UNIVERSITAT DE BARCELONA

Reaction space charting of multicomponent processes: a novel approach in organic and biomedical research

Pau Nadal Rodríguez

Aquesta tesi doctoral està subjecta a la llicència ***Reconeixement 4.0. Espanya de Creative Commons***.

Esta tesis doctoral está sujeta a la licencia ***Reconocimiento 4.0. España de Creative Commons***.

This doctoral thesis is licensed under the ***Creative Commons Attribution 4.0. Spain License***.

UNIVERSITAT DE BARCELONA

FACULTAT DE FARMÀCIA I CIÈNCIES DE L'ALIMENTACIÓ

DEPARTAMENT DE FARMACOLOGIA, TOXICOLOGIA I QUÍMICA TERAPÈUTICA

PROGRAMA DE DOCTORAT DE QUÍMICA ORGÀNICA

REACTION SPACE CHARTING OF MULTICOMPONENT PROCESSES: A NOVEL APPROACH IN ORGANIC AND BIOMEDICAL RESEARCH

PAU NADAL RODRÍGUEZ

BARCELONA, 2024

This thesis was developed in the Laboratory of Medicinal Chemistry, Department of Pharmacology, Toxicology and Therapeutic Chemistry, Faculty of Pharmacy and Food Sciences, University of Barcelona and in the Institute of Advanced Chemistry (IQAC-CISC) from October 2020 to June 2024. This work was supported by the Ministerio de Ciencia e Innovación though (projects PID2019-107991RB-I00, PID2022-139180OB-I00 and predoctoral grant PRE2020-092477).

UNIVERSITAT DE BARCELONA

FACULTAT DE FARMÀCIA I CIÈNCIES DE L'ALIMENTACIÓ

DEPARTAMENT DE FARMACOLOGIA, TOXICOLOGIA I QUÍMICA TERAPÈUTICA

PROGRAMA DE DOCTORAT DE QUÍMICA ORGÀNICA

REACTION SPACE CHARTING OF MULTICOMPONENT PROCESSES: A NOVEL APPROACH IN ORGANIC AND BIOMEDICAL RESEARCH

Memòria presentada per Pau Nadal Rodríguez per optar al títol de doctor per la Universitat de Barcelona

Rodolfo Lavilla Grífols (Director i tutor de tesi)

Ouldouz Ghashghaei (Directora de tesi)

Pau Nadal Rodríguez

Ojo y oreja, que la vista engaña.

Abstract

To discover new scaffolds and to streamline the production of novel chemical entities with biological activity is essential for accelerating drug discovery. In this regard, multicomponent reactions (MCRs) offer efficient access to complex and unconventional connectivities. This thesis applies the reaction space charting strategy to systematically explore and describe MCRs, potentially leading to new scaffolds with biomedical applications. Through this approach, the investigation of the MCR involving carbonyls, amines, and isocyanoacetates revealed new multicomponent processes, yielding unsaturated imidazolones, and novel reactivity of the generated core. These scaffolds show promise in various biomedical applications, such as fluorescent probes. were tested as fluorescent probes and antimicrobial activity. Additionally, the reactivity of indole-2-carboxaldehyde (indole-2-CHO) in MCRs was studied, leading to the discovery of 6-substituted indolo[3,2-*b*]carbazoles (6-ICZs), potent ligands for the Aryl hydrocarbon Receptor (AhR). These synthesised 6-ICZs, obtained in one step, show promising anti-inflammatory activity and offer a tunable platform for AhR drug discovery, addressing key challenges in the field.

Resum

El descobriment de nous esquelets i l'optimització de la producció de noves entitats químiques amb activitat biològica és essencial per accelerar el descobriment de fàrmacs. Les reaccions multicomponent (MCRs) ofereixen un accés eficient a compostos amb connectivitats complexes i no convencionals. Aquesta tesi aplica l'estratègia de cartografiar l'espai de reacció per explorar i descriure sistemàticament les MCRs, amb la possibilitat de conduir a nous esquelets amb aplicacions biomèdiques. D'aquesta manera, l'estudi de la MCR entre carbonils, amines i isocianoacetats va revelar nous processos multicomponent, produint imidazolones insaturades, i nova reactivitat del nucli generat. Aquests esquelets mostren potencial en diverses aplicacions biomèdiques, com sondes fluorescents i activitat antimicrobiana. Addicionalment, es va estudiar la reactivitat de l'indol-2-carboxaldehid (indol-2-CHO) en MCRs, permetent el descobriment de indolo[3,2-*b*]carbazols substituïts a la posició 6 (6-ICZs), lligands potents del receptor d'hidrocarburs aromàtics (AhR). Aquests 6-ICZs, obtinguts en un sol pas, mostren una prometedora activitat antiinflamatòria i ofereixen una plataforma modulable per al descobriment de fàrmacs AhR, abordant problemes importants en el camp.

Table of Contents

Chapter I

Introduction and Objectives

1. ***Introduction and Background***
2. ***Objectives***
3. ***References***

1. Introduction and Background

1.1. New Avenues in Organic Chemistry and Biomedical Research

The quest for new chemical compounds has long been compared to the exploration of the universe due to their seemingly infinite nature. For that reason, chemists termed the collection of all conceivable molecules that have and could ever be synthesised as "chemical space".[1,2] This theoretical, multidimensional entity is defined by the structural attributes and properties of the molecules, allowing to organise them in different clusters of related compounds (Figure 1).[3] Of particular interest is the "drug-like" space, comprising molecules whose structure provide suitable pharmacokinetic – administration, distribution, metabolism, elimination (ADME) – properties, complying with the Lipinsky rules.[4–6] Drug discovery campaigns rely on finding molecules within this space which, albeit being well defined, contains $\approx 10^{60}$ compounds. The magnitude of this value is better appreciated when, following the initial analogy, it is compared to number of atoms in the universe, estimated to be $\approx 10^{80}$. In contrast, the known drug space (KDS) – encompassing described drug-like molecules – is ridiculously small.

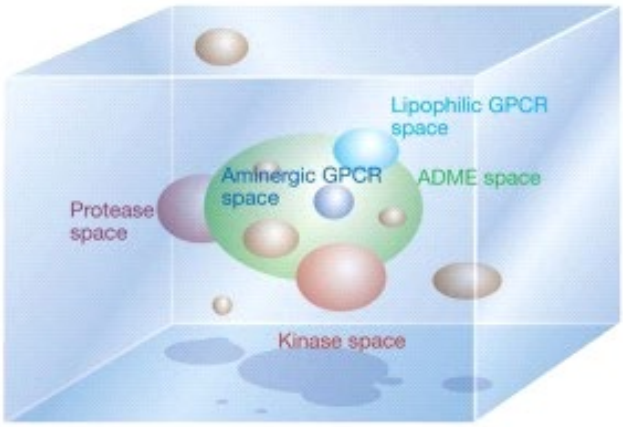

Figure 1. A) Representation of the chemical and "drug-like" spaces, taken from Lipinksi and Hopkins (Ref 5).

To scale the KDS, one could use various figures. For instance, the leading provider of chemical compounds Enamine has curated the REadily AccessibLe (REAL) database, which includes 6.75 billion compounds that can theoretically be synthesised upon request.[7] Other databases such as DrugBank or ChEMBL list between 10 to 20 thousand registered (actually synthesised and characterised) drug-like molecules. Finally, the number of marketed drugs approved by the Food and Drug Administration (FDA) is lower than 2 thousand. These numbers illustrate the hardships of finding new drug candidates,

usually referred to as "looking for a needle in a haystack" by chemists. Therefore, exploring the still dark regions of the drug-like chemical space is pivotal in the discovery of new chemical entities with biological activity.

Synthetic organic chemistry is arguably one of the foundations upon which drug discovery campaigns are built, as typically around ten thousand compounds will need to be prepared for the development of a new drug. At the same time, it is one of the most serious bottlenecks in the entire drug development process.[8–10] The aim is to generate large and diverse collections of compounds, called chemical libraries, which are used in methodologies aimed at identifying bioactive compounds such as high throughput screenings (HTS), quantitative structure-activity relationship studies (QSAR), hit identification and lead optimisation campaigns, etc. Hence, medicinal chemists face the arduous task of designing efficient synthetic routes to biologically active compounds. Historically, medicinal chemistry programs have relied on well-established chemical reactions to generate these chemical libraries. In this regard, the biomedicine oriented organic synthesis is governed by a limited number of transformations such as amide couplings, nucleophilic aromatic substitution, metal catalysed cross-couplings, Boc-protections and deprotections, ester hydrolysis, etc.[11] While offering reliable results, these reactions unavoidably generate scaffolds with similar connectivities, overpopulating known areas of the drug-like chemical space while not efficiently navigating through the unexplored regions.[12] Moreover, the synthetic routes are often lengthy, making the preparation of chemical libraries an inefficient and extremely time- and resource-consuming process.[13,14] This calls for innovative synthetic methodologies that can expedite the discovery of new compounds with optimal structural features for a drug discovery campaign.

Medicinal chemists use the concept of privileged scaffolds to define fundamental skeletal cores that provide a molecule with desirable attributes such as optimal pharmacological properties or propensity to interact with biological targets. Ideally, they should be easy to prepare and amenable to diversification. This concept can be similarly applied to biological probes, tools used to detect, measure, or manipulate biological processes at the molecular, cellular, or organismal level, including fluorescent probes. Of particular interest are aromatic heterocyclic moieties, especially nitrogen heterocycles. They have a proven track record in drug development, as they are present in 60% of FDA-approved drugs (Figure 2A).[15] Heterocycles are highly valued in medicinal chemistry

and drug discovery due to their structural diversity, biological relevance, and suitable physicochemical properties (lipophilicity, solubility, polarity, etc.) leading to favourable pharmacokinetic profiles.[16] Moreover, their structural characteristics offer the possibility of forming valuable interactions with the target receptors, such as hydrogen bonds and π–effects.[17] Finally, their usually conjugated nature provides them with particularly appealing photophysical properties optimal for fluorescent dyes (Figure 2C).[18] Admittedly, the synthetic access to diversly functionalised heterocyclic derivatives is seldom straightforward, illustrating the aforementioned need to investigate new approaches to these privileged structures, as well as studying their intrinsic reactivity.[19]

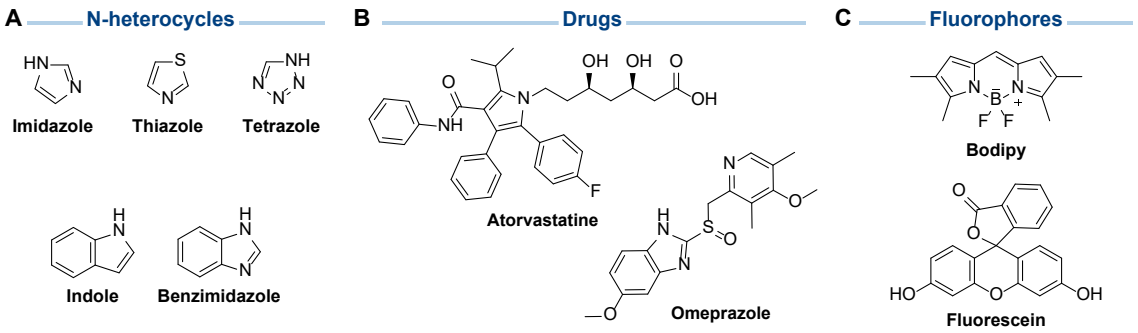

Figure 2. A) Top 5 N-heterocycles found in FDA-approved drugs. B) Examples of marketed drugs containing N-heterocycles. C) The structures of the Bodipy and the Fluorescein, two of the most used dyes, both constituted by a heterocyclic moiety.

Thus, the present thesis is centred on the discovery and development of multicomponent reactions involving heterocycles (either as reactants or products) as a synthetic organic methodology to face the challenges associated to drug discovery. We have focused on two heterocyclic scaffolds with huge projection. Firstly, the conjugated 4-imidazolone core, the key structural feature of the chromophore responsible for the fluorescence of the green fluorescent protein (GFP), which has been a staple in molecular and cellular biology for decades.[20–22] Furthermore, the 4-imidazolone constitutes the core of the natural product coelenterazine (CTZ), a luciferin that causes the bioluminescence of several marine organisms (Figure 3A).[23,24] At the same time, molecules containing the 4-imidazolone core have been reported to have ample biological activity.[25,26] Secondly, the fused polycyclic 5,11-dihydroindolo[3,2-*b*]carbazole (ICZ) scaffold is a ligand of the aryl hydrocarbon receptor (AhR), a transcription factor with promising therapeutic applications in cancer and inflammatory and autoimmune diseases, as illustrated by the endogenous activator 6-formyl ICZ (FICZ). Moreover, ICZ-based compounds have rising relevance in material sciences, such as organic light emitting diodes (OLEDs, Figure 3B).[27,28]

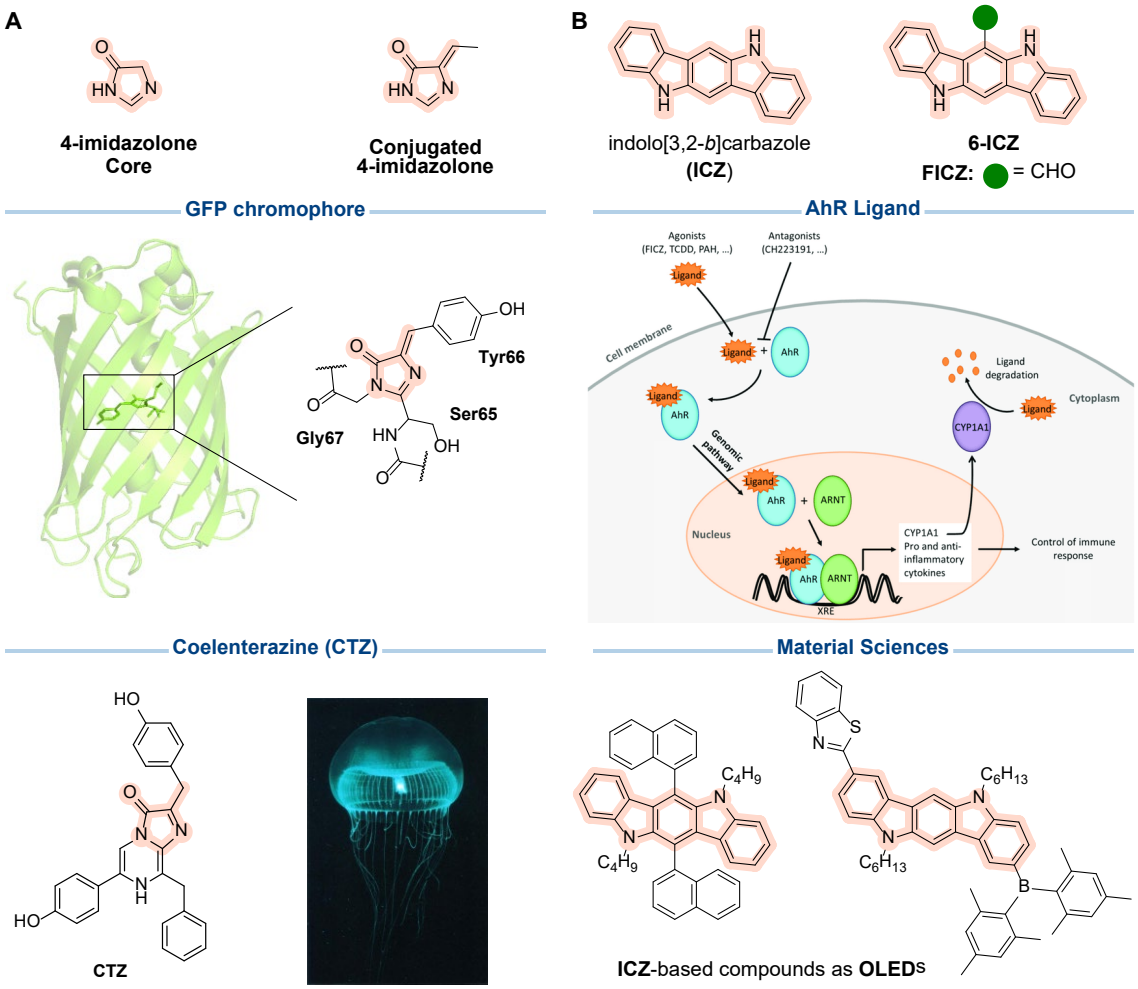

Figure 4. A) Structure of the (conjugated) 4-imidazolone scaffold and occurrence in the natural products: the GFP chromophore and the CTZ. B) Structure of the ICZ scaffold and the endogenous ligand FICZ and applications of ICZ-based compounds in biomedicine and material sciences.

1.2. Discovery and Development of Multicomponent Reactions

Undoubtedly, the ability to streamline the production of new chemical entities is crucial in the discovery of new bioactive molecules, especially outside the boundaries of the KDS. Thus, the generation of novel and meaningful chemical libraries would benefit from enhanced synthetic strategies. In this context, multicomponent reactions (MCRs) are transformations in which three or more starting materials react through a unified mechanism to form an adduct incorporating elements from all reactants.[29] MCRs have become increasingly attractive in medicinal chemistry, especially in the context of drug discovery,[30] due to the ample advantages they offer over classical bimolecular transformations.[31] From an experimental standpoint, MCRs are extremely simple frameworks. All reactants are added simultaneously in the reaction vessel, therefore requiring only one reaction set-up, one work-up, and one product isolation. This results in extremely step-, and time-economic protocols, streamlining the production of

compounds. Furthermore, MCRs provide high bond-forming efficiency (BFE) and atom economy, meaning they allow to generate considerable structural complexity from simple starting materials, decreasing the need for protecting groups. This leads to improved overall yields and reduced waste, which in turn aligns with the principles of Green Chemistry.[32] Additionally, MCRs are modular reactions, facilitating the customisation of the final adducts by simply substituting the building blocks, expediting the generation of chemical libraries (Figure 4A). Finally, MCRs excel at both exploiting the intrinsic reactivity of heterocycles as the reaction inputs,[33] and at generating heterocyclic adducts (Figure 4B).[34]

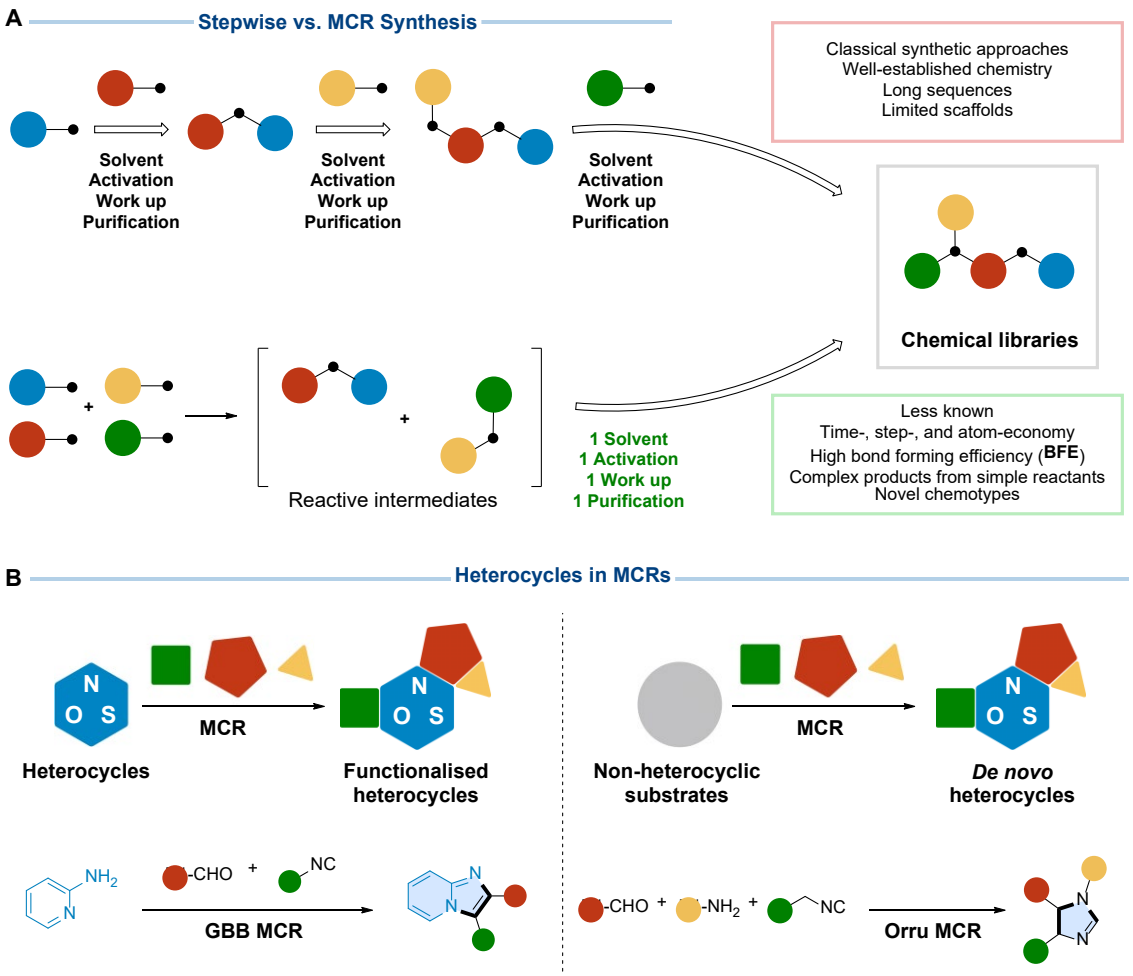

Figure 4. A) Comparison between stepwise strategies and MCRs for the generation of chemical libraries. B) The role of heterocycles in MCRs, both as substrates and products.

Incidentally, MCRs are generally regarded as intermolecular domino reactions. These are processes that involve at least two sequential and spontaneous bond-forming events within the same transformation, without need to isolate intermediates or change the reaction conditions.[35] However, they are often restricted to intramolecular processes, and the preparation of the complex suitable substrates usually requires multi-step

syntheses. In this regard, integration of MCRs and domino reactions lead to the concept of extended MCRs.[36] In these transformations, the substrate suited for a domino process is generated *in-situ* by the MCR from simple, off-the-shelf reactants (Figure 5).

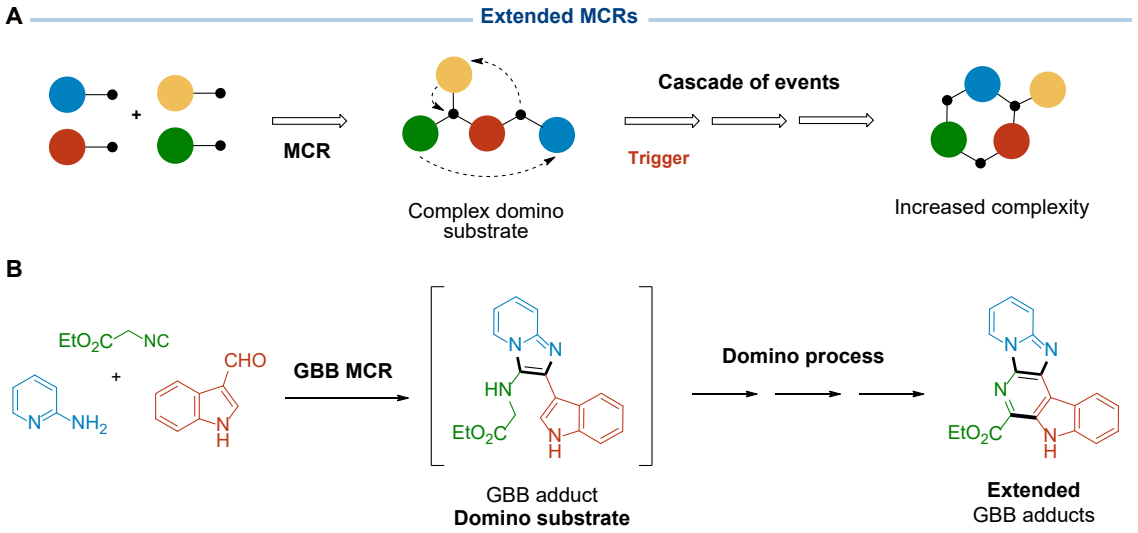

Figure 5. A) The concept of extended MCRs. B) An example of an extended GBB MCR, from Ghashghaei *et al.* (Ref 36).

Yet, the number of known MCRs is extremely low in comparison to bimolecular reactions. Furthermore, since the discovery of the first MCR by Strecker in the 1850s, only a handful of name MCRs have found wide applications in drug discovery, such as the Ugi, Passerini, GBB, Biginelli, Povarov, Orru or Hantzsch (Figure 6A).[37] The under-representation of MCRs in applied organic chemistry is mostly due to the difficulty of discovering new multicomponent processes, an achievement which has been frequently associated to serendipity. Still, remarkable efforts have been made towards the rational design of new MCRs.[38] Nevertheless, the canonical mode of MCR development has always been to promote selective processes. Chemists work towards favouring the formation of a preferred adduct over other minor by-products by carefully controlling reaction conditions and leveraging kinetic or thermodynamic preferences within the reaction, thereby enhancing yield and efficiency. While this prototypic approach has been the basis of impressive developments, one could argue that it suppresses a number of alternative reaction pathways leading to potentially interesting products (Figure 6B).

Thus, the present thesis has explored a novel approach for the study of either known or new multicomponent processes. Rather than optimising the formation of a specific adduct, we propose a thorough description of an MCR through a systematic analysis of the role of various parameters (reactants, reaction conditions, catalysts,

solvents, etc.). In this way, we aim at maximising the potential of these important transformations by trying to develop new connectivity patterns, under expressed in the usual conditions.

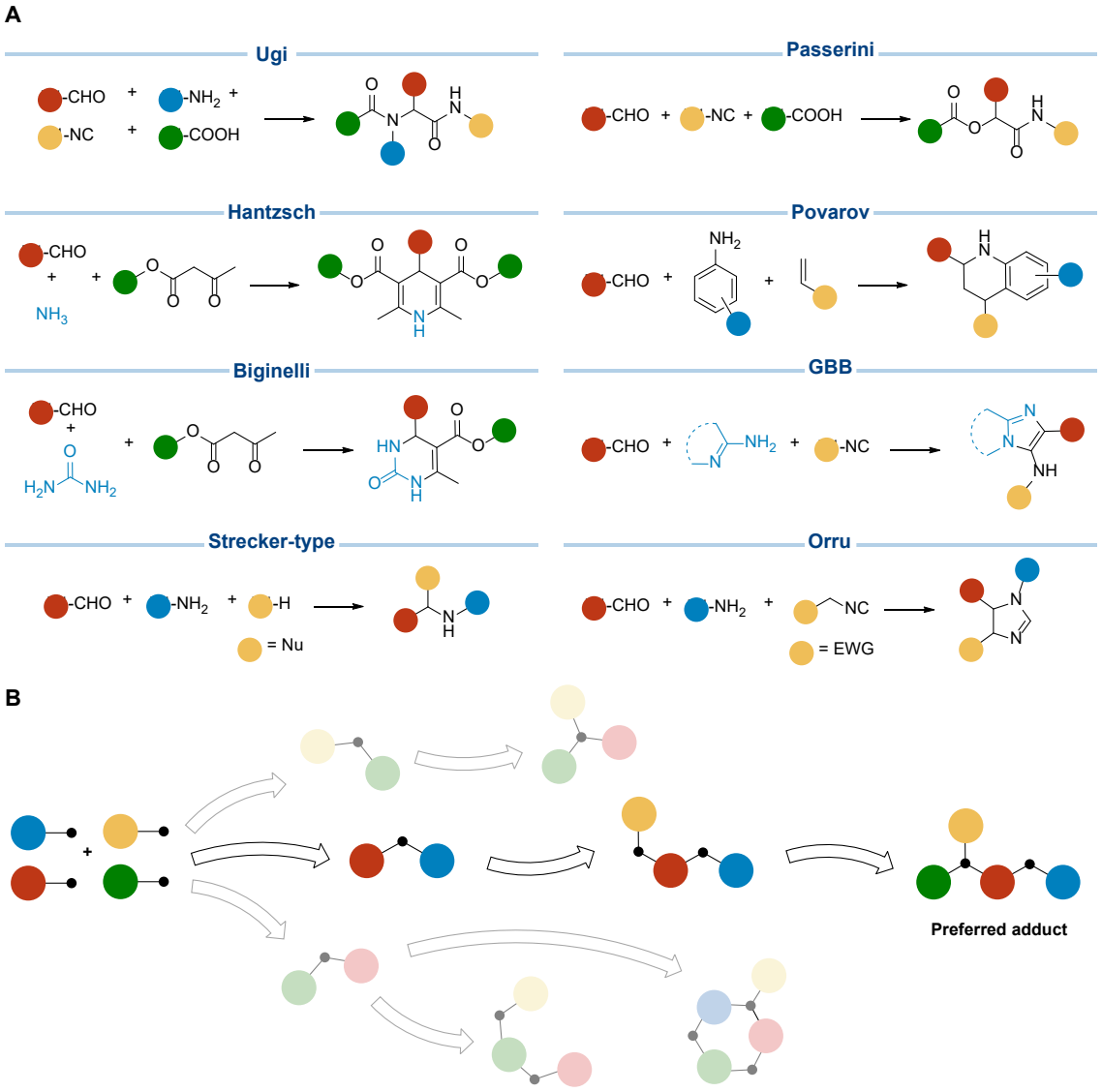

Figure 6. A) Name MCRs with applications in drug discovery and biomedicine. B) Traditional mode of MCR development.

In particular, we have focused on two building blocks which could greatly benefit from this strategy. One the one hand, isocyanides, whose unique electronic structure makes them extremely valuable in the isocyanide-based MCRs (IMCRs), which constitute an important class in the field.[39] The formally divalent isocyanide, featuring both a lone electron pair and a vacant orbital in the carbon atom, can react as a nucleophile and/or electrophile, making it a particularly appealing moiety for the present task (Figure 7A). Even more, the isocyanoacetate subset offers two extra reactivity points in the acidic α carbon and the ester moiety.[40] A paramount example of these reactions is Orru's

synthesis of 2-imidazolines (Figure 7A).[41] On the other hand, the indole-2-carboxaldehyde offers an analogous dual reactivity, an invaluable trait for domino processes and extended MCRs. First, they react as electrophiles due to the intrinsic reactivity of the carbonyl moiety, and then the aromatic ring becomes a nucleophilic partner (Figure 7C). Moreover, indoles represent privileged structures in biomedicine and medicinal chemistry (Figure 7D).[42]

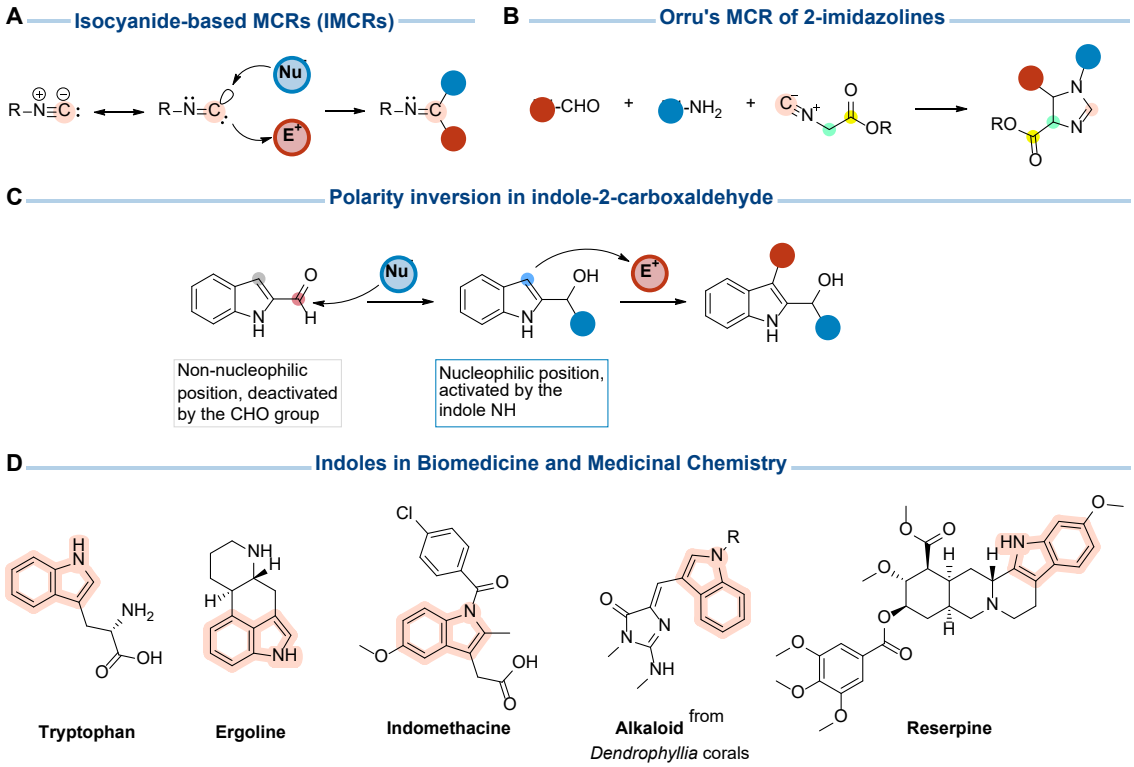

Figure 7. A) The resonant structures of the isocyanide functional group and their dual reactivity towards nucleophiles and electrophiles. B) Orru's multicomponent synthesis of 2-imidazolines from isocyanoacetates. C) The polarity inversion of indole-2-carboxaledehyde after nucleophilic attack. D) Relevant molecules in biomedicine and medicinal chemistry containing an indole heterocycle.

1.3. Reaction Space Charting as a Tool in Reaction Discovery

Charting can be defined as mapping out an unknown or unexplored region. In the context of organic chemistry, reaction space charting refers to the thorough and systematic exploration and description of a chemical transformation to understand all the involved processes.[43] The knowledge gained through this approach can be exploited to expand the reach of the studied system and develop new applications (Figure 8).[44] Additionally, the reaction space charting concept agrees with the systems chemistry, aiming at understanding how the collective interactions between individual components within a chemical network may lead to the emergence of seemingly unpredictable new properties and behaviours.[45]

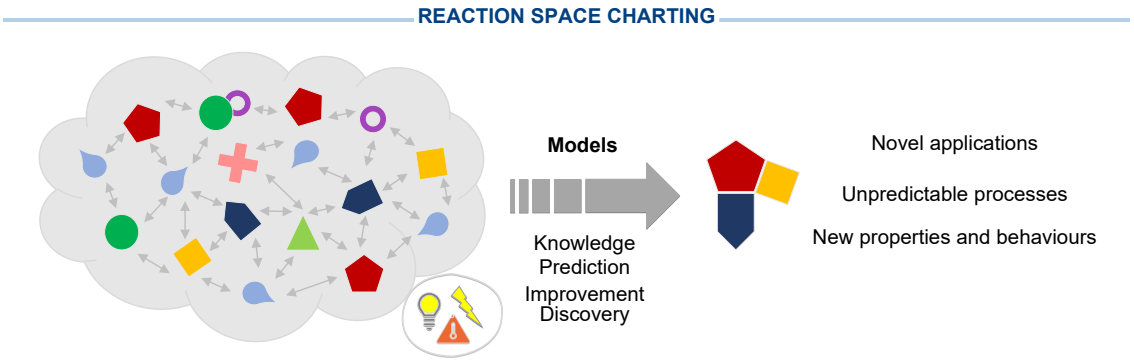

Figure 8. The concept of reaction space charting, adapted from Lozano-Baró *et al*. (Ref 44).

Of particular interest is the power of reaction space charting in the discovery of new chemical reactions.[46] Valuable information may be drawn out of meaningful experimentation such as mechanistic guidelines, optimised reaction conditions, identification of additives to enhance productivity, scope limitations, and even unveiling hidden and unpredictable reaction pathways, potentially leading to novel chemotypes from a single reactant combination. In this context, MCRs can become the ideal playground for the implementation of the reaction space charting strategy due to the innate complexity of the systems involved. Also, it would incorporate MCRs even more into the diversity-oriented synthesis (DOS) strategic approach, which aims at maximising chemical diversity to efficiently explore the chemical space (Figure 9).[47]

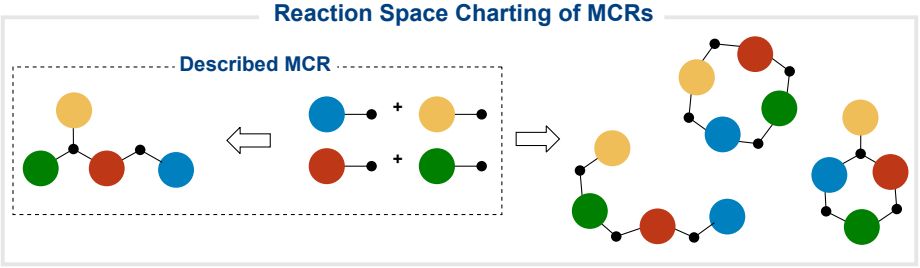

Figure 9. The reaction space charting approach in MCRs.

The present thesis postulates the reaction space charting of multicomponent processes as a novel approach in both organic chemistry and biomedical research. The hypothesis is founded in the potential of the strategy to discover new processes, establish their scope and efficiently generate diverse chemical libraries of biologically relevant molecules, expanding the chemical space to otherwise unavailable regions.

To further expand the knowledge on the two main topics of the thesis, MCRs and reaction space charting, three review articles were written within the frame of the present thesis. As for the MCRs, we generated a comprehensive overview of the group's work in the past 20 years. Firstly, we focused on the development of MCRs involving

heterocycles, exploring the underlying reactivity and its synthetic reach. Secondly, we described the biomedical applications that resulted from the development of said MCRs. Regarding the reaction space charting, we intended to introduce the topic, showcase relevant examples in various fields of organic chemistry, analyse the results and give a broad assessment of the future direction of the methodology. The three review articles are found in the Annex I of the thesis in their respective publication formats.

2. Objectives

The present thesis is focused on the reaction space charting of MCRs as a novel synthetic strategy for organic chemistry and biomedical research. The general objectives are listed below.

- To utilise MCRs to efficiently navigate unexplored regions of the drug-like chemical space.
- To discover and develop new multicomponent processes involving heterocycles and to expand the reach of known MCRs through the reaction space charting approach.
- To leverage the modular nature of MCRs to efficiently generate diverse chemical libraries.
- To generate privileged scaffolds, focusing on the 4-imidazolone and the ICZ cores, and to investigate their biological relevance and intrinsic reactivity.
- To apply the developed chemistry in the context of biomedical research and drug development, by investigating the physicochemical properties and potential biological activities of the synthesised compounds.

The detailed objectives of each chapter are described below.

Chapter II.

The main goal of this chapter was to provide a proof of concept of the hypothesis governing the present thesis: reaction space charting of a multicomponent interaction to better describe the process and discover new connectivities. As a model, the interaction among carbonyls, amines, and isocyanoacetates was chosen. This combination provided an optimal framework for the intended purposes, as the reported literature suggested one well-established reactivity pattern (Orru's 2-imidazolines) albeit with potential

alternative reaction pathways. Thus, we proposed to systematically describe the MCR by screening a broad range of reaction conditions, reactants, catalysts, solvents, etc., as well as to interpret and justify the outcomes through a unified mechanism. Finally, we aimed at finding a potential biomedical application to the generated compounds.

Chapter III.

This chapter aimed at exploring the feasibility of indole 2-CHO as a dual partner in MCRs, exploiting its intrinsic dual reactivity. In particular, we plan to incorporate this reactant in the Yonemitsu MCR and chart the reaction space of its interaction with various nucleophiles. Based in previous work form the group,[36] we expect to generate 6-ICZs through an ABB' process. These adducts have close structural analogy known ligands of the AhR. Thus, we intend to define the MCR and establish the optimal conditions and the scope of the process. Moreover, we plan to prepare a relevant chemical library of 6-ICZ derivatives, analyse their structural features and forward them for biological determinations.

3. References

[1] J.-L. Reymond, *Acc. Chem. Res.* **2015**, *48*, 722–730.

[2] C. M. Dobson, *Nature* **2004**, *432*, 824–828.

[3] J.-L. Reymond, M. Awale, *ACS Chem. Neurosci.* **2012**, 3, 649–657.

[4] C. A. Lipinski, F. Lombardo, B. W. Dominy, P. J. Feeney, *Adv. Drug. Deliv. Rev.* **1997**, *23*, 3–25.

[5] C. Lipinski, A. Hopkins, *Nature* **2004**, *432*, 855–861.

[6] J.-L. Reymond, R. van Deursen, L. C. Blum, L. Ruddigkeit, *Medchemcomm* **2010**, 1, 30–38.

[7] O. O. Grygorenko, D. S. Radchenko, I. Dziuba, A. Chuprina, K. E. Gubina, Y. S. Moroz, *iScience* **2020**, *23*, 101681.

[8] D. C. Blakemore, L. Castro, I. Churcher, D. C. Rees, A. W. Thomas, D. M. Wilson, A. Wood, *Nat. Chem.* **2018**, *10*, 383–394.

[9] O. O. Grygorenko, D. M. Volochnyuk, S. V. Ryabukhin, D. B. Judd, *Chem. Eur. J.* **2020**, *26*, 1196–1237.

[10] G. Wess, M. Urmann, B. Sickenberger, *Angew. Chem. Int. Ed.* **2001**, *40*, 3341–3350.

[11] D. G. Brown, J. Boström, *J. Med. Chem*. **2016**, 59, 4443–4458.

[12] H. Zhao, I. Akritopoulou-Zanze, *Expert Opin. Drug Discov.* **2010**, *5*, 123–134.

[13] T. Newhouse, P. S. Baran, R. W. Hoffmann, *Chem. Soc. Rev.* **2009**, *38*, 3010–3021.

[14] Y. Hayashi, *J. Org. Chem*. **2021**, *86*, 1–23.

[15] E. Vitaku, D. T. Smith, J. T. Njardarson, *J. Med. Chem*. **2014**, *57*, 10257–10274.

[16] A. Gomtsyan, *Chem. Heterocycl. Compd.* **2012**, *48*, 7–10.

[17] R. D. Taylor, M. MacCoss, A. D. G. Lawson, *J. Med. Chem*. **2014**, *57*, 5845–5859.

[18] F. de Moliner, N. Kielland, R. Lavilla, M. Vendrell, *Angew. Chem. Int. Ed.* **2017**, *56*, 3758–3769.

[19] A. P. Taylor, R. P. Robinson, Y. M. Fobian, D. C. Blakemore, L. H. Jones, O. Fadeyi, *Org. Biomol. Chem.* **2016**, *14*, 6611–6637.

[20] R. Y. Tsien, *Annu. Rev. Biochem.* **1998**, *67*, 509–544.

[21] M. Zimmer, *Chem. Rev*. **2002**, *102*, 759–782.

[22] J. Zhang, R. E. Campbell, A. Y. Ting, R. Y. Tsien, *Nat. Rev. Mol. Cell. Biol.* **2002**, *3*, 906–918.

[23] A. Schenkmayerova, M. Toul, D. Pluskal, R. Baatallah, G. Gagnot, G. P. Pinto, V. T. Santana, M. Stuchla, P. Neugebauer, P. Chaiyen, J. Damborsky, D. Bednar, Y. L. Janin, Z. Prokop, M. Marek, *Nat. Catal.* **2023**, *6*, 23–38.

[24] E. P. Coutant, Y. L. Janin, *Chem. Eur. J*. **2015**, *21*, 17158–17171.

[25] M. Debdab, F. Carreaux, S. Renault, M. Soundararajan, O. Fedorov, P. Filippakopoulos, O. Lozach, L. Babault, T. Tahtouh, B. Baratte, Y. Ogawa, M. Hagiwara, A. Eisenreich, U. Rauch, S. Knapp, L. Meijer, J.-P. Bazureau, *J. Med. Chem.* **2011**, *54*, 4172–4186.

[26] A. Kaczor, K. Witek, S. Podlewska, J. Czekajewska, A. Lubelska, E. Żesławska, W. Nitek, G. Latacz, S. Alibert, J.-M. Pagès, E. Karczewska, K. Kieć-Kononowicz, J. Handzlik, *Molecules* **2019**, *24*, 438.

[27] T. Janosik, A. Rannug, U. Rannug, N. Wahlström, J. Slätt, J. Bergman, *Chem. Rev.* **2018**, *118*, 9058–9128.

[28] L. P. Nguyen, C. A. Bradfield, *Chem. Res. Toxicol*. **2008**, *21*, 102–116.

[29] J. Zhu, H. Bienaymé, Eds. *Multicomponent Reactions*, Wiley-VCH, Weinhiem, **2005**.

[30] P. Nadal Rodríguez, O. Ghashghaei, A. Bagán, C. Escolano, R. Lavilla, *Biomedicines* **2022**, *10*, 1488.

[31] P. Slobbe, E. Ruijter, R. V. A. Orru, *Medchemcomm* **2012**, *3*, 1189.

[32] F. A. Etzkorn, Ed. *Green Chemistry: Principles and Case Studies*, RSC Publishing, London, **2019**.

[33] O. Ghashghaei, P. Nadal Rodríguez, R. Lavilla, *Synlett* **2022**, *33*, 822–835.

[34] E. van der Eycken, U. K. Sharma, Eds. *Multicomponent Reactions towards Heterocycles: Concepts and Applications*, Wiley-VCH, Weinheim, **2022**.

[35] L. F. Tietze, G. Brasche, K. Gericke, *Domino Reactions in Organic Synthesis*, Wiley-VCH, Weinheim, **2006**.

[36] O. Ghashghaei, M. Pedrola, F. Seghetti, V. V. Martin, R. Zavarce, M. Babiak, J. Novacek, F. Hartung, K. M. Rolfes, T. Haarmann-Stemmann, R. Lavilla, *Angew. Chem. Int. Ed.* **2021**, *60*, 2603–2608.

[37] A. Dömling, W. Wang, K. Wang, *Chem. Rev*. **2012**, *112*, 3083–3135.

[38] E. Ruijter, R. Scheffelaar, R. V. A. Orru, *Angew. Chem. Int. Ed.* **2011**, *50*, 6234–6246.

[39] A. Dömling, I. Ugi, *Angew. Chem. Int. Ed.* **2000**, *39*, 3168–3210.

[40] N. Elders, E. Ruitjer, V. G. Nenajdenko, R. V. A. Orru, in *Isocyanide Chemistry: Applications in Synthesis and Material Science* (Ed.: V.G. Nenajdenko), Wiley-VCH, Weinheim, **2012**, pp. 75–108.

[41] R. S. Bon, C. Hong, M. J. Bouma, R. F. Schmitz, F. J. J. de Kanter, M. Lutz, A. L. Spek, R. V. A. Orru, *Org. Lett.* **2003**, *5*, 3759–3762.

[42] D. A. Horton, G. T. Bourne, M. L. Smythe, *Chem. Rev*. **2003**, *103*, 893–930.

[43] P. M. Murray, S. N. G. Tyler, J. D. Moseley, *Org. Process Res. Dev.* **2013**, *17*, 40–46.

[44] E. Lozano-Baró, P. Nadal Rodríguez, J. Juárez-Jiménez, O. Ghashghaei, R. Lavilla, *Adv. Synth. Catal.* **2024**, *366*, 551–573.

[45] G. Ashkenasy, T. M. Hermans, S. Otto, A. F. Taylor, *Chem. Soc. Rev.* **2017**, *46*, 2543–2554.

[46] K. D. Collins, T. Gensch, F. Glorius, *Nat. Chem.* **2014**, *6*, 859–871.

[47] M. D. Burke, S. L. Schreiber, *Angew. Chem. Int. Ed.* **2004**, *43*, 46–58.

Chapter II

Reaction Space Charting of an MCR

1. Charting the Reaction Space Around a Multicomponent Combination

Text and figures adapted from the following publication, derived from the present thesis:

P. Nadal Rodríguez, O. Ghashghaei, A.M. Shoepf, S. Benson, M. Vendrell, R. Lavilla, Charting the Chemical Reaction Space around a Multicomponent Combination: Controlled Access to a Diverse Set of Biologically Relevant Scaffolds, *Angew. Chem. Int. Ed.*, **2023**, *135*, e202303889.

1.1. Introduction

In the effort to colonise meaningful regions of the chemical space,[1] access to new scaffolds is a priority.[2] In this regard, multicomponent reactions (MCRs)[3] offer undeniable advantages to combinatorially attain unconventional molecular connectivities, with high bond formation indexes, and exceptional atom, step, and time economies.[4] These intermolecular domino processes[5] comprise 3 or more reactants that form an adduct in a single operation through a unified reaction mechanism. Due to the complexity of an MCR (substrates, solvents, catalysts, conditions, reactive intermediates), the discovery of new processes is challenging, and frequently associated to serendipity. Efforts in recent years have focused on the rational design of new MCRs, including the single reactant replacement approach.[6] However, the prevailing paradigm in MCR research has been to optimise the formation of a specific adduct and suppress potentially interesting by-products.

To drive MCRs into a Diversity Oriented Synthesis context[7] we propose a thorough charting of the reaction space (defined as the network of feasible interactions connecting all species in a given system).[8] Arguably, this would unravel alternative bond formation patterns, expanding the synthetic reach of MCRs (Figure 1).

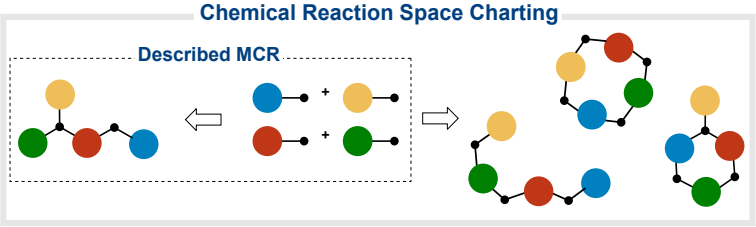

Figure 1. Charting the chemical reaction space of an MCR to generate alternative scaffolds.

In our opinion, the kinetic selection of some pathways over the rest may support this hypothesis. This is in line with relevant findings validating the charting approach in

other areas.[9,10] Initial experiments where an Ugi MCR was switched to a Passerini MCR by using bulky amines seemed to follow this trend [see Experimental Section (ES), Table S1]. Consequently, we propose a systematic screening of the reaction parameters and reactants involved in a given MCR, to rewire known routes and develop new transformations.[11]

As a model combination, we chose carbonyls (aldehydes and ketones), amines, and α-acidic isocyanides.[12] This MCR was previously reported to yield 2-imidazolines through the α-nucleophilic attack on the imine followed by isocyanide insertion. The procedure was developed by Orru et al. and has found wide acceptance in organic chemistry (Scheme 1A).[13] In a related work, Zhu and co-workers described the reaction between amines and α-substituted isocyanoacetates to access 4-imidazolones (Scheme 1B).[14] Moreover, Bischoff et al. recently reported the synthesis of 4-imidazolones through a multistep approach (Scheme 1C).[15] In the present thesis, we describe an extensive exploration of the reaction space around the aforementioned interaction to selectively yield several synthetic outputs in a controlled manner (Scheme 1D).

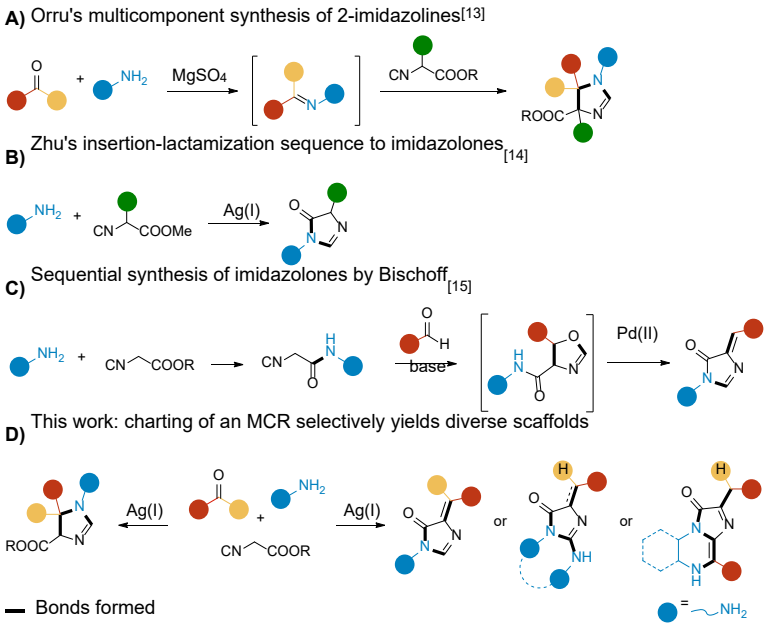

Scheme 1. A) MCR to yield 2-imidazolines by Orru. B) 4-Imidazolone synthesis by Zhu. C) Sequential synthesis of 4-imidazolones by Bischoff. D) This work: charting of the chemical space around the interaction of carbonyls, amines, and isocyanoacetates.

1.2. Charting of a Multicomponent Interaction

The initial experiments with 4-chlorobenzaldehyde, benzylamine, and methyl isocyanoacetate in MeOH without additives gave the expected 2-imidazoline **4a**.

However, we also detected the unsaturated imidazolone **5a** (Figure 2A-B). Incidentally, compound **5a** features a scaffold analogous to the chromophore of the Green Fluorescent Protein (GFP), one of the most used fluorescent tools in biochemistry and cell biology.[16] These findings indicated that this interaction could be more divergent than previously reported, and could also provide a novel MCR-based access to GFP fluorophore derivatives.[15,17] Thus, we launched an extensive charting of the chemical reaction space around this combination (Figure 2B and Table S2-S3).

Sequential protocols, where the imine was pre-formed, only generated the 2-imidazoline **4a**.[13] In contrast, the process could be tuned to afford imidazolone **5a** when subjected to a multicomponent procedure. In this context, some additives had a clear impact on the reaction outcome. Catalyst-free protocols and activation by various metal salts such as Mg(II), Pd(II), and Rh(II) gave a mixture of adducts **4a** and **5a**, illustrating the competitive nature of the interaction. Satisfyingly, the process was selectively driven towards the formation of imidazolone **5a** when the reaction was catalysed by Ag(I) or Cu(II) salts, $AgNO_3$ being the most productive. As for the solvents, MeOH gave the highest conversions to adduct **5a**. The use of other alcohols (EtOH and *i*PrOH) selectively generated compound **5a** as well. However, their fluorinated counterparts, trifluoroethanol (TFE) and hexafluoroisopropanol (HFIP), remarkably reversed the outcome of the MCR to the formation of the 2-imidazoline **4a** in the presence of $AgNO_3$, demonstrating the synthetic potential of a simple modification (Figure 2B and Table S2). Additionally, the outcome was analogous at room temperature (rt) or under microwave (μW) irradiation. These results were reproduced with acetone as the carbonyl component. Although $AgNO_3$ catalysis gave a mixture of both structural types **4aa** and **5aa**, the former could be selectively generated either by pre-formation of the imine or using HFIP as the solvent (Figure 2B and Table S3). Accordingly, we defined the standard conditions to access the imidazolones **5** as a multicomponent protocol in MeOH under $AgNO_3$ catalysis. Notably, the developed procedure conveniently afforded pure analogues after simple filtration, even at gram scale in several cases (see below).

Next, we screened the scope of reactants testing a diverse combination of carbonyls **1a-af** and amines **2a-x** under our defined standard conditions (Figure 2C and ES). The reaction was consistently directed towards the formation of adducts **5** with aromatic aldehydes. A variety of substituted benzaldehydes gave the desired adducts **5a-h** in moderate yields (42-50%). Highly electron-rich aldehydes such as piperonal,

4-(dimethylamino)benzaldehyde, or thiophene-2-carboxaldehyde afforded the respective adducts **5i-m** in higher yields (*ca*. 80%). While 4-hydroxybenzaldehyde and indole-3-carboxaldehyde did not react in the MCR (Table S4), their protected analogues gave adducts **5n-p** in decent yields (43-56%). Subsequent deprotection conveniently afforded compounds **5n'** and **5o'**. Note that Boc removal from compound **5o** gave derivative **5o'** as a mixture of diastereomers (Figure S2). These adducts **5n'-o'** are of particular importance, as they represent close analogues of the wild type chromophores of the green and cyan fluorescent protein, respectively. Contrarily, the electron-deficient 4-formylpyridine reacted poorly in the MCR, but still exclusively yielded adduct **5q** (28%). The corresponding imidazolones were also obtained from indole-2-carboxaldehyde (**5r**, 47%) and *trans*-4-chlorocinnamaldehyde (**5s**, 25%). Formaldehyde and glucose did not participate in the MCR, and simple aliphatic aldehydes gave complex reaction mixtures (Table S4). Notably, the MCR was stereoselective and only the *Z*-diastereomer was generated (Figure 2C). The stereochemistry of the double bond was unequivocally determined by X-ray crystallography of compound **5h** (Table S9).[18] While representative aromatic ketones did not react in the MCR (Table S4), the aliphatic ones always produced mixtures of scaffolds **4** and **5** under the standard conditions. In this way, 2-imidazolines **4aa-ac** (27-51%) and imidazolones **5aa-ac** (12-58%) were generated from acetone, cyclopentanone, and 2-adamantanone. Lastly, the incorporation of isatin resulted in barely productive and complex reaction mixtures (Figures S4-6). In general, the new MCR efficiently leads to the imidazolone scaffold with high appendage diversity in practical yields, which may be further optimised in particular reactant combinations.

The amino input also had a relevant impact on the outcome of the MCR. Imidazolone adducts **5a-v** were obtained from various alkyl amines, including an array of benzylamines, a homoallyl derivative, and tryptamine (25-85%, Figure 2C). Remarkably, the use of deuterated benzylamine **2a-*d*$_2$** conveniently led to the C-2 D labeled imidazolone **5a-*d*** (47%). Moreover, an NH_3 solution in MeOH provided the corresponding *NH* imidazolone **5w** (30%). L-Phenylalanine and its methyl ester did not afford the corresponding imidazolones **5** under standard conditions (Table S4). However, N^{α}-Fmoc-L-lysine allyl ester yielded adduct **5x** (47%) in gram scale, efficiently linking the imidazolone scaffold to an amino acid. The Pd-catalysed deprotection of the allyl residue afforded the GFP chromophore derivative-lysine conjugate **5x'** (55%). Finally, 4-methoxyaniline yielded the corresponding adduct **5y** albeit in a lower yield (12%),

likely due to the decreased insertion rate of the isocyanides into the aniline N-H bond (see the mechanistic implications below).[14] Interestingly, a bulkier input such as *tert*-butylamine directed the process towards the generation of oxazolines **6**. In this way, compounds **6a-b** were obtained from 4-formylpyridine and acetone, respectively, in good yields (55-90%). Even then, traces of the corresponding imidazolones **5** were detected and eventually isolated (**5z**, 2%, Table S5).

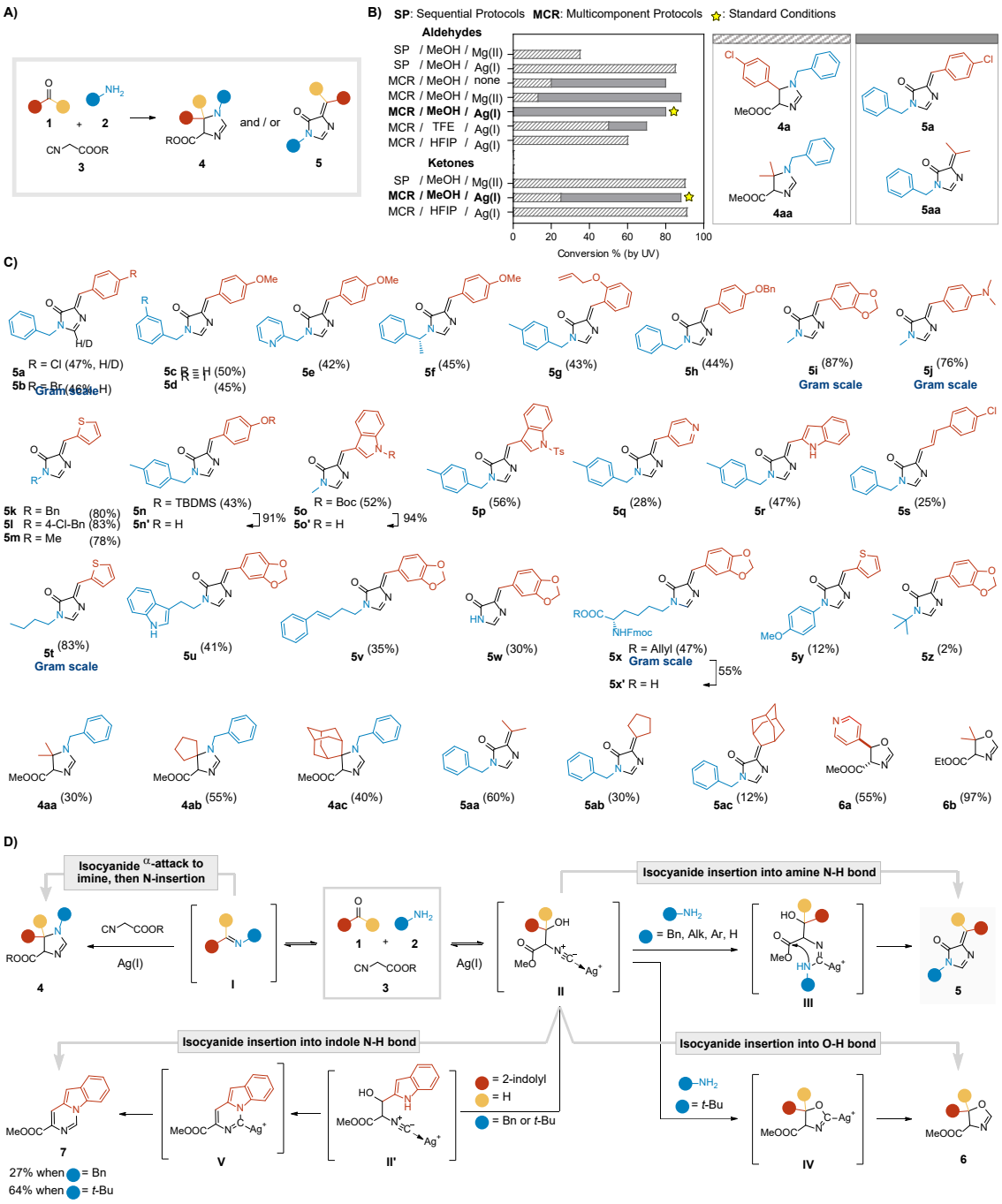

Figure 2. A) Possible outcomes of the MCR between carbonyls, amines, and isocyanoacetates. B) Role of additives and solvents in the process and selected standard conditions. C) Scope of the MCR under the standard conditions [MCR; $AgNO_3$ (10 mol%); MeOH (0.2 M); rt for 17 h or 40 ºC (μW) for 20 min]. D) Proposed reaction pathways and putative mechanisms.

All these results suggest a complex interaction map of divergent reaction pathways (Figure 2D). Small variations in certain parameters may sufficiently alter the competing reaction rates to generate the observed structural diversity. It seems feasible that depending on the reaction medium, imine **I** and the Knoevenagel intermediate **II** may be reversibly generated or kinetically favored. Under suitable conditions, the formation and trapping of the imine **I** leads to the preferential generation of imidazolines **4**.[13] Contrarily, we propose that isocyanide insertion into the N-H bond of the amine may lead to intermediate **III**, which in turn dehydrates and gives adducts **5** after a final lactamisation. However, when N-H insertion is compromised due to the steric hindrance of bulky amines (e.g. *tert*-butylamine), the reaction pathway is directed towards isocyanide insertion into the generated O-H bond to yield oxazolines **6** (Figure 2D).[19] The input of indole-2-carboxaldehyde represented an interesting exception to support this mechanistic hypothesis. In this case, the MCR with benzylamine afforded a mixture of imidazolone **5r** (47%) and indolocarbazole **7** (27%).[20] This outcome is consistent with the intermediacy of putative adduct **II'** and the subsequent insertion of the isocyanide into the indole N-H bond. Additionally, the use of *tert*-butylamine, which inhibits the GFP pathway, resulted in an improved conversion to indolocarbazole **7** (60%, Figures 2D and S7).

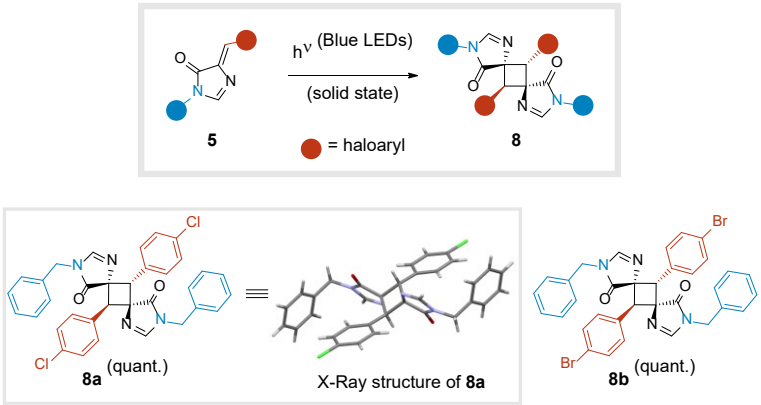

Figure 3. Photocatalysed dimerisation of compounds **5** to give cyclobutanes **8**.

Remarkably, we observed that adducts **5** containing a halogen-substituted aryl group participated in a [2+2] photocycloaddition to generate cyclobutanes **8** in a stereoselective manner. The structural assignment of the centrosymmetric derivative **8a** was confirmed by single crystal X-ray diffraction (Figure 3 and Table S10).[18] Although the reaction takes place spontaneously upon prolonged exposure to sunlight, a blue LED light source served to achieve full dimerisation of **5a-b** in the solid state. Compounds

8a-b were obtained through this simple post-transformation in quantitative yields, expanding the number of scaffolds generated from the initial MCR (Figure 3). Notably, this transformation has not been described for imidazolones **5**.[21]

1.3. Multicomponent Access to Coelenterazine Analogues

The participation of bifunctional inputs in MCRs ponders the question of selectivity, usually generating mono- or bis- adducts.[22] However, the use of ethylenediamine **2m** in our MCR resulted in an extended multicomponent process[23] to give adducts **9**. This process incorporates two aldehyde units in an ABB'C fashion, featuring an impressive bond formation index (Figure 4A). Compounds **9** are analogues of the luciferin coelenterazine, responsible for the bioluminescence in several aquatic organisms (Figure 4A).[24] Remarkably, this scaffold was generated in one step, in a strikingly distinct approach from the biomimetic and reported synthetic procedures.[24b,25]

After adjusting the stoichiometry, we prepared compounds **9a-d** in moderate yields (*ca.* 30%) from a variety of benzaldehydes **1**, ethylenediamine **2m** or (±)-*trans*-1,2-diaminocyclohexane ***trans*-2n**, and methyl isocyanoacetate **3a**, under the standard conditions (Figure 4B). Unexpectedly, with piperonal **1j** and 3,4,5-trimethoxy benzaldehyde **1z**, the desired coelenterazine analogues **9e-f** were only generated under the suboptimal stoichiometry 1:1:1 and consequently isolated in lower yields (*ca.* 13%, Figure 4B). Instead, when applying the optimal ratio of 2:1:1, adducts **9e-imine** (51%) and **9f'** (30%) precipitated from the reaction mixture, respectively (Figure 4C). To justify the observed trends, we propose the following unified mechanism. Likely, the process starts with the silver-mediated formation of the imidazolone precursor **5ad**, whose immediate condensation with a second unit of aldehyde unit gives the intermediate **9-imine**. The activated imine presumably yields the bicyclic intermediate **9'**, which in turn may evolve towards species **9** under acidic catalysis (Figure 4D). The putative mechanism features the intriguing transformation of intermediate **9-imine** to tautomer **9'**. Although arguable, our hypothesis contemplates an unprecedented intramolecular attack of a nucleophilic imidazolone upon an electrophilic activated imine (Figure S12). The potentially nucleophilic nature of imidazolones may be supported by a reported Pd-catalysed C-H activation mechanism at the C-2 position,[26] which served to synthesise compound **10** in 43% yield (Figure 4E, for further mechanistic reflections see ES). As for the isomerisation of **9'** to **9**, preliminary computational studies suggested a variety of

tautomeric structures with comparable stabilities, likely favoring the natural connectivity of adducts **9** (Figures 4D and S14).

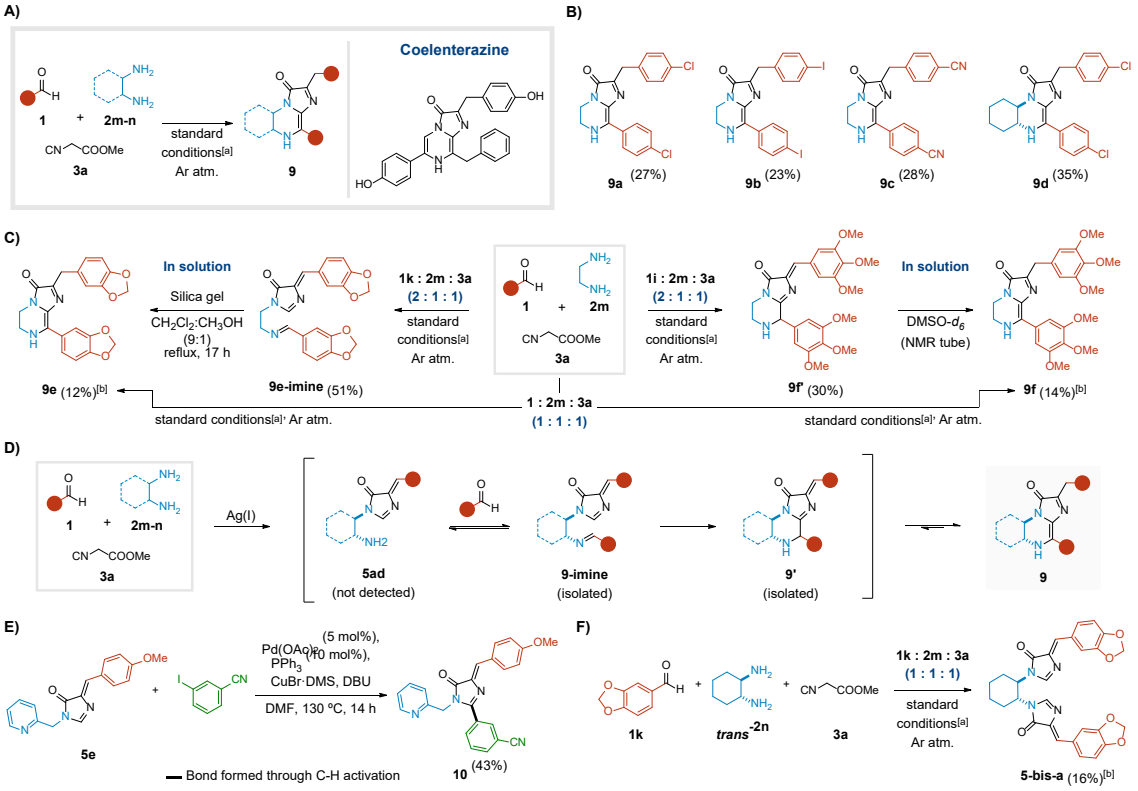

Figure 4. MCR with 1,2-diamines: access to analogues of the natural product coelenterazine. A) General reaction scheme and structure of coelenterazine. B) Scope of the process. C) Isolated intermediates and conversion to the coelenterazine derivatives **9**. D) Proposed reaction mechanism for the formation of adducts **9**. E) The C-H activation reaction. F) Formation of bis-imidazolone adduct **5-bis-a**. [a]Standard conditions: MCR; $AgNO_3$ (10 mol%); MeOH (0.2 M); rt for 17 h or 40 ºC (μW) for 20 min. [b]Unoptimised yield: the reaction was performed with a 1:1:1 ratio of reactants. Nucleophilic Addition to the Imidazolone Core

According to our empirical observations, we speculate that the precipitation of intermediates **9e-imine** and **9f'** in the reaction media might play a role in the interruption of the dynamic pathway towards adducts **9**. Consistently, both intermediates were fully converted to their corresponding coelenterazine isomers **9** in solution (Figures 4C and S12-13). Interestingly, in an independent experiment with equimolar amounts of piperonal **1k**, (±)-*trans*-1,2-diaminocyclohexane ***trans*-2n**, and methyl isocyanoacetate **3a**, we isolated the double imidazolone derivative **5-bis-a** (16%, Figures 4F and S8) as a precipitate.

1.4. Nucleophilic Addition to the Imidazolone Core

Next, we evaluated the impact of longer chain diamines, on the MCR. In the case of 1,6-hexanediamine, no imidazolone-type species were formed (Figure S8). However, with 1,3-propylenediamine **2o**, the MCR unexpectedly yielded guanidine **11a**. Moreover,

we observed trace amounts (*ca*. 10 %) of the corresponding dehydrogenated 2-aminoimidazolone **12a** (Figures 5A and S8). Incidentally, this nucleus has wide-ranging biological and pharmacological relevance. Several natural products from marine sponges and coral species feature this scaffold.[27] Moreover, various analogues have been reported to have promising therapeutic profiles as antibiotics and neuroprotective agents, being potent and selective kinase inhibitors.[28] Finally, they have also been studied as fluorescent probes.[29] In addition, the oxidative conversion of **11a** to **12a** remarkably mimics the biosynthesis of the GFP chromophore,[30] rendering a novel MCR-based approach to 2-aminoimidazolones synthesis.

We were able to reproduce the process intermolecularly by using an excess of methylamine **2i** (10 eq.) in the MCR under the standard conditions. The corresponding intermediates **11b-c** were formed, and again we detected trace amounts of **12b-c** (Figure 5B). Switching to an inert atmosphere allowed for a cleaner formation of guanidines **11**. Several oxidation protocols fully converted compounds **11** to 2-aminoimidazolones **12** (Figure 5A-B and Table S7). Among them, the use stoichiometric amounts of TEMPO minimised a known oxidative cleavage of the imidazolone,[30] providing compounds **12a-c** with fair yields (*ca*. 60% for the oxidation step, Figure 5C). Notably, Boc-deprotection of **12c** directly afforded the natural product **12c'**, an alkaloid present in the *Dendrophyllia* corals (26% overall yield for 3 steps, Figure 5C).[27a]

Moreover, we developed a convenient protocol in which a previously isolated imidazolone **5** was reacted with a nucleophile under inert atmosphere to give adducts **11** quantitively, after simple evaporation or aqueous work-up (Figure 5D). The addition reaction was strongly dependent on the nature of the incoming species (Table S6). Pyrrolidine reacted at room temperature, while more deactivated secondary amines and amylamine needed thermal activation. The reaction with ammonia required copper to promote the addition. Among other nucleophiles, 1-propanethiol was successfully added to the imidazolone scaffold in basic conditions. In contrast, the incorporation of phenols and diethyl phosphite resulted in complex reaction mixtures (see ES). Finally, anilines, sulfinates, or 2-methylindole did not react with adducts **5** under the conditions tested. In this way, guanidines **11d-e** were isolated in quantitative yields and characterised as representative examples (Figure 5E). However, in most cases the crude intermediates **11** were directly dehydrogenated to yield the 2-aminoimidazolones **12d-h** and the sulfa adduct **13** (30-70%, Figure 5E). Notably, the natural product leucettamine B (**12i**, from

Leucetta sponges)[27b] was obtained in a single step from the MCR adduct **5i** and ammonia, likely because the copper additive also promoted the in situ conversion to the oxidised product (20%, Figure 5E).

We assume that scaffold **11** is generated through the unprecedented addition of a second amino functionality to the amidine moiety of the imidazolone core,[28a,31] leading to the intermediate **I**. In turn, a series of tautomeric equilibria *via* the imine tautomer **II** yields the presumably more stable guanidine **11** (Figure 5D). Preliminary computational results and experiments with deuterated species supported the proposed addition mechanism, likely involving the intermediacy of radical species (see ES).[32]

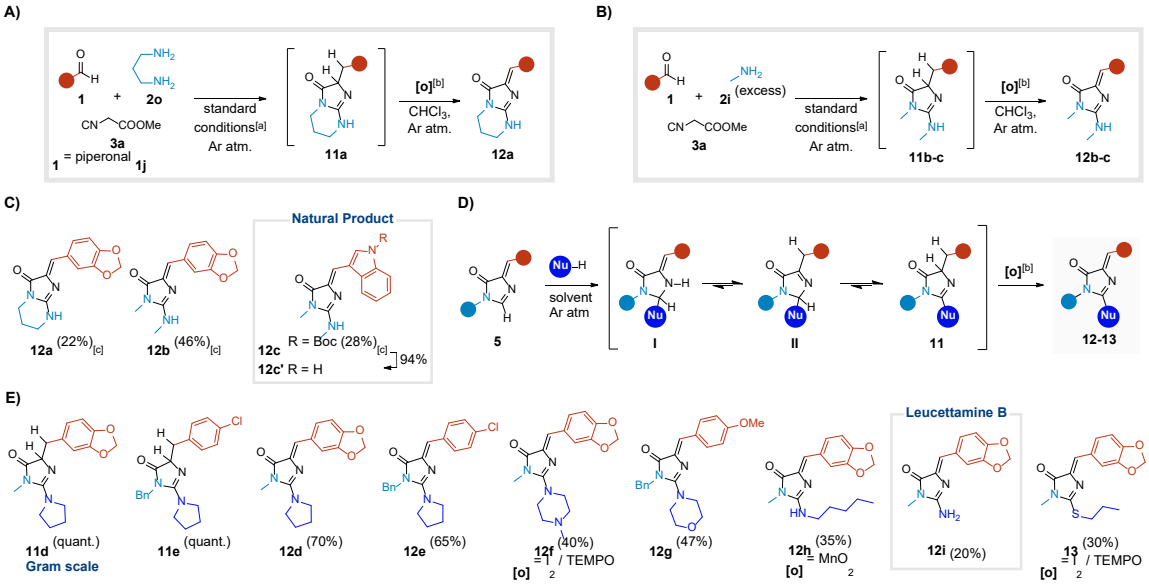

Figure 5. Addition of nucleophiles to the GFP core. A) New MCR with 1,3-diaminopropane. B) Use of an excess of methylamine in the MCR. C) Examples derived from the new MCR-oxidation process. D) Sequential protocol leading to adducts **12** and **13**. E) Scope of the sequential protocol. [a]Standard conditions: MCR; $AgNO_3$ (10 mol%); MeOH (0.2 M); rt for 17 h or 40 ºC (μW) for 20 min. [b]Unless otherwise stated, **[o]** = TEMPO. [c]Yield calculated over 2 steps (MCR-oxidation).

1.5. Fluorescence Applications of (2-Amino)Imidazolones

Considering the close analogy of the synthesised adducts to the GFP chromophore, we investigated their potential as fluorescent probes.[33] The convenient structural tuning of our compounds allows for rapid modifications in their photophysical behaviour. For instance, we observed a 60 nm bathochromic shift in the absorption maximum from adduct **5i** to **5j**. Compound **12d** did not show significant differences to the chromophores **5** in the absorption pattern (Figure 6A). The GFP chromophore does not emit in solution, as its fluorescence emanates from its fixed position in the protein environment.[34] However, it has been shown that modifications such as tuning the central core or restricting the double bond rotation can lead to improved fluorogenic

properties.[29,35] Recently, this was also achieved through binding of the chromophore to other proteins.[36] Indeed, our GFP chromophore-type adducts **5** did not exhibit significant fluorescence in any of the tested solvents (Figure S26). Yet, the incorporation of the amino moiety at the C-2 of the imidazolone resulted in a substantial increase of the fluorescence, as compound **12d** showed over 30-fold increase in the emission intensity in EtOH in respect to its parent adduct **5i** (Figure 6B). In addition, the fluorescence of imidazolone **5i** and its amino derivative **12d** was remarkably increased in hydrophobic environments in comparison to aqueous media (Figures 6C and S27). Interestingly, we observed a significant decrease in the fluorescence intensity of compound **12d** at low pH values (Figure S27).

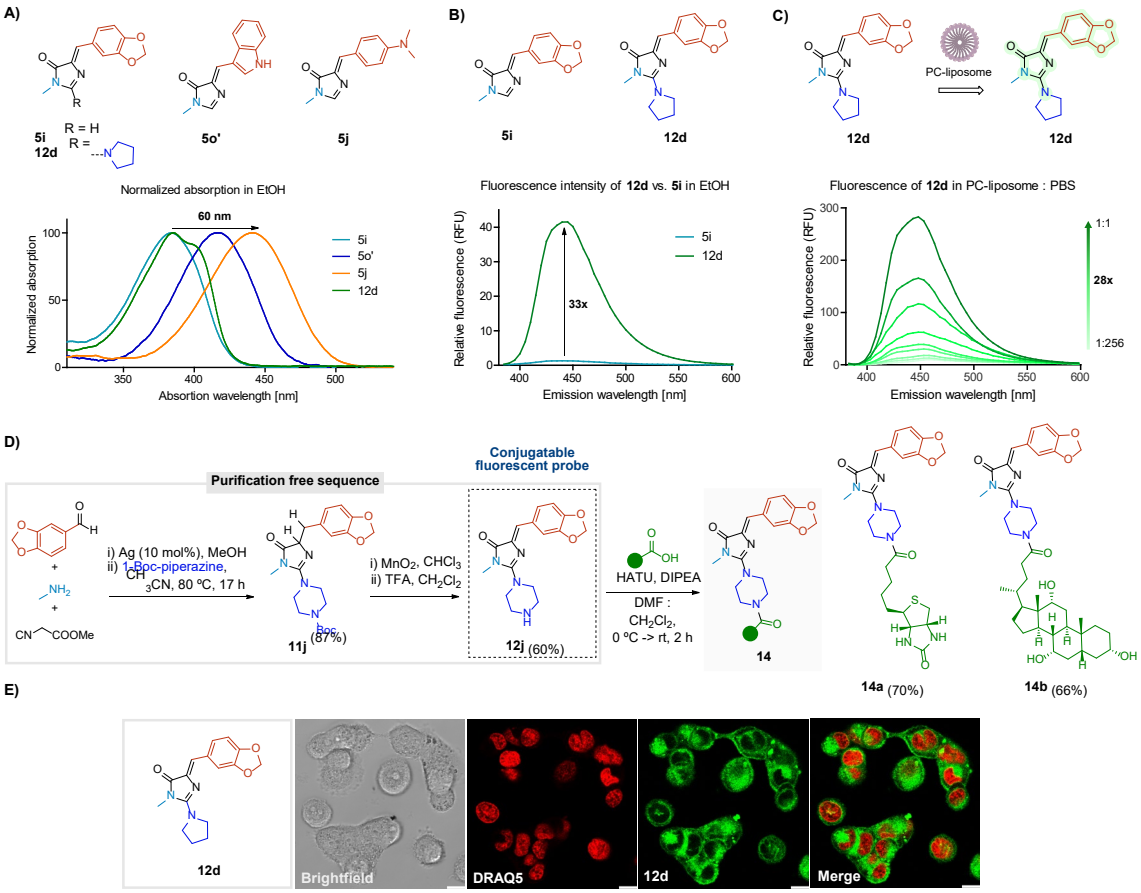

Figure 6. Photophysical studies. A) Normalised absorption spectra of compounds **5i**, **5o'**, **5j**, and **12d** in EtOH (100 µM). B) Emission spectra of **5i** and **12d** in EtOH (100 µM, λ_{ext}: 360 nm). C) Emission spectra of **12d** in increasing concentrations of phosphatidylcholine (PC)-liposome in PBS (100 µM, λ_{ext}: 360 nm). D) Synthesis of probe **12j** and conjugation with biologically relevant carboxylic acids. E) Fluorescence images of **MDA-MB-231** human cancer cells after incubation with compound **12d** (100 µM, 1 h, green) and **DRAQ5** (red) as a nuclear counterstain. Scale bar: 10 µm.

Given the suitable photophysical properties of 2-aminoimidazolones **12**, we envisaged their participation in a bioconjugation process. As a proof of concept, we obtained compound **12j** in a convenient purification-free synthesis with a decent global

yield of 52% and coupled it to biotin and cholic acid to give the final conjugates **14a-b** (*ca.* 70%, Figure 6D). The process was not detrimental to the emission of the final adducts (Figure S26). Lastly, in a collaboration with Prof. Vendrell (University of Edinburgh), we demonstrated the compatibility of compound **12d** for live-cell imaging by incubating MDA-MB-231 cells followed by confocal fluorescence microscopy (Figure 6E). Fluorophore **12d** showed strong intracellular signals, confirming cell permeability and suitability for fluorescence microscopy assays.

1.6. Conclusions

In summary, we have described how a systematic charting of the chemical reaction space around a known MCR not only defines the synthetic reach but, more importantly, leads to the discovery of rerouted and extended processes. In this way, the combination of carbonyls, amines, and isocyanoacetates was inspected to selectively access a wide array of biologically relevant heterocyclic scaffolds: GFP chromophore derivatives, coelenterazine analogues, imidazolines, oxazolines, etc. Incidentally, our approach has also prompted the discovery of new fundamental reactivity of the imidazolone scaffold. In our opinion, subtle kinetic changes within the chemical reaction space dictate the divergency of the MCR. In that sense, the charting approach provides a unified understanding of the possible interactions within a multicomponent combination and may lead to the discovery of new processes. We advocate for such explorations in MCRs to map the still dark regions of the chemical reaction space around these important transformations and expand their impact in Diversity Oriented Synthesis.

2. Experimental Section

2.1. General Information

Unless otherwise stated, all reactions were carried out under normal atmosphere in dried glassware. All chemicals were purchased from commercial sources and were used as received unless otherwise mentioned. Microwave reactions were performed on a Biotage Initiator Classic. Flash column chromatographies were performed on an Isolera Prime Biotage provided with dual UV detection over normal phase silica gel columns (prepacked: 5, 10 and 25 g; or refillable cartridges: 5 – 50 g), reverse-phase C18 columns (prepacked: 6, 12 and 30 g), or neutral aluminum oxide (Al_2O_3) columns (prepacked: 4 g, or refillable cartridges: 5 – 20 g). Thin layer chromatographies were performed on pre-coated Merk silica gel 60 F254 plates and visualised under UV light at 254 nm and 365 nm.

2.1.1. Analysis

The ^{1}H NMR spectra were recorded on a 400 MHz or 500 MHz NMR spectrometer. The ^{13}C NMR spectra were recorded at 101 MHz or 126 MHz. Chemical shifts were reported in ppm(δ) as s (singlet), d (doublet), t (triplet), dd (doublet of doublets), m (multiplet), br s (broad singlet), etc. The residual solvent signals were used as references. The University of Barcelona Mass Spectrometry Service performed the High-Resolution Mass Spectrometry analyses. LC-MS spectra were carried out on Agilent 1260 Infinity II. The analysis was conducted on a Poroshell 120 EC-C15 (4.6 mm × 50 mm, 2.7 μm) at 40 °C with mobile phase A (H_2O + 0.05% formic acid) and B (CH_3CN + 0.05% formic acid) using a gradient elution and flow rate 0.6 mL/min. The DAD detector was set at 254 and 365 nm. The injection volume was 5 μL. EPR spectra were recorded on a Bruker EMX-Plus 10/12 Bruker BioSpin spectrometer with a X-band microwave bridge EMX Premium X, a 10″ERO73 magnet and a power supply of 12 kW (ERO83). The temperature was controlled by a Bruker ER 4111 VT temperature control system. The Science and Technology Park (University of Burgos, Spain) carried out X-ray diffractions.

2.1.2. Photocatalysed Reactions Set-Up

Flexible blue LED strips of 120 cm from buyledstrip.com (Netherlands) were used as the light source for photocatalysed reactions. The light source was placed in a large crystallizing dish, around its inner circumference. The vial or round bottom flask

containing the solid to be irradiated was placed in the center of the dish to ensure even distribution of the irradiation (~ 5 cm of distance between the vessel and the light source). The device was covered with aluminum foil to increase the reaction irradiation and avoid any dangerous exposure to LEDs.

2.2. Results and Discussion

2.2.1. Preliminary Charting Experiments

In preliminary experiments, while performing the following Ugi-4CR with sterically hindered amine and aldehyde components and an aromatic isocyanide (4-methoxyphenyl isocyanide), we also detected the formation of the Passerini adduct in competing yields (Entry 1, Table S1). Interestingly, as we switched to cyclohexyl isocyanide, the formation of the Ugi adduct was fully suppressed and only the Passerini Adduct was detected (Entry 2, Table S1). As the formation of the Ugi adduct is the result of isocyanide attack to the formed imine, we presume that bulky residues slow down/disfavor this attack and give rise to the alternative Passerini pathway. This effect is especially dominant in the case of the non-flat cyclohexyl residue in comparison with a flat methoxyphenyl one. In our opinion these results indicated that an MCR pathway can be rewired by slight alterations, rationalizing the potential usefulness of systematic charting studies around a known MCR combination.

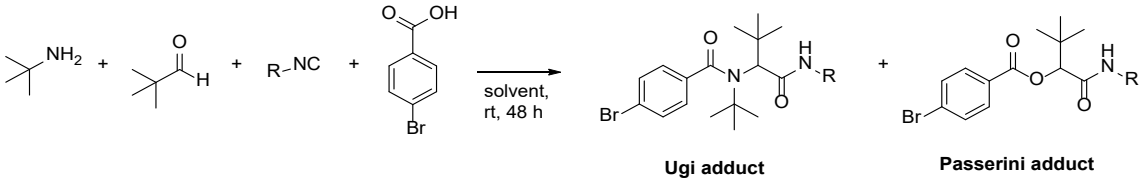

Table S1. Preliminary experiments supporting the need for charting an MCR.

Entry	R	Solvent	Ugi Adduct (%)[a]	Passerini Adduct (%)[a]
1	4-methoxyphenyl	MeOH	28	15
2	cyclohexyl	MeOH	0	25

[a]Conversion % calculated by LC-MS.

2.2.2. Charting of the MCR

Inputs of the MCR

Carbonyls (1a-1af)

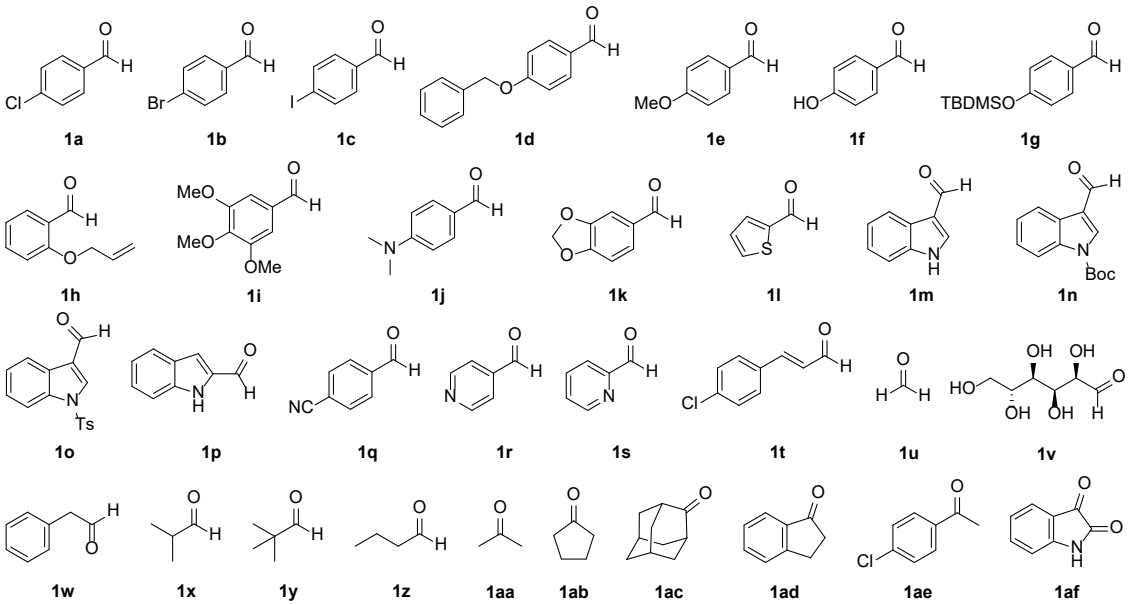

Amines and surrogates (2a-2x)

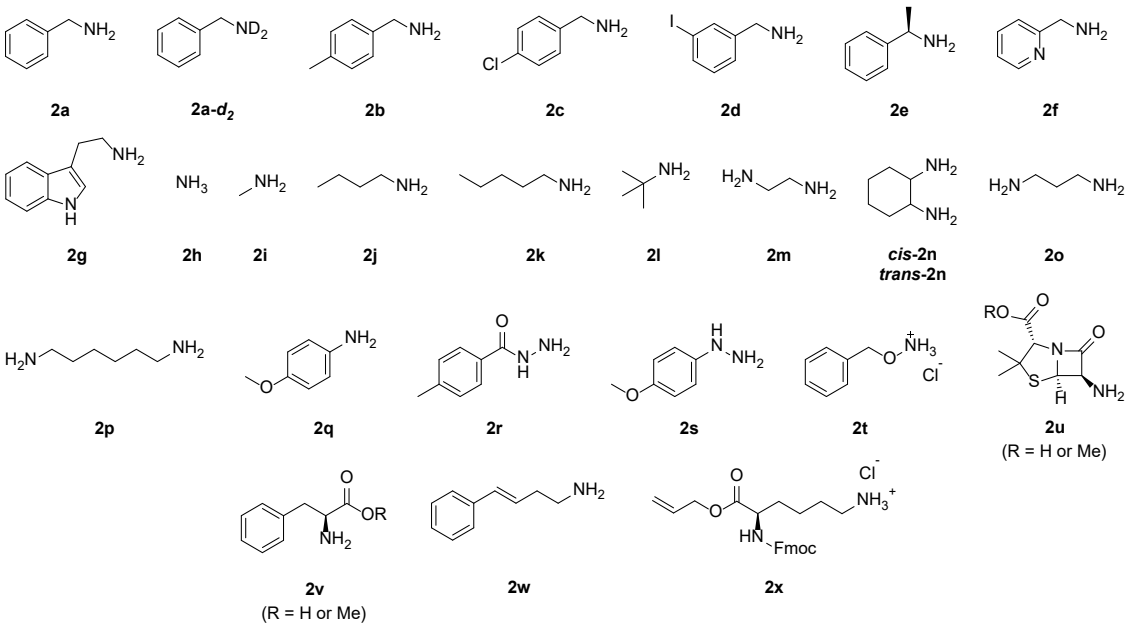

Isocyanoacetates (3a-3b)

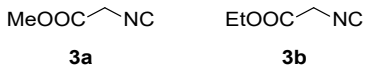

2.2.3. Screening the Reaction Conditions

We studied the outcome of the MCR involving carbonyls, amines and isocyanoacectates depending on reaction conditions, solvent, and catalyst. We started charting the MCR with 4-chlorobenzaldehyde **1a**, benzylamine **2a**, and methyl isocyanoacetate **3a** (Table S2). Experiments in which the imine was preformed, either prior or *in situ*, with or without $MgSO_4$ (entries 1-3) only generated **4a**. Multicomponent protocols with $MgSO_4$ or without additives produced mixtures of **4a** and **5a** (entries 4-5). The use of $AgNO_3$ in a multicomponent protocol resulted in the selective formation of **5a**. Entries 6-10 show how varying the temperature, time and catalyst loading did not affect productivity. However, a change in the stoichiometry (excess of **3a**) decreased the yield of the MCR, although it was still selective towards **5a** (entry 11). As for the solvent, alcohols were the solvents of choice for the formation of **5a**, and addition of water as cosolvent was not detrimental (entries 12-14). Aprotic solvents such as CH_3CN and CH_2Cl_2 were unproductive and gave mostly imine (entries 15-16). The MCR with fluorinated alcohols (and $AgNO_3$) reversed the outcome of the reaction to the formation of **4a** (entries 17-18). Lastly, the effect of the catalyst was studied. Other silver and copper salts selectively gave **5a**, but with lower conversions than $AgNO_3$ (entries 19-22). Other metals gave either low production mixtures of **4a** and **5a** (entries 23-24) or unproductive reactions (entry 25).

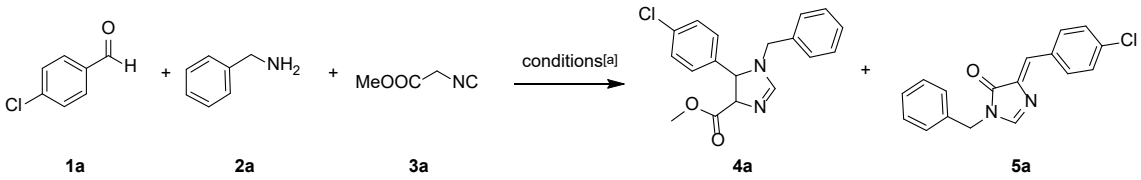

Table S2. Charting of the MCR with 4-chlorobenzaldehyde **1a**.

Entry	Protocol	Solvent	Catalyst (10 mol%)[b]	Temperature (ºC)	Time	Conversion % by LC-MS (isolated yield)	
						4a	**5a**
1	One-pot sequential[c]	MeOH	$MgSO_4$ (1.5 eq.)	rt	48 h	45	0
2	One-pot sequential[c]	MeOH	$AgNO_3$	rt	17 h	85 (70%)	0
3	Stepwise (pre-formed imine)[d]	MeOH	$MgSO_4$ (1.5 eq.)	rt	17 h	65	0

4	MCR	MeOH	$MgSO_4$ (1.5 eq.)	rt	17 h	13	75
5	MCR	MeOH	-	rt	17 h	20	60
6	MCR	MeOH	$AgNO_3$	rt	17 h	0	75 (47%)
7	MCR	MeOH	$AgNO_3$	80	17 h	0	73
8	MCR	MeOH	$AgNO_3$ (20 mol%)	rt	17 h	0	76
9	MCR	MeOH	$AgNO_3$	40 (μW)	20 min	0	76 (46%)
10	MCR	MeOH	$AgNO_3$	80 (μW)	10 min	0	75
11	MCR[e]	MeOH	$AgNO_3$	rt	17 h	0	58 (21%)
12	MCR[f]	EtOH	$AgNO_3$	100 (μW)	10 min	0	69
13	MCR	*i*-PrOH	$AgNO_3$	120 (μW)	10 min	0	64
14	MCR	MeOH / H_2O (8 : 2)	$AgNO_3$	rt	17 h	0	80 (45%)
15	MCR	CH_3CN	$AgNO_3$	40 (μW)	20 min	0	0[g]
16	MCR	CH_2Cl_2	$AgNO_3$	rt	17 h	31	0[g]
17	MCR	TFE	$AgNO_3$	40 (μW)	20 min	50	20
18	MCR	HFIP	$AgNO_3$	40 (μW)	20 min	60	0
19	MCR	MeOH	Ag_2CO_3	40 (μW)	20 min	0	72
20	MCR	MeOH	AgOAc	40 (μW)	20 min	0	56
21	MCR	MeOH	$CuCl_2$	40 (μW)	20 min	0	39
22	MCR	MeOH	$Cu(OAc)_2$	40 (μW)	20 min	0	42
23	MCR	MeOH	$Rh_2(OAc)_4$	40 (μW)	20 min	10	25 (22%)[g]
24	MCR	MeOH	$PdCl_2$	40 (μW)	20 min	10	15 (10%)[g]
25	MCR	MeOH	$AuCl_3$	40 (μW)	20 min	0	0[g]

[a]Unless otherwise stated: **1a** (1.1 mmol), **2a** (1.1 mmol), **3a** (1 mmol), catalyst (0.1 mmol), solvent (5 mL). [b]Amount of catalyst was 10 mol% unless otherwise stated. [c]One-pot sequential protocol: **1a** (1.1 mmol), **2a** (1.1 mmol) and catalyst stirred for 4 h, then added **3a** (1 mmol), solvent (5 mL). [d]Stepwise protocol: *N*-benzyl-1-(4-chlorophenyl)methanimine (1.1 mmol), **3a** (1 mmol), catalyst, solvent (5 mL). [e]Different reaction stoichiometry: **1a** (1 mmol), **2a** (1 mmol),

3a (1.1 mmol), catalyst (0.1 mmol), solvent (5 mL). [f]Ethyl isocyanoacetate **3b** (1 mmol) was used instead of **3a**. [g]Unproductive reactions (low or no amount of **4a** and **5a**) mostly produced *N*-benzyl-1-(4-chlorophenyl)methanimine.

Next, we selected key experiments from the charting with 4-chlorobenzaldehyde **1a** (entries 2, 6 and 18, Table S2) and reproduced them with acetone **1v** (Table S3). The results were comparable. With preformed imine *in situ*, the reaction only yielded **4aa** (entry 1). The MCR with $AgNO_3$ afforded a mixture of **4a** and **5a** (entry 2). Finally, the MCR with HFIP only yielded **4a** (entry 3).

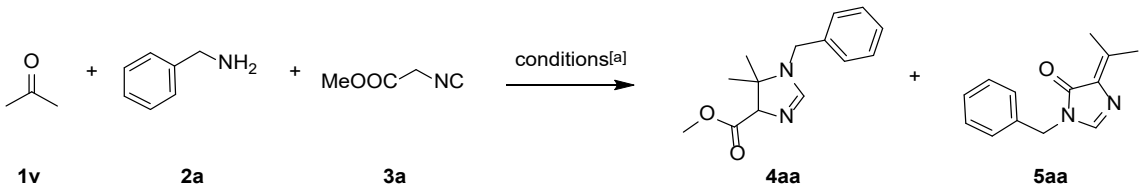

1v **2a** **3a** **4aa** **5aa**

Table S3. Charting of the MCR with acetone **1v**.

Entry	Protocol	Solvent	Catalyst (10 mol%)	Tempe-rature (ºC)	Time	Conversion % by LC-MS (isolated yield)	
						4aa	**5aa**
1	One-pot sequential[b]	MeOH	$AgNO_3$	rt	48 h	90 (90%)	0
2	MCR	MeOH	$AgNO_3$	40 (μW)	20 min	30 (27%)	63 (58%)
3	MCR	HFIP	$AgNO_3$	40 (μW)	20 min	91	0

[a]**1v** (1.1 mmol), **2a** (1.1 mmol), **3a** (1 mmol), catalyst (0.1 mmol), solvent (5 mL). [b]One-pot sequential protocol: **1a** (1.1 mmol), **2a** (1.1 mmol) stirred for 4 h, then added **3a** (1 mmol) and catalyst (10 mol%), solvent (5 mL).

2.2.4. Exploring the Scope of the MCR

The scope of the MCR was explored with two goals: to assess the limitations of the new process, and to study the impact of the inputs of the MCR on its outcome, as part of the charting of the MCR. Unless otherwise stated, all experiments reported in this section were performed under the described standard reaction conditions: **1** (1.1 mmol), **2** (1.1 mmol), **3** (1 mmol) and $AgNO_3$ (10 mol%) in MeOH (0.2 M); rt for 17 h or 40 ºC (mW) for 20 min.

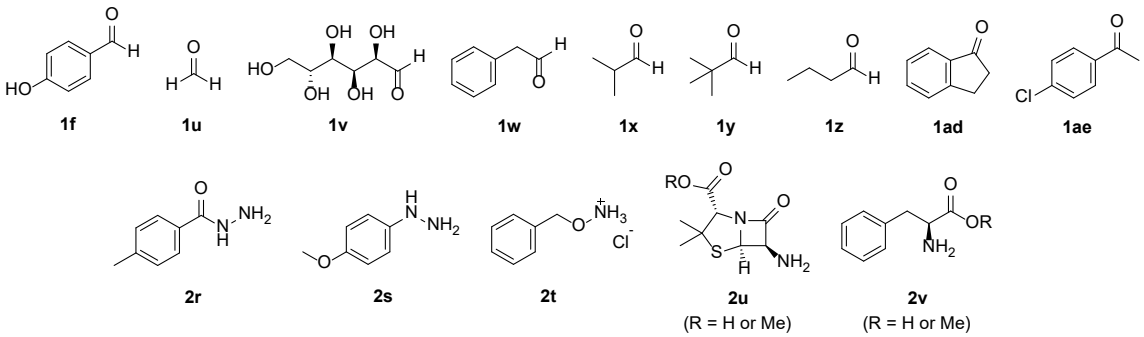

Table S4. The following inputs did not yield any of the expected adducts **4-6** under the described standard conditions.

Entry	**Input**		Result
1	**1f**	4-Hydrozybenzaldehyde	No meaningful reaction was observed under the standard conditions. The lack of the reactivity of 4-hydroxybenzaldehyde **1f** in the MCR may correlate with the failure to generate the Knovenagel adducts under the standard conditions.[37]
2	**1u**	Formaldehyde[a]	Complex reaction mixtures. Likely formation of polymeric adducts.
3	**1v**	Glucose	No reaction observed.
4	**1w-1z**	Aliphatic aldehydes	Complex reaction mixtures. No detection of MCR adducts under the standard conditions.
5	**1ad-1ae**	Aromatic ketones	No reaction observed under the standard conditions. The low level of reactivity of aromatic ketones is likely due to their decreased electrophilicity, compared to dialkyl ketones.[38]
6	**2r**	Hydrazide	No detection of MCR adducts under the standard conditions. Mostly unreacted starting material recovered.
7	**2s**	Hydrazine	No detection of MCR adducts under the standard conditions. Mostly unreacted starting material recovered.
8	**2t**	Hydroxylamine[b]	No detection of MCR adducts under the standard conditions. Mostly unreacted starting material recovered.
9	**2u**	6-Aminopenicillanic acid (6-APA) or 6-APA methyl ester[b]	No reaction observed under the standard conditions. Deactivated primary amines do not yield the MCR adducts, likely due to their reduced nucleophilicity.

10	**2v**	L-phenylalanine or L-phenylalanine methyl ester[b]	No reaction observed under the standard conditions. Deactivated primary amines do not yield the MCR adducts, likely due to their reduced nucleophilicity.

[a]Formaldehyde **1t** was used as its polymer form: paraformaldehyde. [b]The O-benzylhydroxylamine **2t**, the 6-APA methyl ester (**2u**, R = Me), and the L-phenylalanine methyl ester (**2v**, R = Me) were used as the hydrochloride form, which was neutralised by addition of 1 eq. of trimethylamine in the MCR.

Some inputs did react in the MCR but resulted in unconventional results (Figure S1). We describe the corresponding outcome in each particular case.

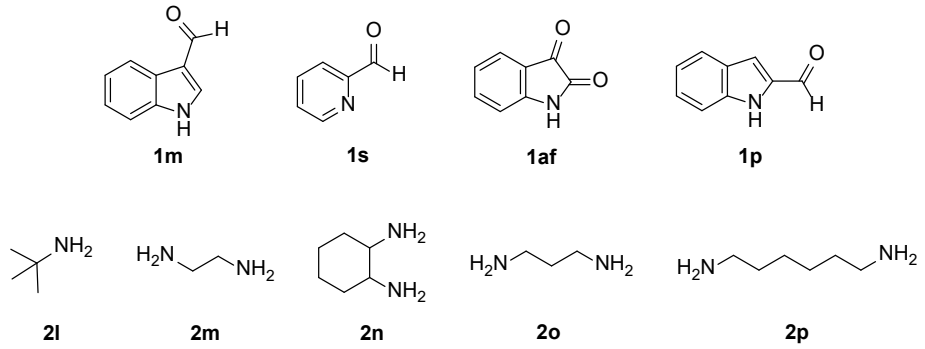

Figure S1. Inputs that resulted in unconventional results.

The case of indole-3-carboxaldehyde **1m**

The unprotected indole-3-carboxaldehyde **1m** did not react in the MCR under the standard conditions. The Boc- and Ts- protected indole-3-carboxaldehydes **1n-o** gave the desired imidazolones **5o-p** in good yields and, consistently with the general trend, were generated as a single diastereomer. However, deprotection of the adduct **5o** gave **5o'** as a mixture of diastereomers (Figure S2).[39]

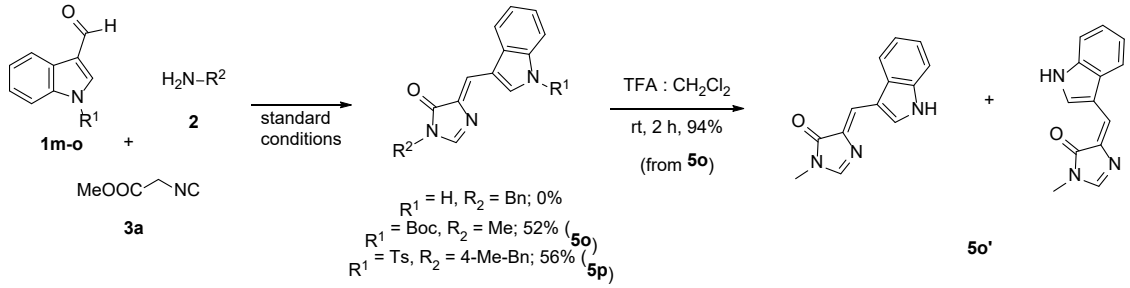

Figure S2. MCR with (un)protected indole-3-carboxaldehyde, amines and methyl isocyanoacetate **3a**.

The cases of 2- formylpyridine **1r** and 4-formylpyridine **1s**

Electron deficient aromatic aldehydes reacted poorly in the MCR under the standard conditions. In this way, the adduct **5q** was formed in 28% yield form 4-

formylpyridine **1r**. With 2-formylpyridine **1s**, we detected the expected *m/z* 298 $[M+H]^+$ by LC-MS. However, the ^1H NMR of the reaction crude suggested a highly complex reaction mixture and the expected imidazolone **S1** could not be isolated after several attempts to purify with chromatography and recrystallisation (Figure S3).

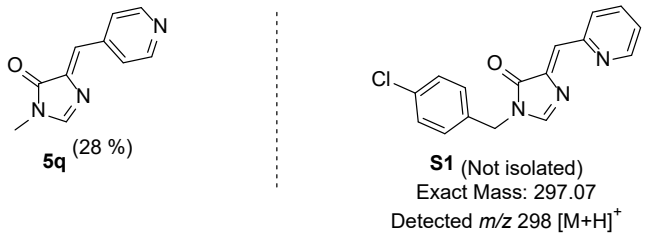

Figure S3. Outcomes of the MCR with pyridine aldehydes.

The case of isatin **1af**

We investigated the participation of an activated carbonyl such as isatin **1af** in the MCR. In the first experiments with an alkyl amine, we did not detect the expected imidazolone adducts **S3,** and LC-MS analysis suggested the presence of a second unit of amine (even when only 1 equivalent of the amine was used in the MCR). We hypothesised that due to the higher reactivity of the imidazolone scaffold with the isatin moiety, the addition of a second unit of the amine was faster than the MCR. Thus, the corresponding adducts **S3** were never observed and the 2-aminoimidazolone **S2** was detected (Figure S4).

The conversion to these presumed adducts was very low and its isolation was problematic, which resulted in very low amounts of impure products after chromatography. Nonetheless, the ^1H NMR and LC-MS data of the impure isolated products showed evidence that is consistent with this hypothesis.

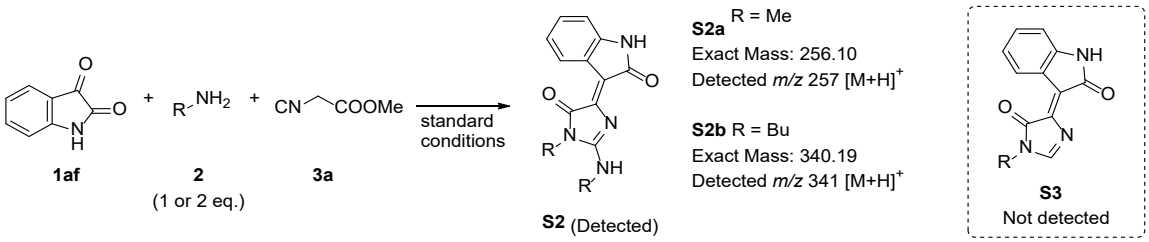

Figure S4. MCR with isatin **1af**, primary aliphatic amines, and methyl isocyanoacetate **3a**.

We also reacted isatin **1af** with 1,3-diaminopropane **2o**, and methyl isocyanoacetate **3a** in an attempt to emulate the result we obtained with piperonal **1j.**

Although the desired *m/z* was detected by LC-MS, again only a very low amount of impure product consistent with **S4** was obtained (Figure S5).

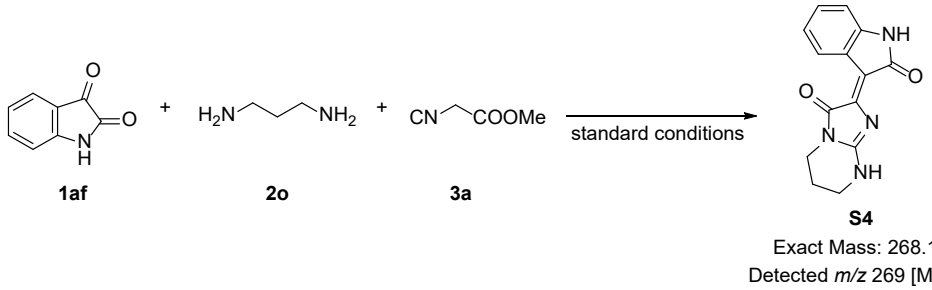

Figure S5. MCR with isatin **1af**, 1,3-propylenediamine **2n**, and methyl isocyanoacetate **3a**.

Lastly, we pondered whether we could develop a new 4-CR by reacting isatin **1af** with butylamine **2j** and 4-methoxyaniline **2q**. The hypothesis was that butylamine **2j** would react in the MCR and the 4-methoxyaniline **2q** would add into the generated imidazolone. This hypothesis was supported by the fact that isocyanides have a lower insertion rate into aromatic N-H bonds.[14] Similar to the other experiments, we obtained very low amounts of an impure sample – although presumably consistent with the expected adduct **S5** – from a highly complex reaction mixture (Figure S6).

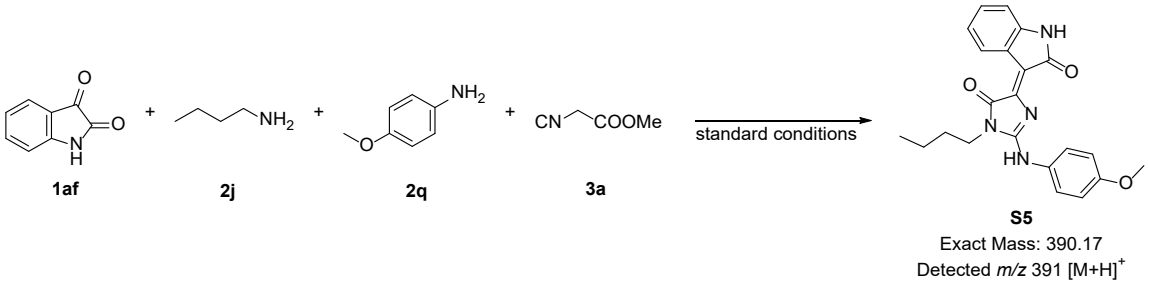

Figure S6. MCR with isatin **1af**, butylamine **2j**, 4-methoxyaniline **2q,** and methyl isocyanoacetate **3a**.

The case of indole-2-carboxaldehyde **1p**

The MCR with indole-2-carboxalehyde **1p** and benzylamine **1a** under the standard conditions gave the expected adduct **5r** (47%) together with indolocarbazole **7** (27%, Figure S7). The formation of this mixture results from the competitive nature of the isocyanide insertion into the benzylamine N-H bond and the indole N-H bond.

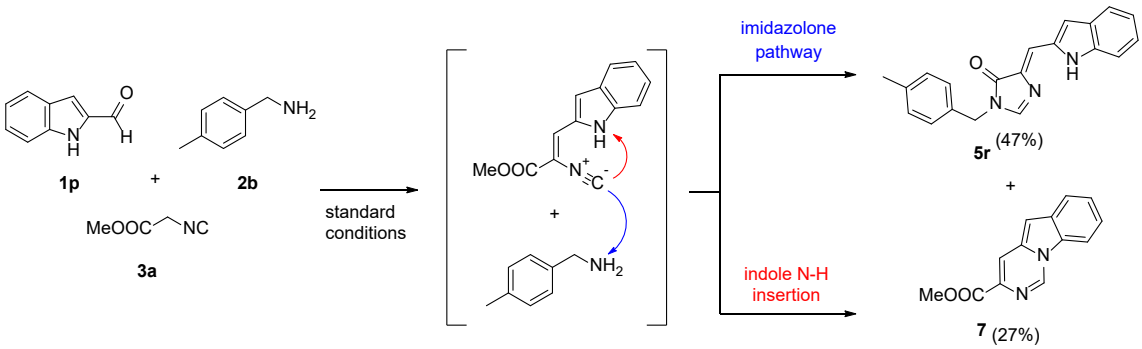

Figure S7. MCR with indole-2-carboxalehyde **1p,** benzylamine **1a** and methyl isocyanoacetate **3a**.

The case of *tert*-butylamine **2l**

The sterically hindered *tert*-butylamine **2l** was subjected to the MCR with a range of carbonyls. We first performed the MCR with acetone **1aa**. In this case neither the imidazoline **4** nor the imidazolone **5** were detected, and oxazoline **6b** was isolated almost quantitatively (Table S5, Entry 1). Then we performed the MCR with aromatic aldehydes. Again, the major products of the MCR were the corresponding oxazolines **6** (Entries 2-3). However, with piperonal **1k** traces of the adduct **5z** were detected, and it could be isolated in 2% yield (Entry 3).

Finally, we pondered whether the formation of indolocarbazole **7** (see above) could be promoted by the participation of *tert*-butylamine **2l** in the MCR with indole-2-carboxalehyde **1p**. Indeed, the formation of indolocarbazole **7** was increased to a 64% yield, and traces of the corresponding oxazoline **6** were detected. The corresponding compounds **4-5** were not detected in this case.

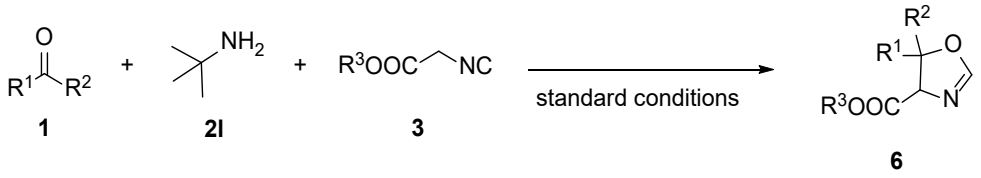

Table S5. Results of the MCR with *tert*-butylamine **1l** and different carbonyls.

Entry	Carbonyl **1**	Isocyanoacetate **3**	Conversion % by LC-MS (isolated yield) 2-imidazoline **4**	imidazolone **5**	oxazoline **6**	indolocarbazole **7**
1[a]	**1aa**	**3b**	0	0	**6b** 99 (97%)	- [b]
2	**1r**	**3a**	0	0	**6a**	- [b]

					60 (55%)	
3	**1k**	**3a**	0	**5z** traces (2%)	58 (not isolated)	- [b]
4	**1p**	**3a**	0	0	traces	**7** 75 (64%)

[a]The result was analogous when a sequential protocol was applied: **1aa**, **2l** and $MgSO_4$ in MeOH stirred for 4h, then **3b**. [b]The generation of compound **7** was not possible.

The case of diamines

The incorporation of diamines in the MCR was a clear example of the importance of charting the chemical reaction space around an MCR. By only altering one parameter in the reaction (i.e. the type of diamine input), the outcome of the MCR was completely altered. Moreover, these variations were in principle unpredictable. Remarkably, the outcome in each scenario was highly selective, as in most cases no mixtures were detected. Here we summarise the results of screening the MCR with equimolar amounts of piperonal **1k**, methyl isocyanoacetate **3a**, and a variety of diamines (Figure S8A).

The experiment with ethylenediamine **2m** exclusively afforded the coelenterazine analogue **9e** and neither of the expected mono- or bis-imidazolone adducts were detected.

In the case of (±)-*trans*-1,2-diaminocyclohexane ***trans*-2n**, the bis-imidazolone adduct **5-bis-a** was isolated as the single adduct (16%). However the *m/z* consistent with the corresponding adduct **5** (*m/z* 314 $[M+H]^+$) and coelenterazine analogue **9** (*m/z* 446 $[M+H]^+$) were also detected by LC-MS, albeit in trace amounts. In contrast, the *cis*-1,2-diaminocyclohexane ***cis*-2n** resulted in a highly complex reaction mixture and none of the imidazolone-type derivatives were detected by LC-MS.

In the case of 1,3-propylenediamine **2o**, the formation of the imidazolone was followed by the intra molecular nucleophilic addition of the second NH_2 to the imidazolone scaffold.

Finally, with the longer chain 1,6-hexanediamine **2p**, a highly insoluble solid – which accounted for 53% of the mass balance – was recovered from the reaction. We hypothesise that the bis-imine **S6** precipitated from the reaction mixture, stopping the evolution to any of the other possible adducts. Structure confirmation of the proposed bis-imine **S6** was challenging due to the low solubility of the product. LC-MS analysis

showed the presence of piperonal **1k**, consistent with *in-situ* hydrolysis of the bis-imine in the acidic aqueous HPLC method.

Note that the use of (±)-*trans*-1,2-diaminocyclohexane ***trans*-2n** in the MCR with 2 equivalents of 4-chlorobenzaldehhde **4a** resulted in the formation of compound **9d**.

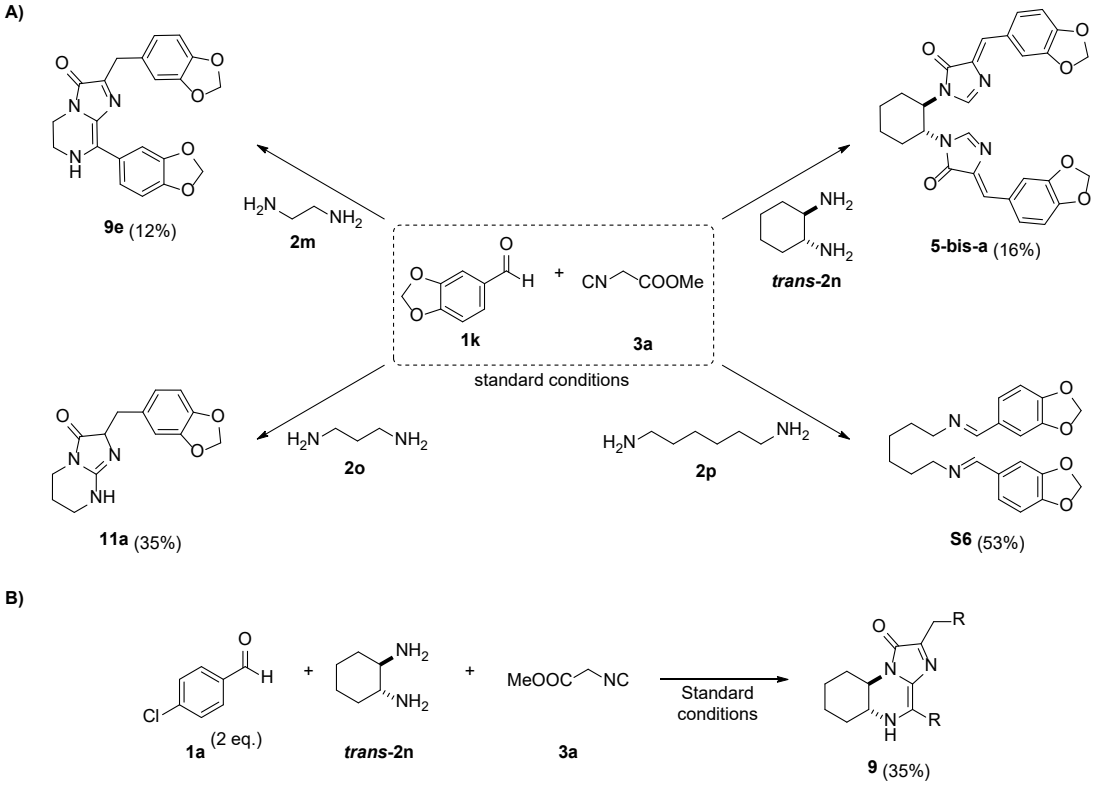

Figure S8. A) Variations in the outcome of the MCR with piperonal **1k**, methyl isocyanoacetate **3a**, and a range of diamines under the standard conditions. B) The MCR with 2 eq. of 4-chlorobenzalehyde **1a**, (±)-*trans*-1,2-diaminocyclohexane ***trans*-2n**, and methyl isocyanoacetate **3a** under the standard conditions.

2.2.5. Study of the Addition-Dehydrogenation Sequence

The following nucleophiles were successfully added to an imidazolone adduct **5** under described conditions.

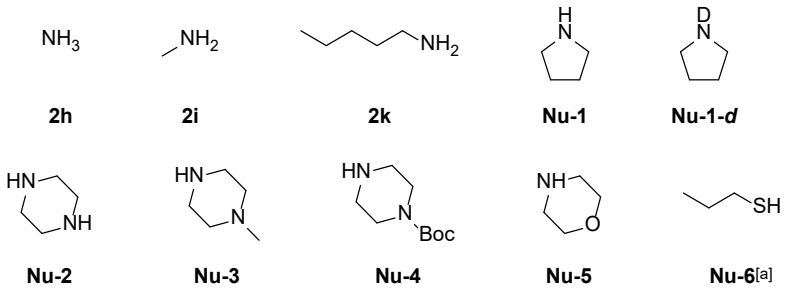

Figure S9. Nucleophiles successfully added to the imidazolone core. [a] Caesium carbonate was added in the reaction.

The following nucleophiles did not give the expected adducts **11** (Figure S10). Generally, the starting material **5** was recovered unreacted. However, with phenols **Nu-13** and **Nu-14** and diethyl phosphite **Nu-15**, the imidazolone **5** was consumed, but the reaction generated highly complex crudes and the corresponding adducts **11** were not detected.

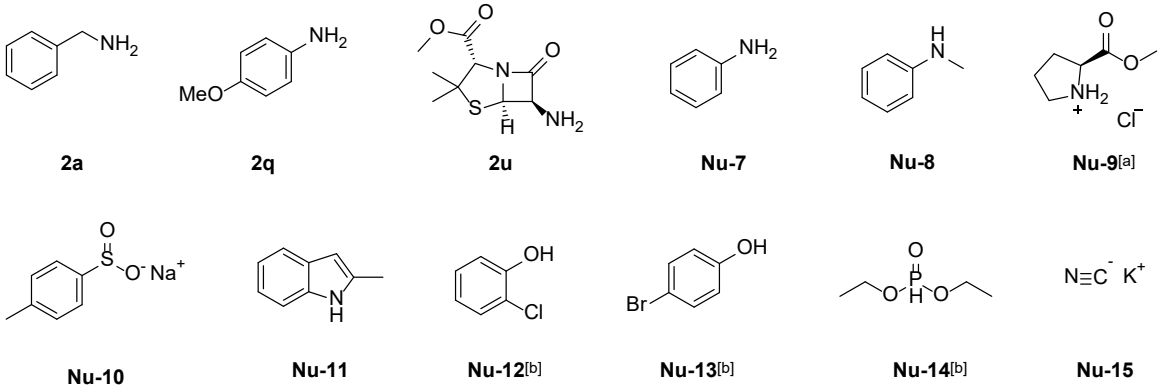

Figure S10. Nucleophiles that failed to give adducts **11**. [a]Triethylamine was added in the reaction. [b]Caesium carbonate was added in the reaction.

Screening the Nucleophilic Addition Conditions

The reaction of imidazolones **5** with a variety of nucleophiles gave adducts **11**. The conditions necessary for the addition varied depending on the nucleophile (Table S6).

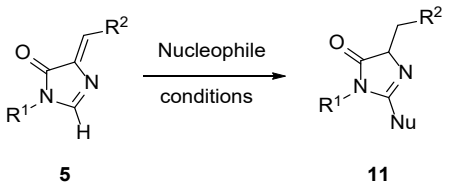

Table S6. Summary of applied reaction conditions for the nucleophilic addition to the imidazolone scaffold **5**. All reactions were performed in CH_3CN (0.1 M) and under argon atmosphere.

Entry	Substrate (imidazolones **5**)	Nucleophile	Nu Eq.	Temperature	Time	Additive	Conversion % to **11** (by LC-MS)
1a	**5i**	NH_3[a]	30	rt	17 h	-	0
1b	**5i**	NH_3[a]	30	80 ºC (µW)	30 min	$CuCl_2$ (1 eq.)	60
2	**5i**	CH_3NH_2[b]	10	rt	17 h	-	100
3a	**5i**		1	rt	17 h	-	80

3b	**5i**		5	rt	8 h	-	100
4a	**5i**	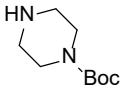	1	80 ºC	17 h	-	20
4b	**5i**	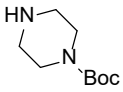	5	80 ºC	17 h	-	100
5a	**5i**	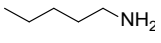	5	rt	17 h	-	0
5b	**5i**	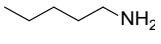	5	80 ºC	17 h	-	100
6a	**5c**		5	rt	17 h	-	0
6b	**5c**		5	80 ºC	17 h	-	100
7	**5i**		5	80 ºC	17 h	-	100
8a	**5i**	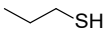	1	rt	17 h	-	0
8b	**5i**	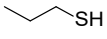	1	rt	3 h	Cs_2CO_3[c] (1.1 eq.)	100

[a]NH_3 was used as a 7 M solution in MeOH. [b]CH_3NH_2 was used as a 9.8 M solution in MeOH.

Dehydrogenation of Compounds 11 to Compounds 12

We observed that adducts **11** were spontaneously converted to **12**, either when the addition reaction was performed under open air or when adducts **11** were stored as solids in open air. In these cases, the average conversion was *ca*. 10% (Figure S11).

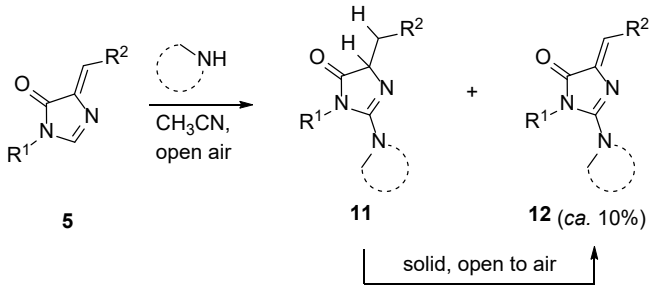

Figure S11. Addition of nucleophiles to the imidazolone scaffold and spontaneous dehydrogenation under open air.

A range of oxidants were tested to transform adduct **11d** to its conjugated counterpart **12d** (Table S7). The use of Iodine or MnO_2 as oxidants resulted in some degradation of imidazolone scaffold via cleavage of the conjugated double bond. This

degradation was consistent with a thorough report by Tsuji *et al*. on the oxidation mechanism of the GFP chromophore[30]. The use of a stoichiometric amounts of TEMPO minimised the observed degradation.

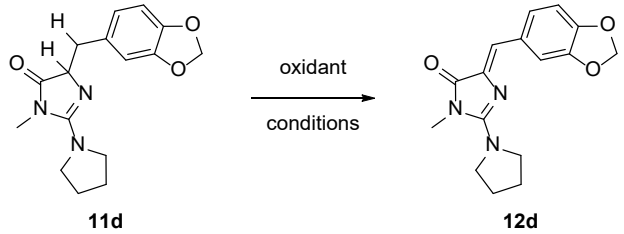

11d **12d**

Table S7. Study of dehydrogenation conditions to convert compound **11d** to compound **12d**. Unless otherwise stated, all reactions were performed under inert atmosphere (argon) for 17 h (overnight).

Entry	Oxidant (eq.)	Solvent	Temperature	Conversion % to **12d** (by LC-MS)
1	Air	$CHCl_3$	rt	10
2[a]	Air	-	rt	10
3	I_2 (1)	$CHCl_3$	rt	75
4	I_2 / TEMPO (1 / 0.1)	$CHCl_3$	rt	87
5	TEMPO (1)	$CHCl_3$	rt	100
6	DDQ (2)	$CHCl_3$	rt	0
7	$FeCl_3$ (3)	$CHCl_3$	rt	0
8	MnO_2 (50)	$CHCl_3$	rt	80
9	H_2O_2 (20)	Water	rt	0
10	H_2O_2 (20)	HFIP	rt	0

[a]**11c** was left as a solid in open air. The conversion did not change after 1 week.

2.2.6. Mechanistic Studies

Mechanistic Considerations on the Formation of Compounds 9

We propose that the formation of coelenterazine analogues **9** starts with the generation of the corresponding imidazolone **5**, which condenses with a second unit of aldehyde **1** to give the imine intermediate **9-imine**. This intermediate then progresses through an intramolecular cyclisation to give coelenterazine tautomer **9'** which finally evolves towards the final coelenterazine adduct **9** (Figure S12A). This process may involve a stepwise tautomerisation through the species **9''** or a direct transformation through a formal 1,5-proton shift involving imine-enamine equilibria, likely via acid-base catalysis.

No reports in the literature were found for the transformation of intermediate **9-imine** to **9'**. We assume that the observed reactivity may be due to the nucleophilic attack of the imidazolone ring upon the activated electrophilic imine moiety. The resonance form depicted in Figure S12B could explain the possible nucleophilic nature of the ring, perhaps via an intramolecular SET process.

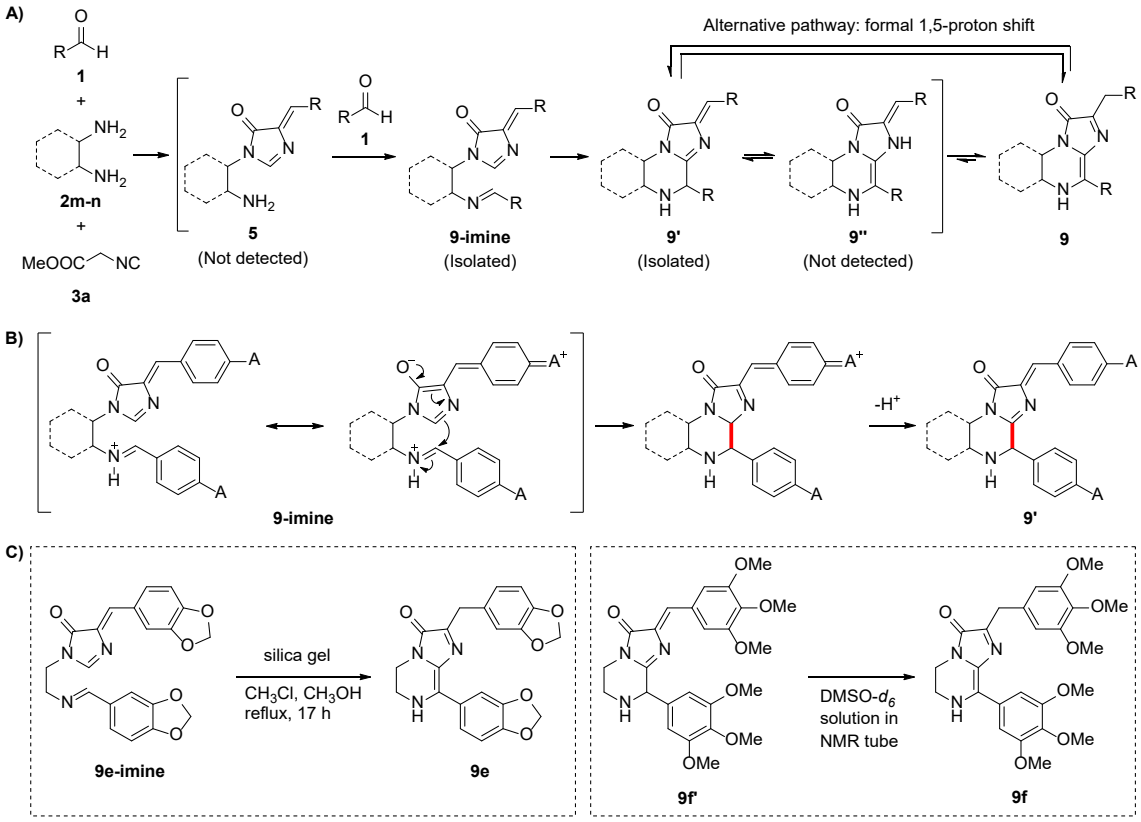

Figure S12. A) Proposed reaction mechanism of the MCR between aldehydes **1**, diamines **2m-n** and methyl isocyanoacetate **3a**. B) Putative transformation of intermediate **9-imine** to **9'**. C) Conversion of intermediates **9e-imine** and **9f'** to the corresponding coelenterazine analogues **9**.

In most cases, the MCR progressed directly to the final adduct **9** under the optimal stoichiometries of 2:1:1 for the reagents **1**, **2** and **3** respectively. However, in the case of piperonal **1k,** the MCR gave the imine intermediate **9e-imine**, and with 3,4,5-trimethoxybenzaldehyde **1i** we isolated the tautomer **9f'**. Notably, in both cases these adducts precipitated from the reaction mixture and were easily isolated by filtration under vacuum. Thus, we propose that precipitation of these intermediates during the reaction stops their progression to their corresponding coelenterazine analogues **9**. Moreover, we observed that when a 1:1:1 ratio of reactants was used with piperonal **1l** or 3,4,5-trimethoxybenzaldehyde **1i**, the isolated products in both cases were the corresponding compounds **9e-f**, and neither one of the intermediates were detected. We believe that in these cases, intermediates **9e-imine** and **9f'** were present in lower concentrations, they did not precipitate from the reaction media and were directly converted to the corresponding compounds **9e-f**. Satisfyingly, we accomplished full conversion of both intermediates **9e-imine** and **9f'** to their respective compounds **9e-f**. Noteworthy, this conversion was only observed when the intermediates were fully dissolved in the reaction mixture (Figure S12C). Moreover, we observed that compound **9f'** spontaneously converted to the coelenterazine analogue **9f** when left to stand in solution (Figure S13A).

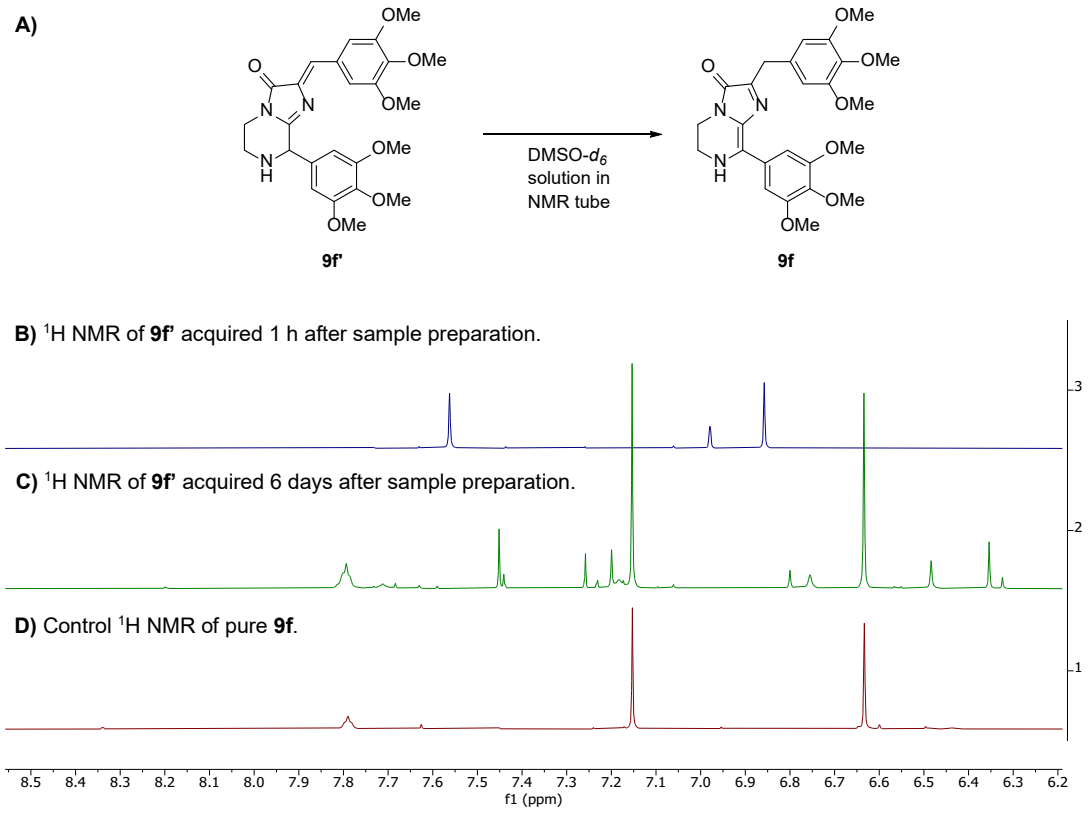

Figure S13. A) Conversion of **9f'** to **9f**. Stacked NMR spectra of B) Compound **9f'** 1 h after sample preparation; C) Compound **9f'** 6 days after sample preparation; D) Pure compound **9f**.

Preliminary computational studies on the conversion of intermediate **9f'** to compound **9f** were consistent with the empirical results. Four possible tautomers of the compounds **9** were modeled in a Spartan suite. We built the structures and minimised the energy with molecular mechanics (MMFF) and semiempirical methods (NMDO) and analysed the equilibrium tautomers. As a model, we used a benzene ring as the aryl substituent to simplify the calculations (Figure S14). We observed a decrease in energy from intermediate **9'** to the coelenterazine analogue **9**.

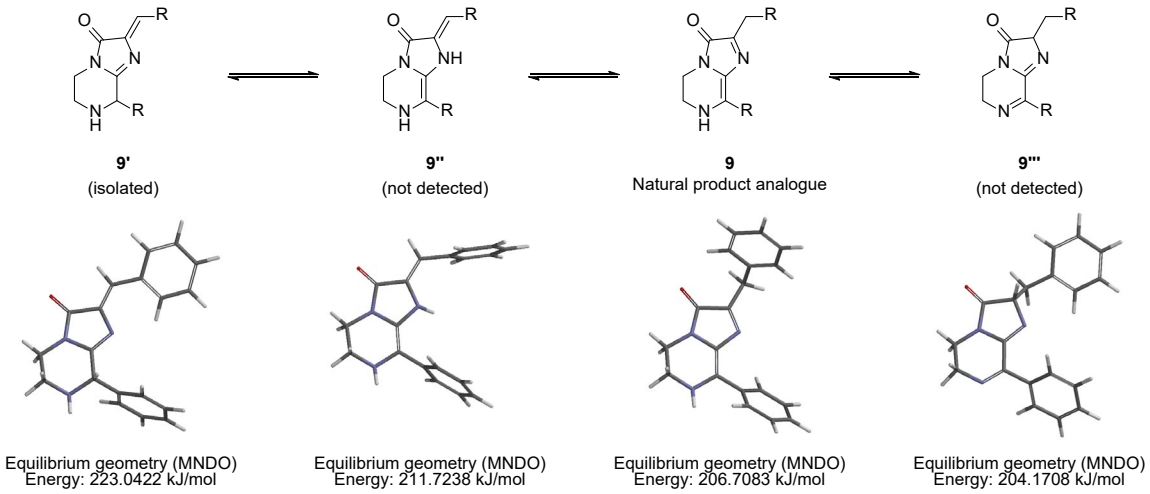

Figure S14. Computational estimated stabilities of the tautomers of coelenterazine analogues **9**.

The following experiment further supported the precipitation hypothesis, as performing the MCR under the standard conditions but in an ultrasonic bath, promoted the precipitation of bis-imine **S7** – a potential by-product of this reaction –, and reduced the conversion to the expected compound **9b** (Figure S15).

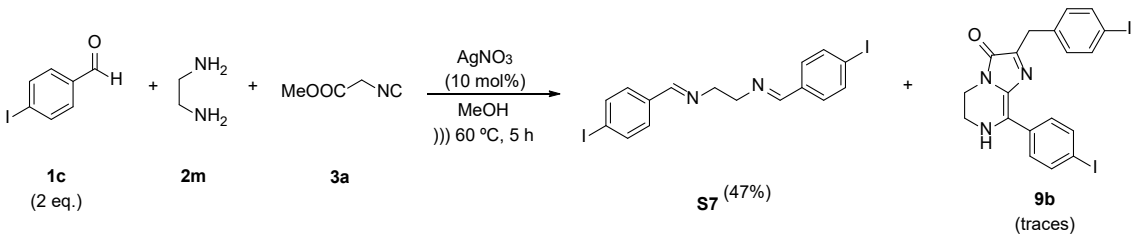

Figure S15. MCR with 4-iodobenzaldehyde **1s**, ethylenediamine **2m**, and methyl isocyanoacetate **3a** in an ultrasonic bath.

Noteworthy, a related MCR reported by Shaabani *et* al. involving carbonyls, diamines, and isocyanides and mediated by acid catalysis yields a similar scaffold.[25] In this case, the transformation starts with the formation of the imine **I** – in equilibrium with its cyclic aminal surrogate **II** – followed by nucleophilic isocyanide attack. The generated nitrilium cation **III** is finally trapped intramolecularly by the free amine to give the final

diaza-heterocycle **IV,** which tautomerizes to the isolated adducts **V** (Figure S16A). Presumably, if the isocyanide input was an isocyanoacetate, this MCR could in principle progress to the formation of our described coelenterazine analogues **9** after lactamisation and incorporation of the second unit of aldehyde *via* a Knoevenagel condensation or vice versa. (Figure S16B). Note that there is one example of this MCR with methyl isocyanoacetate in the literature and it has been reported to give adduct **V**.[25b]

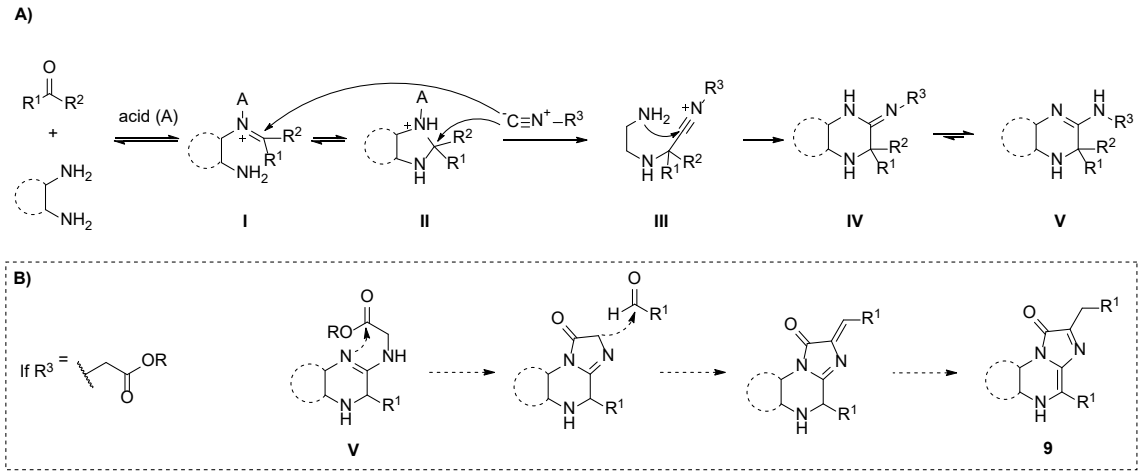

Figure S16. A) Reaction mechanism of the MCR described by Shaabani *et al*. B) Potential evolution of adduct **V** to compound **9** with isocyanoacetates.

To confirm that our MCR does not follow this mechanism, we reproduced Shabaani's conditions by performing our MCR under acid catalysis (Figure S17). We isolated an unstable material in almost quantitative yield, whose structure was assigned to aminal **S8** using ^{1}H NMR, suggesting that isocyanide **3a** does not perform the nucleophilic attack upon the aminal to follow Shabaani's pathway.

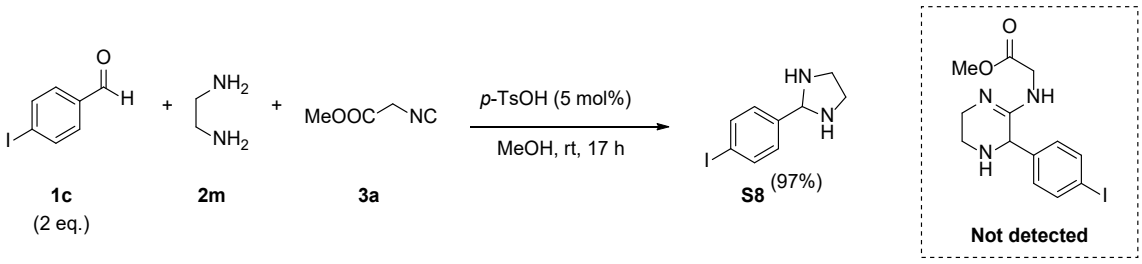

Figure S17. MCR with 4-iodobenzaldehyde **1c**, ethylenediamine **2m**, and methyl isocyanoacetate **3a**.

Moreover, when we changed the isocyanide to cyclohexyl isocyanide – which does not contain an a-acidic position and therefore cannot participate in the Knoevenagel condensation step – the MCR progressed to give the bis-imine **S9** in 86% yield (Figure S18). Thus, we confirmed that silver does not properly catalyse the MCR described by

Shabaani, suggesting that the formation mechanism of our MCR differs from the one previously described.

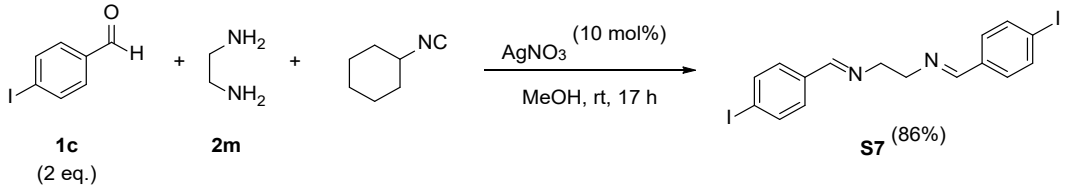

Figure S18. MCR with 4-iodobenzaldehyde **1c**, ethylenediamine **2m**, and cyclohexyl isocyanide **3a**.

Studies on the Addition of Nucleophiles into the Imidazolone Scaffold

Regarding the addition of nucleophilic species into the imidazolones **5**, the productivity of transformation depended on the nucleophilicity of the added species: better nucleophiles reacted at rt while poorer nucleophiles needed thermal activation or did not react at all. This study was consistent with the addition mechanism being of nucleophilic nature (Figure S19A).

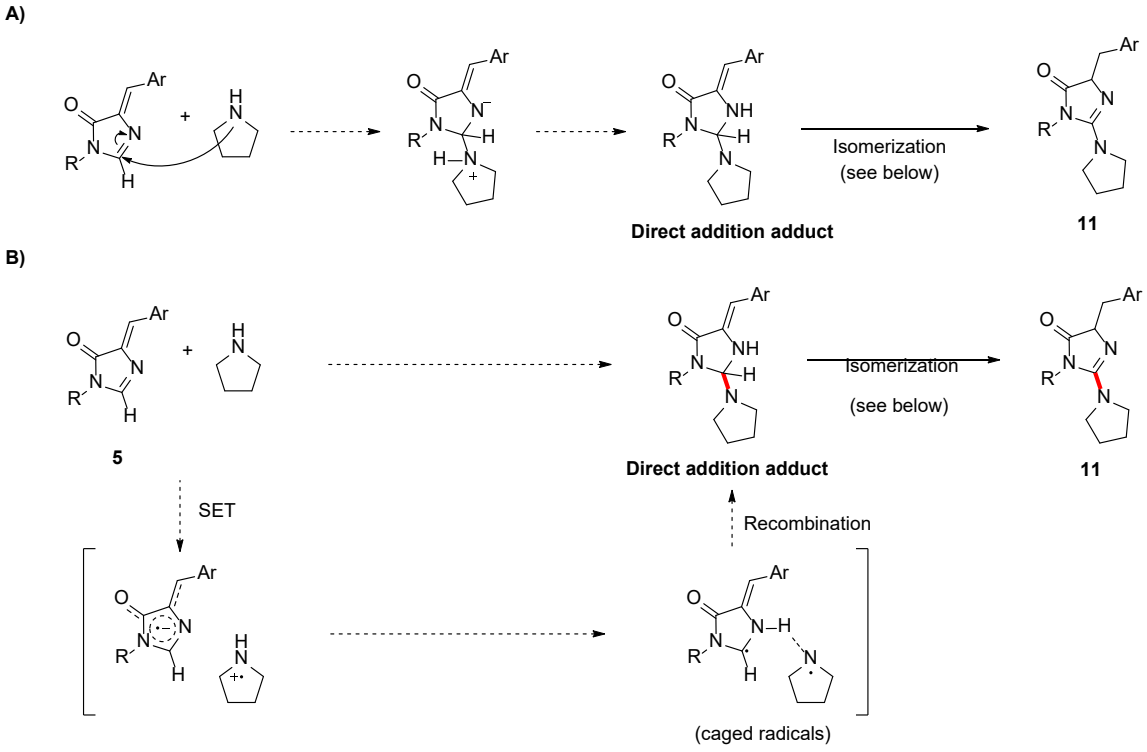

Figure S19. A) Putative ionic mechanism of the addition of nucleophiles to the imidazolone scaffold. B) Participation of complexes and radical intermediates, from SET step.

Interestingly, we observed that upon addition of a nucleophile to a suspension of imidazolone **5** in CH_3CN under argon atmosphere, the mixture quickly turned to a highly intense dark violet color. Moreover, the violet color quickly faded when the reaction was opened to air. This suggested that the transformation may involve radical species (Figure

S19B). A precedent in the literature reported a photocatalysed cross dehydrogenative coupling amination in a similar system.[32] In our case, we established that the transformation was not photocatalysed as the addition still took place when the reaction was performed in the dark, and the presence of a photosensitizer – $Ir(dFppy)_3$ – did not affect the reaction rate or conversion.

We performed a series of experiments to study whether the mechanism of the addition involves a radical process. First, considering the remarkable change in color of the reaction mixture upon addition of a nucleophile, we focused on the detection of the potential occurrence of UV-Vis absorbent charge transfer complex. UV-Vis spectra of all reactants, the product and their combination were recorded to determine whether there were light absorbing species in the reaction mixture (Figure S20). No significant differences were observed in the absorption spectra of the reactant and the reaction mixture. However, it is important to note that the quick loss of coloring after opening the reaction mixture to air – presumably due to radial quenching by atmospheric O_2 – complicated the obtention of representative data.

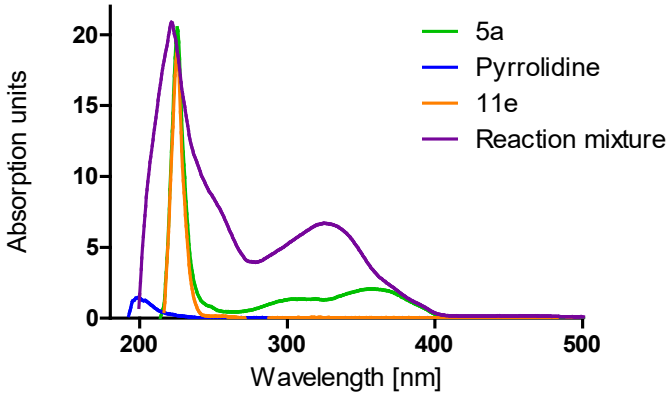

Figure S20. Absorption spectra of the components of the reaction and the reaction mixture.

Next, we focused on trapping the putative radical species, either inter- or intramolecularly. First, we performed the reaction in the presence of the stable radical TEMPO, expecting the reaction to be inhibited by trapping of the putative radical with TEMPO (Figure S21A). However, the product of the reaction was the 2-aminoimidazolone **12e**, suggesting that the addition progressed normally, and TEMPO just acted as an oxidant not trapping the putative radical. Also, we attempted to trap the putative radical species intramolecularly using the adduct **5v** as the substrate. Presumably,

the styrene moiety – a known radical trap – would capture the putative radical to give the fused [5,5] adduct. However, this adduct was not detected (Figure S21B).

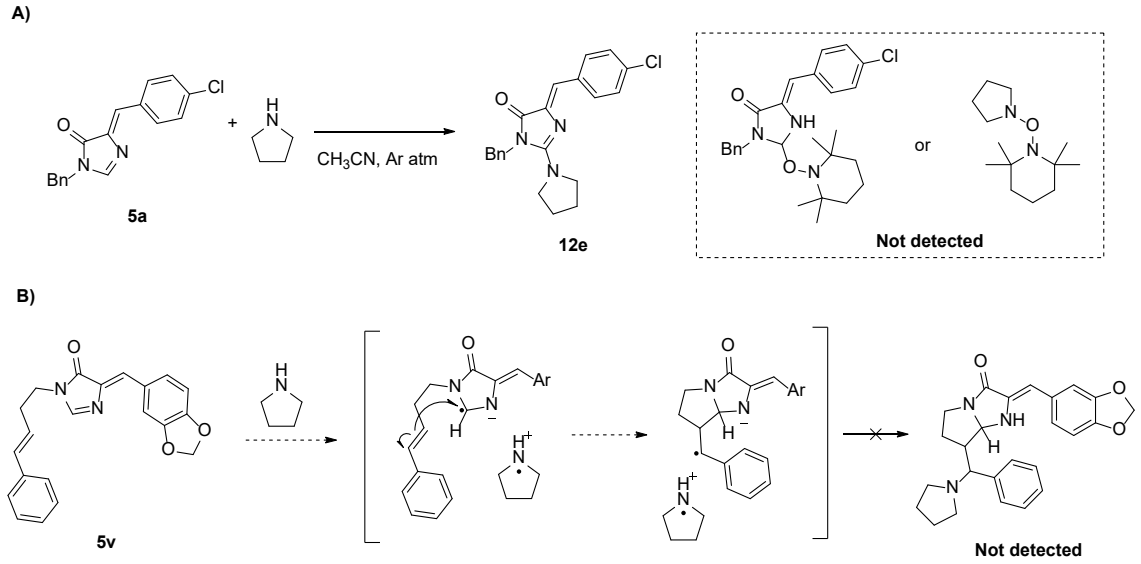

Figure S21. Mechanistic studies on the radical pathway.

Inability to capture the putative radical suggested a very short-lived radical species. Thus, we hypothesised that the use of a spin trap would generate a longer lived radical which could potentially be detected by electron paramagnetic resonance (EPR). According to the proposed hypothesis, the incorporation of DMPO into the reaction mixture would in theory result in the trapping of either the pyrrolidine-DMPO radical or the imidazolone-DMPO radical (Figure S22A). To our delight, we detected a signal, confirming the presence of a radical species in the reaction. The obtained signal was consistent with the pyrrolidine-DMPO radical, as compared with a simulated spectrum from data found in the literature (with morpholine instead of pyrrolidine, Figure S22B).[32]

Experimental procedure for acquiring the EPR spectrum: an EPR tube was purged with cycles of vacuum and argon, and was charged with CH_3CN, compound **5a** (1 eq.), pyrrolidine (10 eq.) and DMPO (20 eq.) and the EPR spectrum was recorded at room temperature. Spectrometer parameters for acquiring spectra: magnetic field, 3520 G with a sweep width of 100 G. A 5.02 mW microwave power at a frequency of 9.858 GHz was used with a modulation amplitude of 2 G and a frequency of 100 kHz. The morpholine-DMPO EPR spectrum was simulated with software from Bruker WIN-EPR system (v 2.22 Rev. 12).

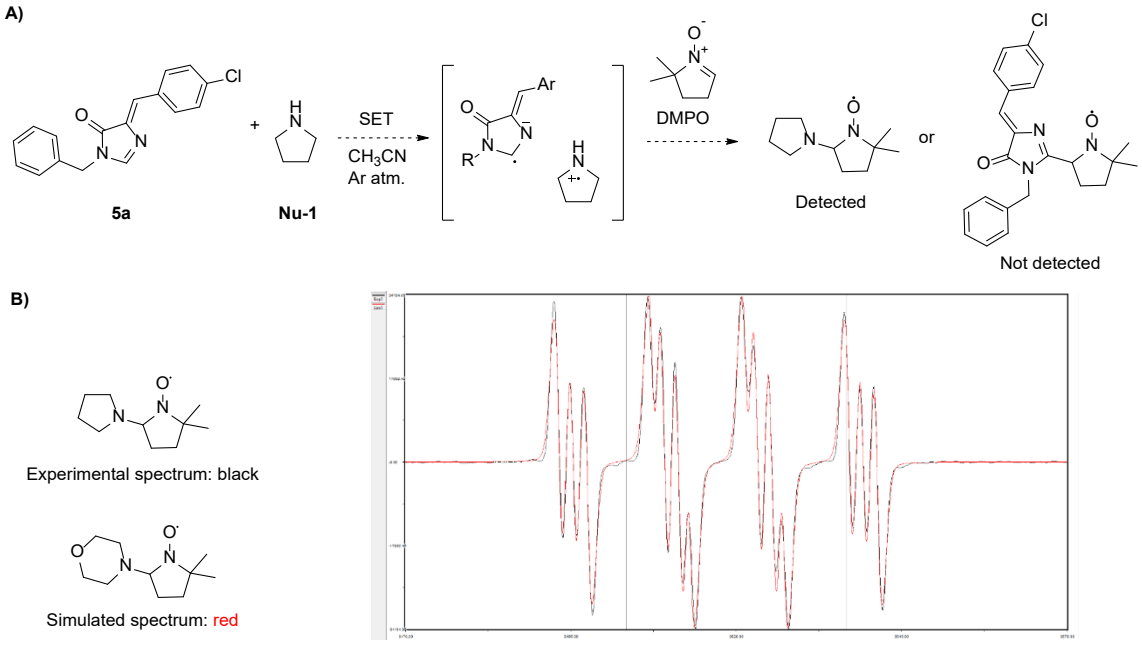

Figure S22. Trapping of the intermediate radical with DMPO.

According to the proposed addition of nucleophiles to the imidazolone **5**, the transformation should result in the direct addition adducts **A**. However, this intermediate was never detected and instead, the reaction readily afforded its tautomer adduct **11**. The structure of compounds **11** was confirmed with spectroscopic methods. Therefore, we hypothesised that after the addition, a series of protic (acid/base) catalysed tautomeric equilibria converts the putative intermediates **A** to the isolated compounds **11**.

We modeled the following adducts and intermediates in a Spartan suite using molecular mechanics and semiempirical method.

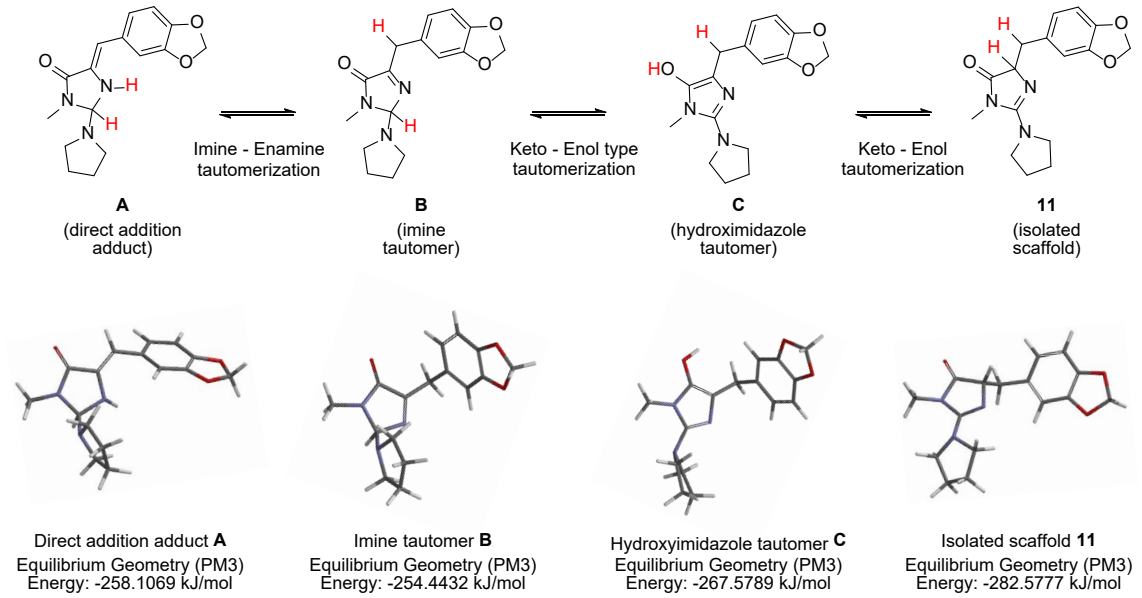

Figure S23. Tautomeric equilibria towards addition product **11** and computationally estimated stabilities.

We built the structures and minimised the energy with molecular mechanics (MMFF) and semi-empirical methods (PM3) and analysed the equilibrium tautomers. We used the addition of pyrrolidine **2z** to adduct **5i** as the model. The computational calculations suggested a decrease in energy in each of the proposed tautomeric equilibria to reach scaffold **11** as the lowest energy structure, being consistent with the proposed hypothesis (Figure S23).

To further study this hypothesis, we performed a series of experiments using deuterated solvents, as well as D-labelled substrate and nucleophile species. We reacted imidazolone **5a** with an excess of pyrrolidine **Nu-1** in protic and non-protic solvents. The performed experiments suggested extensive hydrogen exchange with either the solvent – depending on its nature – or the excess pyrrolidine.

We observed clear differences between protic (methanol) and aprotic (acetonitrile) solvents. In this regard, the experiments with CD_3CN (which does not undergo hydrogen exchange) and non-deuterated pyrrolidine **Nu-1** resulted in the formation of the non-deuterated compound **11e**, even if the substrate was deuterated (Figure S24A) However, the use of CD_3OD (capable of hydrogen exchange) resulted in the obtention of the deuterated adduct **11-*d*$_2$** from non-deuterated reagents (Figure S24B).

Lastly, we detected the triple deuterated adduct **11e-*d*$_3$** by LC-MS after reaction of deuterated imidazolone **5a-*d*** with deuterated pyrrolidine **Nu-1-*d*** in deuterated acetonitrile (CD_3CN). However, after neutral Al_2O_3 flash chromatography we observed replacement of the *a* deuterium for a proton and isolated adduct **11-*d*$_2$** (Figure S24C).

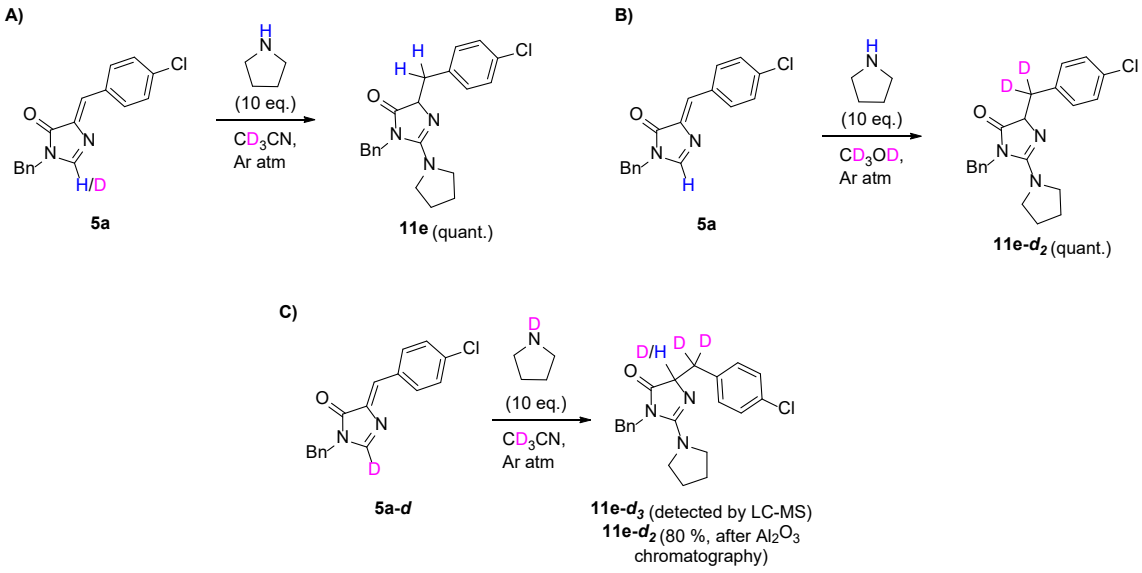

Figure S24. Deuteration experiments.

2.3. Experimental Procedures and Characterisation Data of Selected Compounds

2.3.1. General Synthetic Procedures

General Procedure A: Synthesis of Compounds 4-7 and 9

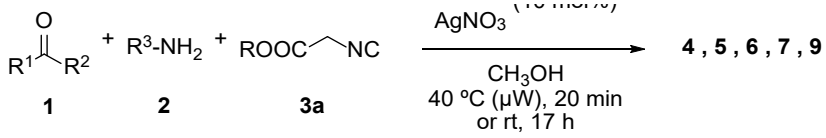

To a mixture of cabonyl **1** (1.1 or 2 eq.), methyl isocyanoacetate **3a** (1 eq.) and $AgNO_3$ (0.1 eq.) in CH_3OH (0.2 M) was added amine **2** (1.1 – 10 eq.). The reaction was either heated to 40 ºC for 20 min under microwave (mW) irradiation (sealed vial) or was stirred at room temperature (rt) for 17 h. After reaction completion (TLC or LC-MS control) the reaction mixture was filtered through Celite® washing with CH_2Cl_2 – to remove the remains of the silver catalyst – and concentrated under reduced pressure to obtain a dark oil. The crude reaction mixture was purified *via* flash chromatography using the indicated solvent system to afford the pure products **4**-**7** and **9**. In the stated cases, compounds **5** or **9** precipitated during the reaction and were collected by filtration under reduced pressure washing with cold MeOH. The solid was dissolved in CH_2Cl_2 and the resulting solution was filtered through Celite® washing with CH_2Cl_2 – to remove the remains of the silver catalyst – and concentrated under reduced pressure to give the pure product **5** or **9**.

General Procedure B: Sequential Synthesis of Compounds 4

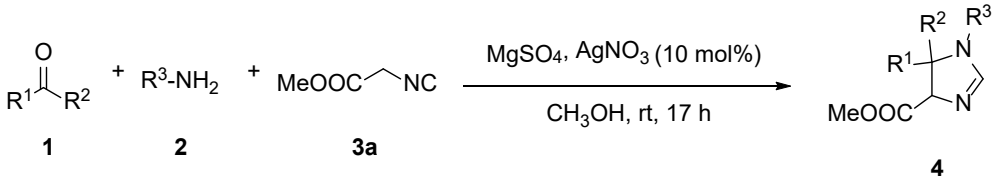

To a solution of aldehyde **1** (1.1 eq.) and amine **2** (1.1 eq.) in CH_3OH (0.2 M) was added $MgSO_4$ (1.5 eq.) and the mixture was stirred at rt for 4 h. After this time, methyl isocyanoacetate **3a** (1 eq.) and $AgNO_3$ (10 mol%) were added as specified, and the reaction was stirred overnight at rt. After reaction completion (TLC control) the mixture was filtered to remove inorganics and the solvent was evaporated under reduced pressure. The residue was absorbed onto silica and purified via silica gel flash chromatography using the indicated solvent system to afford the pure product **4**.

General Procedure C: Synthesis of Compounds 8

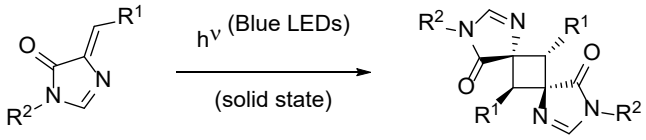

5 **8**

Compound **5** was placed as a solid – in a vial or round bottom flask – under irradiation with a Blue LEDs strip for 12 – 17 h (until analysis by TLC or LC-MS suggested full conversion) to give the pure product **8** without the need for purification.

General Procedure D: Synthesis of Compounds 12a-c

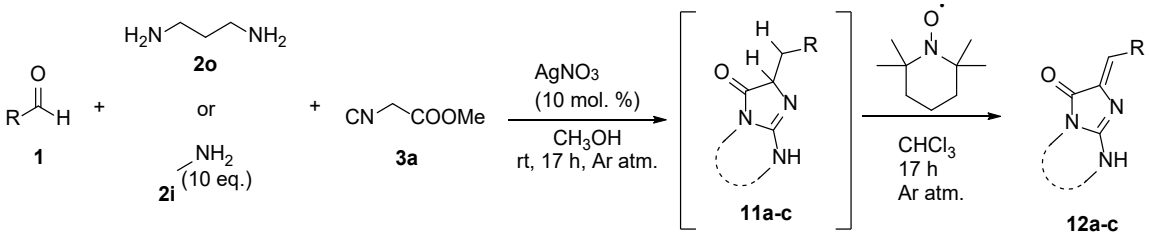

(i) To a mixture of aldehyde **1** (1.1 eq.), methyl isocyanoacetate **3a** (1 eq.), and $AgNO_3$ (0.1 eq.) in CH_3OH (0.2 M) under argon atmosphere was added 1,3-diaminopropane **2o** (1.1 eq.) or a 9.8 M solution of methylamine **2i** in MeOH (10 eq.). The reaction was stirred at room temperature (rt) for 17 h. After reaction completion (LC-MS control), the reaction mixture was filtered through a pad of Celite® washing with CH_2Cl_2. The filtrate was extracted with a 0.5 N aqueous HCl solution (3x). The aqueous layers were combined, basified to pH = 9 and extracted with CH_2Cl_2 (3x). The organic layers were combined, washed with saturated brine, dried over Na_2SO_4, filtered, and concentrated under reduced pressure to give intermediates **11a-c**. Intermediates **11a-c** contained traces of compounds **12a-c** and were used in the next step without further purification.

(ii) To a solution of intermediate **11a-c** (1 eq.) in dry CH_3Cl (0.1 M) under argon atmosphere was added TEMPO (2 eq.) and the reaction was stirred at room temperature (rt) for 17 h. The pure products **12a-c** precipitated from the reaction mixture and were collected by filtration under reduced pressure washing with cold $CHCl_3$.

General Procedure E: Synthesis of Compounds 12d-h and 13

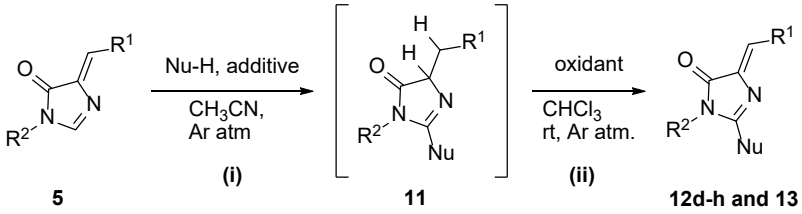

(i) To a suspension of **5** (1 eq.) in CH_3CN (0.1 M) under argon atmosphere was added the corresponding nucleophile (1.1 – 10 eq.) and an additive when specified. Upon addition the mixture turned to a dark purple solution. The reaction was stirred at the indicated temperature for 17 h. After reaction completion (TLC or LC-MS control) the solvent was evaporated under reduced pressure and the excess nucleophile was removed by evaporation under reduced pressure or *via* aqueous work-up, to give the corresponding intermediate **11**. In most cases, intermediates **11** were only checked by LC-MS and directly subjected to the dehydrogenation protocol. Compounds **11d-e** and **11j** were characterised without the need for further purification.

(ii) To a solution of intermediate **11** (1 eq.) in dry CH_3Cl (0.1 M) under argon atmosphere was added the indicated oxidant and the reaction was stirred at room temperature until analysis by LC-MS suggested consumption of starting material. The appropriate work-up was performed according to the oxidant used in each case. The crude product was purified *via* neutral Al_2O_3 flash chromatography using the indicated solvent system to afford the pure products **12d-h** and **13**.

Experimental procedures according to the oxidant used:

TEMPO: TEMPO (2 eq.) was added to a solution of **5** in $CHCl_3$ under argon atmosphere. After reaction completion (LC-MS control), the reaction was diluted with CH_2Cl_2 and washed with a 1:1 mixture of a saturated aqueous solution of $Na_2S_2O_3$ and a saturated aqueous solution of Na_2CO_3. The organic layer was washed with saturated brine, dried over Na_2SO_4, filtered, and concentrated under reduced pressure to afford the crude product.

I_2 / TEMPO: A solution of I_2 (0.9 eq.) in $CHCl_3$ and TEMPO (0.1 eq.) were added to a solution of **5** in $CHCl_3$ under argon atmosphere. After reaction completion (LC-MS control), the reaction was diluted with CH_2Cl_2 and washed with a 1:1 mixture of a saturated aqueous solution of $Na_2S_2O_3$ and a saturated aqueous solution of Na_2CO_3. The

organic layer was washed with saturated brine, dried over Na_2SO_4, filtered, and concentrated under reduced pressure to afford the crude product.

MnO_2: MnO_2 (50 eq.) was added to a solution of **5** in $CHCl_3$ under argon atmosphere. After reaction completion (LC-MS control), the reaction was filtered through a pad of Celite® washing with CH_2Cl_2. The filtrate was concentrated under reduced pressure to afford the crude product.

General Procedure F: Synthesis of Compounds 14

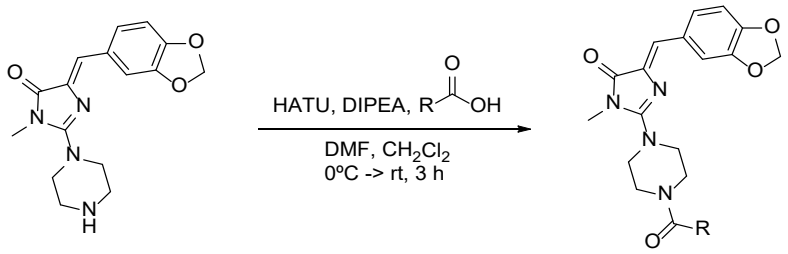

12j **14**

A Schlenk flask in an ice bath was charged with DMF (0.1 M), the corresponding carboxylic acid (1.2 eq.), HATU (1.2 eq.), and DIPEA (4 eq.). The reaction was purged with cycles of vacuum and argon, was allowed to warm up to rt and was stirred for 1 h. After this time the reaction was cooled to 0 ºC and a solution of **12j** (1 eq.) in CH_2Cl_2 (0.2 M) was added dropwise. The reaction was allowed to warm up to rt and was stirred for 2 h. The reaction was diluted with CH_2Cl_2 and washed with a saturated aqueous Na_2CO_3 solution and saturated brine. The organic layer was dried over Na_2SO_4, filtered, and concentrated under reduced pressure. The crude product was purified *via* neutral Al_2O_3 flash chromatography using the indicated solvent system to afford the pure product **14**.

Special Case I: Synthesis of Compound 10

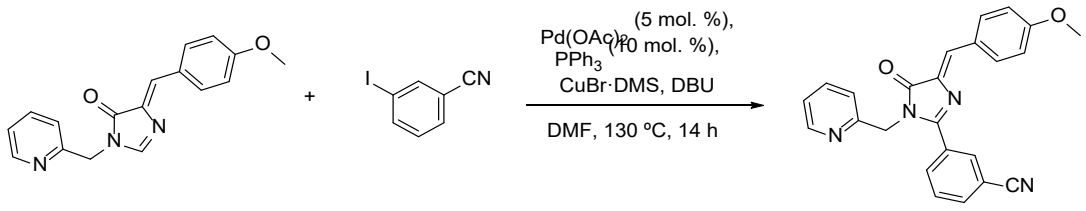

5e **10**

The title compound **10** was synthesised following a protocol described in the literature.[26]

A Schlenk tube was sequentially charged with **5e** (1 eq.), $Pd(OAc)_2$ (0.05 eq.), PPh_3 (0.1 eq.), DBU (1 eq.), CuBr·DMS (1 eq.), and a solution of 3-iodobenzonitrile (1 eq.) in DMF (0.05 M). The reaction was purged with cycles of argon and vacuum (3x)

and was heated to 130 ºC and stirred for 14 h. After reaction completion (TLC control), the reaction mixture diluted with CH_2Cl_2 was filtered through Celite® washing with CH_2Cl_2. The filtrate was washed with a 10% aqueous NH_3 solution (3x) and saturated brine. The organic layer was dried over Na_2SO_4, filtered, and concentrated under reduced pressure. The crude product was purified *via* silica gel flash chromatography (EtOAc/hexane gradient from 0:100 to 50:50 v/v) to afford the pure product **10**.

Special Case II: Synthesis of Compound 12j

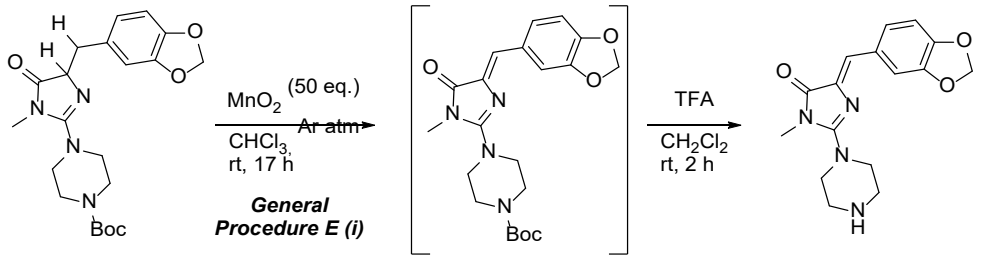

To a solution of **11j** (1 eq.) in dry $CHCl_3$ (0.1 M) was added MnO_2 (50 eq.) and the reaction was stirred at rt for 17 h. After reaction completion (LC-MS control), the inorganics were filtered with a pad of Celite® washing with CH_2Cl_2. The filtrate was concentrated under reduced pressure to give the intermediate **Boc-12j** which was not isolated. The crude product was dissolved in CH_2Cl_2 (0.1 M) and was added TFA (100 eq.) and the reaction was stirred at rt for 2h, until analysis by TLC suggested consumption of starting material. The reaction mixture was partitioned between CH_2Cl_2 and water. The aqueous layer (containing the ionised title compound **12j**) was basified by the portion wise addition of solid Na_2CO_3 until pH = 11 and was extracted with CH_2Cl_2 (3x). The combined organic layers were washed with saturated brine, dried over Na_2SO_4, filtered, and concentrated under reduced pressure to afford the title compound **12j**.

2.3.2. Characterisation Data of Isolated Compounds

Methyl 1-benzyl-5-(4-chlorophenyl)-4,5-dihydro-1*H*-imidazole-4-carboxylate (4a)

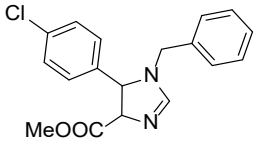

Following *General Procedure B*, compound **4a** was obtained as a pale brown oil (500 mg, 76%) from **1a** (309 mg, 2.2 mmol), **2a** (235 mL, 2.2 mmol), **3a** (181 mL, 2

mmol), Mg_2SO_4 (361 mg, 3 mmol) and $AgNO_3$ (34 mg, 0.2 mmol) in CH_3OH (10 mL) after flash chromatography purification ($MeOH/CH_2Cl_2$ gradient from 0:100 to 10:90 v/v). Compound **4a** was obtained as an 85 : 15 mixture of *trans* : *cis* diastereomers. NMR data reported of the major diastereomer. **^{1}H NMR** (400 MHz, $CDCl_3$) δ 7.36 – 7.28 (m, 5H), 7.25 – 7.21 (m, 2H), 7.12 (dd, *J* = 4.7, 2.0 Hz, 2H), 7.09 (d, *J* = 1.6 Hz, 1H), 4.66 (d, *J* = 9.5 Hz, 1H), 4.52 (dd, *J* = 9.5, 1.9 Hz, 1H), 4.40 (d, *J* = 15.0 Hz, 1H), 3.95 (d, *J* = 14.9 Hz, 1H), 3.75 (s, 3H). **^{13}C NMR** (101 MHz, $CDCl_3$) δ 171.90, 156.85, 138.16, 135.31, 134.12, 129.21, 128.89, 128.71, 128.06, 128.02, 78.05, 64.88, 52.57, 49.27. **HRMS:** *m/z* calcd. for $C_{18}H_{18}ClN_2O_2^+$ $[M+H]^+$: 329.1051; found: 329.1052.

Methyl (1r,3r,5r,7r)-3'-benzyl-3',5'-dihydrospiro[adamantane-2,4'-imidazole]-5'-carboxylate (4ac)

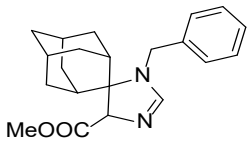

Following *General Procedure A* under mW irradiation, compound **4ac** was obtained as a pale brown oil (270 mg, 40%) from **1ac** (330 mg, 2.2 mmol), **2a** (240 mL, 2.2 mmol), **3a** (181 mL, 2 mmol) and $AgNO_3$ (34 mg, 0.2 mmol) in CH_3OH (10 mL) after flash chromatography purification (EtOAc/hexane gradient from 0:100 to 100:0 v/v). **^{1}H NMR** (400 MHz, $CDCl_3$) δ 7.48 – 7.42 (m, 2H), 7.40 – 7.33 (m, 2H), 7.31 – 7.27 (m, 1H), 6.93 (d, *J* = 1.1 Hz, 1H), 4.85 (s, 2H), 4.79 (d, *J* = 1.1 Hz, 1H), 3.73 (s, 3H), 2.25 – 2.14 (m, 4H), 2.02 – 1.96 (m, 1H), 1.95 – 1.89 (m, 1H), 1.86 – 1.81 (m, 1H), 1.80 – 1.77 (m, 1H), 1.76 – 1.69 (m, 4H), 1.66 – 1.60 (m, 1H), 1.53 – 1.46 (m, 1H). **^{13}C NMR** (101 MHz, $CDCl_3$) δ 171.50, 160.40, 139.30, 128.59, 127.33, 126.96, 76.37, 71.99, 51.86, 51.74, 38.79, 37.44, 36.26, 35.15, 33.59, 32.76, 31.21, 26.80, 26.60. **HRMS:** *m/z* calcd. for $C_{21}H_{27}N_2O_2^+$ $[M+H]^+$: 339.2067; found: 339.2078.

Compound **4ac** was isolated from the same reaction mixture as compound **5ac**.

(*Z*)-3-Benzyl-5-(4-chlorobenzylidene)-3,5-dihydro-4*H*-imidazol-4-one (5a)

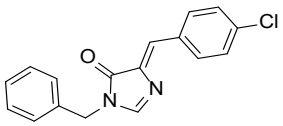

Following *General Procedure A* under mW irradiation, compound **5a** was obtained as a golden colored solid (0.95 g, 47%) from **1a** (1.02 g, 7.3 mmol), **2a** (793 mL,

7.3 mmol), **3a** (600 mL, 6.6 mmol) and $AgNO_3$ (112 mg, 0.66 mmol) in CH_3OH (20 mL, 0.33 M). The product precipitated from the reaction mixture and was isolated by filtration under reduced pressure. **^{1}H NMR** (400 MHz, DMSO-*d6*) δ 8.44 (d, *J* = 1.7 Hz, 1H), 8.29 (d, *J* = 8.6 Hz, 2H), 7.56 (d, *J* = 8.7 Hz, 2H), 7.46 – 7.38 (m, 2H), 7.38 – 7.30 (m, 3H), 7.22 (d, *J* = 1.7 Hz, 1H), 4.84 (s, 2H). **^{13}C NMR** (101 MHz, DMSO-d_6) δ 169.55, 156.66, 139.41, 137.14, 135.70, 134.33, 133.09, 129.35, 129.22, 128.17, 127.90, 127.42, 44.66. **HRMS**: *m/z* calcd. for $C_{17}H_{14}ClN_2O^+$ $[M+H]^+$: 297.0789; found: 297.0797.

(*Z*)-3-Benzyl-5-(4-chlorobenzylidene)-3,5-dihydro-4*H*-imidazol-4-one-2-*d* (5a-*d*)

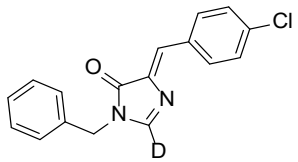

Following *General Procedure A* under mW irradiation, compound **5a** was obtained as a golden colored solid (850 mg, 47%) from **1a** (0.93 mg, 6.6 mmol), **2a-*d*$_2$** (734 mL, 6.6 mmol), **3a** (544 mL, 6 mmol) and $AgNO_3$ (102 mg, 0.6 mmol) in CD_3OD (20 mL, 0.3 M). The product precipitated from the reaction mixture and was isolated by filtration under reduced pressure. **^{1}H NMR** (500 MHz, $CDCl_3$) δ 8.09 – 8.05 (m, 2H), 7.41 – 7.38 (m, 2H), 7.38 – 7.31 (m, 3H), 7.30 – 7.27 (m, 2H), 7.20 (s, 1H), 4.77 (s, 2H). **^{13}C NMR** (126 MHz, $CDCl_3$) δ 168.49, 152.11 (t), 137.69, 135.84, 134.36, 132.63, 131.23, 128.24, 128.11, 128.08, 127.34, 126.77, 44.00. **HRMS:** *m/z* calcd. for $C_{17}H_{13}DClN_2O^+$ $[M+H]^+$: 298.0852; found: 298.0851.

(*Z*)-3-(3-iodobenzyl)-5-(4-methoxybenzylidene)-3,5-dihydro-4*H*-imidazol-4-one (5d)

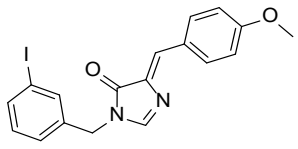

Following *General Procedure A* under mW irradiation, compound **5d** was obtained as a dark yellow solid (565 mg, 45%) from **1e** (402 mL, 3.3 mmol), **2d** (440 mL, 3.3 mmol), **3a** (272 mL, 3 mmol) and $AgNO_3$ (51 mg, 0.3 mmol) in CH_3OH (10 mL, 0.3 M) after flash chromatography purification (EtOAc/hexane gradient from 0:100 to 40:60 v/v). **^{1}H NMR** (400 MHz, DMSO-d_6) δ 8.30 (d, *J* = 1.6 Hz, 1H), 8.26 – 8.17 (m, 2H), 7.71 (t, *J* = 1.8 Hz, 1H), 7.70 – 7.64 (m, 1H), 7.36 – 7.29 (m, 1H), 7.17 (t, *J* = 7.8 Hz, 1H), 7.13 (d, *J* = 1.7 Hz, 1H), 7.08 – 7.01 (m, 2H), 4.75 (s, 2H), 3.83 (s, 3H). **^{13}C NMR** (101 MHz, DMSO-d_6) δ 169.57, 161.86, 154.53, 139.92, 136.89, 136.86, 136.51, 134.92,

131.37, 129.42, 127.39, 126.86, 114.92, 95.52, 55.89, 43.88. **HRMS:** *m/z* calcd. for $C_{18}H_{16}IN_2O_2^+$ $[M+H]^+$: 419.0251; found: 419.0252.

(*R,Z*)-5-(4-Methoxybenzylidene)-3-(1-phenylethyl)-3,5-dihydro-4*H*-imidazol-4-one (5f)

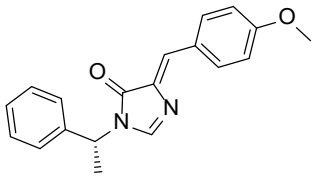

Following *General Procedure A* at rt, compound **5f** was obtained as a yellow solid (140 mg, 45%) from **1e** (134 mL, 1.1 mmol) **2e** (140 mL, 1.1 mmol), **3a** (91 mL, 1 mmol) and $AgNO_3$ (17 mg, 0.1 mmol) in CH_3OH (5 mL) after flash chromatography purification (EtOAc/hexane gradient from 0:100 to 20:80 v/v). **^{1}H NMR** (400 MHz, DMSO-*d*$_6$) δ 8.45 (d, *J* = 1.7 Hz, 1H), 8.21 (d, *J* = 9.1 Hz, 2H), 7.42 – 7.24 (m, 5H), 7.12 (d, *J* = 1.6 Hz, 1H), 7.04 (d, *J* = 9.1 Hz, 2H), 5.24 (q, *J* = 7.2 Hz, 1H), 3.83 (s, 3H), 1.73 (d, *J* = 7.3 Hz, 3H). **^{13}C NMR** (101 MHz, DMSO-*d*$_6$) δ 169.13, 161.78, 153.03, 141.85, 137.46, 134.85, 129.17, 129.07, 128.06, 126.98, 126.68, 114.91, 55.87, 50.95, 20.13. **HRMS:** *m/z* calcd. for $C_{19}H_{19}N_2O_2^+$ $[M+H]^+$: 307.1441; found: 307.1440.

(*Z*)-5-(2-(allyloxy)benzylidene)-3-(4-methylbenzyl)-3,5-dihydro-4*H*-imidazol-4-one (5g)

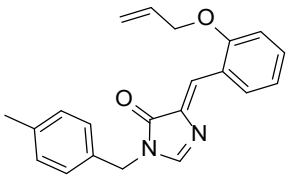

Following *General Procedure A* under mW irradiation, compound **5g** was obtained as a yellow solid (150 mg, 43%) from **1h** (178 mg, 1.1 mmol), **2b** (140 mL, 1.1 mmol), **3a** (91 mL, 1 mmol) and $AgNO_3$ (17 mg, 0.1 mmol) in CH_3OH (5 mL) after flash chromatography purification (EtOAc/hexane gradient from 0:100 to 30:70 v/v). **^{1}H NMR** (400 MHz, $CDCl_3$) δ 8.68 (dd, *J* = 7.9, 1.7 Hz, 1H), 7.90 (d, *J* = 1.7 Hz, 1H), 7.67 (d, *J* = 1.8 Hz, 1H), 7.34 (ddd, *J* = 8.7, 7.3, 1.8 Hz, 1H), 7.22 – 7.14 (m, 5H), 7.05 – 6.98 (m, 1H), 6.89 (dd, *J* = 8.4, 1.1 Hz, 1H), 6.08 (ddt, *J* = 17.3, 10.4, 5.2 Hz, 1H), 5.43 (dq, *J* = 17.3, 1.6 Hz, 1H), 5.31 (dq, *J* = 10.2, 1.2 Hz, 1H), 4.73 (s, 2H), 4.63 (dt, *J* = 5.2, 1.6 Hz, 2H), 2.34 (s, 3H). **^{13}C NMR** (101 MHz, $CDCl_3$) δ 169.64, 158.41, 152.61, 138.05, 138.03, 133.26, 132.85, 132.65, 132.28, 129.72, 127.83, 125.11, 123.12, 121.06, 117.91, 112.03,

69.28, 44.77, 21.14. **HRMS:** *m/z* calcd. for $C_{21}H_{21}N_2O_2^+$ $[M+H]^+$: 333.1598; found: 333.1600.

(*Z*)-3-Benzyl-5-(4-(benzyloxy)benzylidene)-3,5-dihydro-4*H*-imidazol-4-one (5h)

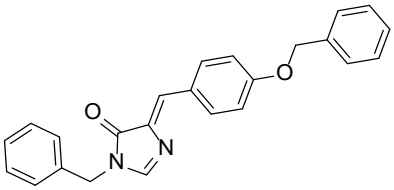

Following *General Procedure A* at rt, compound **5h** was obtained as a yellow solid (171 mg, 44%) from **1d** (234 mg, 1.1 mmol), **2a** (120 mL, 1.1 mmol), **3a** (91 mL, 1 mmol) and $AgNO_3$ (17 mg, 0.1 mmol) in CH_3OH (5 mL) after flash chromatography purification (EtOAc/hexane gradient from 0:100 to 20:80 v/v). **^{1}H NMR** (400 MHz, DMSO-*d*$_6$) δ 8.34 (d, *J* = 1.6 Hz, 1H), 8.26 (d, *J* = 8.9 Hz, 2H), 7.55 – 7.48 (m, 2H), 7.48 – 7.38 (m, 5H), 7.18 (d, *J* = 1.5 Hz, 1H), 7.16 (d, *J* = 8.8 Hz, 2H), 5.23 (s, 2H), 4.83 (s, 2H). **^{13}C NMR** (101 MHz, DMSO-*d*$_6$) δ 169.57, 160.88, 154.79, 137.37, 137.12, 137.05, 134.86, 129.20, 129.10, 128.96, 128.47, 128.32, 128.11, 127.87, 127.12, 115.70, 69.90, 44.55. **HRMS:** *m/z* calcd. for $C_2H_{21}N_2O_2^+$ $[M+H]^+$: 369.1598; found: 369.1601.

Crystals suitable for single X-ray diffraction were grown by slow diffusion of Et_2O into a CH_2Cl_2 solution of the pure compound **5h** through layering.

(*Z*)-5-(Benzo[d][1,3]dioxol-5-ylmethylene)-3-methyl-3,5-dihydro-4*H*-imidazol-4-one (5i)

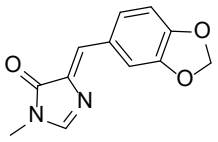

Following *General Procedure A* under mW irradiation, compound **5i** was obtained as a brown solid (2.05 g, 87%) from **1k** (1.65 g, 11 mmol), **2i** (9.8 M solution in MeOH, 1.1 mL, 11 mmol), **3a** (0.91 mL, 10 mmol) and $AgNO_3$ (170 mg, 1 mmol) in CH_3OH (20 mL, 0.5 M). The product precipitated from the reaction mixture and was isolated by filtration under reduced pressure. **^{1}H NMR** (400 MHz, $CDCl_3$) δ 7.90 (d, *J* = 1.7 Hz, 1H), 7.62 (d, *J* = 1.7 Hz, 1H), 7.37 (dd, *J* = 8.1, 1.7 Hz, 1H), 7.07 (d, *J* = 1.7 Hz, 1H), 6.78 (d, *J* = 8.1 Hz, 1H), 5.95 (s, 2H), 3.16 (s, 3H). **^{13}C NMR** (101 MHz, $CDCl_3$) δ 170.15, 152.82, 150.12, 148.27, 136.78, 130.57, 129.16, 128.36, 111.40, 108.59, 101.66, 27.74. **HRMS:** *m/z* calcd. for $C_{12}H_{11}N_2O_3^+$ $[M+H]^+$: 231.0764; found: 231.0762.

(*Z*)-5-(4-(Dimethylamino)benzylidene)-3-methyl-3,5-dihydro-4*H*-imidazol-4-one (5j)

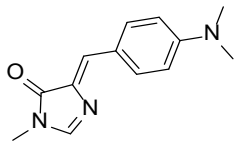

Following *General Procedure A* under mW irradiation, compound **5j** was obtained as an orange solid (0.92 g, 76%) from **1j** (789 mg, 5.8 mmol), **2i** (9.8 M solution in MeOH, 594 mL, 5.8 mmol), **3a** (480 mL, 5.3 mmol) and $AgNO_3$ (95 mg, 0.5 mmol) in CH_3OH (15 mL, 0.35 M). The product precipitated from the reaction mixture and was isolated by filtration under reduced pressure. **^{1}H NMR** (400 MHz, $CDCl_3$) δ 8.08 – 8.02 (m, 2H), 7.60 (d, *J* = 1.6 Hz, 1H), 7.19 (d, *J* = 1.6 Hz, 1H), 6.72 – 6.66 (m, 2H), 3.22 (s, 3H), 3.05 (s, 6H). **^{13}C NMR** (101 MHz, $CDCl_3$) δ 170.16, 151.95, 150.49, 134.73, 134.33, 132.03, 121.84, 111.73, 40.04, 27.68. **HRMS:** *m/z* calcd. for $C_{13}H_{16}N_3O^+$ $[M+H]^+$: 230.1288; found: 230.1286.

(*Z*)-3-(4-chlorobenzyl)-5-(thiophen-2-ylmethylene)-3,5-dihydro-4*H*-imidazol-4-one (5l)

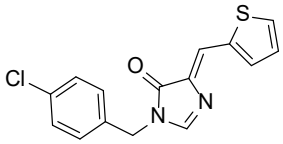

Following *General Procedure A* at rt, compound **5l** was obtained as a yellow solid (250 mg, 83%) from **1l** (93 mg, 1.1 mmol), **2c** (134 mL, 1.1 mmol), **3a** (91 mL, 1 mmol) and $AgNO_3$ (17 mg, 0.1 mmol) in CH_3OH (5 mL) after flash chromatography purification (EtOAc/hexane gradient from 0:100 to 25:75 v/v). **^{1}H NMR** (400 MHz, $CDCl_3$) δ 7.60 (d, *J* = 5.1, 1H), 7.59 (s, 1H), 7.48 (d, *J* = 3.7 Hz, 1H), 7.44 (s, 1H), 7.27 (d, *J* = 8.5 Hz, 2H), 7.16 (d, *J* = 8.5 Hz, 1H), 7.05 (dd, *J* = 5.1, 3.7 Hz, 1H), 4.67 (s, 2H). **^{13}C NMR** (101 MHz, $CDCl_3$) δ 168.79, 151.37, 137.33, 135.86, 135.66, 134.96, 134.27, 134.10, 129.27, 129.11, 127.77, 124.57, 44.39. **HRMS:** *m/z* calcd. for $C_{15}H_{12}ClN_2OS^+$ $[M+H]^+$: 303.0353; found: 303.0359.

(*Z*)-5-(4-((*tert*-Butyldimethylsilyl)oxy)benzylidene)-3-(4-methylbenzyl)-3,5-dihydro-4*H*-imidazol-4-one (5n)

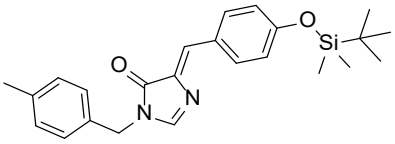

Following *General Procedure A* at rt, compound **5n** was obtained as a pale-yellow solid (185 mg, 43%) from **1g** (236 mg, 1.1 mmol), **2b** (140 mL, 1.1 mmol), **3a** (91 mL, 1 mmol) and $AgNO_3$ (17 mg, 0.1 mmol) in CH_3OH (5 mL) after flash chromatography purification (EtOAc/hexane gradient from 0:100 to 30:70 v/v). **^{1}H NMR** (400 MHz, $CDCl_3$) δ 8.05 (d, *J* = 8.5 Hz, 2H), 7.65 (s, 1H), 7.24 (s, 1H), 7.17 (s, 4H), 6.88 (d, *J* = 8.4 Hz, 2H), 4.73 (s, 2H), 2.34 (s, 3H), 0.98 (s, 9H), 0.23 (s, 6H). **^{13}C NMR** (101 MHz, $CDCl_3$) δ 169.62, 158.57, 151.93, 138.08, 136.57, 134.55, 132.58, 131.01, 129.73, 127.81, 127.25, 120.62, 44.76, 25.63, 21.13, 18.29, -4.32. **HRMS:** *m/z* calcd. for $C_{24}H_{31}N_2O_2Si^+$ $[M+H]^+$: 407.2149; found: 407.2150.

(*Z*)-5-(4-Hydroxybenzylidene)-3-(4-methylbenzyl)-3,5-dihydro-4*H*-imidazol-4-one (5n')

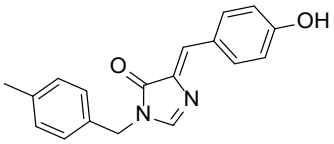

To a 0 ºC solution of compound **5n** (52 mg, 0.13 mmol, 1 eq.) in THF (1.5 mL) was added a solution of TBAF·$3H_2O$ (60 mg, 0.19 mmol, 1.5 eq.) in THF (0.5 mL). The reaction was stirred at 0 ºC for 30 min. After consumption of starting material (TLC control), the reaction was quenched with the addition of water (20 mL) and the mixture was partitioned between EtOAc (60 mL) and water. The organic layer was washed with saturated NH_4Cl aqueous solution (3 x 20 mL) and saturated brine, dried over Na_2SO_4, filtered, and concentrated under reduced pressure to afford the title compound **5n'** as a yellow solid (33 mg, 91%). **^{1}H NMR** (400 MHz, DMSO-d_6) δ 10.23 (s, 1H), 8.21 (s, 1H), 8.10 (d, *J* = 8.4 Hz, 2H), 7.22 – 7.13 (m, 4H), 7.07 (s, 1H), 6.85 (d, *J* = 8.8, 2H), 4.71 (s, 2H), 2.27 (s, 3H). **^{13}C NMR** (101 MHz, DMSO-d_6) δ 169.52, 160.71, 154.06, 137.32, 136.33, 135.17, 134.42, 129.71, 129.64, 127.89, 125.46, 116.36, 44.25, 21.14. **HRMS:** *m/z* calcd. for $C_{18}H_{17}N_2O_2^+$ $[M+H]^+$: 293.1285; found: 293.1286.

Compound **5n'** was also obtained as an "*in-situ* deprotection" minor by-product in the synthesis of **5n**, in a 5% yield.

***Tert*-butyl (*Z*)-3-((1-methyl-5-oxo-1,5-dihydro-4*H*-imidazol-4-ylidene)methyl)-1*H*-indole-1-carboxylate (5o)**

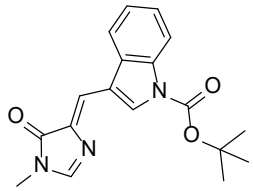

Following *General Procedure A* at rt, compound **5o** was obtained as a yellow solid (170 mg, 52%) from **1n** (269 mg, 1.1 mmol), **2i** (9.8 M solution in MeOH, 112 mL, 1.1 mmol) **3a** (91 mL, 1 mmol) and $AgNO_3$ (17 mg, 0.1 mmol) in CH_3OH (5 mL) after flash chromatography purification (EtOAc/hexane gradient from 0:100 to 20:80 v/v). **^{1}H NMR** (400 MHz, $CDCl_3$) δ 8.69 (d, *J* = 0.9 Hz, 1H), 8.21 – 8.16 (m, 1H), 7.97 – 7.92 (m, 1H), 7.68 (d, *J* = 1.7 Hz, 1H), 7.50 (dd, *J* = 1.7, 0.9 Hz, 1H), 7.36 (pd, *J* = 7.3, 1.5 Hz, 2H), 3.25 (s, 3H), 1.70 (s, 9H). **^{13}C NMR** (101 MHz, $CDCl_3$) δ 169.55, 152.43, 149.19, 137.58, 135.37, 131.97, 129.39, 125.21, 123.62, 121.45, 119.25, 115.42, 115.13, 84.79, 28.13, 27.76. **HRMS:** *m/z* calcd. for $C_{18}H_{20}N_3O_3^+$ $[M+H]^+$: 326.1499; found: 326.1501.

(*Z*)-5-((1H-indol-3-yl)methylene)-3-methyl-3,5-dihydro-4H-imidazol-4-one (5o')

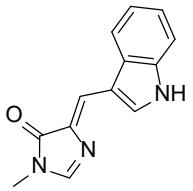

To a 0 ºC solution of compound **5o** (100 mg, 0.307 mmol) in CH_2Cl_2 (4 mL) was slowly added TFA (2.4 mL). The reaction was allowed to warm up to room temperature and was stirred for 2 h, until analysis by TLC suggested consumption of starting material. The solvent and excess TFA were evaporated with a stream of argon. The residue was triturated with CH_2Cl_2 / hexanes and evaporated to dryness to give the pure product **5o'** (65 mg, 94%) as a bright orange solid. Compound **5o'** was obtained as a 90:10 mixture of diastereomers. NMR data is only given of the major diastereomer due to peaks overlapping. **^{1}H NMR** (400 MHz, DMSO-*d*$_6$) δ 12.05 (s, 1H), 8.39 (s, 1H), 8.31 (d, *J* = 7.3 Hz, 1H), 8.01 (d, *J* = 1.6 Hz, 1H), 7.47 (ddd, *J* = 8.0, 1.4, 0.8 Hz, 1H), 7.43 (dd, *J* = 1.6, 0.7 Hz, 1H), 7.24 – 7.14 (m, 2H), 3.14 (s, 3H). **^{13}C NMR** (101 MHz, DMSO-*d*$_6$) δ

169.43, 152.01, 137.06, 134.41, 133.98, 127.03, 123.32, 123.20, 121.44, 120.61, 112.71, 111.74, 27.81. **HRMS:** *m/z* calcd. for $C_{13}H_{12}N_3O^+$ $[M+H]^+$: 226.0975; found: 226.0973.

(*Z*)-3-(4-Methylbenzyl)-5-(pyridin-4-ylmethylene)-3,5-dihydro-4*H*-imidazol-4-one (5q)

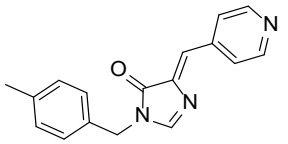

Following *General Procedure A* under mW irradiation, compound **5q** was obtained as a pale brown solid (70 mg, 28%) from **1r** (104 mg, 1.1 mmol), **2b** (140 mL, 1.1 mmol), **3a** (91 mL, 1 mmol) and $AgNO_3$ (17 mg, 0.1 mmol) in CH_3OH (5 mL) after flash chromatography purification (EtOAc/hexane gradient from 10:90 to 60:40 v/v). **^{1}H NMR** (400 MHz, $CDCl_3$) δ 8.70 – 8.66 (m, 2H), 7.94 – 7.90 (m, 2H), 7.75 (d, *J* = 1.7 Hz, 1H), 7.18 (s, 4H), 7.13 (d, *J* = 1.7 Hz, 1H), 4.73 (s, 2H), 2.35 (s, 3H). **^{13}C NMR** (101 MHz, $CDCl_3$) δ 169.21, 155.40, 150.34, 141.97, 140.55, 138.41, 131.98, 129.86, 127.88, 126.97, 125.40, 44.97, 21.14. **HRMS:** *m/z* calcd. for $C_{17}H_{16}N_3O^+$ $[M+H]^+$: 278.1288; found: 278.1228.

(*Z*)-5-((1*H*-Indol-2-yl)methylene)-3-(4-methylbenzyl)-3,5-dihydro-4*H*-imidazol-4-one (5r)

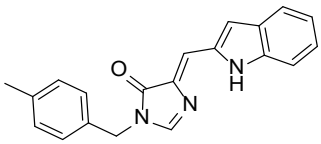

Following *General Procedure A* under mW irradiation, compound **5r** was obtained as a pale green solid (59 mg, 47%) from **1p** (64 mg, 0.44 mmol), **2b** (56 mL, 0.44 mmol), **3a** (36 mL, 0.4 mmol) and $AgNO_3$ (7 mg, 0.04 mmol) in CH_3OH (2 mL). The product precipitated from the reaction mixture and was isolated by filtration under reduced pressure. **^{1}H NMR** (400 MHz, $CDCl_3$) δ 10.77 (s, 1H), 7.67 (d, *J* = 1.6 Hz, 1H), 7.64 (dq, *J* = 8.1, 1.0 Hz, 1H), 7.41 (dq, *J* = 8.4, 1.0 Hz, 1H), 7.33 (d, *J* = 1.6 Hz, 1H), 7.31 – 7.26 (m, 1H), 7.23 – 7.16 (m, 4H), 7.14 – 7.05 (m, 1H), 7.01 (d, *J* = 2.1 Hz, 1H), 4.76 (s, 2H), 2.35 (s, 3H). **^{13}C NMR** (101 MHz, $CDCl_3$) δ 168.43, 150.81, 139.33, 138.20, 136.35, 133.90, 132.50, 129.79, 128.00, 127.90, 125.67, 122.04, 120.54, 120.27, 113.32, 111.65, 44.83, 21.15. **HRMS:** *m/z* calcd. for $C_{20}H_{18}N_3O^+$ $[M+H]^+$: 316.1444; found: 316.1448.

(*Z*)-3-Benzyl-5-((*E*)-3-(4-chlorophenyl)allylidene)-3,5-dihydro-4*H*-imidazol-4-one (5s)

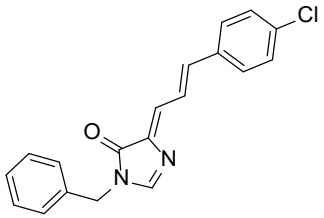

Following *General Procedure A* at rt, compound **5s** was obtained as an orange solid (64 mg, 20%) from **1t** (183 mg, 1.1 mmol), **2a** (120 mL, 1.1 mmol), **3a** (91 mL, 1 mmol) and $AgNO_3$ (17 mg, 0.1 mmol) in CH_3OH (5 mL) after flash chromatography purification (EtOAc/hexane gradient from 20:80 to 80:20 v/v). **^{1}H NMR** (400 MHz, $CDCl_3$) δ 7.55 (d, *J* = 1.6 Hz, 1H), 7.52 (dd, *J* = 15.7, 11.6 Hz, 1H), 7.45 – 7.40 (m, 2H), 7.33 – 7.25 (m, 5H, complex overlapped aromatic signals), 7.23 – 7.20 (m, 2H), 7.06 (dt, *J* = 11.7, 1.3 Hz, 1H), 6.97 (d, *J* = 15.7 Hz, 1H), 4.69 (s, 2H). **^{13}C NMR** (101 MHz, $CDCl_3$) δ 168.48, 151.59, 142.02, 139.40, 135.50, 134.60, 131.63, 129.16, 129.12, 128.90, 128.33, 127.82, 123.65, 45.01. **HRMS:** *m/z* calcd. for $C_{19}H_{16}ClN_2O^+$ $[M+H]^+$: 323.0946; found: 323.0951.

(*Z*)-3-Butyl-5-(thiophen-2-ylmethylene)-3,5-dihydro-4*H*-imidazol-4-one (5t)

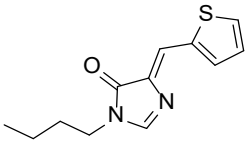

Following *General Procedure A* under mW irradiation, compound **5t** was obtained as a golden colored solid (0.97 g, 83%) from **1l** (514 mg, 5.5 mmol), **2j** (541 mL, 5.5 mmol), **3a** (454 mL, 5 mmol) and $AgNO_3$ (85 mg, 0.5 mmol) in CH_3OH (15 mL, 0.33 M) after flash chromatography purification (EtOAc/hexane gradient from 0:100 to 15:85 v/v). **1H NMR** (400 MHz, CDCl3) δ 7.65 (d, J = 1.6 Hz, 1H), 7.59 (d, J = 5.0 Hz, 1H), 7.46 (d, J = 3.8 Hz, 1H), 7.39 (d, J = 1.7 Hz, 1H), 7.05 (dd, J = 5.1, 3.7 Hz, 1H), 3.53 (t, J = 7.2 Hz, 2H), 1.65 – 1.53 (m, 3H), 1.37 – 1.24 (m, 2H), 0.88 (t, J = 7.4 Hz, 3H). **^{13}C NMR** (101 MHz, $CDCl_3$) δ 169.14, 152.35, 137.47, 136.45, 135.21, 134.44, 127.66, 123.66, 41.19, 31.33, 19.85, 13.55. **HRMS:** *m/z* calcd. for $C_{12}H_{15}N_2OS^+$ $[M+H]^+$: 235.0900; found: 235.0906.

(*Z*)-3-(2-(1*H*-Indol-3-yl)ethyl)-5-(benzo[*d*][1,3]dioxol-5-ylmethylene)-3,5-dihydro-4*H*-imidazol-4-one (5u)

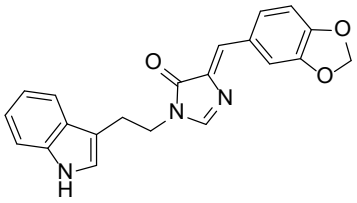

Following *General Procedure A* under mW irradiation, compound **5u** was obtained as a yellow solid (160 mg, 42%) from **1k** (165 mg, 1.1 mmol), **2g** (176 mg, 1.1 mmol), **3a** (91 mL, 1 mmol) and $AgNO_3$ (17 mg, 0.1 mmol) in CH_3OH (5 mL) after flash chromatography purification (EtOAc/hexane gradient from 0:100 to 45:55 v/v). **^{1}H NMR** (400 MHz, DMSO-d_6) δ 10.87 (s, 1H), 8.01 (d, J = 14.2, 2H), 7.61 (d, J = 8.3, 1H), 7.58 (d, J = 7.8 Hz, 1H), 7.35 (d, J = 8.0 Hz, 1H), 7.15 (s, 1H), 7.12 – 6.95 (m, 4H, complex signal), 6.10 (s, 2H), 3.84 (t, J = 7.2 Hz, 2H), 3.05 (t, J = 7.2 Hz, 2H). **^{13}C NMR** (101 MHz, DMSO-d_6) δ 169.67, 155.15, 149.91, 148.19, 137.69, 136.72, 129.32, 128.66, 128.36, 127.43, 123.62, 121.55, 118.88, 118.70, 111.94, 111.10, 110.85, 109.11, 102.21, 41.78, 24.95. **HRMS:** *m/z* calcd. for $C_{21}H_{18}N_3O_3^+$ $[M+H]^+$: 360.1343; found: 360.1344.

(*Z*)-5-(Benzo[d][1,3]dioxol-5-ylmethylene)-3-((*E*)-4-phenylbut-3-en-1-yl)-3,5-dihydro-4*H*-imidazol-4-one (5v)

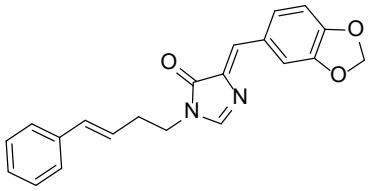

Following *General Procedure A* at rt, compound **5v** was obtained as a golden colored solid (120 mg, 35%) from **1k** (164 mg, 1.1 mmol), **2w** (165 mg, 1.1 mmol), **3a** (91 mL, 1 mmol) and $AgNO_3$ (17 mg, 0.1 mmol) in CH_3OH (5 mL). The product precipitated from the reaction mixture and was isolated by filtration under reduced pressure. **^{1}H NMR** (400 MHz, $CDCl_3$) δ 7.95 (d, J = 1.6 Hz, 1H), 7.70 (d, J = 1.7 Hz, 1H), 7.44 (dd, J = 8.2, 1.7 Hz, 1H), 7.35 – 7.27 (m, 5H), 7.25 – 7.19 (m, 1H), 7.15 (d, J = 1.6 Hz, 1H), 6.85 (d, J = 8.1 Hz, 1H), 6.46 (d, J = 15.9 Hz, 1H), 6.19 – 6.09 (m, 1H), 6.02 (s, 2H), 3.75 (t, J = 6.9 Hz, 2H), 2.64 – 2.56 (m, 2H). **^{13}C NMR** (101 MHz, $CDCl_3$) δ 169.82, 152.29, 150.09, 148.26, 137.01, 136.85, 133.52, 130.52, 129.13, 128.58,

128.39, 127.55, 126.18, 125.19, 111.39, 108.57, 101.64, 41.20, 32.87. **HRMS:** *m/z* calcd. for $C_{21}H_{19}N_2O_3^+$ $[M+H]^+$: 347.1390; found: 347.1394.

(*Z*)-5-(Benzo[d][1,3]dioxol-5-ylmethylene)-3,5-dihydro-4*H*-imidazol-4-one (5w)

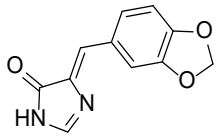

Following *General Procedure A* at rt, compound **5w** was obtained as a light brown solid (130 mg, 30%) from **1k** (330 mg, 2.2 mmol), **2h** (7 M solution in MeOH, 290 mL, 2.2 mmol), **3a** (181 mL, 2 mmol) and $AgNO_3$ (34 mg, 0.2 mmol) in CH_3OH (10 mL) after flash chromatography purification (EtOAc/hexane gradient from 25:75 to 75:25 v/v). **^{1}H NMR** (400 MHz, DMSO-d_6) δ 11.33 (brs, 1H), 8.13 (d, J = 1.7 Hz, 1H), 8.01 (d, J = 1.6 Hz, 1H), 7.60 (dd, J = 8.3, 1.7 Hz, 1H), 7.00 (d, J = 8.1 Hz, 1H), 6.96 (d, J = 1.7 Hz, 1H), 6.10 (s, 2H). **^{13}C NMR** (101 MHz, DMSO-d_6) δ 171.47, 153.73, 149.71, 148.18, 137.63, 129.04, 128.78, 127.19, 110.99, 109.09, 102.15. **HRMS:** *m/z* calcd. for $C_{11}H_9N_2O_3^+$ $[M+H]^+$: 217.0608; found: 217.0611.

Allyl (*S*,*Z*)-2-((((9*H*-fluoren-9-yl)methoxy)carbonyl)amino)-6-(4-(benzo[*d*][1,3]dioxol-5-ylmethylene)-5-oxo-4,5-dihydro-1*H*-imidazol-1-yl)hexanoate (5x)

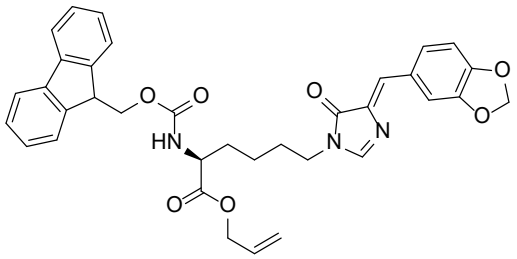

Following *General Procedure A* at rt, compound **5x** was obtained as a light brown solid (0.95 g, 47%) from **1k** (553 mg, 3.7 mmol), **2x** (1.64 g, 1.1 mmol), **3a** (304 mL, 1 mmol), $AgNO_3$ (114 mg, 0.1 mmol) and triethylamine (536 mL, 1.2 mmol) in CH_3OH (17 mL) after flash chromatography purification (EtOAc/hexane gradient from 0:100 to 35:65 v/v). **^{1}H NMR** (400 MHz, DMSO-d_6) δ 8.22 (d, J = 1.6 Hz, 1H), 8.02 (d, J = 1.6 Hz, 1H), 7.88 (d, J = 7.5 Hz, 2H), 7.80 (d, J = 7.8 Hz, 1H), 7.73 – 7.67 (m, 2H), 7.62 (dd, J = 8.3, 1.7 Hz, 1H), 7.40 (t, J = 7.4 Hz, 2H), 7.34 – 7.29 (m, 2H), 7.05 (d, J = 1.6 Hz, 1H), 7.01 (d, J = 8.1 Hz, 1H), 6.10 (s, 2H), 5.93 – 5.81 (m, 1H), 5.29 (dq, J = 17.3, 1.7 Hz, 1H), 5.18 (dq, J = 10.6, 1.5 Hz, 1H), 4.56 (dq, J = 5.5, 1.4 Hz, 2H), 4.29 (d, J = 6.3

Hz, 2H), 4.21 (t, *J* = 7.0 Hz, 1H), 4.07 – 3.99 (m, 1H), 3.53 (t, *J* = 6.9 Hz, 2H), 1.79 – 1.55 (m, 4H), 1.37 – 1.26 (m, 2H). **^{13}C NMR** (101 MHz, DMSO-*d*$_6$) δ 172.50, 169.73, 156.62, 155.25, 149.93, 148.20, 144.25, 141.20, 137.67, 132.84, 129.35, 128.67, 128.49, 128.09, 127.52, 125.68, 120.58, 118.22, 111.09, 109.11, 102.22, 66.12, 65.25, 54.28, 47.09, 40.85, 30.63, 28.54, 23.11. **HRMS:** *m/z* calcd. for $C_{35}H_{34}N_3O_7^+$ $[M+H]^+$: 608.2391; found: 608.2393.

(*S*,*Z*)-2-((((9*H*-fluoren-9-yl)methoxy)carbonyl)amino)-6-(4-(benzo[*d*][1,3]dioxol-5-ylmethylene)-5-oxo-4,5-dihydro-1*H*-imidazol-1-yl)hexanoic acid (5x')

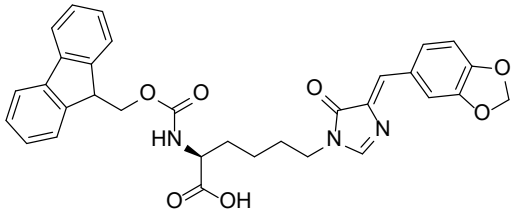

To a solution of **5x** (156 mg, 0.26 mmol, 1 eq.) and tetrakis(triphenylphosphine)palladium(0) (119 mg, 0.1 mmol, 0.4 eq.) in dry CH_2Cl_2 (5.1 mL, 0.05 M) under argon atmosphere, was added 1,3-dimethylbarbituric acid (200 mg, 1.3 mmol, 5 eq.) and the reaction was stirred at rt for 1 h. After reaction completion (LC-MS control) the reaction mixture was concentrated under reduced pressure. The crude product was purified *via* reverse phase C18 chromatography (CH_3CN + 0.1% HCOOH / H_2O + 0.1% HCOOH gradient from 5:95 to 80:20 v/v) to afford the title compound **5x'** as a pale-yellow solid (80 mg, 55%). **^{1}H NMR** (400 MHz, DMSO-*d*$_6$) δ 8.22 (d, *J* = 1.7 Hz, 1H), 8.01 (d, *J* = 1.6 Hz, 1H), 7.88 (d, *J* = 7.5 Hz, 2H), 7.70 (d, *J* = 7.5 Hz, 2H), 7.64 – 7.59 (m, 2H), 7.53 – 7.48 (m, 1H), 7.39 (t, *J* = 7.4 Hz, 2H), 7.32 (td, *J* = 7.2, 2.3 Hz, 2H), 7.05 (d, *J* = 1.7 Hz, 1H), 7.00 (d, *J* = 8.0 Hz, 1H), 6.10 (s, 2H), 4.28 – 4.19 (m, 3H), 3.94 – 3.84 (m, 1H), 3.53 (t, *J* = 6.9 Hz, 2H), 1.77 – 1.54 (m, 4H), 1.37 – 1.27 (m, 2H). **^{13}C NMR** (101 MHz, DMSO-*d*$_6$) δ 174.37, 169.71, 156.57, 155.28, 149.92, 148.20, 144.28, 141.16, 137.67, 131.91, 129.29, 128.47, 128.08, 127.53, 125.71, 120.56, 111.09, 109.11, 102.21, 66.04, 54.25, 47.12, 40.90, 30.81, 28.64, 23.19. **HRMS:** *m/z* calcd. for $C_{32}H_{27}N_3O_7^-$ $[M-H]^-$: 566.1933; found: 567.1931.

(*Z*)-3-(4-Methoxyphenyl)-5-(thiophen-2-ylmethylene)-3,5-dihydro-4*H*-imidazol-4-one (5y)

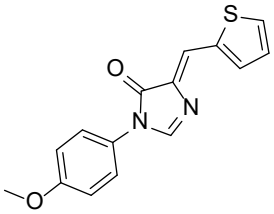

Following *General Procedure A* at rt, compound **5y** was obtained as a light brown solid (35 mg, 12%) from **1l** (103 mL, 1.1 mmol), **2q** (135 mg, 1.1 mmol), **3a** (91 mL, 1 mmol) and $AgNO_3$ (17 mg, 0.1 mmol) in CH_3OH (5 mL). The product and unreacted aniline were collected by filtration washing with cold MeOH. The solid was dissolved in CH_2Cl_2 and was filtered through Celite®® – to remove the remains of the silver catalyst. The solution was washed with 0.5 M aqueous HCl (3x) and saturated brine. The organic layer was dried over Na_2SO_4, filtered, and concentrated under reduced pressure to give the crude product **5y**. The pure product **5y** was obtained after crystallisation by slow diffusion of Et_2O into a CH_2Cl_2 solution of the pure product through layering. **^{1}H NMR** (400 MHz, $CDCl_3$) δ 7.95 (d, *J* = 1.6 Hz, 1H), 7.70 (dt, *J* = 5.1, 1.0 Hz, 1H), 7.59 – 7.55 (m, 2H, overlapped signals), 7.40 – 7.33 (m, 2H), 7.14 (dd, *J* = 5.1, 3.7 Hz, 1H), 7.03 – 6.96 (m, 2H), 3.84 (s, 3H). **^{13}C NMR** (101 MHz, $CDCl_3$) δ 167.68, 158.94, 151.09, 137.42, 136.20, 135.56, 134.84, 127.76, 126.83, 124.64, 124.25, 114.85, 55.59. **HRMS:** *m/z* calcd. for $C_{15}H_{13}N_2O_2S^+$ $[M+H]^+$: 285.0692; found: 285.0693.

(*Z*)-5-(Benzo[d][1,3]dioxol-5-ylmethylene)-3-(tert-butyl)-3,5-dihydro-4*H*-imidazol-4-one (5z)

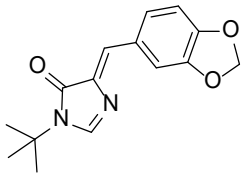

Following *General Procedure A* under mW irradiation, compound **5z** was obtained as a pale yellow solid (10 mg, 2%) from **1k** (330 mg, 2.2 mmol), **2l** (231 mL, 2.2 mmol), **3a** (181 mL, 2 mmol) and $AgNO_3$ (34 mg, 0.2 mmol) in CH_3OH (10 mL) after flash chromatography purification (EtOAc/hexane gradient from 20:80 to 70:30 v/v). **^{1}H NMR** (400 MHz, $CDCl_3$) δ 7.95 (d, *J* = 1.7 Hz, 1H), 7.83 (d, *J* = 1.7 Hz, 1H), 7.43 (dd, *J* = 8.1, 1.6 Hz, 1H), 7.05 (d, *J* = 1.6 Hz, 1H), 6.85 (d, *J* = 8.1 Hz, 1H), 6.02 (s, 2H), 1.57

(s, 9H). **^{13}C NMR** (101 MHz, $CDCl_3$) δ 170.35, 151.14, 149.82, 148.21, 138.47, 129.47, 128.77, 128.63, 111.27, 108.55, 101.58, 55.11, 28.16. **HRMS:** *m/z* calcd. for $C_{15}H_{17}N_2O_3^+$ $[M+H]^+$: 273.1234; found: 273.1237.

3-Benzyl-5-(propan-2-ylidene)-3,5-dihydro-4*H*-imidazol-4-one (5aa)

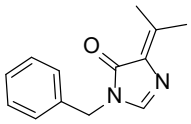

Following *General Procedure A* under mW irradiation, compound **5aa** was obtained as a pale brown oil (130 mg, 60%) from **1aa** (81 mL, 1.1 mmol), **2a** (120 mL, 2.2 mmol), **3a** (91 mL, 1 mmol) and $AgNO_3$ (17 mg, 0.1 mmol) in CH_3OH (5 mL) after flash chromatography purification (EtOAc/hexane gradient from 0:100 to 60:40 v/v). **^{1}H NMR** (400 MHz, $CDCl_3$) δ 7.46 (s, 1H), 7.38 – 7.29 (m, 3H), 7.27 – 7.24 (m, 2H), 4.71 (s, 2H), 2.44 (s, 3H), 2.27 (s, 3H). **^{13}C NMR** (101 MHz, $CDCl_3$) δ 167.40, 152.84, 147.89, 136.69, 135.92, 129.00, 128.10, 127.74, 44.65, 22.44, 19.62. **HRMS:** *m/z* calcd. for $C_{18}H_{15}N_2O^+$ $[M+H]^+$: 215.1179; found: 215.1177.

Compound **5aa** was isolated from the same reaction mixture as compound **4aa**.

5-((1*r*,3*r*)-adamantan-2-ylidene)-3-benzyl-3,5-dihydro-4*H*-imidazol-4-one (5ac)

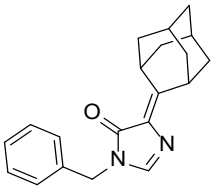

Following *General Procedure A* under mW irradiation, compound **5ac** was obtained as an off-white oil (75 mg, 12%) from **1ac** (330 mg, 2.2 mmol), **2a** (240 mL, 2.2 mmol), **3a** (181 mL, 2 mmol) and $AgNO_3$ (34 mg, 0.2 mmol) in CH_3OH (10 mL) after flash chromatography purification (EtOAc/hexane gradient from 0:100 to 40:60 v/v). **^{1}H NMR** (400 MHz, $CDCl_3$) δ 7.41 (s, 1H), 7.38 – 7.26 (m, 5H), 4.71 (s, 2H), 4.45 – 4.40 (m, 1H), 3.64 – 3.54 (m, 1H), 2.12 – 2.04 (m, 4H), 2.04 – 1.98 (m, 2H), 1.97 – 1.89 (m, 6H). **^{13}C NMR** (101 MHz, $CDCl_3$) δ 168.86, 166.90, 146.59, 134.94, 130.03, 127.95, 127.05, 126.87, 43.61, 38.99, 38.91, 35.76, 33.71, 30.62, 26.78. **HRMS:** *m/z* calcd. for $C_{20}H_{23}N_2O^+$ $[M+H]^+$: 307.1805; found: 307.1805.

Compound **5ac** was isolated from the same reaction mixture as compound **4ac**.

(5Z,5'Z)-3,3'-(Cyclohexane-1,2-diyl)bis(5-(benzo[d][1,3]dioxol-5-ylmethylene)-3,5-dihydro-4H-imidazol-4-one) (5-bis-a)

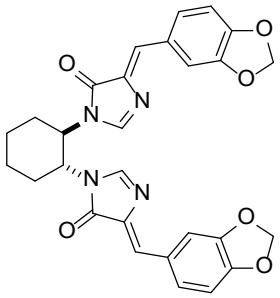

Following *General Procedure A* at rt, compound **9** was obtained as a yellow solid (120 mg, 19%) from **1k** (330 mg, 2.2 mmol), ***trans*-2n** (251 mg, 2.2 mmol), **3a** (181 mL, 2 mmol) and $AgNO_3$ (34 mg, 0.2 mmol) in CH_3OH (10 mL). The precipitate formed during the reaction was filtered under vacuum to give the crude product as a pale-yellow solid. The pure product **9** was obtained after crystallisation by slow diffusion of Et_2O into a CH_2Cl_2 solution of the crude product through layering. **^{1}H NMR** (400 MHz, DMSO-d_6) δ 8.47 (d, J = 1.6 Hz, 1H), 8.00 (d, J = 1.6 Hz, 1H), 7.63 (dd, J = 8.2, 1.7 Hz, 1H), 7.04 (d, J = 8.1 Hz, 1H, overlapped), 7.03 (d, J = 1.6 Hz, 1H, overlapped), 6.15 (s, 2H), 4.32 – 4.22 (m, 1H), 2.10 – 1.99 (m, 1H), 2.00 – 1.92 (m, 1H), 1.92 – 1.85 (m, 1H), 1.56 – 1.47 (m, 1H). **^{13}C NMR** (101 MHz, DMSO-d_6) δ 173.67, 157.67, 154.76, 152.93, 141.95, 134.22, 133.65, 133.23, 115.87, 113.87, 106.97, 58.02, 35.63, 29.52. **HRMS:** *m/z* calcd. for $C_{28}H_{25}N_4O_6^+$ $[M+H]^+$: 513.1769; found: 513.1766.

(5*R*,6*R*,7*S*,12*S*)-3,10-Dibenzyl-6,12-bis(4-chlorophenyl)-1,3,8,10-tetraazadispiro[4.1.4^7.1^5]dodeca-1,8-diene-4,11-dione (8a)

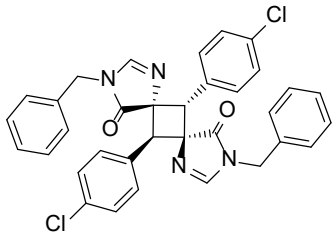

Compound **5a** (150 mg, 0.5 mmol) was dissolved in CH_2Cl_2 and evaporated under reduced pressure using a 50 mL RBF, ensuring an even distribution along the flask. Compound **5a** had a golden color. The flask was then placed under blue LEDs irradiation for 17 h. After irradiation the solid was recovered to give the title compound **8a** as a white solid (150 mg, 100%). **^{1}H NMR** (400 MHz, DMSO-d_6) δ 8.15 (s, 1H), 7.52 – 7.47 (m, 2H), 7.32 – 7.25 (m, 2H), 7.24 – 7.18 (m, 1H), 7.18 – 7.12 (m, 2H), 6.72 – 6.67 (m, 2H),

4.61 (s, 1H), 4.53 (d, *J* = 15.8 Hz, 1H), 4.43 (d, *J* = 15.9 Hz, 1H). **^{13}C NMR** (101 MHz, DMSO-*d*$_6$) δ 179.98, 155.89, 136.77, 132.93, 132.83, 132.60, 128.83, 128.03, 127.80, 127.05, 73.89, 53.10, 44.06. **HRMS**: *m/z* calcd. for $C_{34}H_{27}Cl_2N_4O_2$ $[M+H]^+$: 593.1506; found: 593.1495.

Crystals suitable for single X-ray diffraction were grown by slow diffusion of Et_2O into a $CHCl_3$ solution of the pure compound **8a** through layering.

2-(4-Chlorobenzyl)-8-(4-chlorophenyl)-6,7-dihydroimidazo[1,2-*a*]pyrazin-3(5*H*)-one (9a)

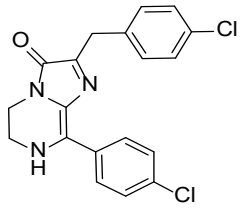

Following *General Procedure A* at rt under argon atm., compound **9a** was obtained as a yellow solid (30 mg, 8%) from **1a** (140 mg, 1.1 mmol), **2m** (74 mL, 1.1 mmol), **3a** (91 mL, 1 mmol) and $AgNO_3$ (17 mg, 0.1 mmol) in CH_3OH (5 mL) after flash chromatography purification (CH_2Cl_2/hexane gradient from 0:100 to 80:20 v/v). **^{1}H NMR** (400 MHz, DMSO-*d*$_6$) δ 7.95 (br s, 1H), 7.83 – 7.78 (m, 2H), 7.60 – 7.54 (m, 2H), 7.34 – 7.27 (m, 4H), 3.82 (s, 2H), 3.81 – 3.74 (m, 2H), 3.59 – 3.54 (m, 2H). **^{13}C NMR** (101 MHz, DMSO-*d*$_6$) δ 159.97, 150.09, 137.88, 135.18, 133.91, 131.53, 131.25, 131.01, 130.84, 128.79, 128.69, 126.58, 40.67 (overlapped with the residual solvent signal), 38.32, 33.18. **HRMS:** *m/z* calcd. for $C_{19}H_{16}Cl_2N_3O$ $[M+H]^+$: 372.0665; found: 372.0670.

4-(2-(4-Cyanobenzyl)-3-oxo-3,5,6,7-tetrahydroimidazo[1,2-*a*]pyrazin-8-yl)benzonitrile (9c)

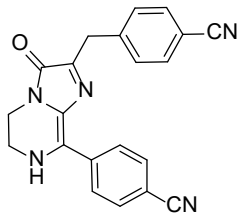

Following *General Procedure A* at rt under argon atm., compound **9c** was obtained as a bright orange solid (80 mg, 9%) from **1q** (360 mg, 2.75 mmol), **2m** (184 mL, 2.75 mmol), **3a** (227 mL, 2.5 mmol) and $AgNO_3$ (43 mg, 0.25 mmol) in CH_3OH (12.5 mL) after flash chromatography (CH_2Cl_2/hexane gradient from 0:100 to 80:20 v/v).

^{1}H NMR (400 MHz, DMSO-d_6) δ 8.05 (br s, 1H), 7.99 – 7.93 (m, 4H), 7.76 – 7.71 (m, 2H), 7.51 – 7.46 (m, 2H), 3.95 (s, 2H), 3.79 (dd, J = 6.6, 4.6 Hz, 2H), 3.58 (t, J = 5.7 Hz, 2H). ^{13}C NMR (101 MHz, DMSO-d_6) δ 160.01, 150.47, 144.58, 136.42, 133.19, 132.74, 132.53, 130.50, 130.29, 127.49, 119.41, 118.99, 112.51, 109.55, 40.67 (overlapped with the residual solvent signal), 38.32, 33.96. **HRMS:** *m/z* calcd. for $C_{21}H_{15}N_5O$ $[M+H]^+$: 354.1349; found: 354.1350.

(5a*R*,9a*R*)-2-(4-Chlorobenzyl)-4-(4-chlorophenyl)-5a,6,7,8,9,9a-hexahydroimidazo[1,2-*a*]quinoxalin-1(5*H*)-one (9d)

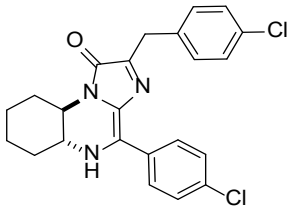

Following *General Procedure A* at rt under argon atm., compound **9c** was obtained as a yellow solid (150 mg, 35%) from **1a** (281 mg, 2 mmol), **2m** (126 mg, 1.1 mmol), **3a** (91 mL, 1 mmol) and $AgNO_3$ (17 mg, 0.1 mmol) in CH_3OH (5 mL) after flash chromatography purification (CH_2Cl_2/hexane gradient from 0:100 to 50:50 v/v). **^{1}H NMR** (400 MHz, DMSO-d_6) δ 7.78 – 7.72 (m, 2H), 7.63 (br s, 1H), 7.57 – 7.51 (m, 2H), 7.35 – 7.30 (m, 2H), 7.30 – 7.25 (m, 2H), 3.78 (d, J = 14.9 Hz, 1H), 3.73 (d, J = 14.9 Hz, 1H), 3.65 (td, J = 11.0, 3.7 Hz, 1H), 3.30 – 3.23 (m, 1H), 2.18 – 2.10 (m, 1H), 1.80 – 1.69 (m, 2H), 1.54 – 1.22 (m, 5H). **^{13}C NMR** (101 MHz, DMSO-d_6) δ 161.50, 151.17, 137.80, 134.91, 133.79, 131.91, 131.25, 131.05, 131.02, 128.69, 128.54, 127.53, 58.30, 56.68, 32.99, 29.28, 27.10, 24.04, 23.94. **HRMS:** *m/z* calcd. for $C_{23}H_{22}Cl_2N_3O^+$ $[M+H]^+$: 426.1134; found: 426.1136.

8-(Benzo[d][1,3]dioxol-5-yl)-2-(benzo[d][1,3]dioxol-5-ylmethyl)-6,7-dihydroimidazo[1,2-*a*]pyrazin-3(5*H*)-one (9e)

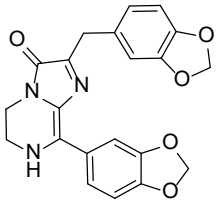

Following *General Procedure A* at rt under argon atm., compound **9e** was obtained as a bright yellow solid (230 mg, 12%) from **1k** (826 mg, 5.5 mmol), **2m** (367 mL, 5.5 mmol), **3a** (454 mL, 5 mmol) and $AgNO_3$ (85 mg, 0.5 mmol) in CH_3OH (25 mL)

after flash chromatography purification (MeOH/CH_2Cl_2 gradient from 0:100 to 5:100 v/v). **^{1}H NMR** (400 MHz, $CDCl_3$) δ 7.29 (d, *J* = 1.8 Hz, 1H), 7.20 (dd, *J* = 8.2, 1.8 Hz, 1H), 6.91 (d, *J* = 1.7 Hz, 1H), 6.86 (d, *J* = 8.2 Hz, 1H, overlapped), 6.85 (dd, *J* = 7.9, 1.7 Hz, 1H, overlapped) 6.71 (d, *J* = 7.9 Hz, 1H), 6.01 (s, 2H), 5.88 (s, 2H), 5.02 (t, *J* = 3.5 Hz, 1H), 3.88 (s, 2H), 3.88 – 3.85 (m, 2H), 3.63 – 3.57 (m, 2H). **^{13}C NMR** (101 MHz, $CDCl_3$) δ 160.61, 153.27, 149.62, 148.01, 147.52, 146.03, 133.14, 131.58, 127.14, 125.76, 123.20, 122.07, 109.82, 109.68, 108.57, 108.19, 101.66, 100.77, 40.58, 38.48, 33.93. **HRMS:** *m/z* calcd. for $C_{21}H_{18}N_3O_5$ $[M+H]^+$: 392.1241; found: 392.1241. Compound **9e** contains residual solvent from chromatography. The connectivity of compound **9e** was further studied with bidimensional NMR spectroscopy (COSY).

2-(3,4,5-Trimethoxybenzyl)-8-(3,4,5-trimethoxyphenyl)-6,7-dihydroimidazo[1,2-*a*]pyrazin-3(5*H*)-one (9f)

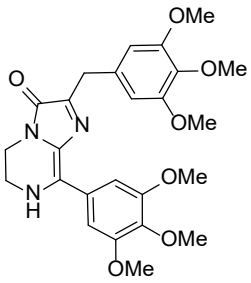

Following *General Procedure A* at rt under argon atm, compound **9f** was obtained as a greenish solid (70 mg, 14%) from **1i** (215 mg, 1.1 mmol), **2m** (73 mL, 1.1 mmol), **3a** (91 mL, 1 mmol) and $AgNO_3$ (17 mg, 0.1 mmol) in CH_3OH (5 mL) after flash chromatography purification eluting with (CH_2Cl_2/hexane gradient from 0:100 to 80:20 v/v). **^{1}H NMR** (400 MHz, DMSO-d_6) δ 7.80 (t, *J* = 3.3 Hz, 1H), 7.15 (s, 2H), 6.63 (s, 2H), 3.77 – 3.74 (m, 10H; complex signal), 3.71 (s, 6H), 3.71 (s, 3H), 3.61 (s, 3H), 3.58 – 3.55 (m, 2H). **^{13}C NMR** (101 MHz, DMSO-d_6) δ 159.92, 153.10, 152.82, 149.96, 139.51, 136.39, 134.57, 134.55, 127.14, 126.28, 107.57, 106.88, 60.60, 60.41, 56.30, 56.23, 40.67 (overlapped with residual solvent signal), 38.37, 34.33. **HRMS:** *m/z* calcd. for $C_{25}H_{30}N_3O_7^+$ $[M+H]^+$: 484.2078; found: 484.2081.

Compound **9f** contains residual solvent from chromatography.

(*Z*)-5-(benzo[*d*][1,3]dioxol-5-ylmethylene)-3-(2-(((*E*)-benzo[*d*][1,3]dioxol-5-ylmethylene)amino)ethyl)-3,5-dihydro-4*H*-imidazol-4-one (9e-imine)

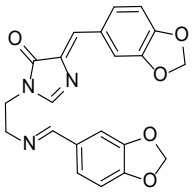

Following *General Procedure A* at rt under argon atm., compound **9e-imine** was obtained as a light brown solid (200 mg, 51%) from **1k** (300 mg, 2 mmol), **2m** (73 mL, 1.1 mmol), **3a** (91 mL, 1 mmol) and $AgNO_3$ (17 mg, 0.1 mmol) in CH_3OH (5 mL). The product precipitated from the reaction mixture and was isolated by filtration under reduced pressure. **^{1}H NMR** (400 MHz, DMSO-d_6) δ 8.20 (br s, 1H), 8.13 (d, J = 1.6 Hz, 1H), 7.98 (d, J = 1.6 Hz, 1H), 7.61 (dd, J = 8.2, 1.7 Hz, 1H), 7.29 (d, J = 1.5 Hz, 1H), 7.17 (dd, J = 8.1, 1.6 Hz, 1H), 7.05 (d, J = 1.7 Hz, 1H), 7.00 (d, J = 8.1 Hz, 1H), 6.96 (d, J = 8.0 Hz, 1H), 6.09 (s, 2H), 6.07 (s, 2H), 3.87 – 3.81 (m, 2H), 3.76 – 3.70 (m, 2H). **^{13}C NMR** (101 MHz, DMSO-d_6) δ 169.56, 162.46, 155.54, 150.14, 149.94, 148.35, 148.20, 137.52, 131.02, 129.35, 128.60, 128.42, 124.94, 111.09, 109.12, 108.68, 106.35, 102.21, 102.01, 58.73, 42.11. **HRMS:** *m/z* calcd. for $C_{21}H_{18}N_3O_5^+$ $[M+H]^+$: 392.1241; found: 392.1245. The connectivity of compound **9e-imine** was further studied with bidimensional NMR spectroscopy (HSQC, HMBC).

5-(Benzo[*d*][1,3]dioxol-5-ylmethyl)-3-methyl-2-(pyrrolidin-1-yl)-3,5-dihydro-4*H*-imidazol-4-one (11d)

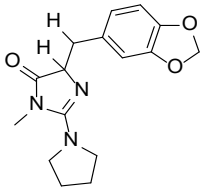

Following the *General Procedure (i)* at rt, compound **11d** was obtained as a pale brown solid (1.06 g, 100%) from **5i** (806 mg, 3.5 mmol) and **Nu-1** (578 mL, 7 mmol, 2 eq.) in CH_3CN (35 mL). The solvent and excess pyrrolidine were evaporated, and the residue was triturated with CH_2Cl_2 / hexanes to afford the pure compound **11d** without further purification. **^{1}H NMR** (500 MHz, $CDCl_3$) δ 6.75 (t, J = 1.0 Hz, 1H), 6.66 (d, J = 1.0 Hz, 2H), 5.89 – 5.87 (m, 2H), 4.22 (t, J = 5.3 Hz, 1H), 3.45 – 3.38 (m, 2H), 3.38 – 3.32 (m, 2H), 3.07 (dd, J = 13.6, 5.0 Hz, 1H), 2.96 (s, 3H), 2.94 (dd, J = 13.5, 5.6 Hz, 1H), 1.93 – 1.86 (m, 4H). **^{13}C NMR** (101 MHz, $CDCl_3$) δ 182.03, 157.96, 146.92, 146.06,

130.10, 122.93, 110.43, 107.62, 100.67, 66.29, 48.71, 37.59, 28.62, 25.35. **HRMS:** *m/z* calcd. for $C_{16}H_{20}N_3O_3^+$ $[M+H]^+$: 302.1499; found: 302.1506.

The connectivity of compound **11d** was further studied with bidimensional NMR spectroscopy (**COSY**, **HSQC**, **HMBC**).

3-Benzyl-5-(4-chlorobenzyl)-2-(pyrrolidin-1-yl)-3,5-dihydro-4*H*-imidazol-4-one (11e)

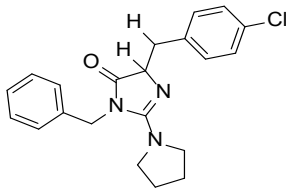

Following the *General Procedure E (i)* at rt, compound **11e** was obtained as a light brown solid (131 mg, 100%) from **5a** (100 mg, 0.34 mmol) and **Nu-1** (278 mL, 3.4 mmol, 10 eq.) in CH_3CN (3.4 mL). The solvent and excess pyrrolidine were evaporated and the residue was triturated with CH_2Cl_2 / hexanes to afford the pure compound **11e** without further purification. **^{1}H NMR** (400 MHz, $CDCl_3$) δ 7.21 (s, 4H), 7.20 – 7.18 (m, 3H), 6.54 – 6.48 (m, 2H), 4.83 (d, *J* = 17.0 Hz, 1H), 4.46 (d, *J* = 16.9 Hz, 1H), 4.43 (t, *J* = 4.7 Hz, 1H), 3.34 – 3.22 (m, 3H), 3.20 – 3.13 (m, 3H), 1.78 – 1.72 (m, 4H). **^{13}C NMR** (101 MHz, $CDCl_3$) δ 182.67, 157.23, 136.10, 134.79, 132.50, 131.81, 128.63, 127.98, 127.19, 125.27, 66.28, 48.31, 44.74, 36.69, 25.24. **HRMS:** *m/z* calcd. for $C_{21}H_{23}ClN_3O^+$ $[M+H]^+$: 368.1524; found: 368.1528.

3-Benzyl-5-((4-chlorophenyl)methyl-*d*$_2$)-2-(pyrrolidin-1-yl)-3,5-dihydro-4*H*-imidazol-4-one (11e-*d*$_2$)

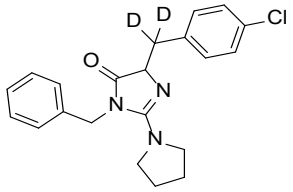

Following the *General Procedure E (i)* at rt, compound **11e-*d*$_2$** was obtained as a light brown solid (117 mg, 99%) from **5a** (95 mg, 0.32 mmol), **Nu-1** (266 mL, 3.2 mmol, 10 eq.) in CD_3OD (3 mL). The solvent and excess pyrrolidine were evaporated and the residue was triturated with CH_2Cl_2 / hexanes to afford the pure compound **11e-*d*$_2$** without further purification. **^{1}H NMR** (400 MHz, $CDCl_3$) δ 7.22 (s, 4H), 7.20 – 7.17 (m, 3H), 6.54 – 6.47 (m, 2H), 4.83 (d, *J* = 16.8 Hz, 1H), 4.46 (d, *J* = 17.0 Hz, 1H), 4.42 (s, 1H),

3.34 – 3.25 (m, 2H), 3.21 – 3.12 (m, 2H), 1.77 – 1.72 (m, 4H). **^{13}C NMR** (101 MHz, $CDCl_3$) δ 182.70, 157.24, 136.10, 134.71, 132.48, 131.78, 128.61, 127.96, 127.17, 125.27, 66.18, 48.29, 44.72, 25.23, 10.12. **HRMS:** *m/z* calcd. for $C_{21}H_{21}D_2ClN_3O^+$ $[M+H]^+$: 370.1650; found: 370.1650.

(*Z*)-2-(benzo[*d*][1,3]dioxol-5-ylmethylene)-5,6,7,8-tetrahydroimidazo[1,2-*a*]pyrimidin-3(2*H*)-one (12a)

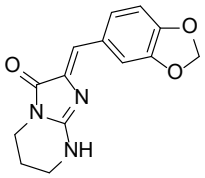

Following the *General Procedure D*, compound **12a** was obtained as a light-yellow solid (290 mg, 22% over two steps). The crude intermediate **11a** (480 mg, 1.76 mmol) was subjected to the dehydrogenation protocol with TEMPO (550 mg, 3.52 mmol) in $CHCl_3$ (18 mL) to afford the title compound **12a**. **^{1}H NMR** (400 MHz, DMSO-d_6) δ 8.30 (s, 1H), 7.89 (d, *J* = 1.6 Hz, 1H), 7.37 (dd, *J* = 8.5, 1.6 Hz, 1H), 6.89 (d, *J* = 8.1 Hz, 1H), 6.28 (s, 1H), 6.00 (s, 2H), 3.52 (t, *J* = 5.8 Hz, 2H), 3.30 – 3.25 (m, 2H), 1.96 – 1.87 (m, 2H). **^{13}C NMR** (101 MHz, DMSO-d_6) δ 168.66, 156.07, 147.20, 146.44, 138.95, 130.54, 124.80, 111.34, 109.33, 108.25, 100.98, 38.26, 37.40, 20.61. **HRMS:** *m/z* calcd.for $C_{14}H_{14}N_3O_3^+$ $[M+H]^+$: 272.1030; found: 272.1032.

***tert*-Butyl (*Z*)-3-((1-methyl-2-(methylamino)-5-oxo-1,5-dihydro-4*H*-imidazol-4-ylidene)methyl)-1*H*-indole-1-carboxylate (12c)**

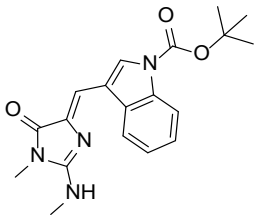

Following the *General Procedure D*, compound **12c** was obtained as a yellow solid (100 mg, 28% over two steps). The crude intermediate **11c** (173 mg, 0.49 mmol) was subjected to the dehydrogenation protocol with TEMPO (153 mg, 0.98 mmol) in $CHCl_3$ (5 mL) to afford the title compound **12c**. **^{1}H NMR** (400 MHz, DMSO-d_6) δ 8.71 (d, *J* = 0.8 Hz, 1H), 8.10 (d, *J* = 8.2 Hz, 1H), 7.96 (d, *J* = 7.9 Hz, 1H), 7.74 (br s, 1H), 7.37 (td, *J* = 7.2, 1.4 Hz, 1H), 7.31 (td, *J* = 7.5, 1.2 Hz, 1H), 6.66 (d, *J* = 0.8 Hz, 1H), 3.06 (s, 3H), 3.02 (s, 3H), 1.65 (s, 9H). **^{13}C NMR** (101 MHz, DMSO-d_6) δ 169.23, 158.96,

149.35, 140.76, 134.90, 129.85, 128.22, 125.17, 123.50, 119.73, 116.65, 115.18, 102.91, 84.29, 28.07, 28.03, 25.95. **HRMS:** *m/z* calcd. for $C_{19}H_{23}N_4O_3^+$ $[M+H]^+$: 355.1765; found: 355.1770.

(*Z*)-5-((1*H*-Indol-3-yl)methylene)-3-methyl-2-(methylamino)-3,5-dihydro-4*H*-imidazol-4-one (12c')

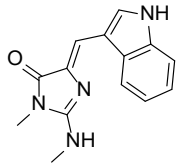

To a solution of **12c** (19 mg, 0.05 mmol) in CH_2Cl_2 (1.1 mL, 0.05 mmol) was added TFA (411 mL, 5.4 mmol, 100 eq.) and the reaction was stirred at rt for 2 h, until analysis by TLC suggested consumption of starting material. The reaction was diluted with EtOAc and it was slowly added a saturated aqueous solution of Na_2CO_3 until pH = 11. The aqueous layer was extracted with EtOAc (3x). The organic layers were combined, washed with saturated brine, dried over Na_2SO_4, filtered, and concentrated under reduced pressure to afford the title compound **12c'** as a yellow solid (13 mg, 94%). **^{1}H NMR** (400 MHz, DMSO-*d*$_6$) δ 11.49 (br s, 1H), 8.29 (d, *J* = 2.7 Hz, 1H), 7.95 (d, *J* = 8.1 Hz, 1H), 7.41 (dt, *J* = 8.0, 1.0 Hz, 1H), 7.36 (q, *J* = 4.6 Hz, 1H), 7.14 (ddd, *J* = 8.1, 7.0, 1.3 Hz, 1H), 7.08 (ddd, *J* = 8.0, 7.0, 1.2 Hz, 1H), 6.78 (s, 1H), 3.03 (s, 3H), 2.99 (d, *J* = 4.6 Hz, 3H). NMR data are in agreement with those previously reported in literature.[27a]

(*Z*)-5-(Benzo[*d*][1,3]dioxol-5-ylmethylene)-3-methyl-2-(pyrrolidin-1-yl)-3,5-dihydro-4*H*-imidazol-4-one (12d)

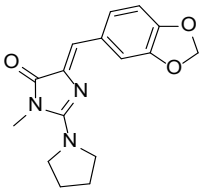

Following the *General Procedure E (ii)*, compound **12d** was obtained as a light brown solid (70 mg, 71%) from **11d** (100 mg, 0.33 mmol) and TEMPO (104 mg, 0.66 mmol) in $CHCl_3$ (3.3 mL) after flash chromatography purification (EtOAc/hexane gradient from 0:100 to 40:60 v/v). **^{1}H NMR** (400 MHz, $CDCl_3$) δ 7.98 (d, *J* = 1.6 Hz, 1H), 7.35 (dd, *J* = 8.1, 1.7 Hz, 1H), 6.81 (d, *J* = 8.1 Hz, 1H), 6.61 (s, 1H), 5.97 (s, 2H), 3.80 – 3.70 (m, 4H), 3.33 (s, 3H), 2.05 – 1.97 (m, 4H). **^{13}C NMR** (101 MHz, $CDCl_3$) δ 171.82, 157.99, 147.67, 147.37, 137.94, 130.57, 126.02, 116.29, 110.25, 108.34, 101.03,

48.81, 28.87, 25.44. **HRMS:** *m/z* calcd. for $C_{16}H_{18}N_3O_3^+$ $[M+H]^+$: 300.1343; found: 300.1351.

(*Z*)-3-Benzyl-5-(4-chlorobenzylidene)-2-(pyrrolidin-1-yl)-3,5-dihydro-4*H*-imidazol-4-one (12e)

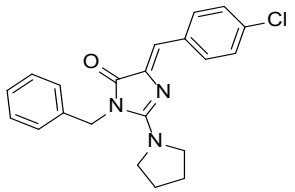

Following the *General Procedure E (ii)*, compound **12e** was obtained as a light brown solid (32 mg, 65%) from **11e** (50 mg, 0.14 mmol) and TEMPO (43 mg, 0.27 mmol) in $CHCl_3$ (1.4 mL) after flash chromatography purification (EtOAc/hexane gradient from 0:100 to 40:60 v/v). **^{1}H NMR** (400 MHz, $CDCl_3$) δ 8.09 – 8.03 (m, 2H), 7.38 – 7.32 (m, 2H, overlapped), 7.35 – 7.24 (m, 3H, overlapped), 7.17 – 7.12 (m, 2H), 6.67 (s, 1H), 5.04 (s, 2H), 3.69 – 3.55 (m, 4H), 1.93 – 1.84 (m, 4H). **^{13}C NMR** (101 MHz, $CDCl_3$) δ 172.02, 157.72, 139.33, 136.71, 134.60, 133.30, 131.87, 128.99, 128.61, 127.59, 125.66, 114.42, 48.71, 44.97, 25.30. **HRMS:** *m/z* calcd. for $C_{21}H_{21}ClN_3O^+$ $[M+H]^+$: 366.1368; found: 366.1366.

(*Z*)-3-Benzyl-5-(4-methoxybenzylidene)-2-morpholino-3,5-dihydro-4*H*-imidazol-4-one (12g)

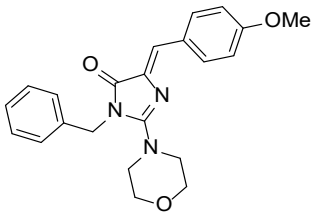

Following the *General Procedure E*, compound **12g** was obtained as a yellow solid (90 mg, 47% over two steps). The corresponding intermediate **11** was obtained in quantitative conversion following the *General Procedure E (i)* from **5c** (150 mg, 0.51 mmol) and **Nu-5** (447 mL, 5.1 mmol, 10 eq.) in CH_3CN (5.1 mL) at 80 ºC for 17 h. The crude intermediate was directly subjected to the dehydrogenation protocol with TEMPO (160 mg, 1.03 mmol) in $CHCl_3$ (5 mL) which afforded the title compound **12g** after flash chromatography purification (EtOAc/hexane gradient from 0:100 to 40:60 v/v). **^{1}H NMR** (400 MHz, $CDCl_3$) δ 8.11 – 8.05 (m, 2H), 7.37 – 7.27 (m, 3H), 7.21 – 7.15 (m, 2H), 6.96 – 6.91 (m, 2H), 6.90 (s, 1H), 4.88 (s, 2H), 3.85 (s, 3H), 3.66 – 3.60 (m, 4H), 3.43 – 3.38

(m, 4H). **^{13}C NMR** (101 MHz, $CDCl_3$) δ 172.18, 160.22, 159.75, 136.12, 136.03, 133.00, 128.96, 128.09, 127.74, 126.21, 120.64, 114.13, 66.09, 55.31, 47.94, 46.04. **HRMS:** *m/z* calcd. for $C_{22}H_{24}N_3O_3^+$ $[M+H]^+$: 378.1812; found: 378.1814.

(*Z*)-5-(Benzo[*d*][1,3]dioxol-5-ylmethylene)-3-methyl-2-(pentylamino)-3,5-dihydro-4*H*-imidazol-4-oneone (12h)

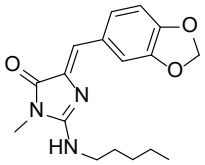

Following the *General Procedure E*, compound **12g** was obtained as a yellow solid (58 mg, 37% over two steps). The corresponding intermediate **11** was obtained in quantitative conversion following the *General Procedure E (i)* from **5i** (115 mg, 0.5 mmol) and **2k** (290 mL, 2.5 mmol, 5 eq.) in CH_3CN (5 mL) at 80 ºC for 17 h. The crude intermediate was directly subjected to the dehydrogenation protocol with MnO_2 (2.2 g, 25 mmol) in $CHCl_3$ (5 mL) which afforded the title compound **12g** after flash chromatography purification (EtOAc/hexane gradient from 0:100 to 40:60 v/v). **^{1}H NMR** (400 MHz, $CDCl_3$) δ 7.98 (d, *J* = 1.6 Hz, 1H), 7.35 (dd, *J* = 8.1, 1.6 Hz, 1H), 6.81 (d, *J* = 8.1 Hz, 1H), 6.65 (s, 1H), 5.98 (s, 2H), 4.49 (br s, 1H), 3.63 – 3.53 (m, 2H), 3.11 (s, 3H), 1.74 – 1.67 (m, 2H), 1.44 – 1.36 (m, 4H), 0.98 – 0.91 (m, 3H). **^{13}C NMR** (126 MHz, $CDCl_3$) δ 170.22, 157.06, 147.71, 147.57, 138.04, 130.26, 126.15, 117.11, 110.35, 108.33, 101.07, 42.00, 29.28, 29.02, 25.08, 22.36, 13.99. **HRMS:** *m/z* calcd. for $C_{17}H_{22}N_3O_3^+$ $[M+H]^+$: 316.1655; found: 316.1656.

(*Z*)-2-Amino-5-(benzo[*d*][1,3]dioxol-5-ylmethylene)-3-methyl-3,5-dihydro-4*H*-imidazol-4-one (12i, Leucettamine B)

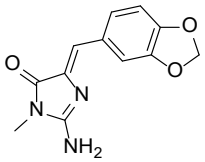

A 0.5-2 mL Biotage microwave vial was charged with **5i** (50 mg, 0.22 mmol, 1 eq.), a 7M NH_3 solution in CH_3OH (1 mL, 7 mmol, 32 eq.) and $CuCl_2$ (29 mg, 0.22 mmol, 1 eq.). The vial was sealed, and the reaction was stirred at 80 ºC for 30 min under mW irradiation. After reaction completion (LC-MS control), the reaction mixture was diluted with CH_2Cl_2 and washed with a saturated aqueous solution of NH_4Cl (5x), water and

saturated brine. The organic layer was dried over Na_2SO_4, filtered, and concentrated under reduced pressure to give a dark solid. The crude product was purified *via* neutral Al_2O_3 flash chromatography (EtOAc/hexane gradient from 30:70 to 100:0 v/v) to afford the title compound **12i** as a yellow solid (11 mg, 20 %). **^{1}H NMR** (500 MHz, DMSO-d_6) δ 7.93 (d, J = 1.6 Hz, 1H), 7.50 (s, 2H), 7.40 (dd, J = 8.1, 1.5 Hz, 1H), 6.91 (d, J = 8.0 Hz, 1H), 6.34 (s, 1H), 6.02 (s, 2H), 3.04 (s, 3H). NMR data are in agreement with those previously reported in literature.[28a]

The ^{1}H NMR spectra of compound **12i** contains 0.5 eq. of THF which was not removed under high vacuum.

(*Z*)-5-(Benzo[*d*][1,3]dioxol-5-ylmethylene)-3-methyl-2-(piperazin-1-yl)-3,5-dihydro-4*H*-imidazol-4-one (12j)

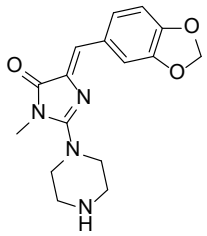

Following the *Special Case I*, compound **12j** was obtained as a yellow solid (295 mg, 60%). The intermediate **Boc-12j** was obtained from **11j** (650 mg, 1.6 mmol) and MnO_2 (6.8 g, 78 mmol) in $CHCl_3$ (15.6 mL) at rt for 17 h. The title compound **12j** was obtained from Boc-deprotection of intermediate **Boc-12j** with TFA (12 mL, 156 mmol) in CH_2Cl_2 (15 mL) at rt for 2 h. Compound **12j** was used in the next step (Synthesis of Compounds **14**) without further purification. **^{1}H NMR** (400 MHz, $CDCl_3$) δ 7.97 (d, J = 1.7 Hz, 1H), 7.35 (dd, J = 8.1, 1.6 Hz, 1H), 6.82 (d, J = 8.1 Hz, 1H), 6.75 (s, 1H), 5.99 (s, 2H), 3.51 (dd, J = 6.1, 3.9 Hz, 4H), 3.23 (s, 3H), 3.03 (dd, J = 6.2, 3.7 Hz, 5H). **^{13}C NMR** (101 MHz, $CDCl_3$) δ 172.00, 160.89, 148.04, 147.78, 137.14, 129.91, 126.78, 119.63, 110.46, 108.40, 101.18, 48.68, 45.52, 29.74. **HRMS:** *m/z* calcd. for $C_{16}H_{19}N_4O_3^+$ $[M+H]^+$: 315.1452; found: 315.1452.

(*Z*)-5-(Benzo[*d*][1,3]dioxol-5-ylmethylene)-3-methyl-2-(propylthio)-3,5-dihydro-4*H*-imidazol-4-one (13)

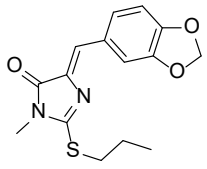

Following the *General Procedure E*, compound **12g** was obtained as a yellow solid (58 mg, 37% over two steps). The corresponding intermediate **11** was obtained in quantitative conversion following the *General Procedure E (i)* from **5i** (50 mg, 0.22 mmol), **Nu-6** (23 mL, 0.25 mmol, 1.2 eq.) in CH_3CN (2 mL) at rt for 3 h. The crude intermediate was directly subjected to the dehydrogenation protocol with I_2 (50 mg, 0.2 mmol) / TEMPO (4 mg, 0.02 mmol) in $CDCl_3$ (2 mL) which afforded the title compound **12g** after flash chromatography purification (EtOAc/hexane gradient from 0:100 to 20:80 v/v). **^{1}H NMR** (400 MHz, $CDCl_3$) δ 8.06 (t, *J* = 1.3 Hz, 1H), 7.37 (dt, *J* = 8.4, 1.1 Hz, 1H), 6.86 (s, 1H), 6.83 (dd, *J* = 8.1, 1.0 Hz, 1H), 6.01 (d, *J* = 1.1 Hz, 2H), 3.32 (td, *J* = 7.2, 1.0 Hz, 2H), 3.15 (d, *J* = 1.0 Hz, 3H), 1.89 (hd, *J* = 7.4, 1.0 Hz, 2H), 1.11 (td, *J* = 7.4, 1.0 Hz, 3H). **^{13}C NMR** (101 MHz, $CDCl_3$) δ 169.94, 163.87, 149.07, 147.99, 137.14, 129.19, 127.98, 123.58, 110.83, 108.44, 101.41, 32.61, 26.53, 22.54, 13.47. **HRMS:** *m/z* calcd. for $C_{15}H_{17}N_2O_3S^+$ $[M+H]^+$: 305.0954; found: 305.0959.

(3a*S*,4*R*,6a*R*)-4-(5-(4-((*Z*)-4-(Benzo[*d*][1,3]dioxol-5-ylmethylene)-1-methyl-5-oxo-4,5-dihydro-1*H*-imidazol-2-yl)piperazin-1-yl)-5-oxopentyl)tetrahydro-1*H*-thieno[3,4-*d*]imidazol-2(3*H*)-one (14a)

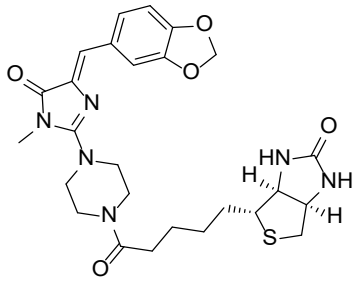

Following the *General Procedure F*, compound **14a** was obtained as a pale yellow solid (30 mg, 70%) from **12j** (25 mg, 0.08 mmol), biotin (23 mg, 0.095 mmol), HATU (36 mg, 0.095 mmol), and DIPEA (55 mL, 0.32 mmol) in DMF (0.8 mL) and CH_2Cl_2 (0.4 mL) after flash chromatography purification (EtOAc/hexane gradient from 0:100 to 30:70 v/v). **^{1}H NMR** (400 MHz, $CDCl_3$) δ 7.93 (d, *J* = 1.6 Hz, 1H), 7.34 (dd, *J* = 8.4, 1.6 Hz, 1H), 6.82 (d, *J* = 8.1 Hz, 1H), 6.79 (s, 1H), 5.99 (s, 2H), 5.79 (s, 1H), 5.10 (s, 1H), 4.53 – 4.45 (m, 1H), 4.36 – 4.28 (m, 1H), 3.84 – 3.74 (m, 2H), 3.71 – 3.63 (m, 2H), 3.63 – 3.54 (m, 2H), 3.48 (t, *J* = 5.2 Hz, 2H), 3.23 (s, 3H), 3.21 – 3.14 (m, 1H), 2.90 (dd, *J* = 12.8, 5.0 Hz, 1H), 2.72 (d, *J* = 12.9 Hz, 1H), 2.41 (t, *J* = 7.4 Hz, 2H), 1.84 – 1.62 (m, 4H, overlapped with water signal), 1.57 – 1.42 (m, 2H). **^{13}C NMR** (101 MHz, $CDCl_3$) δ 171.72, 171.62, 163.36, 160.60, 148.36, 147.84, 136.70, 129.57, 127.08, 120.88, 110.46,

108.47, 101.28, 61.81, 60.11, 55.29, 47.55, 44.83, 40.85, 40.57, 32.59, 29.44, 28.28, 24.96. **HRMS:** *m/z* calcd. for $C_{26}H_{33}N_6O_5S^+$ $[M+H]^+$: 541.2228; found: 541.2227.

(*Z*)-5-(Benzo[*d*][1,3]dioxol-5-ylmethylene)-3-methyl-2-(4-((*R*)-4-((3*S*,5*R*,7*S*,8*S*,9*R*,10*R*,12*R*,13*S*,14*R*,17*S*)-3,7,12-trihydroxy-10,13-dimethylhexadecahydro-1*H*-cyclopenta[*a*]phenanthren-17-yl)pentanoyl)piperazin-1-yl)-3,5-dihydro-4*H*-imidazol-4-one (14b)

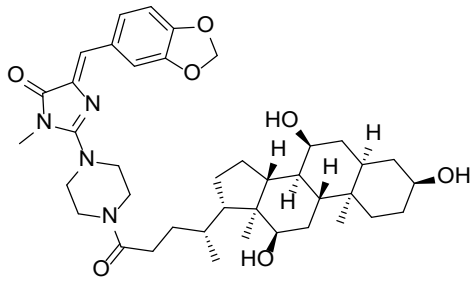

Following the *General Procedure F*, compound **14b** was obtained as a pale yellow solid (30 mg, 70%) from **12j** (25 mg, 0.08 mmol), biotin (23 mg, 0.095 mmol), HATU (36 mg, 0.095 mmol), and DIPEA (55 mL, 0.32 mmol) in DMF (0.8 mL) and CH_2Cl_2 (0.4 mL) after flash chromatography purification (EtOAc/hexane gradient from 0:100 to 30:70 v/v). **^{1}H NMR** (400 MHz, $CDCl_3$) δ 7.94 (d, *J* = 1.6 Hz, 1H), 7.34 (dd, *J* = 8.5, 1.7 Hz, 1H), 6.82 (d, *J* = 8.1 Hz, 1H), 6.80 (s, 1H), 5.99 (s, 2H), 4.01 – 3.96 (m, 1H), 3.87 – 3.83 (m, 1H), 3.80 – 3.75 (m, 2H), 3.70 – 3.64 (m, 2H), 3.60 – 3.54 (m, 2H), 3.49 – 3.44 (m, 2H), 3.24 (s, 3H), 2.50 – 2.40 (m, 1H), 2.33 – 2.16 (m, 4H), 1.98 – 1.65 (m, 15H, complex signal), 1.60 – 1.26 (m, 12H, complex signal), 1.19 – 1.07 (m, 1H), 1.03 (d, *J* = 6.3 Hz, 3H), 0.93 – 1.02 (m, 1H), 0.89 (m, 5H, overlapped signals), 0.70 (s, 3H).**^{13}C NMR** (101 MHz, $CDCl_3$) δ 172.52, 171.65, 160.59, 148.36, 147.84, 136.71, 129.59, 127.09, 120.93, 110.49, 108.46, 101.28, 72.98, 71.93, 68.40, 47.57, 46.89, 46.51, 44.83, 41.90, 41.45, 40.83, 39.71, 39.55, 35.38, 35.24, 34.71, 31.21, 30.53, 29.99, 29.44, 28.33, 27.57, 26.57, 23.24, 22.52, 17.57, 12.57. **HRMS:** *m/z* calcd. for $C_{40}H_{56}N_4O_7^+$ $[M+H]^+$: 705.4222; found: 705.4214.

The spectra contain traces of hexane (from the chromatography) and pentane (used in an attempt to remove the remaining hexane), which were not removed under high vacuum.

2.4. Fluorescence Studies

2.4.1. In vitro Spectroscopy

A representative set of the synthesised compounds were chosen for spectroscopic studies (Figure S25).

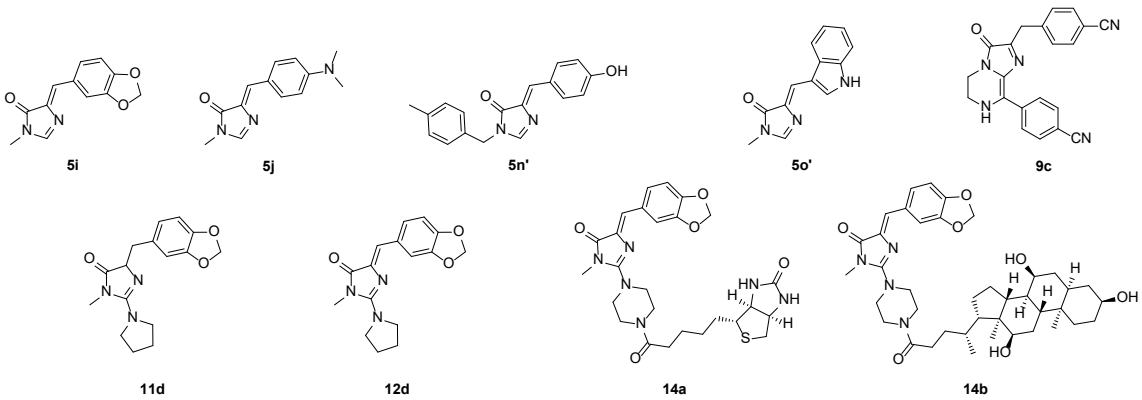

Absorption spectra were recorded with NanoDrop. Step 0.5 nm. Emission spectra were recorded with Varioskan. (Step: 5 nm, excitation bandwidth: 12 nm, measurement time: 100 ms, dynamic range: automatic). Selected compounds were dissolved in DMSO and were diluted to 100 µM. The spectra were recorded at room temperature. The spectra are represented as means from two independent experiments with n=3 (Figure S26).

Figure S25. Selected compounds for UV-Vis spectroscopy studies.

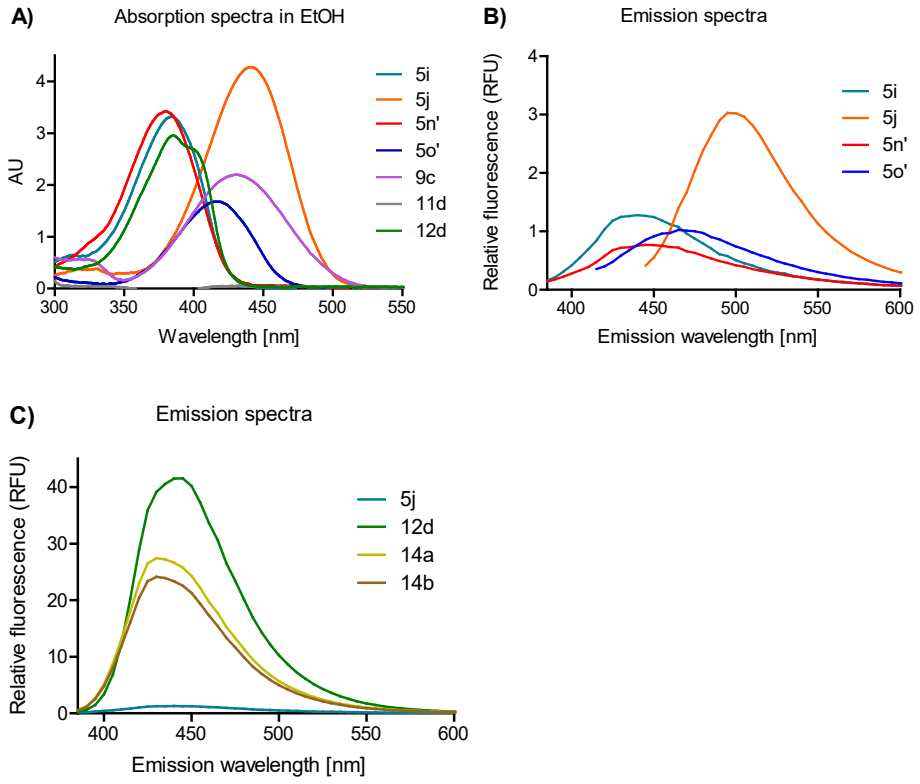

Table S8. Absorption and emission maxima values of selected compounds in different solvents (100 mM).

Compound	Absorption maxima wavelength (nm)			Emission maxima wavelength (nm)			Excitation wavelength (nm)
	DMSO	EtOH	PBS	DMSO	EtOH	PBS	
5i	385	385	387	450	440	465	360
5j	437	441	455	505	495	530	420
5n'	383	380	376	445	445	465	355
5o'	412	416	414	465	465	450	390
9c	439	430	424	610	595	595	400
12d	388	386	392	450	445	460	360
14a	-	383	-	-	430	-	360
14b	-	385	-	-	430	-	360

The fluorescence intensity of compounds **5i** and **12d** was significally increased the presence of phosphatidylcholine (PC)-based lyposome, a viscous hydrophobic environment that restricts the rotation around the aryl-alkene bond (Figure S27B). Moreover, the fluorescence of 2-aminoimidazolone **12d** was reduced at lower pH values (Figure S27A).

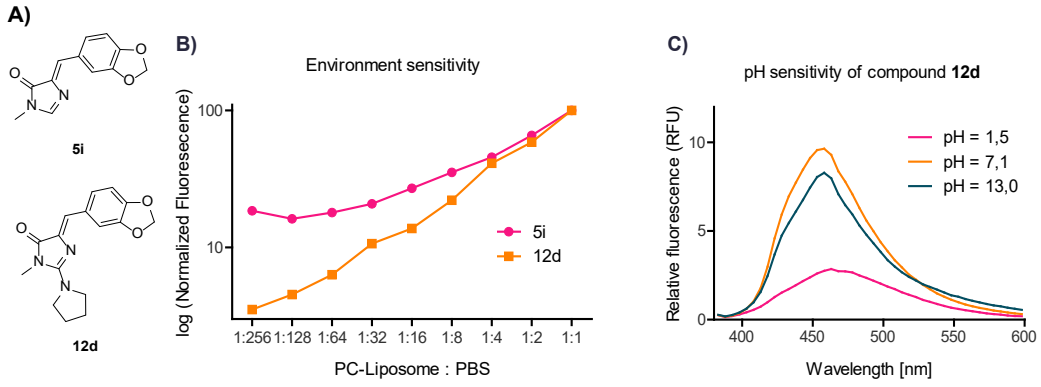

Figure S27. Environment-sensitive fluorescence of compounds 5i and 12d (100 mM). A) Structure of compounds **5i** and **12d**. B) Fluorescence emission at different PC-liposome: PBS ratios (l_{exc}: 360 nm). C) Fluorescence emission of compound **12d** in 1 :1 mixtures of MeOH : water at different pH values (l_{exc}: 360 nm).

2.5. Crystallographic Data

Table S9. Crystal data and structure refinement of compound **5h.**

CCCD Number	**2240654**[18]
Crystal data	
Chemical formula	$C_{24}H_{20}N_2O_2$
M_r	368.42
Crystal system, space group	Monoclinic, $P2_1$
Temperature (K)	180
a, b, c (Å)	5.9189 (7), 7.4198 (8), 21.621 (2)
β (°)	97.764 (4)
V (Å^3)	940.84 (18)
Z	2
Radiation type	Cu $K\alpha$
μ (mm^{-1})	0.66
Crystal size (mm)	0.4 × 0.15 × 0.05
Data collection	
Diffractometer	Bruker *APEX*-II CCD
Absorption correction	Multi-scan *SADABS2016*/2 (Bruker,2016/2) was used for absorption correction. wR2(int) was 0.1552 before and 0.0979 after correction. The Ratio of minimum to maximum transmission is 0.7054. The λ/2 correction factor is Not present.
T_{min}, T_{max}	0.532, 0.754
No. of measured, independent and observed [$I > 2\sigma(I)$] reflections	16392, 3583, 3341
R_{int}	0.067
$(\sin \theta/\lambda)_{max}$ (Å^{-1})	0.620
Refinement	
$R[F^2 > 2\sigma(F^2)]$, $wR(F^2)$, S	0.043, 0.114, 1.04
No. of reflections	3583
No. of parameters	255
No. of restraints	1
H-atom treatment	H-atom parameters constrained
$\Delta\rho_{max}$, $\Delta\rho_{min}$ (e Å^{-3})	0.15, −0.16
Absolute structure	Refined as an inversion twin.
Absolute structure parameter	−0.1 (3)

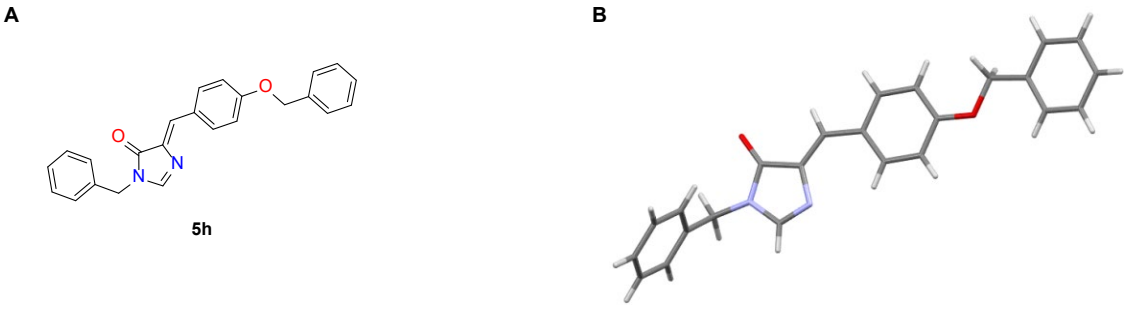

Figure S28 A) Structure of **5h**. B) X-Ray molecular structure of **5h**.

Table S10. Crystal data and structure refinement of compound **8a.**

CCDC number	**2240652**[18]
Crystal data	
Chemical formula	$C_{34}H_{26}Cl_2N_4O_2$
M_r	593.49
Crystal system, space group	Monoclinic, $P2_1/c$
Temperature (K)	180
a, b, c (Å)	15.815 (2), 7.4619 (10), 12.7516 (16)
β (°)	103.016 (9)
V (Å^3)	1466.2 (3)
Z	2
Radiation type	Cu $K\alpha$
μ (mm^{-1})	2.30
Crystal size (mm)	0.1 × 0.08 × 0.01
Data collection	
Diffractometer	Bruker *APEX*-II CCD
Absorption correction	Multi-scan *SADABS2016*/2 (Bruker,2016/2) was used for absorption correction. wR2(int) was 0.1374 before and 0.0955 after correction. The Ratio of minimum to maximum transmission is 0.7157. The λ/2 correction factor is Not present.
T_{min}, T_{max}	0.538, 0.752
No. of measured, independent and observed [$I > 2\sigma(I)$] reflections	20711, 2182, 1356
R_{int}	0.094
θ_{max} (°)	60.1
$(\sin\theta/\lambda)_{max}$ (Å^{-1})	0.562
Refinement	
$R[F^2 > 2\sigma(F^2)]$, $wR(F^2)$, S	0.065, 0.225, 1.10
No. of reflections	2182
No. of parameters	190
H-atom treatment	H-atom parameters constrained
$\Delta\rho_{max}$, $\Delta\rho_{min}$ (e Å^{-3})	0.30, −0.36

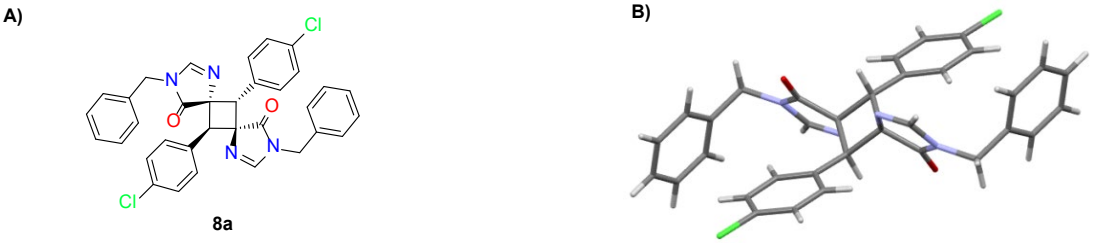

Figure S29. A) Structure of **8a**. B) X-Ray molecular structure of **8a**.

2.6. Selected Copies of NMR Spectra

Methyl 1-benzyl-5-(4-chlorophenyl)-4,5-dihydro-1H-imidazole-4-carboxylate (**4a**)

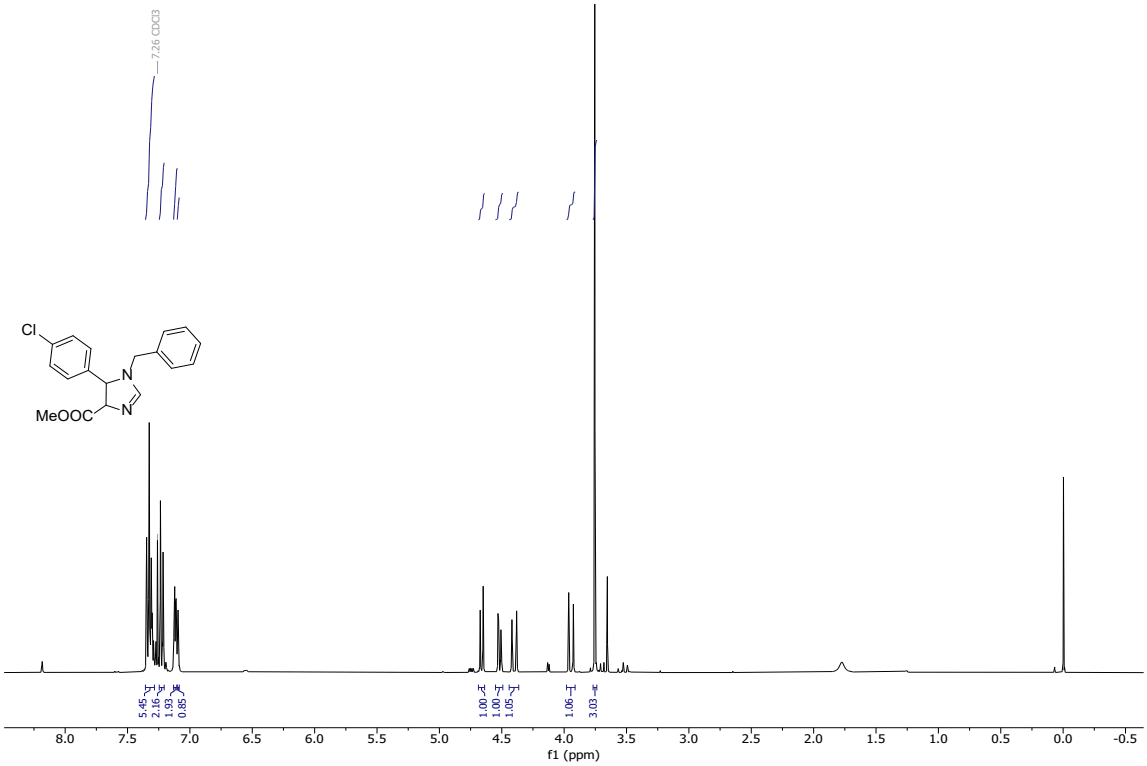

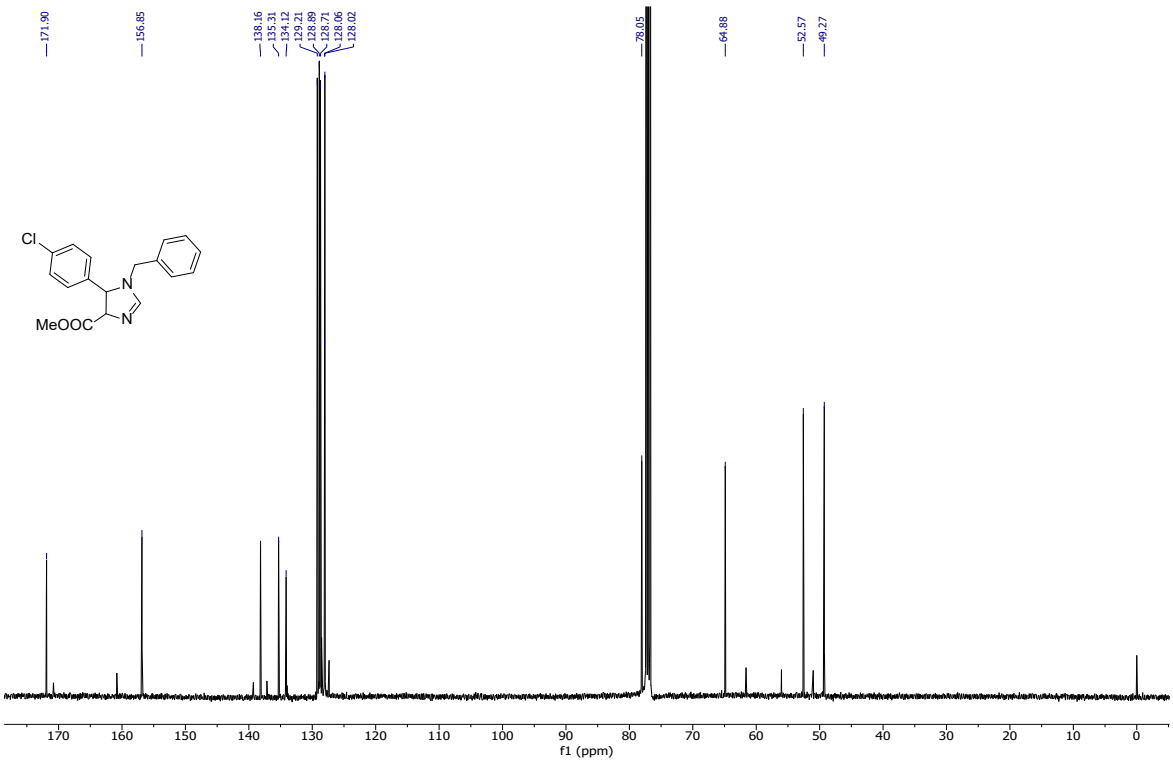

Methyl (1r,3r,5r,7r)-3'-benzyl-3',5'-dihydrospiro[adamantane-2,4'-imidazole]-5'-carboxylate (4ac)

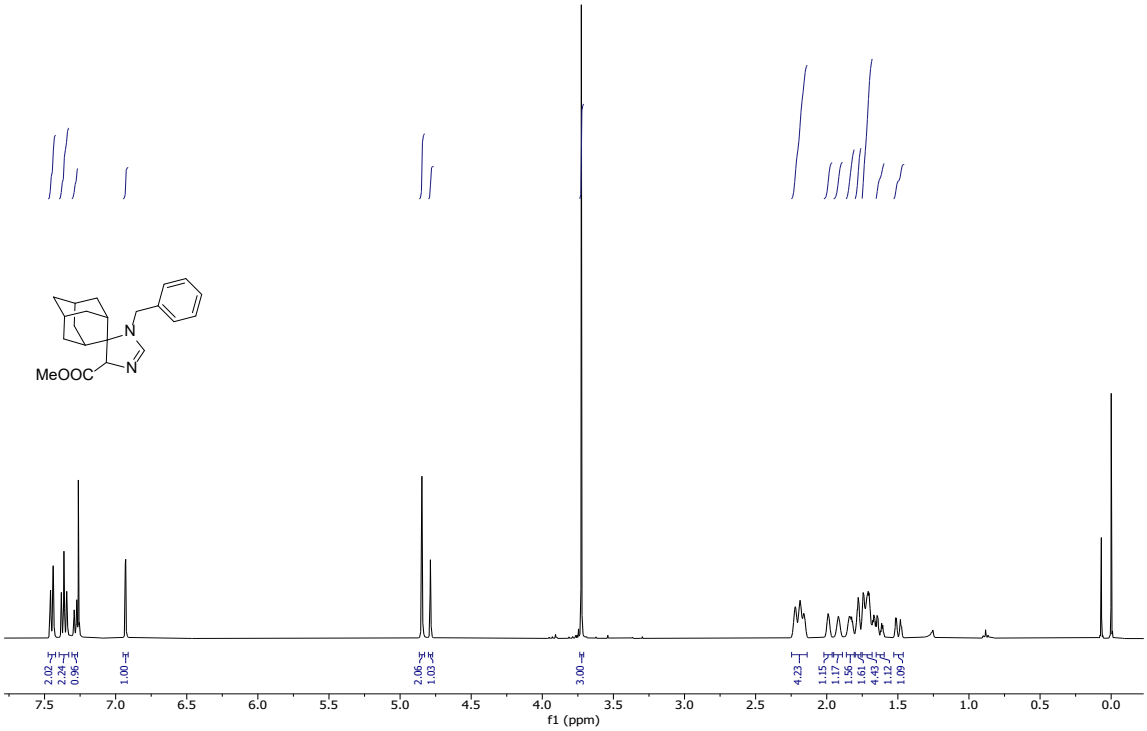

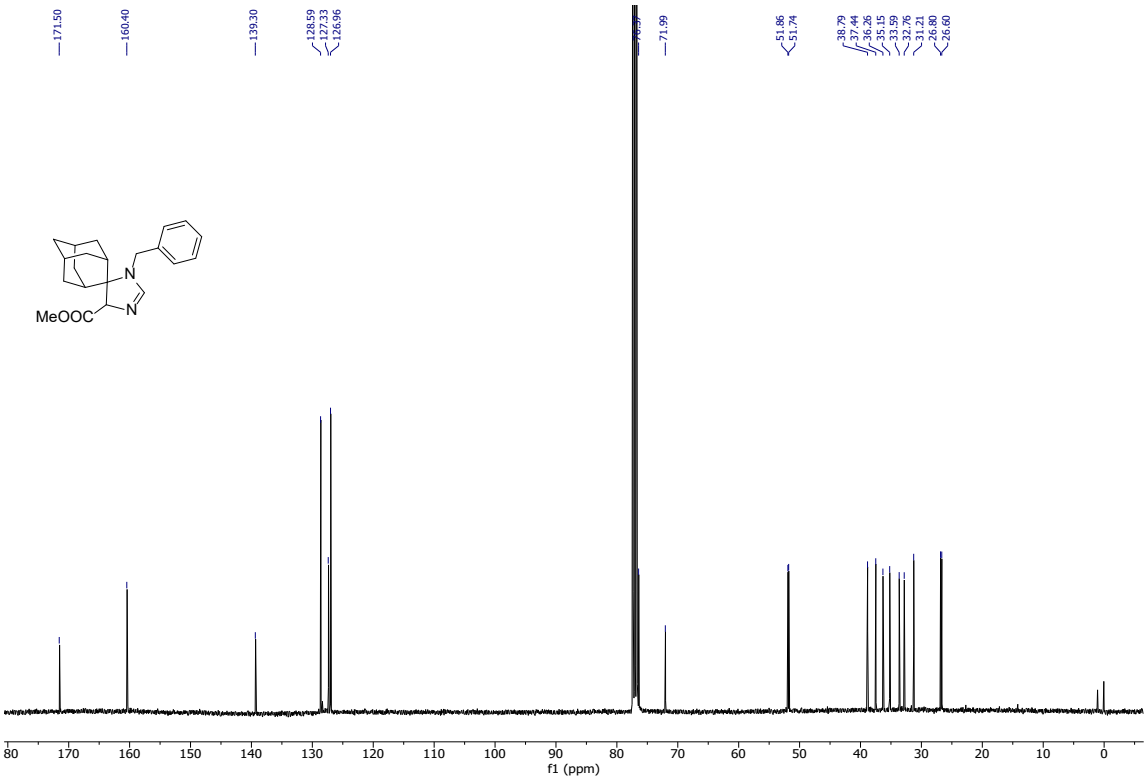

(*Z*)-3-Benzyl-5-(4-chlorobenzylidene)-3,5-dihydro-4*H*-imidazol-4-one (5a)

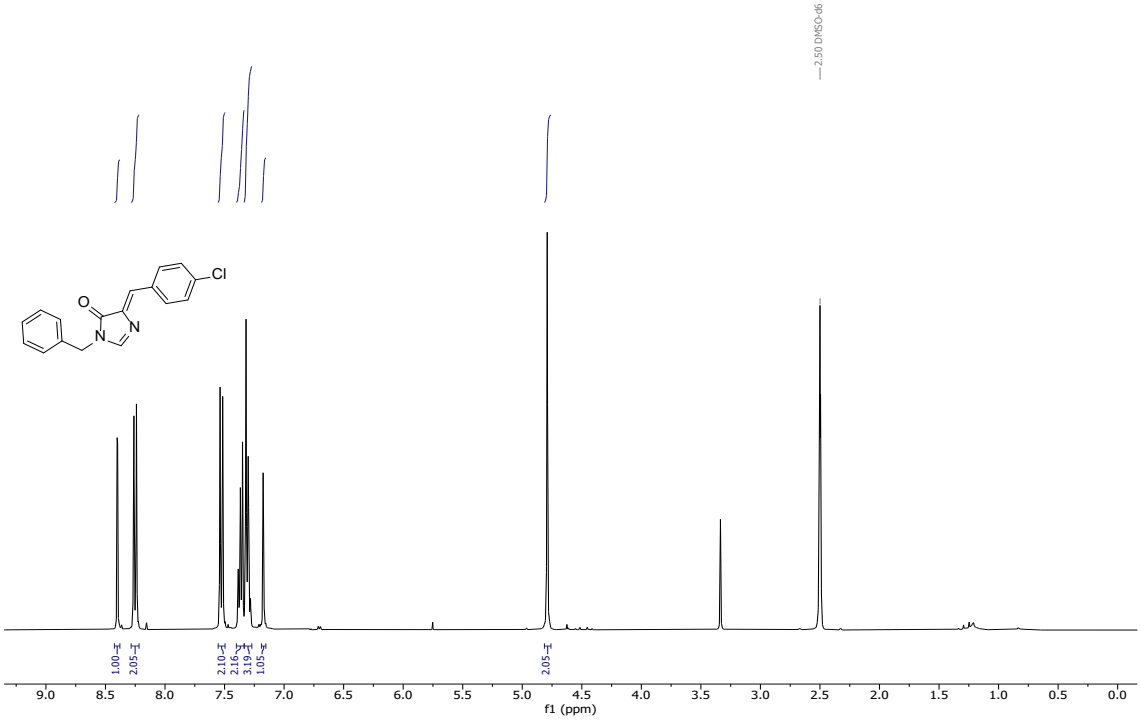

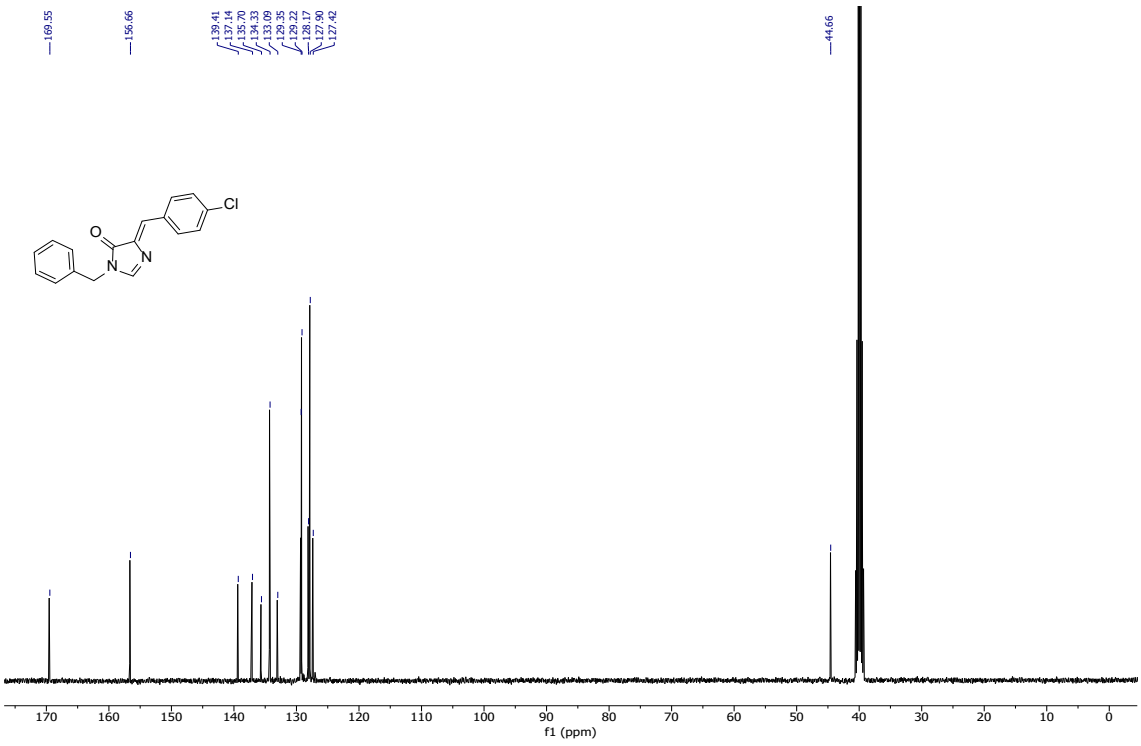

(*Z*)-3-Benzyl-5-(4-chlorobenzylidene)-3,5-dihydro-4*H*-imidazol-4-one-2-*d* (5a-*d*)

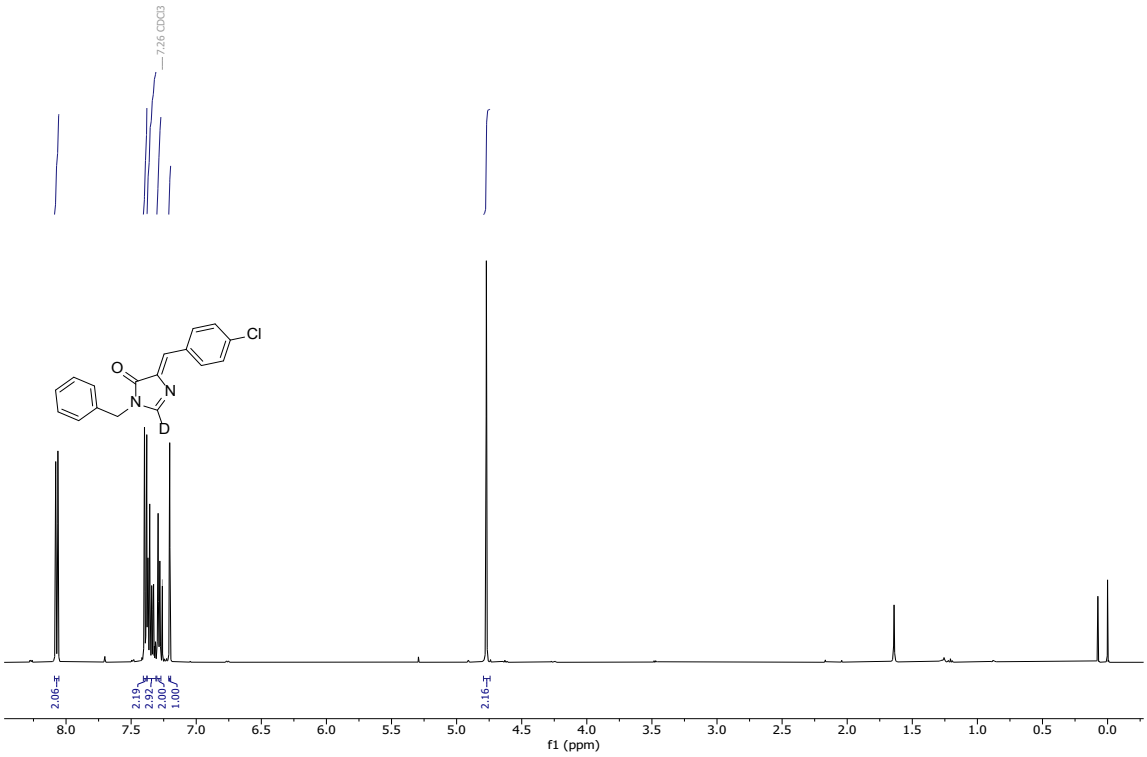

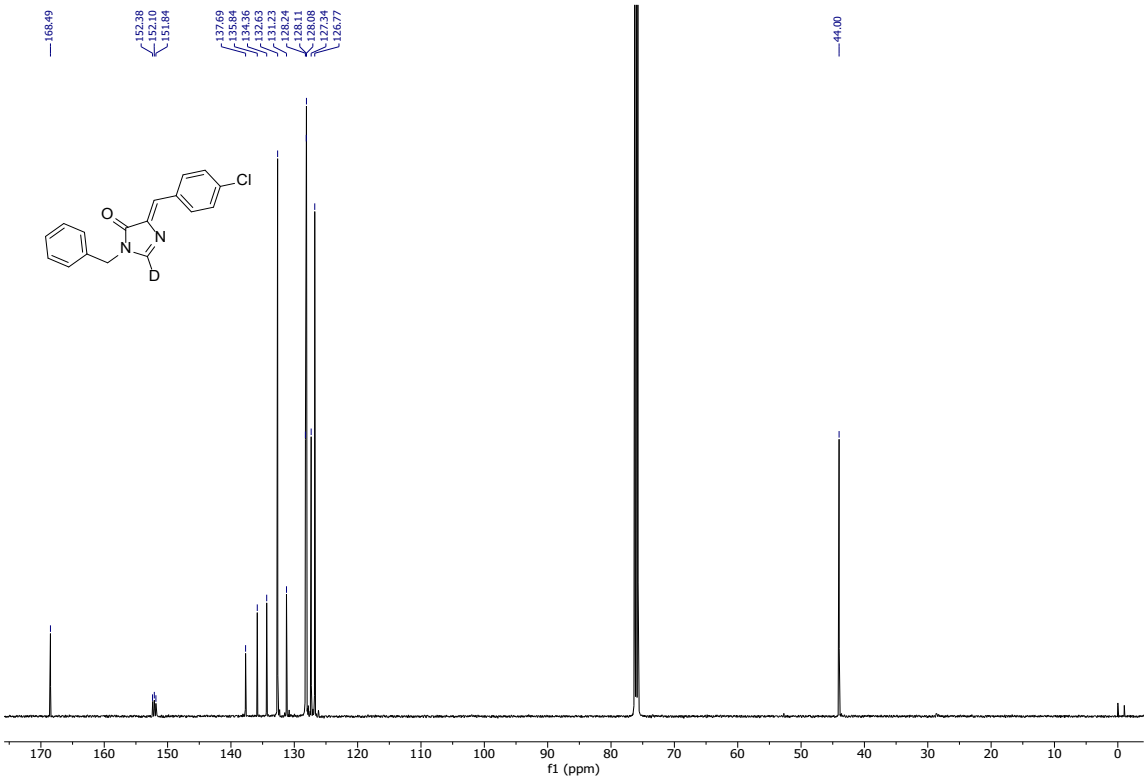

(*Z*)-3-(3-iodobenzyl)-5-(4-methoxybenzylidene)-3,5-dihydro-4*H*-imidazol-4-one (5d)

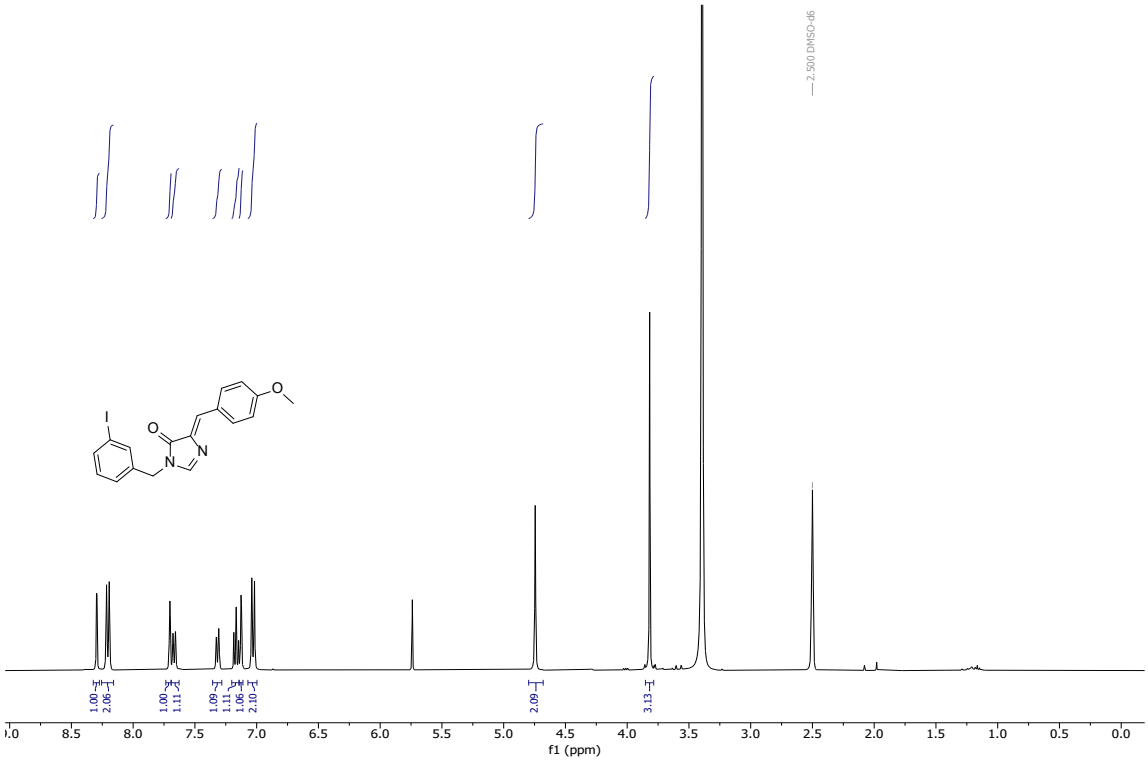

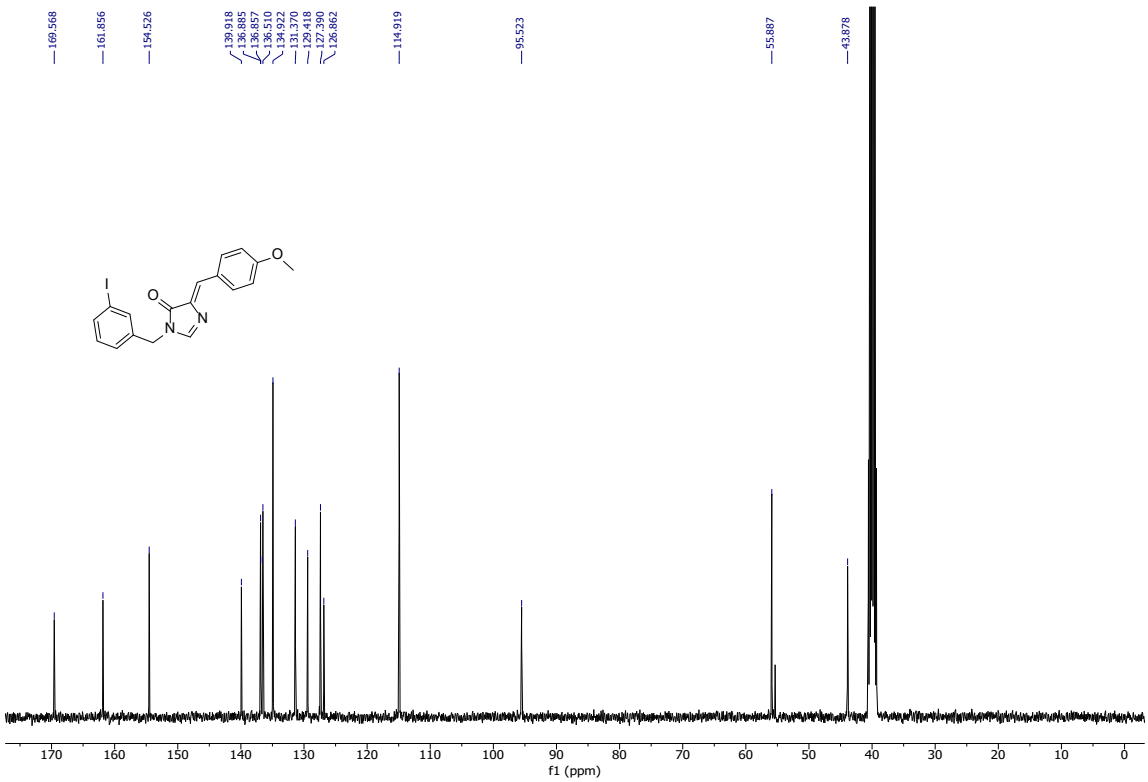

(*R*,*Z*)-5-(4-Methoxybenzylidene)-3-(1-phenylethyl)-3,5-dihydro-4*H*-imidazol-4-one (5f)

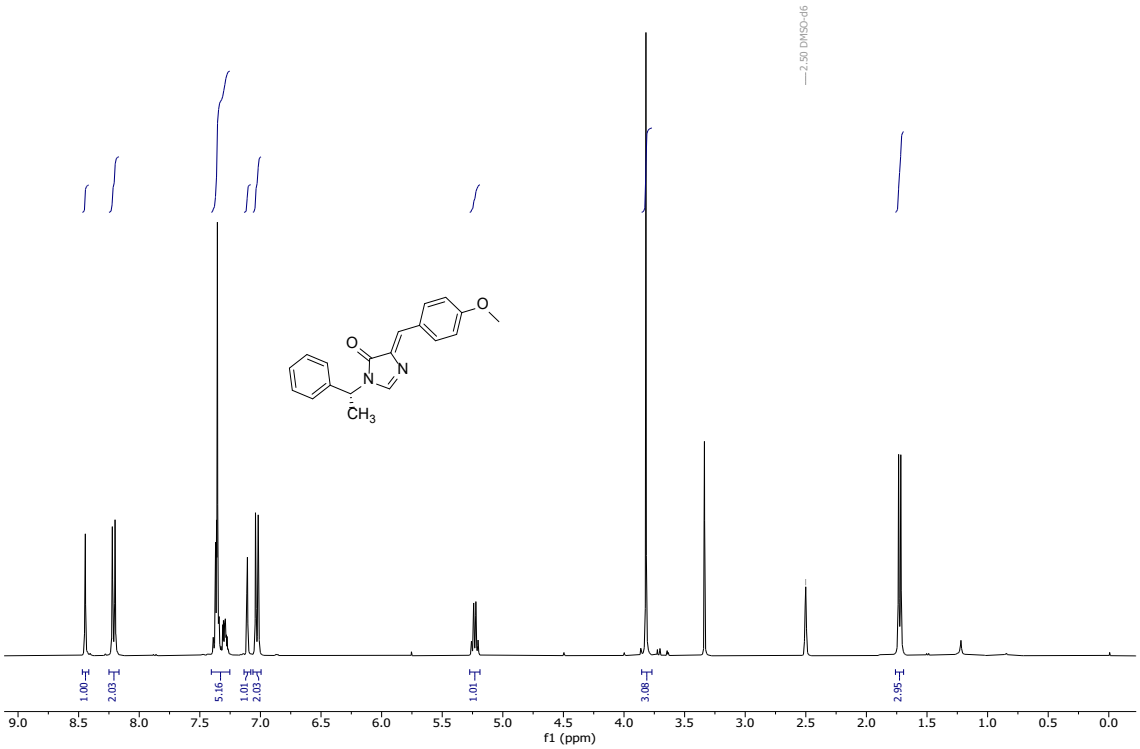

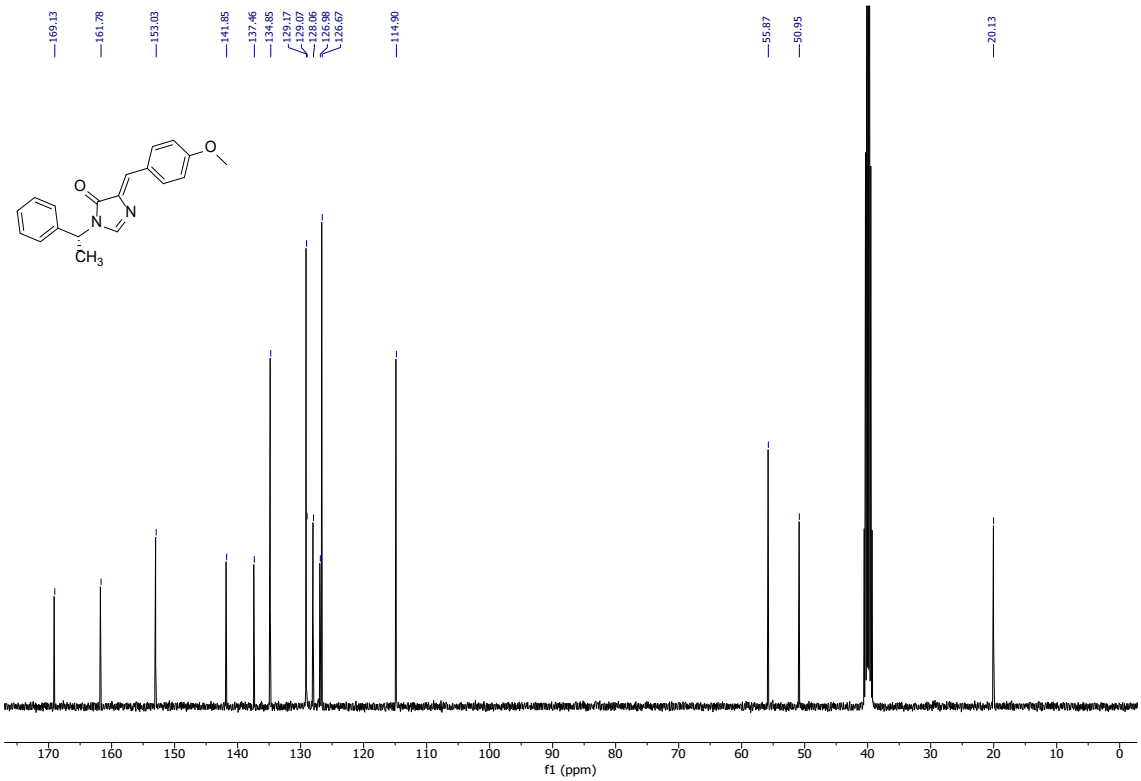

(*Z*)-5-(2-(allyloxy)benzylidene)-3-(4-methylbenzyl)-3,5-dihydro-4*H*-imidazol-4-one (5g)

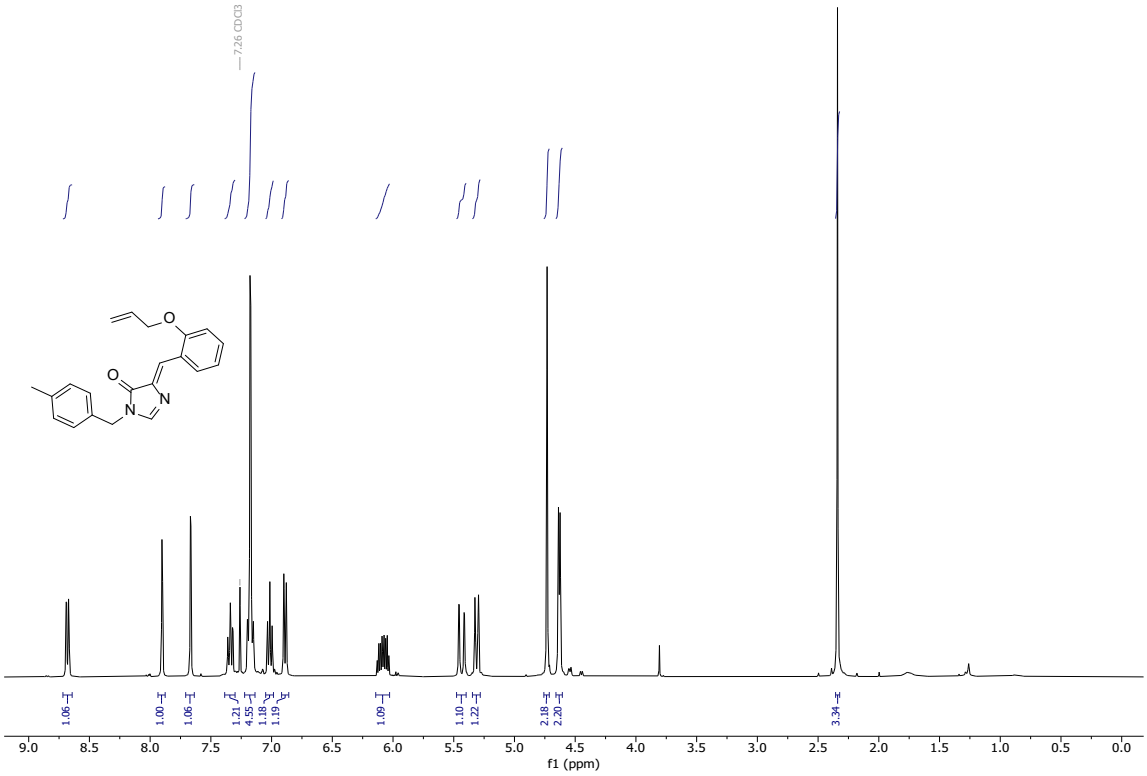

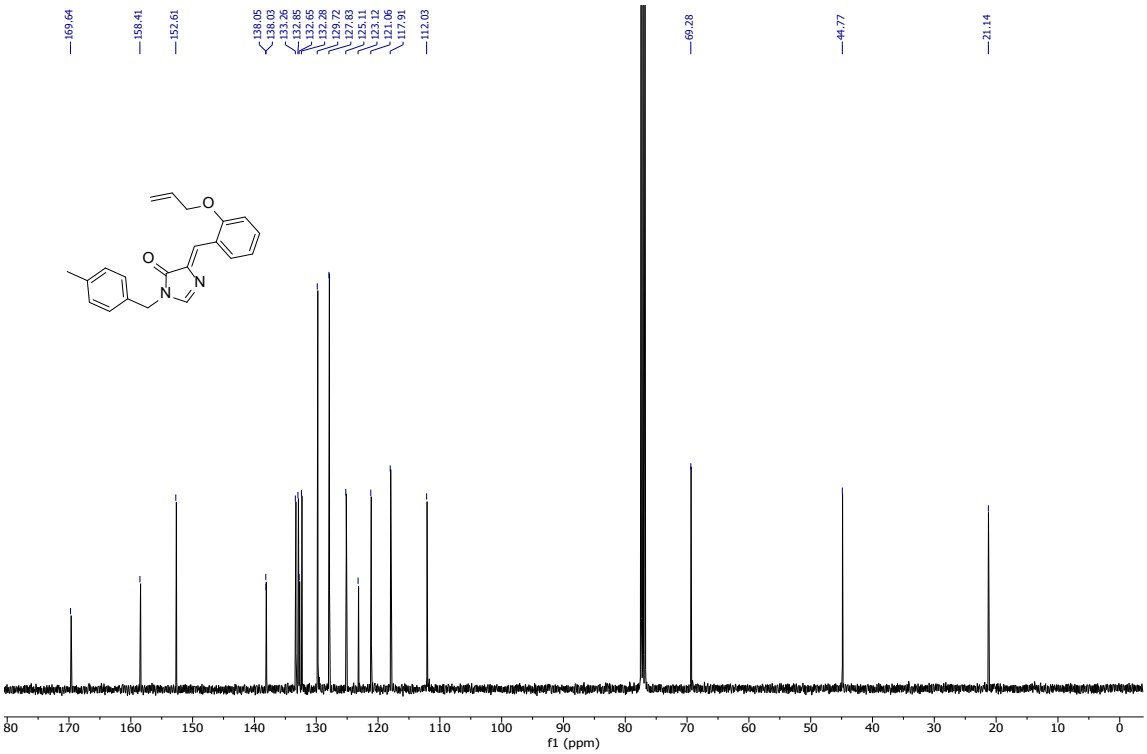

(*Z*)-3-Benzyl-5-(4-(benzyloxy)benzylidene)-3,5-dihydro-4*H*-imidazol-4-one (5h)

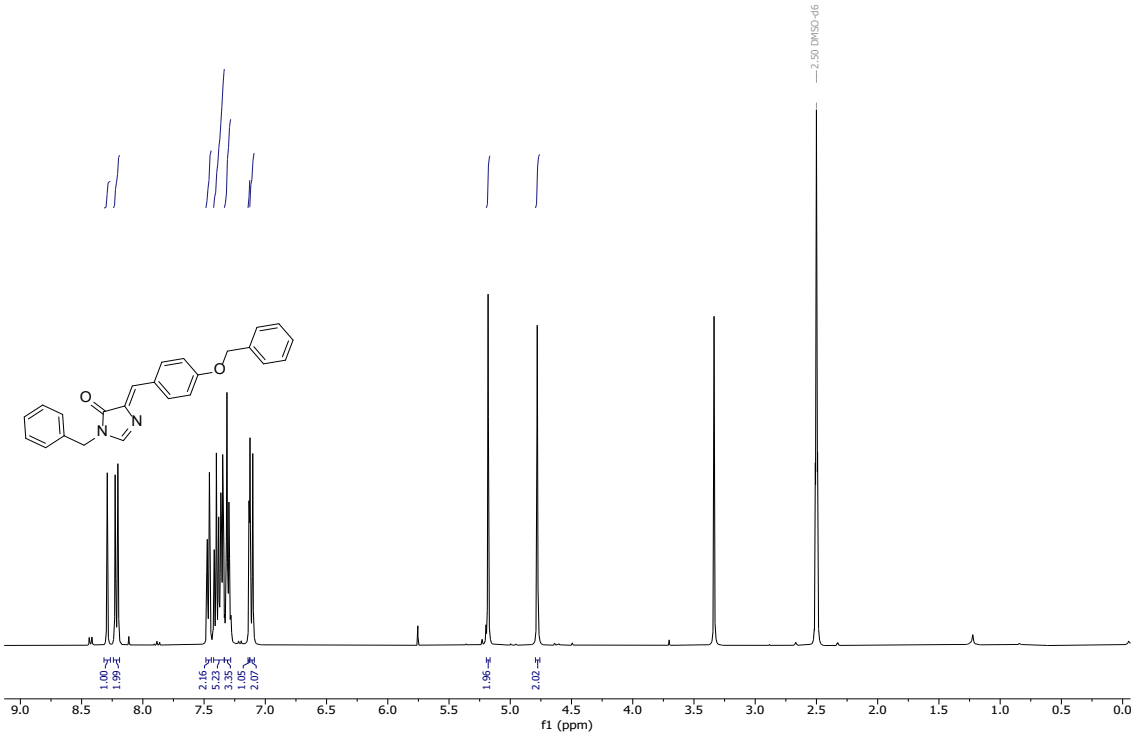

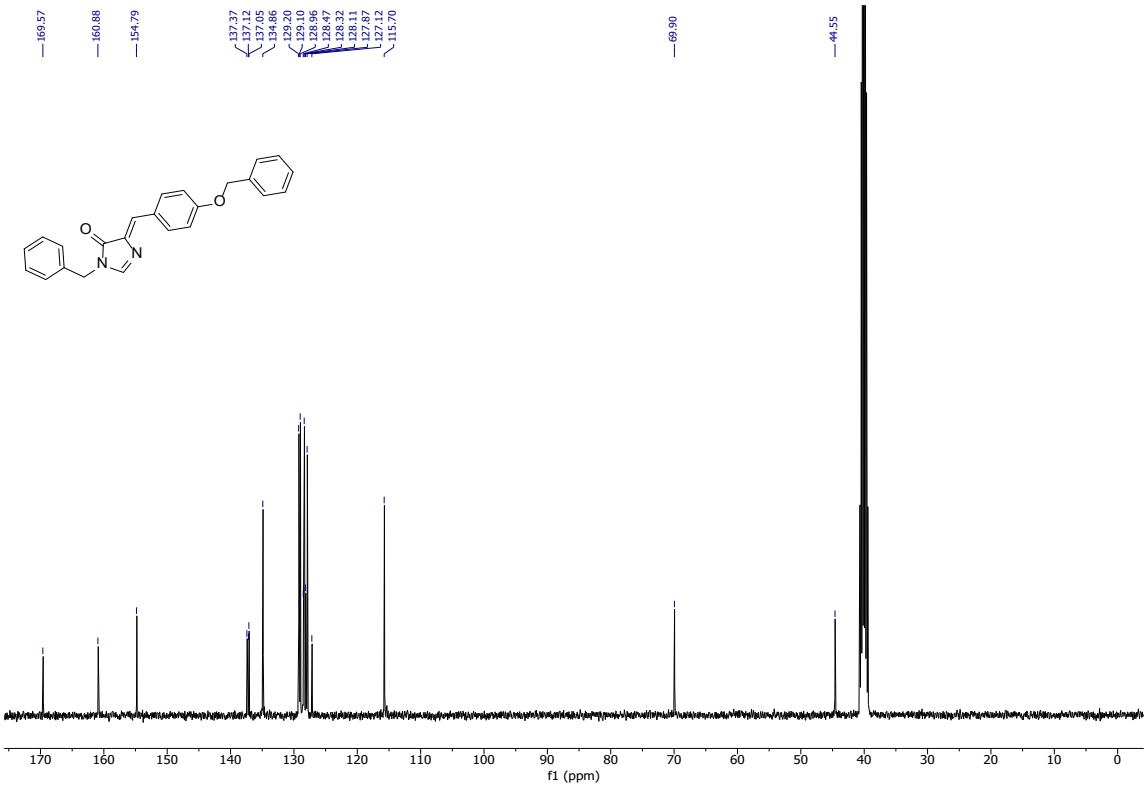

(*Z*)-5-(Benzo[*d*][1,3]dioxol-5-ylmethylene)-3-methyl-3,5-dihydro-4*H*-imidazol-4-one (5i)

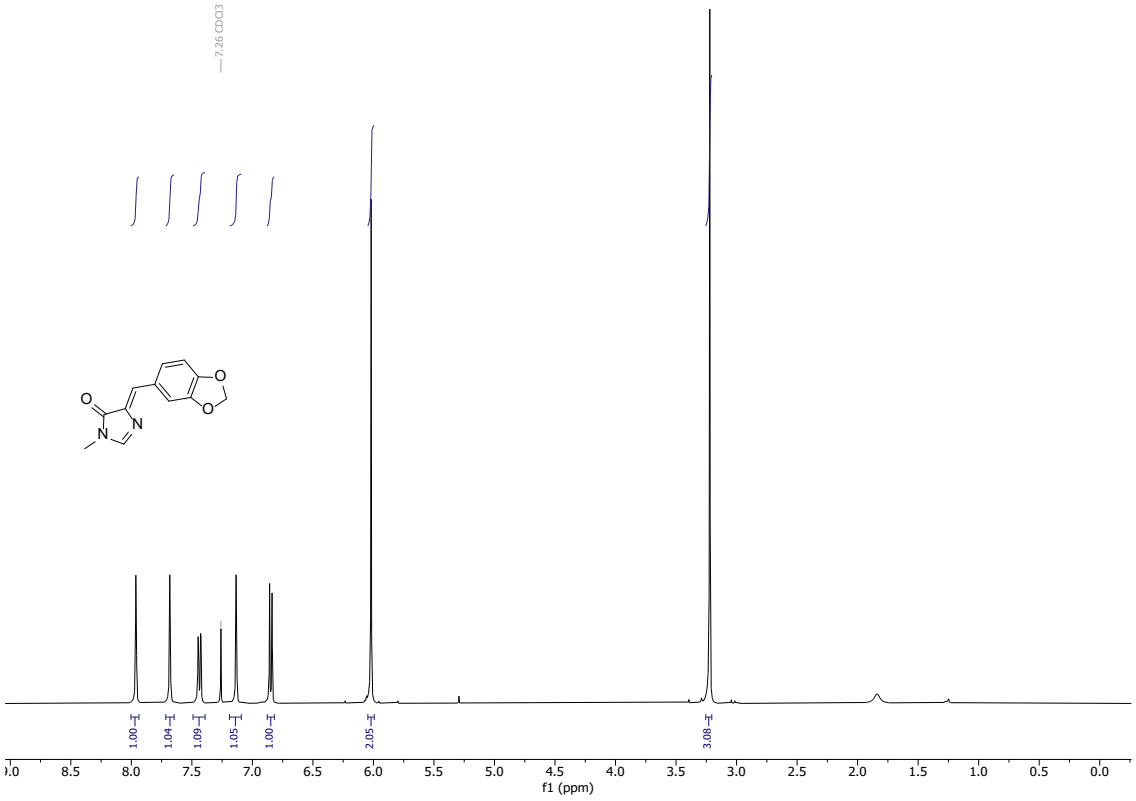

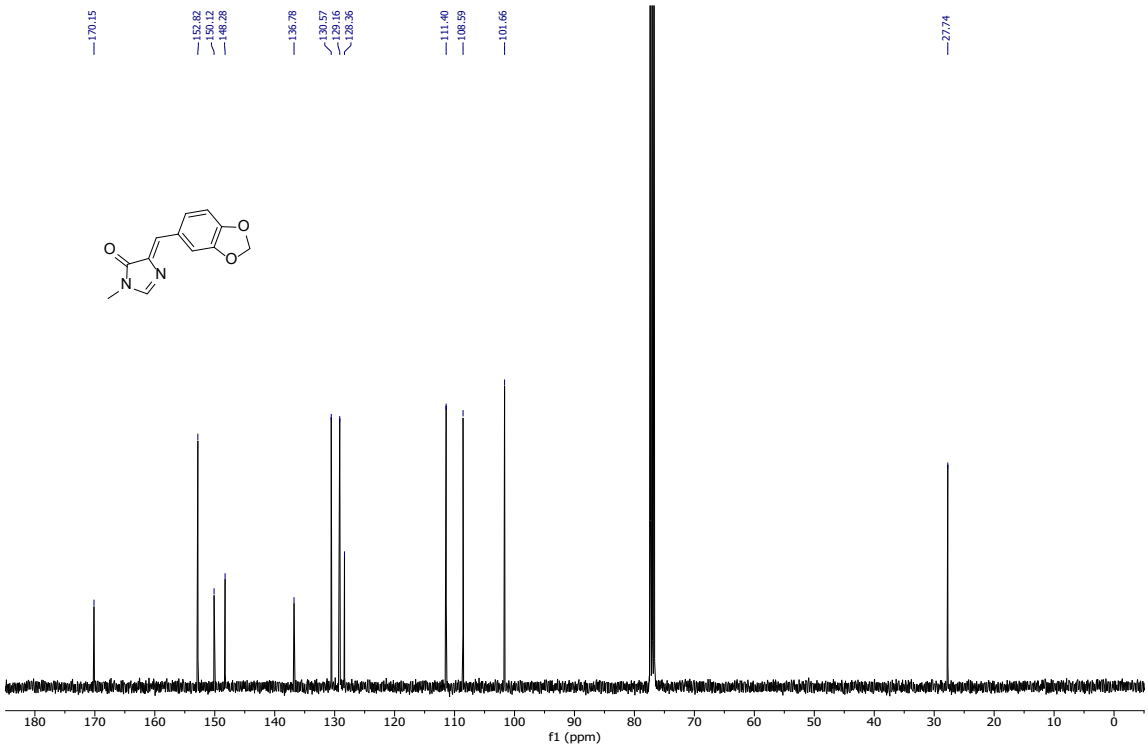

(*Z*)-5-(4-(Dimethylamino)benzylidene)-3-methyl-3,5-dihydro-4*H*-imidazol-4-one (5j)

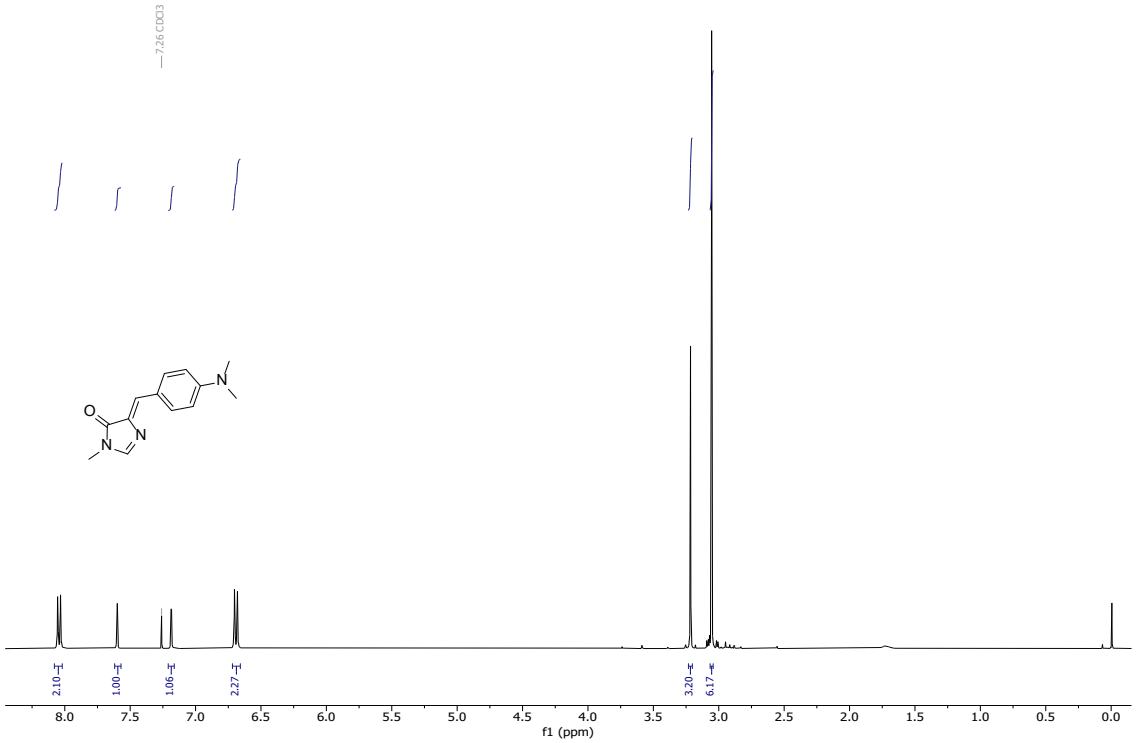

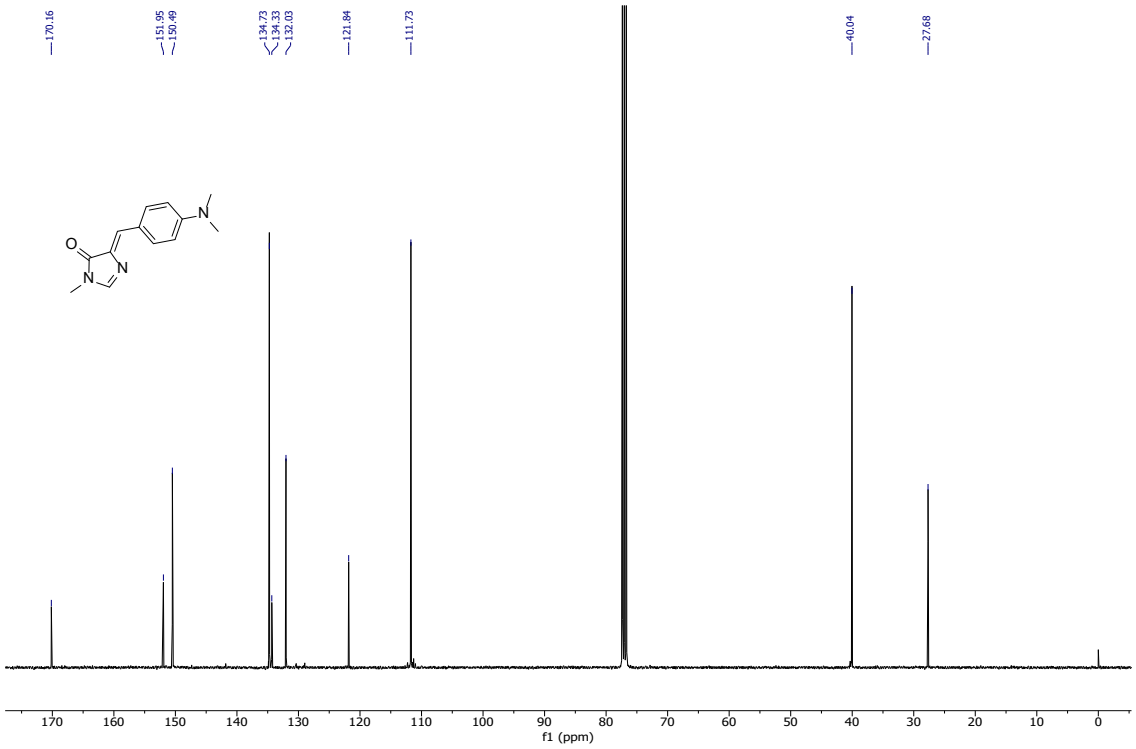

(*Z*)-3-(4-chlorobenzyl)-5-(thiophen-2-ylmethylene)-3,5-dihydro-4*H*-imidazol-4-one (5l)

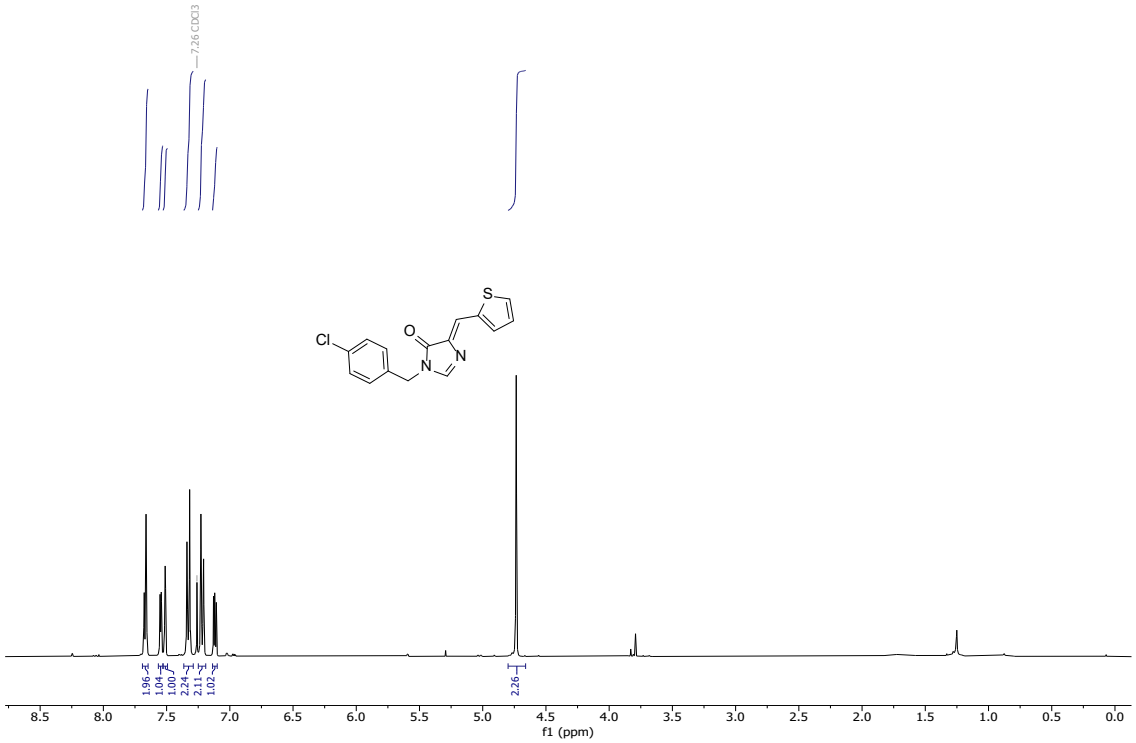

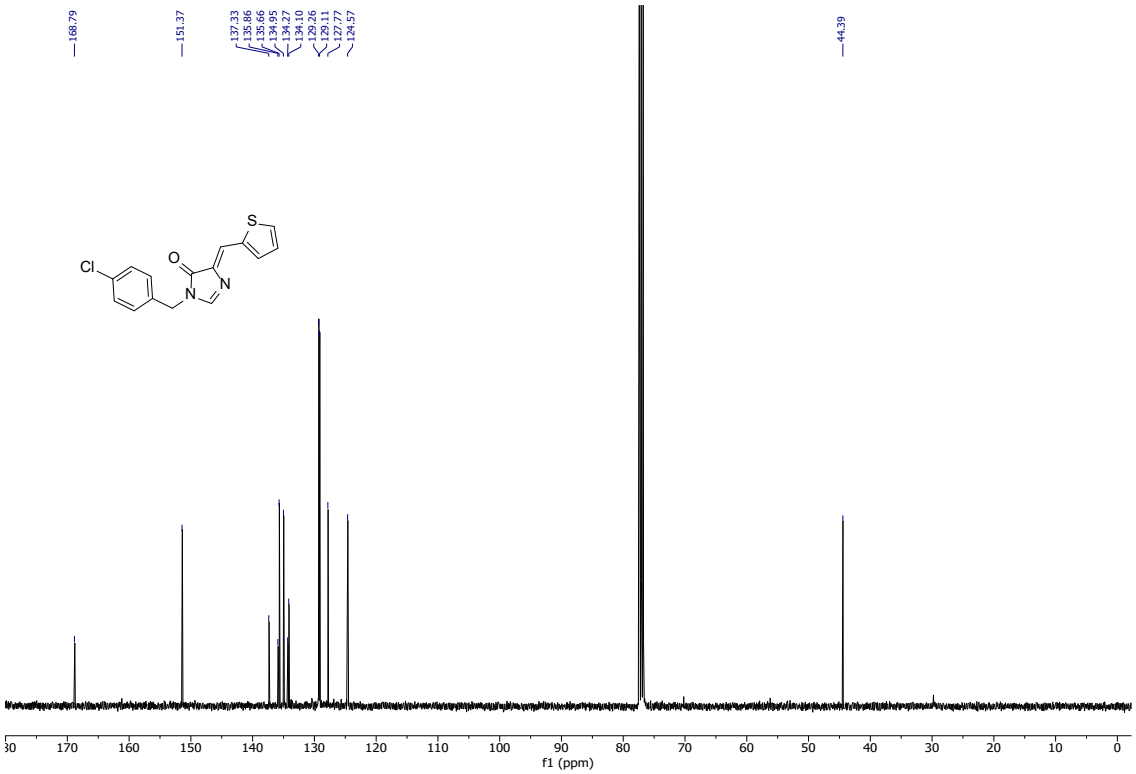

(*Z*)-5-(4-((*tert*-Butyldimethylsilyl)oxy)benzylidene)-3-(4-methylbenzyl)-3,5-dihydro-4*H*-imidazol-4-one (5n)

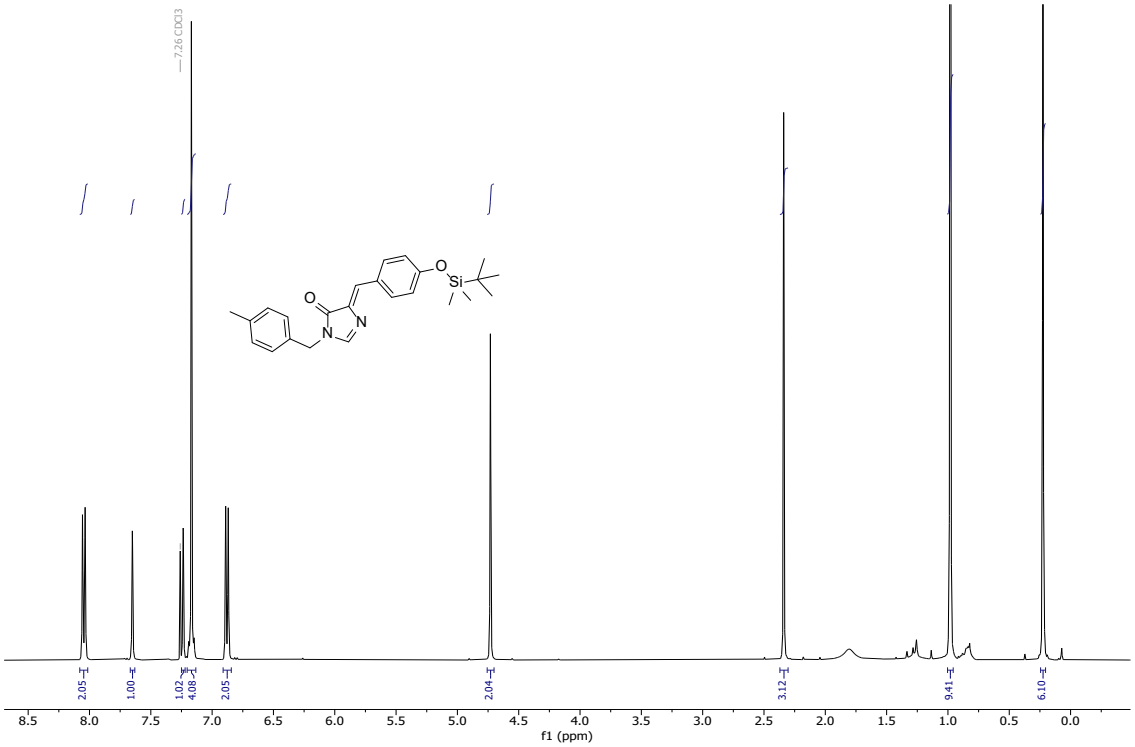

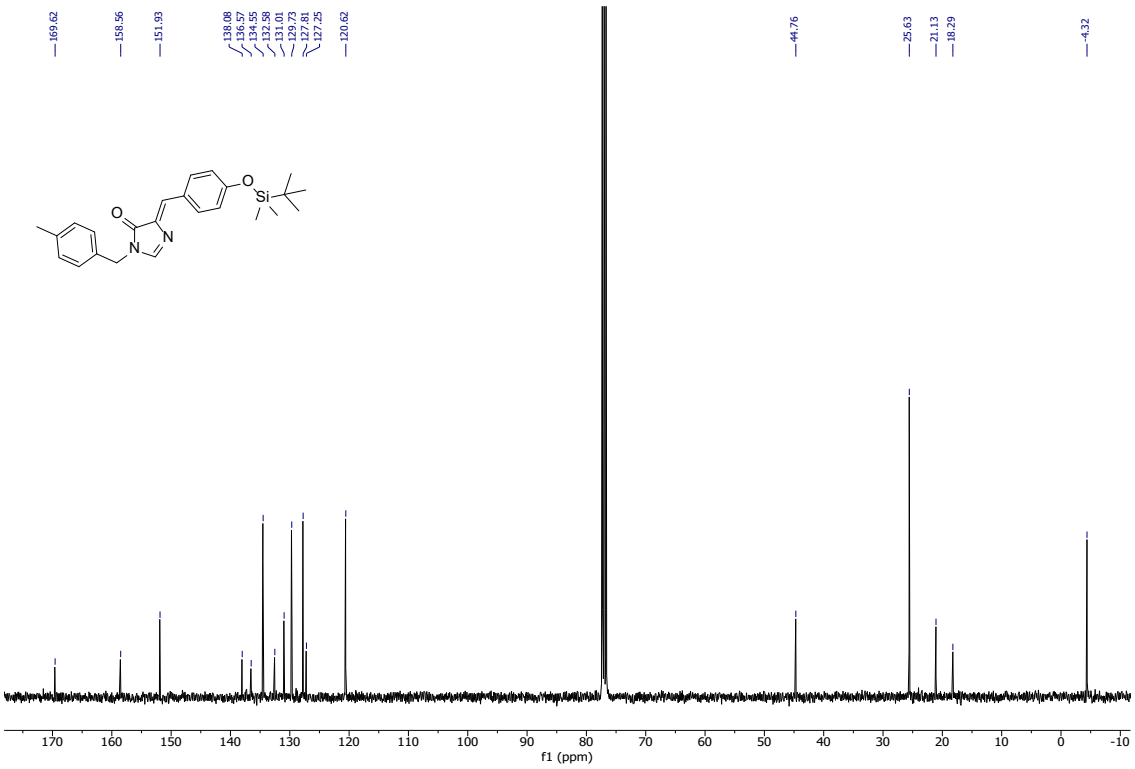

(*Z*)-5-(4-Hydroxybenzylidene)-3-(4-methylbenzyl)-3,5-dihydro-4*H*-imidazol-4-one (5n')

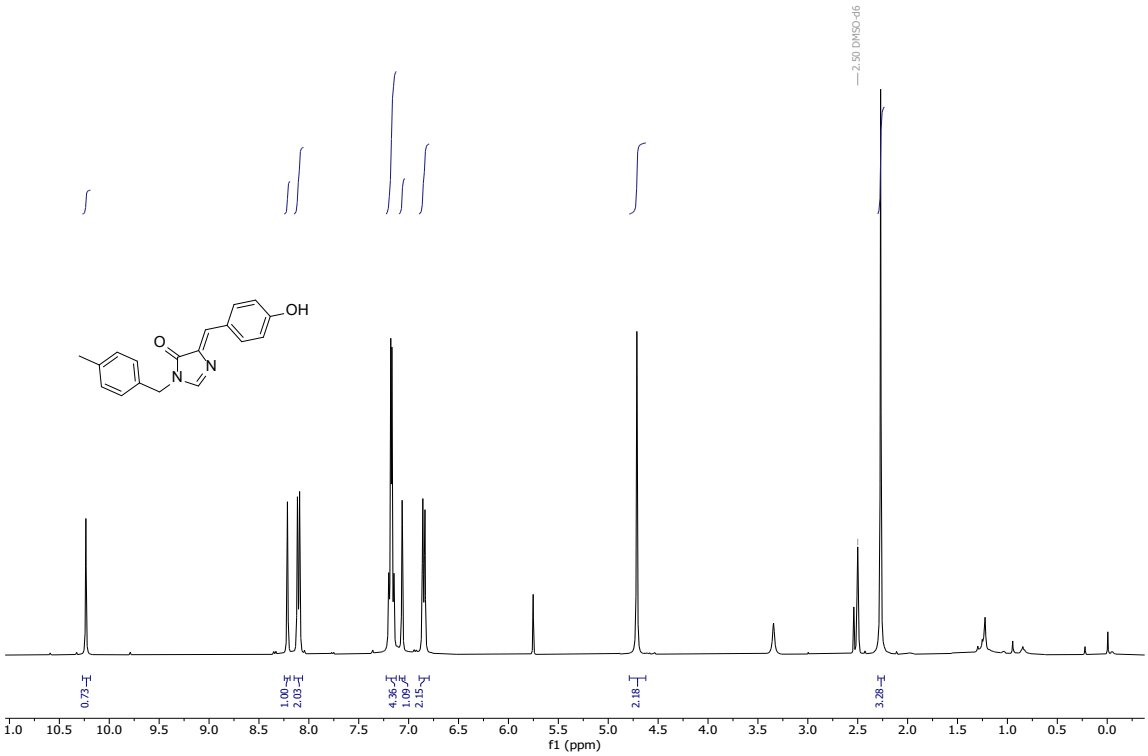

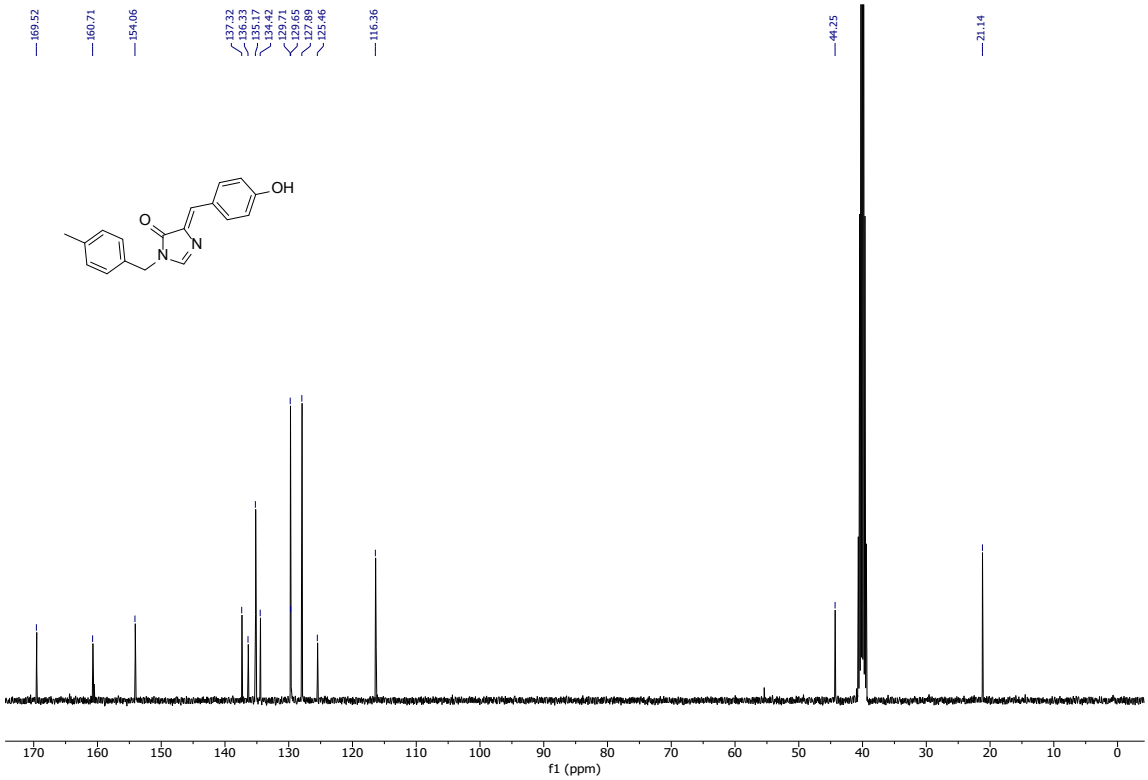

Tert-butyl (_Z_)-3-((1-methyl-5-oxo-1,5-dihydro-4_H_-imidazol-4-ylidene)methyl)-1_H_-indole-1-carboxylate (5o')

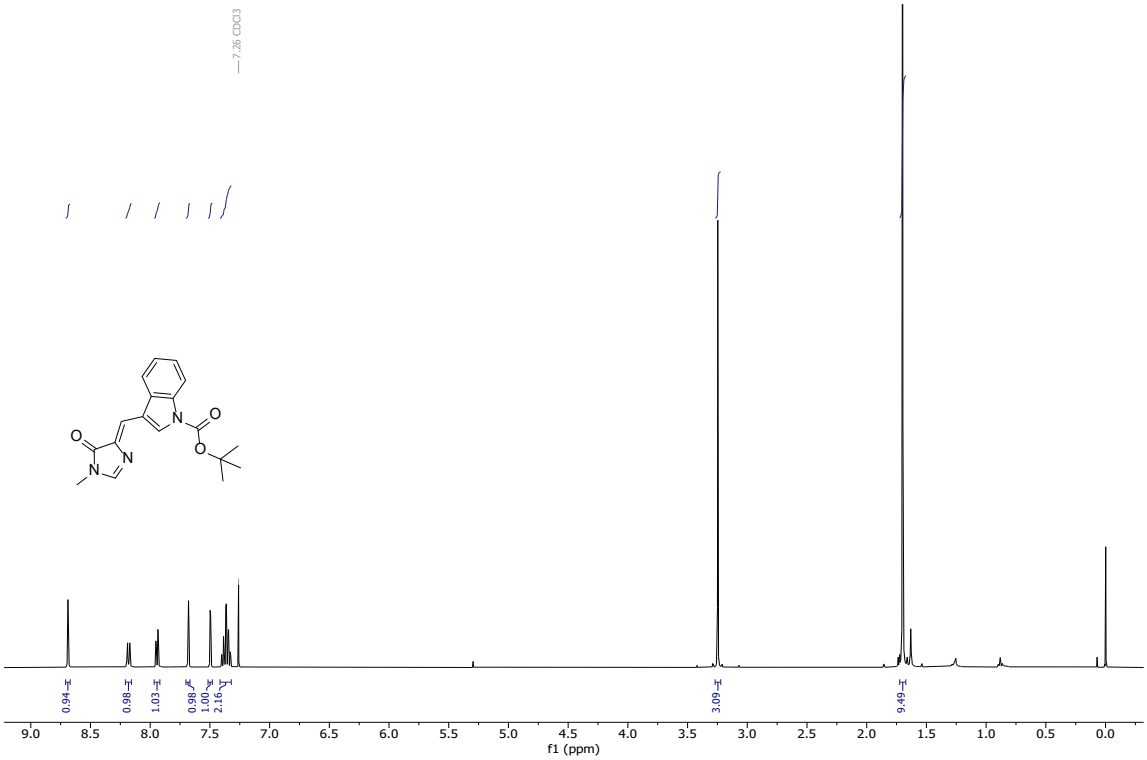

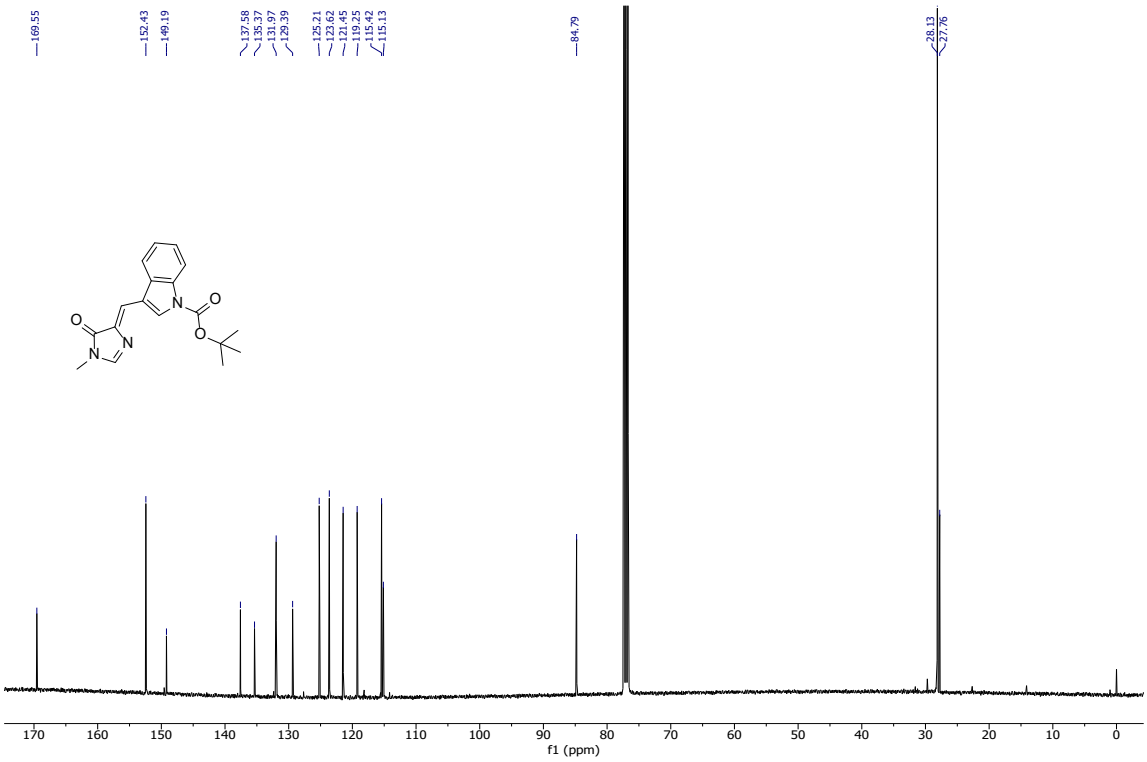

(*Z*)-5-((1H-indol-3-yl)methylene)-3-methyl-3,5-dihydro-4H-imidazol-4-one (5o')

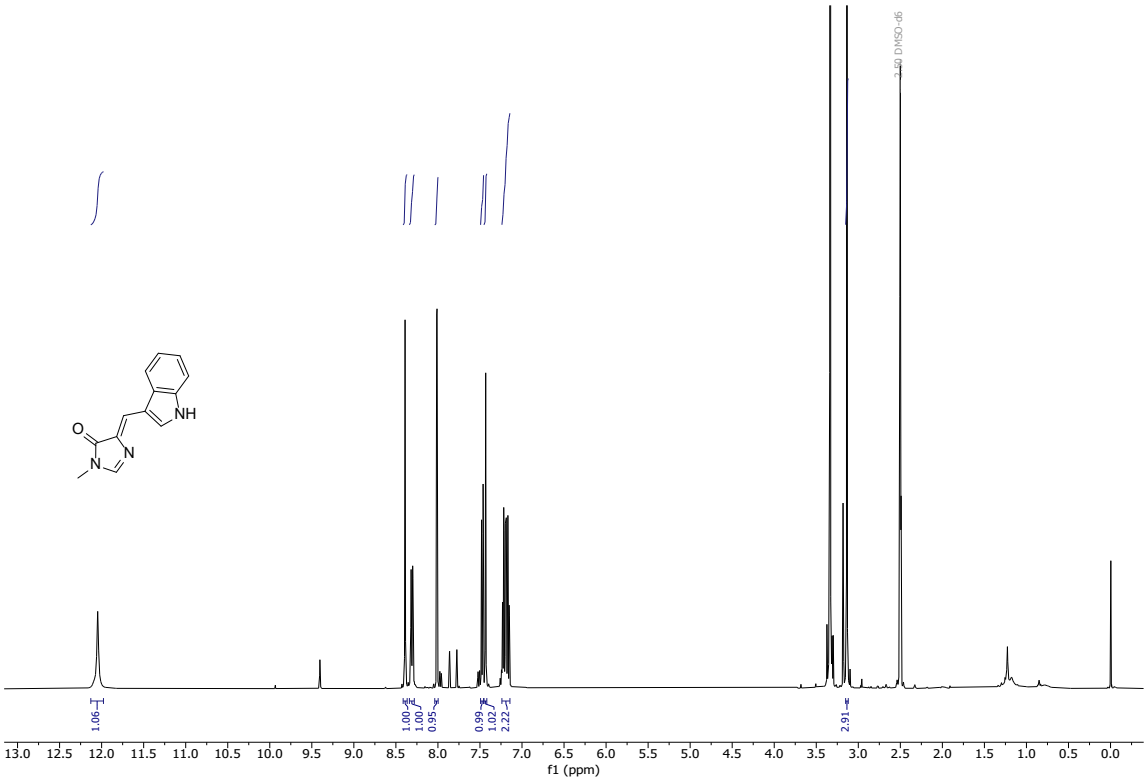

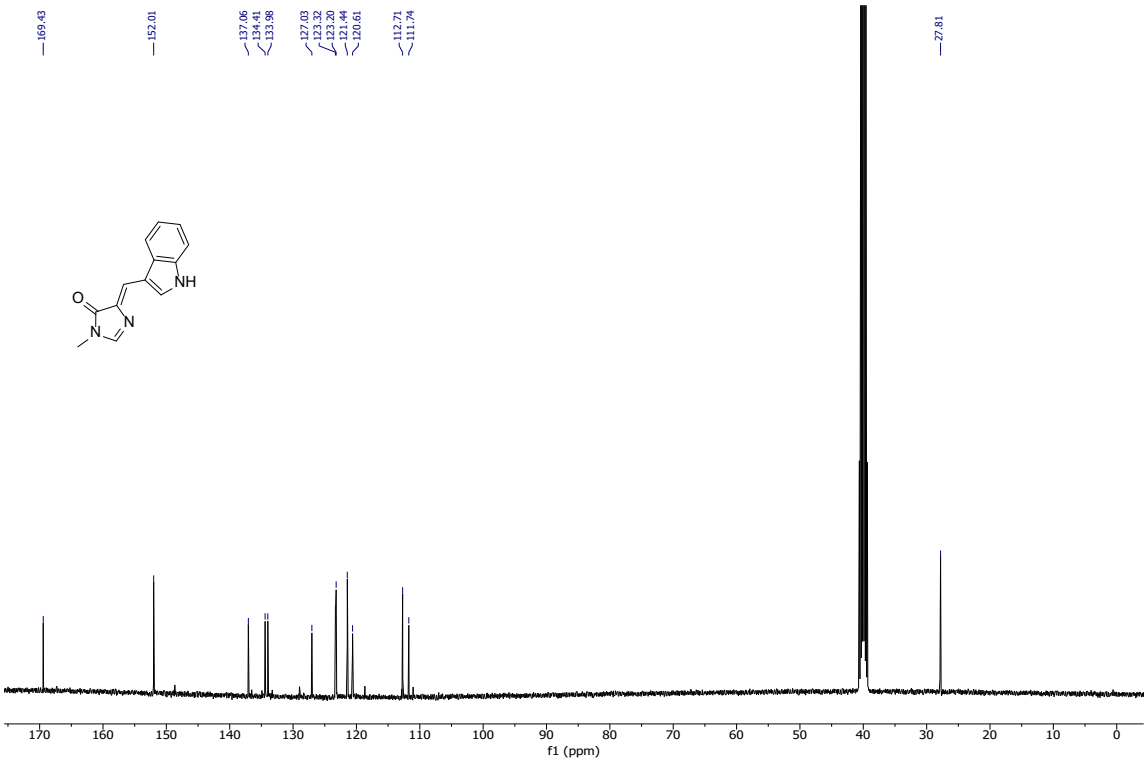

(*Z*)-3-(4-methylbenzyl)-5-(pyridin-4-ylmethylene)-3,5-dihydro-4*H*-imidazol-4-one (5q)

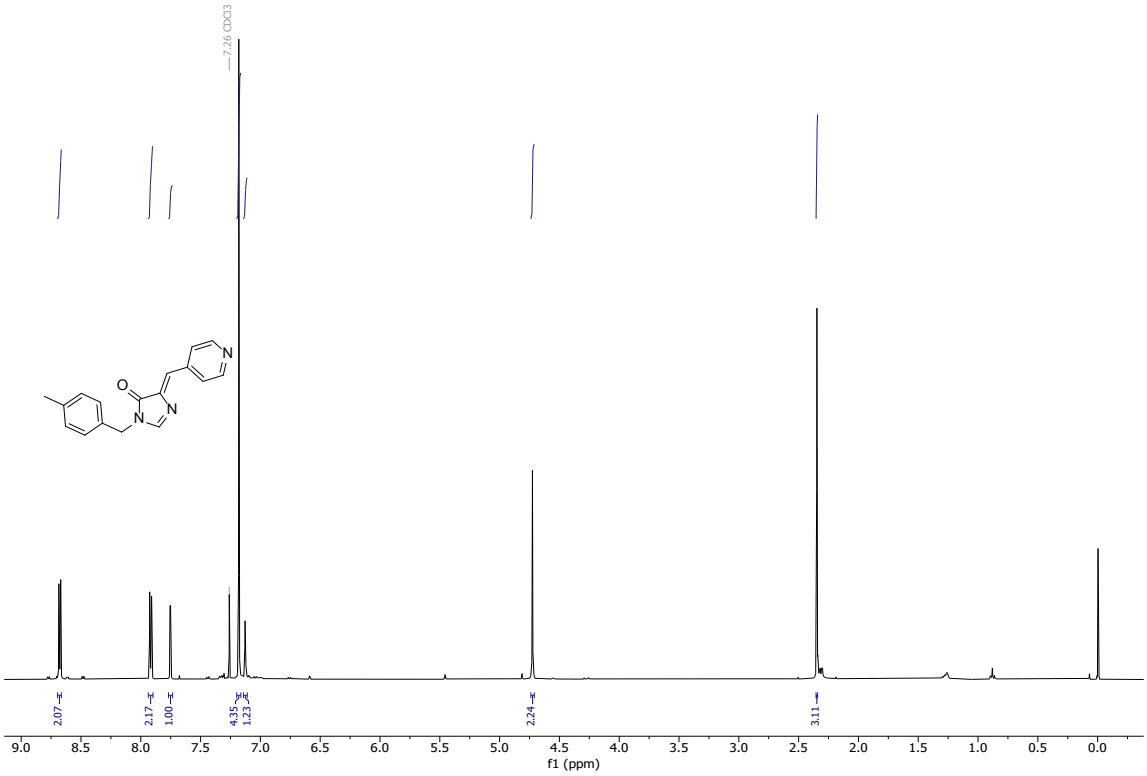

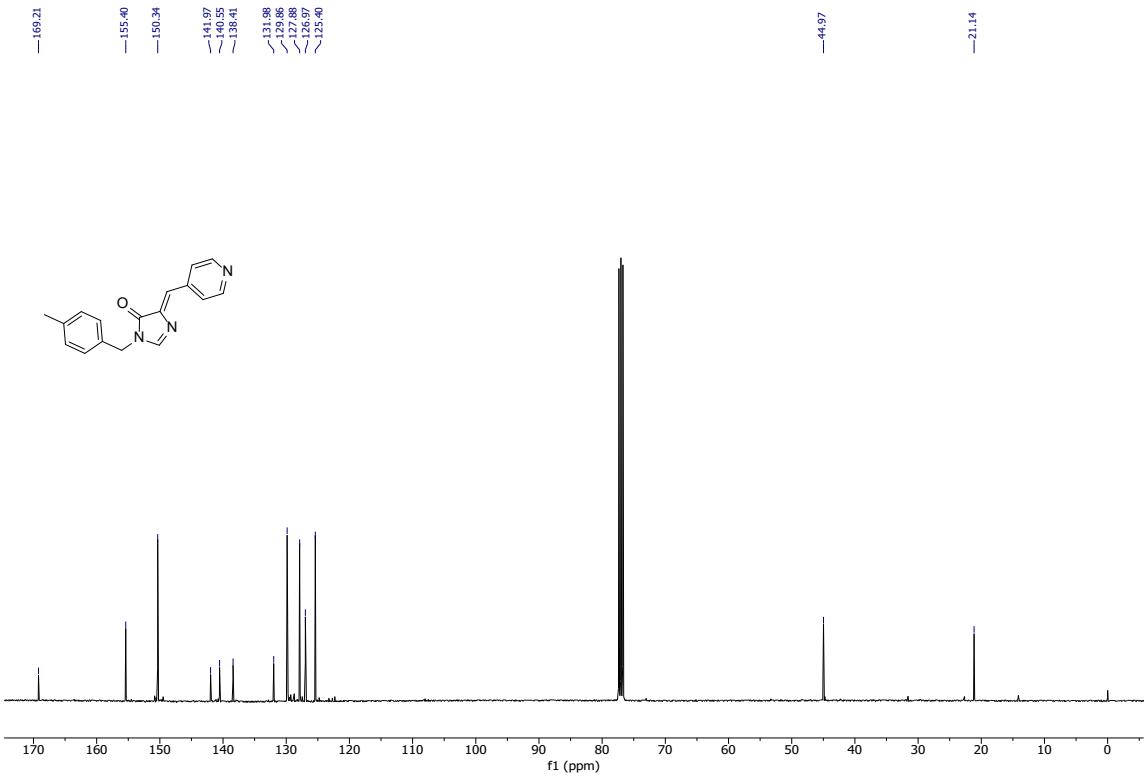

(*Z*)-5-((1*H*-indol-2-yl)methylene)-3-(4-methylbenzyl)-3,5-dihydro-4*H*-imidazol-4-one (5r)

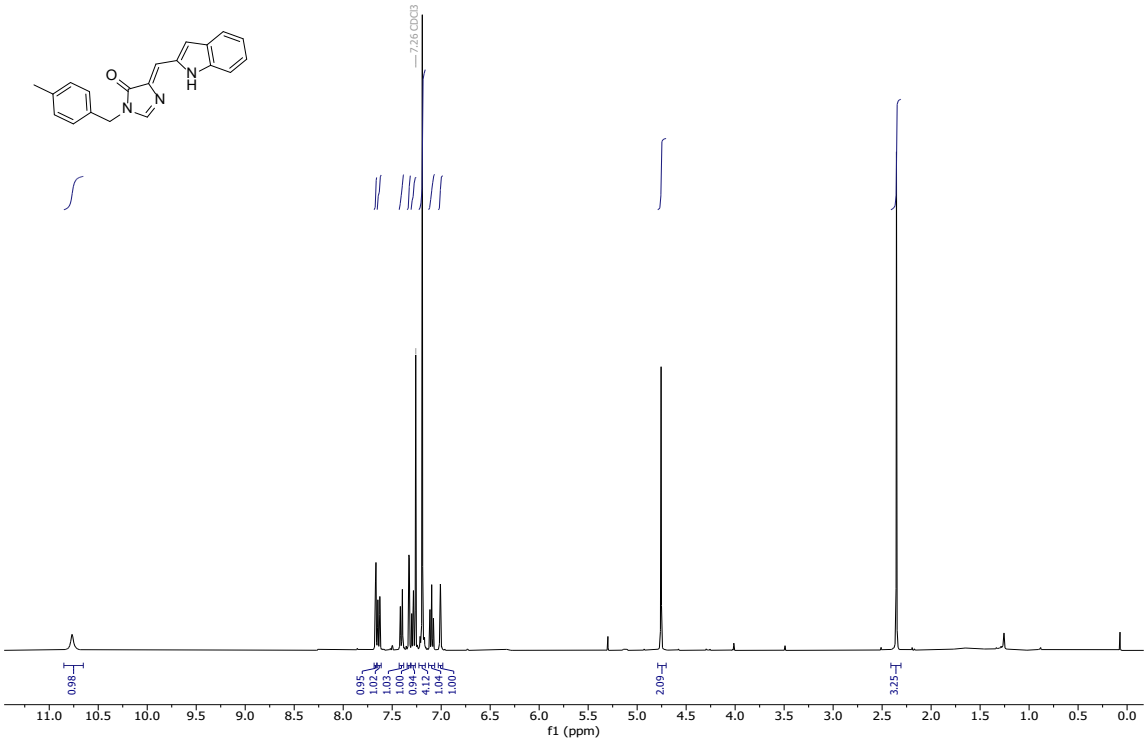

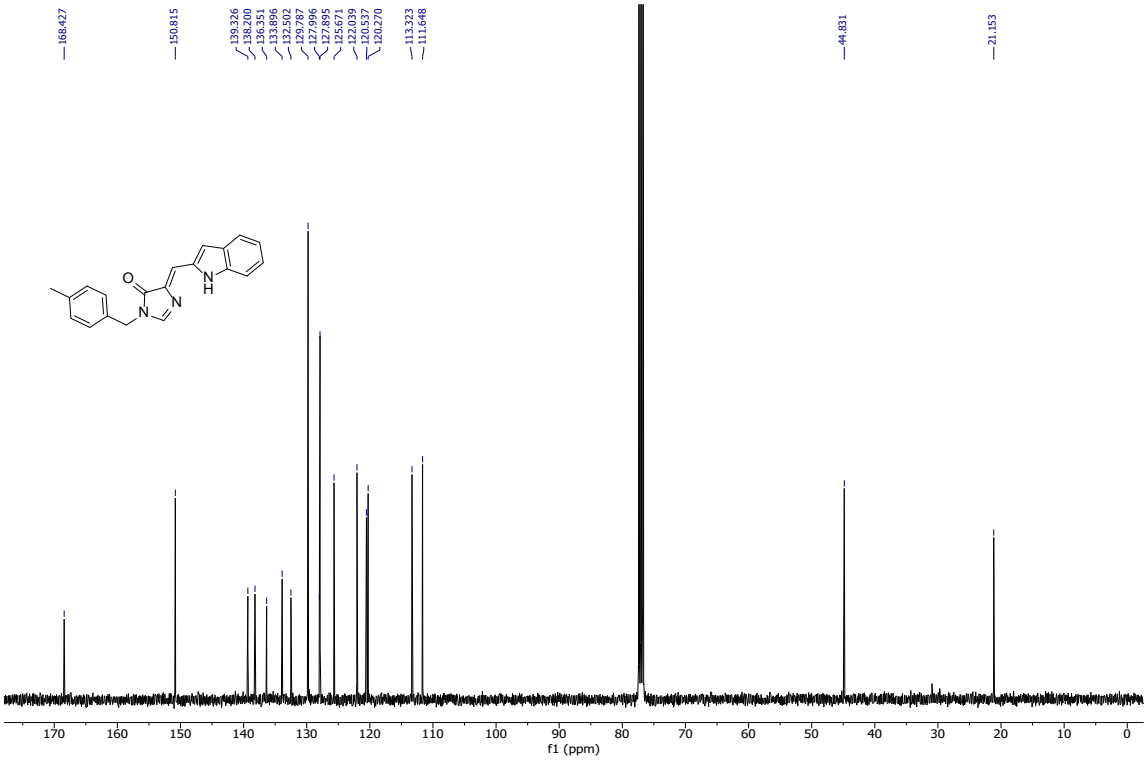

(*Z*)-3-Benzyl-5-((*E*)-3-(4-chlorophenyl)allylidene)-3,5-dihydro-4*H*-imidazol-4-one (5s)

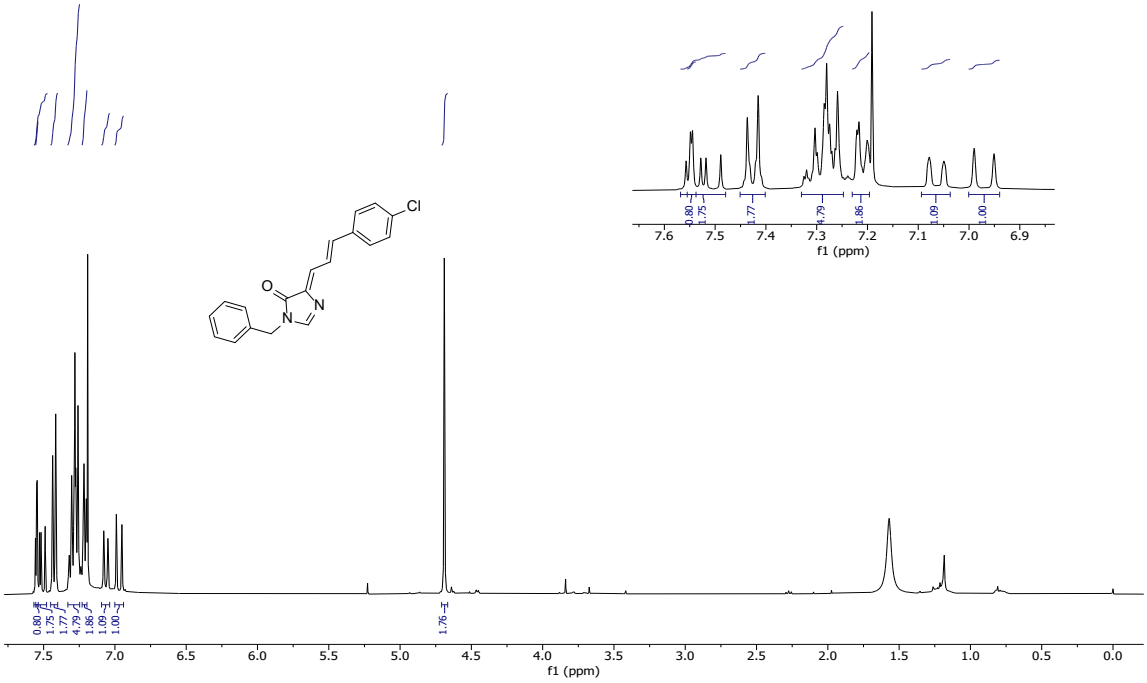

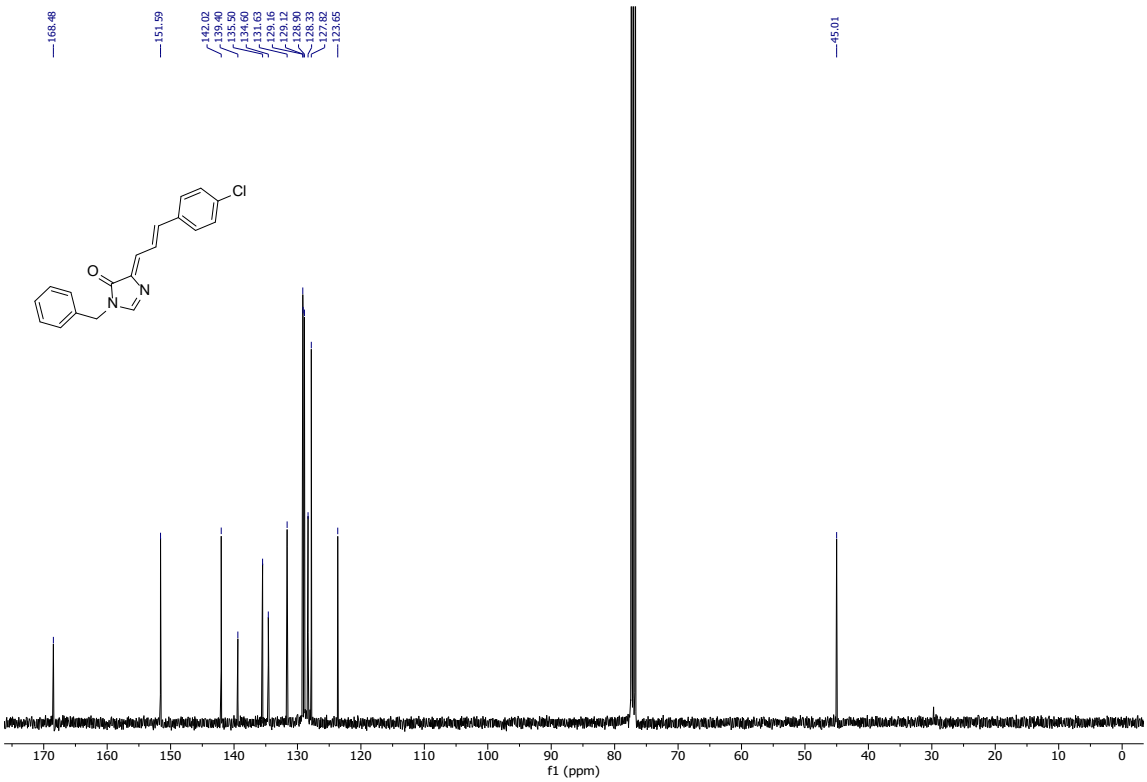

(*Z*)-3-butyl-5-(thiophen-2-ylmethylene)-3,5-dihydro-4*H*-imidazol-4-one (5t)

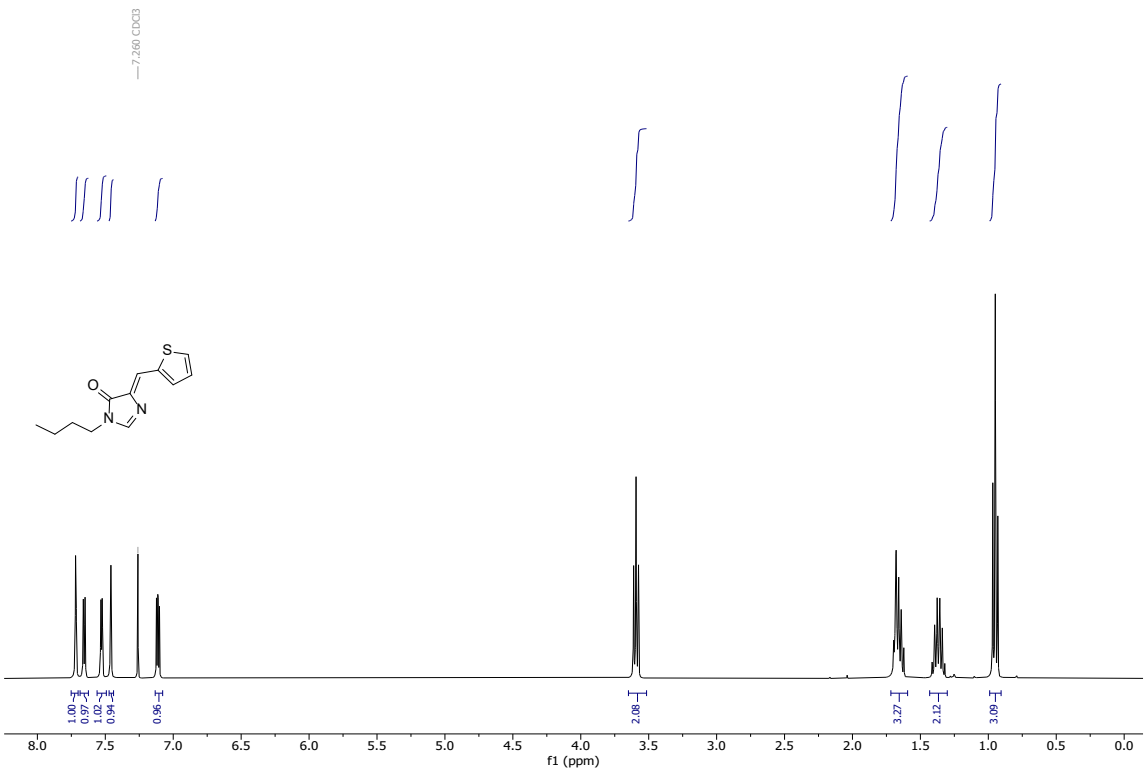

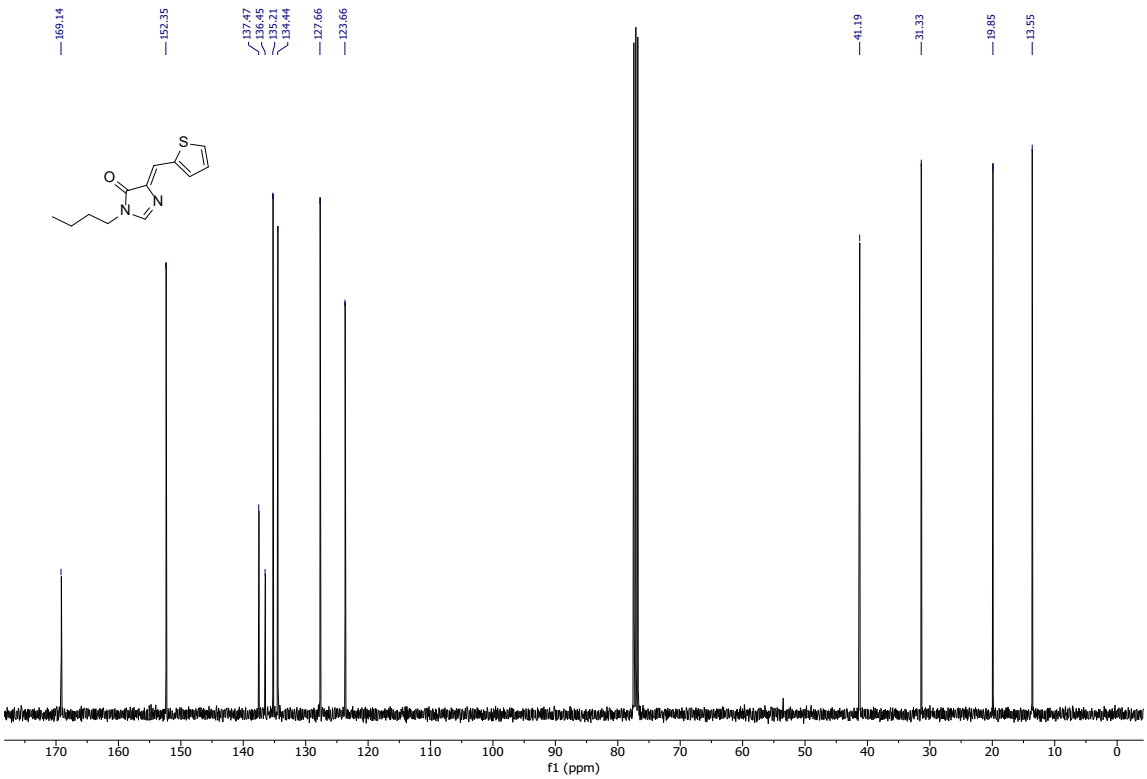

(*Z*)-3-(2-(1*H*-Indol-3-yl)ethyl)-5-(benzo[*d*][1,3]dioxol-5-ylmethylene)-3,5-dihydro-4*H*-imidazol-4-one (5u)

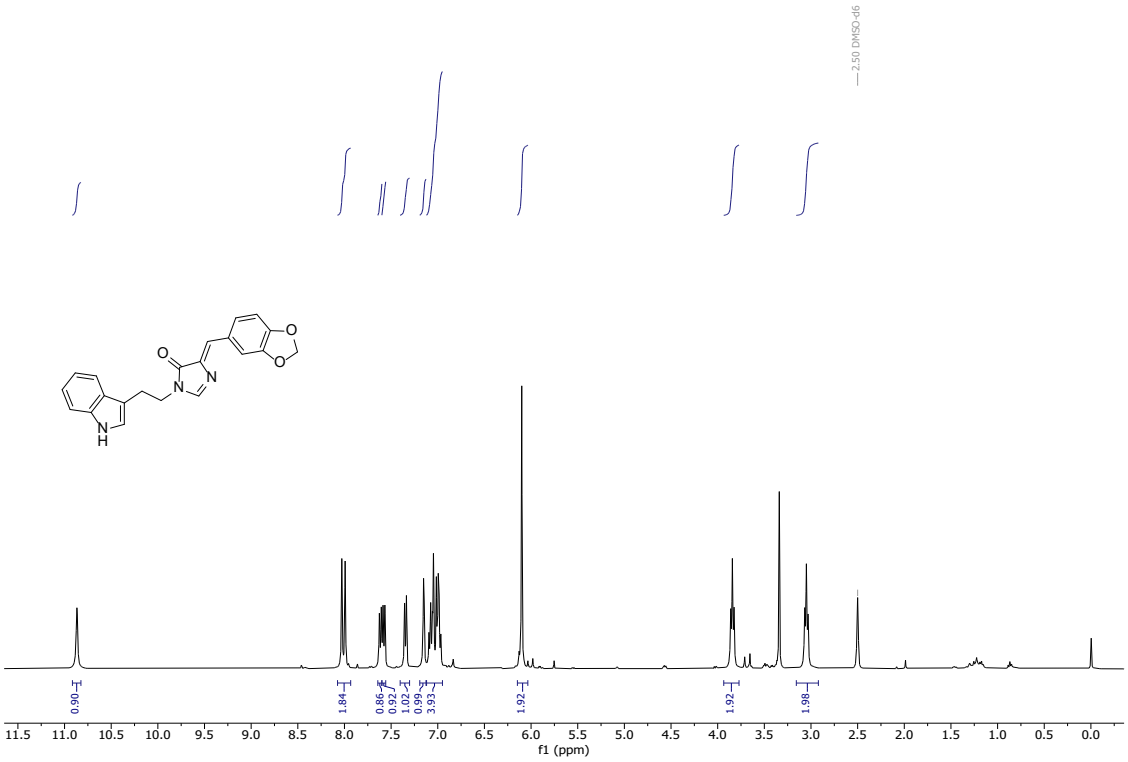

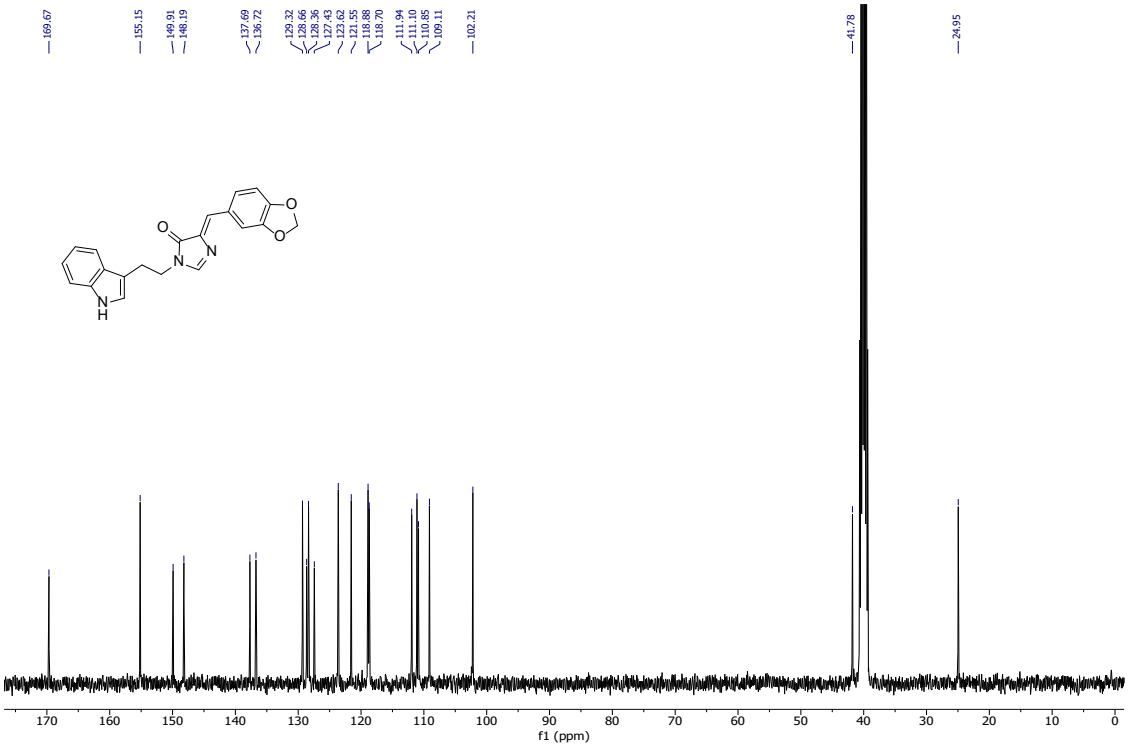

(*Z*)-5-(Benzo[*d*][1,3]dioxol-5-ylmethylene)-3-((*E*)-4-phenylbut-3-en-1-yl)-3,5-dihydro-4*H*-imidazol-4-one (5v)

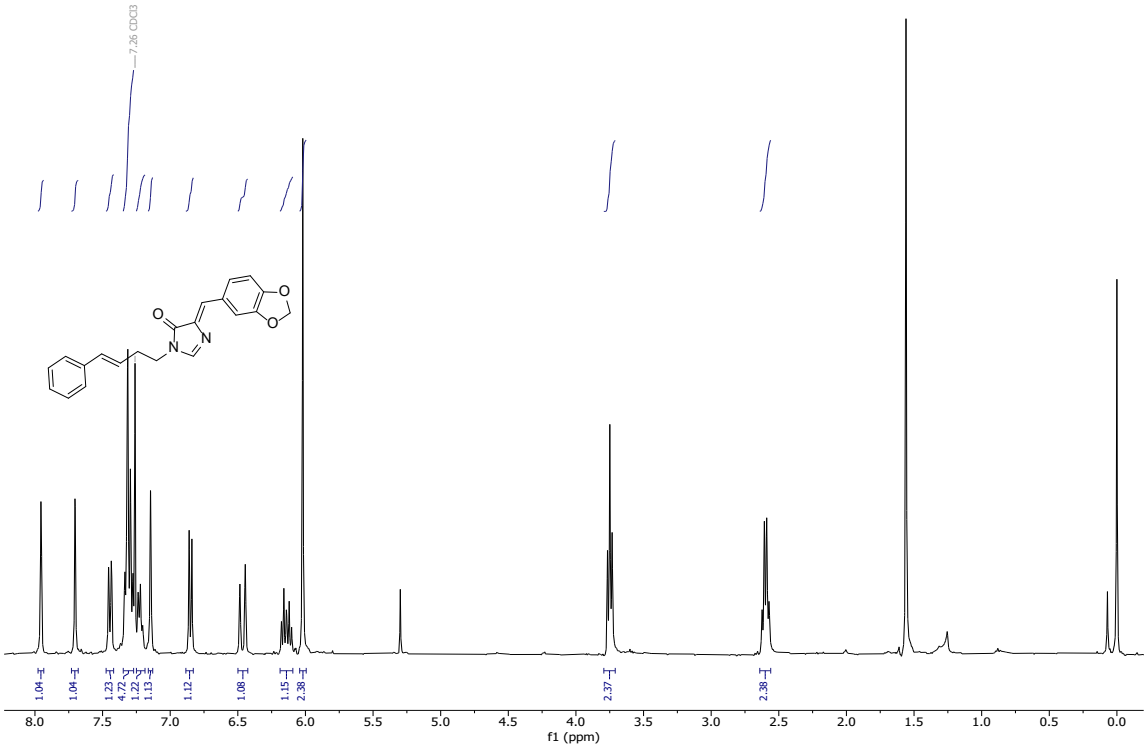

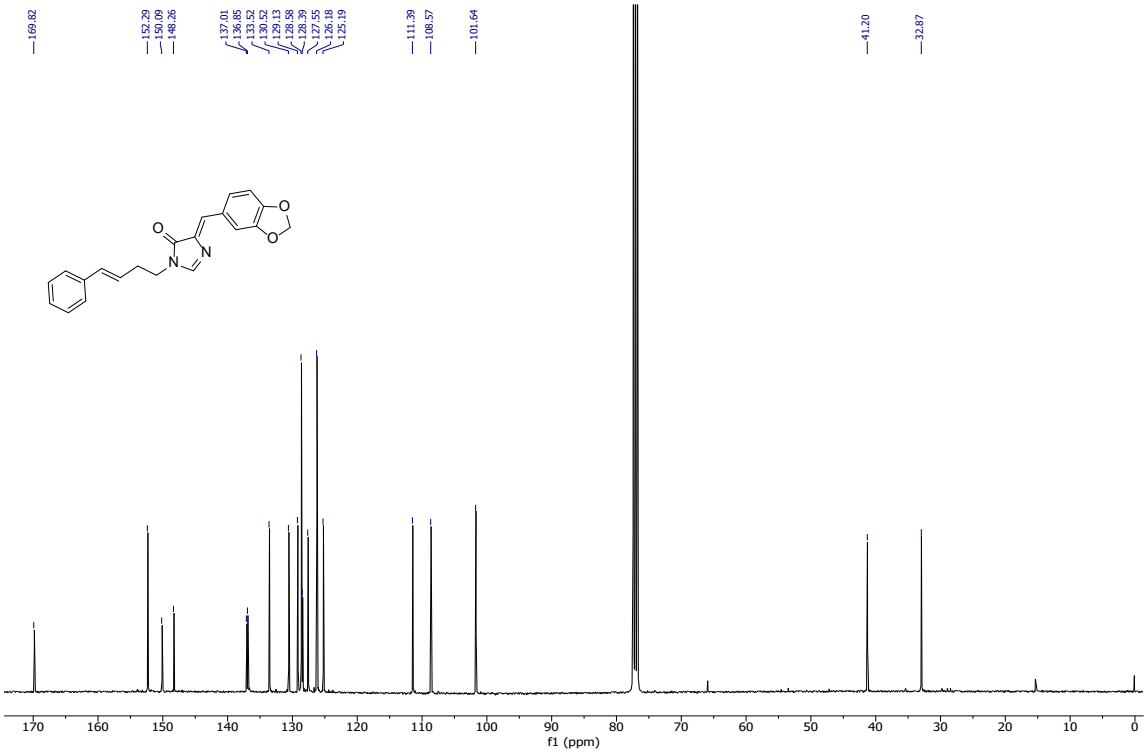

(*Z*)-5-(Benzo[*d*][1,3]dioxol-5-ylmethylene)-3,5-dihydro-4*H*-imidazol-4-one (5w)

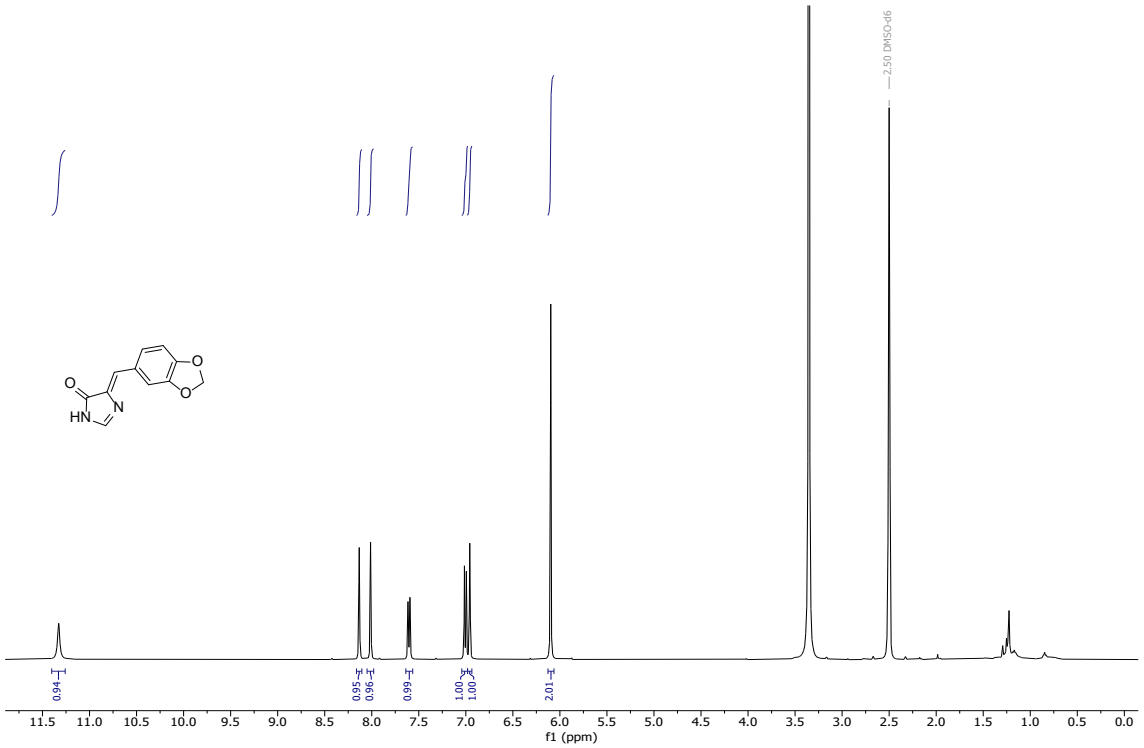

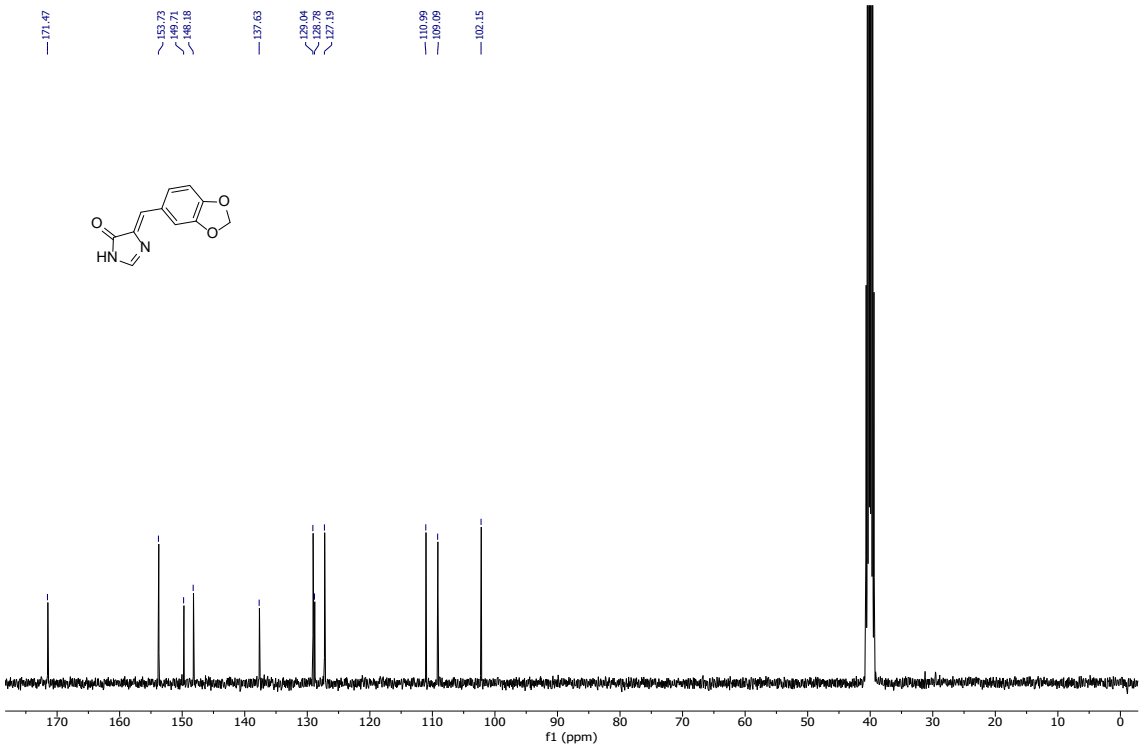

Allyl (*S*,*Z*)-2-((((9*H*-fluoren-9-yl)methoxy)carbonyl)amino)-6-(4-(benzo[*d*][1,3]dioxol-5-ylmethylene)-5-oxo-4,5-dihydro-1*H*-imidazol-1-yl)hexanoate (5x)

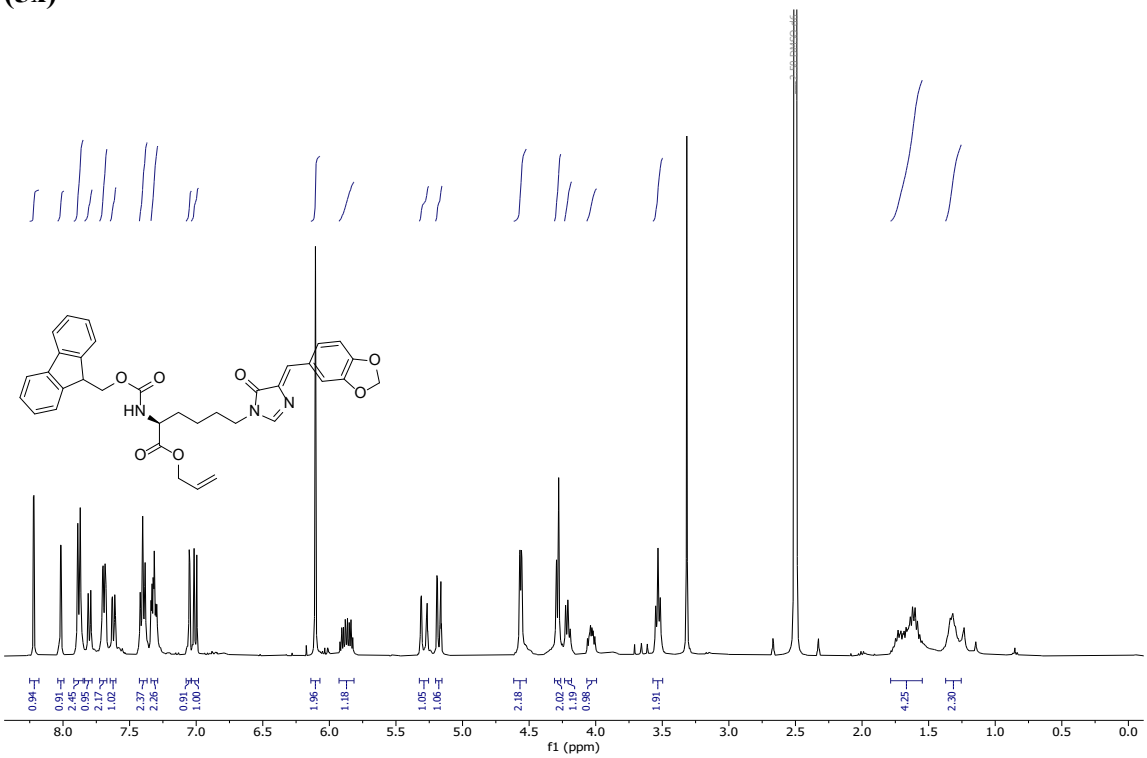

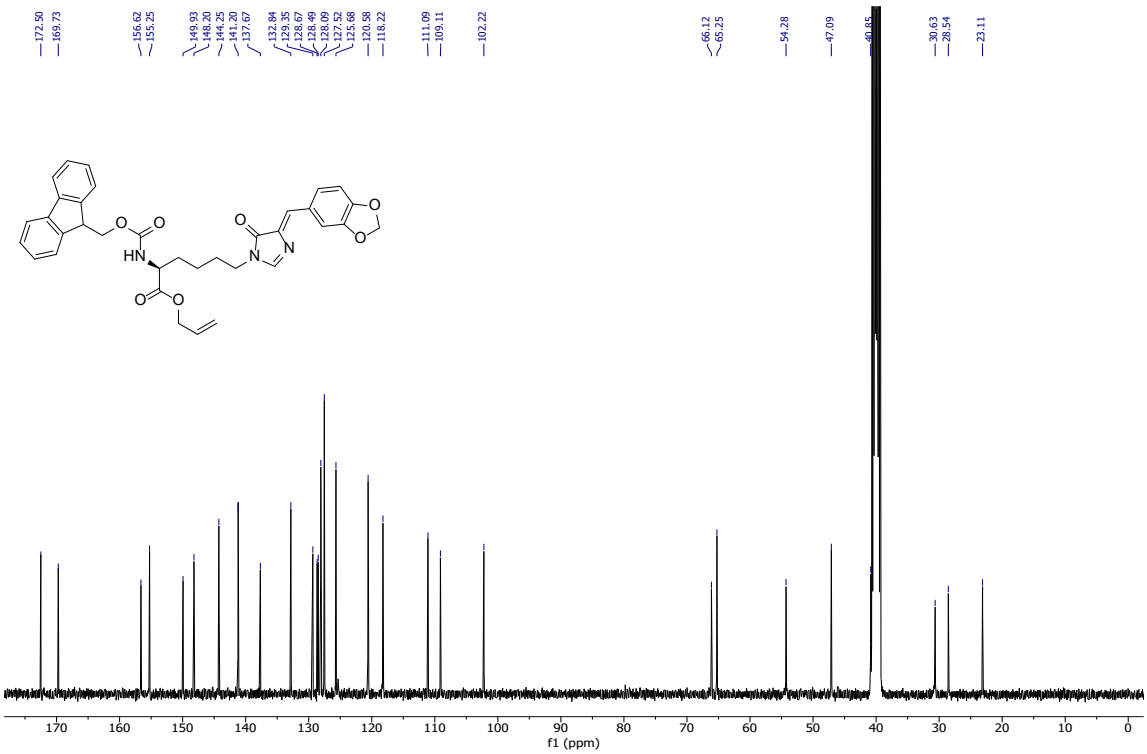

(*S*,*Z*)-2-((((9*H*-Fluoren-9-yl)methoxy)carbonyl)amino)-6-(4-(benzo[*d*][1,3]dioxol-5-ylmethylene)-5-oxo-4,5-dihydro-1*H*-imidazol-1-yl)hexanoic acid (5x')

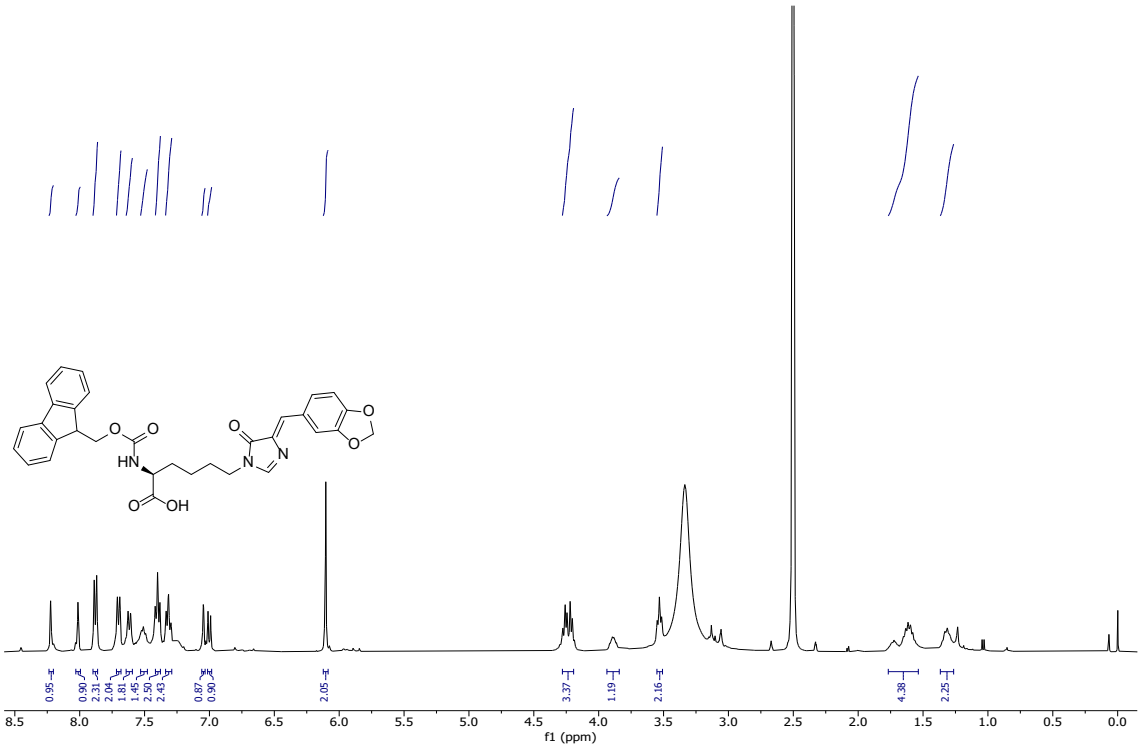

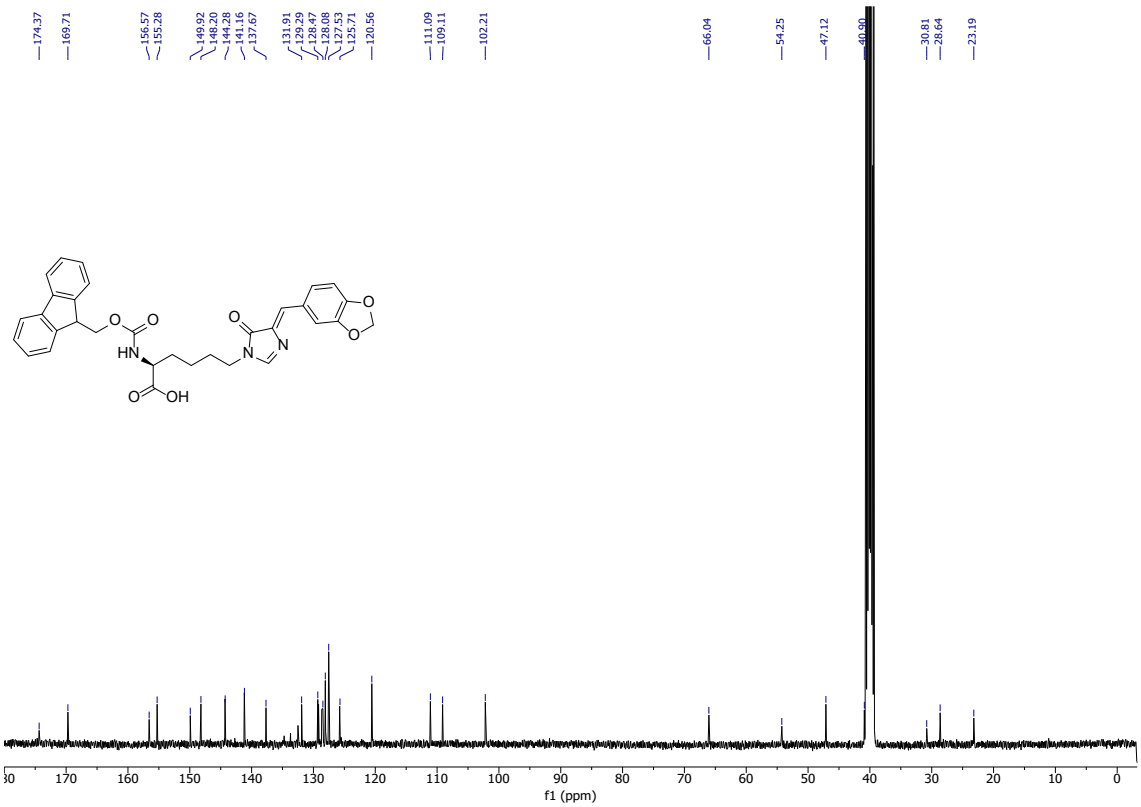

(*Z*)-3-(4-Methoxyphenyl)-5-(thiophen-2-ylmethylene)-3,5-dihydro-4*H*-imidazol-4-one (5y)

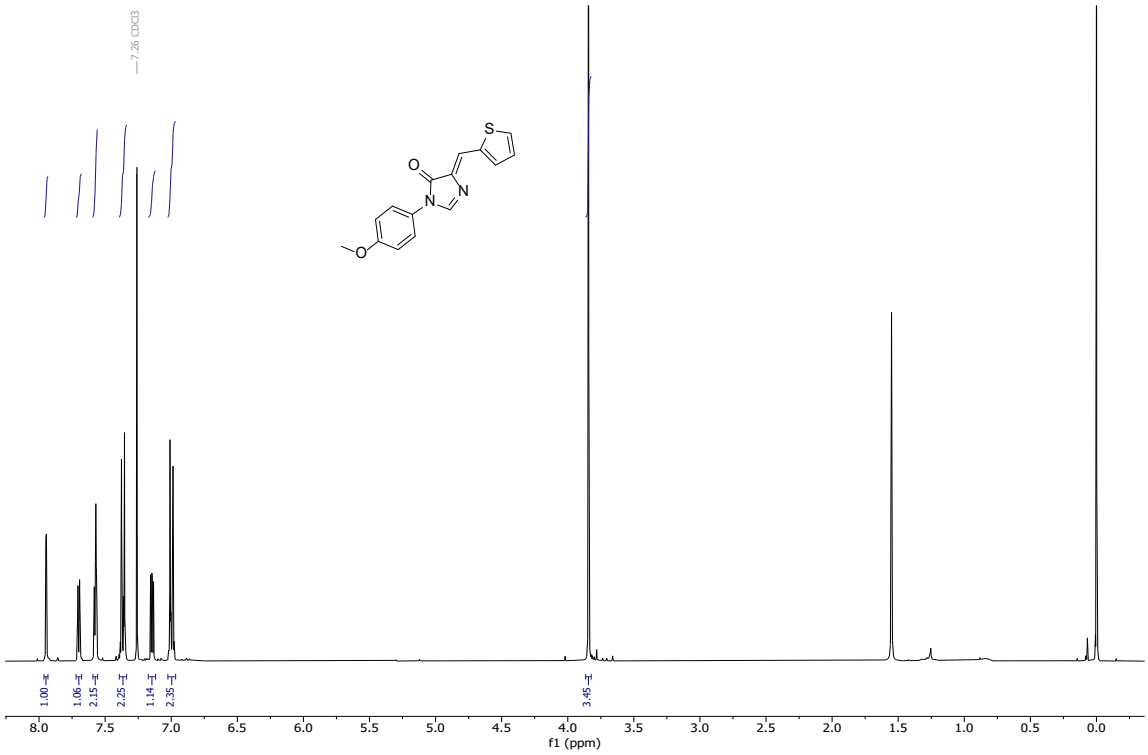

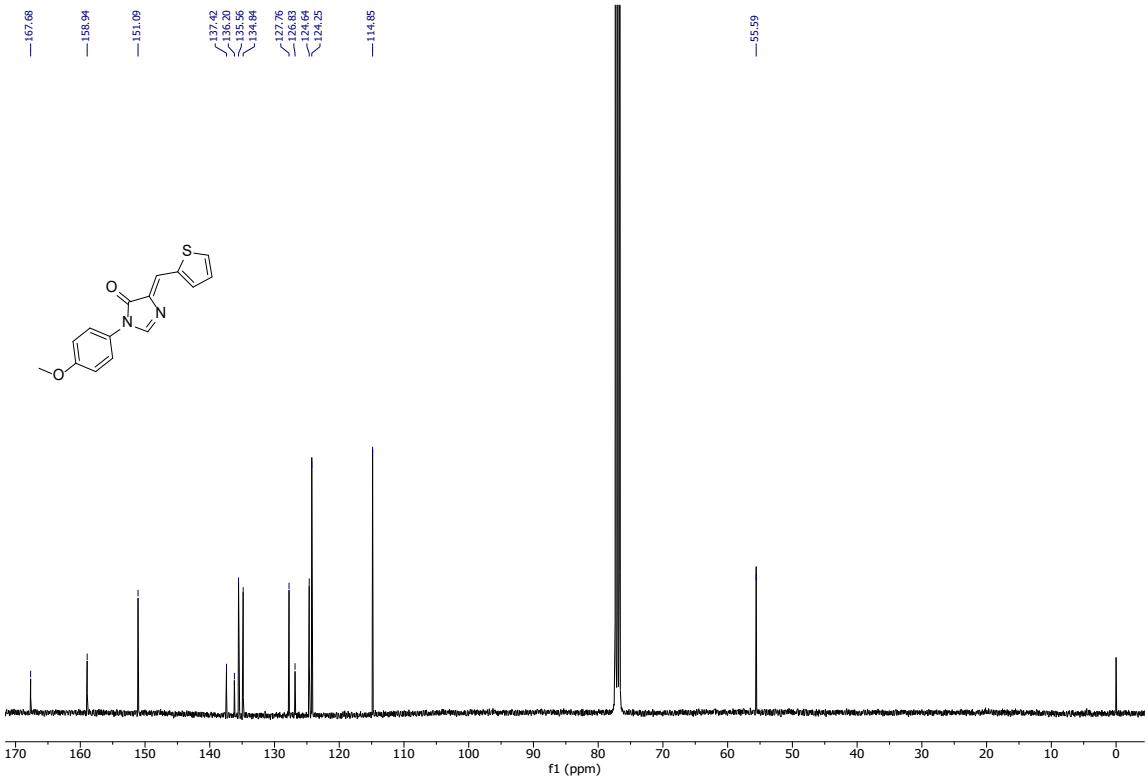

(*Z*)-5-(Benzo[d][1,3]dioxol-5-ylmethylene)-3-(tert-butyl)-3,5-dihydro-4*H*-imidazol-4-one (5z)

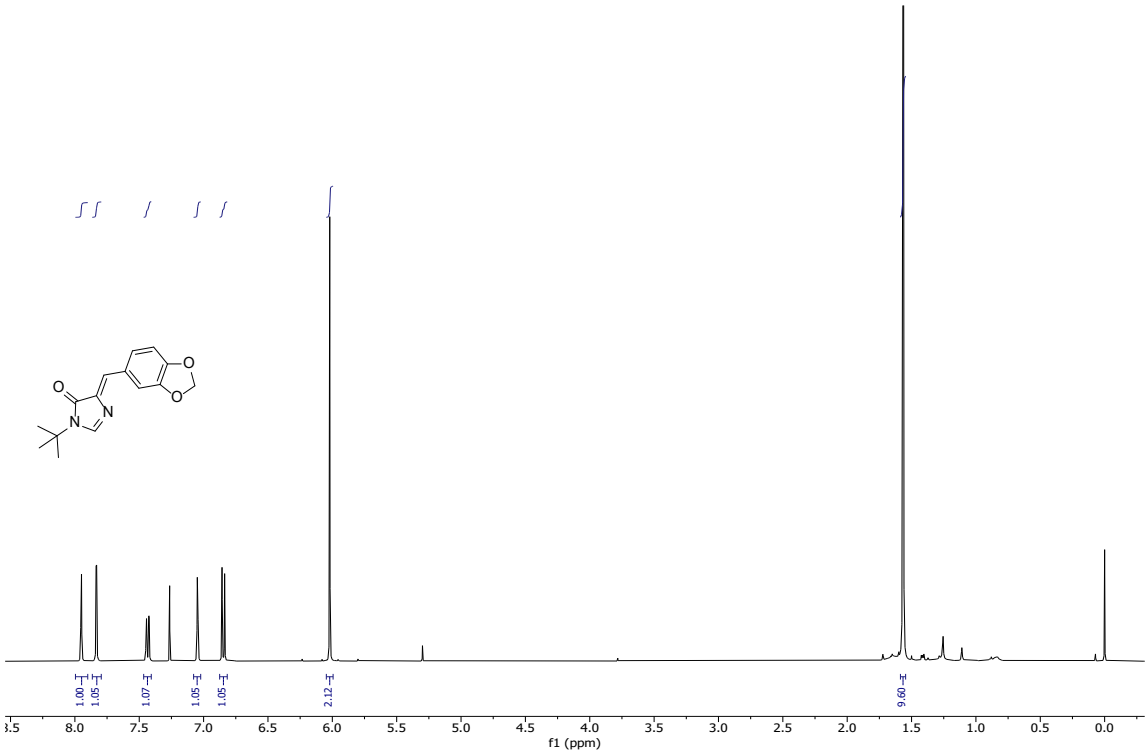

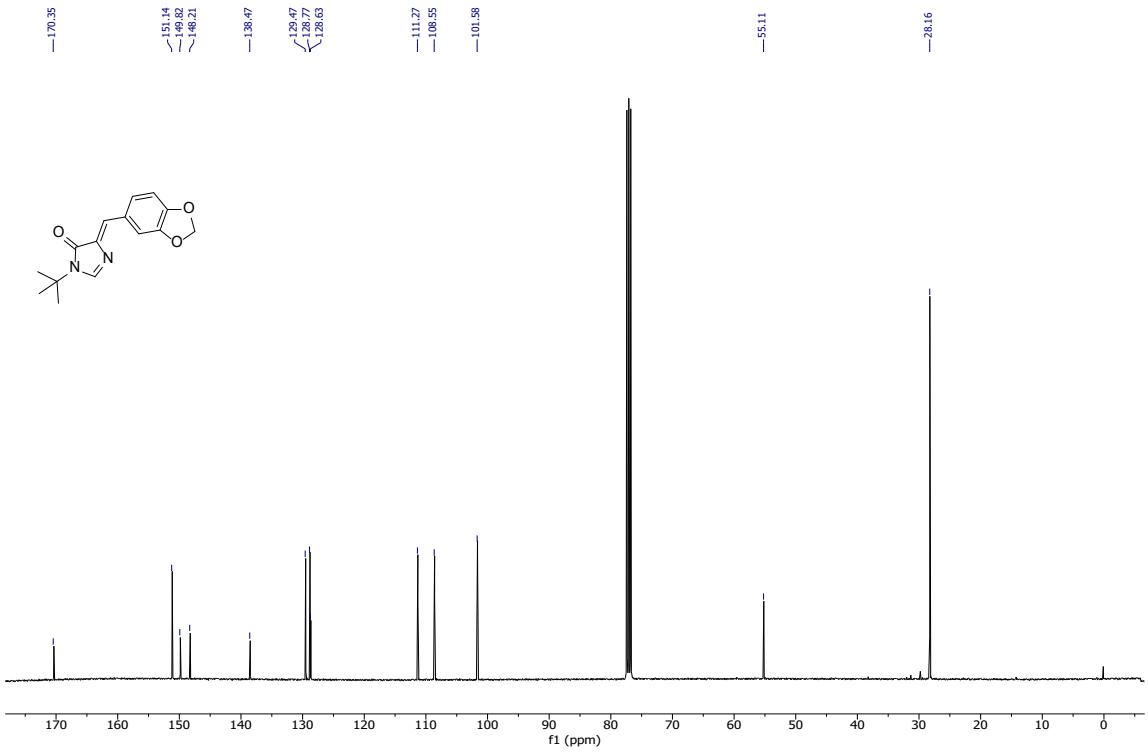

3-Benzyl-5-(propan-2-ylidene)-3,5-dihydro-4*H*-imidazol-4-one (5aa)

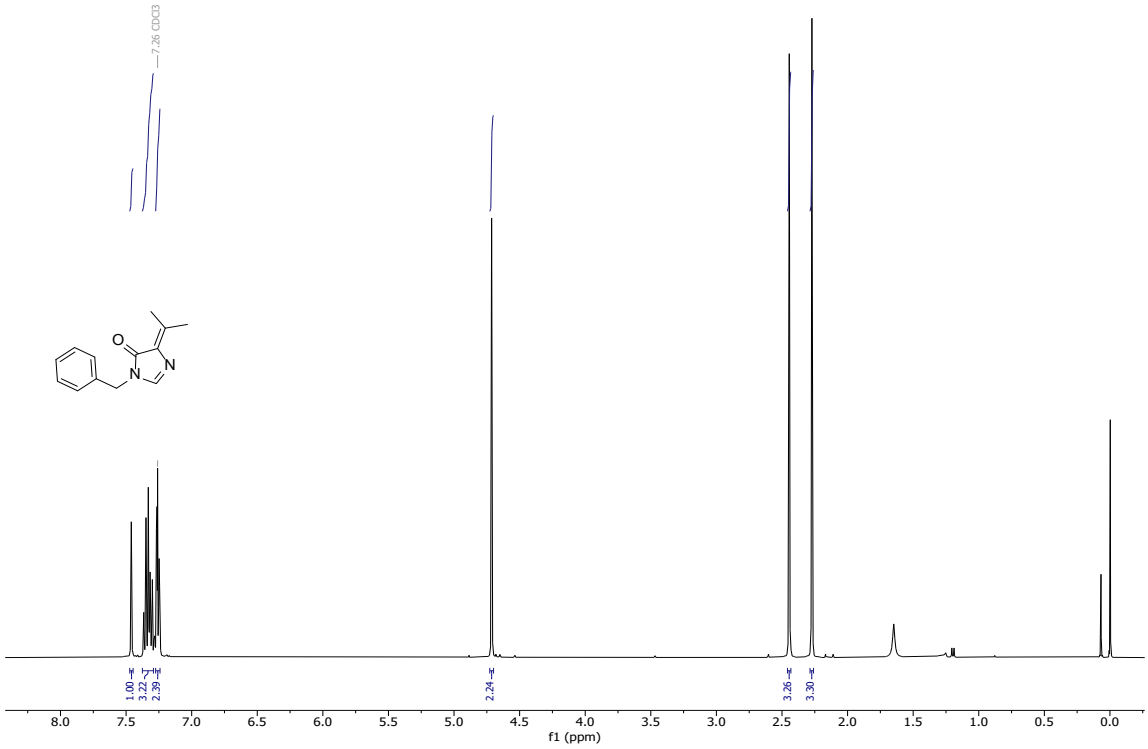

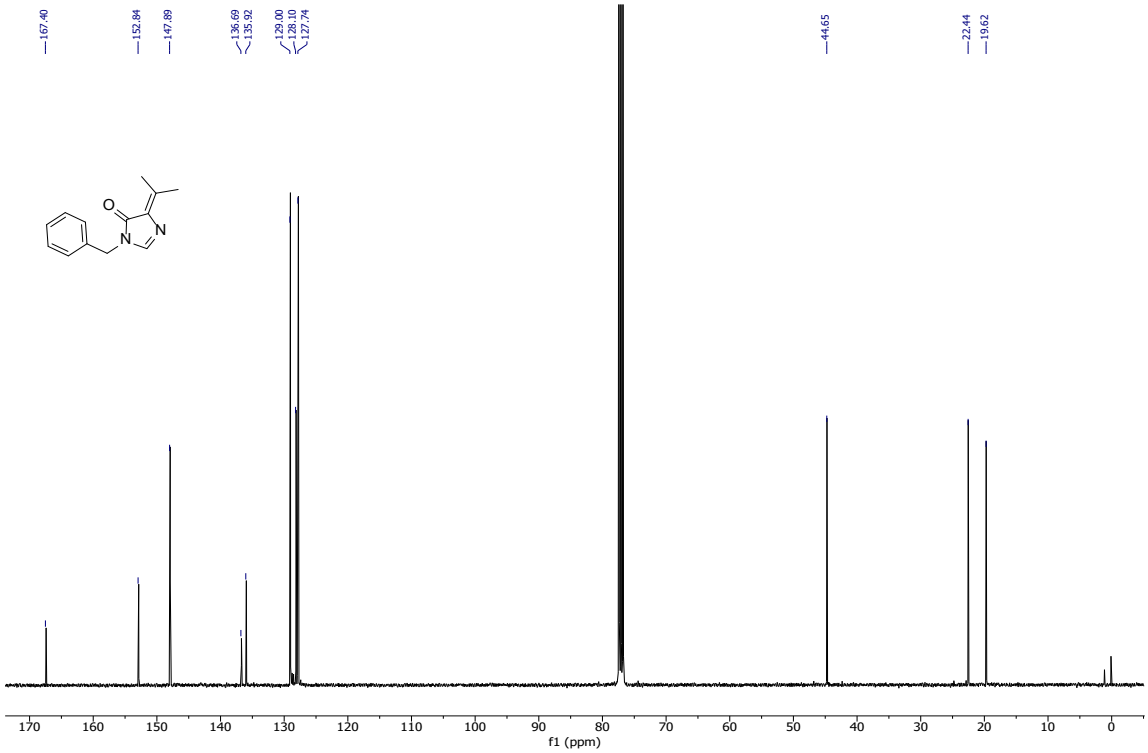

5-((1*r*,3*r*)-adamantan-2-ylidene)-3-benzyl-3,5-dihydro-4*H*-imidazol-4-one (5ac)

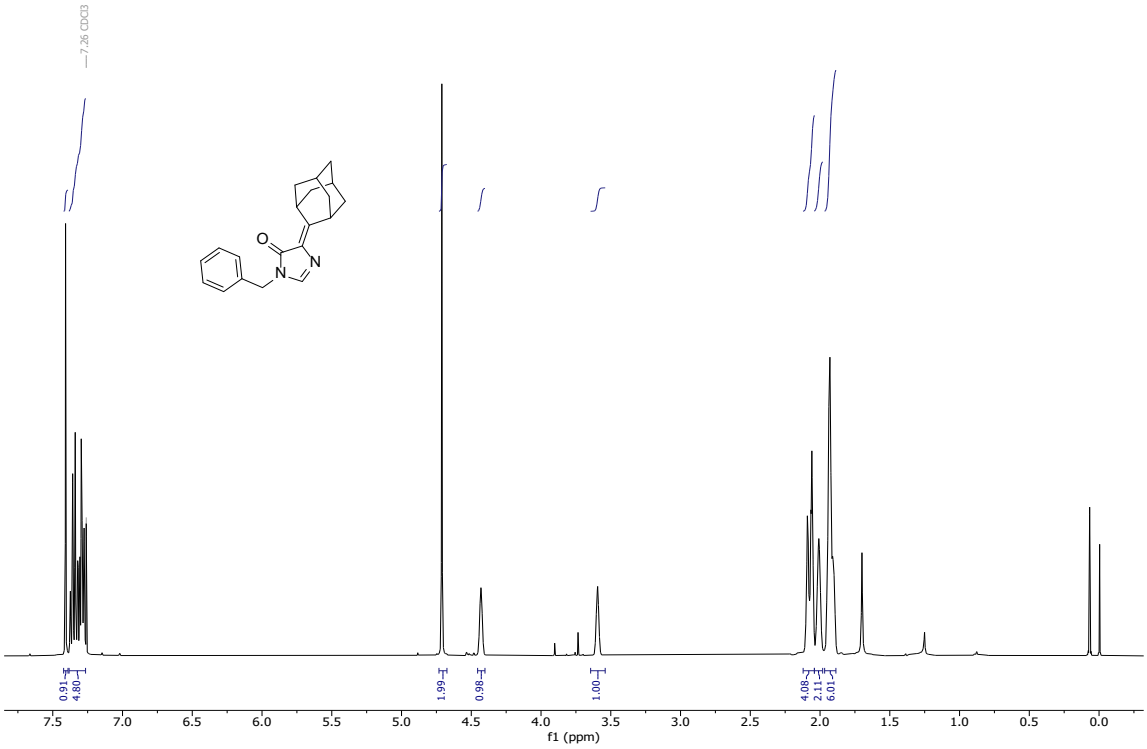

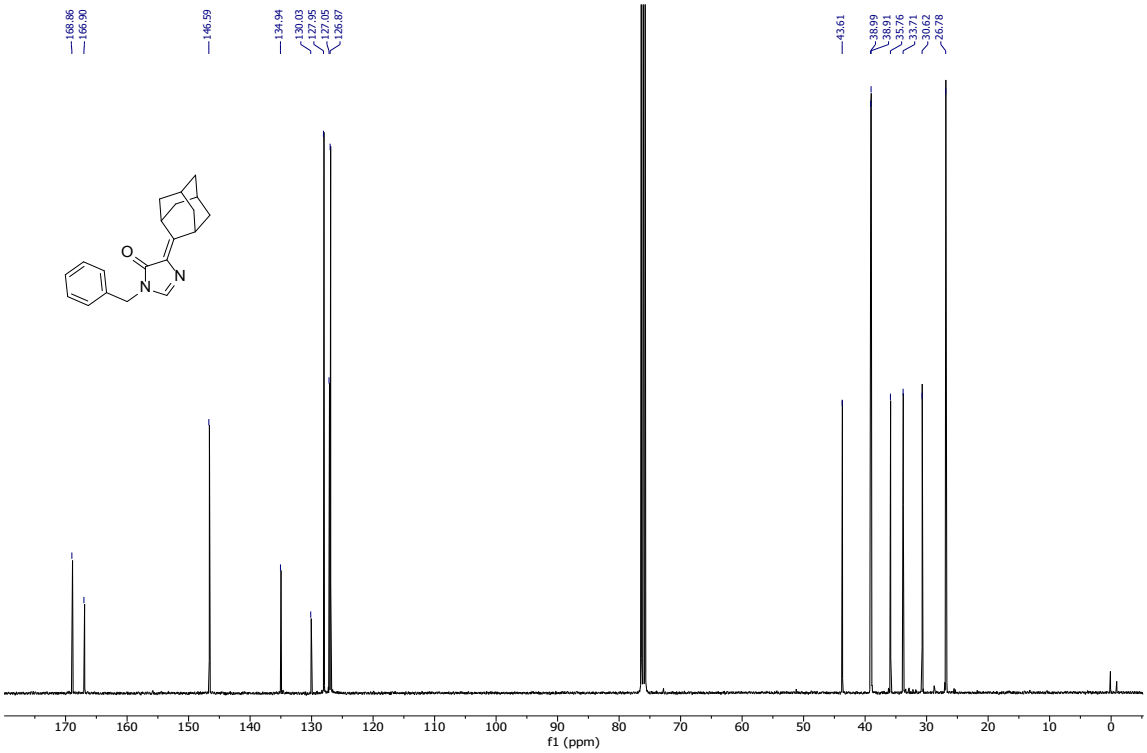

(5Z,5'Z)-3,3'-(Cyclohexane-1,2-diyl)bis(5-(benzo[d][1,3]dioxol-5-ylmethylene)-3,5-dihydro-4H-imidazol-4-one) (5-bis-a)

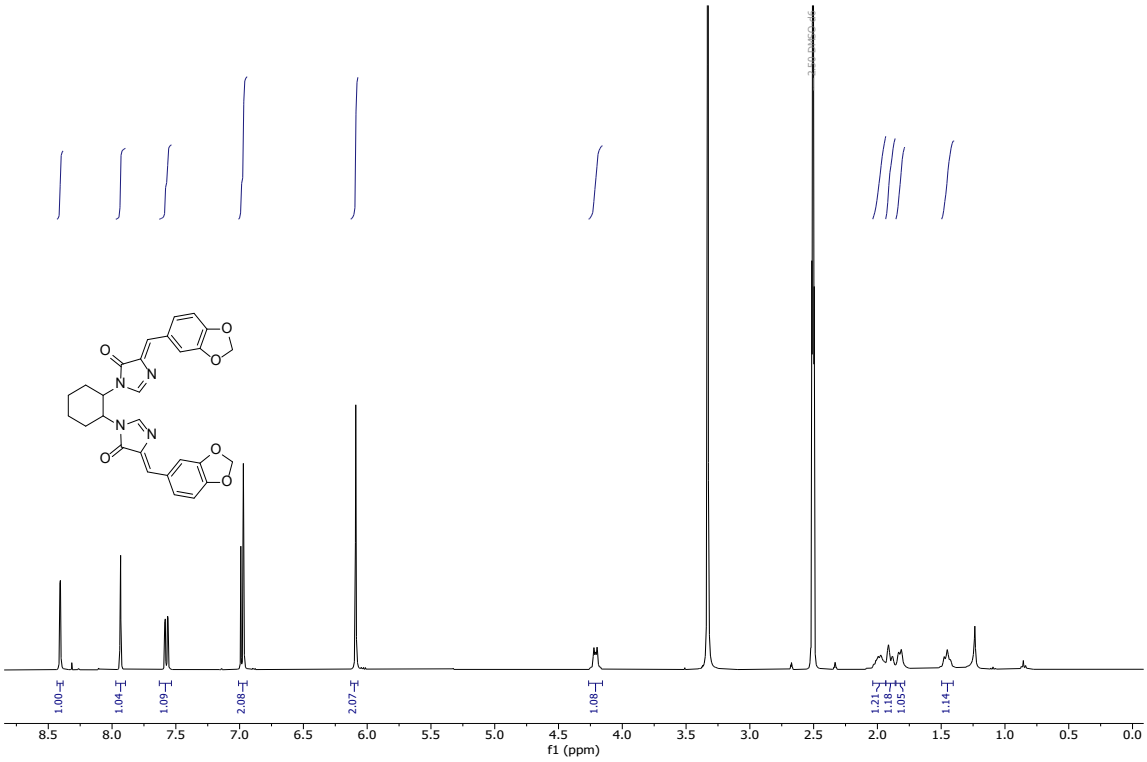

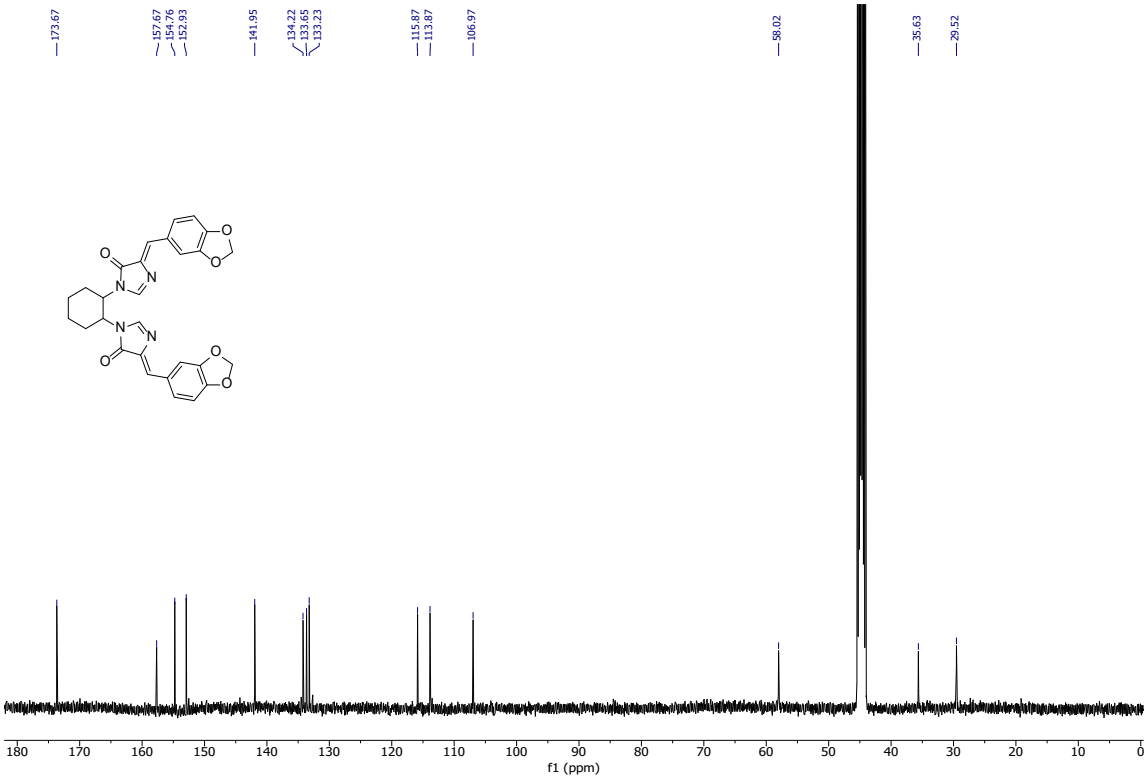

(5*R*,6*R*,7*S*,12*S*)-3,10-dibenzyl-6,12-bis(4-chlorophenyl)-1,3,8,10-tetraazadispiro[4.1.4^{7}.1^{5}]dodeca-1,8-diene-4,11-dione (8a)

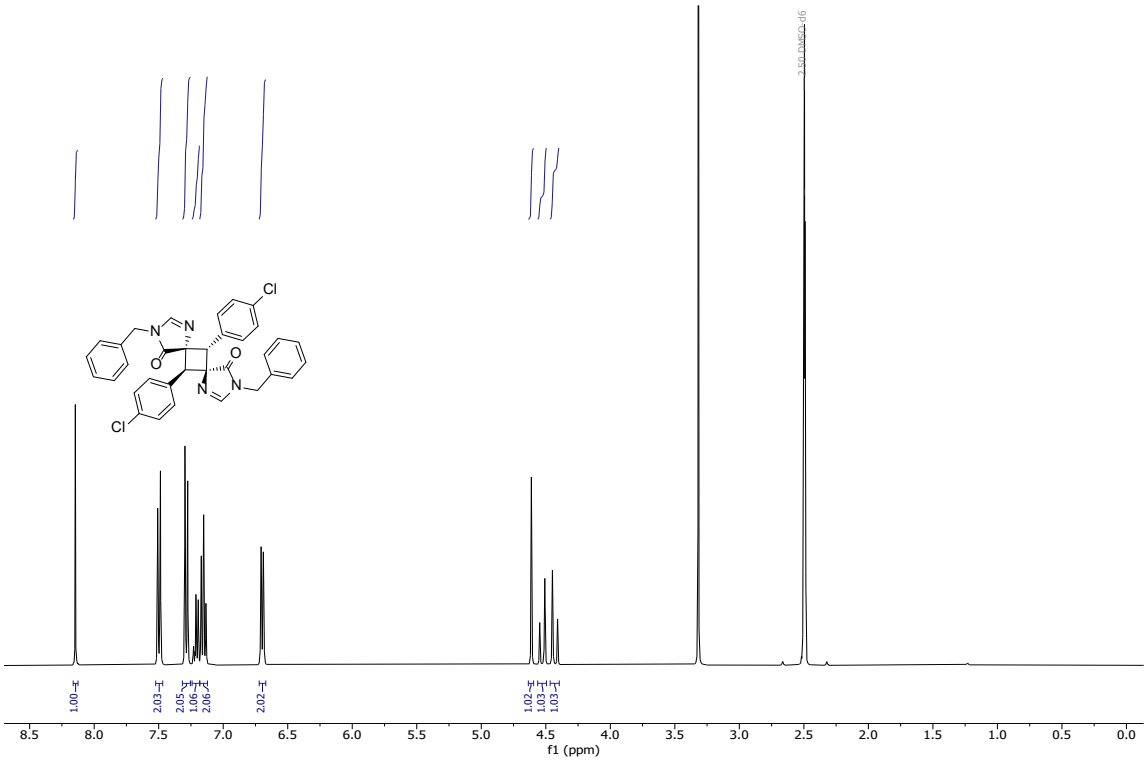

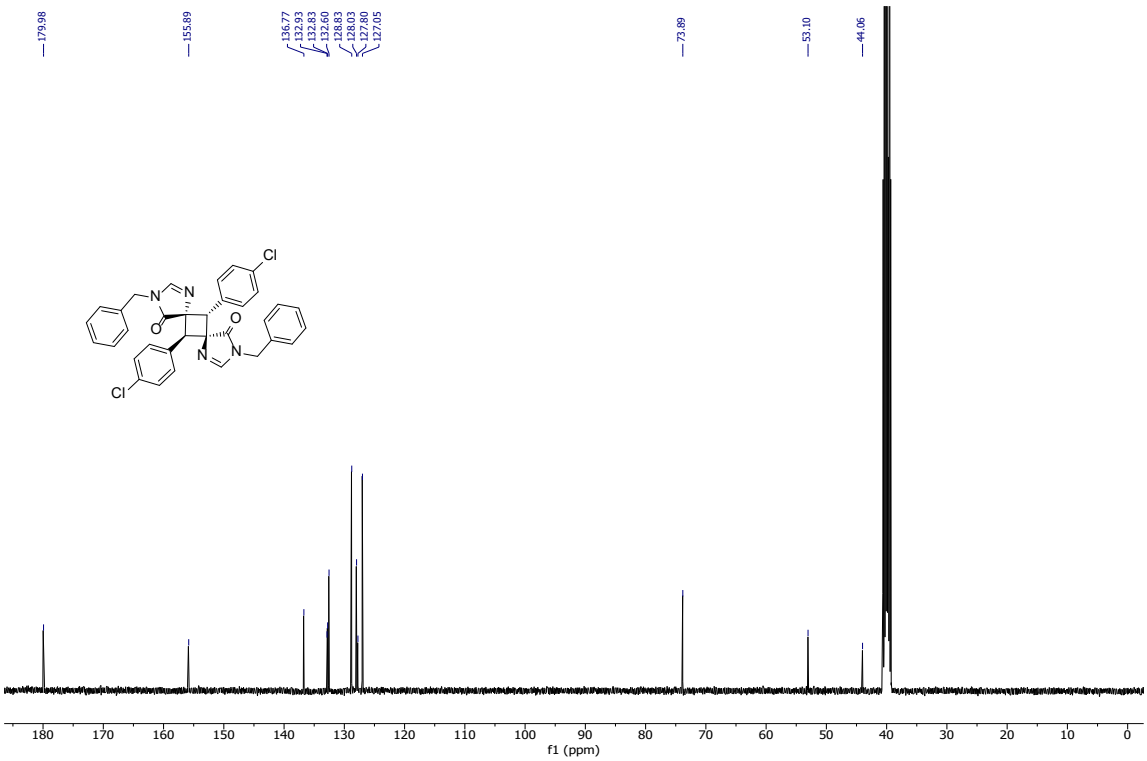

2-(4-Chlorobenzyl)-8-(4-chlorophenyl)-6,7-dihydroimidazo[1,2-a]pyrazin-3(5*H*)-one (9a)

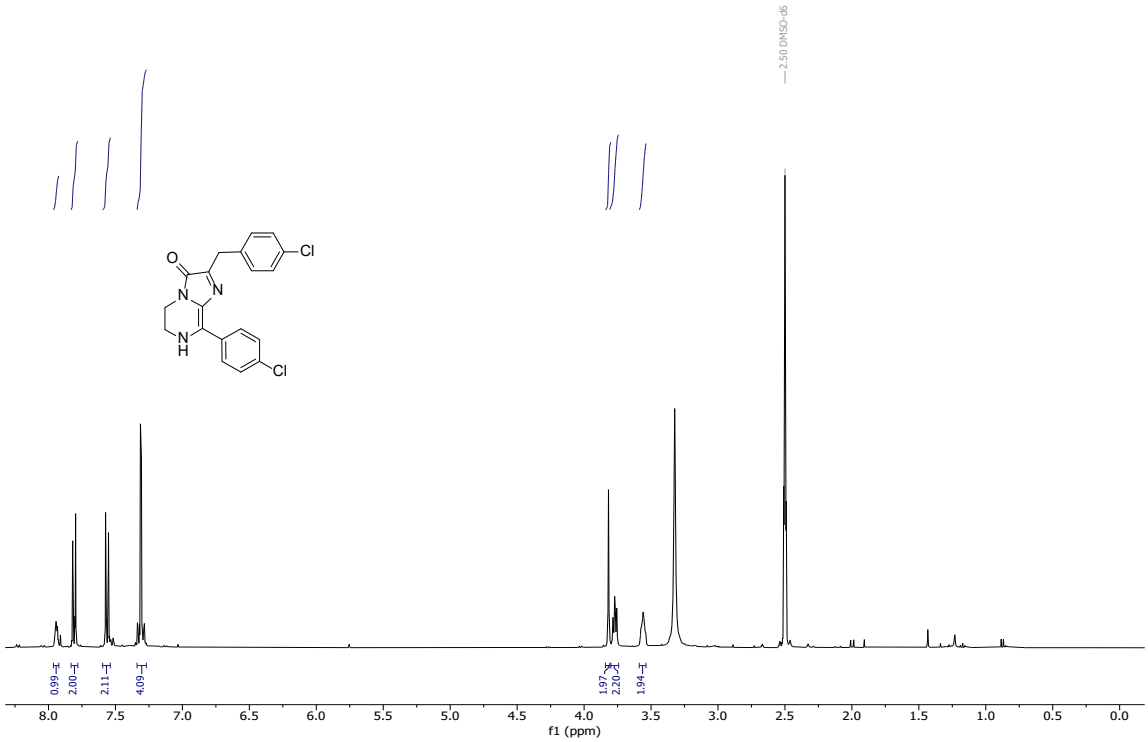

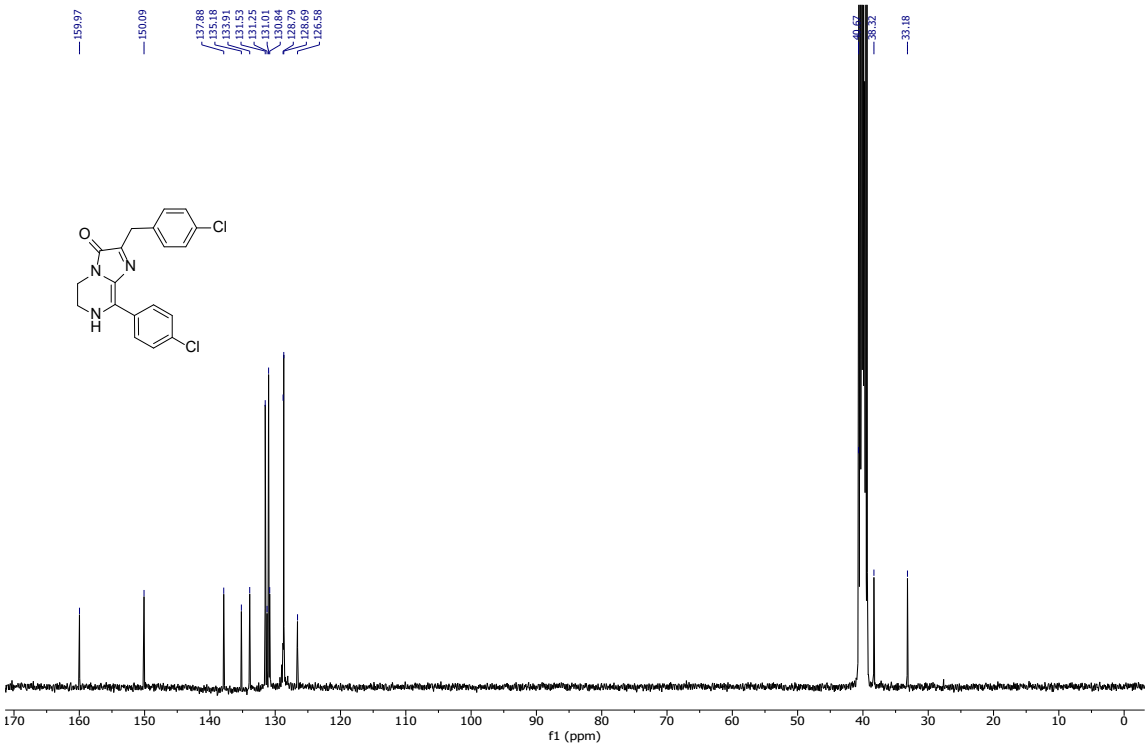

4-(2-(4-Cyanobenzyl)-3-oxo-3,5,6,7-tetrahydroimidazo[1,2-a]pyrazin-8-yl)benzonitrile (9c)

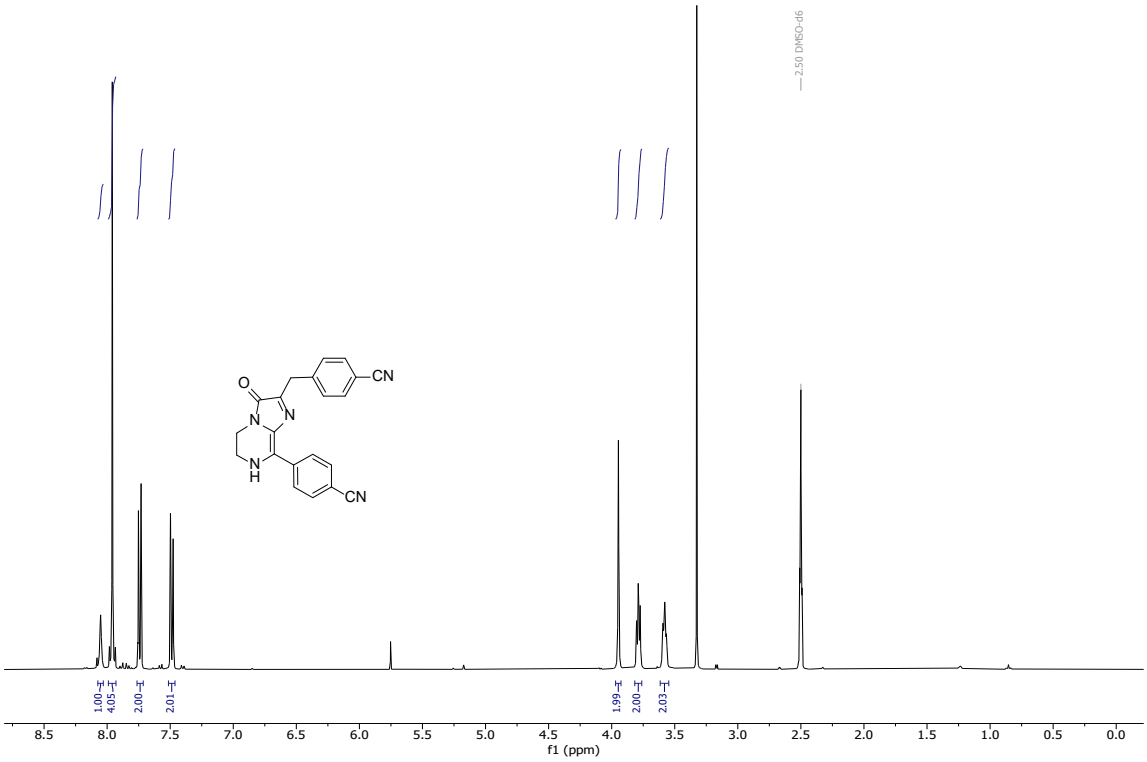

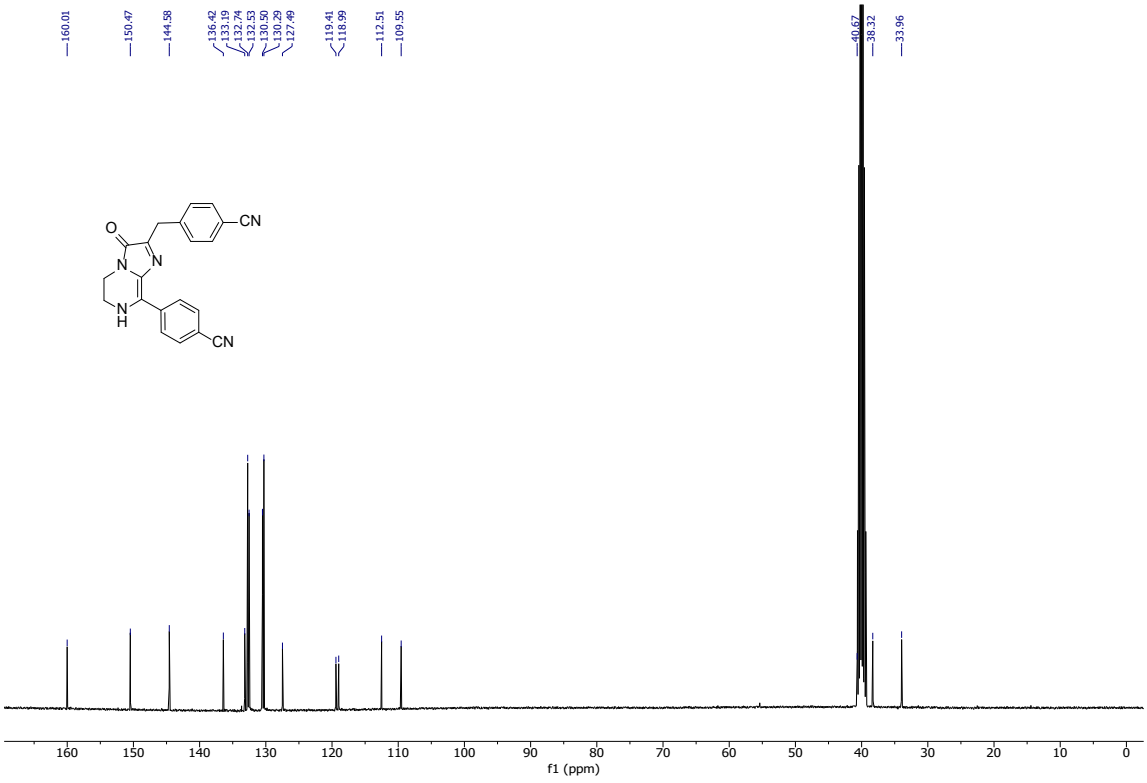

(5a*R*,9a*R*)-2-(4-Chlorobenzyl)-4-(4-chlorophenyl)-5a,6,7,8,9,9a-hexahydroimidazo[1,2-*a*]quinoxalin-1(5*H*)-one (9d)

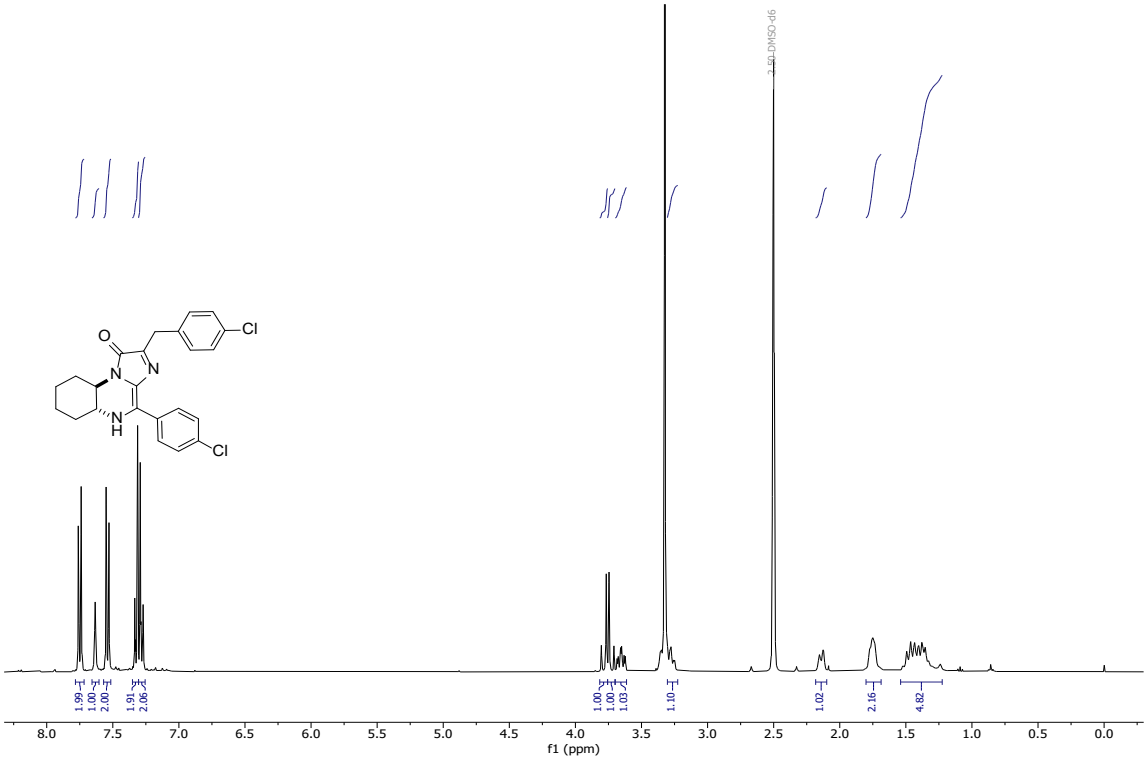

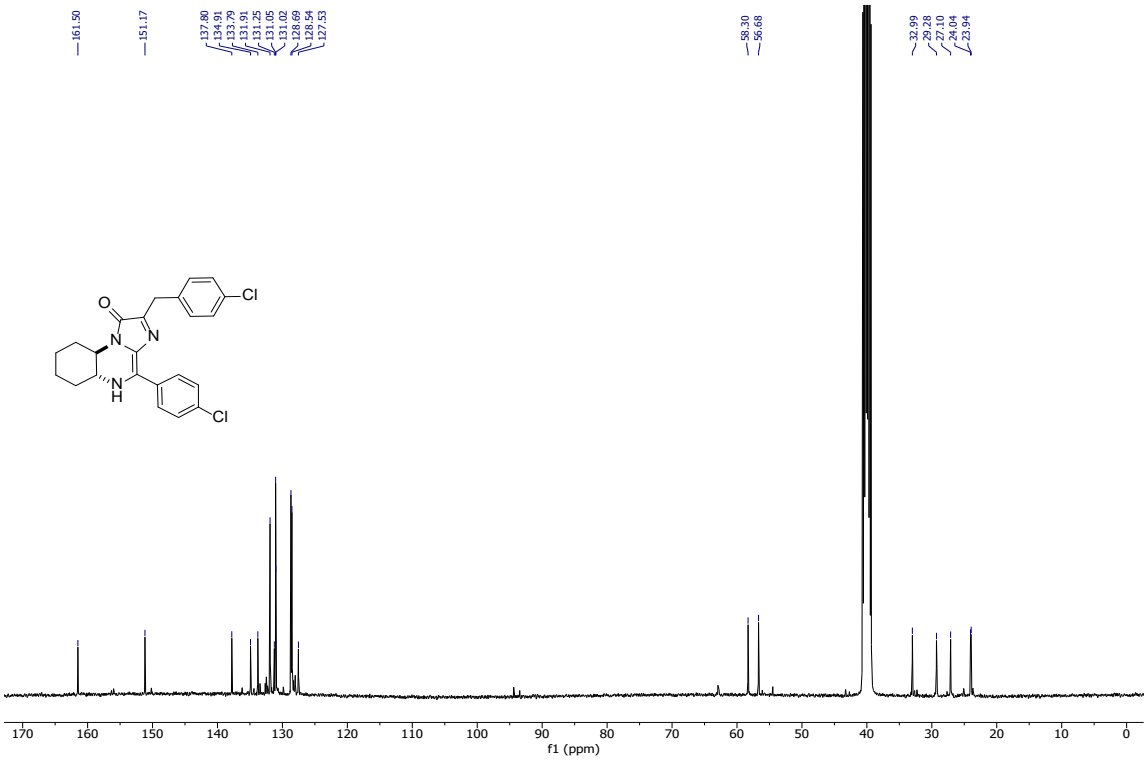

8-(Benzo[d][1,3]dioxol-5-yl)-2-(benzo[d][1,3]dioxol-5-ylmethyl)-6,7-dihydroimidazo[1,2-a]pyrazin-3(5*H*)-one (9e)

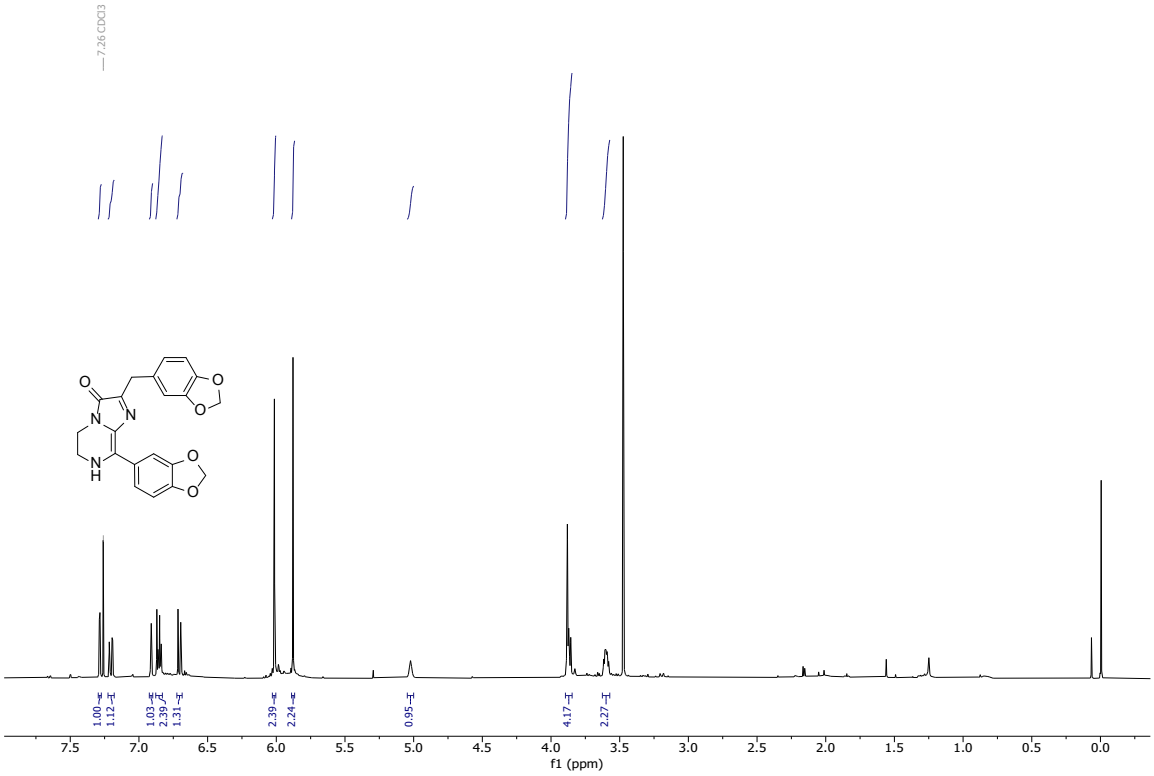

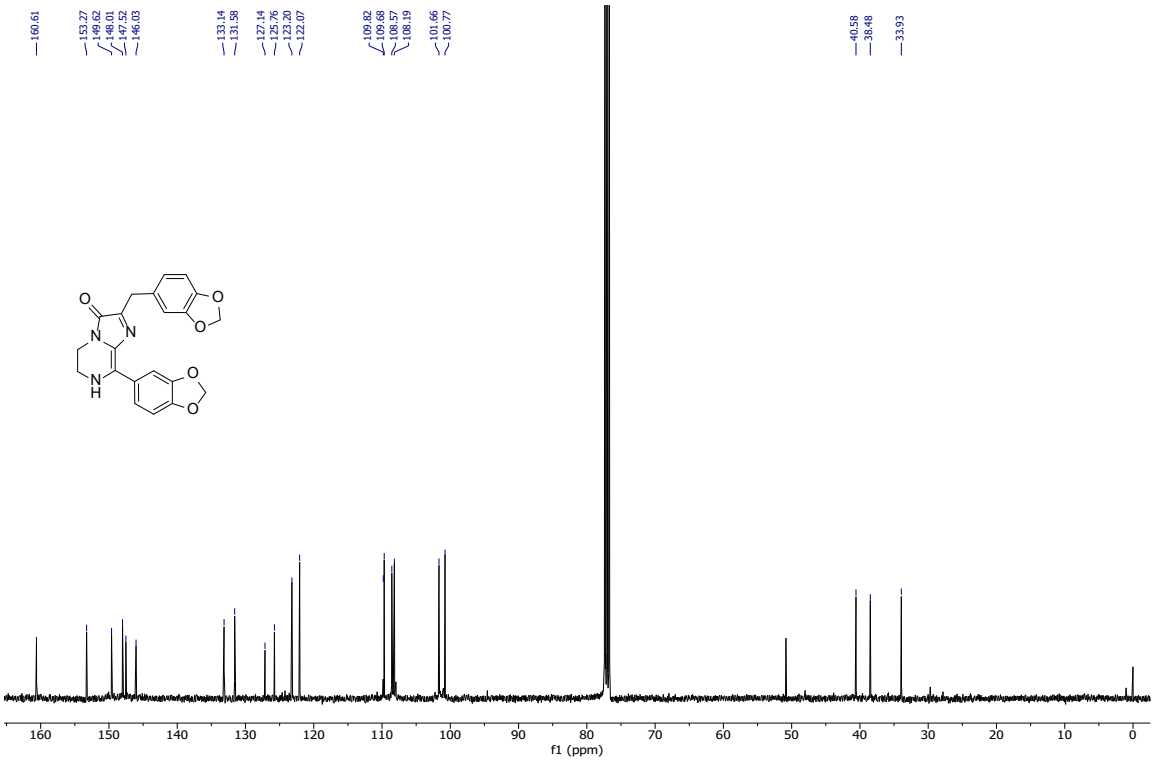

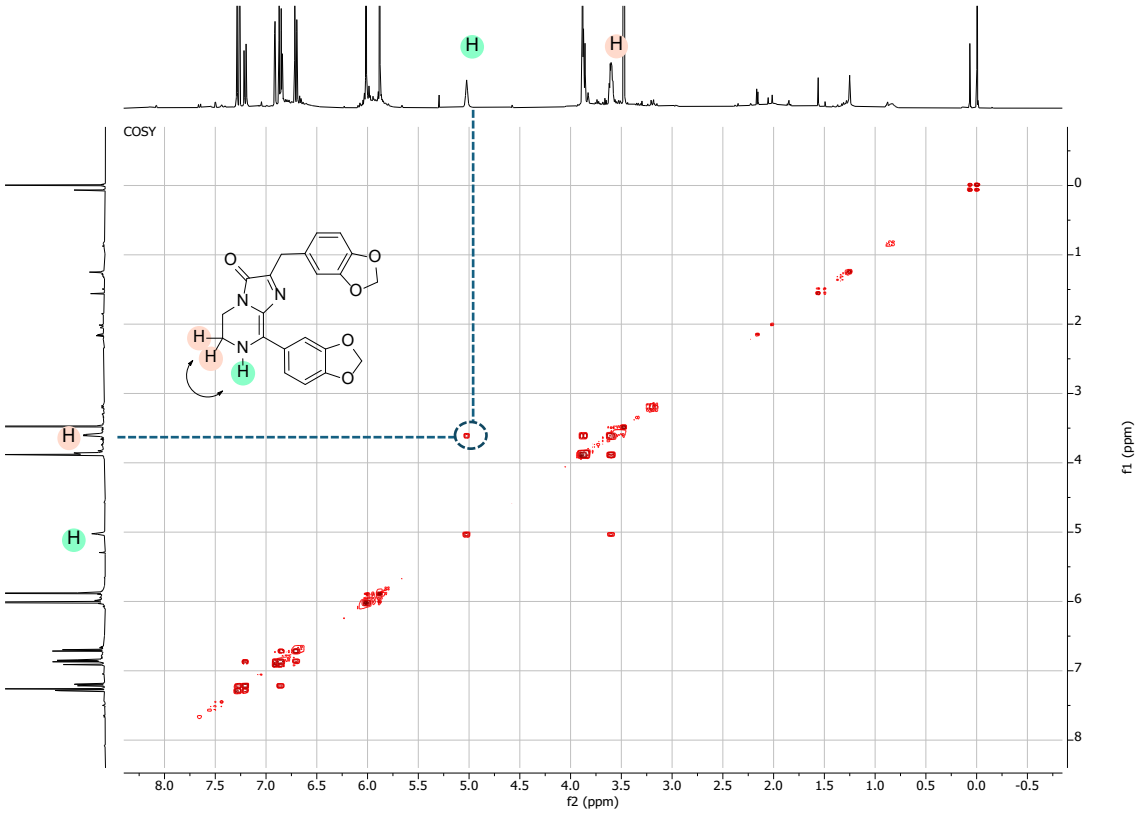
COSY
H
H
H
H
O
O
O
O
N
N
N
H
H
H
f2 (ppm)
f1 (ppm)
8.0
7.5
7.0
6.5
6.0
5.5
5.0
4.5
4.0
3.5
3.0
2.5
2.0
1.5
1.0
0.5
0.0
-0.5
0
1
2
3
4
5
6
7
8

2-(3,4,5-Trimethoxybenzyl)-8-(3,4,5-trimethoxyphenyl)-6,7-dihydroimidazo[1,2-*a*]pyrazin-3(5*H*)-one (9f)

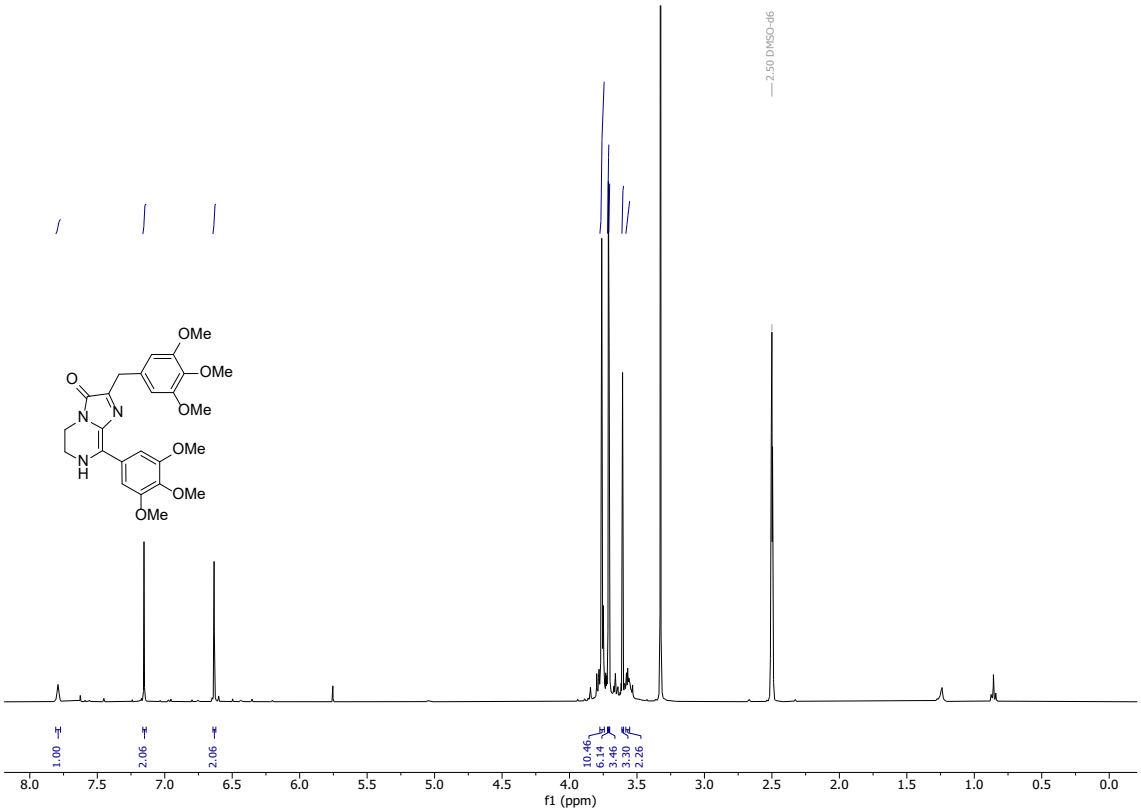

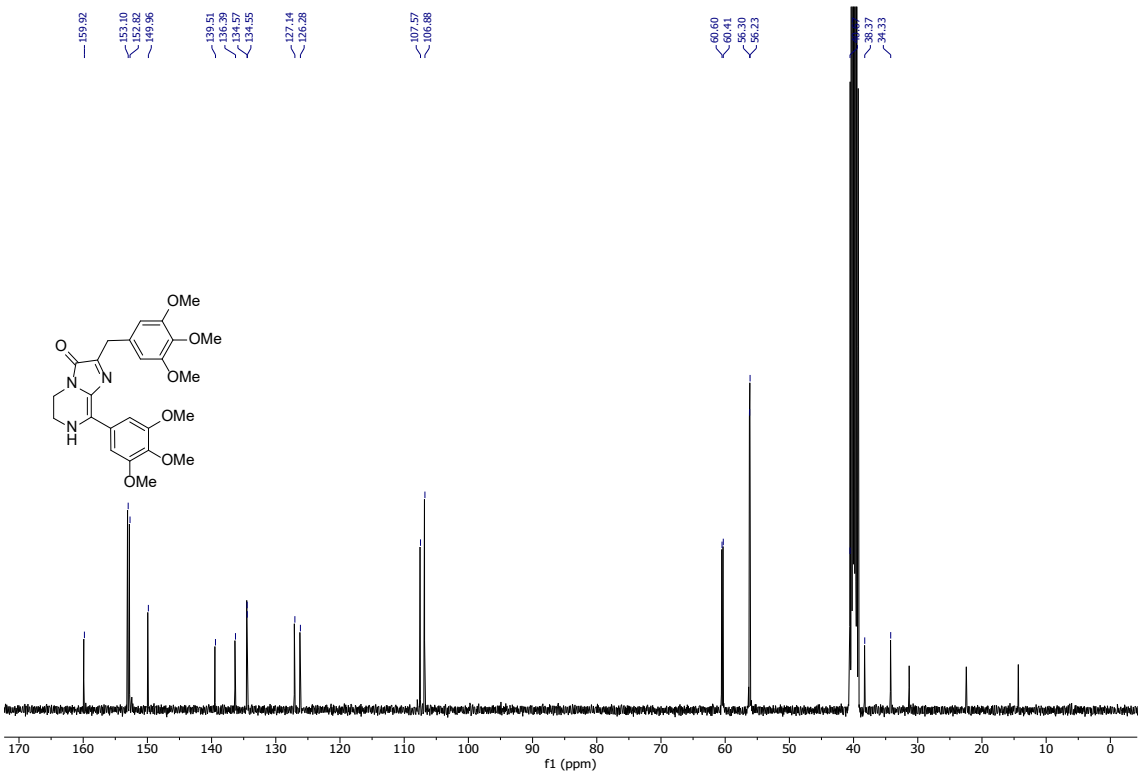

(*Z*)-8-(benzo[*d*][1,3]dioxol-5-yl)-2-(benzo[*d*][1,3]dioxol-5-ylmethylene)-1,5,6,7-tetrahydroimidazo[1,2-*a*]pyrazin-3(2*H*)-one (9e-imine)

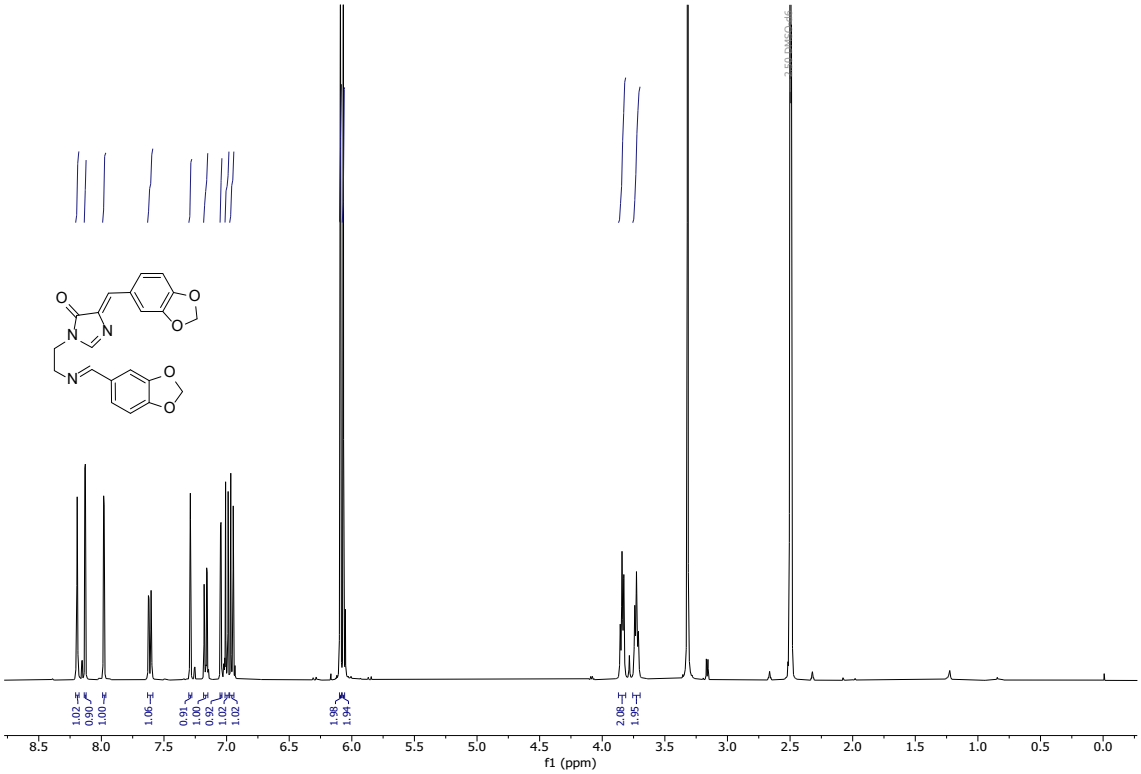

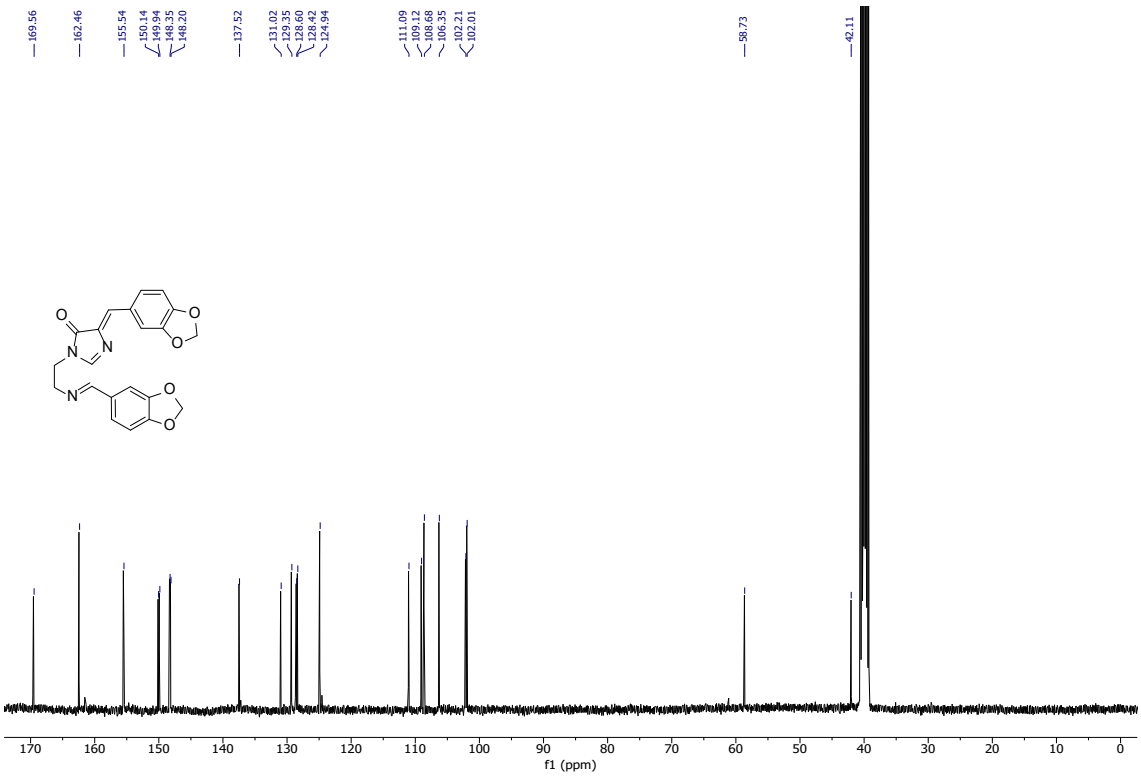

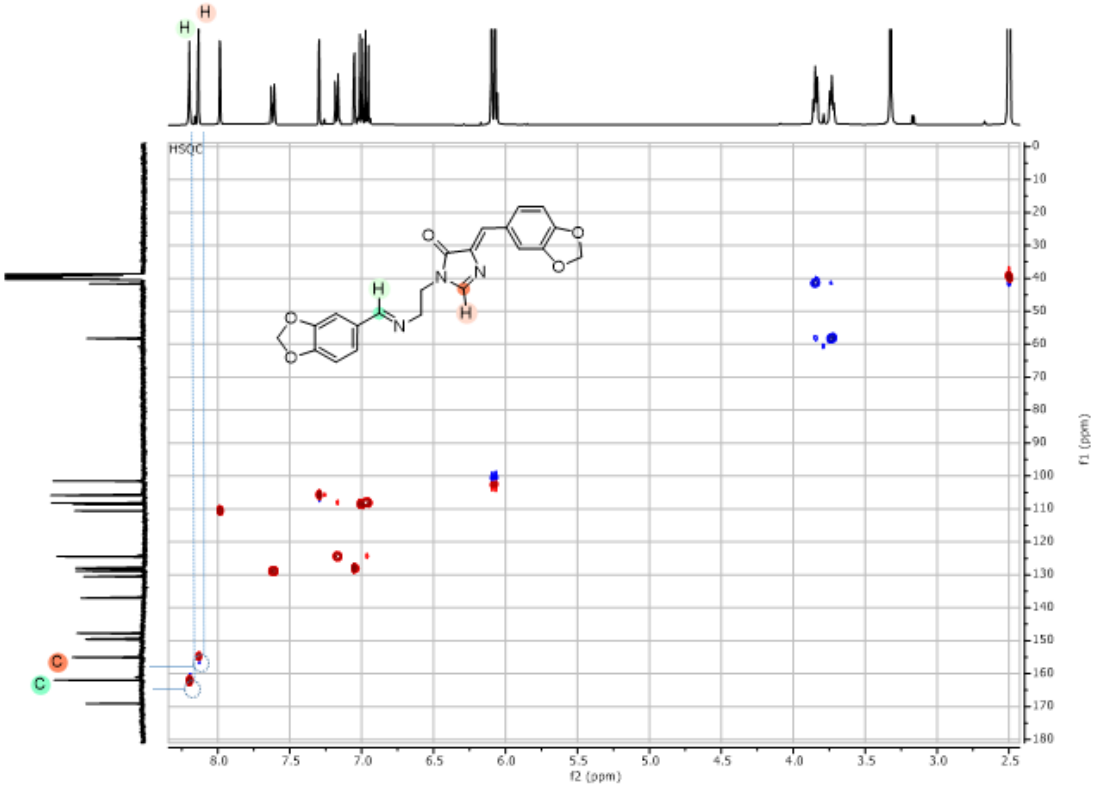
HSQC
f2 (ppm)
f1 (ppm)

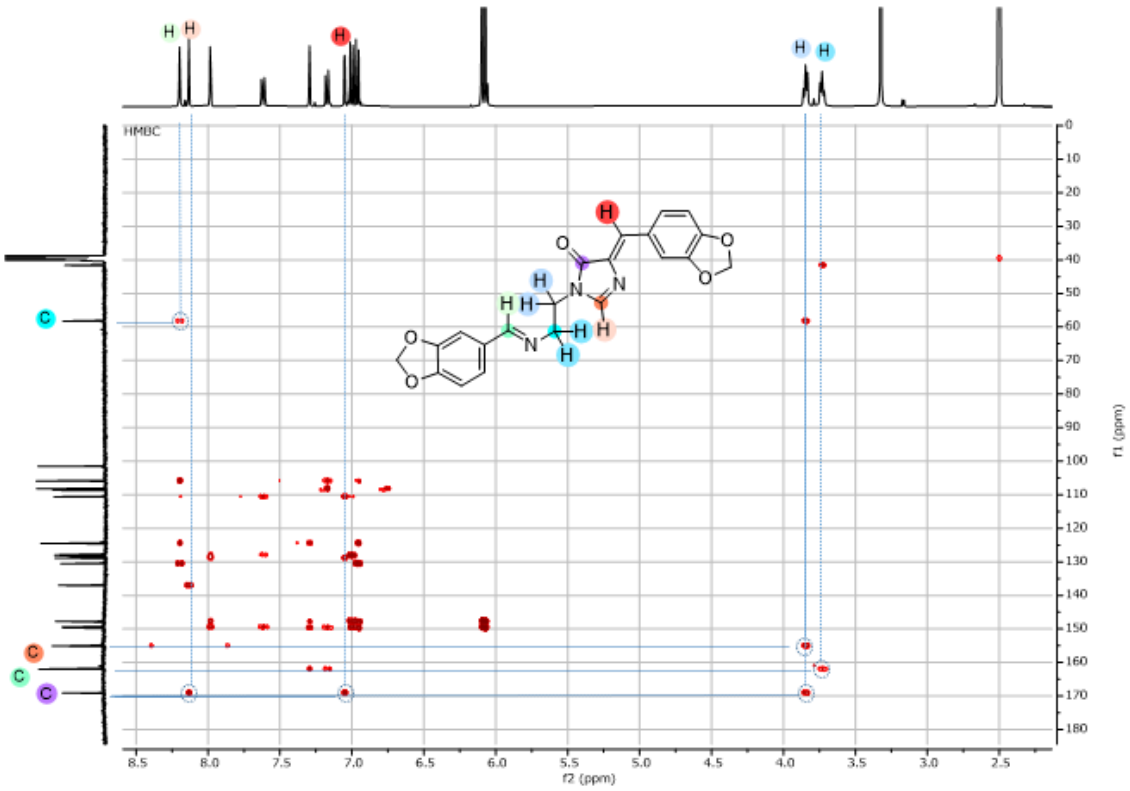
HMBC
f2 (ppm)
f1 (ppm)

5-(Benzo[*d*][1,3]dioxol-5-ylmethyl)-3-methyl-2-(pyrrolidin-1-yl)-3,5-dihydro-4*H*-imidazol-4-one (11d)

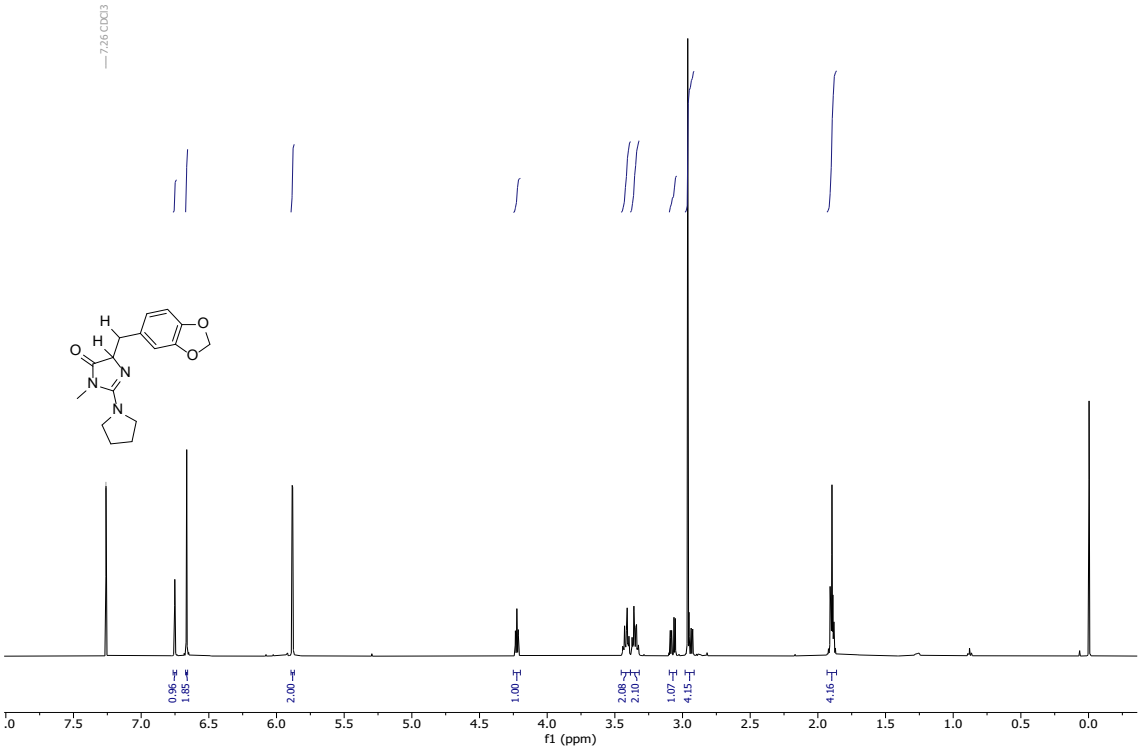

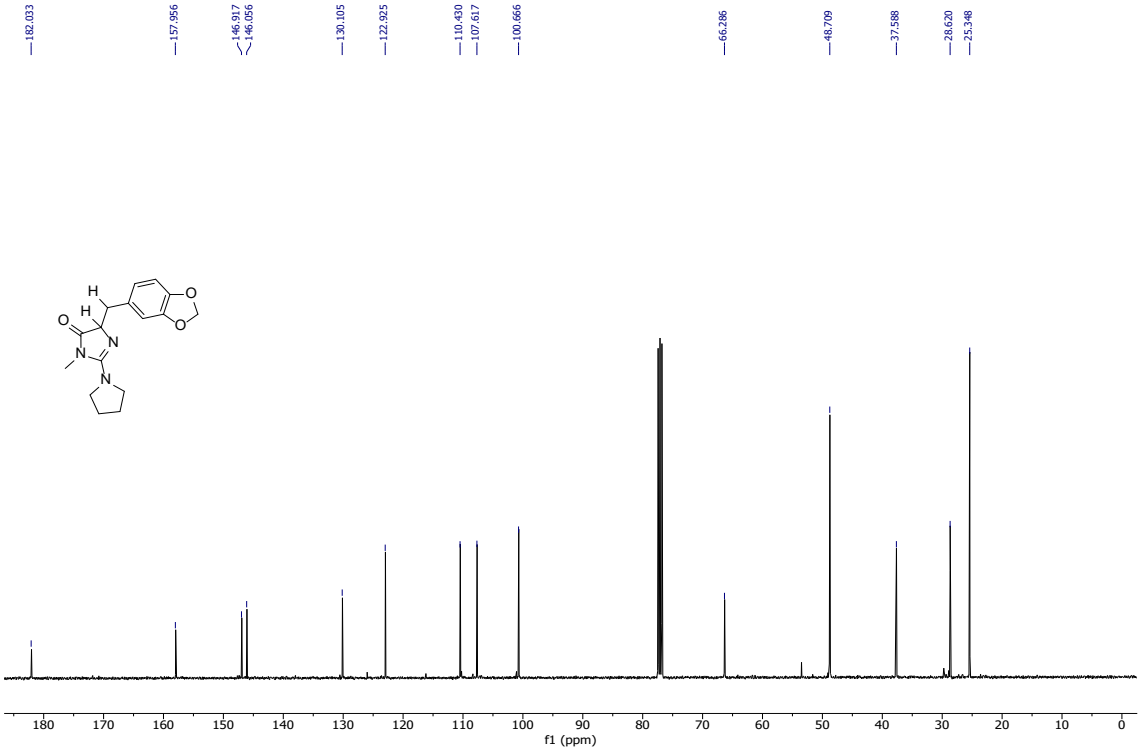

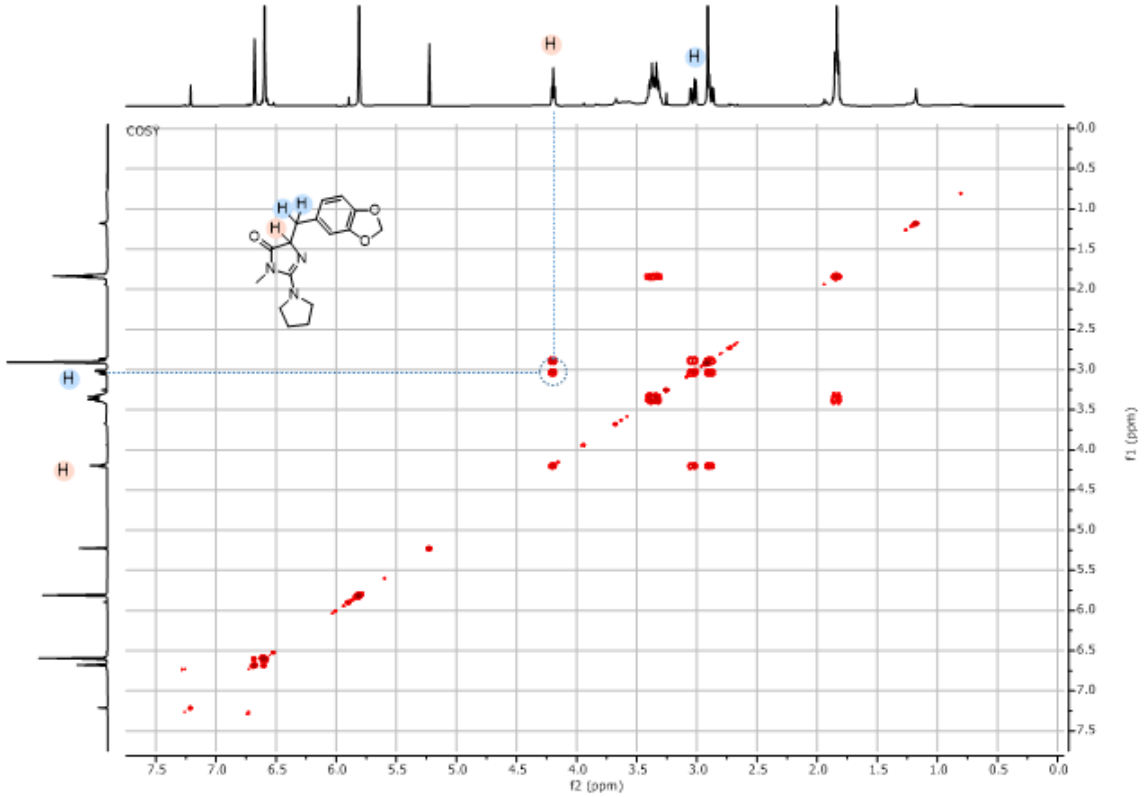
COSY
H
H
H
H
f2 (ppm)
f1 (ppm)

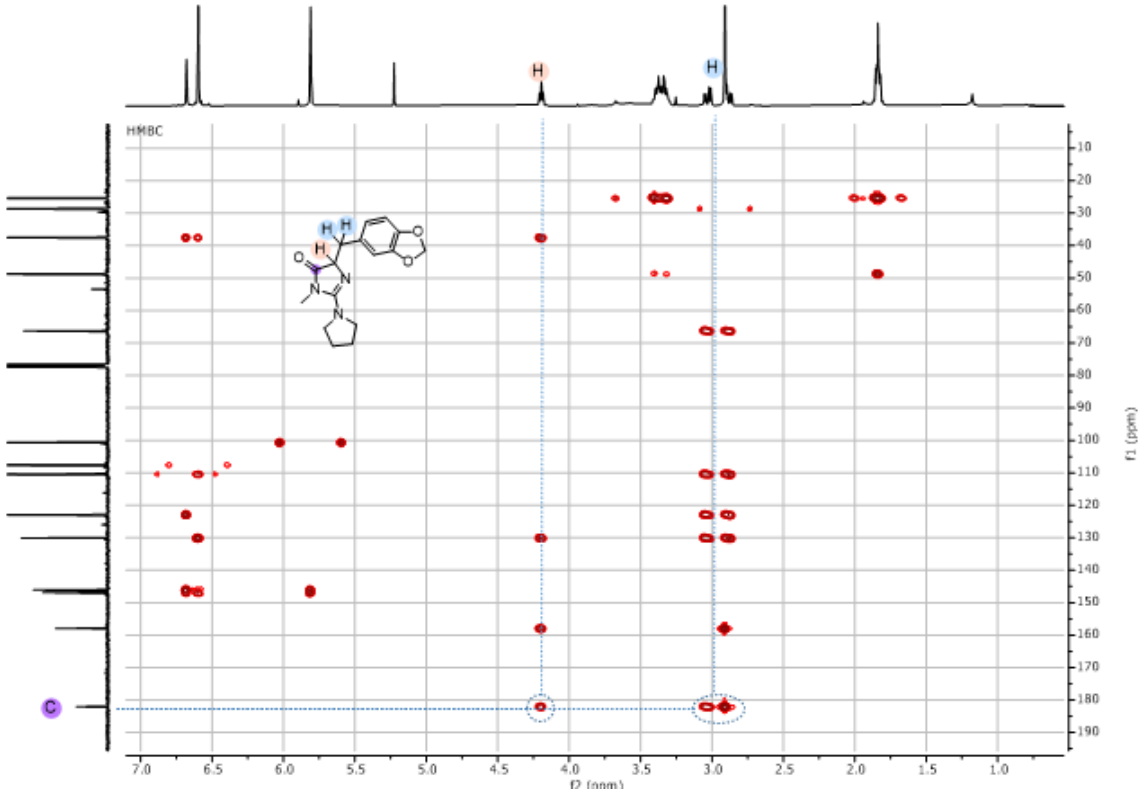
HMBC
H
H
C
f2 (ppm)
f1 (ppm)

3-Benzyl-5-(4-chlorobenzyl)-2-(pyrrolidin-1-yl)-3,5-dihydro-4*H*-imidazol-4-one (11e)

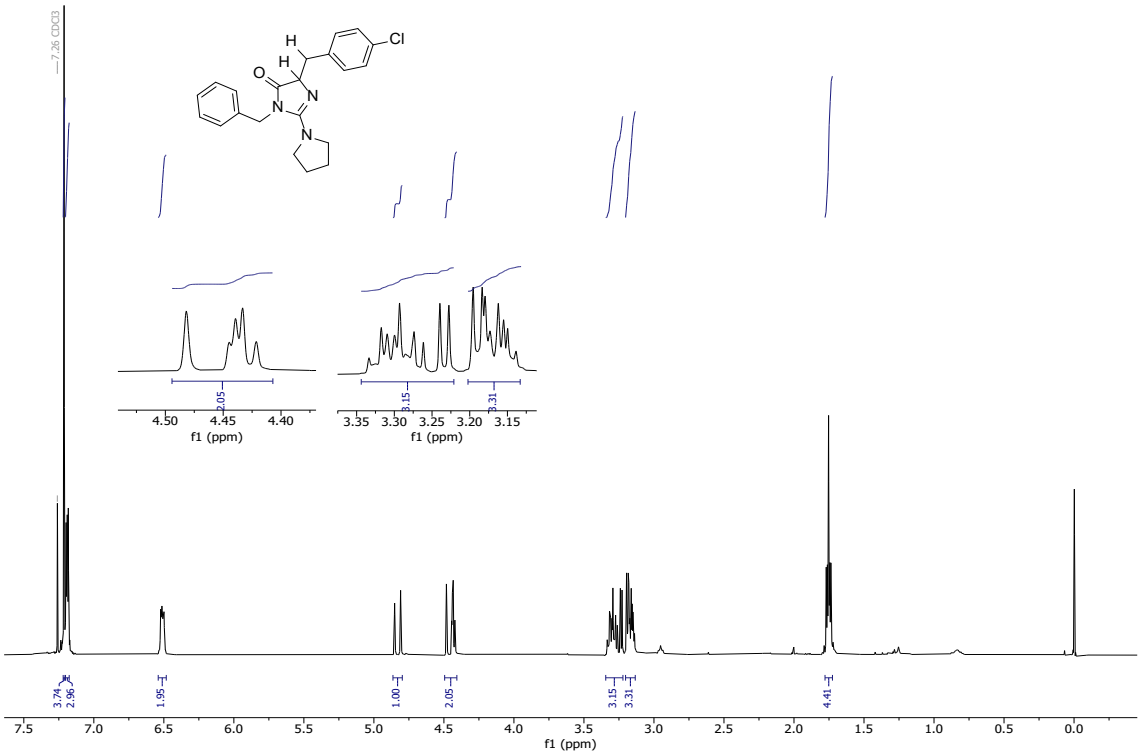

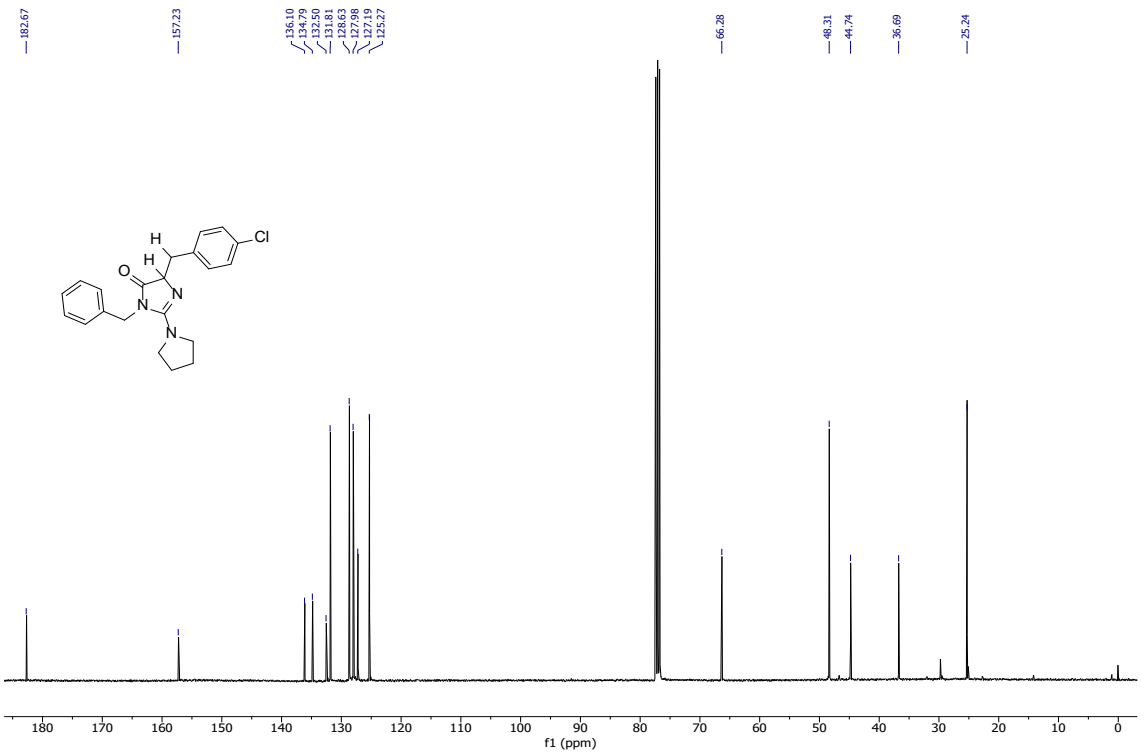

3-Benzyl-5-((4-chlorophenyl)methyl-d_2)-2-(pyrrolidin-1-yl)-3,5-dihydro-4*H*-imidazol-4-one (11e-d_2)

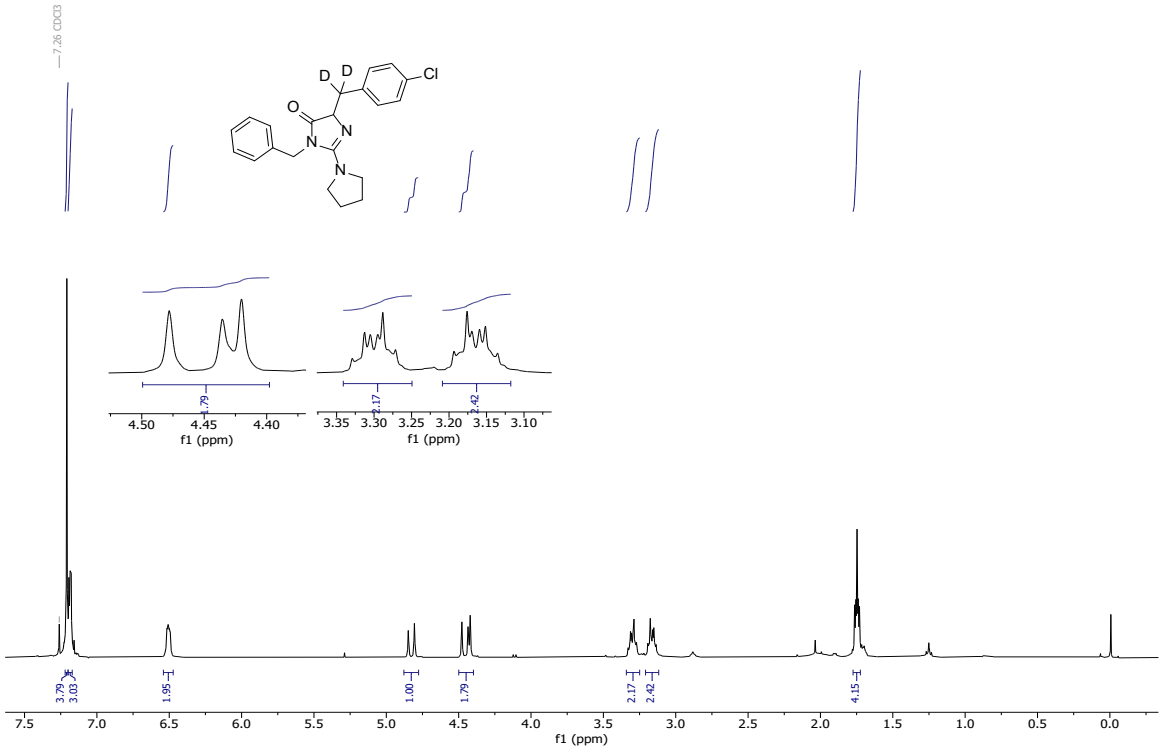

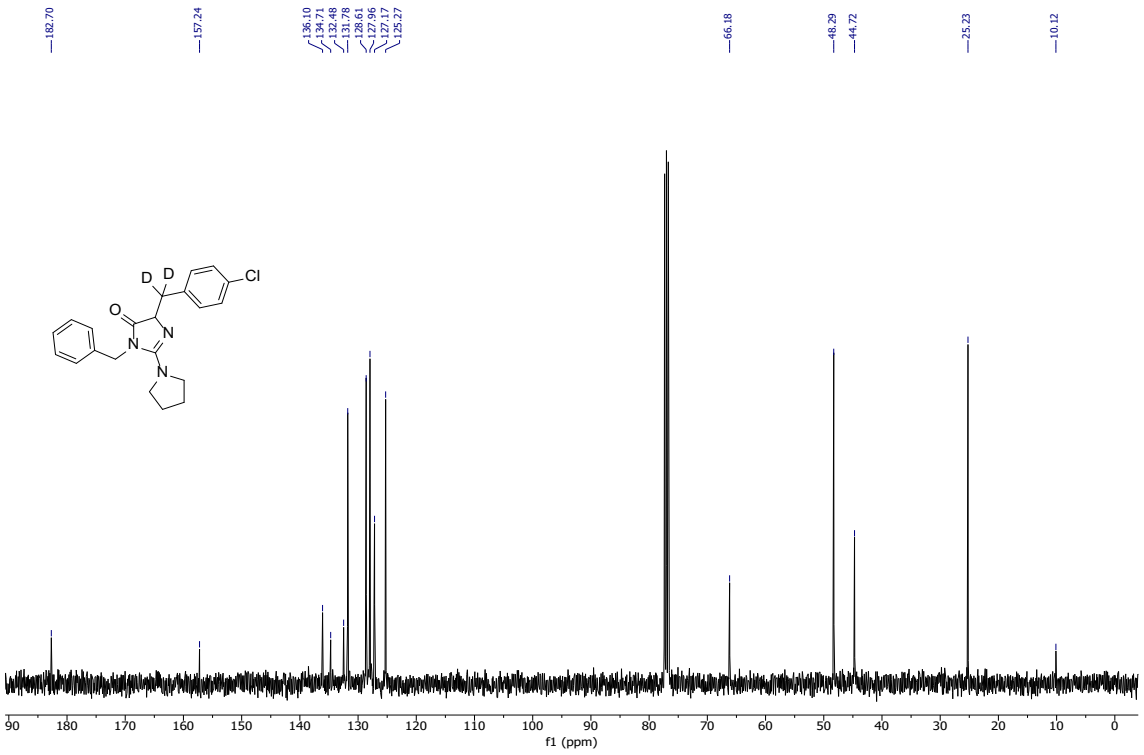

(*Z*)-2-(benzo[*d*][1,3]dioxol-5-ylmethylene)-5,6,7,8-tetrahydroimidazo[1,2-*a*]pyrimidin-3(2*H*)-one (12a)

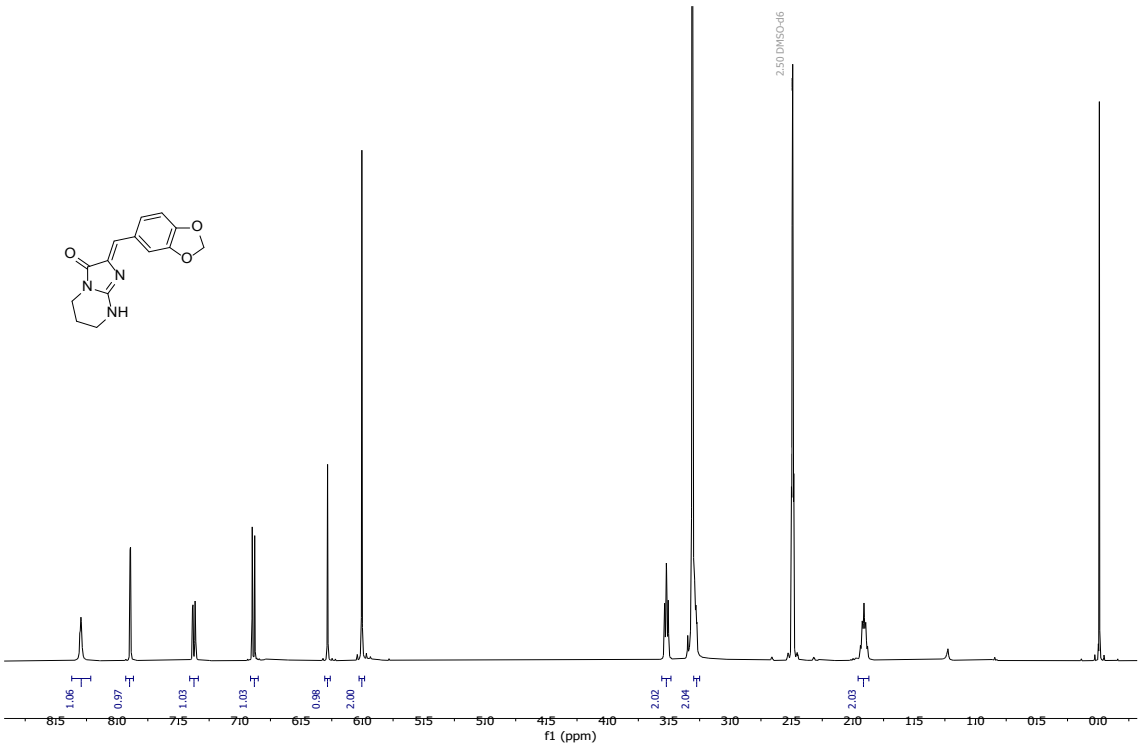

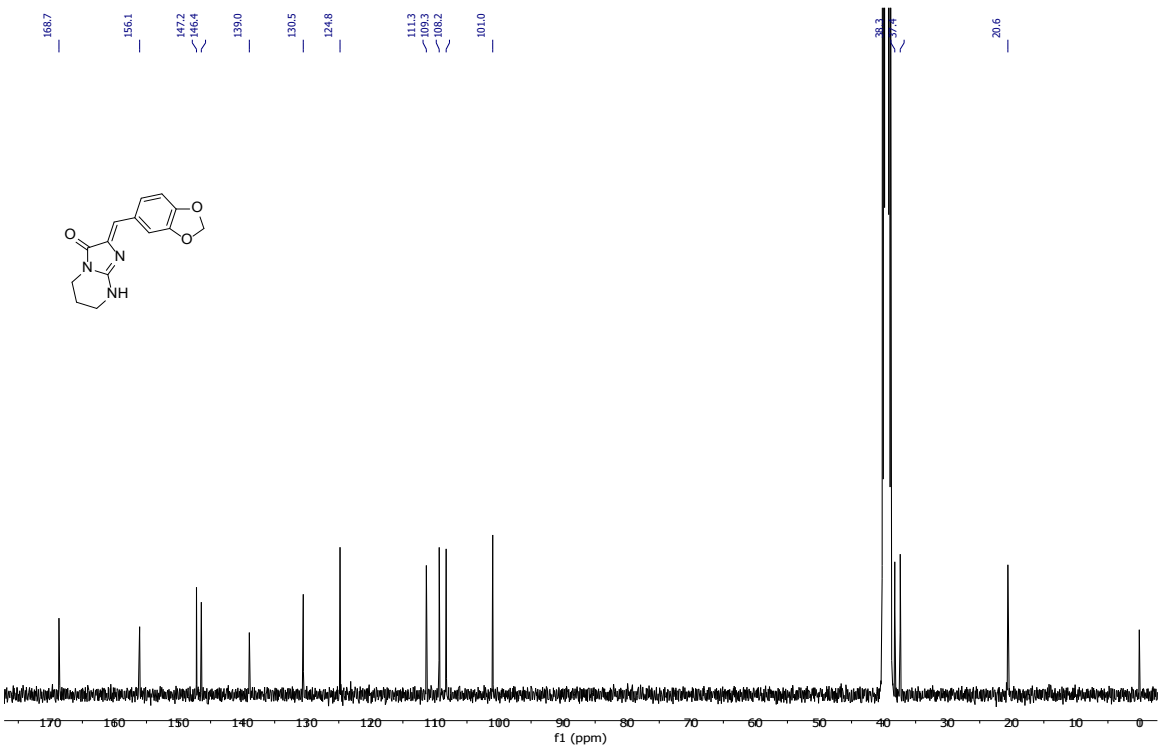

tert-Butyl (_Z_)-3-((1-methyl-2-(methylamino)-5-oxo-1,5-dihydro-4_H_-imidazol-4-ylidene)methyl)-1_H_-indole-1-carboxylate (12c)

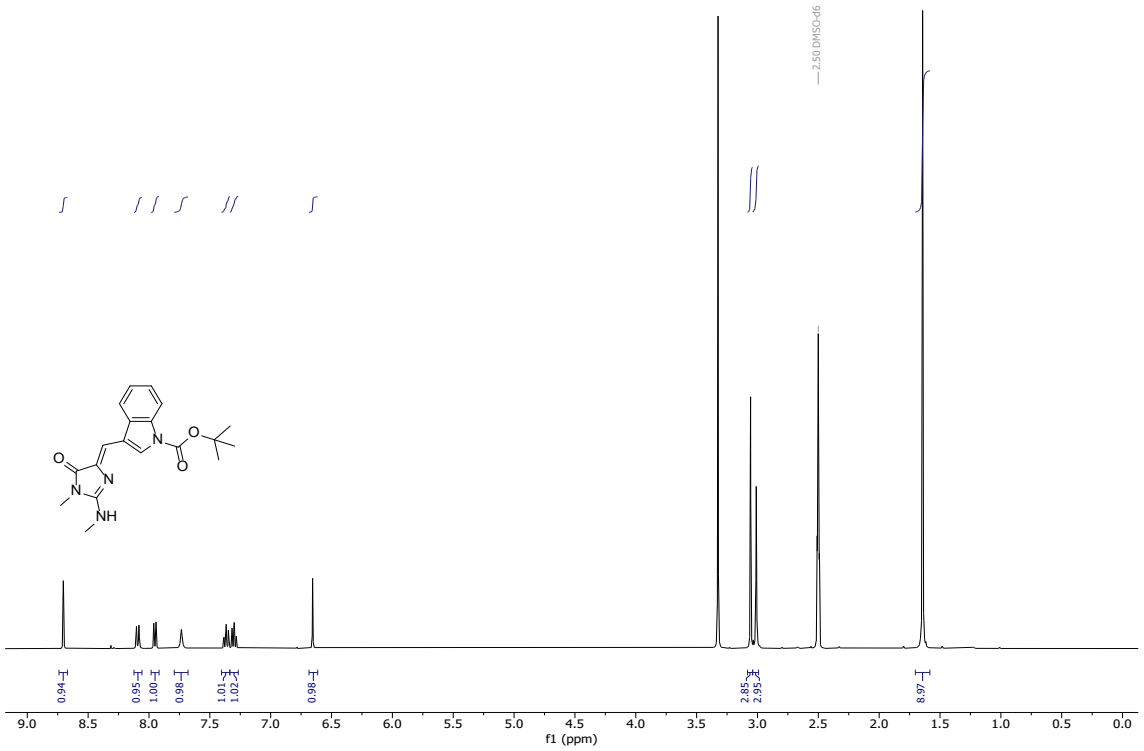

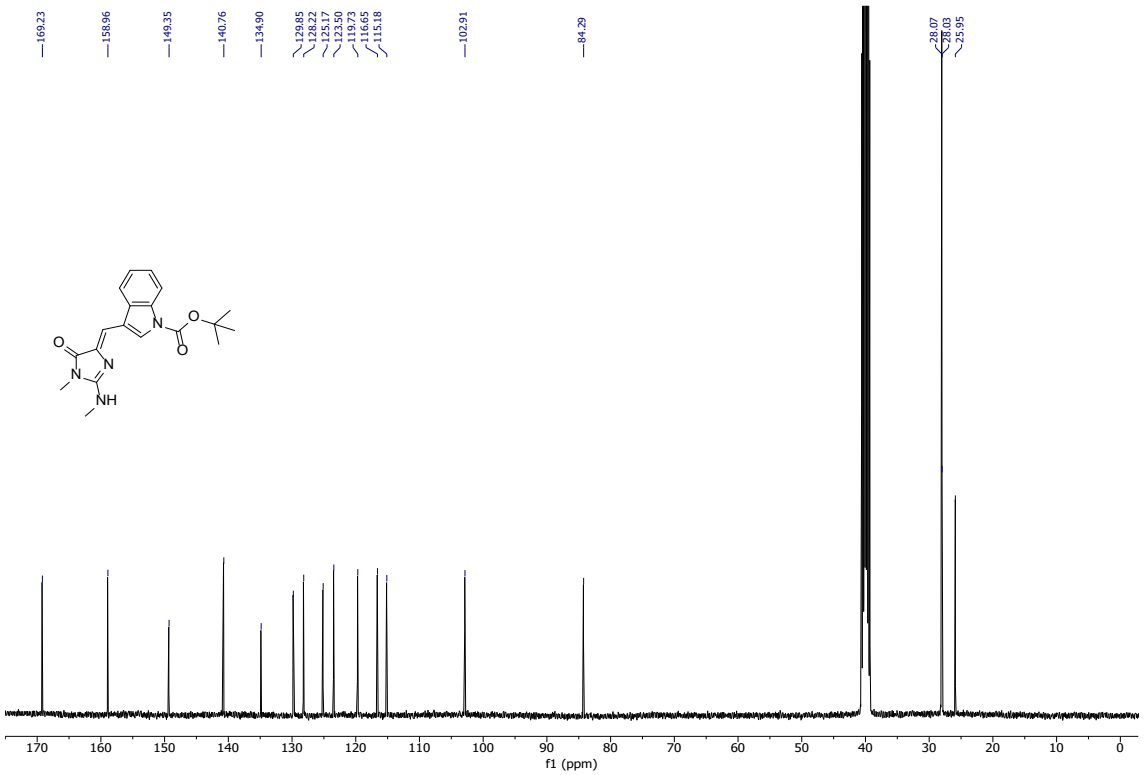

(*Z*)-5-((1*H*-Indol-3-yl)methylene)-3-methyl-2-(methylamino)-3,5-dihydro-4*H*-imidazol-4-one (12c')

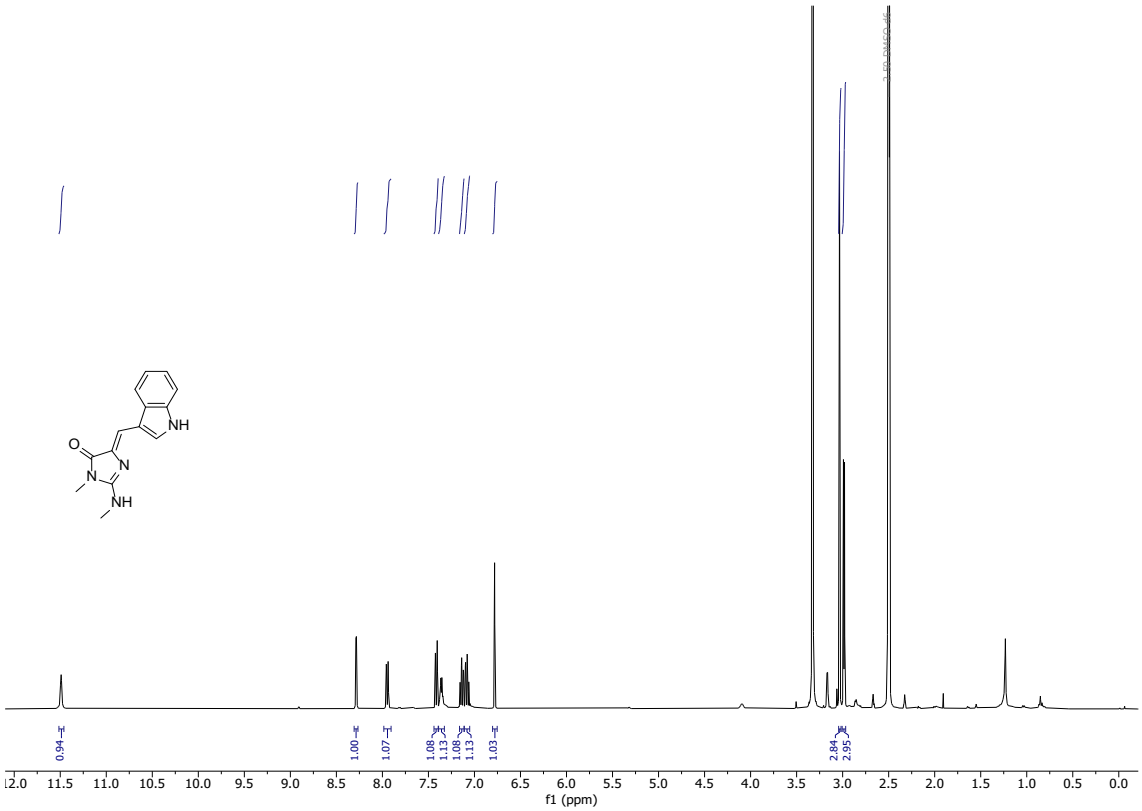

(*Z*)-5-(Benzo[*d*][1,3]dioxol-5-ylmethylene)-3-methyl-2-(pyrrolidin-1-yl)-3,5-dihydro-4*H*-imidazol-4-one (12d)

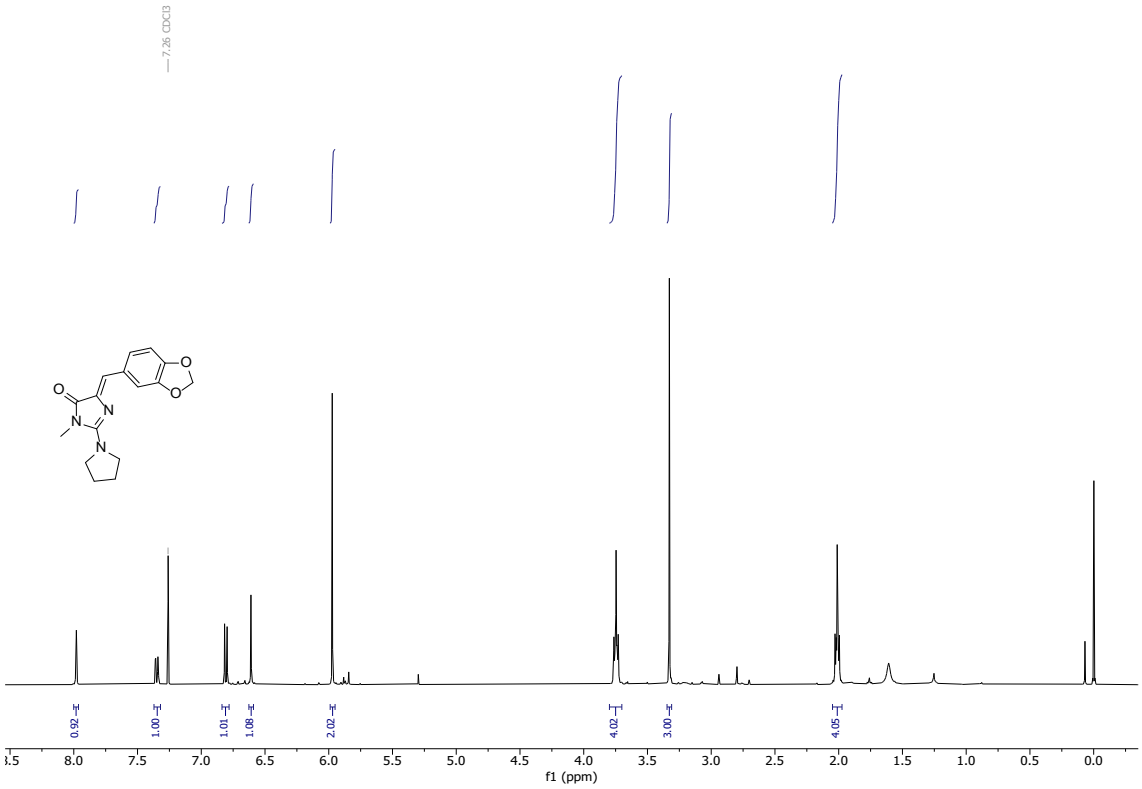

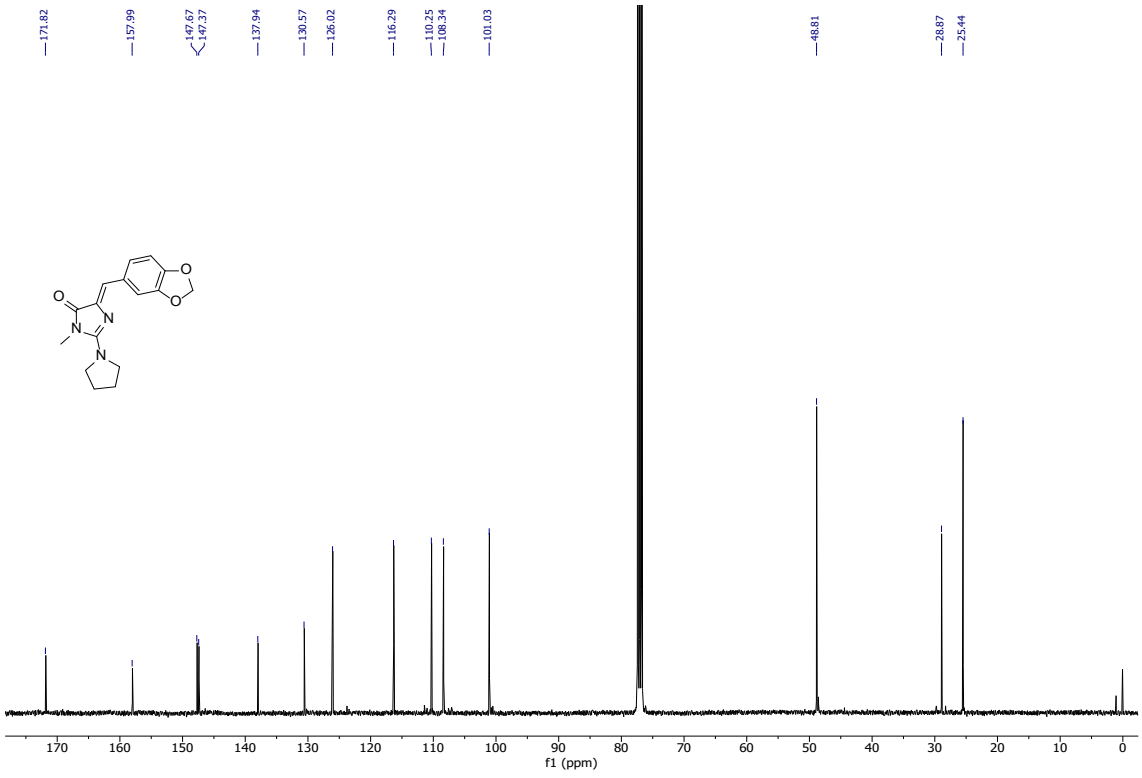

(*Z*)-3-Benzyl-5-(4-chlorobenzylidene)-2-(pyrrolidin-1-yl)-3,5-dihydro-4*H*-imidazol-4-one (12e)

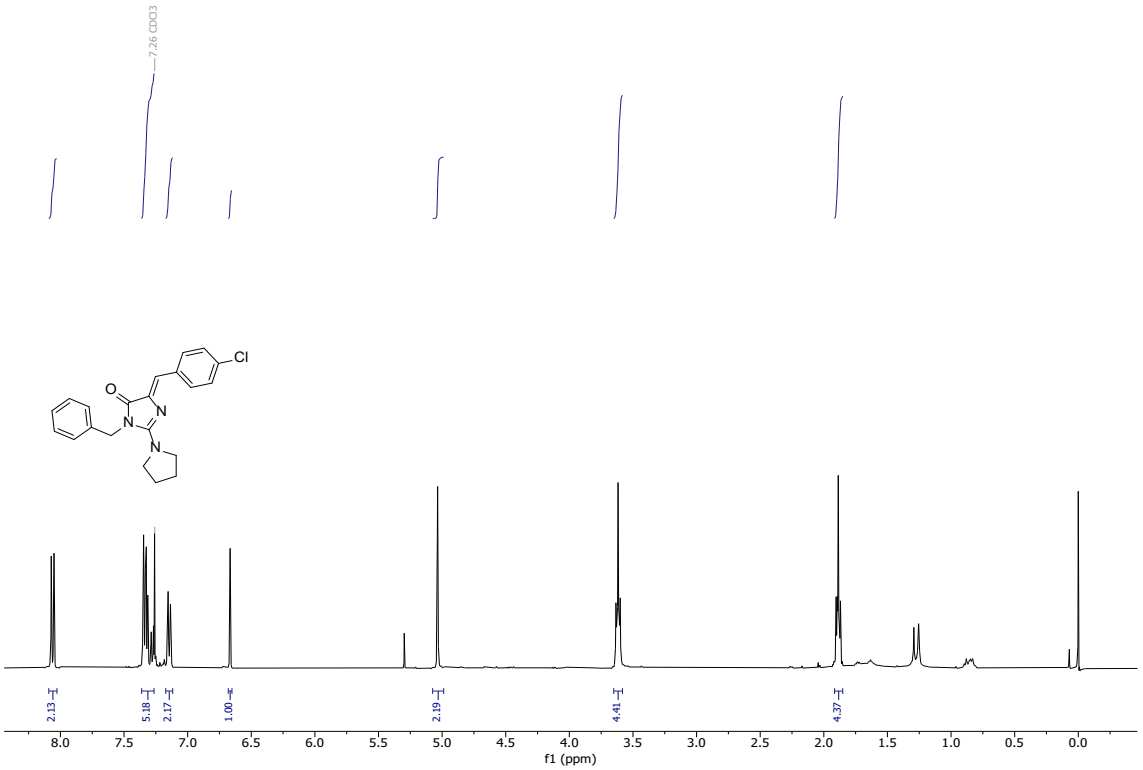

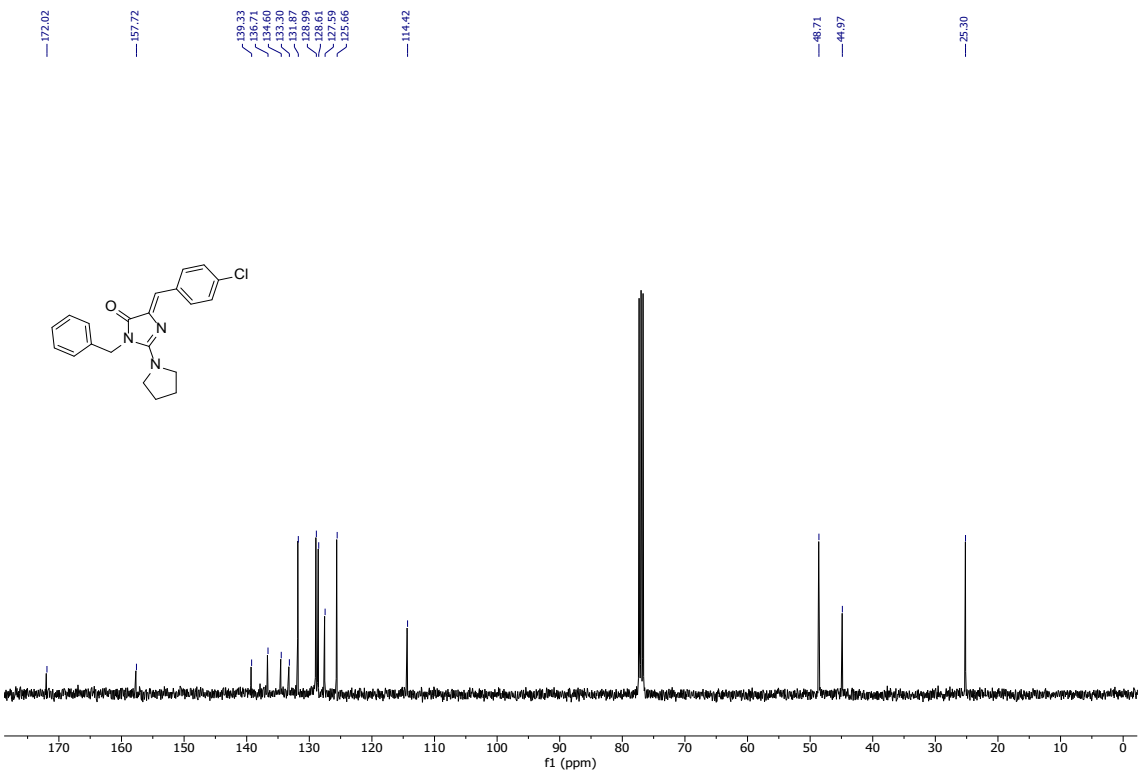

(*Z*)-3-Benzyl-5-(4-methoxybenzylidene)-2-morpholino-3,5-dihydro-4*H*-imidazol-4-one (12g)

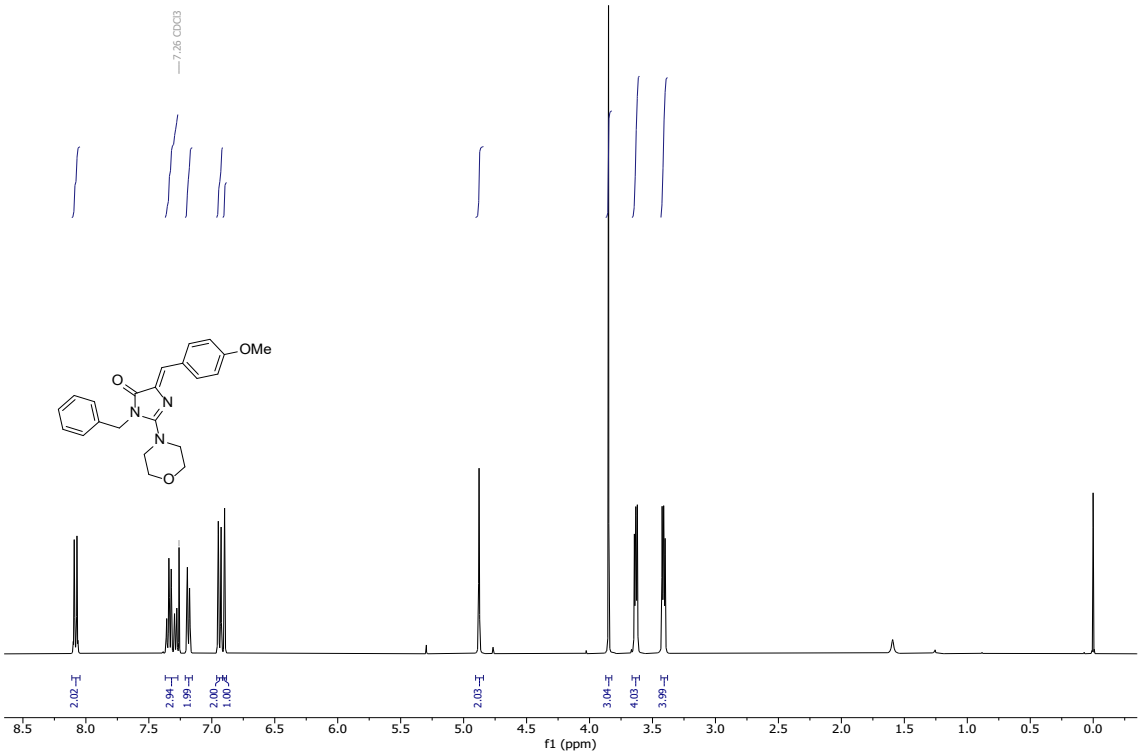

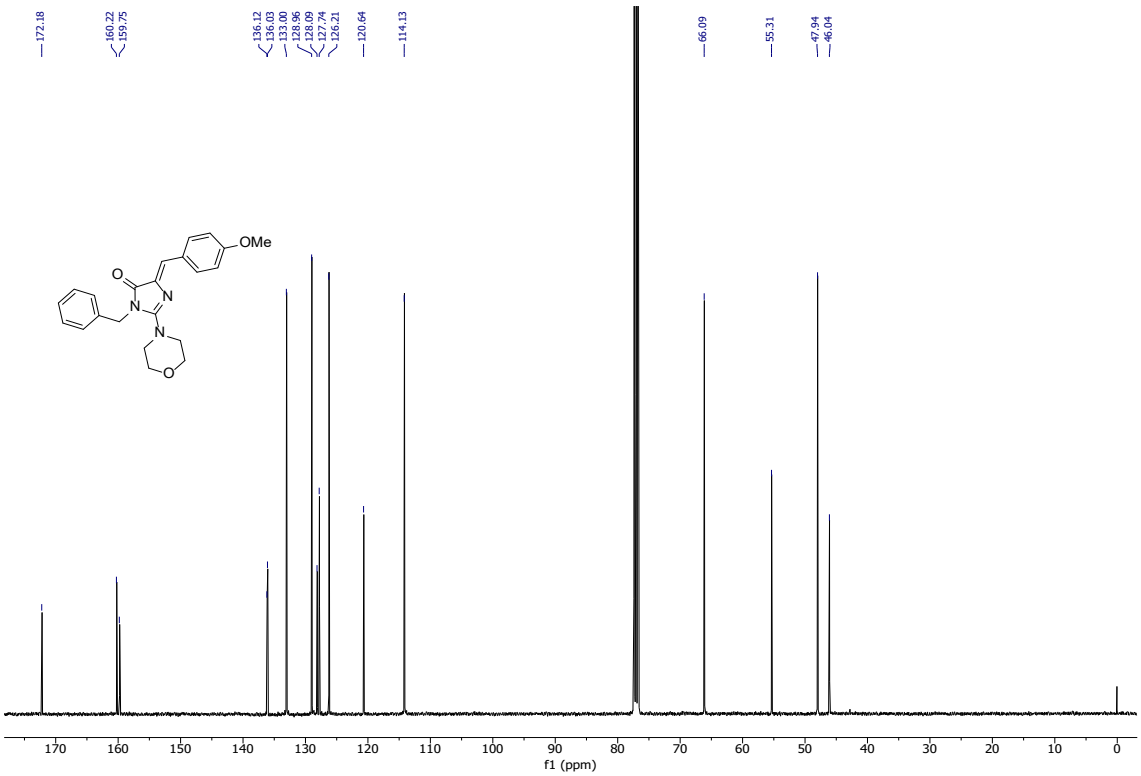

(*Z*)-5-(Benzo[*d*][1,3]dioxol-5-ylmethylene)-3-methyl-2-(pentylamino)-3,5-dihydro-4*H*-imidazol-4-oneone (12h)

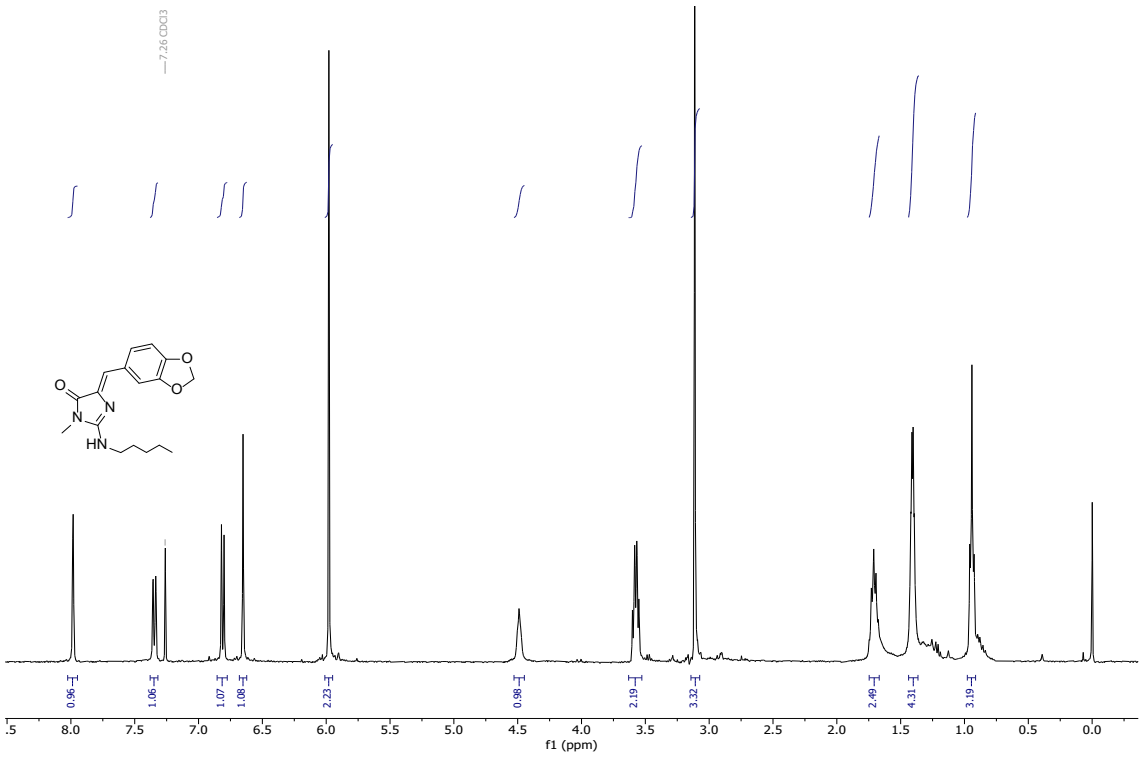

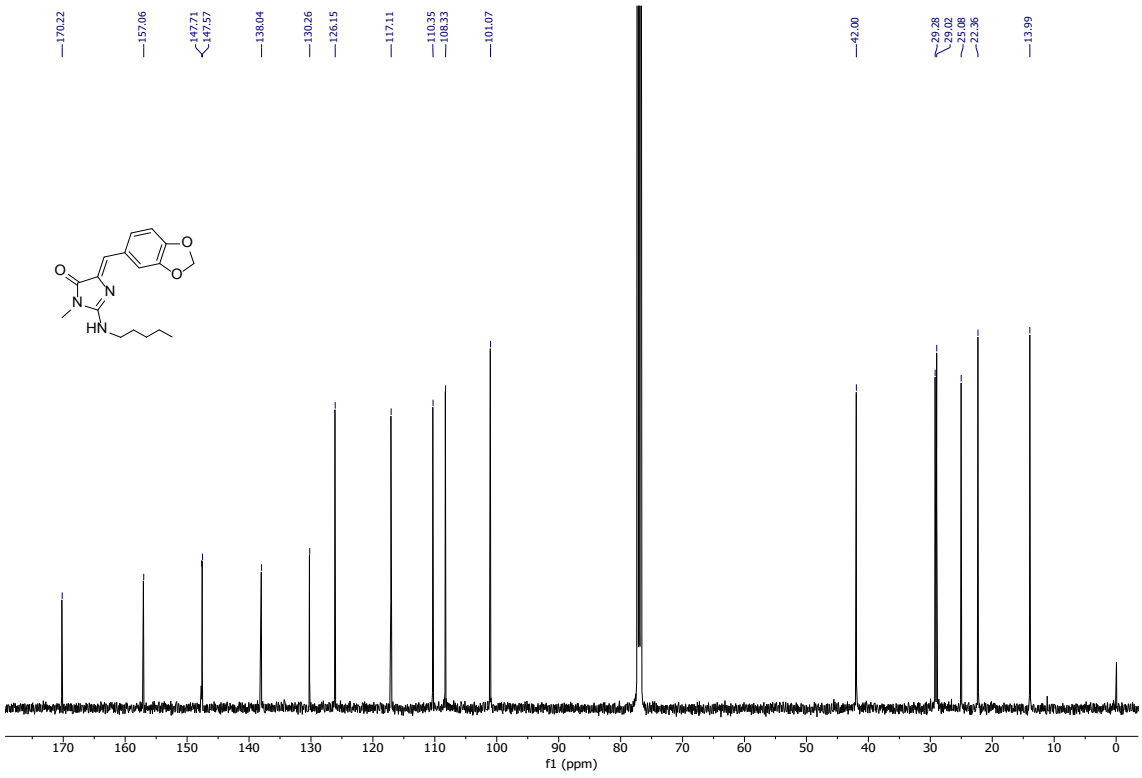

(*Z*)-2-Amino-5-(benzo[*d*][1,3]dioxol-5-ylmethylene)-3-methyl-3,5-dihydro-4*H*-imidazol-4-one (12i, Leucettamine B))

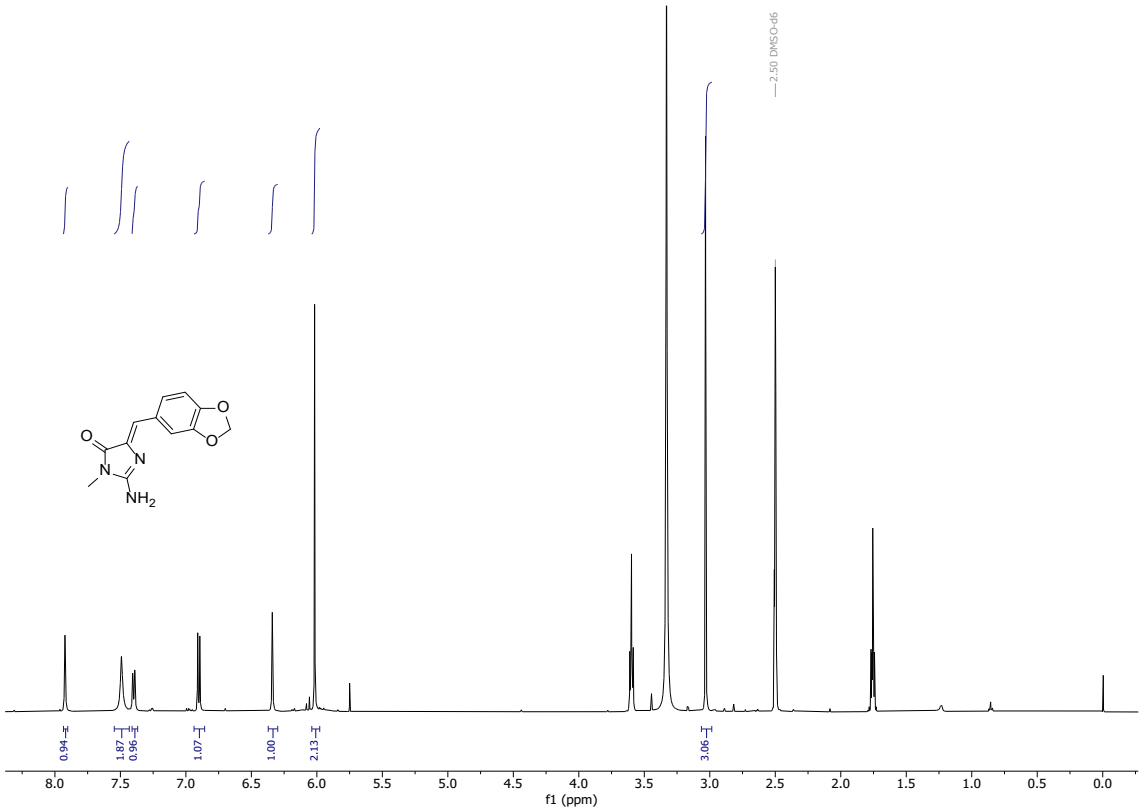

(*Z*)-5-(Benzo[*d*][1,3]dioxol-5-ylmethylene)-3-methyl-2-(piperazin-1-yl)-3,5-dihydro-4*H*-imidazol-4-one (12j)

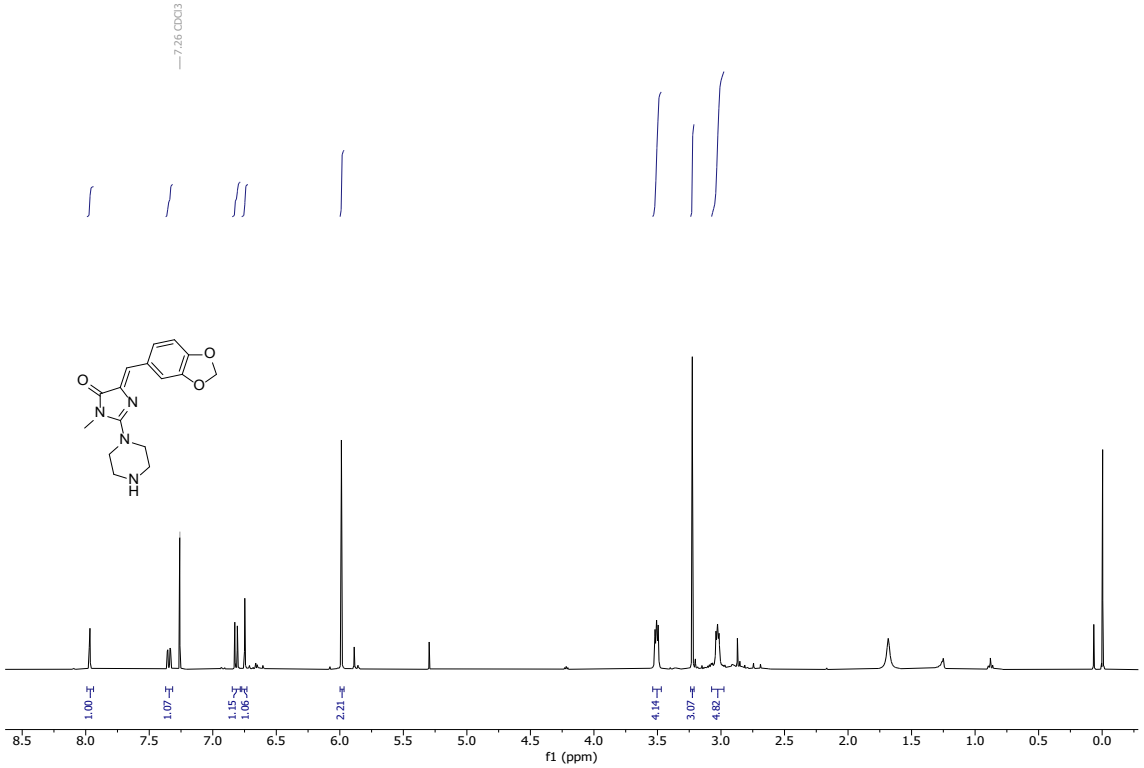

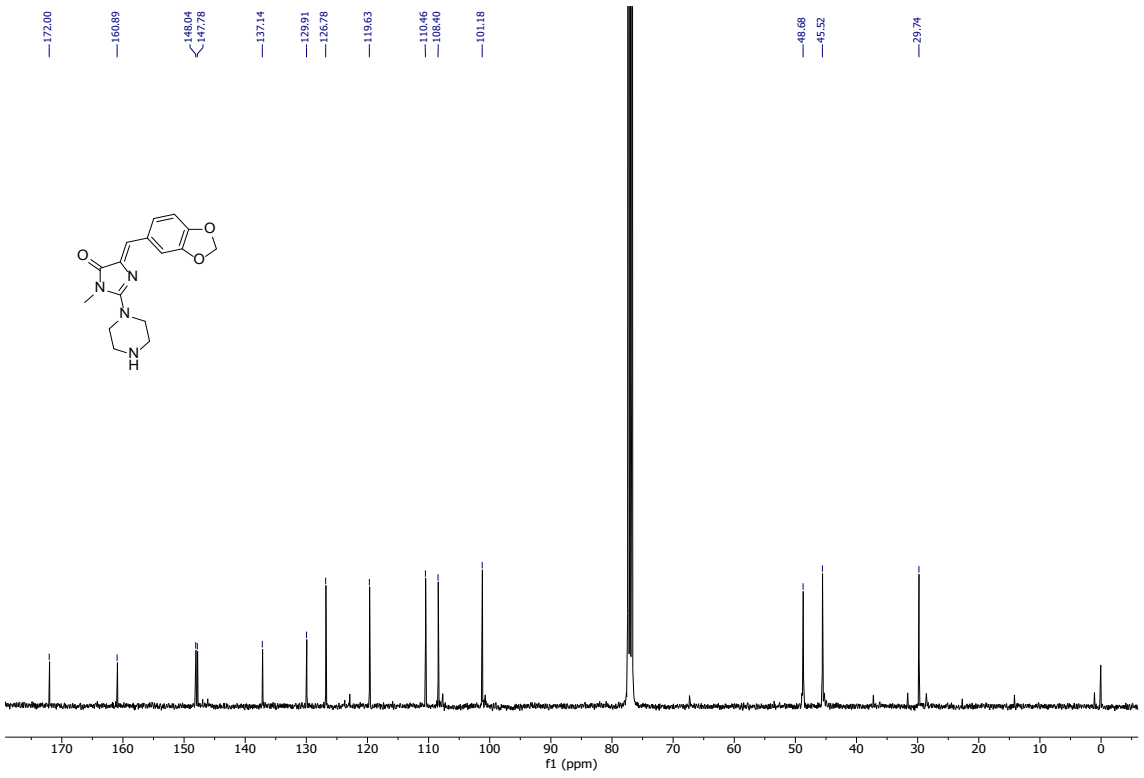

(*Z*)-5-(Benzo[*d*][1,3]dioxol-5-ylmethylene)-3-methyl-2-(propylthio)-3,5-dihydro-4*H*-imidazol-4-one (13)

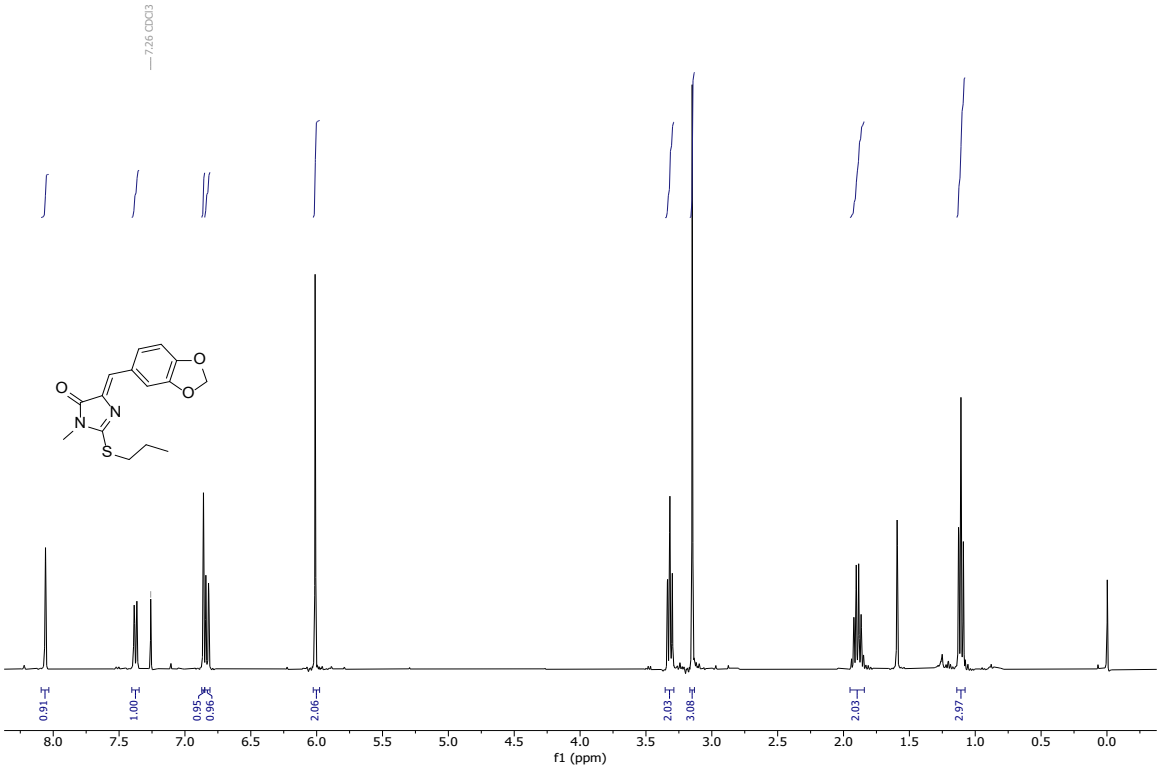

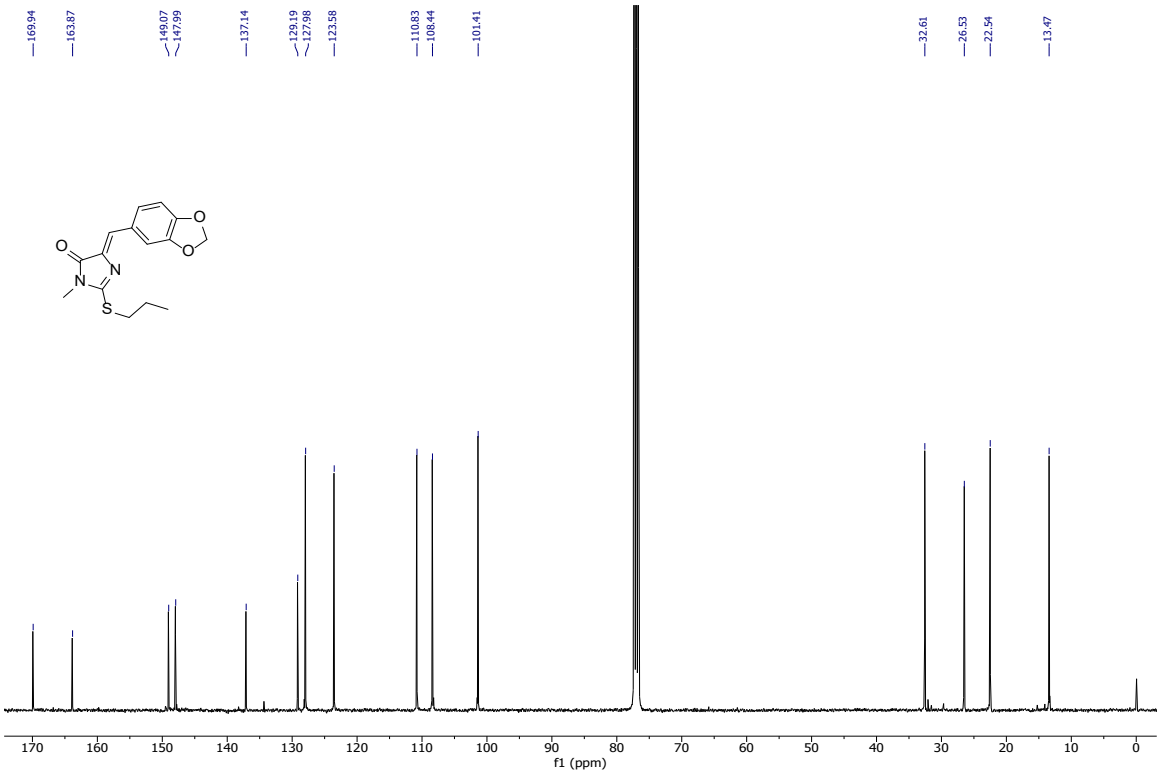

(3a*S*,4*R*,6a*R*)-4-(5-(4-((*Z*)-4-(Benzo[*d*][1,3]dioxol-5-ylmethylene)-1-methyl-5-oxo-4,5-dihydro-1*H*-imidazol-2-yl)piperazin-1-yl)-5-oxopentyl)tetrahydro-1*H*-thieno[3,4-*d*]imidazol-2(3*H*)-one (14a)

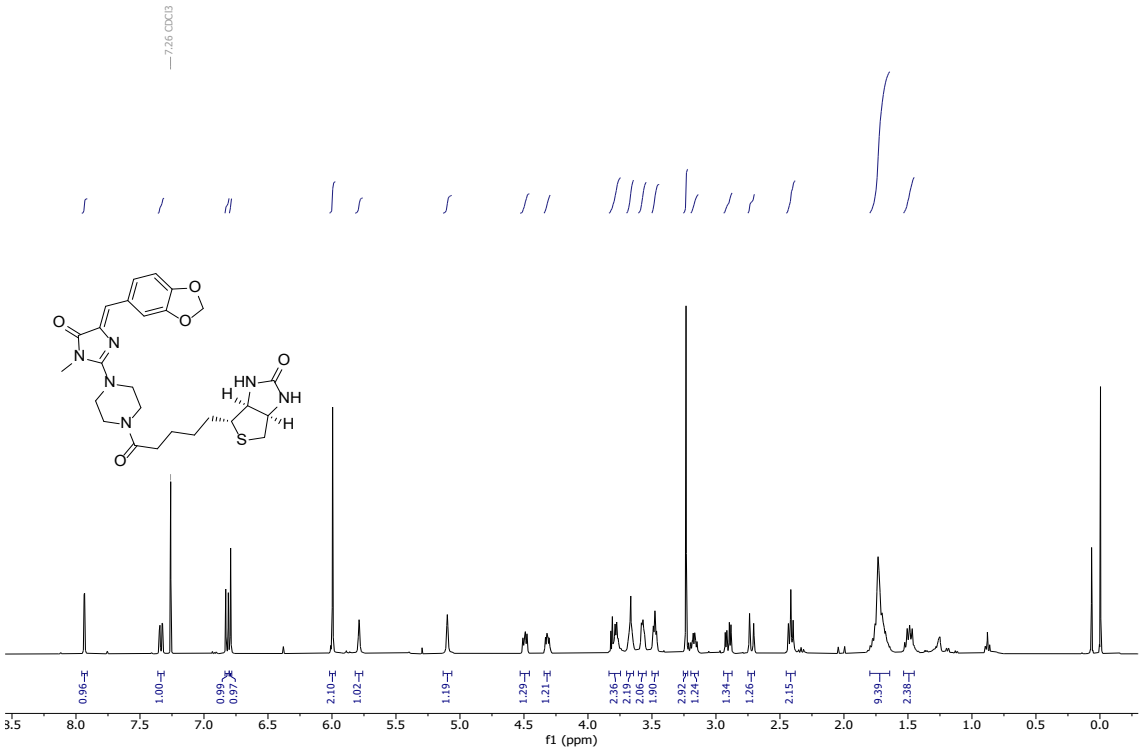

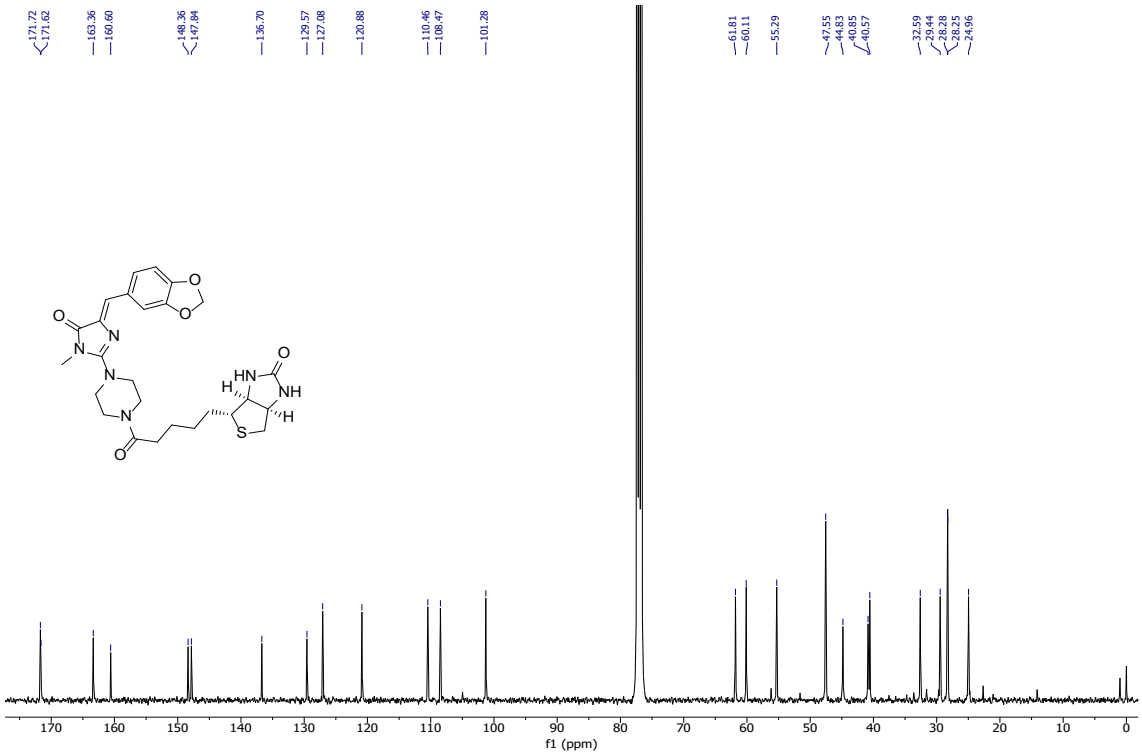

(*Z*)-5-(Benzo[*d*][1,3]dioxol-5-ylmethylene)-3-methyl-2-(4-((*R*)-4-((3*S*,5*R*,7*S*,8*S*,9*R*,10*R*,12*R*,13*S*,14*R*,17*S*)-3,7,12-trihydroxy-10,13-dimethylhexadecahydro-1*H*-cyclopenta[*a*]phenanthren-17-yl)pentanoyl)piperazin-1-yl)-3,5-dihydro-4*H*-imidazol-4-one (14b)

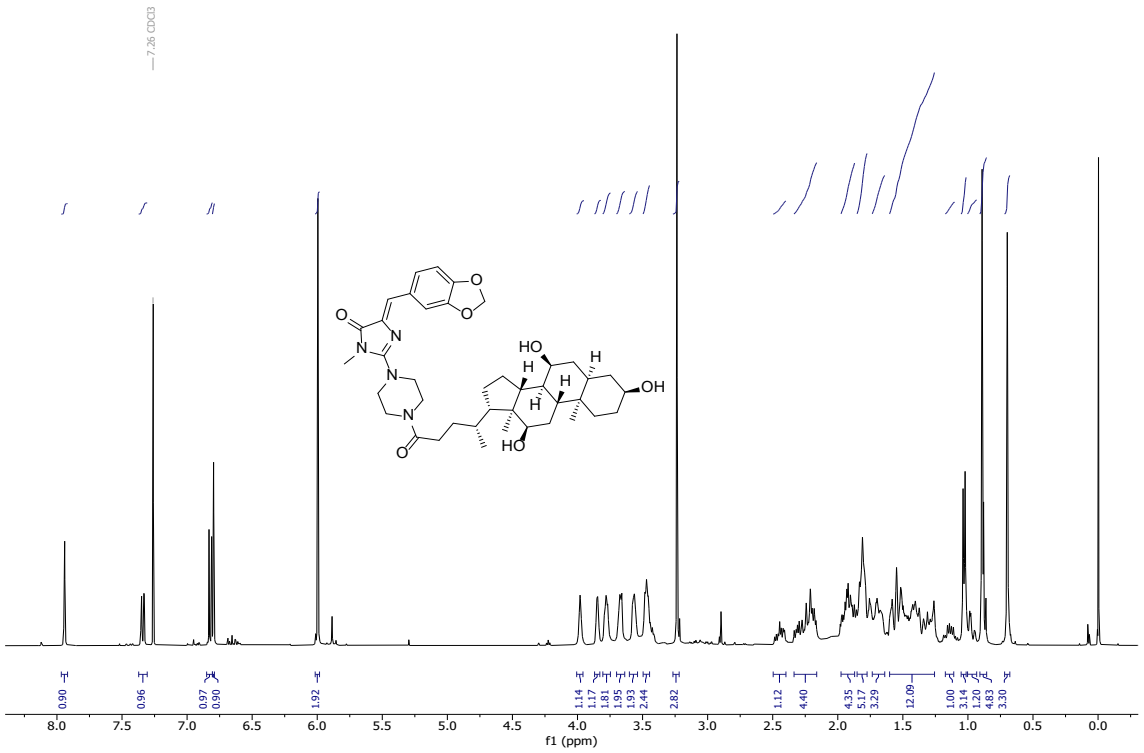

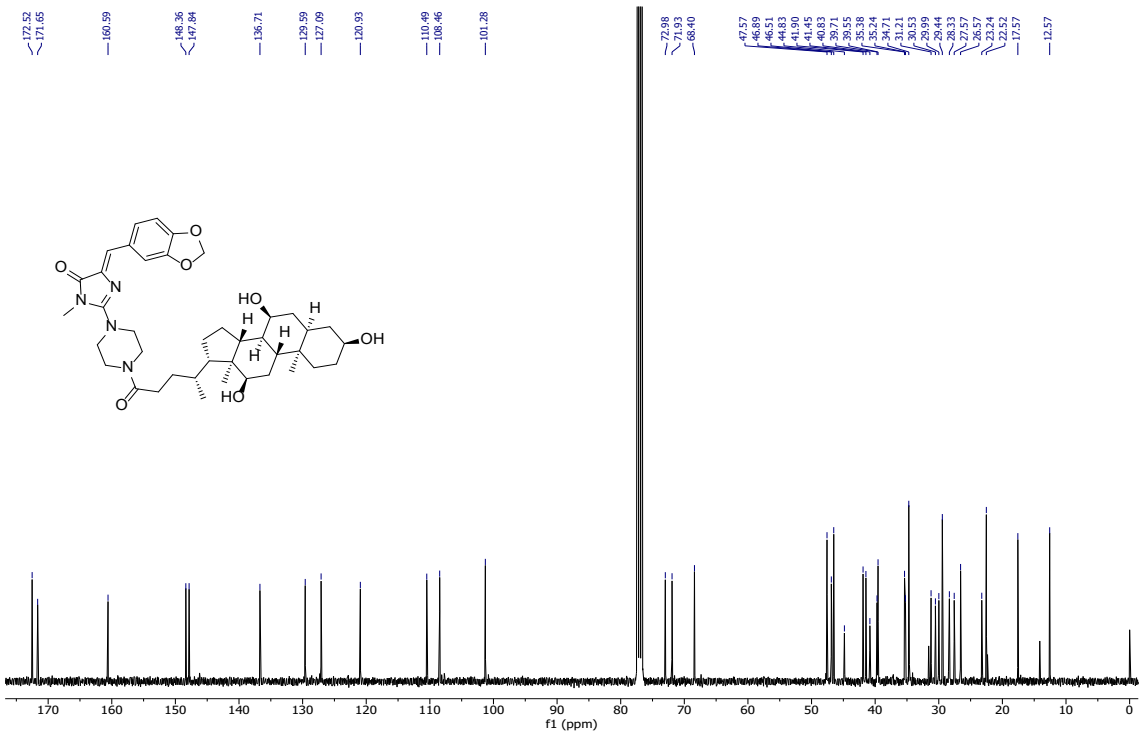

3. Addendum to Chapter II: Predoctoral Research Stay

In Chapter II we described an extended MCR leading to compounds with structural analogy to the natural product coelenterazine (CTZ), which has particularly attractive photophysical properties making it a valuable asset in chemical biology (ChemBio) applications. During the predoctoral research stay at the Philipps-Universität Marburg under the supervision of Prof. Dr. Olalla Vázquez (Apr. – Jul. 2023), these potential applications were studied. Incidentally, the research stay in a ChemBio laboratory was planned to develop a deeper understanding of biological systems and gain hands-on experience in ChemBio experimental techniques. In this way, the research stay served to acquire new skills and knowledge to complement the organic chemistry expertise achieved through the present thesis.

3.1. Introduction

Bioluminescence is the emission of light by a living organism. It results from a chemical reaction on a substrate (luciferin) catalysed by an enzyme (luciferase), typically involving the participation of dioxygen (O_2), metal cations, or cofactors such as ATP. Several luciferins have been discovered, such as the CTZ, which is the substrate of many luciferases found in a wide range of aquatic organisms. Of note is the *Renilla* luciferase (RLuc) found in the sea pansy *Renilla renifromis*, which quickly became the staple in the field as the reaction only requires O_2 to generate a blue photon (Figure 1A-B). As such, it has been exploited in ChemBio research to study cellular processes such as gene expression or enzyme activity and for *in vivo* imaging.[24a,40]

Due to the enormous impact of the CTZ – RLuc system, synthetic analogues of the CTZ with optimised properties have appeared in the last decades. One example is the coelenterazine 400a or DeepBlueC (Figure 1C). The DeepBlueC is chemically more stable than the CTZ, ensuring consistent performance over time. Moreover, an engineered luciferase named NanoLuc has become one of the most used systems in bioluminescence assays due to the enhanced properties compared to other luciferases (Figure 1D).[41] Its main advantages are its reduced size (19 kDa), increased stability *in vitro* and *in vivo*, and significantly brighter luminescence. In this context, the host group used the DeepBlueC luciferin in conjunction with a split luciferase based on the NanoLuc luciferase, named NanoBiT. The NanoBiT is a complementation system formed by two luciferase fragments: a larger part which constitutes a major part of the enzyme's sequence, named

LgBiT, and a small peptide with high affinity for the LgBiT, named HiBiT (Figure 1D). Upon being in close proximity and binding, the full enzyme and its catalytic pocket are reconstituted, providing a working luciferase equivalent to NanoLuc.[42] From a practical standpoint, the experiments require a previous incubation of the two fragments to generate the functional luciferase enzyme [see the Materials and Methods (MM) section below].

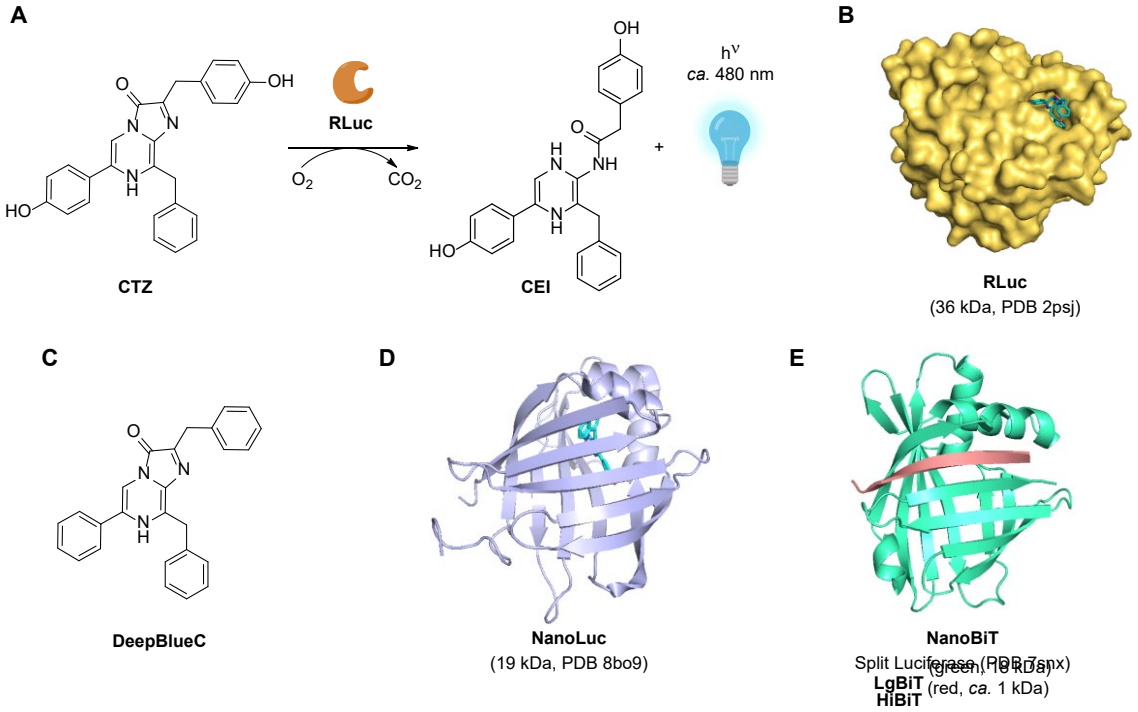

Figure 1. A) Bioluminescence reaction of CTZ with RLuc, to generate product CEI and a blue photon. C) Crystall structure of RLuc with CEI bound. C) Chemical structure of CTZ analogue DeepBlueC, used in the enzymatic assays described in this section. D) Crystall structure of NanoLuc with a non-reactive CTZ analogue bound. E) NanoBiT split luciferase complementation system. LgBiT (green) and HiBiT (red).

3.2. Objectives of the Research Stay

- To design and conduct enzymatic assays to test the potential bioluminescence of the synthesised adducts MCR-CTZ-1 and MCR-CTZ-2 (Figure 2A).
- To design a synthetic route based on an MCR approach to obtain closer analogues to the substrate DeepBlueC, namely two missing features in the MCR-CTZs: the phenyl residue (pink) and the double bond in the pyrazine ring (green, Figure 2B).

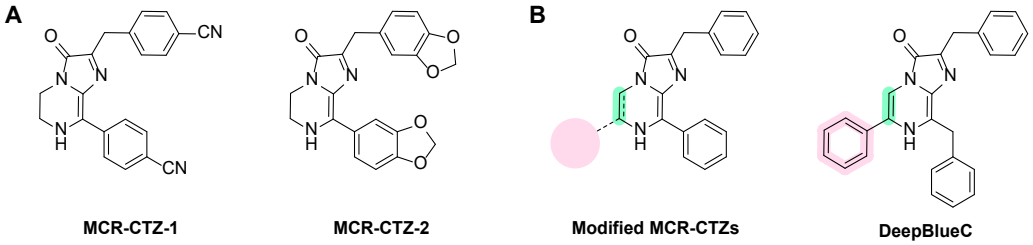

Figure 2. A) Structure of the tested compounds MCR-CTZ-1 and MCR-CTZ-2. B) Main structural differences between the MCR-CTZs and the DeepBlueC substrate.

3.3. Results and Discussion

First, the luminescence enzymatic assays were performed using DeepBlueC as the substrate and the NanoBiT complementation system as the luciferase. The assay conditions were optimised and the kinetic parameters were determined using the GraphPad software (see MM). With the optimised assay, adducts MCR-CTZ-1 and MCR-CTZ-2 were tested, but neither of them produced bioluminescence (Figure 3A-B).

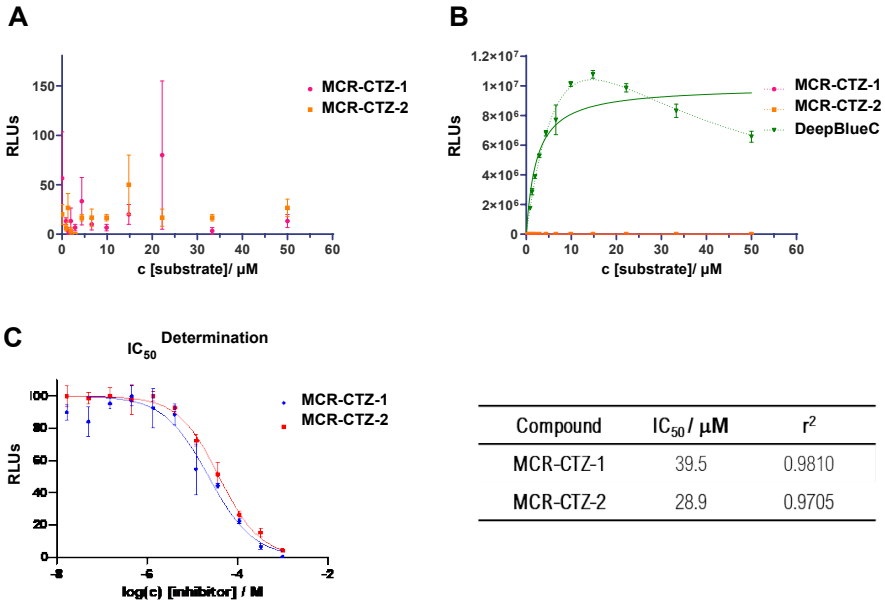

Compound	IC_{50} / µM	r^2
MCR-CTZ-1	39.5	0.9810
MCR-CTZ-2	28.9	0.9705

Figure 3. A) Luminescence enzymatic assays with MCR-CTZ-1 and MCR-CTZ-2 showed no significant signal. B) Results from the MCR-CTZ adducts compared to those obtained with the DeepBlueC substrate. C) IC_{50} determination of inhibitors MCR-CTZ-1 and MCR-CTZ-2. DeepBlueC was used as substrate.

Nevertheless, due to the structural similarity, it was hypothesised whether the MCR-CTZ adducts could act as inhibitors of the NanoBiT system. Thus, competitive inhibition experiments were designed and performed.[43] The results suggested that the MCR-CTZs act as competitive inhibitors of the DeepBlueC substrate in the NanoBiT split luciferase system. The IC_{50} K_I for both compounds was determined by fitting the data using GraphPad (Figure 3C and MM). Notably, whereas there are more potent inhibitors for the NanoLuc luciferase,[44] there are no reported inhibitors for the NanoBiT system.

Next, synthetic work was performed in an attempt to obtain closer analogues to the enzyme substrates. As shown above, the MCR-CTZ compounds are lacking two main attributes to the CTZ or the DeepBlueC: a phenyl ring substitution and a double bond in the pyrazine ring. First, we focused on the design of a synthetic route to MCR-CTZ

analogues bearing the phenyl ring residue. To that end, the following retrosynthesis was proposed (Scheme 1).

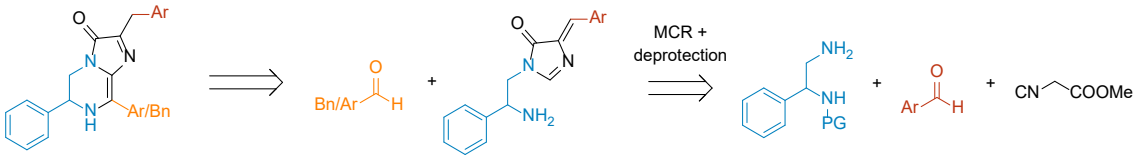

Scheme 1. Proposed retrosynthetic route.

As the protected 2-phenyl diamines are not commercially available, its synthesis was designed and performed. Two protecting groups, with distinct deprotection conditions, were considered: an acyl group and a Boc group. Thus, the protected diamines **1a-b** were synthesised following described protocols (Scheme 2A-B).[45-48]

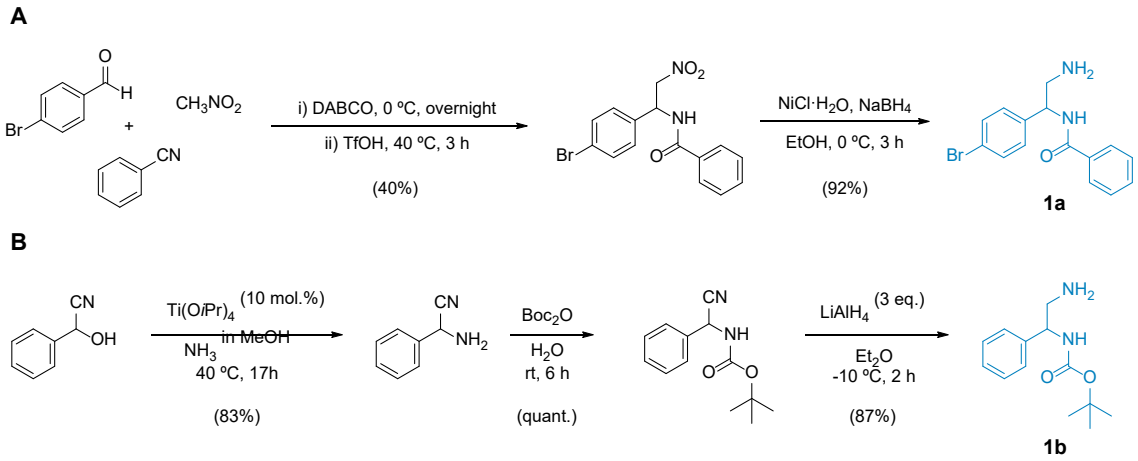

Scheme 2. A) Synthesis of the acyl-protected diamine **1a**. B) Synthesis of the Boc-protected diamine **1b**.

Then, the MCR was successfully performed with both diamines with different aldehydes **2a-b** and methyl isocyanacetate **3** to obtain compounds **4a-b** (Scheme 3A). As for the deprotections, the acyl hydrolysis resulted in high degradation of the lactam core of compound **4a**, as presumably it is unstable under the necessary harsh, basic conditions. In contrast, the removal of the Boc protecting group in **4b** was successful under milder conditions, generating the free amine GFP-chromophore **5b** (Scheme 3B). Subsequently, compound **5b** was coupled to 4-chlorobenzaldehyde to give imine **6** (Scheme 3C).

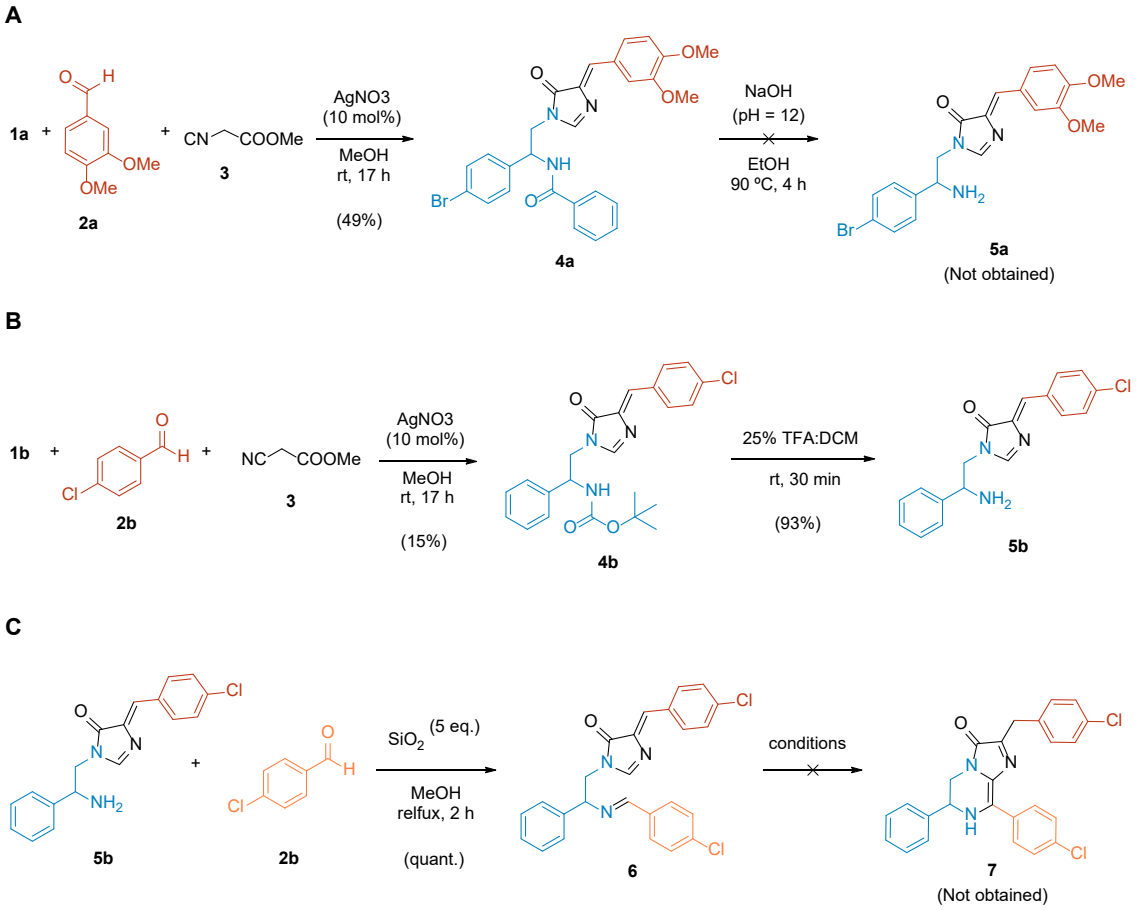

Scheme 3. A) MCR with acylated diamine and failed deprotection. B) MCR with Boc-protected diamine and deprotection. C) Imine formation and failed cyclisation.

Unfortunately, the intramolecular cyclisation to give the desired analogue **7** was unsuccessful under the tested conditions (Scheme 3C and Table 1).

Table 1. Conditions tested for the cyclisation of **6**. All reactions performed overnight at reflux temperature. No conversion observed under any of the tested conditions (TLC analysis).

Entry	Solvent	Additive
A	MeOH	SiO_2 (10 eq.)
B	MeOH	*p*-TsOH (5 mol%)
C	Toluene	*p*-TsOH (10 mol%)
D	MeOH / DCM	$AgNO_3$ (10 mol%)
E	MeOH / DCM	DMAP (10 mol%)
F	MeOH / DCM	DABCO (10 mol%)

Finally, we attempted to obtain the missing double bond in the pyrazine ring. For that purpose, two strategies were considered: i) direct generation the desired product **8** by dehydrogenation of the MCR-CTZ-3 adduct; ii) oxidation of the **MCR-CTZ-3** compound

to its fully unsaturated derivative **9**, and subsequent partial reduction to the desired isomer **8**, following a precedent in the literature (Scheme 4).[49]

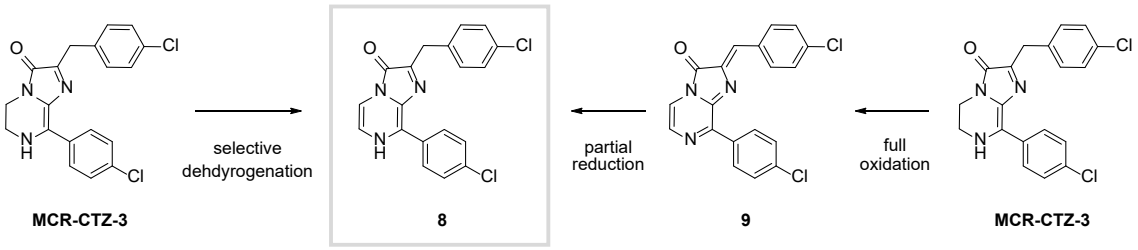

Scheme 4. Synthetic approach to the desired compound **8** from **MCR-CTZ-3**.

Thus, the oxidation of compound **MCR-CTZ-3** was attempted under a range of conditions (Scheme 5 and Table 2). In the majority of cases, the isolated compound was the undesired isomer **10**, presumably more stable due to the more extended conjugation compared to the desired isomer **8**, which was not detected under any of the tested conditions. Moreover, only traces of the fully oxidised compound **9** were detected in one case. Importantly, an oxidative dimerisation was discovered when the oxidant was MnO_2 (entry G), leading to the dimer **11** (as a mixture of diastereomers), likely through the dimerisation of a precursor radical intermediate. The structure of the major stereoisomer was confirmed by X-Ray crystallography (see the Characterisation Data section).

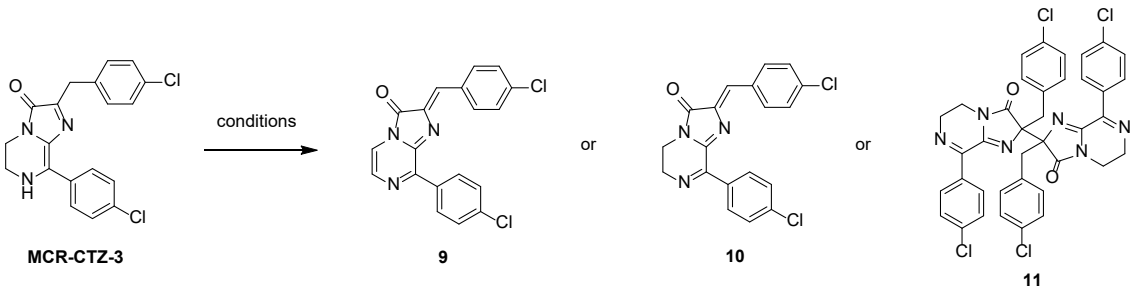

Scheme 5. Products derived from the oxidation of **MCR-CTZ-3** under a range of conditions.

Table 2. Tested conditions for the oxidation of **MCR-CTZ-3** and the respective outcome. [a]Unless otherwise stated, 1 eq. of oxidant was used. [b]Not isolated.

Entry	Oxidant[a]	Solvent	Time /Temp.	Outcome (yield)
A	TEMPO (2 eq.)	DCM	5 h / rt	**10** (60%)
B	DDQ	DCM	3 h / rt	**10**[b]
C	I_2	DCM	5 h / rt	No reaction
D	DMP	DCM	5 h / rt	No reaction
E	NCS / Et_3N	DCM	8 h / 0 ºC to rt	**10** (60%) + **9** (5%)
F	Pd / C (10 mol%)	DMF	100 ºC / 60 h	No reaction
G	MnO_2 (50 eq.)	DCM	0 ºC / 5 min	**11** (75%)

3.4. Characterisation Data

N-(1-(4-Bromophenyl)-2-nitroethyl)benzamide

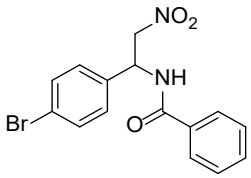

A solution of 4-bromobenzaldehyde (925 mg, 5 mmol, 1 eq), nitromethane (1.07 mL, 20 mmol, 4 eq), benzonitrile (2.5 mL, 25 mmol, 5 eq), and DABCO (275 µL, 2.5 mmol, 0.5 eq) in DCM (7.5 mL) was stirred at 0 ºC (ice bath) overnight. In the morning the temperature of the batch was 5 ºC. The reaction was allowed to warm to rt and was added triflic acid (1.3 mL, 15 mmol, 3 eq). The reaction was heated to 40 ºC and stirred for 3 h. The reaction was quenched by addition of aqueous sat. sodium bicarbonate and extracted with DCM. The organic layer was dried over magnesium sulphate, filtered, and concentrated under reduced pressure to give a brown gum. The residue was purified via silica gel flash chromatography eluting with 0 – 30 % EtOAc : pentane. The appropriate fractions were combined to afford the title compound as an off white solid (640 mg, 40 %). **^{1}H NMR** (300 MHz, $CDCl_3$) δ 7.89 – 7.77 (m, 2H), 7.66 – 7.41 (m, 5H), 7.31 – 7.26 (m, 2H), 7.16 (d, *J* = 8.0 Hz, 1H), 5.86 (dt, *J* = 7.9, 5.6 Hz, 1H), 5.04 (dd, *J* = 13.1, 6.2 Hz, 1H), 4.86 (dd, *J* = 13.2, 5.0 Hz, 1H).

N-(2-Amino-1-(4-bromophenyl)ethyl)benzamide (1a)

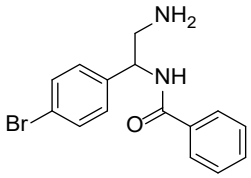

To a 0 ºC (ice bath) solution of *N*-(1-(4-bromophenyl)-2-nitroethyl)benzamide (450 mg, 1.3 mmol, 1 eq), and $NiCl{\cdot}6H_2O$ (337 mg, 1.4 mmol, 1.1 eq) in EtOH (2.5 mL) was added $NaBH_4$ (491 mg, 13 mmol, 10 eq) under N_2 atmosphere. The reaction was stirred at rt for 2 h, until starting material consumption (TLC control). The reaction was quenched by the addition of aqueous sat. NH_4Cl (50 mL) and extracted with DCM (2 x 100 mL). The organic layer was washed with sat. brine, dried over magnesium sulphate, filtered, and concentrated under reduced pressure to afford the title compound as an off white solid (380 mg, 92 %). **^{1}H NMR** (300 MHz, DMSO) δ 8.72 (d, *J* = 7.5 Hz, 1H), 7.91

(d, *J* = 7.4 Hz, 2H), 7.51 (p, *J* = 6.2 Hz, 5H), 7.33 (d, *J* = 8.1 Hz, 2H), 4.91 (s, 1H), 2.88 (d, *J* = 10.8 Hz, 2H), 1.64 (s, 1H).

2-Amino-2-phenylacetonitrile

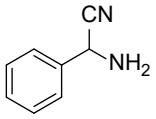

To a solution of mandelonitrile (6.65 g, 50 mmol, 1 eq) and NH_3 (7 M in MeOH, 30 mL) in MeOH (50 mL) under nitrogen atmosphere was added $Ti(OPr)_4$ (1.48 mL, 5 mmol, 0.1 eq) and the reaction was stirred at 40 ºC for 17 h. After reaction completion (TLC control), the inorganics were filtered off washing with MeOH. The filtrate was evaporated, dissolved in EtOAc and washed with 2 M aqueous HCl until no amine was detected in the organic layer (aprox 4 – 5 washes). The aqueous layer was neutralised by the addition of solid Na_2CO_3 until pH > 7 and was extracted with DCM. The organic layer was dried over magnesium sulphate, filtered, and concentrated under reduced pressure to give the crude product. The pure title product was obtained after crystallisation with DCM/pentane (5.3 g, 80 %). **^{1}H NMR** (300 MHz, $CDCl_3$) δ 7.62 – 7.52 (m, 2H), 7.52 – 7.36 (m, 3H), 4.96 (s, 1H). **^{13}C NMR** (75 MHz, DMSO) δ 138.89, 129.10, 128.63, 127.14, 122.70, 46.83.

***tert*-Butyl (cyano(phenyl)methyl)carbamate**

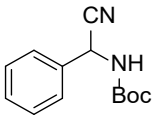

To a suspension of 2-Amino-2-phenylacetonitrile (450 mg, 3.4 mmol, 1 eq) in water (5 mL) was added Boc_2O (820 mg, 3.75 mmol, 1.1 eq.). Upon addition, effervescence was observed and the suspension turned into a solution. The reaction was stirred at rt for 2 h. During the reaction, the solution turned back into a suspension, and the precipitate was filtered washing with water and dried under high vacuum to afford the title compound as an off white solid (700 mg, 88 %). **^{1}H NMR** (300 MHz, $CDCl_3$) δ 7.46 (ddd, *J* = 17.2, 6.8, 4.3 Hz, 5H), 5.79 (s, 1H), 5.09 (s, 1H), 1.49 (s, 9H). **^{13}C NMR** (75 MHz, $CDCl_3$) δ 129.53, 129.35, 126.91, 117.75, 28.24, 27.43.

tert-Butyl (2-amino-1-phenylethyl)carbamate (1b)

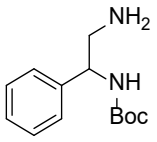

To a -5 ºC (acetone/ice bath) suspension of $LiAlH_4$ (2 g, 51 mmol, 3 eq) in Et_2O (40 mL) was slowly added a solution of *tert*-butyl (cyano(phenyl)methyl)carbamate (3 g, 13 mmol, 1 eq) in Et_2O (20 mL) during 30 min. The reaction was further stirred at -5 ºC for 30 min. After reaction completion (TLC control), the reaction was quenched by sequential slow addition of water (3 mL), 15 % aqueous NaOH (3 mL) and water (5 mL). The reaction was allowed to warm to rt and was stirred for 20 min. Then was added magnesium sulphate and the reaction was stirred at rt for 20 min. The salts were filtered off washing with Et_2O. The filtrate was concentrated under reduced pressure to give the crude title product, which was used in the next step without further purification. **^{1}H NMR** (300 MHz, $CDCl_3$) δ 7.32 – 7.16 (m, 9H), 5.26 (d, *J* = 7.8 Hz, 1H), 4.66 – 4.57 (m, 1H), 2.94 (d, *J* = 5.8 Hz, 2H), 1.35 (s, 12H).

(*Z*)-*N*-(1-(4-Bromophenyl)-2-(4-(3,4-dimethoxybenzylidene)-5-oxo-4,5-dihydro-1*H*-imidazol-1-yl)ethyl)benzamide (4a)

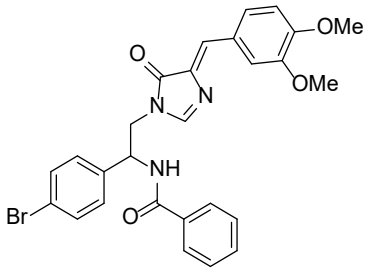

To a mixture of 3,4-dimethoxybenzaldehyde (92 mg, 0.55 mmol, 1.1 eq), methyl isocyanoacetate (45 µL, 0.5 mmol, 1 eq) and $AgNO_3$ (8.5 mg, 0.05 mmol, 0.1 eq) in MeOH (2.5 mL, 0.2 M) was added *N*-(1-(4-bromophenyl)-2-nitroethyl)benzamide (175 mg, 0.55 mmol, 1.1 eq) and the reaction was stirred overnight at rt. After this time, a precipitate was formed, and was collected by filtration washing with cold methanol to afford the title compound as a light brown solid (130 mg, 49 %). **^{1}H NMR** (300 MHz, DMSO-*d*$_6$) δ 9.01 (d, *J* = 8.6 Hz, 1H), 8.16 (d, *J* = 1.6 Hz, 1H), 8.02 (d, *J* = 1.9 Hz, 1H), 7.85 (dt, *J* = 6.9, 1.5 Hz, 2H), 7.71 (dd, *J* = 8.7, 1.9 Hz, 1H), 7.64 – 7.42 (m, 7H), 7.09 (d, *J* = 1.6 Hz, 1H), 7.05 (d, *J* = 8.5 Hz, 1H), 5.42 (q, *J* = 7.8 Hz, 1H), 4.11 – 3.93 (m, 2H). **^{13}C NMR** (75 MHz, DMSO- *d*$_6$) δ 169.74, 166.75, 154.45, 151.85, 149.12, 139.84,

136.81, 134.45, 131.91, 129.69, 129.46, 128.83, 127.80, 126.99, 121.18, 115.07, 112.06, 56.09, 55.95, 52.32, 45.44. **HRMS:** *m/z* calcd for $C_{27}H_{24}BrN_3O_4Na^+$ $[M+Na]^+$: 556.0842, 558.0823; found: 556.0832, 558.0809.

***tert*-Butyl (*Z*)-(2-(4-(4-chlorobenzylidene)-5-oxo-4,5-dihydro-1*H*-imidazol-1-yl)-1-phenylethyl)carbamate (4b)**

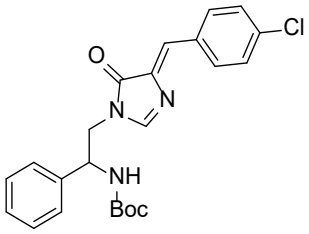

To a mixture of 4-chlorobenzaldehyde (588 mg, 4.2 mmol, 1.1 eq), methyl isocyanoacetate (345 µL, 3.8 mmol, 1 eq), and $AgNO_3$ (65 mg, 0.38, 0.1 eq) in MeOH (20 mL) was added *tert*-butyl (2-amino-1-phenylethyl)carbamate (990 mg, 4.2 mmol, 1.1 eq) and the reaction was stirred overnight at rt. The precipitate was filtered washing with cold MeOH to afford the title compound as w light brown solid (200 mg, 12 %). **^{1}H NMR** (300 MHz, $CDCl_3$) δ 8.05 (dd, *J* = 8.7, 2.3 Hz, 2H), 7.49 (s, 1H), 7.43 – 7.27 (m, 7H), 7.16 (s, 1H), 5.38 (d, *J* = 7.5 Hz, 1H), 4.96 (s, 1H), 3.93 (t, *J* = 6.6 Hz, 2H), 1.38 (s, 8H). **^{13}C NMR** (75 MHz, $CDCl_3$) δ 170.20, 155.23, 153.49, 138.24, 136.96, 133.69, 132.17, 129.38, 129.12, 128.33, 126.38, 77.22, 46.60, 28.26. **HRMS:** *m/z* calcd for $C_{23}H_{24}ClN_3O_3Na^+$ $[M+H]^+$: 448.1398; found: 448.1391.

(*Z*)-3-(2-Amino-2-phenylethyl)-5-(4-chlorobenzylidene)-3,5-dihydro-4*H*-imidazol-4-one (5b)

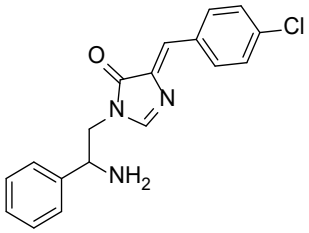

A solution of **4b** (100 mg, 0.236 mmol, 1 eq) in DCM:TFA (3:1, 3 mL) was stirred rt for 30 min. The reaction was diluted with DCM and aqueous sat. Na_2CO_3 was added until pH > 7. The organic layer was dried over magnesium sulphate, filtered, and concentrated under reduced pressure to afford the title compound as a yellow solid (70 mg, 93 %). **^{1}H NMR** (300 MHz, $CDCl_3$) δ 8.01 – 7.91 (m, 2H), 7.35 – 7.22 (m, 8H), 7.17 (d, *J* = 1.4 Hz, 1H), 7.05 (s, 1H), 4.17 (t, *J* = 6.4 Hz, 1H), 3.67 (d, *J* = 6.5 Hz, 2H). **^{13}C**

NMR (75 MHz, $CDCl_3$) δ 169.96, 154.21, 142.04, 138.63, 136.77, 133.62, 132.31, 129.07, 129.01, 128.83, 128.17, 126.44, 77.22, 55.09, 49.27.

5-((*Z*)-4-Chlorobenzylidene)-3-(2-(((*E*)-4-chlorobenzylidene)amino)-2-phenylethyl)-3,5-dihydro-4*H*-imidazol-4-one (6)

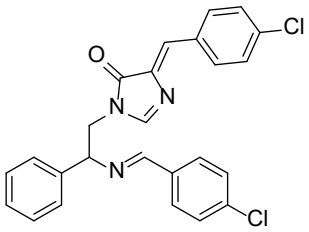

To a solution of **5b** (100 mg, 0.31 mmol, 1 eq) and 4-chlorobenzaldehyde (44 mg, 0.31 mmol, 1 eq) in MeOH:DCM (1:1) was added silica gel (100 mg) and the reaction was stirred at 60 ºC for 17 h. After reaction completion, the DCM was evaporated the solid was filtered washing with cold MeOH. Then, further DCM was added to dissolve the product and the silica gel was removed by filtration. The filtrate was evaporated under reduced pressure to afford the title compound as a pale brown solid (140 mg, 100%). **^{1}H NMR** (300 MHz, $CDCl_3$) δ 8.16 (s, 1H), 7.95 (d, *J* = 8.1 Hz, 2H), 7.68 – 7.59 (m, 2H), 7.53 (d, *J* = 1.9 Hz, 1H), 7.42 – 7.21 (m, 9H), 7.19 (d, *J* = 1.4 Hz, 1H), 7.07 (s, 1H), 4.57 (dd, *J* = 8.5, 4.5 Hz, 1H), 4.05 (dt, *J* = 14.7, 4.4 Hz, 1H), 3.90 (dd, *J* = 13.9, 8.5 Hz, 1H). **HRMS:** *m/z* calcd for $C_{25}H_{19}Cl_2N_3ONa^+$ $[M+H]^+$: 470.0797; found: 470.0793.

(*Z*)-2-(4-Chlorobenzylidene)-8-(4-chlorophenyl)imidazo[1,2-*a*]pyrazin-3(2*H*)-one (9)

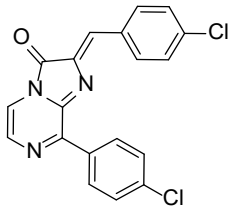

To a solution of **MCR-CTZ-3** (50 mg, 0.13 mmol, 1 eq) in DCM was added NCS (18 mg, 0.13 mmol, 1 eq) under nitrogen atmosphere and the reaction was stirred at rt for 2 h. After this time was added triethylamine (19 µL, 0.13 mmol, 1 eq) and the reaction was stirred overnight at rt. After reaction completion (TLC control) the solvent was evaporated under reduced pressure and the residue was purified via silica gel flash chromatography eluting with 20 – 60% EtOAc : pentane to afford the title compound as a red solid (3 mg, 5 %). **^{1}H NMR** (300 MHz, $CDCl_3$) δ 8.53 (d, *J* = 8.2 Hz, 1H), 8.14 (d,

J = 8.1 Hz, 1H), 7.48 – 7.32 (m, 4H), 7.19 (s, 1H). **HRMS:** *m/z* calcd for $C_{19}H_{12}Cl_2N_3O^+$ $[M+H]^+$: 368.0352; found: 368.0348.

(*Z*)-2-(4-Chlorobenzylidene)-8-(4-chlorophenyl)-5,6-dihydroimidazo[1,2-*a*]pyrazin-3(2*H*)-one (10)

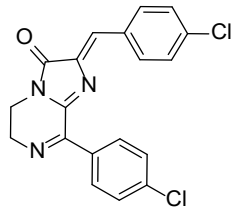

To a solution of **MCR-CTZ-3** (100 mg, 0.26 mmol, 1 eq) in DCM (2 mL) was added TEMPO (84 mg, 0.52 mmol, 2 eq) under nitrogen atmosphere and the reaction was stirred at rt for 5 h. After reaction completion (TLC control) the solvent was evaporated under reduced pressure and the residue was purified via silica gel flash chromatography eluting with 50 – 100 % DCM:pentane. The appropriate fractions were combined and concentrated under reduced pressure to afford a yellow solid (60 mg, 60 %). **^{1}H NMR** (300 MHz, $CDCl_3$) δ 8.22 (d, *J* = 8.2 Hz, 2H), 8.12 (d, *J* = 8.2 Hz, 2H), 7.54 – 7.38 (m, 5H), 4.27 (t, *J* = 6.3 Hz, 3H), 3.85 (t, *J* = 6.2 Hz, 2H).

(2*R*,2'*R*)-2,2'-bis(4-Chlorobenzyl)-8,8'-bis(4-chlorophenyl)-5,5',6,6'-tetrahydro-[2,2'-biimidazo[1,2-*a*]pyrazine]-3,3'(2*H*,2'*H*)-dione (11)

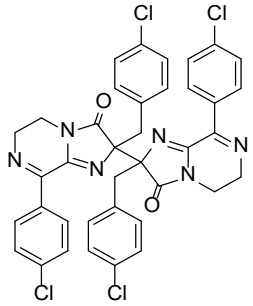

To a 0 ºC (ice bath) solution of **MCR-CTZ-3** (100 mg, 0.27 mmol, 1 eq) in DCM (10 mL) under inert atmosphere was added MnO_2 (1.1 g, 13.5 mmol, 50 eq) and the reaction was stirred at 0 ºC for 10 min. Analysis after this time by TLC (2% MeOH : DCM) suggested consumption of starting material and formation of a new product. The reaction was filtered through Celite washing with DCM and the filtrate was concentrated under reduced pressure. The residue was purified via silica gel flash chromatography eluting with 75 – 100% DCM : pentane. The appropriate fractions were concentrated under reduced pressure to afford the title compound as a light-yellow solid. **^{1}H NMR**

(400 MHz, DMSO- d_6) δ 7.73 (d, J = 8.4 Hz, 2H), 7.57 – 7.43 (m, 2H), 7.34 – 7.21 (m, 2H), 7.08 – 6.93 (m, 2H), 3.92 (d, J = 13.0 Hz, 1H), 3.75 (dt, J = 16.8, 5.0 Hz, 1H), 3.53 (d, J = 13.0 Hz, 1H), 3.38 (q, J = 6.4 Hz, 2H), 3.11 (dt, J = 16.6, 6.5 Hz, 1H).

Characterisation data only reported for the major diastereomer. Crystals suitable for X-Ray crystallography were obtained by slow diffusion of pentane into a solution of pure compound in DCM (Figure 4).

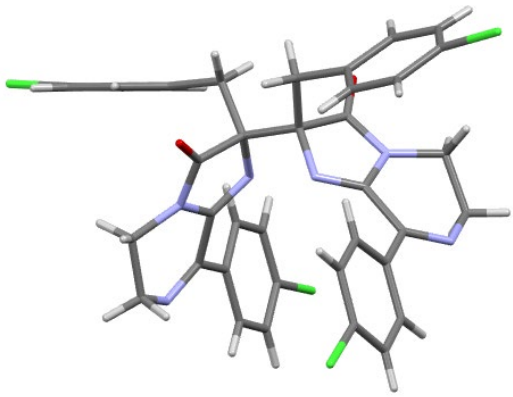

Figure 4. X-Ray crystallography of compound **11**.

3.5. Selected Copies of NMR Spectra

(*Z*)-*N*-(1-(4-Bromophenyl)-2-(4-(3,4-dimethoxybenzylidene)-5-oxo-4,5-dihydro-1*H*-imidazol-1-yl)ethyl)benzamide (4a)

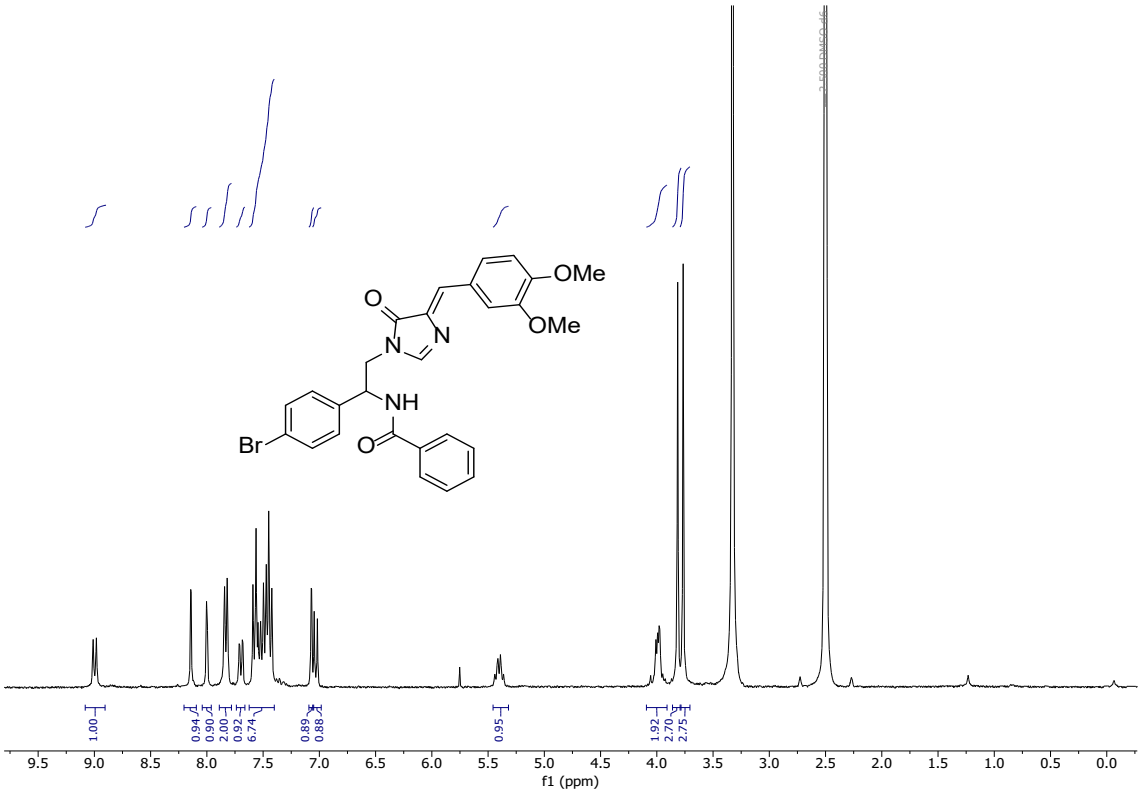

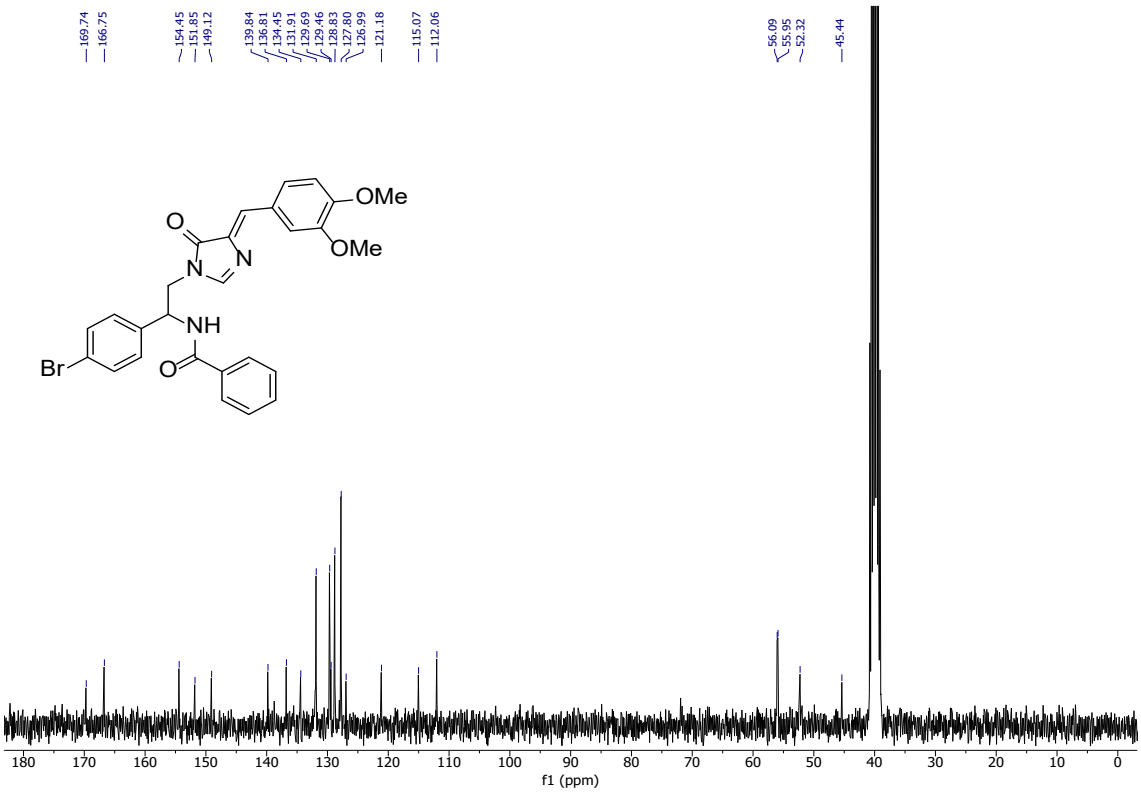

tert-Butyl (_Z_)-(2-(4-(4-chlorobenzylidene)-5-oxo-4,5-dihydro-1_H_-imidazol-1-yl)-1-phenylethyl)carbamate (4b)

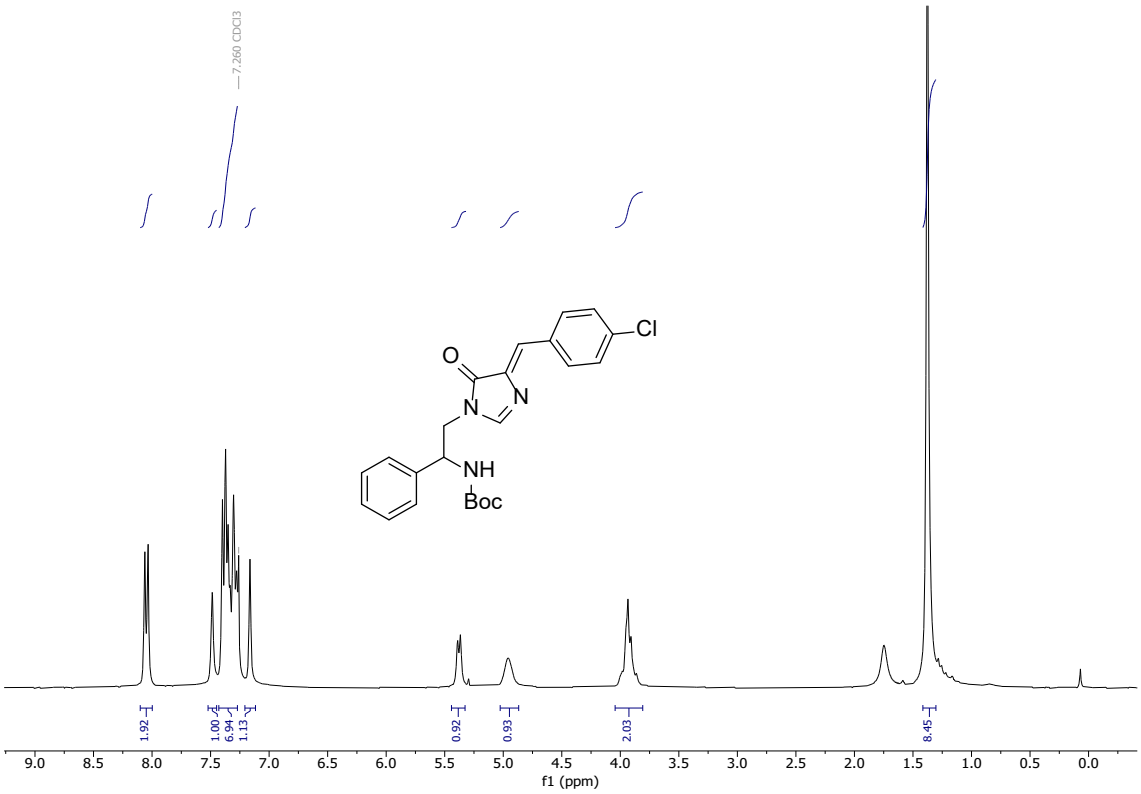

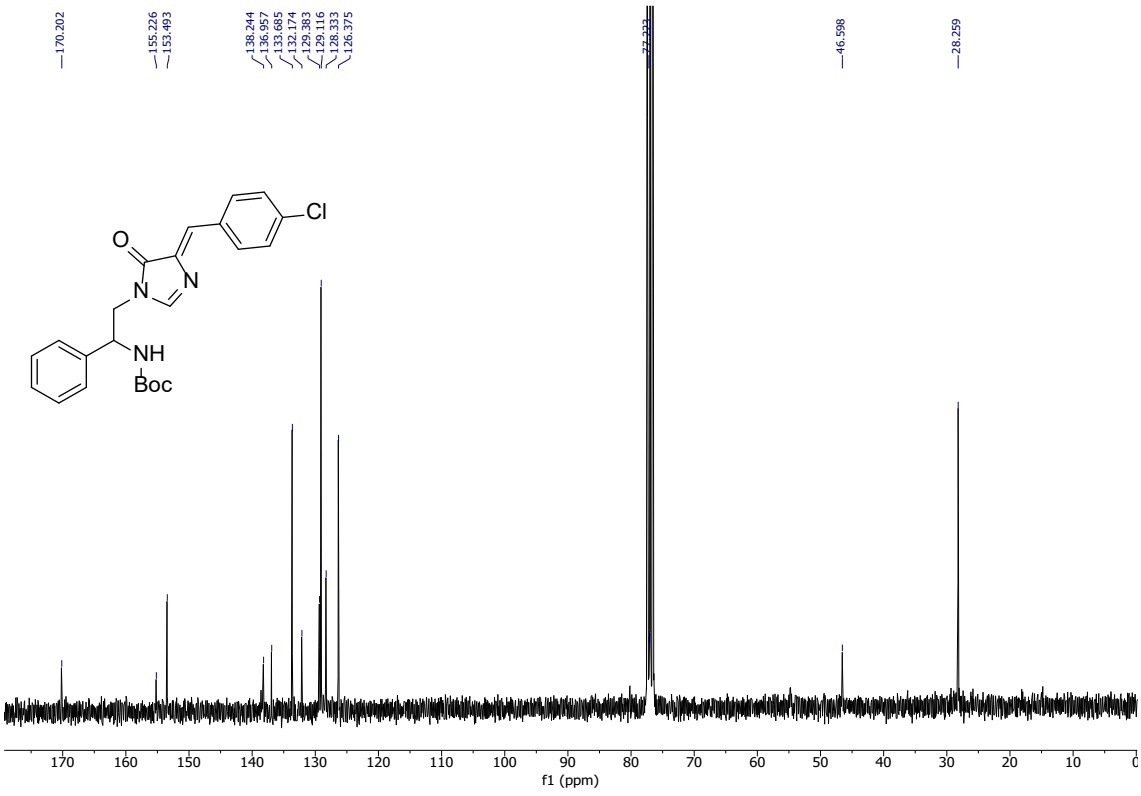

(*Z*)-3-(2-Amino-2-phenylethyl)-5-(4-chlorobenzylidene)-3,5-dihydro-4*H*-imidazol-4-one (5b)

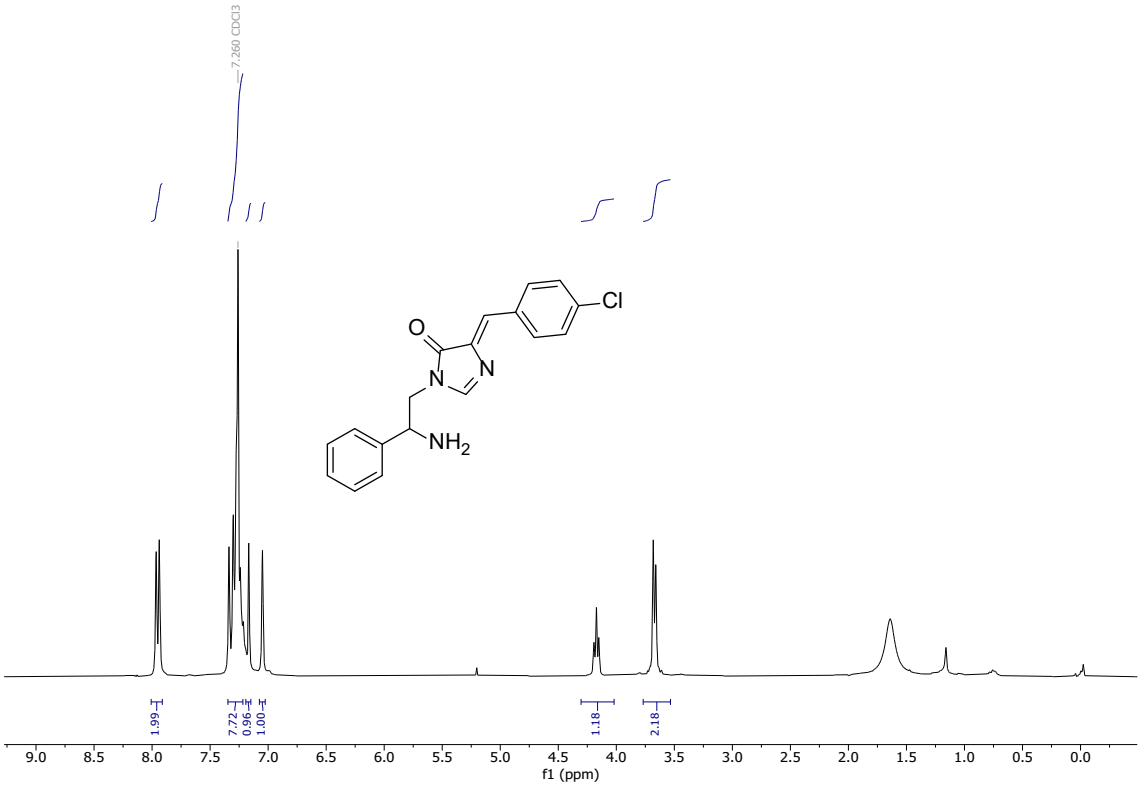

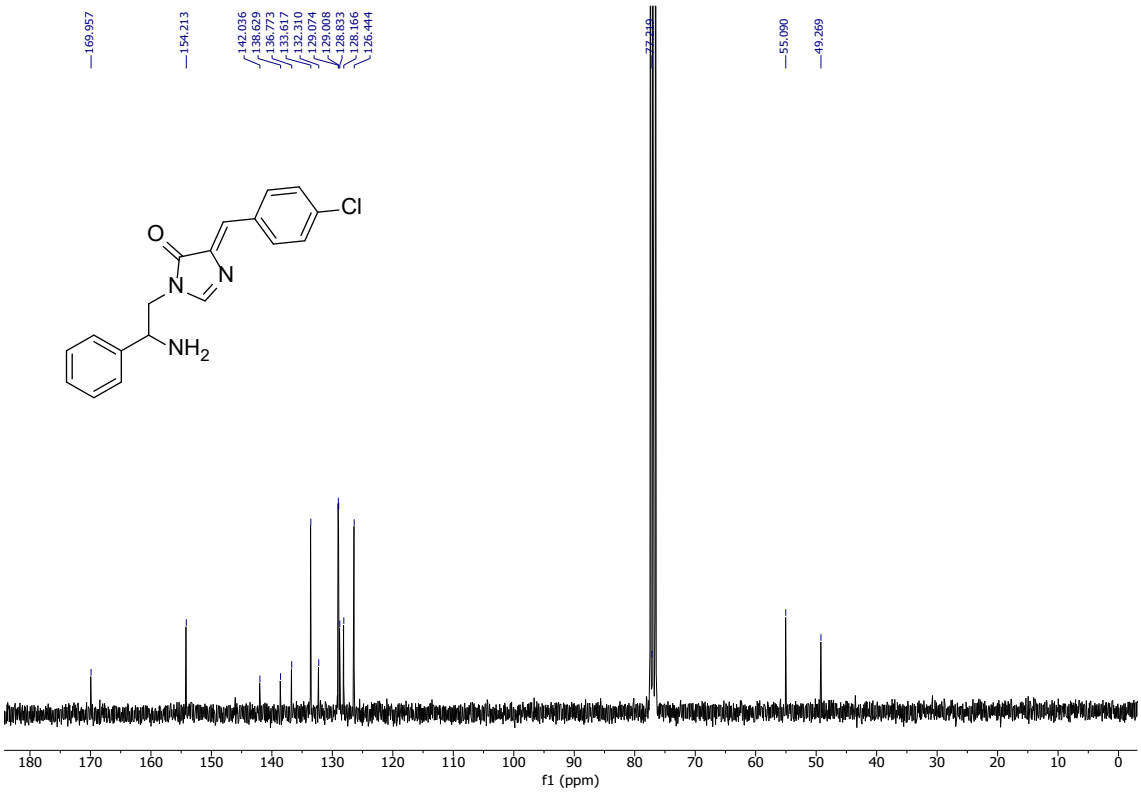

5-((*Z*)-4-Chlorobenzylidene)-3-(2-(((*E*)-4-chlorobenzylidene)amino)-2-phenylethyl)-3,5-dihydro-4*H*-imidazol-4-one (6)

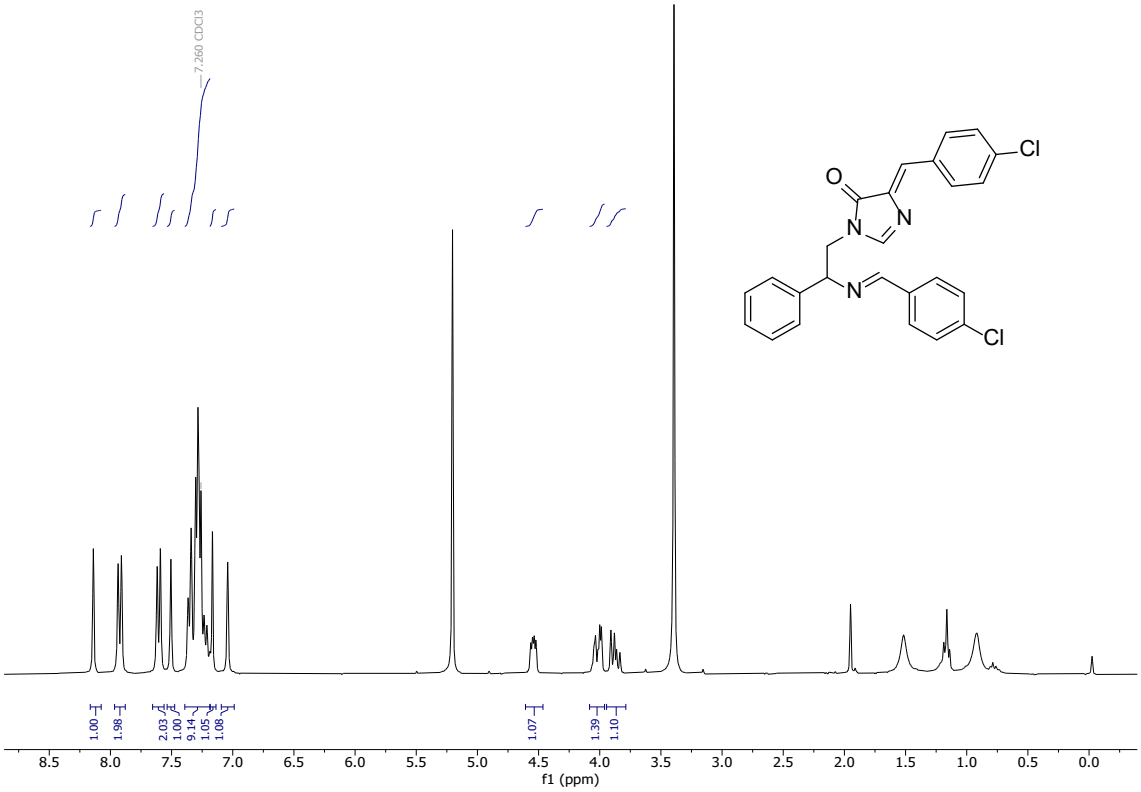

(*Z*)-2-(4-Chlorobenzylidene)-8-(4-chlorophenyl)imidazo[1,2-*a*]pyrazin-3(2*H*)-one (9)

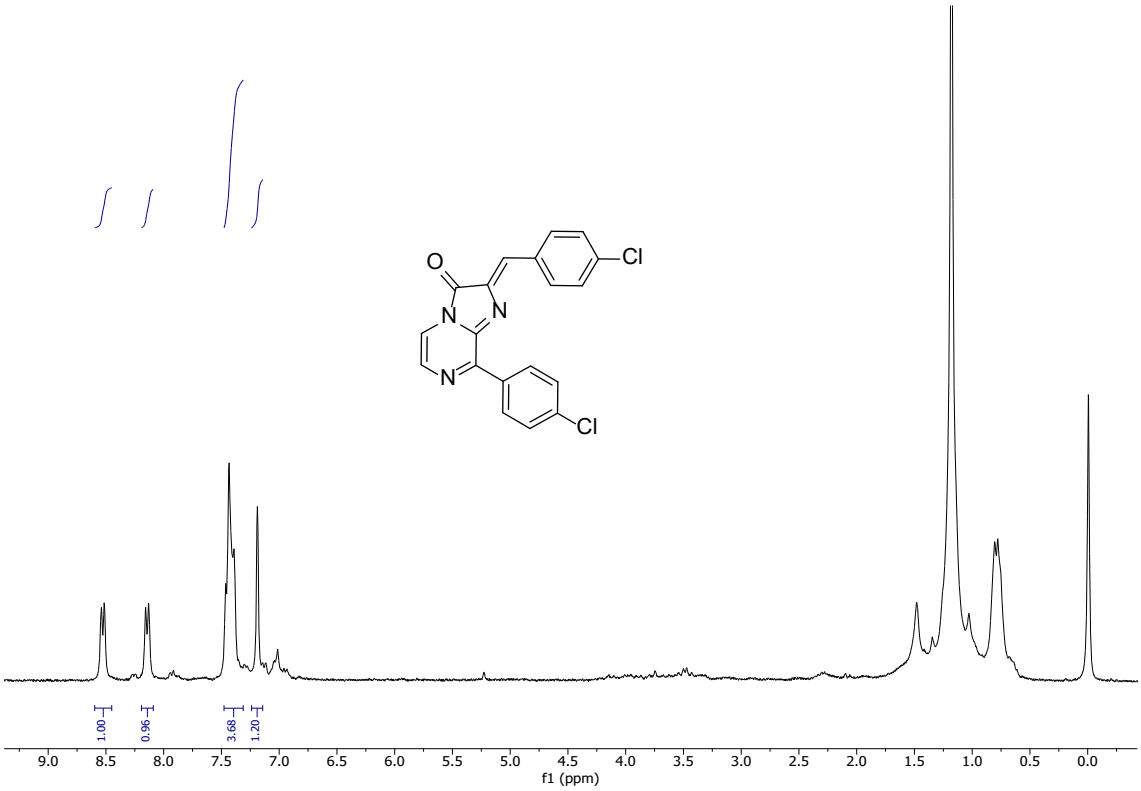

(*Z*)-2-(4-Chlorobenzylidene)-8-(4-chlorophenyl)-5,6-dihydroimidazo[1,2-*a*]pyrazin-3(2*H*)-one (10)

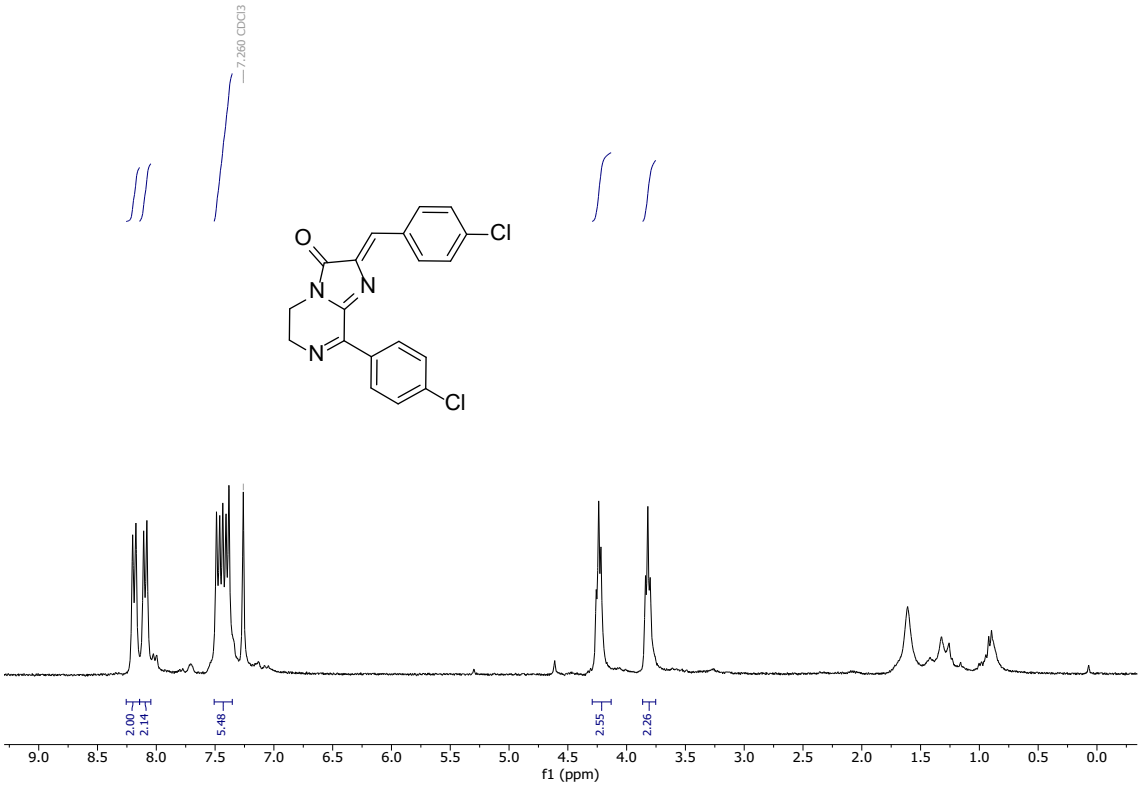

(2*R*,2'*R*)-2,2'-bis(4-Chlorobenzyl)-8,8'-bis(4-chlorophenyl)-5,5',6,6'-tetrahydro-[2,2'-biimidazo[1,2-*a*]pyrazine]-3,3'(2H,2'*H*)-dione (11)

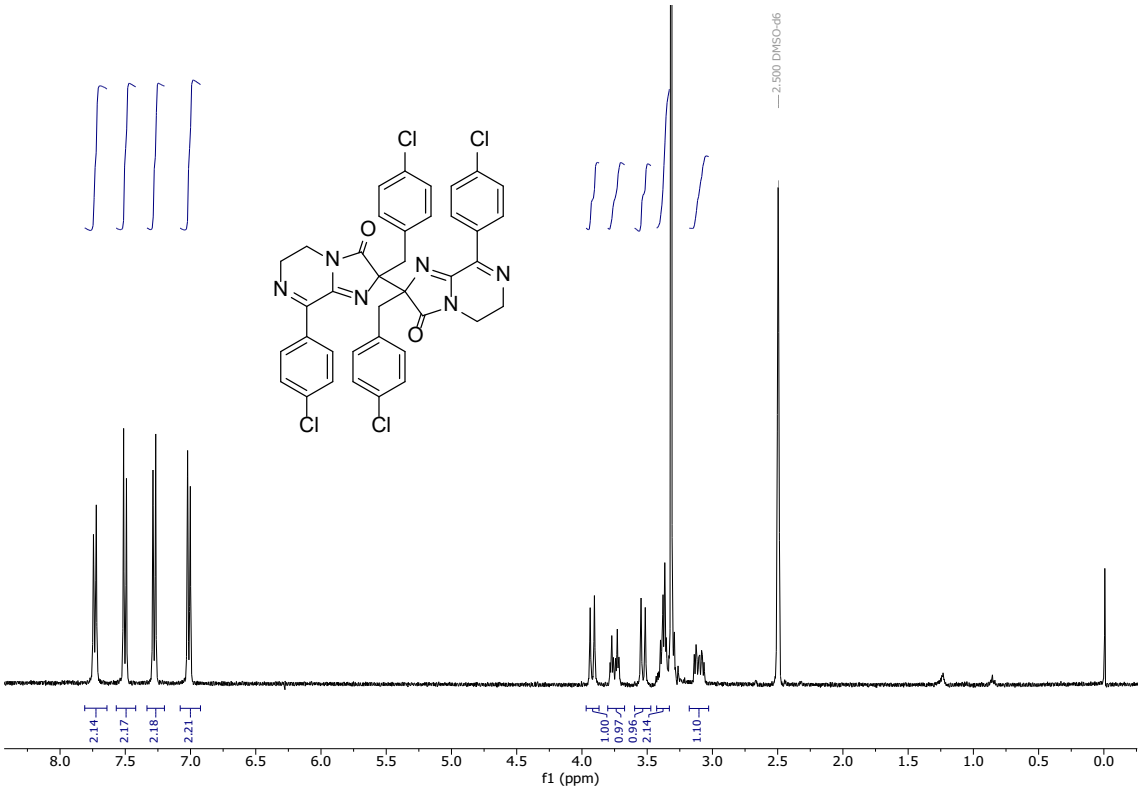

3.6. Materials and Methods for the Enzymatic Assays

3.6.1. K_M Determination Experiments

Instrument: luminescence was measured with a Berthold Orion Microplate Luminometer.

Buffer: Tris·HCl + 0.1 mg/mL BSA (pH =7.5).

Enzyme mix:

- LgBiT: to ensure proper conservation of the enzyme, the LgBiT is stocked as a 1μM solution at -20 ºC. Dilute 3.2 μL of LgBiT stock into a final volume of 100 μL of buffer. Further dilute 1:10 to a final volume of 100 μL. [LgBiT] = 3.2 nM
- HiBiT: to ensure proper conservation of the peptide, the HiBiT is lyophilised and stored at -20 ºC. An aliquot of HiBiT is taken up in water and its concentration is determined by UV-Vis absorption (ε_{HiBiT} = 5800 $M^{-1}\cdot cm^{-1}$). Prepare a 1.6 μM solution of HiBiT (500 eq. in respect to LgBiT) in buffer, final volume 200 μL.
- Enzyme incubation: 100 μL of HiBiT solution + 100 μL of LgBiT solution. Mix thoroughly in in a shaker for 5 min. Take 150 μL and dilute with buffer to a final volume of 3 mL. Incubate in a shaker at 300 rpm for 30 min. This constitutes the enzyme mix.

Substrate: 11-point $(2/3)^n$ dilution. Prepare a 100 μM solution of the substrate in buffer, final volume 1.2 mL. Take 600 μL of this solution and add it to 300 μL of buffer. Repeat until a 11-point dilution series (50 – 0.9 μM).

Plate layout and reading (Figure 5): a 96-well plate is used for the measurements. First, the buffer and substrate are added into the plate. Right before the reading, the enzyme mix is added into the plate. Average time from enzyme mix addition to first reading is 2 minutes. Readings were taken approximately every 75 seconds. The plate was automatically shaken in-between readings.

L = 20 μL of buffer + 40 μL of substrate solution + 20 μL of enzyme solution.

E = 60 μL of buffer + 20 μL of enzyme mix.

S = 40 μL of buffer + 40 μL of substrate.

B = 80 μL of buffer.

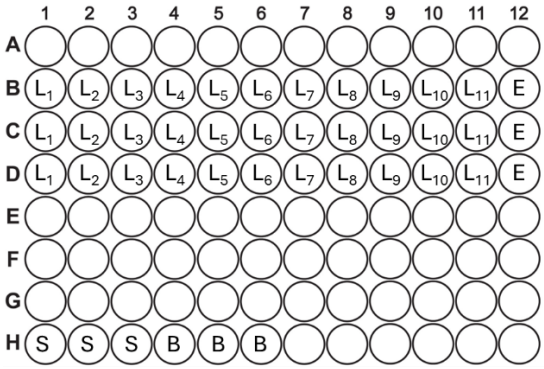

Figure 5. Plate layout for the enzymatic assays.

The final concentrations of the optimised assay in the 96-well plate are: enzyme mix = 20 pM, substrate 0 – 50 µM.

To select the optimal enzyme concentration for the assays, three experiments were conducted with enzyme concentrations of 200 pM, 20 pM and 5 pM. The results indicated good correlation between the enzyme and the signal intensity. However, saturation of the instrument was observed in some cases at an enzyme concentration of 200 pM. Thus, 20 pM was selected as the optimal concentration (Figure 6).

With the experiments at an enzyme concentration of 20 pM, the K_M was determined using the GraphPad software. The data was fitted to a Michalis-Menten model both considering inhibition by the substrate (dotted lines) and no substrate inhibition (plain lines). In agreement with previous reports, the data was better fitted with a substrate inhibition model.[43]

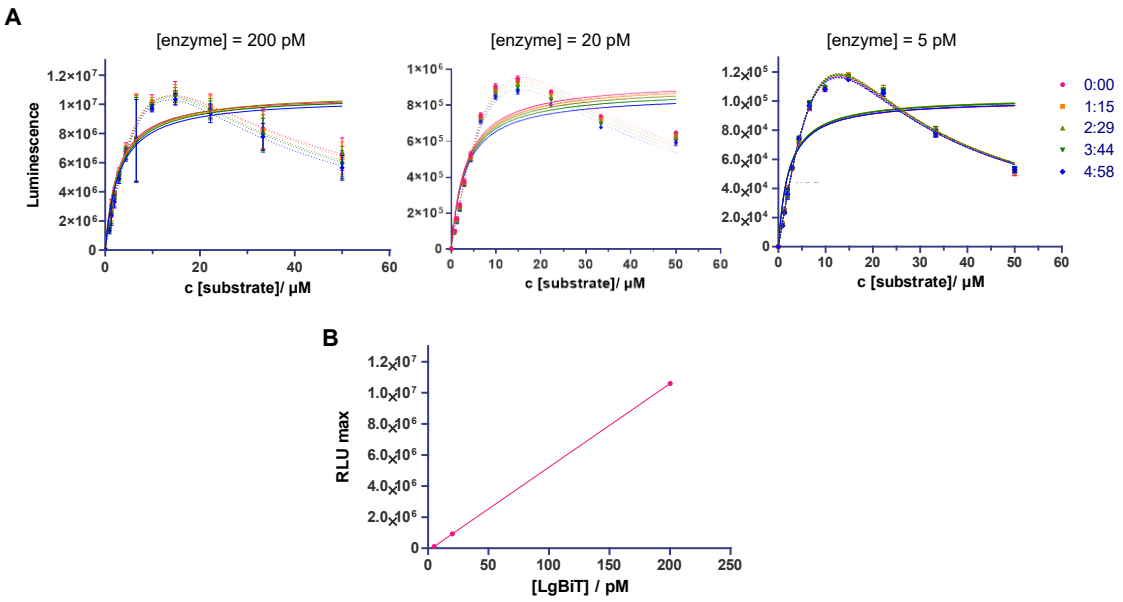

Figure 6. A) Luminescence measurements at different enzyme concentrations. B) Correlation between the enzyme and the luminescence signal intensity.

3.6.2. IC_{50} Determination Experiments

The buffer and enzyme mix preparation for the IC_{50} determination of the inhibitors MCR-CTZ-1 and MCR-CTZ-2 were prepared exactly as indicated in the previous section.

Inhibitor: 11-point $(1/3)^n$ dilution. Prepare a 100 μM solution of the substrate in buffer, final volume 600 μL. Take 300 μL of this solution and add it to 300 μL of buffer. Repeat until a 11-point dilution series (1 mM – 19 nM). The inhibitor was added into the enzyme mix after 10 min incubation. The mixture was further incubated for 20 min at 300 rpm.

Substrate: for the IC_{50} determination, the substrate was used at a final concentration of 5 μM.

3.7. Conclusions

The bioluminescence of the MCR-CTZ compounds was tested. The necessary enzymatic experiments were designed and conducted. Unfortunately, no bioluminescence was observed in the tested compounds, presumably due to the lack of structural attributes such as the pyrazine double bond.

The adducts MCR-CTZ were found to be competitive inhibitors of the NanoBiT split luciferase, in the micromolar range. Importantly, there are no described inhibitors for this complementation system, making our compounds promising tools for such a task. Moreover, the easy, one-step access to the MCR-CTZ compounds would provide a facile approach to a chemical library to further study their inhibitory potential. This work is in progress in our laboratory.

A synthetic approach based on an MCR to generate closer analogues to the CTZ was designed. The proposed synthesis was applied; however, several unproductive reactions hindered the initial objective. Nevertheless, through the experimental work, new reactivity of our MCR-CTZ adducts was found, leading to interesting dimeric species. The generality of this process and its application on similar cores is currently being pursued in our laboratories.

4. References

[1] C. M. Dobson, *Nature* **2004**, *432*, 824–828.

[2] a) C. Lipinski, A. Hopkins, *Nature* **2004**, *432*, 855–861; b) H. Zhao, I. Akritopoulou-Zanze, *Expert Opin. Drug Discov.* **2010**, *5*, 123–134.

[3] a) J. Zhu, H. Bienaymé, Eds. *Multicomponent Reactions*, Wiley-VCH, Weinhiem, **2005**; b) J. Zhu, Q. Wang, M. X. Wang, Eds. *Multicomponent Reactions in Organic Synthesis*, Wiley-VCH, Weinheim, **2015**; c) A. Dömling, I. Ugi, *Angew. Chem. Int. Ed.* **2000**, *39*, 3168–3210; d) E. van der Eycken, U. K. Sharma, Eds. *Multicomponent Reactions towards Heterocycles: Concepts and Applications*, Wiley-VCH, Weinheim, **2022**.

[4] a) T. Newhouse, P. S. Baran, R. W. Hoffmann, *Chem. Soc. Rev.* **2009**, *38*, 3010–3021; b) T. Gaich, P. S. Baran, *J. Org. Chem.* **2010**, *75*, 4657– 4673; c) Y. Hayashi, *J. Org. Chem.* **2021**, *86*, 1–23.

[5] L. F. Tietze, G. Brasche, K. Gericke, *Domino Reactions in Organic Synthesis*, Wiley-VCH, Weinheim, **2006**.

[6] E. Ruijter, R. Scheffelaar, R. V. A. Orru, *Angew. Chem. Int. Ed.* **2011**, *50*, 6234–6246.

[7] a) M. D.Burke, S. L. Schreiber*, Angew. Chem. Int. Ed.* **2004**, *43*, 46–58; b) For a precedent work on condition-based divergency in MCRs, see: N. Elders, E. Ruijter, F. J. J. de Kanter, M. B. Groen, R. V. A. Orru, *Chem. Eur. J.* **2008**, *14*, 4961–4973.

[8] P. M. Murray, S. N. G. Tyler, J. D. Moseley. *Org. Process Res. Dev.* **2013**, *17*, 40−46.

[9] For examples of reaction discovery see: a) D. H. H. Barton, *Aldrichimica Acta* **1990**, *23*, 3–10; b) Y. Chen, A. S. Kamlet, J. B. Steinman, D. R. Liu, *Nat. Chem.* **2011**, *3*, 146–153; c) D. W. Robbins, J. F. Hartwig, *Science* **2011**, *333*, 1423–1427; d) A. McNally, C. K. Prier, D. W. C. MacMillan, *Science* **2011**, *334*, 1114–1117.

[10] For examples of systematic charting, see: a) K. D. Collins, F. Glorius, *Nat. Chem.* **2013**, *5*, 597–601; b) C. N. Prieto Kullmer, J. A. Kautzky, S. W. Krska, T. Nowak, S. D. Dreher, D. W. C. MacMillan, *Science* **2022**, *376*, 532–539; c) J. J. Dotson. L. van Dijk. J. C. Timmerman, S. Grosslight, R. C. Walroth, F. Gosselin, K. Püntener, K. A. Mack, M. S. Sigman. *J. Am. Chem. Soc*. **2023**, *145*, 110−121.

[11] V. Trudel, C.-H. Tien, A. Trofimova, A. K. Yudin, *Nat. Rev. Chem.* **2021**, *5*, 604–623.

[12] a) A. v. Gulevich, A. G. Zhdanko, R. V. A. Orru, V. G. Nenajdenko, *Chem. Rev.* **2010**, *110*, 5235–5331; b) N. Elders, E. Ruitjer, V. G. Nenajdenko, R. V. A. Orru, in *Isocyanide Chemistry: Applications in Synthesis and Material Science* (Ed.: V.G. Nenajdenko), Wiley-VCH, Weinheim, **2012**, pp. 75–108; c) M. Giustiniano, A. Basso, V. Mercalli, A. Massarotti, E. Novellino, G. C. Tron, J. Zhu, *Chem. Soc. Rev.* **2017**, *46*, 1295–1357.

[13] R. S. Bon, C. Hong, M. J. Bouma, R. F. Schmitz, F. J. J. de Kanter, M. Lutz, A. L. Spek, R. V. A. Orru, *Org. Lett.* **2003**, *5*, 3759–3762.

[14] A. Clemenceau, Q. Wang, J. Zhu, *Org. Lett.* **2017**, *19*, 4872–4875.

[15] S. Frippiat, C. Sarre, C. Baudequin, C. Hoarau, L. Bischoff, *J. Org. Chem.* **2022**, *87*, 7464–7473.

[16] a) M. Zimmer, *Chem. Rev.* **2002**, *102*, 759–782; c) J. Zhang, R. E. Campbell, A. Y. Ting, R. Y. Tsien, *Nat. Rev. Mol. Cell. Biol.* **2002**, *3*, 906–918.

[17] a) A. Baldridge, J. Kowalik, L. Tolbert, *Synthesis* **2010**, *14*, 2424–2436; b) X. Gong, H. Yang, H. Liu, Y. Jiang, Y. Zhao, H. Fu, *Org. Lett.* **2010**, *12*, 3128–3131. c) S. Gutiérrez, M. Morón, M. Griera, D. Sucunza, L. Calleros, A. García-Jérez, C. Coderch, F. J. Hermoso, C. Burgos, M. Rodríguez-Puyol, B. de Pascual-Teresa, M. L. Diez-Marques, A. Jimenez, M. Toro-Londoño, D. Rodríguez-Puyol, J. J. Vaquero, *Eur. J. Med. Chem.* **2018**, *157*, 946–959.

[18] Compound **5h**: Rodolfo Lavilla; 2023; CCDC 2240654; Experimental Crystal Structure Determination; DOI: 10.5517/ccdc.csd.cc2f6l5f. Compound **8a**: Rodolfo Lavilla; 2023; CCDC 2240652; Experimental Crystal Structure Determination; DOI: 10.5517/ccdc.csd.cc2f6l3c.

[19] S. Sakai, A. Fujioka, K. Imai, K. Uchiyama, Y. Shimizu, K. Higashida, M. Sawamura, *Adv. Synth. Catal.* **2022**, *364*, 2333–2339.

[20] J. Mendiola, J. M. Minguez, J. Alvarez-Builla, J. J. Vaquero. *Org. Lett*. **2000**, *2*, 3253–3256.

[21] a) Remarkably, the UV-photodimerisation of a related GFP derivative leads to a steroisomeric cyclobutane: P. Naumov, J. Kowalik, K. M. Solntsev, A. Baldridge, J. S. Moon, C. Kranz, L. M. Tolbert, *J. Am. Chem. Soc*. **2010**, *132*, 5845–5857; b) I. F. S. Marra, A. M. de Almeida, L. P. Silva, P. P. de Castro, C. C. Corrêa, G. W. Amarante, *J. Org. Chem.* **2018**, *83*, 15144–15154.

[22] O. Ghashghaei, F. Seghetti, R. Lavilla, *Beilstein. J. Org. Chem*, **2019**, *15*, 521–534.

[23] O. Ghashghaei, M. Pedrola, F. Seghetti, V. V. Martin, R. Zavarce, M. Babiak, J. Novacek, F. Hartung, K. M. Rolfes, T. Haarmann-Stemmann, R. Lavilla, *Angew. Chem. Int. Ed.* **2021**, *60*, 2603-2608.

[24] a) A. Schenkmayerova, M. Toul, D. Pluskal, R. Baatallah, G. Gagnot, G. P. Pinto, V. T. Santana, M. Stuchla, P. Neugebauer, P. Chaiyen, J. Damborsky, D. Bednar, Y. L. Janin, Z. Prokop, M. Marek, *Nat. Catal.* **2023**, *6*, 23–38; b) E. P. Coutant, Y. L. Janin, *Chem. Eur. J.* **2015**, *21*, 17158–17171.

[25] For reports that yield related adducts through different mechanistic pathways, see: a) A. Shaabani, A. Maleki, H. Mofakham, H. R. Khavasi, *J. Comb. Chem.* **2008**, *10*, 323–326; b) V. Kysil, A. Khvat, S. Tsirulnikov, S. Tkachenko, C. Williams, M. Churakova, A. Ivachtchenko, *Eur. J. Org. Chem.* **2010**, *2010*, 1525–1543.

[26] M. Muselli, C. Baudequin, C. Perrio, C. Hoarau, L. Bischoff, *Chem. Eur. J.* **2016**, *22*, 5520–5524.

[27] a) G. Guella, I. Mancini, H. Zibrowius, F. Pietra, *Helv. Chim. Acta.* **1989**, *72*, 1444–1450; b) P. Crews, D. P. Clark, K. Tenney, *J. Nat. Prod.* **2003**, *66*, 177–182.

[28] a) M. Debdab, F. Carreaux, S. Renault, M. Soundararajan, O. Fedorov, P. Filippakopoulos, O. Lozach, L. Babault, T. Tahtouh, B. Baratte, Y. Ogawa, M. Hagiwara, A. Eisenreich, U. Rauch, S. Knapp, L. Meijer, J.-P. Bazureau, *J. Med. Chem.* **2011**, *54*, 4172–4186; b) A. Kaczor, K. Witek, S. Podlewska, J. Czekajewska, A. Lubelska, E. Żesławska, W. Nitek, G. Latacz, S. Alibert, J.-M. Pagès, E. Karczewska, K. Kieć-Kononowicz, J. Handzlik, *Molecules* **2019**, *24*, 438.

[29] a) S. Gutiérrez, D. Martínez-López, M. Morón, D. Sucunza, D. Sampedro, A. Domingo, A. Salgado, J. J. Vaquero, *Chem. Eur. J.* **2015**, *21*, 18758–18763.

[30] S. Kojima, T. Hirano, H. Niwa, M. Ohashi, S. Inouye, F. I. Tsuji, *Tetrahedron Lett.* **1997**, *38*, 2875–2878.

[31] For alternative processes, see: a) Q. Wang, S. L. Schreiber, *Org. Lett.* **2009**, *11*, 5178–5180; b) Y. Park, Y. Kim, S. Chang, *Chem. Rev.* **2017**, *117*, 9247–9301; c) M. Morón, C. Burgos, J. Alvarez-Builla, A. Salgado, M. E. G. Mosquera, J. J. Vaquero. *Chem. Commun*. **2012**, *48*, 9171–9173.

[32] W. Wei, L. Wang, P. Bao, Y. Shao, H. Yue, D. Yang, X. Yang, X. Zhao, H. Wang. *Org. Lett*. **2018**, *20*, 7125–7130.

[33] F. de Moliner, N. Kielland, R. Lavilla, M. Vendrell, *Angew. Chem. Int. Ed.* **2017**, *56*, 3758–3769.

[34] S. R. Meech, *Chem. Soc. Rev.* **2009**, *38*, 2922–2934.

[35] a) L. Wu, K. Burgess, *J. Am. Chem. Soc.* **2008**, *130*, 4089–4096; b) K. Y. Chen, Y. M. Cheng, C. H. Lai, C. C. Hsu, M. L. Ho, G. H. Lee, P. T. Chou, *J. Am. Chem. Soc.* **2007**, *129*, 4534–4535; c) A. Baldridge, K. M. Solntsev, C. Song, T. Tanioka, J. Kowalik, K. Hardcastle, L. M. Tolbert, *Chem. Commun.* **2010**, *46*, 5686–5688; d) A. Baldridge, S. R. Samanta, N. Jayaraj, V. Ramamurthy, L. M. Tolbert, *J. Am. Chem. Soc.* **2010**, *132*, 1498–1499.

[36] C. Chen, S. R. Tachibana, N. S. Baleeva, I. N. Myasnyanko, A. M. Bogdanov, A. S. Gavrikov, A. S. Mishin, K. K. Malyshevskaya, M. S. Baranov, C. Fang, *Chem. Eur. J.* **2021**, *27*, 8946–8950.

[37] G. Jones, in *Organic Reactions*, John Wiley & Sons, Inc., Hoboken, **2011**, pp. 204–599.

[38] M. B. Smith, J. March, in *March's Advanced Organic Chemistry: Reactions, Mechanisms, and Structure, 5th ed.*, John Wiley & Sons, Inc., Hoboken, **2006**, p. 1174.

[39] V. Voliani, R. Bizzarri, R. Nifosì, S. Abbruzzetti, E. Grandi, C. Viappiani, F. Beltram, *J. Phys. Chem. B.* **2008**, *112*, 10714–10722.

[40] V.V. Krasitskaya, E.E. Bashmakova, L.A. Frank, *Int. J. Mol. Sci.* **2020**, *21*, 7465.

[41] C. G. England, E. B. Ehlerding, W. Cai, *Bioconjugate Chem.* **2016**, *27*, 1175–1187.

[42] A. S. Dixon, M. K. Schwinn, M. P. Hall, K. Zimmerman, P. Otto, T H. Lubben, B. L. Butler, B. F. Binkowski, T. Machleidt, T. A. Kirkland, M. G. Wood, C. T. Eggers, L. P. Encell, K. V. Wood, *ACS Chem. Biol.* **2016**, *11*, 400–408.

[43] A. Schenkmayerova, M. Toul, D. Pluskal, R. Baatallah, G. Gagnot, G. P. Pinto, V. T. Santana, M. Stuchla, P. Neugebauer, P. Chaiyen, J. Damborsky, D. Bednar, Y. L. Janin, Z. Prokop, M. Marek, *Nat. Catal.* **2023**, *6*, 23–38.

[44] Walker, J. R.; Hall, M. P.; Zimprich, C. A.; Robers, M. B.; Duellman, S. J.; Machleidt, T.; Rodriguez, J.; Zhou, W, *ACS Chem. Biol.* **2017**, *12*, 1028–1037.

[45] A. Wensi, S. Ronghua, Z. Liyan, J. Dehong, M. Xiaobo, Y. Jilan, W. Zhouyu, *RSC Adv.*, **2015**, *5*, 24044–24048.

[46] Q.-H. Li, Z.-F. Li, J. Tao, W.-F. Li, L.-Q. Ren, Q. Li, Y.-G. Peng, T.-L. Liu, *Org. Lett.* **2019**, *21*, 8429– 8433.

[47] M. Somi Reddy, M. Narender, Y. V. D. Nageswar, K. Rama Rao, *Synlett* **2006**, *7*, 1110–1112.

[48] A. Järvinen, M. Cerrada-Gimenez, N. A. Grigorenko, A. R. Khomutov, J. J. Vepsäläinen, R. M. Sinervirta, T. A. Keinänen, L. I. Alhonen, J. E. Jänne, *J. Med. Chem.* **2006**, *49*, 399–406.

[49] S. Inoue, H. Taguchi, M. Murata, H. Kakoi, T. Goto, *Chem. Lett.* **1977**, *6*, 259–262.

Chapter III

New Avenues in AhR Modulation

1. ***A Multicomponent Reaction Platform for AhR Modulation***
2. ***Experimental Section***
3. ***References***

1. A Multicomponent Reaction Platform for AhR Modulation

1.1. Introduction

The aryl hydrocarbon receptor (AhR) is a transcription factor with key roles in xenobiotic metabolism and immunity.[1] The regulation of AhR is a promising strategy against several autoimmune and inflammatory diseases, cancers, and viral infections.[2] Nevertheless, AhR-based drug discovery faces several challenges: i) the ambivalent outcome of AhR activation depends not only on the chemical features of the ligand,[4] but also on the cellular context; ii) known AhR ligands are difficult to synthesise, have limited structural diversity and raise serious toxicity concerns; iii) with the existing structural information on AhR,[5] the development of improved ligands heavily relies on screening approaches rather than on rational design. In this context, the bacterial metabolite tapinarof is the only FDA-approved AhR ligand to date, for psoriasis treatment and, as said above, was discovered through screening (Figure 1A).[3]

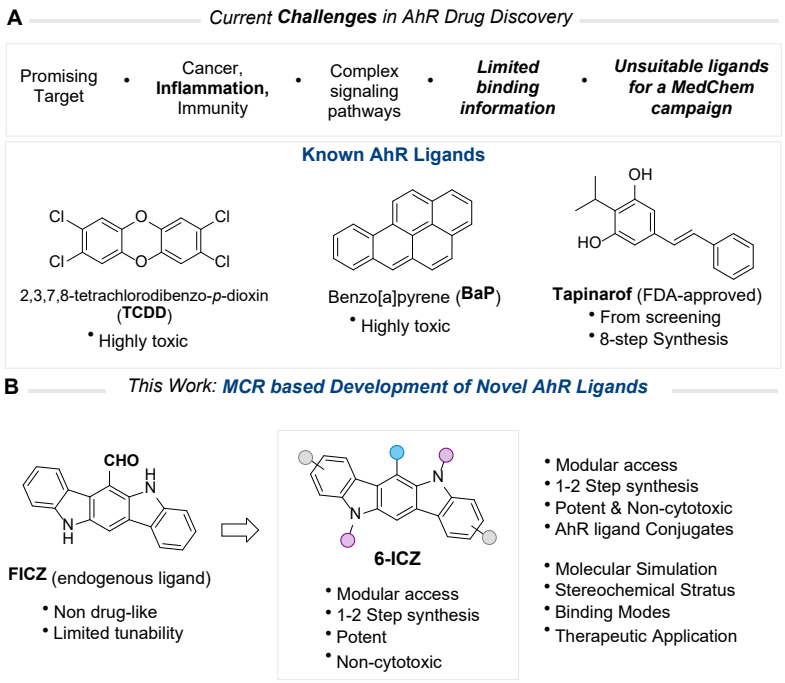

Figure 1. AhR-based drug discovery. A) Current status, challenges, and known ligands. B) This work: MCR access to the 6-ICZ scaffold offers novel avenues in AhR research.

A known family of AhR ligands are fused (hetero)aromatic systems.[6] Among them, 6-formylindolo[3,2-*b*]carbazole (FICZ, Figure 1B) is an endogenous, highly potent, and selective probe. However, its long synthesis with limited options for diversification,[7] and unsuitable drug-like features, restrict its therapeutic projection. Moreover,

6-substituted indolo[3,2-*b*]carbazole (6-ICZ) scaffold is an attractive pseudo-natural product skeleton,[8] with relevant applications in material sciences.[9] Thus, we considered it as the synthetic target for a novel AhR-based drug discovery campaign (Figure 1B). This would require short, modular, and efficient access to 6-ICZs. However, in contrast to their symmetrically disubstituted 6,12-ICZ counterparts, a reliable synthetic approach to the 6-ICZ scaffold remains almost unexplored.[10] In this regard, Multicomponent Reactions (MCRs) offer remarkable capabilities to build diverse and modular chemical libraries, particularly appealing for MedChem.[11] Recently, a family of aminobenzimidazoles bearing ICZ residues were obtained through an extended MCR.[12] However, despite being AhR activators, they were not suitable for biomedical applications due to their large size and structural complexity. Thus, we designed a new MCR to foster simpler, tunable and drug-like 6-ICZs.

1.2. Rewired Yonemitsu MCR to yield 6-ICZs

We envisioned that Yonemitsu MCR, combining aldehydes **1**, 1,3-dicarbonyls **2** and indoles **3** (Figure 2A),[13] could be rewired using indole aldehydes,[14] exploiting their dual role in domino processes,[15] first as electrophiles and subsequently as nucleophilic partners. A previous report showed that indole 3-carboxaldehyde (indole-3-CHO) yields standard Yonemitsu adducts.[16] In sharp contrast, our initial experiments with indole-2-carboxaldehyde (indole-2-CHO) **1a**, dimedone **2a** and indoles **3a-b** generated 6-ICZ adducts **4a** or **5a** in a single step through an ABB' process.[17] The competitive incorporation of the incoming species **2-3** depending on their relative nucleophilicity (Figure 2B),[18] suggested the feasibility of a new MCR with indole-2-CHO and a nucleophilic partner (Figure 2C).

After tuning the stoichiometry and reaction conditions, the scope of the MCR was studied [see Experimental Section (ES)]. Regarding nucleophiles, 1,3-dicarbonyls including dimedone, tetronic acid, and 4-hydroxycoumarin conveniently afforded the adducts **4a**-**4d** in good yields (40-97%, Figure 3A). Highly enolizable 1,3-dicarbonyls only yielded the Knoevenagel adducts **6a** (44%) and **6b** (93%), and acyclic 1,3-dicarbonyls did not participate in the MCR (Figure 3A and ES). Concerning heterocyclic nucleophiles, a variety of indoles (naked, *N*-, 2-, 4-, 5-, and 7-substituted) consistently gave the expected adducts **5a-5l** (9-86%). The structure of **5b** was confirmed by X-ray crystallography (Figure 3A).[19] These processes included several gram-scale outputs. Other nucleophiles, including heterocycles,[20] phenols, isocyanides, cyanide,

and nitromethane led to complex mixtures, competitive processes or unproductive reactions (see ES). Regarding the aldehyde partner, substituted indole-2-CHOs were allowed and adducts **4g** (40%), **5k** (72%), **5k** (38%) and **5l** (45%) were synthesised from 1-Me, 5-F and 5-OMe indole-2-CHO derivatives. In contrast, the electron deficient *N*-sulfonyl indole-2-CHO only yielded the tris-indolylmethane **7a** (36%, Figure 3A and ES).

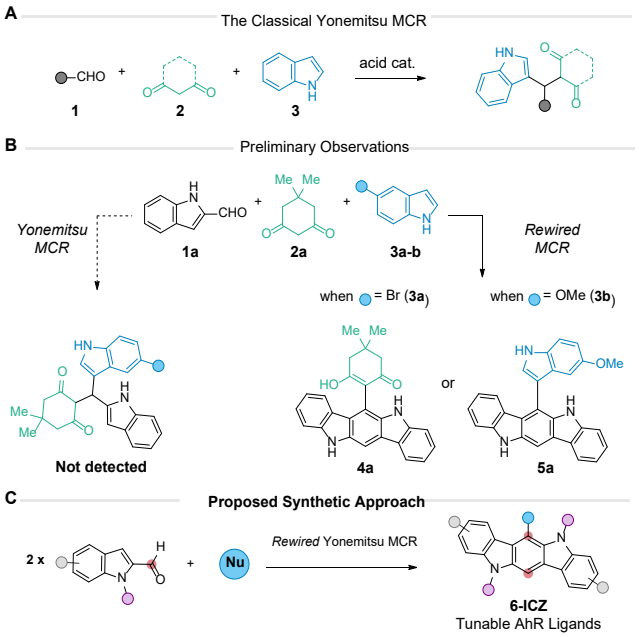

Figure 2. MCR access to 6-ICZs A) Classical Yonemitsu MCR. B) Initial experiments with indole-2-CHO. C) The rewired MCR approach to access 6-ICZs.

To extend the reach of the MCR approach as well as expanding the chemical diversity of the synthesised 6-ICZs, several post-transformation reactions were performed. In this context, the bromo adduct **5b** offered the possibility of post modifications, leading to the indolyl C-5 substituted compounds **8a** (83%) and **8b** (53%) after Suzuki and Sonogashira cross-couplings, respectively (Figure 3B). Moreover, to obtain analogues of FICZ, bearing a carbonyl motif linked to the ICZ, we considered the oxidative cleavage of the indolyl residue in compound **5e** with *m*CPBA.[21] Remarkably this process yielded the ketoamide **9** (86%) in a chemoselective manner. Interestingly, its subsequent oxidation afforded the spiro adduct **10** (74%), bypassing the Baeyer–Villiger route. The structure of **10** was confirmed by X-Ray crystallography (Figure 3C).[22] Finally, due to the rising interest in dual entities such as PROteolysis TArgeting Chimeras (PROTACs) and labelled probes, we exploited our MCR platform to prepare AhR ligand conjugates. In this regard, indole-6-carboxylic acid **3j** readily generated compound **5m** (17%, unoptimised), which stood out as a linkable 6-ICZ.

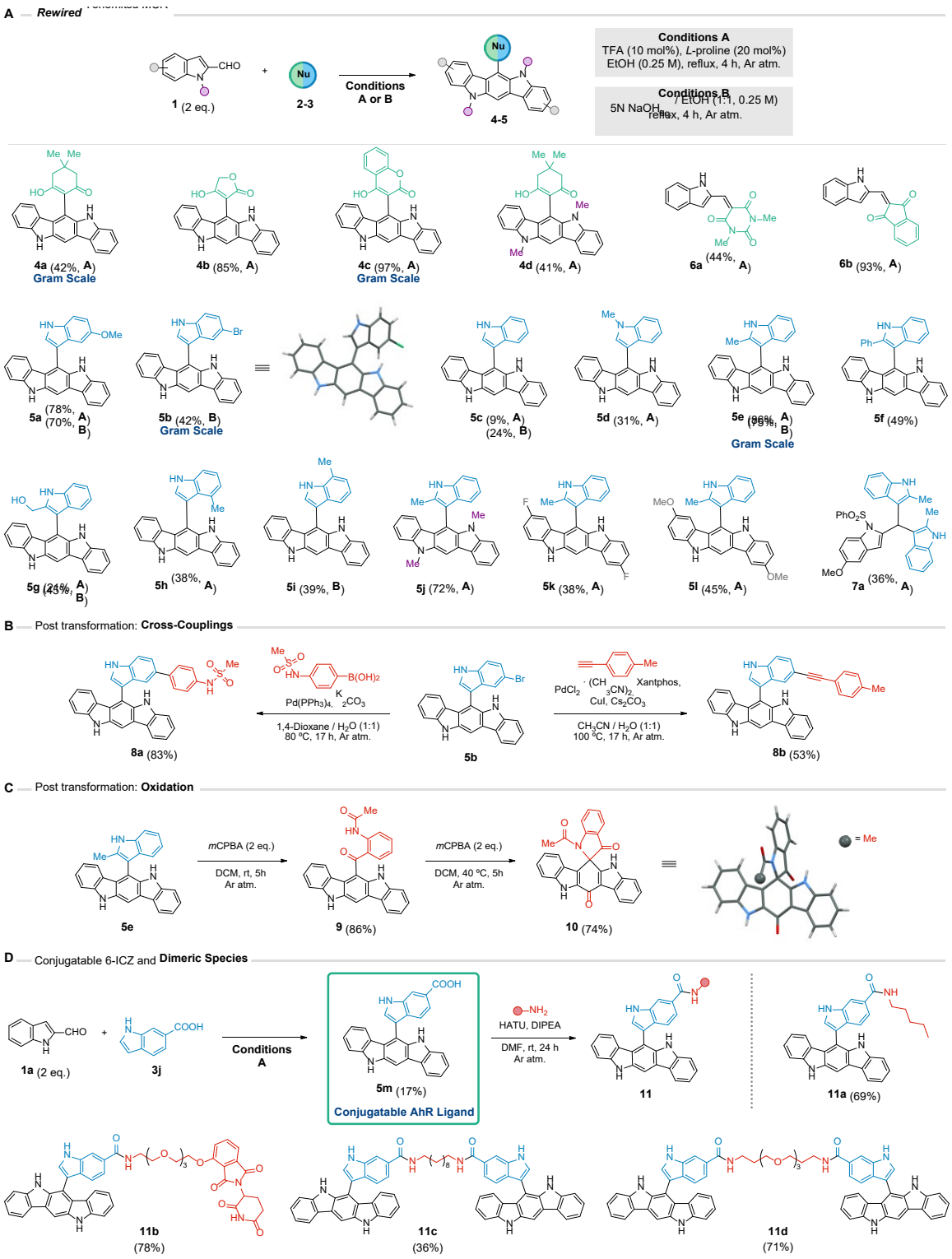

Figure 3. MCR access to 6-ICZs and ensuing chemistry. A) Optimised process and scope. In brackets, isolated yield and conditions used. B) Cross-coupling reactions with adduct **5b**. C) Oxidation of adduct **5e**. D) Amide couplings with adduct **5m.**

Note that the indolyl C-6 position was rationally selected after molecular docking (MD) simulations (see below). In this way, a conventional amide coupling of the acid **5m** with amylamine gave the model adduct **11a** (69%). We also linked a commercially available thalidomide-PEG-amine to **5m** to conveniently obtain compound **11b** (78%).

Notably, the dimeric species **11c** (36%) and **11d** (71%) were synthesised in a single step from unprotected diamine-type linkers (Figure 3D).

Likely, the reaction mechanism starts with the addition of nucleophiles **2-3** to indole-2-CHO **1a** to yield the putative carbinols **I**. Then, addition of a second indole-2-CHO **1a** leads to a domino process that includes an electrophilic cyclisation and a final dehydrative aromatisation to generate 6-ICZs **4-5** (Figure 4A).[12] Presumably, the incorporation of the second unit of aldehyde and the ensuing cascade are faster than the first nucleophilic addition, which challenged the detection of carbinols **I**. Notably, similar carbinols usually evolve towards the Knoevenagel adducts **6** *via* dehydration or to bis/tris-indolylmethanes **7** upon subsequent indole addition,[23] as was observed in some cases (Figure 4A). In this regard, there is a clear dichotomy with indole-3-CHO, which exclusively affords the Knoevenagel adducts **6** (see ES). Importantly, the adducts **6-7** were not converted to 6-ICZs **4-5** under tested conditions (Figure 4A). Moreover, the reaction of indole-2-CHO **1a** with preformed carbinols **Ia-d**, gave the corresponding 6-indolyl-ICZs **5g** and **5n-p**, bypassing the alternative intramolecular cyclisation (Figure 4B).

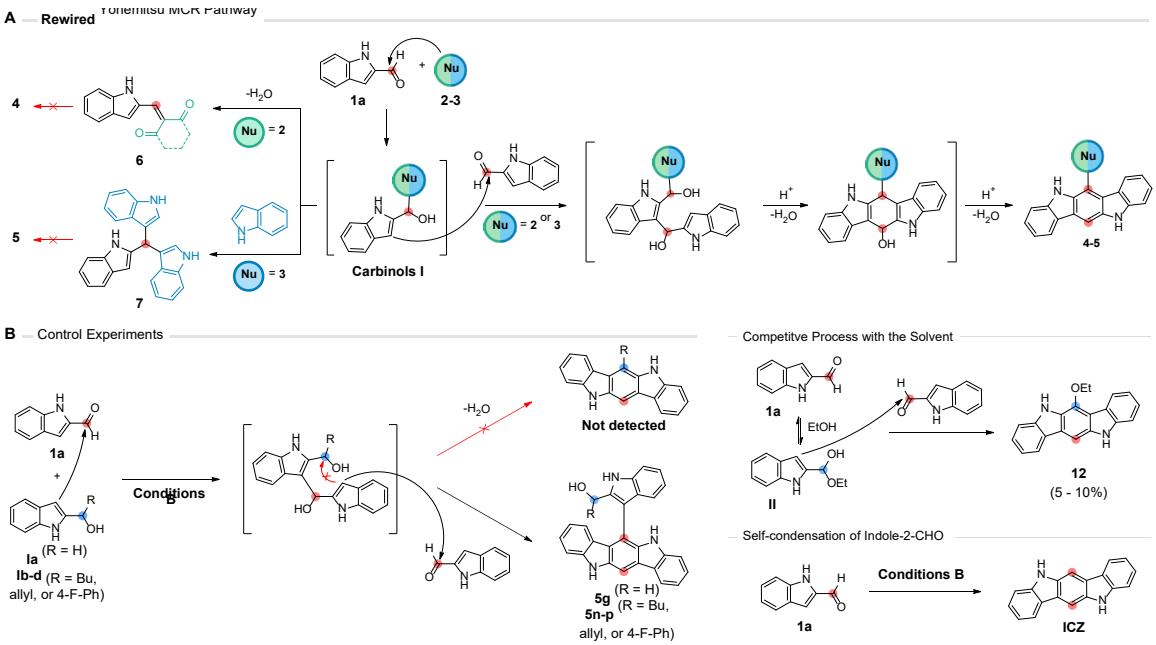

Figure 4. Mechanistic considerations. A) Proposed hypothesis on the rewired MCR and competitive pathways. B) Control experiments.

Significantly, a competitive incorporation of the solvent EtOH was observed in many cases leading to small amounts of 6-ethoxy-ICZ **12**, likely generated from the hemiacetal intermediate **II** (Figure 2B). Lastly, the self-condensation of indole-2-CHO under strong basic conditions afforded the unsubstituted **ICZ** (Figure 4B and ES).

1.3. Stereochemical Status of the 6-ICZs

The stereochemical status of these adducts is a potential concern in therapeutic applications. Substituents at the C-6 position of the ICZ nucleus may induce axial chirality due to steric clashes preventing full bond rotation.[24] The existence of atropoisomers was unambiguously confirmed in compounds **4a-b** and **5g** (diastereotopic ^{1}H NMR signals), and **5e** (peak splitting in chiral HPLC). However, no evidence was found to support chirality in adducts **5b** and **5m**, featuring 2-*H* indolyl substituents on ICZ, suggesting a free rotation around the ICZ-indolyl axis in case of an unencumbered framework (Figure 5A and ES).To explore the effect of the indolyl C-2 substitution on the rotational behaviour of **5c** (R = H) and **5e** (R = Me), density functional theory (M062X/6-31G(d,p)) calculations were performed in collaboration with Prof. Luque (Universitat de Barcelona, UB). We defined the dihedral (φ) and butterfly (α) angles to describe the ICZ-indolyl rotation and the planarity of the ICZ pentacycle, respectively (Figure 5B). Both compounds adopt minimum energy structures (**M**) characterised by the rotation of the indole residues (**M1**: φ ~ 50º, **M2**: φ ~ 122º) relative to the planar ICZ (α < 4.5º, Figure 5C). These values are close to the arrangement found in the X-Ray structure of adduct **5b** (φ = 122.1º, α < 3.8º). Rotation of the indole residue is hindered by strong steric clashes at dihedral angles φ close to 0º and 180º. However, the hindrance is alleviated through the concerted distortion of the ICZ and the indolyl residue in the transition state (**TS**) structures. This involves the bending of the indole towards one face of the molecular plane, accompanied by the synchronous, butterfly-like warp of the ICZ towards the opposite face to angles α up to 30º – 40º (Figure 5C). The free energy barriers reflected a marked destabilisation of **TS1** and **TS3** for **5e** (gray, *ca*. 35 kcal/mol) in contrast to **5c** (green, 20 – 30 kcal/mol). These values reflect the energy strain caused by the bending of ICZ, as noted in previous studies for acenes,[25] and the steric clash of the substitution at the indolyl C-2 with the bent ICZ. Remarkably, the geometrical distortion of **5c** in one direction (**TS3**, 20.9 kcal/mol) is more favorable than the reverse sense (**TS1**, 29.0 kcal/mol). The former value, which is in line with the rotational barrier reported for C2-unsubstituted naphthyl indoles,[24c] underscores a preferred pathway for the racemisation of **5c**. Importantly, intrinsic reaction coordinate (IRC) calculations confirmed that the proposed TS leads to the minimum energy structures (Figure 4D). Similar trends were observed in the energy profiles determined from MP2 calculations. Interestingly, variable temperature NMR studies with compound **5g** did not result in the

coalescence of the diastereotopic signals up to 150 ºC, in agreement with the calculated energy barriers (see ES). This behavior opens a new perspective to understand the structural features of 6-ICZs and analogous systems, so far described as permanently flat arrangements,[26] establishing the suitability of our derivatives for biological uses, either as single compounds or separable racemic mixtures.

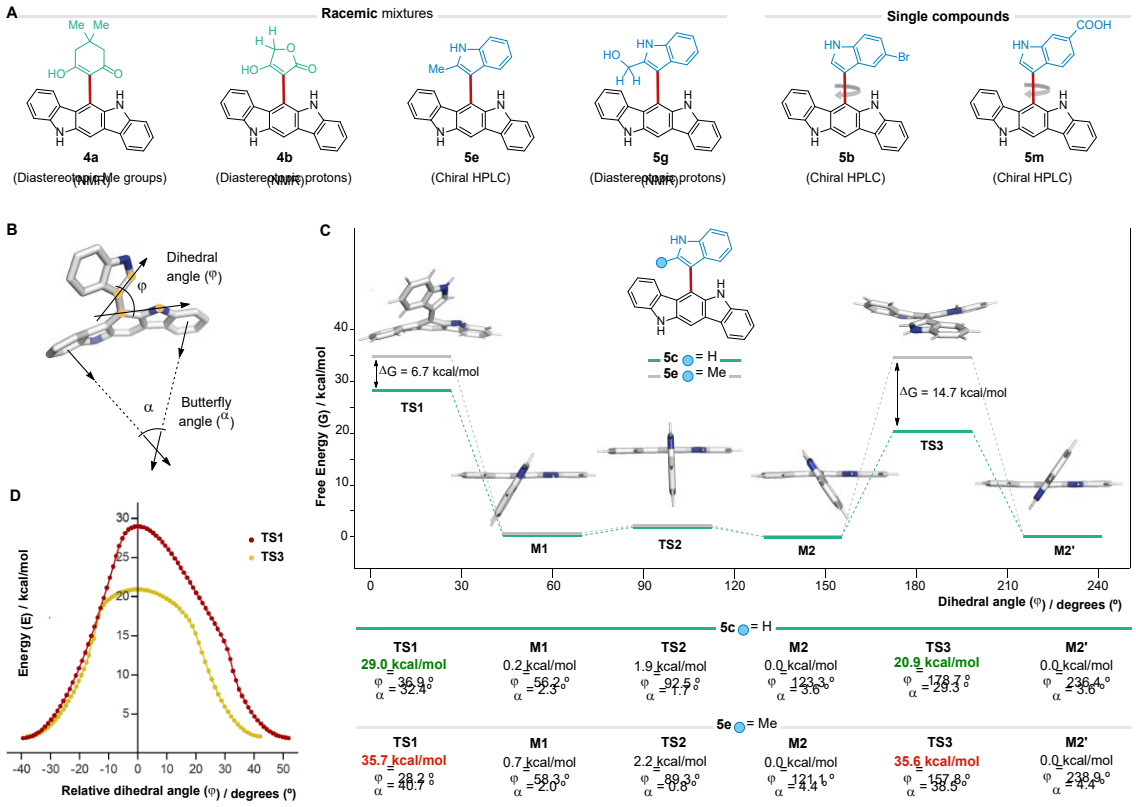

Figure 5. Axial chirality of 6-ICZs. A) Experimental observations. B) Definition of the dihedral (**φ**) and butterfly (**α**) angles. C) Energy barrier diagram for the ICZ-indolyl axis rotation for compounds **5c** (green) and **5e** (gray). Only the snapshots of **5c** are shown. D) IRC analysis of **TS1** and **TS3** for compound **5c**.

1.4. Molecular Docking Studies

Next, also in collaboration with Prof. Luque (UB), molecular docking (MD) simulations were performed to assess the ability of **5c** to mimic FICZ as an AhR binder. First, docking of the isoenergetic conformers **M2** and **M2'** (Figure 6A-B) pointed out that the ICZ moiety can bind to the hydrophobic cavity of AhR, leading to a close overlap with indirubin as found in its X-Ray complex with AhR (Figure 6A-B).[27] Noteworthy, binding of the conformers **M2** and **M2'** primarily affects the arrangement of the loops located between βA and βB and between helices C and E, while the heterodimer interface remains unaltered (Figure 6A). Therefore, binding of **5c** does not affect the interaction of AhR with the other complex subunits. In agreement with previous studies,[28] the $N_{11}H$ unit of **M2** forms a hydrogen bond (HB) with S365. In contrast, **M2'** adopts a pose where

the ICZ moiety is rotated ~180°, and S365 forms a C_7–H··· O bond with ICZ (Figure 6B-C). Furthermore, the poses of **M2** and **M2'** are reinforced by an HB network connecting Q383, T289 and H291, which in turn interacts with S320 and G321 (Figure C).

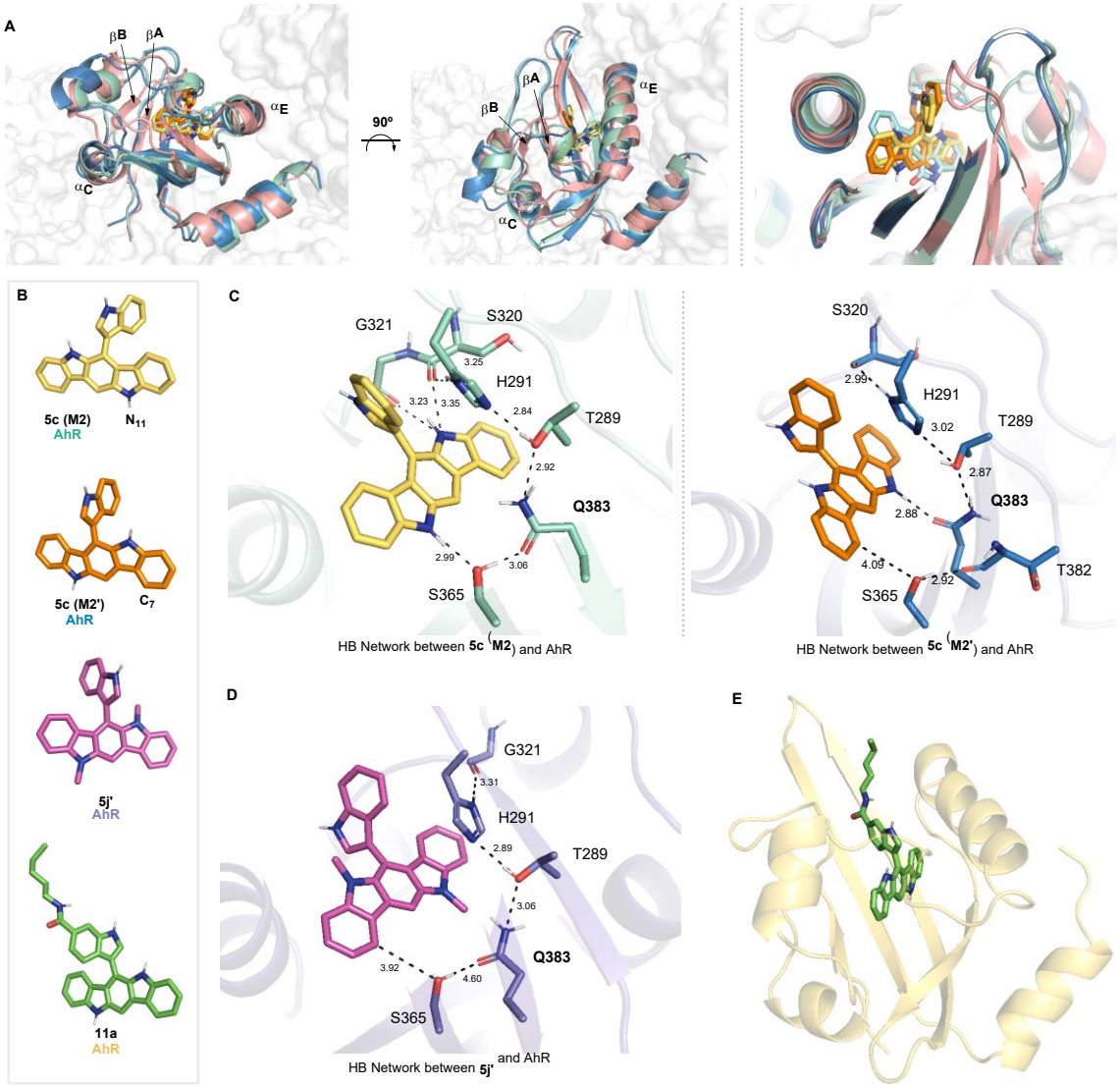

Figure 6. AhR binding of compounds **5c** and **5j'**. A) Superposition of the cryo-EM structure of the AhR-indirubin complex (PDB ID 7ZUB; AhR: pale red cartoon; indirubin: light blue cartoon) and the last snapshot taken from the MD simulation of AhR with **5c** (**M2** and **M2'**). The surface of the interface of AhR with the neighbouring subunits is shown in grey. B) Colour of the ligands and their respective AhR protein used throughout the figure. C) The HB network formed in the binding pocket of the AhR complex with **5c** (**M2** and **M2'**). D) The HB network formed in the binding pocket of the AhR complex with **5j'**. Distances (Å) denote the average value determined in the last 250 ns of the trajectory (the standard deviation generally varies between 0.2 and 0.4 Å). Labels denote the numbering of residues in the cryo-EM structure. E) The last snapshot taken from the MD simulation of AhR with **11a** (green: ligand; yellow: AhR).

Remarkably, the establishment of this network is facilitated by the readjustment of the Q383 side chain, adopting distinct conformations in the two poses (Figure 6C). MD simulations supported the structural stability of the two binding modes [RMSD of 2.2 ± 0.1 Å (**M2**) and 1.8 ± 0.2 Å (**M2'**)].

1.5. Biological Activity of the Prepared Adducts

Then, in collaboration with Prof. Haarmann-Stemmann (IUF – Leibniz Research Institute for Environmental Medicine), we studied the potential AhR-stimulating activity of the prepared 6-ICZs. Almost all the tested compounds increased the AhR/XRE-dependent reporter gene activity in hepatoma cells in a dose-dependent manner, with several analogues in the sub-μM range, indolyl 6-ICZs **5** being more promising than the 1,3-dicarbonyls counterparts **4** (Figure 7A). Several adducts also induced the expression of cytochrome P450 (*CYP*) *1A1* and *CYP1B1* in wildtype HaCaT keratinocytes. Notably, the activity was AhR-dependent, as no expression was induced in AhR-deficient (DU26) HaCaT cells. In this regard, 6-ICZs **5a-e**, **5h**, **9**, and **12** were comparable to the reference compounds tapinarof (**T**, 3 μM) and benzo[*a*]pyrene (**BaP**, 2.5 μM, Figure 7A-B). These results are in good agreement with the proposed *in silico* model. Relevantly, the activity of the *N*, *N*'-Me derivative **5j** is reduced by only 2.3-fold compared to its *N*, *N*'-H analog **5e** (Figure 7A). In this regard, MD simulations of the model structure **5j'** pointed out that *N*-methylated ICZs bind to the AhR mimicking the pose of **5c** (**M2'**), retaining the HB network facilitated by the conformational rearrangement of Q383 (Figures 6D). Importantly, none of the 6-ICZ compounds induced apoptotic cell death or cytotoxicity at concentrations of 10 μM, as tested by our collaborator Prof. Gil (UB).

At this point, we envisaged the design of conjugatable AhR ligands as building blocks for dual entities. Molecular modeling studies suggested the incoming indole's C-6 position as a suitable extension point. Indeed, MD simulations confirmed the ability of compound **11a** to bind to AhR, as the alkyl chain protrudes into the bulk solvent without interfering with the AhR heteromeric complex (Figures 6E). This was confirmed as the IC_{50} values of **11a** and **5c** were comparabale (Figure 7A). Considering the agonistic character of our 6-ICZs, we believed that compounds **11b-d** may have potential as AhR dual probes. Accordingly, the 6-ICZ conjugate **11d** was postulated as a PROTAC, as thalidomide is a ligand of the E3 ubiquitin ligase Cereblon.[29] The dimeric species **11b-c** may act as proximity agents or as homo-PROTACs, i.e. two AhR proteins brought in spatial proximity targeting each other, since AhR is also known to serve as an E3 ligase.[30] Treatment of HaCaT cells with adducts **11b-d** caused a transient decline of the AhR protein level, albeit still potently inducing AhR/XRE-dependent luciferase activity and *CYP1A1*/*CYP1B1* gene expression (Figures 7A-B). These results indicated that 6-ICZ

conjugates behave as AhR agonists, which typically induce proteolysis of the receptor after being exported from the nucleus.[31]

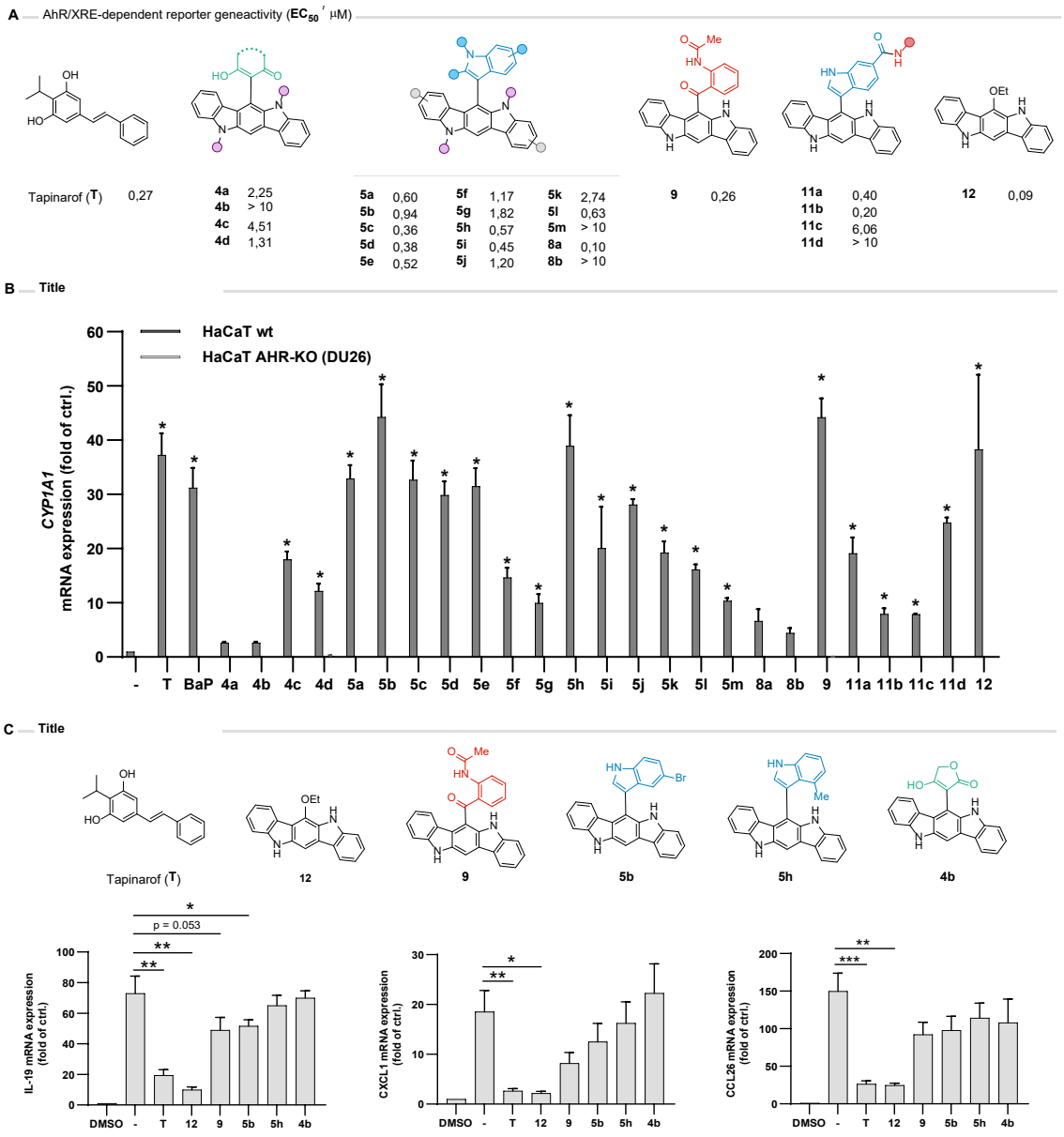

Figure 7. The 6-ICZs bioactivity profile. A) AhR/XRE-dependent reporter gene activity results (EC_{50} - µM). B) *CYP1A1* enzyme activity results. *CYP1A1* induction expressed as fold of 0.1% DMSO control (-) in HaCaT wt cells (grey) *vs*. HaCaT AhR-KO cells (white). Used concentrations. ICZs and Tapinarof (**T**): 3 µM. **BaP**: 2,5 µM C) Anti-inflammatory effect of the 6-ICZs against IL-13 promoted inflammation: Induced gene expression of proinflammatory IL-19, CXCL1, and CCL26 expressed as fold of 0.1% DMSO control. HaCaT keratinocytes were treated with IL-13 (10 ng/mL) for 24 h, then either untreated (-) or treated with positive control **T** (1 µM) or 6-ICZs (1 µM). *$p \leq 0.05$, **$p \leq 0.01$, ***$p \leq 0.001$.

However, co-immunoprecipitation analysis in HaCaT cells revealed the interaction of AhR with Cullin 4B, an essential component of the AhR E3 ubiquitin ligase complex. These results suggested that other parameters may determine the performance of

compounds **11**. Altogether, our convenient synthetic access to AhR-binding conjugates may serve as promising platform for the development of AhR-targeting dual entities.

As the activation of AhR is beneficial for pathologies including chronic inflammatory skin diseases,[32] we assessed the potential anti-inflammatory role of our ligands by co-treating HaCaT keratinocytes with the pro-inflammatory cytokine IL-13 and a selection of 6-ICZs. A 24h treatment with IL-13 alone induced the gene expression of the proinflammatory IL-19, CXCL1 and CCL26,[33] whereas a co-treatment with compound **12** significantly reduced the IL-13-triggered induction of those genes. Notably, compound **12** was slightly more potent than the positive control tapinarof, indicating that our 6-ICZs may potentially serve as scaffolds for the development of novel AhR-targeting anti-inflammatory drugs (Figure 7C).

1.6. Conclusions

To sum up, a rewired MCR with indole 2-CHOs was designed to develop novel AhR activators. This specific, yet exceptionally relevant process, gives unique access to a highly valuable scaffold. The conformational dynamics of these indolocarbazoles revealed the presence of bent species, explaining important structural features regarding their axial chirality. The MD studies confirmed the binding of these ligands to the AhR adaptative pocket allowing the rational design of conjugated derivatives. Finally, these compounds significantly reduced IL-13 induced inflammation. The streamlined synthetic access, tunability, low cytotoxicity, potency and selectivity of our compounds together with the remarkable biomedical consequences of our approach open new avenues in the modulation of AhR, an important, yet underexplored target.

2. Experimental Section

2.1. General Information

All chemicals were purchased from commercial sources and were used as received unless otherwise stated. All reactions were performed under argon in dried glassware, unless otherwise stated. Microwave-irradiated reactions were carried out using a Biotage Initiator Classic. Column chromatographies were carried out on commercial silica gel. Flash column chromatographies were carried out using an Isolera Prime Biotage equipped with dual UV detection over prepacked normal phase silica gel columns (4, 12 and 24 g) or the prepacked reverse phase C18 columns (12g). Thin layer chromatographies (TLC) were done using pre-coated Merk silica gel 60 F254 plates and visualised under UV light at 254 nm and 365 nm. The ^{1}H NMR spectra were recorded on 400 MHz or 600 MHz NMR spectrometers. The ^{13}C NMR spectra were recorded at 100 MHz or 150 MHz. Chemical shifts were reported in ppm(δ) as s (singlet), d (doublet), t (triplet), dd (doublet of doublet), m (multiplet), brs (broad singlet), etc. The residual solvent signals were used as references. HPLC-MS spectra were carried out using the following settings: a) Agilent 1260 Infinity II. The analysis was conducted on a Poroshell 120 EC-C15 (4.6 mm × 50 mm, 2.7 μm) at 40 °C with mobile phase A (H_2O + 0.05% formic acid) and B (ACN + 0.05% formic acid) using a gradient elution and flow rate 0.6 mL/min. The DAD detector was set at 254 or 220 nm, the injection volume was 5 μL and oven temperature was 40 °C. b) Waters 2795 Alliance A ZORBOX Extended-C181 (2.1 mm × 50 mm, 3.5 μm) at 35 °C with mobile phase A (H_2O + 0.05% formic acid) and B (ACN + 0.05% formic acid) using a gradient elution and flow rate 0.7 mL/min. The DAD detector was set to the range of 210-600 nm and the injection volume was 5 μL. The High-Resolution Mass Spectrometry was performed by the Mass Spectrometry and Molecular Characterisation Unit from the Scientific and Technological Centers in Universitat de Barcelona (CCiTUB).

2.2. Results and Discussion

2.2.1. Reaction Conditions Optimisation

The reaction conditions for the generation of ICZs **4-5** was performed using indole-2-carboxalehyde **1a** and 2-methyl-1*H*-indole **3f** (Table S1). We started the optimisation by performing the MCR under inert atmosphere and TFA catalysis, which afforded the desired 6-ICZ **5e** in a good yield (78%, entry A). Moreover, based on

bibliographic precedents we considered the use of *L*-proline as a co-catalyst,[34] which increased the productivity (86%, entry B). The reaction did not take place under *L*-proline catalysis without TFA (entry C). Using metal complexes as Lewis Acids and *L*-proline co-catalysis, the reaction also proceeded to the formation of the expected 6-ICZ **5e** with a clean profile and in an acceptable yield (*ca*. 70%, entry D).[35] The MCR also worked in open air, albeit with lower yields (60%, entry E). Finally, the 6-ICZ **5e** was also generated in basic conditions in a similar yield to the acidic ones (entry F, 75%).

The best conditions were replicated with dimedone **2a** as the nucleophile (Table S1, entries G-H). Conditions in entries B and G were defined as **standard conditions A**, and conditions in entry F were defined as **standard conditions B**.

Table S1. Tested reaction conditions.

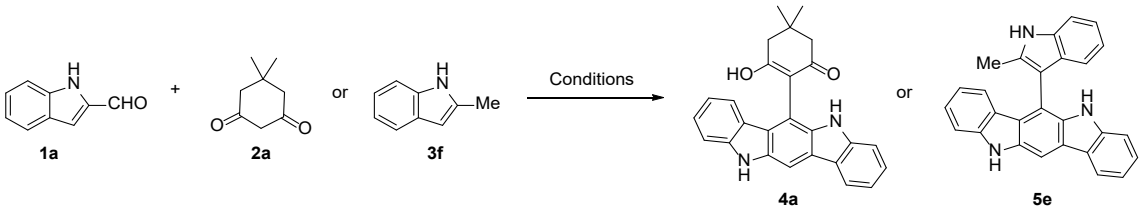

Entry	Nu.	Solvent	Time Temperature	Atm.	Additive (mol %)	Co-catalyst	Product (Yield %)[a]
A	**3f**	EtOH	4 h 80 ºC	Argon	TFA (20%)	-	**5e** (78)
B	**3f**	EtOH	4 h 80 ºC	Argon	TFA (20%)	L-proline (10%)	**5e** (86)
E	**3f**	EtOH	4 h 80 ºC	Argon	-	L-proline (10%)	No conversion
D	**3f**	EtOH	4 h 80 ºC	Argon	$M(OTf)_3$ [b] (10%)	L-proline (10%)	**5e** (*73%*)[c]
E	**3f**	EtOH	4 h 80 ºC	Open air	TFA (20%)	L-proline (10%)	**5e** (60)
F	**3f**	EtOH / H_2O	2 h 90 ºC	Argon	NaOH (10 eq.)	-	**5e** (75)
G	**2a**	EtOH	4 h 80 ºC	Argon	TFA (20%)	L-proline (10%)	**4a** (42)
H	**2a**	Toluene	4 h 110 ºC	Open air	Piperidine (40%)	-	**4a** (50)

[a] Yield obtained after purifying the reaction crude. [b] Three different Lewis Acid have been tested: $In(OTf)_3$ 10% mmol, $Eu(OTf)_3$ 10% mmol, and $Y(OTf)_3$ 10% mmol. All of them provided comparable conversions by LC-MS. [c] After purifying the crude corresponding to the reaction with $In(OTf)_3$, we obtained 73% of yield.

2.2.2. Reaction Scope

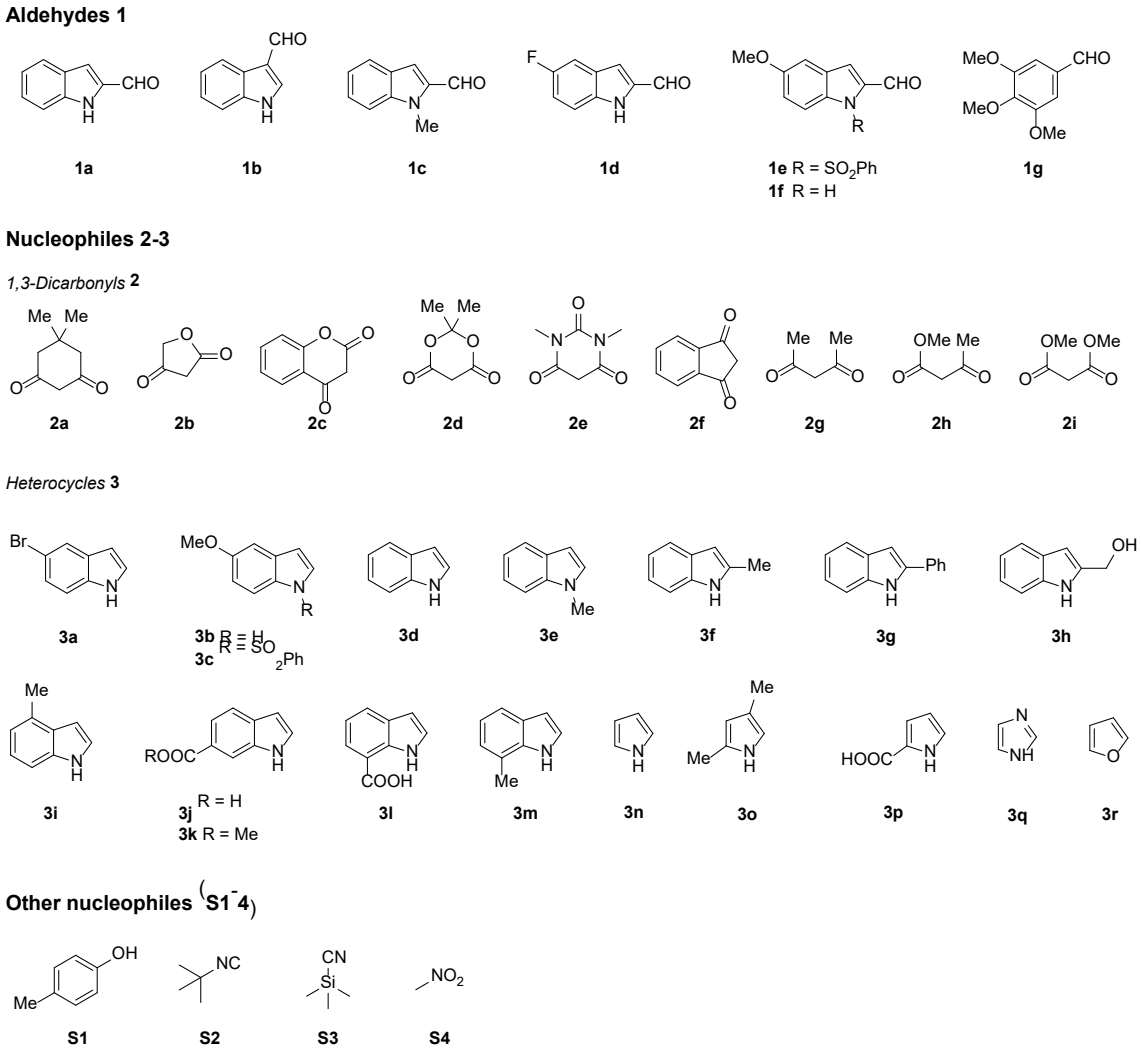

Figure S1. The reactants (commercially available or synthesised) used in the MCR.

2.2.3. Scope Limitations

Depending on the nature of the inputs of the MCR, certain limitations arose resulting in unproductive reactions or alternative results.

Aldehydes

Indole-3-carboxaldehyde 1b did not evolve to the desired indolocarbazoles **4**-**5** in any case. With most 1,3-dicarbonyls **2**, the reaction proceeded to the Knoevenagel adducts **6c-f**. With indoles **3**, in some cases compounds **7** were detected (Figure S2).

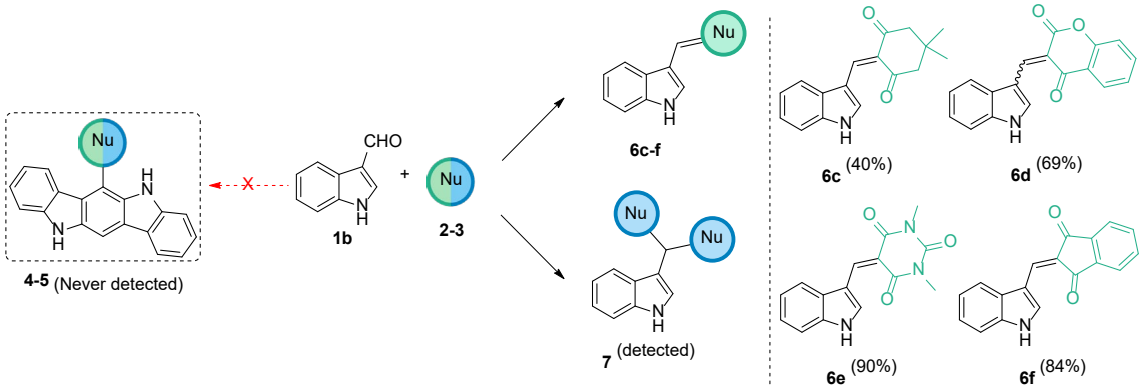

Figure S2. Pathways of the MCR with indole-3-carboxaldehydes depending on the nucleophile and scope of the Knoevenagel adducts **6** with indole-3-carboxalehyde **1b**.

With 5-methoxy-1-(phenylsulfonyl)-1*H*-indole-2-carbaldehyde **1e** and 3,4,5-trimethoxybenzalehyde **1g**, the MCR with 2-methyl-1*H*-indole **3f** did not yield the desired indolocarbazoles **5** under the **standard conditions A**, and instead adducts **7a-b** were isolated from the respective reaction mixtures (Figure S3).

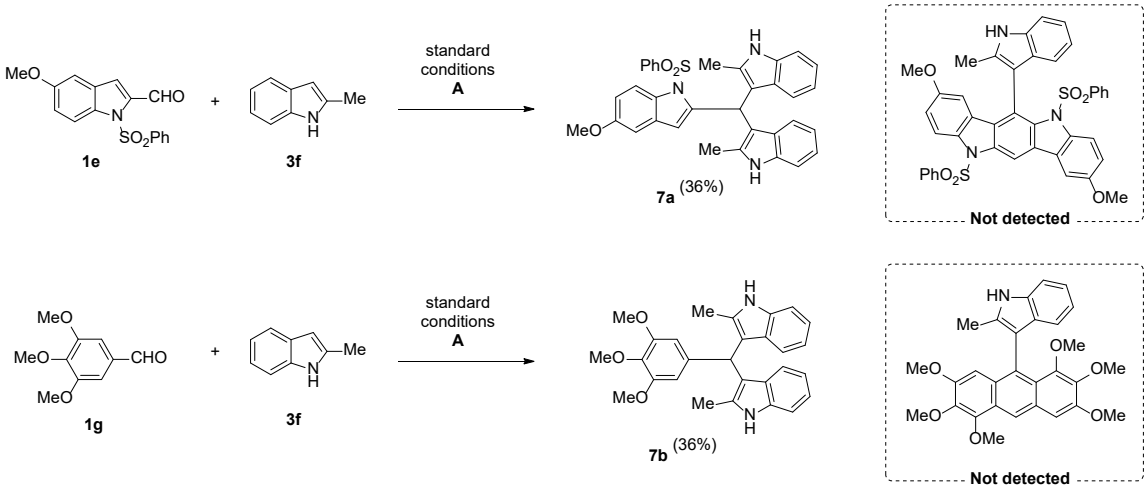

Figure S3. MCR with indole **3f** and aldehydes **1e** and **1g**.

Nucleophiles 2-3 and S1-4

Table S2. Reaction of indole-2-carboxaldehyde **1a** with various nucleophilic species and observed results.

Entry	Input		Observations
A	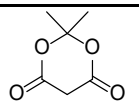	**2d**	No consumption of SM. After increasing the reaction time up to 4 days, a trace of product was detected through LC-MS.
B	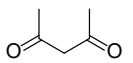	**2g**	No consumption of SM. After increasing the reaction time up to 4 days, a trace of product was detected through LC-MS.
C	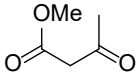	**2h**	No consumption of SM
D	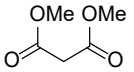	**2i**	No consumption of SM

E	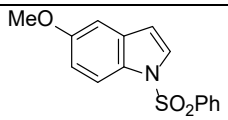	**3c**	Full consumption of **1a** and **3c**. Highly complex crude. LC-MS analysis suggested trace formation of the putative trimer of indole-2-CHO **S5** (Figure S9).
H	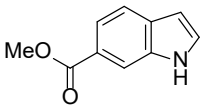	**3k**	Full consumption of **1a** and **3k.** Highly complex crude. LC-MS analysis suggested trace formation of the putative trimer of indole-2-CHO **S5** (Figure S9).
I	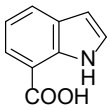	**3l**	Full consumption of **1a** and **3l**. Highly complex crude.
J		**3n**	Full consumption of **1a** and **3n**. Excessive polymerisation and highly complex crudes. Vague evidence on the formation of bis-ICZ **S6** (Figure S4).
K	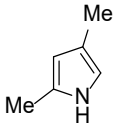	**3o**	Full consumption of **1a** and **3o**. Excessive polymerisation and highly complex crudes. Vague evidence on the formation of bis-ICZ **S7** (Figure S4).
L	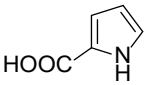	**3p**	Full consumption of **1a** and **3p**. Excessive polymerisation and highly complex crudes.
M		**3q**	No consumption of SM.
N		**3r**	No consumption of SM. Analogous results were observed for thiophene.
O	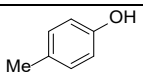	**S1**	Complex mixture.
P		**S2**	^{1}H NMR of the crude suggested mostly unreacted **1a**. LC-MS analysis suggested trace formation of the putative trimer of indole-2-CHO **S5** (Figure S9).
Q	CN^-	**S3**	^{1}H NMR of the crude suggested mostly unreacted **1a**. Formation of cyanohydrin **S9** and trace formation of ether **XX** (Figure S7).
R		**S4**	No consumption of SM.

With pyrroles **3n** and **3o**, the detected masses suggested the formation of the putative bis-indolocarbazole structures. They could not be isolated in their pure forms and fully characterised due to the very low conversion and dirty crudes. However, the ^{1}H NMR spectra of the isolated mg-scale fractions also indicated similar evidence. For instance, for the adduct arising from 2,4-dimethyl pyrrole **3o**, the NMR signals corresponding to the non-symmetric bis-indolocarbazole **S7** with 2 methyl groups, 5 azole NH peaks and the characteristic two singlet peaks of indolocarbazole residues were detectable (Figure S4A). For the assumably symmetric pyrrole **3n**-derived adduct **S6**, the NH signals with 1:2:2 ratio as well as the singlet for the indolocarbazole residue (in blue) were observed (Figure S4B). These hypothetical structures are consistent with the higher reactivity of pyrroles and their tendency to polymerise compared to indoles.

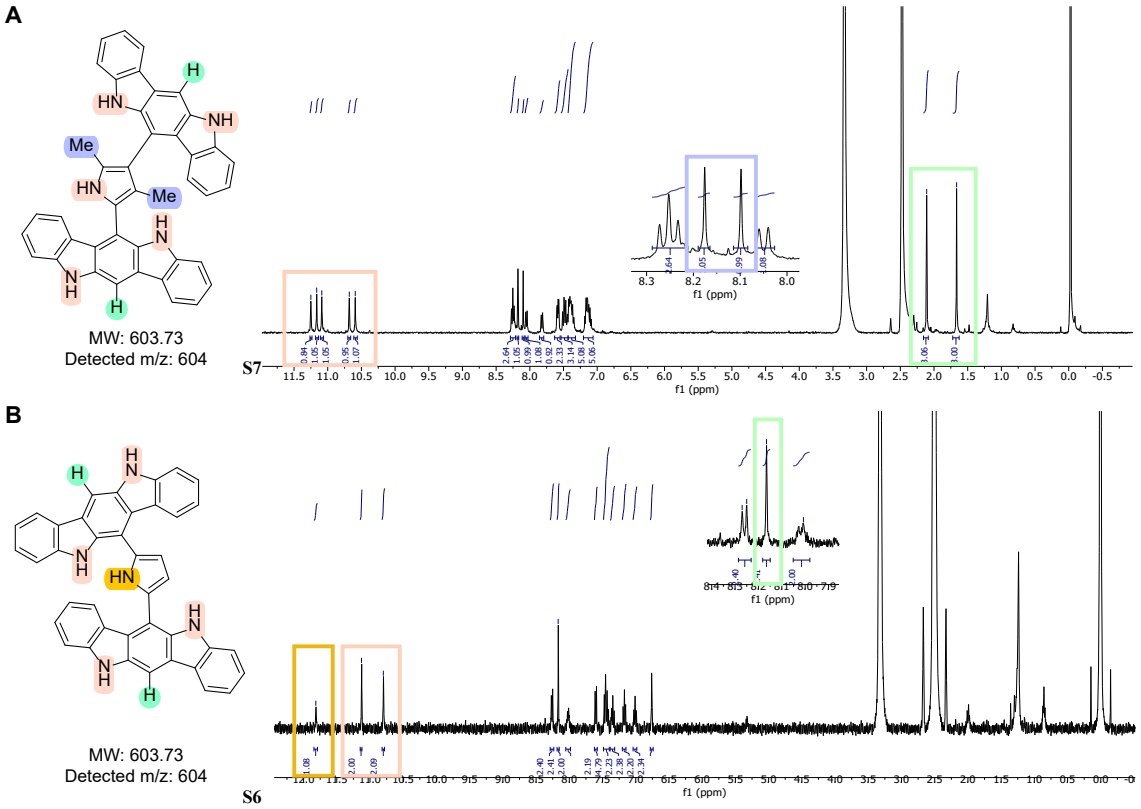

Figure S4. Experimental evidence on the putative bis-ICZ species arising from the interaction indole-2-CHO and pyrroles **3n-o**. A) ^{1}H NMR and LC-MS data of the putative adduct **S7** with 2,4-methyl pyrrole **3o**. B) ^{1}H NMR and LC-MS data of the putative adduct **S6** with pyrrole **3n**.

2.3. Mechanistic Studies

2.3.1. Experimental Observations

Note: all percentages given in this section represent approximate conversion calculated by crude ^{1}H NMR. Percentages in brackets represent isolated yields. Quant. = quantitative conversion. Nd = not detected.

The reaction of indole-2-carboxaldehyde **1a** with indoles **3** mostly only gave the 6-ICZ **5** under the **standard conditions A** and **B** (Figure S5A). However, with lesser nucleophilic species such as 5-bromoindole **3a** and *p*-cresol **S1** under basic conditions, we detected the competitive formation of ICZs **12** and **S8** (Figure S5B-C). Remarkably, we discovered that indole-2-carboxalehyde **1a** auto condensates in basic conditions to give ICZ **Y** quantitively, although in our hands the crude was untreatable to obtain pure samples (Figure S5D and S6). Other electron rich aldehydes did not follow this pattern, and instead proceeded through the expected Cannizzaro rearrangement.

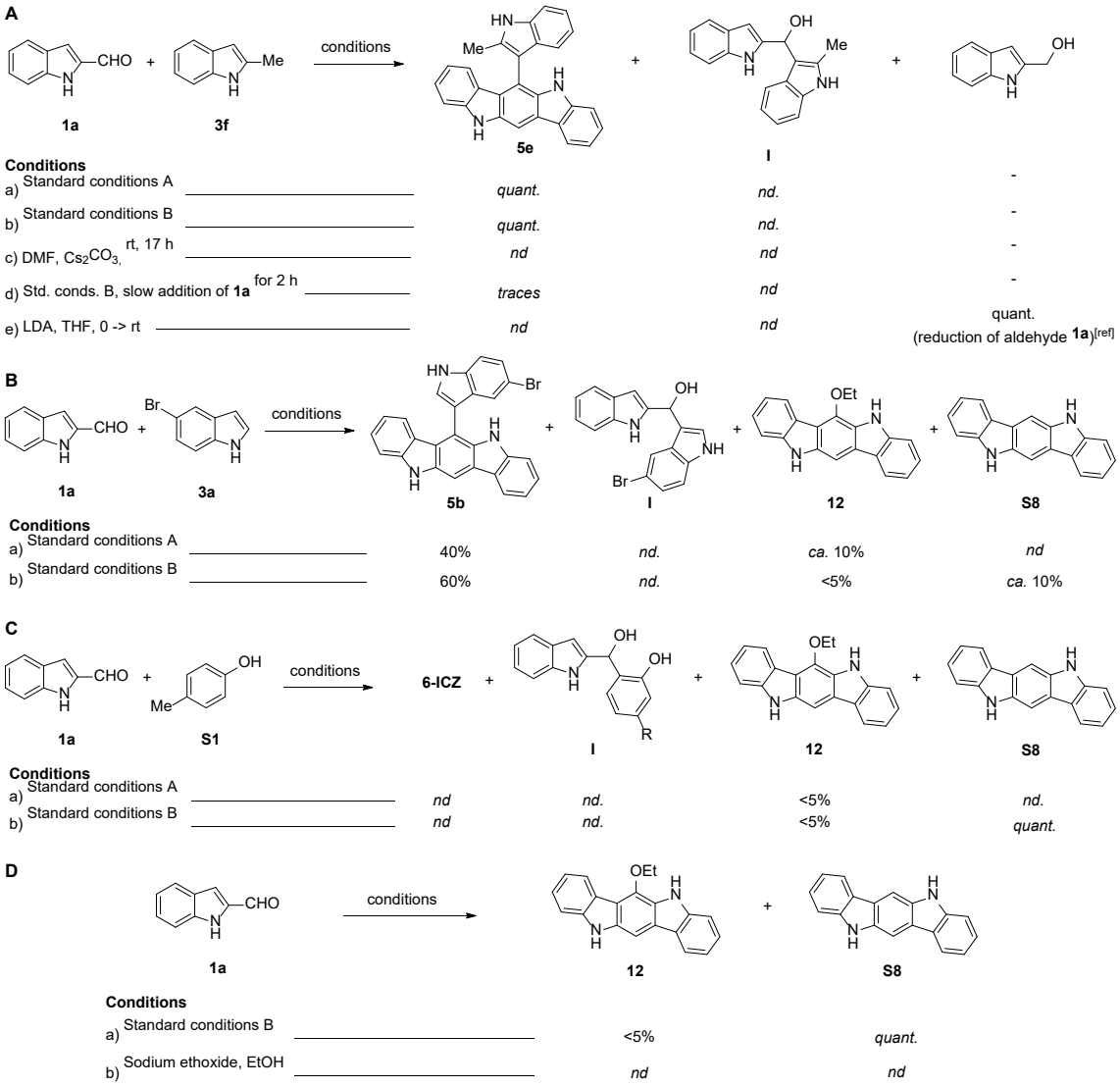

Figure S5. A) Outcomes of the reaction between **1a** and **3f** under different conditions. B) Outcomes of the reaction between **1a** and **3a** under different conditions. C) Outcomes of the reaction between **1a** and **S4** under different conditions. D) Outcomes of the self-condensation of **1a** under different conditions.

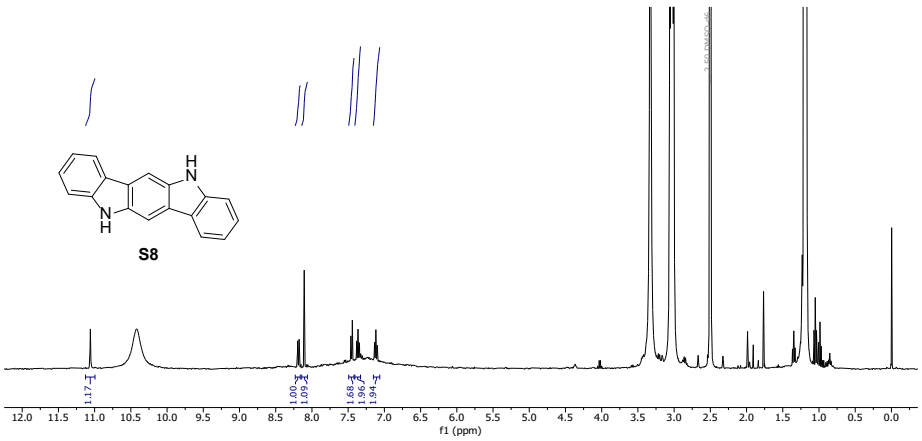

Figure S6. Reaction crude ^{1}H NMR spectra of the auto condensation of indole-2-CHO **1a** under **standard conditions B**. **^{1}H NMR** (400 MHz, DMSO) δ 11.06 (s, 1H), 8.19 (d, *J* = 7.7 Hz, 1H), 8.11 (s, 1H), 7.45 (d, *J* = 8.0 Hz, 1H), 7.36 (ddd, *J* = 8.1, 7.0, 1.2 Hz, 1H), 7.12 (ddd, *J* = 7.4, 6.9, 1.1 Hz, 1H). NMR data are consistent with those previously reported in the literature.

Other nucleophiles were used in the attempt to generate the putative reactive carbinol **I**. With cyanide **S3**, the cyanohydrin **S9** was detected. It was only isolated in trace amounts due to its instability, and it was not converted to the desired 6-ICZ **S11** adduct, likely due to the lower reactivity of the indolyl C-3 due to the electron withdrawing effect of the -CN residue (Figure S7A). With nitromethane **S4**, nitroaldol **S12** was never detected, and the reaction mostly resulted in the dehydration Henry adduct **S13**, which failed to convert to the desired 6-ICZ **S14**, consistently with the proposed reaction mechanism (Figure S7B).

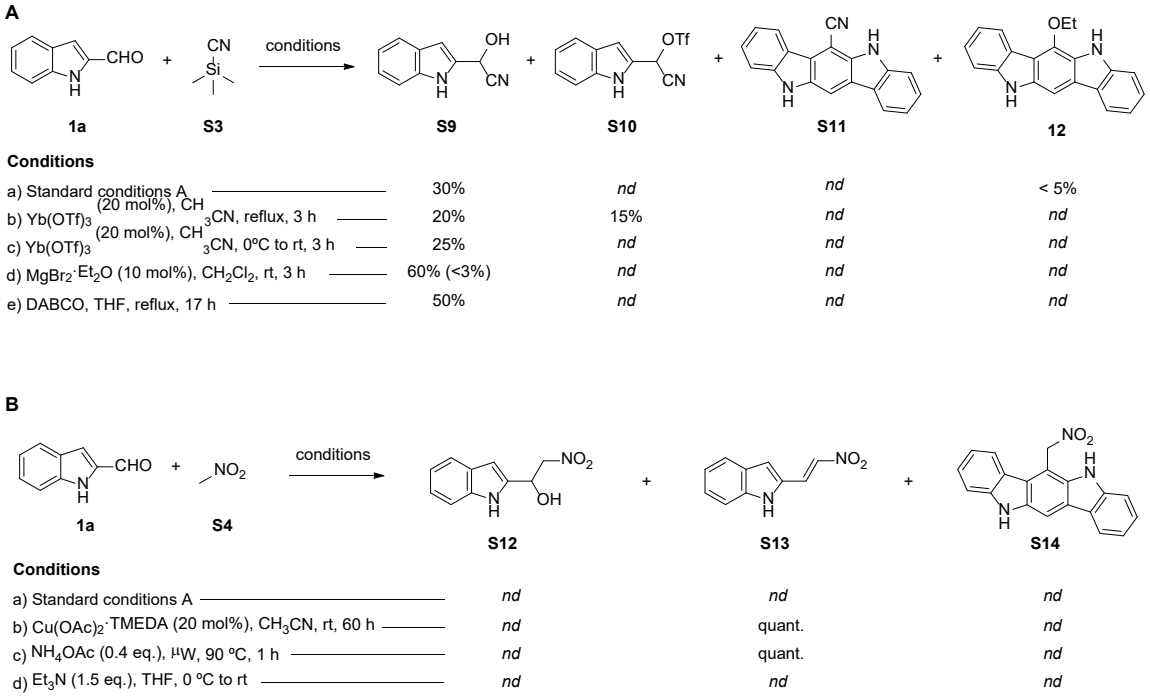

Figure S7. A) Outcomes of the reaction between **1a** and **S3** under different conditions. B) Outcomes of the reaction between **1a** and **S4** under different conditions.

Next, it was proposed to react **1a** with a preformed carbinol. We hypothesised that the intermediate arising from the first nucleophilic attack of the carbinols **3** onto aldehyde **1a** could bypass the domino process to cyclise intramolecularly to adducts **S15**. However, carbinols **3h** and **3i** reacted as usual to give 6-ICZs **5g** and **S16**, respectively. Notably, this means that the intermolecular domino process is faster / preferred over the intramolecular cyclisation (Figure S8).

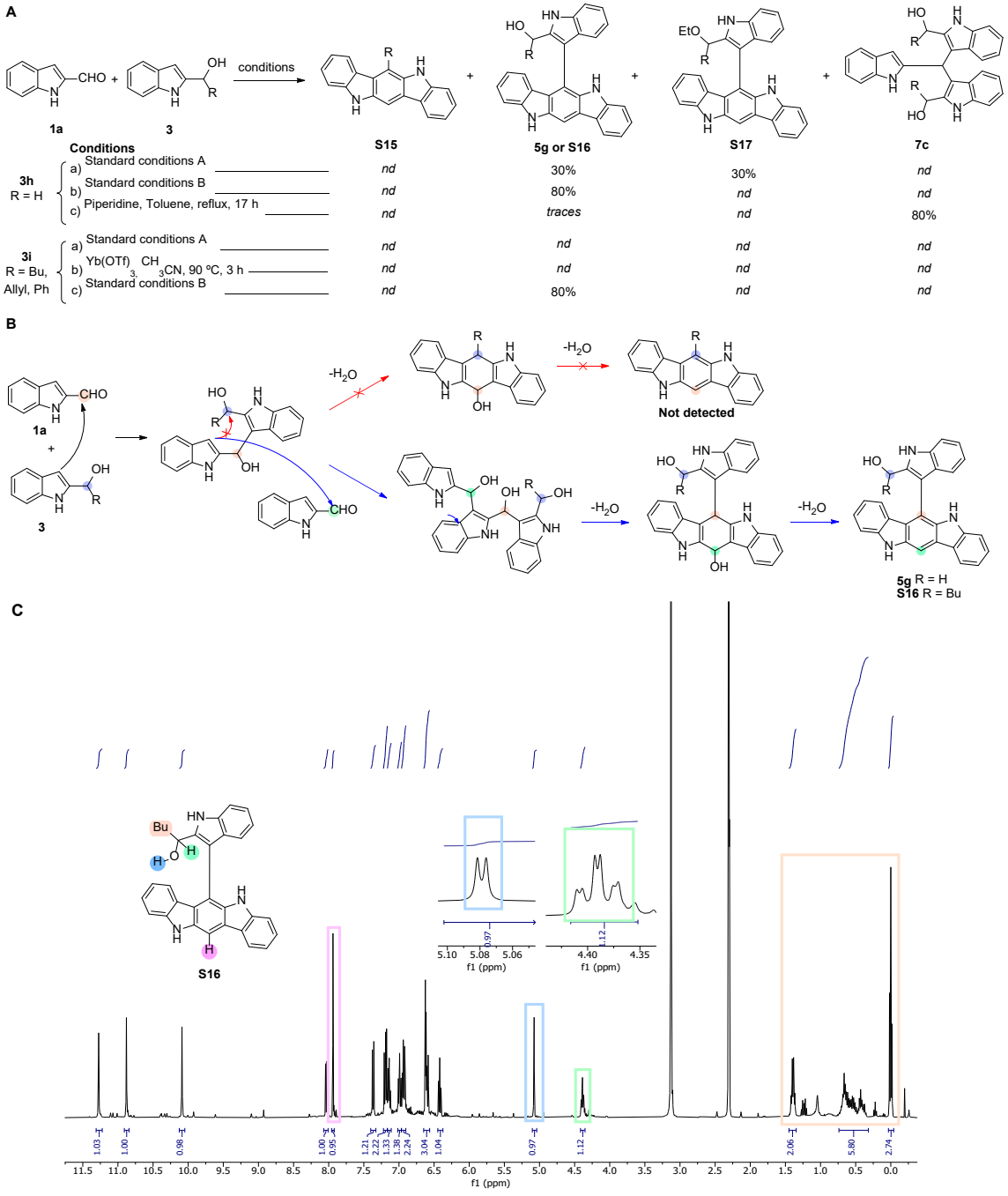

Figure S8. A) Outcomes of the reaction between **1a** and carbinols **3h-i** under different conditions. B) Possible pathways arising from the interaction of **1a** and carbinols **3**. C) ^{1}H NMR of the isolated product **S16**.

In the stated precedent cases, putative trimers of the indole-2-CHO **1a** were observed. In blank experiments, the self-oligomerisation of the substrate was ruled out as no evolution was observed under **standard conditions A**. However, in the presence of a weak nucleophiles complex mixtures were produced, allowing the obtention of samples containing the supposed trimer **S5**. These materials were either detected by LC-MS or were isolated in mg-scale amounts. They were not fully characterised due to their possibly unstable nature and small isolated amounts. Thus, we cannot fully confirm their

structures. However, their ^{1}H NMR and LC-MS data suggested some evidence regarding the presence of putative trimer **S5**. Hypothetically, their formation would arise from a reversible addition of the nucleophile upon the carbonyl, followed by the usual domino process leading to the indolocarbazole trimer or ensuing structures. Their instability may come from the reactive aldehyde moiety in the adduct or from the cationic heterocyclic arrangement (Figure S9).

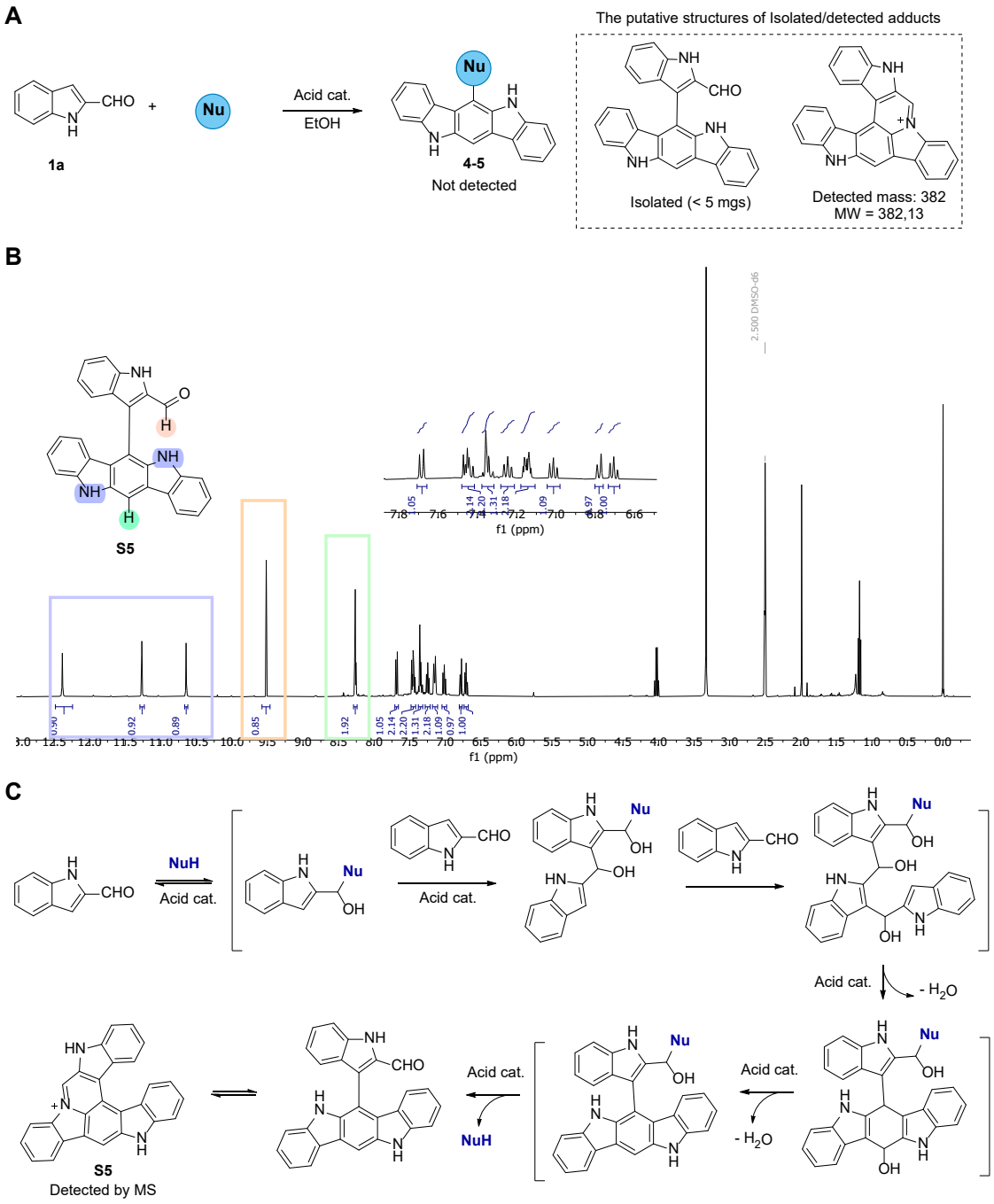

Figure S9. Experimental evidence on the formation of putative trimeric species of **1a**. A) The reaction profiles using weak nucleophiles. B) The ^{1}HNMR of the isolated trimer **S5** from the reaction of **1a** with 4-bromophenol and representative signals. C) The proposed mechanism.

*2.3.2. Computational Studies on the Reactivity Trends of Aldehydes **1a-b** with 1,3-Dicarbonyls **3***

According to the proposed mechanism, indole aldehydes **1** and 1,3-dicarbonyls **2** would react to give carbinol intermediates **I**, which in turn could either react with another equivalent of aldehyde to generate ICZ **4** or dehydrate to form the Knoevenagel adduct **6**. A clear dichotomy was observed, as indole-2-caboxaldehyde **1a** generally proceeded to 6-ICZs **4**, while indole-3-carboxaldehyde **1b** always gave Knoevenagel adducts **6** (Figure S10).

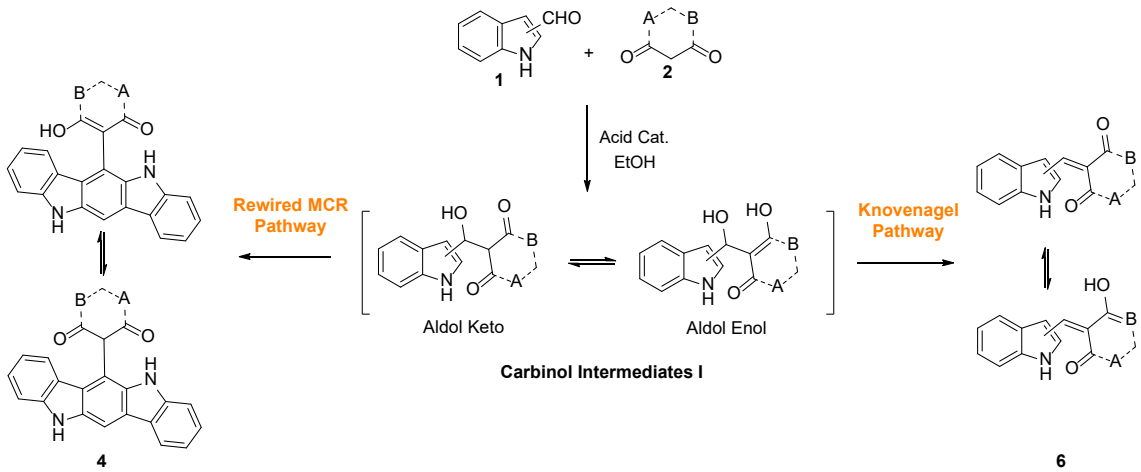

Figure S10. Reaction profile for the formation of indolocarbazoles **4** and Knoevenagel adducts **6** from 1,3-dicarbonyl compounds **2**.

Table S3. Tested combinations of **1a-b** and **2a-f** and results.

	2a	**2b**	**2c**	**2d**	**2e**	**2f**
1a	**4a**	**4f**	**4g**	**4** (traces, by LC-MS)	**6a**	**6b**
1b	**6c**	**6** (traces, by LC-MS)	**6d**	**6** (traces, by LC-MS)	**6e**	**6c**

The results from the reaction of indole-2-CHO **1a** with N-methyl baribituric acid **2e** and indanone **2f** can be explained by the degree of enolisation of the 1,3-dicarbonyl residues in carbinols **I**. In this regard, a lower enolisation degree can relatively slow down the dehydration leading to the Knoevenagel adduct, whereas the opposite trend would favor the ICZ formation, by coordination with an incoming aldehyde (Figure S11).

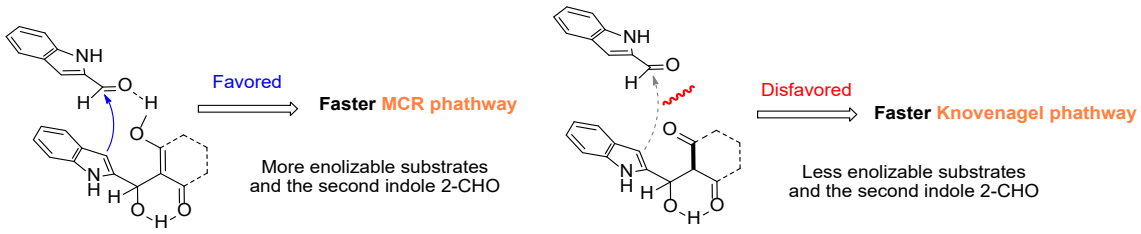

Figure S11. Putative enolisation influences the Indolocarbazole formation.

As for the dichotomy observed between the indole-2-CHO **1a** and indole-3-CHO **1b**, it was hypothesised that the dehydration of the intermediate carbinols **I** was favored in the latter, in agreement with the facilitated activation of indole 3-carbinols due to the more efficient electron donation from the aromatic nucleus (Figure S12).

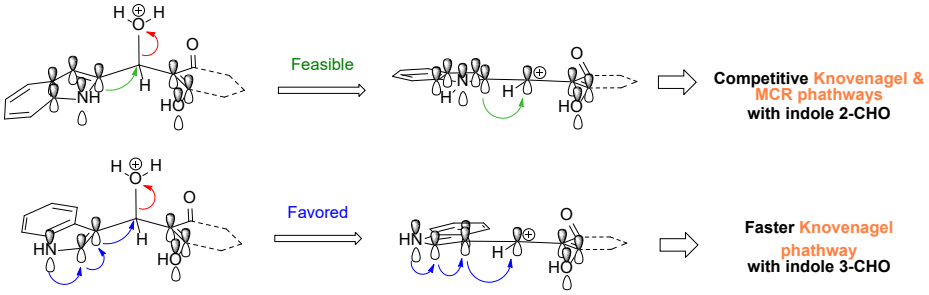

Figure S12. Favored dehydration form indole 3-derivatives in route to Knoevenagel adducts.

Moreover, the stability of intermediates shown in Figure S11 were calculated in vacuo after optimisation through molecular mechanics (MMF) and semiempirical (PM3) methods using a SPARTAN suite (Figures S13-S16).[36] As seen, in practically all series, the Knoevenagel adducts coming from indole-3-CHO are more stable than their 2-CHO counterparts. We anticipate that reaction barriers may parallel the differences in energies, justifying the observed facts in a qualitative manner.

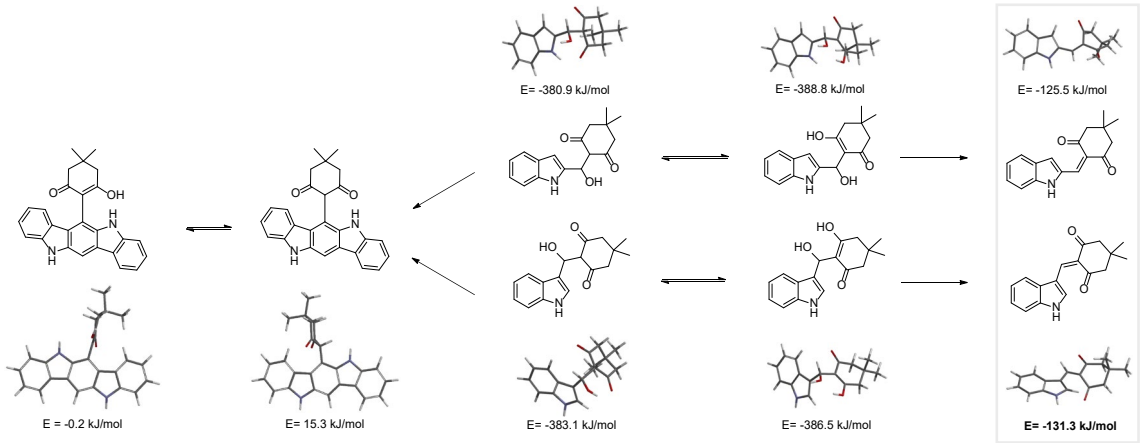

Figure S13. Calculated geometries and energies for the species arising from the interaction of dimedone **2a** with indole 2-CHO **1a** (top) and indole-3-CHO **1b** (bottom).

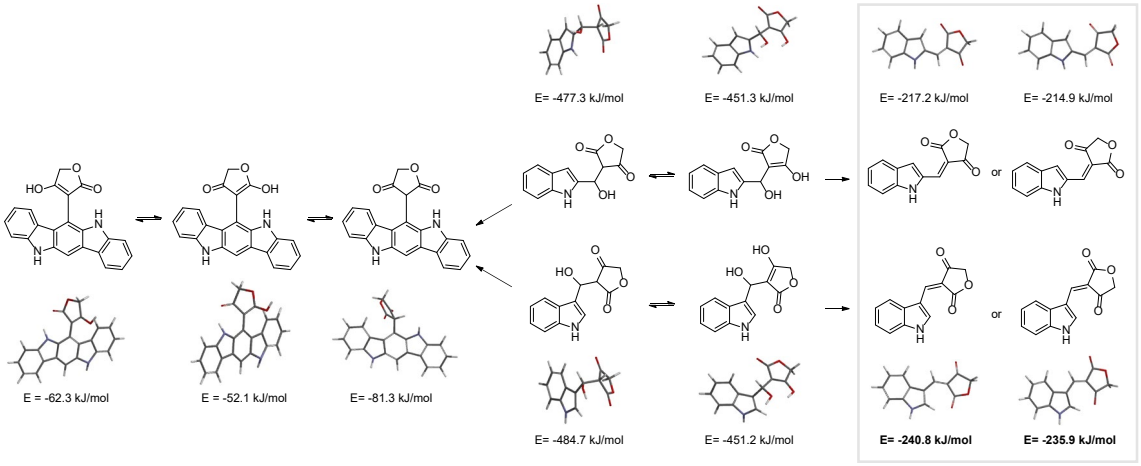

Figure S14. Calculated geometries and energies for the species arising from the interaction of tetronic acid **2b** with indole-2-CHO **1a** (top) and indole-3-CHO **1b** (bottom).

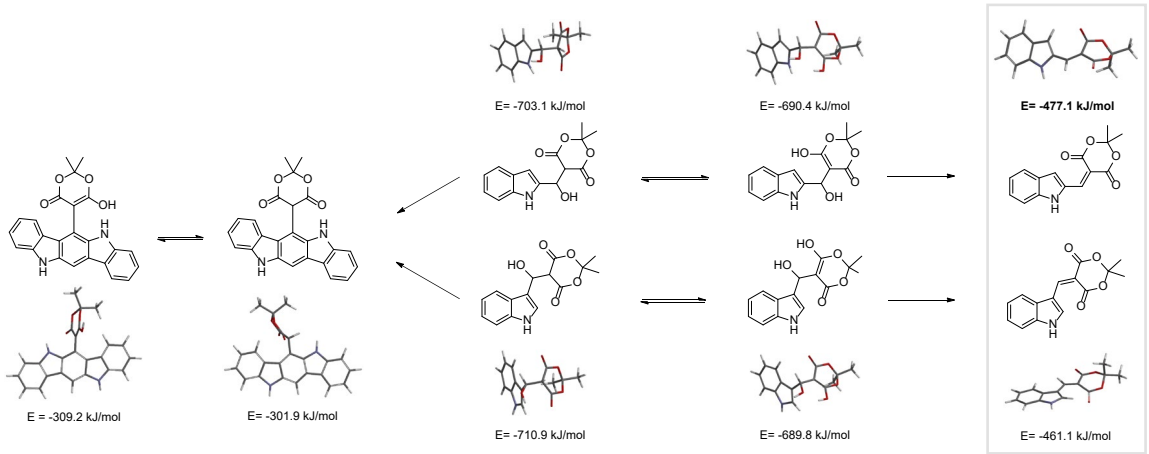

Figure S15. Calculated geometries and energies for the species arising from the interaction of Meldrum's acid **2d** with indole-2-CHO **1a** (top) and indole-3-CHO **1b** (bottom).

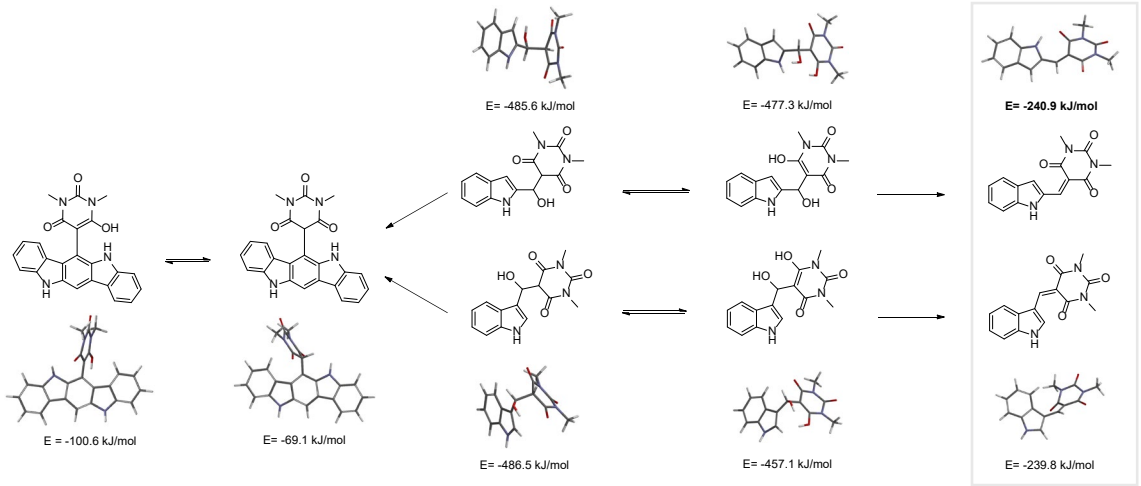

Figure S16. Calculated geometries and energies for the species arising from the interaction of N-methyl barbituric acid **2e** with indole-2-CHO **1a** (top) and indole-3-CHO **1b** (bottom).

2.4. Axial Chirality of 6-ICZs

The rotation of the bond linking the ICZ residue with the substituents at C-6 were studied to determine the axial chirality aspects of the synthesised 6-ICZs (Figure S17).

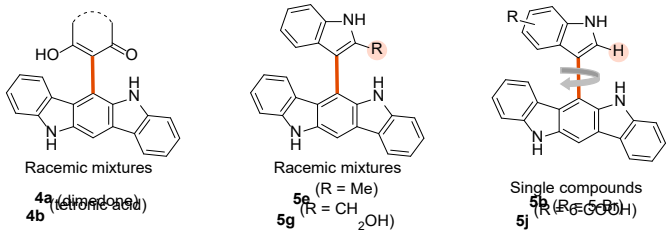

Figure S17. Bond rotation in substituted indolocarbazoles.

2.4.1. Experimental Evidence

Chiral HPLC was run of three selected representatives: **5b**, **5e**, and **5m** (Figure S18). Chiral column**:** CHIRALPAK AD-H (Daicel Chemical Ind.) of 4.6 mm x 250 mm (particle size 5 µm). Chiral HPLC methods (50 minutes): I) Acidic media: CH_3CN + 0.07% TFA / H_2O + 0.1% TFA. II) Neutral media: CH_3CN / H_2O

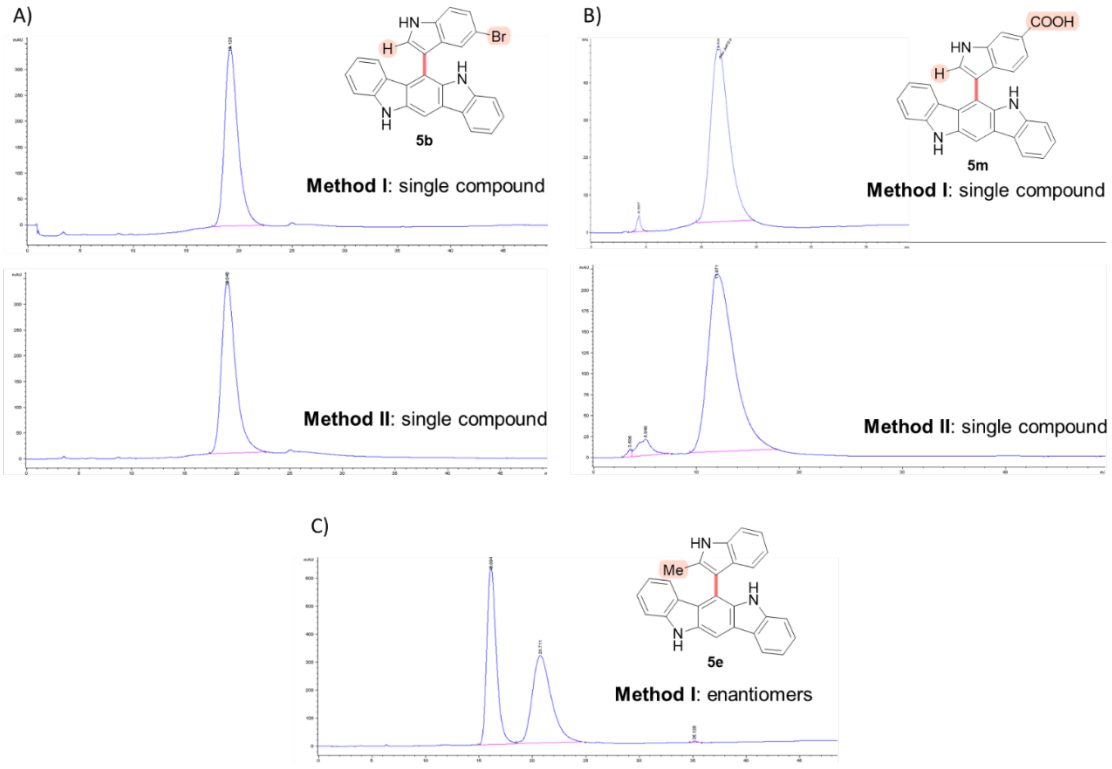

Figure S18. A) The chiral HPLC profile of the compound **5b** (bearing a substituent at **C-5** and no substituent at **C-2**), was studied using two different methods: acidic and neutral media. In both cases a single peak was detected, at 19.128 min (acidic media) and 19.046 min (neutral media), indicating the existence of a single compound. B) The chiral HPLC profile of the compound **5m** (bearing a substituent at **C-6** and no substituent at **C-2**), was studied using the two different methods: acidic and neutral media. In both cases a single peak was detected, at 11.536 min (acidic media) and 11.971 min (neutral media), indicating the existence of a single compound. C) The chiral HPLC profile of compound **5e** (bearing a

substituent at **C-2**) in acidic media showed two peaks, with retention times of 19.094 min and 20.711 min, respectively, indicating the existence of two enantiomers.

Moreover, a representative set of diastereotopic signals was observed on the ^{1}H NMR spectra of compounds **4a**, **4b** and **5g**, suggestive of axial chirality (Figure S19).

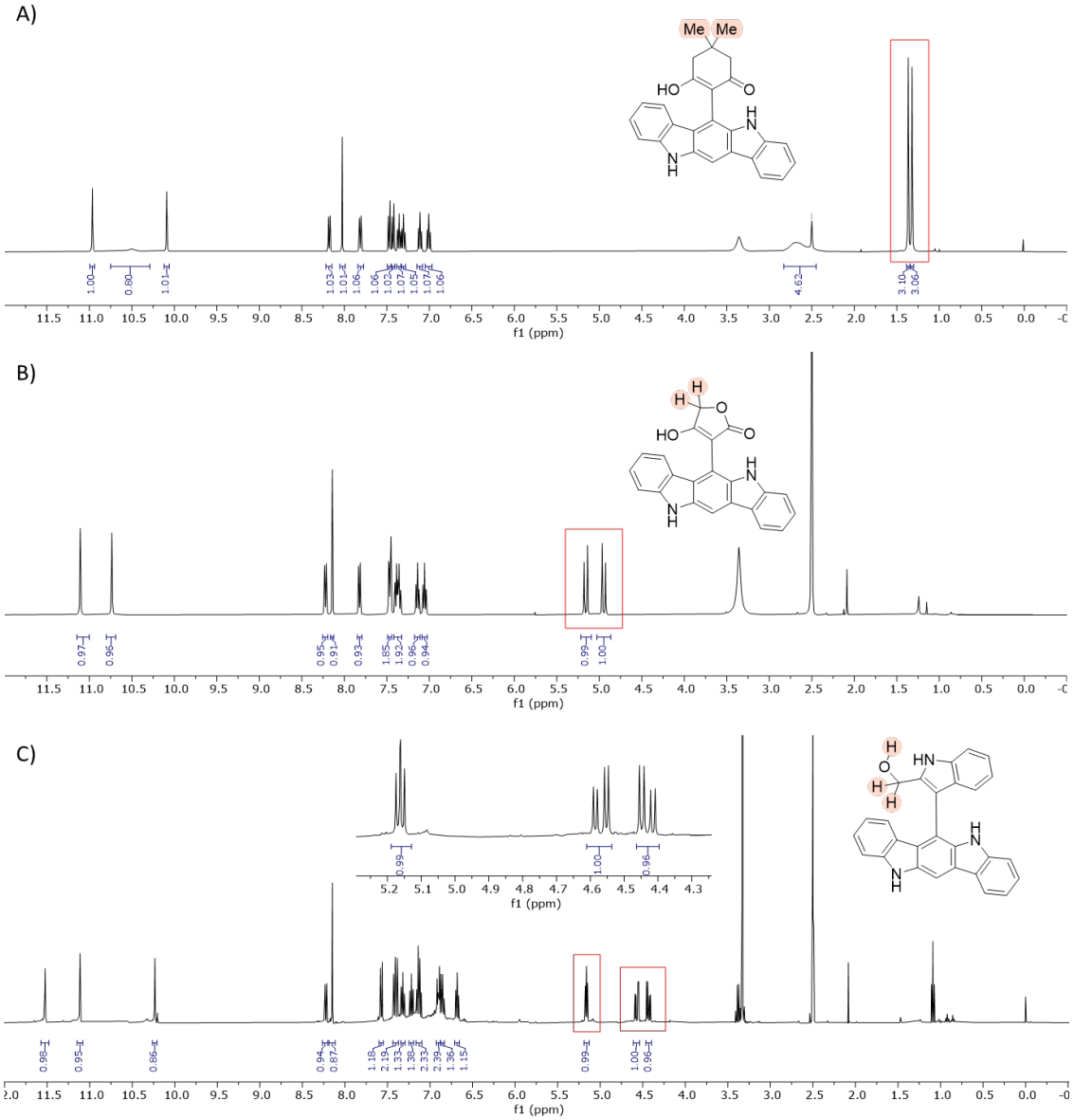

Figure S19. Structures and diastereotopic groups in compounds **4a**, **4b**, and **5g**. A) ^{1}H NMR spectra of **4a**, where the highlighted methyl groups appear as a diastereotopic set of signals. B) ^{1}H NMR spectra of **4b**, where the highlighted hydrogens of the methylene group appear as a diastereotopic set of signals. C) ^{1}H NMR spectra of **5g**, where the highlighted hydrogens of the methylene group and the hydrogen of the hydroxyl group appear as a diastereotopic set of signals.

2.4.2. Variable Temperature NMR Experiment

According to the computational studies, the energy barrier for the rotation of the ICZ-indolyl bond in compound **5c** is *ca.* 20 kcal/mol, and in compound **5e** is *ca*. 35 kcal/mol (Figure S20A). To challenge these computational results, a variable temperature

NMR experiment with compound **5g** was performed to check the coalescence of the diastereotopic ^{1}H NMR signals observed at room temperature (Figure S20B). ^{1}H NMR spectra were acquired at increasing temperatures from 298 K (25 ºC) to 423 K (150 ºC). The upper temperature was determined by the apparatus limitations. Lastly, a spectrum was acquired again at 25 ºC to exclude any degradation after the experiment.

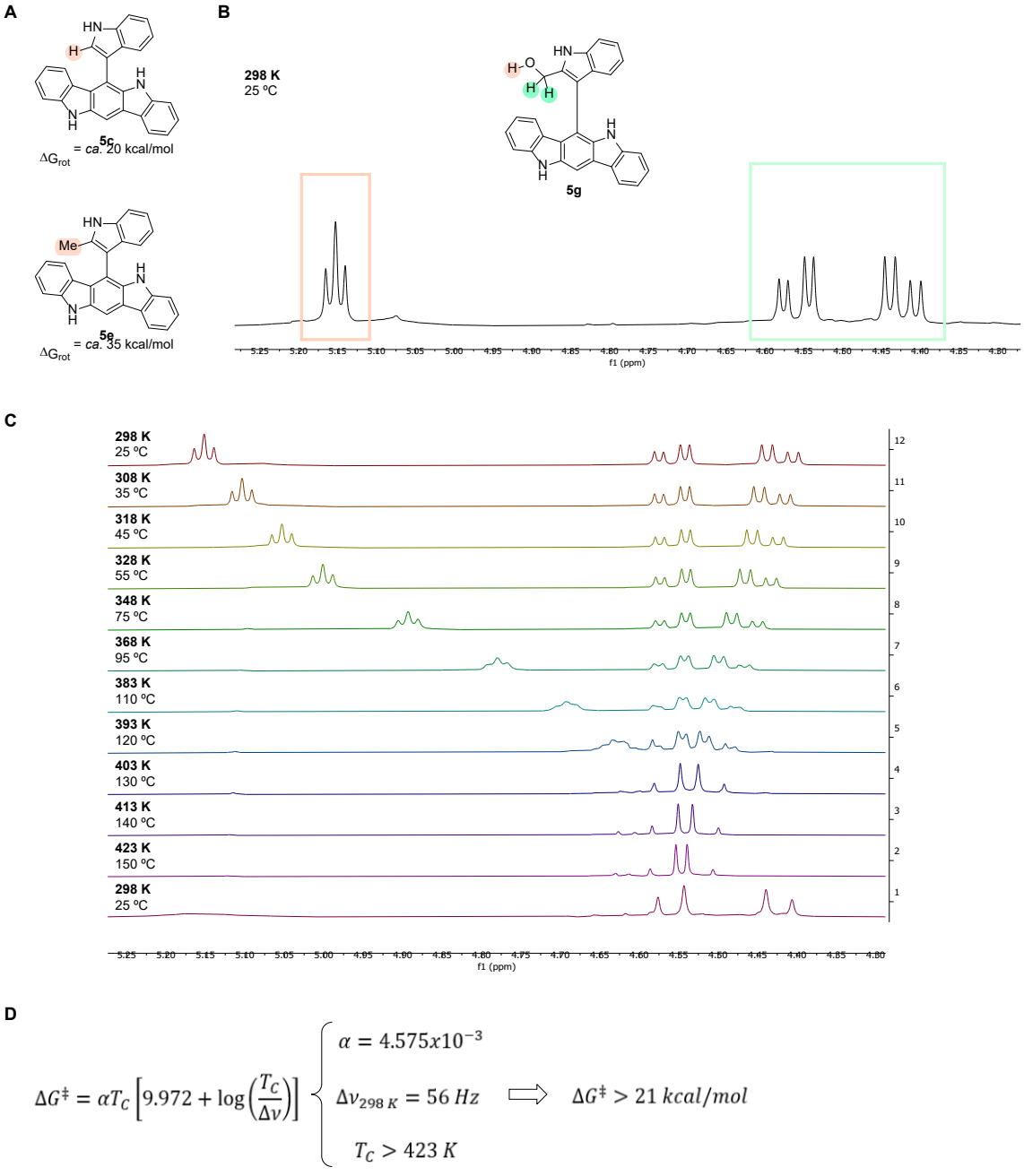

Figure S20. A) Structure and predicted rotation energy barriers of compound **5c** and **5e**. B) Zoomed ^{1}H NMR spectra of compound **5g** at 25 ºC and highlighted diastereotopic signals. C) Variable temperature NMR experiment. D) Energy barrier estimation of compound **5g** using the Eyring equation.

Clearly, no coalescence was observed between the signals of the methylene hydrogens, while we did observe coalescence with the -OH signal between 120 – 130 ºC

(Figure S20C). In this regard, the last spectra at 25 ºC showed loss of multiplicity of the key signals, likely due to -OH exchange. Using the Eyring equation, the energy barrier was roughly estimated to be higher than 21 kcal/mol, consistently with the computational predictions (Figure S20D). Interestingly, the rise of temperature resulted in the downfield shift of one of the methylene hydrogens of about 0.1 ppm (Figure S20C).

2.5. Experimental Procedures and Characterisation Data of Selected Compounds

2.5.1. General Synthetic Procedures

General Procedure A

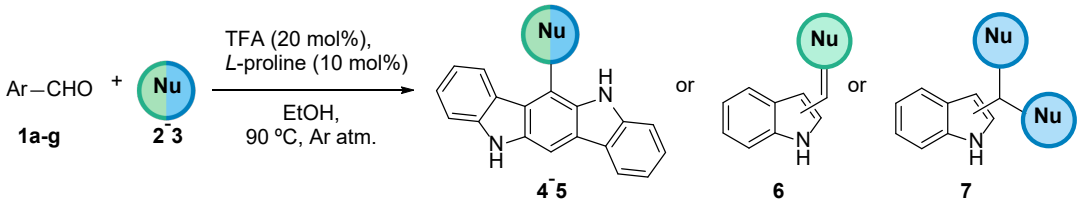

To a solution of aldehyde **1** (2 eq.) and nucleophile **2** or **3** (1 eq.) in EtOH (0.25 M) under inert atmosphere was added *L*-proline (10 mol%) and trifluoroacetic acid (TFA, 20 mol%). The reaction was purged with vacuum-argon cycles, heated to 80 ºC and stirred for 4 h or until full consumption of starting materials (TLC or LC-MS control). The reaction was diluted with EtOAc and washed with a saturated aqueous solution of $NaHCO_3$ and saturated brine. The organic layer was dried over sodium sulfate, filtered, and concentrated under reduced pressure. The residue was purified using the indicated purification protocol to afford the pure products **4**-**6**. In the stated cases, the precipitate formed during the reaction was filtered washing with cold EtOH to afford the pure products **4**-**7**.

General Procedure B

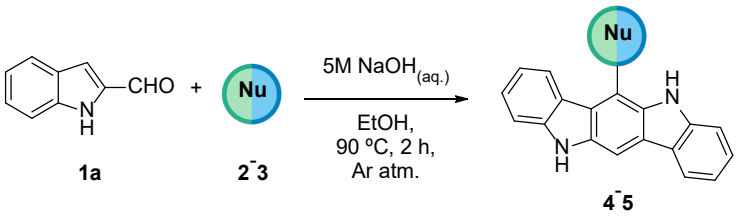

A solution of aldehyde **1a** (2 eq.) and nucleophile **2** or **3** (1 eq.) in EtOH / 5M $NaOH_{(aq)}$ (1:1, 0.25 M) under inert atmosphere was heated to 90 ºC and stirred for 2 h or until full consumption of starting materials (TLC or LC-MS control). The reaction was diluted with EtOAc and washed with 1M aqueous HCl solution, water, and saturated brine. The organic layer was dried over sodium sulfate, filtered, and concentrated under

reduced pressure. The crude was purified using the indicated purification protocol to afford the pure products **4**-**5**.

General Procedure C

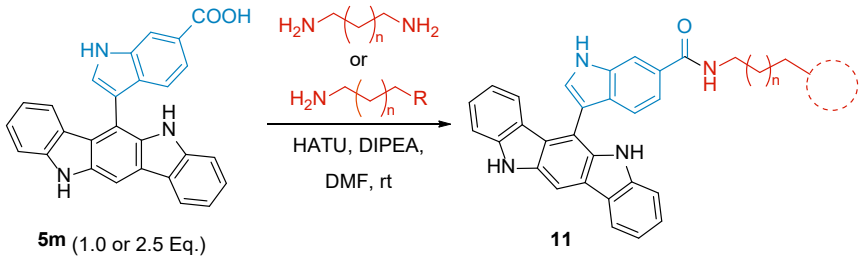

To a solution of **5m** (1.0 eq. or 2.5 eq.) in dry DMF (0.025 M) under argon atmosphere was added DIPEA (1.0 – 5.0 Eq.) and the mixture was stirred for 5 min. Then was added HATU (1.2 eq.) and the mixture was stirred for 10 min. Then was added a solution of the amine or linker (1.1 Eq.) in 0.5 mL of DMF and the reaction was left to stir at room temperature for the indicated time. After reaction completion (TLC control) the reaction mixture was partitioned between EtOAc and water. The aqueous layer was extracted with EtOAc (3 x 40 mL), and the combined organic layers were washed with saturated brine (20 mL), dried over $MgSO_4$, filtered, and concentrated under reduced pressure. The residue was purified via silica gel flash chromatography using the indicated solvent system to afford the pure products **11**.

2.5.2. Characterisation Data of Isolated Compounds

2-(5,11-Dihydroindolo[3,2-*b*]carbazol-6-yl)-3-hydroxy-5,5-dimethylcyclohex-2-en-1-one (4a)

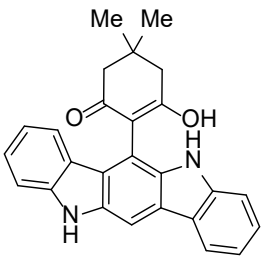

Following the *General Procedure A*, compound **4a** was obtained as an orange powder (83 mg, 42%) from **1a** (145 mg, 1.0 mmol, 2 eq.), **2a** (70 mg, 0.5 mmol, 1.0 eq), *L*-proline (6 mg, 0.05 mmol, 0.1 eq.), and TFA (8 mL, 0.1 mmol, 0.2 eq.) in EtOH (2 mL, 0.25 M) after stirring for 30 min. The product precipitated from the reaction mixture and was isolated by filtration under vacuum. **^{1}H NMR** (400 MHz, DMSO-d_6) δ 10.97 (s, 1H), 10.51 (s, 1H), 10.09 (s, 1H), 8.17 (d, J = 7.7 Hz, 1H), 8.02 (s, 1H), 7.80 (d, J = 7.8 Hz,

1H), 7.47 (dt, *J* = 8.1, 1.0 Hz, 1H), 7.42 (dt, *J* = 8.1, 0.9 Hz, 1H), 7.35 (ddd, *J* = 8.2, 7.1, 1.2 Hz, 1H), 7.30 (ddd, *J* = 8.1, 7.1, 1.2 Hz, 1H), 7.10 (ddd, *J* = 7.9, 7.0, 1.0 Hz, 1H), 7.00 (ddd, *J* = 8.1, 7.1, 1.1 Hz, 1H), 2.85 – 2.40 (m, 4H, overlapped with residual solvent signal), 1.36 (s, 3H), 1.32 (s, 3H). **^{13}C NMR** (101 MHz, DMSO-*d*$_6$) δ 195.80, 172.20, 141.14, 140.94, 135.41, 134.65, 125.13, 124.64, 123.13, 122.87, 121.95, 121.77, 121.70, 120.04, 117.36, 117.18, 110.52, 110.27, 110.02, 98.92, 50.82, 43.28, 31.56, 29.65, 28.40. **HRMS:** m/z calcd for $C_{26}H_{23}N_2O_2^+$ $[M+H]^+$: 395.1754; found 395.1753.

3-(5,11-Dihydroindolo[3,2-b]carbazol-6-yl)-4-hydroxyfuran-2(5H)-one (4b)

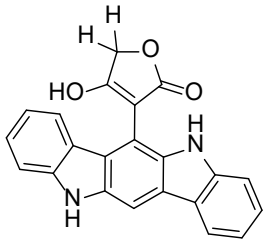

Following the *General Procedure A*, compound **4b** was obtained as dark brown powder (151 mg, 85%) from **1a** (145 mg, 1.0 mmol, 2 eq.), **2b** (50 mg, 0.5 mmol, 1.0 eq), *L*-proline (6 mg, 0.05 mmol, 0.1 eq.), and TFA (8 mL, 0.1 mmol, 0.2 eq.) in EtOH (2 mL, 0.25 M). The product precipitated from the reaction mixture and was isolated by filtration under vacuum. **^{1}H NMR** (400 MHz, DMSO-*d*$_6$) δ 12.43 (s, 1H), 11.11 (s, 1H), 10.74 (s, 1H), 8.22 (d, *J* = 7.7 Hz, 1H), 8.14 (s, 1H), 7.82 (d, *J* = 7.8 Hz, 1H), 7.49 – 7.44 (m, 2H, overlapped signals), 7.42 – 7.33 (m, 2H, overlapped signals), 7.17 – 7.11 (m, 1H), 7.09 – 7.02 (m, 1H), 5.16 (d, *J* = 16.0 Hz, 1H), 4.95 (d, *J* = 15.9 Hz, 1H). **^{13}C NMR** (101 MHz, DMSO-*d*$_6$) δ 176.22, 173.14, 141.24, 140.94, 135.19, 134.83, 125.50, 125.14, 122.60, 122.52, 122.01, 121.82, 121.39, 120.32, 117.64, 117.58, 110.47, 110.23, 104.39, 100.29, 96.58, 67.50. **HRMS:** m/z calcd for $C_{22}H_{15}N_2O_3^+$ $[M+H]^+$: 355.1077; found 355.1068.

6-(5-Methoxy-1*H*-indol-3-yl)-5,11-dihydroindolo[3,2-*b*]carbazole (5a)

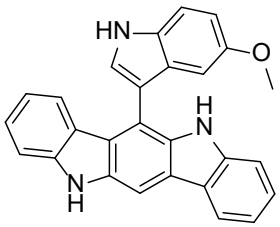

Following the *General Procedure B*, compound **5a** was obtained as a light brown powder (140 mg, 70%) from from **1a** (145 mg, 1.0 mmol, 2 eq.), **3b** (74 mg, 0.5 mmol, 1.0 eq), 5M $NaOH_{(aq)}$ (1 mL, 5 mmol, 10 eq.) in EtOH (1 mL, final concentration 0.25

M) after silica gel flash chromatography purification (DCM / hexane gradient from 0:100 to 40:60 v/v). **^{1}H NMR** (400 MHz, DMSO-d_6) δ 11.43 (d, J = 2.5 Hz, 1H), 11.09 (s, 1H), 10.33 (s, 1H), 8.22 (d, J = 7.4 Hz, 1H), 8.13 (s, 1H), 7.67 (d, J = 2.5 Hz, 1H), 7.52 (dd, J = 8.8, 0.5 Hz, 1H), 7.46 – 7.39 (m, 2H, overlapped signals), 7.32 (ddd, J = 8.2, 7.0, 1.2 Hz, 1H), 7.24 (ddd, J = 8.2, 7.0, 1.2 Hz, 1H), 7.11 (ddd, J = 8.0, 7.0, 1.0 Hz, 1H), 7.07 (d, J = 8.1 Hz, 1H), 6.85 (dd, J = 8.8, 2.5 Hz, 1H), 6.73 (ddd, J = 8.1, 7.1, 1.1 Hz, 1H), 6.46 (d, J = 2.4 Hz, 1H), 3.42 (s, 3H). **^{13}C NMR** (101 MHz, DMSO-d_6) δ 153.89, 141.73, 141.69, 135.97, 135.45, 132.17, 127.66, 125.99, 125.69, 125.27, 123.22, 123.19, 122.62, 122.44, 121.91, 120.62, 118.00, 117.42, 113.07, 112.16, 111.48, 111.34, 110.50, 110.45, 101.66, 99.51, 55.63. **HRMS:** m/z calcd for $C_{27}H_{20}N_3O^+$ $[M+H]^+$: 402.1601; found 402.1606.

6-(5-Bromo-1*H*-indol-3-yl)-5,11-dihydroindolo[3,2-*b*]carbazole (5b)

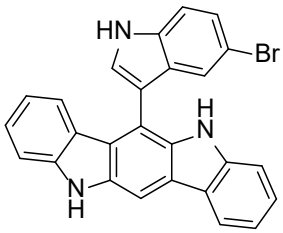

Following the *General Procedure A*, compound **5b** was obtained as a yellow powder (155 mg, 42%), from **1a** (290 mg, 2.0 mmol, 2 eq.), **3a** (196 mg, 1 mmol, 1 eq), *L*-proline (12 mg, 0.1 mmol, 0.1 eq.), and TFA (16 mL, 0.2 mmol, 0.2 eq.) in EtOH (4 mL, 0.25 M) after silica gel flash chromatography purification (DCM / hexane gradient from 0:100 to 50:50 v/v). The title compound **5b** crystallised from the column fractions containing *ca.* 50:50 DCM / hexane mixture (v/v). The crystals were filtered washing with DCM, dried under high vacuum and used for NMR characterisation and X-Ray crystallography. The residual DCM present in the sample and observed in the NMR copies could not be removed even under high vacuum. **^{1}H NMR** (400 MHz, DMSO-d_6) δ 11.80 (d, J = 2.5 Hz, 1H), 11.15 (s, 1H), 10.40 (s, 1H), 8.23 (d, J = 7.8 Hz, 1H), 8.16 (s, 1H), 7.80 (d, J = 2.4 Hz, 1H), 7.61 (dd, J = 8.6, 0.6 Hz, 1H), 7.44 (dt, J = 8.0, 0.9 Hz, 1H), 7.41 (dt, J = 8.1, 1.0 Hz, 1H), 7.33 (ddd, J = 8.2, 7.0, 1.2 Hz, 2H), 7.31 (dd, J = 8.6, 2.0 Hz, 1H), 7.25 (ddd, J = 8.2, 7.0, 1.2 Hz, 1H), 7.12 (ddd, J = 8.0, 7.0, 1.1 Hz, 1H), 7.07 (d, J = 1.9 Hz, 1H), 6.97 (d, J = 8.1 Hz, 1H), 6.74 (ddd, J = 8.0, 7.1, 1.0 Hz, 1H). **^{13}C NMR** (101 MHz, DMSO-d_6) δ 141.75, 141.70, 135.88, 135.78, 135.55, 129.23, 127.08, 125.80, 125.41, 124.35, 123.18, 122.99, 122.71, 121.99, 121.88, 121.82, 120.70, 118.10,

117.59, 114.48, 112.06, 111.42, 110.69, 110.39, 110.09, 99.99. **HRMS:** m/z calcd for $C_{26}H_{17}N_3Br^+$ $[M+H]^+$: 450.0600, 452.0580; found 450.0613, 452.0592.

6-(1-Methyl-1*H*-indol-3-yl)-5,11-dihydroindolo[3,2-*b*]carbazole (5d)

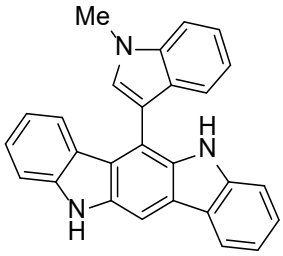

Following the *General Procedure A*, compound **5d** was obtained as an off-white powder (60 mg, 31%) from **1a** (145 mg, 1 mmol, 2 eq.), **3e** (66 mg, 0.5 mmol, 1 eq.), *L*-proline (6 mg, 0.05 mmol, 0.1 eq.), and TFA (8 mL, 0.1 mmol, 0.2 eq.) in EtOH (2 mL, 0.25 M) after silica gel flash chromatography purification (DCM / hexane gradient from 0:100 to 50:50 v/v). **^{1}H NMR** (400 MHz, DMSO-d_6) δ 11.11 (s, 1H), 10.38 (s, 1H), 8.22 (d, J = 7.8 Hz, 1H), 8.13 (s, 1H), 7.73 (s, 1H), 7.66 (dt, J = 8.3, 0.9 Hz, 1H), 7.45 – 7.37 (m, 2H, overlapped signals), 7.32 (ddd, J = 8.2, 7.0, 1.2 Hz, 1H), 7.29 – 7.19 (m, 2H, overlapped signals), 7.12 (ddd, J = 8.0, 7.0, 1.1 Hz, 1H), 7.04 – 6.98 (m, 2H, overlapped signals), 6.95 (ddd, J = 7.9, 6.8, 0.9 Hz, 1H), 6.68 (ddd, J = 8.1, 7.1, 1.0 Hz, 1H), 4.04 (s, 3H). **^{13}C NMR** (101 MHz, DMSO-d_6) δ 141.76, 141.62, 137.48, 135.98, 135.52, 129.67, 127.62, 125.74, 125.28, 123.22, 123.11, 122.62, 122.41, 121.93, 121.82, 120.67, 120.33, 119.56, 118.04, 117.46, 111.33, 110.78, 110.61, 110.52, 109.82, 99.64, 33.31. **HRMS:** m/z calcd for $C_{27}H_{19}N_3^{\cdot+}$ $[M^{\cdot}]^+$: 385.1573; found 385.1576.

6-(2-Methyl-1*H*-indol-3-yl)-5,11-dihydroindolo[3,2-*b*]carbazole (5e)

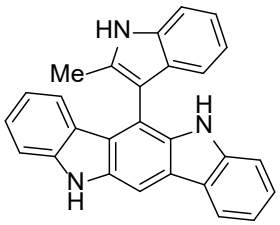

Following the *General Procedure A*, compound **5e** was obtained as a light brown powder (1.65 g, 86%) from **1a** (1.46 g, 10.06 mmol, 2 eq.), **3f** (0.66 g, 5.03 mmol, 1.0 eq), *L*-proline (58 mg, 0.5 mmol, 0.1 eq.), and TFA (77 mL, 1 mmol, 0.2 eq.) in EtOH (10 mL, 0.5 M) after silica gel flash chromatography purification (DCM / hexane gradient from 0:100 to 40:60 v/v). **^{1}H NMR** (400 MHz, DMSO-d_6) δ 11.40 (s, 1H), 11.10 (s, 1H), 10.29 (s, 1H), 8.22 (d, J = 7.8 Hz, 1H), 8.14 (s, 1H), 7.50 (d, J = 8.1 Hz, 1H), 7.46 – 7.37

(m, 2H, overlapped signals), 7.31 (ddd, *J* = 8.2, 7.0, 1.2 Hz, 1H), 7.23 (ddd, *J* = 8.2, 7.0, 1.2 Hz, 1H), 7.11 (m, 2H), 6.94 (d, *J* = 7.9 Hz, 1H), 6.91 – 6.80 (m, 2H), 6.71 (ddd, *J* = 8.0, 7.0, 1.0 Hz, 1H), 2.25 (s, 3H). **^{13}C NMR** (101 MHz, DMSO-*d*$_6$) δ 141.73, 141.70, 136.45, 135.88, 135.41, 134.19, 128.33, 125.64, 125.23, 123.25, 123.23, 122.53, 122.20, 122.10, 120.92, 120.62, 119.20, 119.06, 117.95, 117.59, 111.40, 111.35, 110.75, 110.48, 107.78, 99.60, 12.89. **HRMS:** m/z calcd for $C_{27}H_{20}N_3^+$ $[M+H]^+$: 386.1652; found 386.1600.

(3-(5,11-Dihydroindolo[3,2-*b*]carbazol-6-yl)-1*H*-indol-2-yl)methanol (5g)

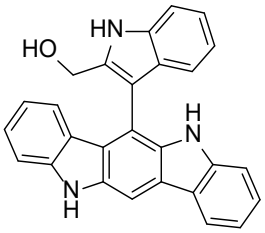

Following the *General Procedure B*, compound **5g** was obtained as an off-white solid (180 mg, 45%) from **1a** (290 mg, 2 mmol, 2 eq.), **3h** (147 mg, 1 mmol, 1 eq.), 5M $NaOH_{aq.}$ (2 mL, 10 mmol, 10 eq.) in EtOH (2 mL, final concentration 0.25 M) after silica gel flash chromatography purification (DCM / hexane gradient from 50:50 to 100:0 v/v). **^{1}H NMR** (400 MHz, DMSO-*d*$_6$) δ 11.52 (s, 1H), 11.11 (s, 1H), 10.23 (s, 1H), 8.22 (d, *J* = 7.8 Hz, 1H), 8.15 (s, 1H), 7.57 (dt, *J* = 8.2, 0.9 Hz, 1H), 7.44 – 7.37 (m, 2H, overlapped signals), 7.32 (ddd, *J* = 8.1, 7.0, 1.2 Hz, 1H), 7.22 (ddd, *J* = 8.2, 7.1, 1.2 Hz, 1H), 7.16 – 7.10 (m, 2H, overlapped signals), 6.93 – 6.88 (m, 2H, overlapped signals), 6.85 (ddd, *J* = 7.9, 6.7, 1.0 Hz, 1H), 6.68 (ddd, *J* = 8.0, 7.1, 1.0 Hz, 1H), 5.16 (dd, *J* = 5.5, 4.6 Hz, 1H), 4.57 (dd, *J* = 13.2, 4.6 Hz, 1H), 4.43 (dd, *J* = 13.1, 5.4 Hz, 1H). **^{13}C NMR** (101 MHz, DMSO-*d*$_6$) δ 141.73, 141.64, 137.48, 136.79, 135.89, 135.45, 127.76, 125.71, 125.26, 123.26, 123.16, 122.56, 122.34, 122.23, 121.59, 120.66, 119.70, 119.29, 118.07, 117.54, 112.05, 111.37, 110.45, 110.26, 107.25, 99.76, 56.25. **HRMS:** m/z calcd for $C_{27}H_{19}N_3O^{\cdot+}$ $[M^{\cdot}]^+$: 401.1523; found 401.1524.

6-(4-Methyl-1*H*-indol-3-yl)-5,11-dihydroindolo[3,2-*b*]carbazole (5h)

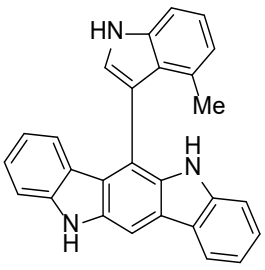

Following the *General Procedure A*, compound **5h** was obtained as a pale brown solid (300 mg, 38%) from **1a** (580 mg, 4 mmol, 2 eq.), **3j** (262 mg, 2 mmol, 1 eq.), *L*-proline (23 mg, 0.2 mmol, 0.1 eq.), and TFA (31 mL, 0.4 mmol, 0.2 eq.) in EtOH (8 mL, 0.25 M) after silica gel flash chromatography purification (DCM / hexane gradient from 0:100 to 50:50 v/v). **^{1}H NMR** (400 MHz, DMSO-d_6) δ 11.46 (s, 1H), 11.04 (s, 1H), 10.36 (s, 1H), 8.21 (d, J = 7.8 Hz, 1H), 8.11 (s, 1H), 7.48 (d, J = 2.4 Hz, 1H), 7.45 – 7.37 (m, 3H, overlapped signals), 7.31 (ddd, J = 8.2, 7.0, 1.2 Hz, 1H), 7.21 (ddd, J = 8.2, 7.0, 1.3 Hz, 1H), 7.13 – 7.04 (m, 3H, overlapped signals), 6.84 (d, J = 7.9 Hz, 1H), 6.71 – 6.63 (m, 2H, overlapped signals), 1.65 (s, 3H). **^{13}C NMR** (101 MHz, DMSO-d_6) δ 141.76, 141.63, 137.25, 136.41, 135.48, 130.58, 126.45, 125.60, 125.26, 124.73, 123.75, 123.38, 123.21, 122.22, 121.82, 121.51, 120.66, 120.49, 117.92, 117.62, 113.27, 111.37, 110.79, 110.57, 110.21, 99.63, 18.62. **HRMS:** m/z calcd for $C_{27}H_{20}N_3^+$ $[M+H]^+$: 386.1652; found 386.1664.

6-(7-Methyl-1*H*-indol-3-yl)-5,11-dihydroindolo[3,2-*b*]carbazole (5i)

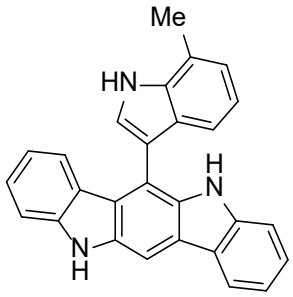

Following the *General Procedure B*, compound **5i** was obtained as white powder (300 mg, 39%), from **1a** (580 mg, 4 mmol, 2 eq.), **3o** (262 mg, 2 mmol, 1.0 eq), 5M $NaOH_{aq.}$ (4 mL, 20 mmol, 10 eq.) in EtOH (4 mL, final concentration 0.25 M) after silica gel flash chromatography purification (DCM / hexane gradient from 20:80 to 80:20 v/v). **^{1}H NMR** (400 MHz, DMSO-d_6) δ 11.54 (d, J = 2.5 Hz, 1H), 11.09 (s, 1H), 10.32 (s, 1H), 8.24 – 8.19 (m, 1H), 8.12 (d, J = 0.5 Hz, 1H), 7.69 (d, J = 2.5 Hz, 1H), 7.44 – 7.38 (m, 2H, overlapped signals), 7.31 (ddd, J = 8.2, 7.0, 1.2 Hz, 1H), 7.22 (ddd, J = 8.2, 7.1, 1.2 Hz, 1H), 7.11 (ddd, J = 7.9, 7.0, 1.1 Hz, 1H), 7.05 – 7.01 (m, 1H), 6.99 (ddd, J = 5.7, 2.4, 1.0 Hz, 1H), 6.87 – 6.79 (m, 2H, overlapped signals), 6.69 (ddd, J = 8.0, 7.1, 1.0 Hz, 1H), 2.68 – 2.61 (m, 3H). **^{13}C NMR** (101 MHz, DMSO-d_6) δ 141.74, 141.66, 136.54, 135.95, 135.52, 127.02, 125.65, 125.23, 124.96, 123.24, 123.20, 122.59, 122.37 (2 overlapped signals), 121.95, 121.44, 120.62, 119.63, 117.97, 117.72, 117.42, 111.46, 111.43, 111.12, 110.48, 99.52, 17.47. **HRMS:** m/z calcd for $C_{27}H_{19}N_3^{\cdot+}$ $[M^{\cdot}]^+$: 385.1573; found 385.1575.

5,11-Dimethyl-6-(2-methyl-1*H*-indol-3-yl)-5,11-dihydroindolo[3,2-*b*]carbazole (5j)

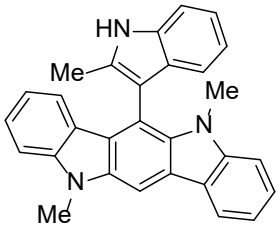

Following the *General Procedure A*, compound **5j** was obtained as a pale yellow solid (150 mg, 72%), from **1c** (160 mg, 1 mmol, 2 eq.), **3f** (66 mg, 0.5 mmol, 1.0 eq), *L*-proline (6 mg, 0.05 mmol, 0.1 eq.), and TFA (8 mL, 0.1 mmol, 0.2 eq.) in EtOH (2 mL, 0.25 M) after silica gel flash chromatography purification (DCM / hexane gradient from 0:100 to 20:80 v/v). **^{1}H NMR** (400 MHz, DMSO-d_6) δ 11.46 (s, 1H), 8.44 (s, 1H), 8.38 (d, *J* = 7.7 Hz, 1H), 7.59 – 7.53 (m, 2H, overlapped signals), 7.53 – 7.45 (m, 2H, overlapped signals), 7.36 (ddd, *J* = 8.3, 7.0, 1.3 Hz, 1H), 7.27 (ddd, *J* = 7.9, 6.1, 1.9 Hz, 1H), 7.16 (ddd, *J* = 8.2, 6.4, 1.8 Hz, 1H), 6.97 – 6.88 (m, 2H, overlapped signals), 6.79 (ddd, *J* = 8.0, 7.0, 1.0 Hz, 1H), 6.71 (ddd, *J* = 7.9, 1.3, 0.6 Hz, 1H), 4.06 (s, 3H), 3.37 (s, 3H), 2.20 (s, 3H). **^{13}C NMR** (101 MHz, DMSO-d_6) δ 143.08, 142.36, 136.83, 135.98, 135.60, 134.15, 129.87, 126.19, 125.57, 123.36, 123.03, 123.00, 122.75, 121.58, 121.21, 120.51, 119.66, 118.70, 118.58, 118.07, 111.47, 111.16, 109.24, 108.71, 108.44, 98.80, 30.82, 29.63, 12.43. **HRMS:** m/z calcd for $C_{29}H_{23}N_3^{\cdot+}$ $[M^{\cdot}]^+$: 413.1886; found 413.1889.

2,8-Difluoro-6-(2-methyl-1*H*-indol-3-yl)-5,11-dihydroindolo[3,2-*b*]carbazole (5k)

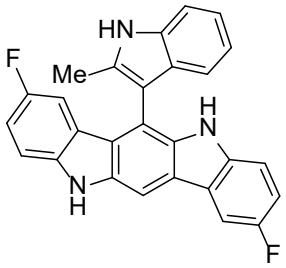

Following the *General Procedure A*, compound **5k** was obtained as a light green solid (80 mg, 38%), from **1d** (163 mg, 1 mmol, 2 eq.), **3f** (66 mg, 0.5 mmol, 1.0 eq), *L*-proline (6 mg, 0.05 mmol, 0.1 eq.), and TFA (8 mL, 0.1 mmol, 0.2 eq.) in EtOH (2 mL, 0.25 M) after silica gel flash chromatography purification (DCM / hexane gradient from 0:100 to 40:60 v/v). **^{1}H NMR** (400 MHz, DMSO-d_6) δ 11.47 (s, 1H), 11.20 (s, 1H), 10.37 (s, 1H), 8.18 (s, 1H), 8.09 (dd, *J* = 9.5, 2.6 Hz, 1H), 7.51 (dt, *J* = 8.2, 0.9 Hz, 1H), 7.44 – 7.35 (m, 2H, overlapped signals), 7.18 (ddd, *J* = 9.4, 8.7, 2.6 Hz, 1H), 7.15 – 7.07 (m,

2H, overlapped signals), 6.91 – 6.83 (m, 2H, overlapped signals), 6.54 (dd, *J* = 10.2, 2.7 Hz, 1H), 2.25 (s, 3H). **^{13}C NMR** (101 MHz, DMSO-*d*$_6$) δ 157.21 (d, *J* = 59.1 Hz), 154.92 (d, *J* = 57.8 Hz), 138.42, 138.35, 136.82, 136.41, 136.31, 134.33, 128.09, 123.45 (d, *J* = 9.6 Hz), 123.29 (d, *J* = 9.8 Hz), 122.94 (d, *J* = 4.0 Hz), 122.32 (d, *J* = 4.2 Hz), 121.12, 119.41, 118.95, 113.48 (d, *J* = 25.1 Hz), 112.95 (d, *J* = 25.1 Hz), 112.10 (d, *J* = 8.7 Hz), 111.47, 111.13 (d, *J* = 9.5 Hz), 111.08, 107.32 (d, *J* = 24.3 Hz), 107.15, 106.38 (d, *J* = 23.5 Hz), 100.34, 12.84. **^{19}F NMR** (376 MHz, DMSO) δ -126.11 (td, *J* = 9.6, 4.8 Hz), -126.41 (td, *J* = 9.7, 4.4 Hz). **HRMS:** m/z calcd for $C_{27}H_{17}F_2N_3^{\cdot+}$ $[M^{\cdot}]^+$: 421.1385; found 421.1384.

2,8-Dimethoxy-6-(2-methyl-1*H*-indol-3-yl)-5,11-dihydroindolo[3,2-*b*]carbazole (5l)

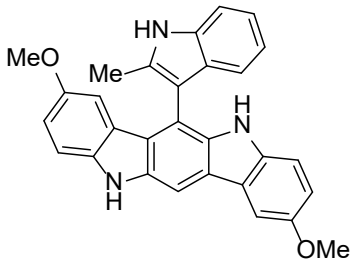

Following the *General Procedure A*, compound **5l** was obtained as a pale brown solid (55 mg, 45%), from **1f** (96 mg, 0.55 mmol, 2 eq.), **3f** (36 mg, 0.27 mmol, 1.0 eq), *L*-proline (3 mg, 0.03 mmol, 0.1 eq.), and TFA (4 mL, 0.05 mmol, 0.2 eq.) in EtOH (1.1 mL, 0.25 M) after silica gel flash chromatography purification (DCM / hexane gradient from 0:100 to 50:50 v/v). **^{1}H NMR** (400 MHz, DMSO-*d*$_6$) δ 11.39 (s, 1H), 10.82 (s, 1H), 10.07 (s, 1H), 8.08 (s, 1H), 7.78 (d, *J* = 2.5 Hz, 1H), 7.49 (dt, *J* = 8.0, 0.9 Hz, 1H), 7.31 (dd, *J* = 3.5, 0.5 Hz, 1H), 7.29 (dd, *J* = 3.6, 0.5 Hz, 1H), 7.09 (ddd, *J* = 8.2, 5.7, 2.5 Hz, 1H), 6.96 (dd, *J* = 8.7, 2.5 Hz, 1H), 6.90 – 6.85 (m, 3H, overlapped signals), 6.41 (d, *J* = 2.6 Hz, 1H), 3.88 (s, 3H), 3.26 (s, 3H), 2.26 (s, 3H). **^{13}C NMR** (101 MHz, DMSO-*d*$_6$) δ 152.81, 151.99, 136.81, 136.72, 136.52, 136.40, 135.86, 134.22, 128.33, 123.56, 123.50, 122.80, 122.21, 120.88, 119.32, 119.17, 114.91, 113.65, 112.00, 111.28, 110.70, 110.58, 107.74, 106.06, 103.64, 99.61, 56.18, 55.17, 12.97. **HRMS:** m/z calcd for $C_{29}H_{23}N_3O_2^{\cdot+}$ $[M^{\cdot}]^+$: 445.1785; found 445.1785.

3-(5,11-Dihidroindolo[3,2-*b*]carbazole-6-yl)-1*H*-indole-6-carboxylic acid (5m)

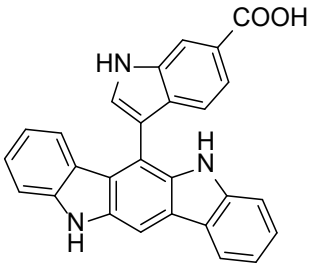

Following the *General Procedure A*, compound **5m** was obtained as a dark red powder (210 mg, 17%), from **1a** (870 mg, 6 mmol, 2 eq.), **3l** (483 mg, 3 mmol, 1.0 eq), *L*-proline (35 mg, 0.3 mmol, 0.1 eq.), and TFA (46 mL, 0.6 mmol, 0.2 eq.) in EtOH (12 mL, 0.25 M) after silica gel flash chromatography purification (EtOAc + 1% Et_3N / hexane gradient from 0:100 to 85:15 v/v). **^{1}H NMR** (400 MHz, DMSO-d_6) δ 12.53 (s, 1H), 11.96 (s, 1H), 11.14 (s, 1H), 10.41 (s, 1H), 8.28 (s, 1H), 8.23 (d, *J* = 7.8 Hz, 1H), 8.16 (s, 1H), 7.97 (d, *J* = 2.5 Hz, 1H), 7.54 (dd, *J* = 8.3, 1.5 Hz, 1H), 7.43 (d, *J* = 8.0 Hz, 1H), 7.40 (d, *J* = 8.0 Hz, 1H), 7.32 (t, *J* = 8.1 Hz, 1H), 7.23 (t, *J* = 8.2 Hz, 1H), 7.12 (t, *J* = 6.9 Hz, 1H), 7.06 (d, *J* = 8.3 Hz, 1H), 6.95 (d, *J* = 7.9 Hz, 1H), 6.70 (t, *J* = 7.5 Hz, 1H). **^{13}C NMR** (101 MHz, DMSO-d_6) δ 168.43, 141.31, 141.24, 135.92, 135.47, 135.05, 130.23, 128.62, 125.32, 124.89, 123.61, 122.72, 122.58, 122.25, 121.65, 121.42, 120.23, 120.04, 119.19, 117.63, 117.08, 114.05, 110.94, 110.74, 110.17, 109.90, 99.45. **HRMS:** m/z calcd for $C_{27}H_{18}N_3O_2^+$ $[M+H]^+$: 416.1394; found 416.1399.

A replicate of the reaction during longer time (24 hours) or lower temperature (50 ºC) resulted in similar final yields.

***N*-(4-(3-(5,11-Dihydroindolo[3,2-*b*]carbazol-6-yl)-1*H*-indol-5-yl)phenyl)methane-sulfonamide (8a)**

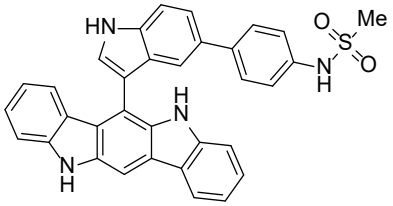

A Schlenk flask was charged with **5b** (50 mg, 0.11 mmol, 1 eq.), 4-methanesulfonamidephenylboronic acid (26 mg, 0.12 mmol, 1.1 eq.), K_2CO_3 (46 mg, 0.33 mmol, 3 eq.), 1,4-dioxane (1 mL), and water (1 mL, final concentration 0.5 M). The reaction mixture was degassed and purged with vacuum-argon cycles (3x). Then was added $Pd(PPh_3)_4$ (6.5 mg, 0.006 mmol, 0.05 eq.) and the reaction was heated to 80 ºC and

stirred for 17 h. After reaction completion (TLC control), the reaction was filtered through a pad of celite. The filtrate was partitioned between EtOAc and water. The organic layer was washed with sat. brine, dried over sodium sulfate, filtered, and concentrated under reduced pressure. The crude product was purified *via* silica gel flash chromatography (DCM / hexane gradient from 50:50 to 100:0 v/v then EtOH / DCM gradient from 0:100 to 10:90 v/v) to afford the pure title compound **8a** (50 mg, 83 %) as an off-white solid. **^{1}H NMR** (400 MHz, DMSO-d_6) δ 11.65 (d, J = 2.5 Hz, 1H), 11.13 (s, 1H), 10.39 (s, 1H), 9.61 (s, 1H), 8.23 (d, J = 7.7 Hz, 1H), 8.15 (s, 1H), 7.76 (d, J = 2.5 Hz, 1H), 7.69 (dd, J = 8.5, 0.7 Hz, 1H), 7.48 (dd, J = 8.5, 1.8 Hz, 1H), 7.43 (dt, J = 3.6, 0.9 Hz, 1H), 7.41 (dt, J = 3.6, 0.9 Hz, 1H), 7.38 – 7.28 (m, 3H, overlapped signals), 7.22 (ddd, J = 8.2, 7.1, 1.2 Hz, 1H), 7.18 (d, J = 1.7 Hz, 1H), 7.15 – 7.05 (m, 4H, overlapped signals), 6.69 (ddd, J = 8.1, 7.1, 1.1 Hz, 1H), 2.89 (s, 3H). **^{13}C NMR** (101 MHz, DMSO-d_6) δ 141.74, 141.70, 137.97, 137.08, 136.56, 135.97, 135.53, 131.49, 127.85, 127.82, 126.26, 125.73, 125.31, 123.21, 123.15, 122.69, 122.30, 121.94, 121.21, 120.66, 118.04, 117.68, 117.44, 111.46, 111.09, 111.01, 110.59, 99.68. The missing ^{13}C signal (-SO_2CH_3), likely to overlap with residual solvent according to predictions. **HRMS:** m/z calcd for $C_{33}H_{25}N_4O_2S^+$ $[M+H]^+$: 541.1693; found 541.1712.

6-(5-(*p*-Tolylethynyl)-1*H*-indol-3-yl)-5,11-dihydroindolo[3,2-*b*]carbazole (8b)

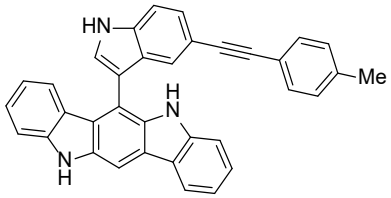

A Schlenk flask was charged with **5b** (30 mg, 0.07 mmol, 1 eq.), 4-ethynyltoluene (25 mL, 0.20 mmol, 3 eq.), Cs_2CO_3 (54 mg, 0.17 mmol, 2.5 eq.), Xantphos (8 mg, 0.13 mmol, 0.2 eq.), CuI (2 mg, 0.01 mmol, 0.15 eq.), CH_3CN (0.6 mL), and water (0.6 mL, final concentration 0.05 M). The reaction mixture was degassed and purged with vacuum-argon cycles (3x). Then was added Bis(acetonitrile)dichloropalladium(II) (1 mg, 0.003 mmol, 0.05 eq.) and the reaction was heated to 100 ºC and stirred for 17 h. After reaction completion (TLC control), the reaction was filtered through a pad of celite. The filtrate was partitioned between EtOAc and water. The organic layer was washed with sat. brine, dried over sodium sulfate, filtered, and concentrated under reduced pressure. The crude product was purified *via* silica gel flash chromatography (EtOAc / hexane gradient from 20:80 to 100:0) to afford the pure title compound **8b** (17 mg, 53 %) as pale brown solid.

^{1}H NMR (400 MHz, DMSO-d_6) δ 11.81 (d, J = 2.5 Hz, 1H), 11.15 (s, 1H), 10.41 (s, 1H), 8.24 (d, J = 7.8 Hz, 1H), 8.17 (s, 1H), 7.80 (d, J = 2.4 Hz, 1H), 7.66 (dd, J = 8.5, 0.8 Hz, 1H), 7.44 (dt, J = 8.1, 0.9 Hz, 2H), 7.41 (dt, J = 8.1, 1.0 Hz, 1H), 7.37 – 7.30 (m, 2H, overlapped signals), 7.28 – 7.21 (m, 3H, overlapped signals), 7.14 (d, J = 1.0 Hz, 1H), 7.13 – 7.10 (m, 1H), 7.09 (d, J = 7.9 Hz, 1H), 6.97 (d, J = 7.4 Hz, 1H), 6.72 (ddd, J = 8.0, 7.1, 1.0 Hz, 1H), 2.25 (s, 3H). **^{13}C NMR** (101 MHz, DMSO-d_6) δ 141.75, 141.69, 138.10, 136.81, 135.88, 135.61, 131.37, 129.61, 127.46, 126.68, 125.78, 125.39, 125.19, 123.27, 123.19, 123.07, 122.70, 122.03, 121.98, 120.71, 120.37, 118.07, 117.60, 113.22, 112.95, 111.41, 111.00, 110.68, 110.28, 99.94, 91.10, 87.34, 21.40. **HRMS:** m/z calcd for $C_{35}H_{24}N_3^+$ $[M+H]^+$: 486.1965; found 486.1965.

***N*-(2-(5,11-Dihydroindolo[3,2-*b*]carbazole-6-carbonyl)phenyl)acetamide (9)**

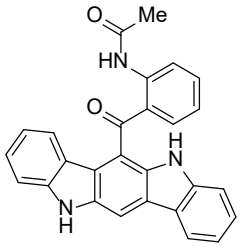

To a solution of **5d** (500 mg, 1.3 mmol, 1 eq.) in dry DCM (8 mL, final 0.1 M) under inert atmosphere was added dropwise a suspension of MCPBA (70% w/w, 569 mg, 2.6 mmol, 2 eq.) in DCM (5 mL). The vessel was sealed, and the reaction was stirred at rt for 5 h, until full consumption of starting material (TLC control). The reaction was diluted with DCM and washed with saturated $NaHCO_3$, saturated brine and water. The organic layer was dried over sodium sulfate, filtered, and concentrated under reduced pressure. The crude residue was purified *via* silica gel flash chromatography (DCM / hexane gradient from 0:100 to 50:0 v/v) to afford the pure title compound **9** (450 mg, 83%) as a bright orange solid. **^{1}H NMR** (400 MHz, DMSO-d_6) δ 11.57 (s, 1H), 11.43 (s, 1H), 10.92 (s, 1H), 8.55 (dd, J = 8.4, 1.1 Hz, 1H), 8.39 (d, J = 0.5 Hz, 1H), 8.28 (d, J = 7.9 Hz, 1H), 7.67 – 7.58 (m, 1H), 7.50 (dt, J = 8.1, 0.9 Hz, 1H), 7.46 – 7.30 (m, 5H, overlapped signals), 7.21 – 7.15 (m, 1H), 6.95 – 6.91 (m, 1H), 6.91 – 6.86 (m, 1H), 2.28 (s, 3H). **^{13}C NMR** (101 MHz, DMSO-d_6) δ 199.80, 169.70, 141.91, 141.82, 141.01, 135.65, 135.23, 134.07, 133.35, 126.62, 126.24, 124.86, 123.68, 122.47, 122.34, 121.41, 121.20, 120.95, 119.39, 118.88, 118.35, 114.63, 111.45, 111.39, 104.31, 25.47. **HRMS:** m/z calcd for $C_{27}H_{20}N_3O_2^+$ $[M+H]^+$: 418.1550; found 418.1548.

1-Acetyl-5'*H*-spiro[indoline-2,6'-indolo[3,2-*b*]carbazole]-3,12'(11'*H*)-dione (10)

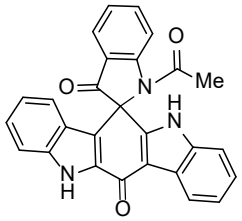

To a solution of **9** (260 mg, 0.6 mmol, 1 eq.) in dry DCM (4 mL, final 0.1 M) under inert atmosphere was added dropwise a suspension of MCPBA (70% w/w, 287 mg, 1.2 mmol, 2 eq.) in DCM (2 mL). The vessel was sealed, and the reaction was stirred at reflux temperature for 5 h, until full consumption of starting material (TLC control). The reaction was diluted with DCM and washed with saturated $NaHCO_3$, saturated brine and water. The organic layer was dried over sodium sulfate, filtered, and concentrated under reduced pressure. The crude residue was purified *via* silica gel flash chromatography (DCM / hexane gradient from 30:70 to 70:30 v/v) to afford the title compound **10** (200 mg, 74%) as a light brown solid. Samples for X-Ray crystallography were obtained by slow evaporation of a THF solution of the pure compound **10**. **^{1}H NMR** (400 MHz, MeOD) δ 8.88 (d, *J* = 7.2 Hz, 1H), 8.27 – 8.20 (m, 1H), 7.93 (ddd, *J* = 8.6, 7.3, 1.5 Hz, 1H), 7.77 (ddd, *J* = 7.7, 1.5, 0.7 Hz, 1H), 7.47 (dt, *J* = 8.4, 0.9 Hz, 1H), 7.38 (td, *J* = 7.5, 0.8 Hz, 1H), 7.35 – 7.30 (m, 1H), 7.24 – 7.20 (m, 2H, overlapped signals), 7.17 (ddd, *J* = 8.3, 7.0, 1.1 Hz, 1H), 6.83 (ddd, *J* = 8.0, 7.0, 1.0 Hz, 1H), 6.72 (dt, *J* = 8.2, 1.0 Hz, 1H), 1.53 (s, 3H). **^{13}C NMR** (101 MHz, MeOD) δ 191.81, 175.75, 170.08, 154.53, 144.92, 138.64, 137.99, 137.38, 134.14, 125.36, 125.26, 124.35, 124.01, 122.36, 122.29, 121.67, 120.98, 120.97, 119.16, 118.54, 116.51, 114.74, 113.09, 111.83, 69.16, 21.83. **HRMS:** m/z calcd for $C_{27}H_{18}N_3O_3^+$ $[M+H]^+$: 432.1343; found 432.1344.

3-(5,11-Dihydroindolo[3,2-*b*]carbazole-6-yl)-*N*-pentyl-1*H*-indole-6-carboxamide (11a)

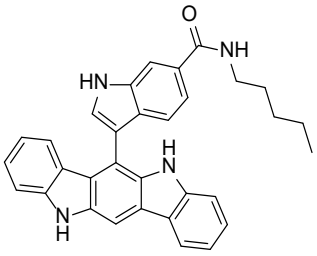

Following the *General Procedure C*, compound **11a** was obtained as a pale brown solid (16 mg, 69%), from **4j** (20 mg, 0.05 mmol, 1 eq.), amylamine (6 mL, 0.053 mmol,

1.1 eq.), HATU (22 mg, 0.06 mmol, 1.2 eq.), and DIPEA (6.2 mg, 0.05 mmol, 1.0 eq.) in DMF (2 mL) after stirring for 24 h. The pure compound **11a** was obtained after flash chromatography purification (EtOAc / hexane gradient from 0:100 to 80:20 v/v). **^{1}H NMR** (400 MHz, DMSO-d_6) δ 11.85 (d, J = 2.4 Hz, 1H), 11.12 (s, 1H), 10.39 (s, 1H), 8.39 (t, J = 5.7 Hz, 1H), 8.25 – 8.20 (m, 1H), 8.16 (dd, J = 1.6, 0.7 Hz, 1H), 8.14 (d, J = 0.5 Hz, 1H), 7.88 (d, J = 2.5 Hz, 1H), 7.45 – 7.42 (m, 1H), 7.40 (dt, J = 9.1, 0.9 Hz, 1H), 7.32 (ddd, J = 8.1, 7.0, 1.2 Hz, 1H), 7.22 (ddd, J = 8.2, 7.1, 1.2 Hz, 1H), 7.12 (ddd, J = 7.9, 7.0, 1.1 Hz, 1H), 7.01 (d, J = 8.4 Hz, 1H), 6.97 – 6.93 (m, 1H), 6.69 (ddd, J = 8.1, 7.1, 1.1 Hz, 1H), 3.29 – 3.25 (m, 2H), 1-58 – 1.51 (m, 2H), 1.36 – 1.26 (m, 4H), 0.93 – 0.83 (m, 3H). **^{13}C NMR** (101 MHz, DMSO-d_6) δ 166.99, 141.28, 141.20, 135.99, 135.46, 135.00, 128.81, 128.11, 127.45, 125.27, 124.82, 122.72, 122.61, 122.21, 121.70, 121.42, 120.19, 118.86, 118.02, 117.58, 117.02, 111.73, 110.93, 110.42, 110.20, 110.11, 99.29, 29.00, 28.79, 21.94, 13.98, 0.11. **HRMS:** m/z calcd for $C_{32}H_{28}N_4O^+$ $[M+H]^+$: 484.2336; found 484.2268.

Indolocarbazole-PEG3-thalidomide (11b)

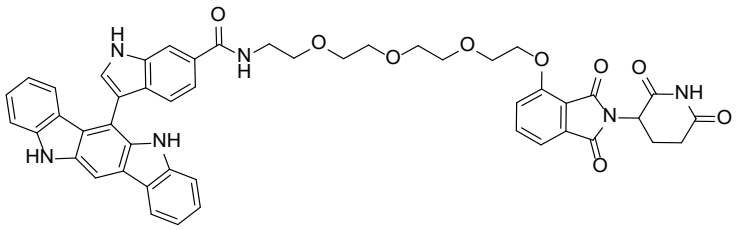

Following the *General Procedure C*, compound **11b** was obtained as a cream solid (0.040 g, 78%) from 0.057 mmol of **4j** (1.1 Eq., 0.024 g), 0.052 mmol of the commercial **Thalidomide 4'-ether-PEG3-amine** (1.0 Eq., 0.025 g), HATU (1.2 Eq., 0.062 mmol, 0.025 g) and DIPEA (4.5 Eq., 0.232 mmol, 40 µL) in 2.1 mL of DMF after stirring for 14 h. The pure product **11b** was obtained from a reverse phase purification by automated column chromatography, using H_2O+TFA (0.05%) / ACN+TFA (0.05%) (gradient from 2:98 to 100:00, v/v) as solvent system. **^{1}H NMR** (400 MHz, DMSO-d_6) δ 11.87 (d, J = 2.6 Hz, 1H), 11.12 (s, 1H), 11.09 (s, 1H), 10.40 (s, 1H), 8.43 (t, J = 5.6 Hz, 1H), 8.22 (d, J = 7.7 Hz, 1H), 8.17 (dd, J = 1.5, 0.7 Hz, 1H), 8.16 – 8.14 (m, 1H), 7.89 (d, J = 2.5 Hz, 1H), 7.76 (dd, J = 8.5, 7.3 Hz, 1H), 7.47 (d, J = 8.5 Hz, 1H), 7.45 – 7.38 (m, 4H), 7.32 (ddd, J = 8.2, 7.0, 1.2 Hz, 1H), 7.22 (ddd, J = 8.2, 7.1, 1.2 Hz, 1H), 7.12 (ddd, J = 8.0, 7.0, 1.1 Hz, 1H), 7.01 (d, J = 8.4 Hz, 1H), 6.94 (d, J = 8.0 Hz, 1H), 6.68 (ddd, J = 8.1, 7.1, 1.1 Hz, 1H), 5.07 (dd, J = 12.8, 5.4 Hz, 1H), 4.29 (dd, J = 5.6, 3.5 Hz, 2H), 3.76 (dd,

J = 5.4, 3.5 Hz, 2H), 3.64 – 3.59 (m, 2H), 3.54 (d, *J* = 4.9 Hz, 7H), 3.44 (q, *J* = 5.9 Hz, 2H), 2.91 – 2.82 (m, 1H), 2.59 (d, *J* = 3.7 Hz, 1H), 2.06 – 1.96 (m, 2H). **HRMS:** m/z calcd for $C_{48}H_{43}N_6O_9^+$ $[M+H]^+$: 847.3086; found 847.3080.

Diaminodecane-HomoPROTAC (11c)

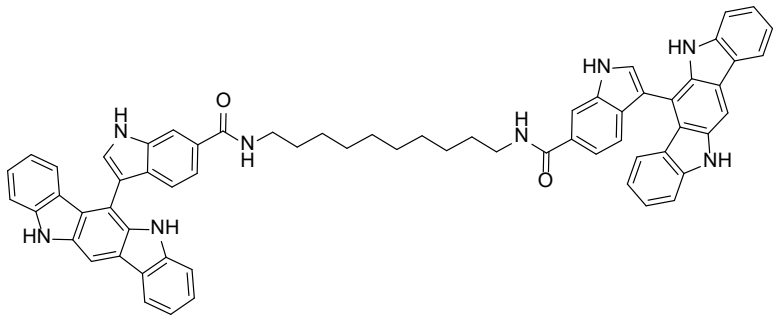

Following the *General Procedure C*, compound **11c** was obtained as a dark red solid (0.016 g, 36%) from 0.108 mmol of **4j** (2.3 Eq., 0.045 g), 0.046 mmol of **1,10-diaminodecane** (1.0 Eq., 8 mg), HATU (3.0 Eq., 0.139 mmol, 0.053 g) and DIPEA (6.5 Eq., 0.302 mmol, 0.053 mL) in 0.500 mL of DMF after stirring for 24 h. The pure product **11c** was obtained from a column chromatography, using Hexane / EtOAc (gradient from 100:0 to 0:100, v/v) and then EtOAc / EtOH (95:5, v/v) as solvent system. **^{1}H NMR** (400 MHz, DMSO-*d*$_6$) δ 11.85 (d, *J* = 2.6 Hz, 2H), 11.12 (s, 2H), 10.39 (s, 2H), 8.38 (t, *J* = 5.6 Hz, 2H), 8.22 (d, *J* = 7.7 Hz, 2H), 8.16 (t, *J* = 1.0 Hz, 2H), 8.14 (s, 2H), 7.88 (d, *J* = 2.5 Hz, 2H), 7.45 – 7.38 (m, 5H), 7.32 (t, *J* = 8.2 Hz, 3H), 7.21 (t, *J* = 7.6 Hz, 3H), 7.11 (t, *J* = 8.0 Hz, 3H), 7.01 (d, *J* = 8.4 Hz, 2H), 6.95 (d, *J* = 7.9 Hz, 2H), 6.68 (t, *J* = 8.0 Hz, 2H), 3.30 – 3.26 (m, 4H), 1.54 (s, 4H), 1.30 (t, *J* = 5.6 Hz, 12H). **^{13}C NMR** (101 MHz, DMSO-*d*$_6$) δ 167.01, 141.28, 141.21, 136.00, 135.47, 135.00, 128.82, 128.11, 127.45, 125.28, 124.82, 122.72, 122.62, 122.22, 121.71, 121.42, 120.19, 118.87, 118.02, 117.59, 117.03, 111.74, 110.94, 110.43, 110.20, 110.12, 99.30, 29.33, 29.05, 28.87, 26.60. The signal corresponding to the amide carbons is overlapped with the solvent signal (estimated at around 40 ppm). **HRMS:** m/z calcd for $C_{64}H_{55}N_8O_2^+$ $[M+H]^+$: 967.4442; found 966.4373.

PEG3-HomoPROTAC (11d)

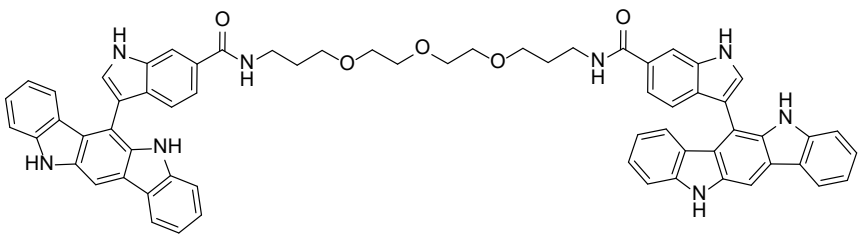

Following the *General Procedure C*, compound **11d** was obtained as a pink solid (0.056 g, 71%) from 0.193 mmol of **4j** (2.5 Eq., 0.080 g), 0.077 mmol of **PEG-3-diamine** (1.0 Eq., 0.017 g), HATU (3.0 Eq., 0.231 mmol, 0.090 g) and DIPEA (6.3 Eq., 0.481 mmol, 0.084 mL) in 1.6 mL of DMF after stirring for 24 h. The pure product **11d** was obtained from a column chromatography, using Hexane / EtOAc (gradient from 100:0 to 0:100, v/v) and then EtOAc / EtOH (95:5, v/v) as solvent system. **^{1}H NMR** (400 MHz, DMSO-d_6) δ 11.86 (d, J = 2.5 Hz, 2H), 11.12 (d, J = 3.2 Hz, 2H), 10.39 (s, 2H), 8.44 (s, 1H), 8.39 (t, J = 5.6 Hz, 2H), 8.22 (d, J = 8.1 Hz, 4H), 8.16 (s, 4H), 8.14 (s, 4H), 7.88 (d, J = 2.5 Hz, 2H), 7.45 – 7.38 (m, 5H), 7.32 (t, J = 9.1 Hz, 3H), 7.21 (t, J = 8.2 Hz, 3H), 7.11 (t, J = 7.4 Hz, 3H), 7.01 (d, J = 8.4 Hz, 2H), 6.95 (d, J = 7.5 Hz, 2H), 6.68 (t, J = 8.1 Hz, 2H), 3.56 – 3.45 (m, 16H), 1.78 (t, J = 6.7 Hz, 4H). **^{13}C NMR** (101 MHz, DMSO-d_6) δ 167.10, 141.27, 141.20, 135.98, 135.46, 134.99, 128.85, 127.99, 127.49, 125.26, 124.81, 122.71, 122.61, 122.21, 121.70, 121.41, 120.18, 118.88, 117.99, 117.57, 117.02, 111.74, 110.93, 110.43, 110.18, 110.10, 99.29, 69.79, 69.58, 68.42, 54.91, 36.74, 29.55. **HRMS:** m/z calcd for $C_{64}H_{53}N_8O_5^-$ $[M-H]^-$: 1014.1795; found 1014.4218.

6-Ethoxy-5,11-dihydroindolo[3,2-*b*]carbazole (12)

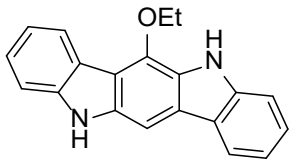

The title compound **12** was obtained as a side product in the synthesis of some adducts **5**. For the characterisation and the biological tests, it was isolated from the reaction mixture of the synthesis of compound **5b**. **^{1}H NMR** (400 MHz, DMSO-d_6) δ 11.07 (s, 1H), 10.97 (s, 1H), 8.23 (dt, J = 7.8, 1.3 Hz, 1H), 8.17 (dt, J = 7.8, 1.3 Hz, 1H), 7.87 (s, 1H), 7.49 (dt, J = 8.1, 0.9 Hz, 1H), 7.45 (dt, J = 8.1, 1.0 Hz, 1H), 7.42 – 7.34 (m, 2H, overlapped signals), 7.18 – 7.09 (m, 2H, overlapped signals), 4.39 (q, J = 7.0 Hz, 2H), 1.56 (t, J = 7.0 Hz, 3H). **^{13}C NMR** (101 MHz, DMSO-d_6) δ 141.61, 141.21, 138.01, 136.72, 127.73, 126.11, 125.55, 125.10, 123.34, 122.42, 121.74, 120.82, 118.40, 118.28, 115.50, 111.35, 110.66, 96.40, 68.46, 16.31. **HRMS:** m/z calcd for $C_{20}H_{17}N_2O^+$ $[M+H]^+$: 301.1335; found 301.1337.

2.6. Selected Copies of NMR Spectra

2-(5,11-Dihydroindolo[3,2-*b*]carbazol-6-yl)-3-hydroxy-5,5-dimethylcyclohex-2-en-1-one (4a)

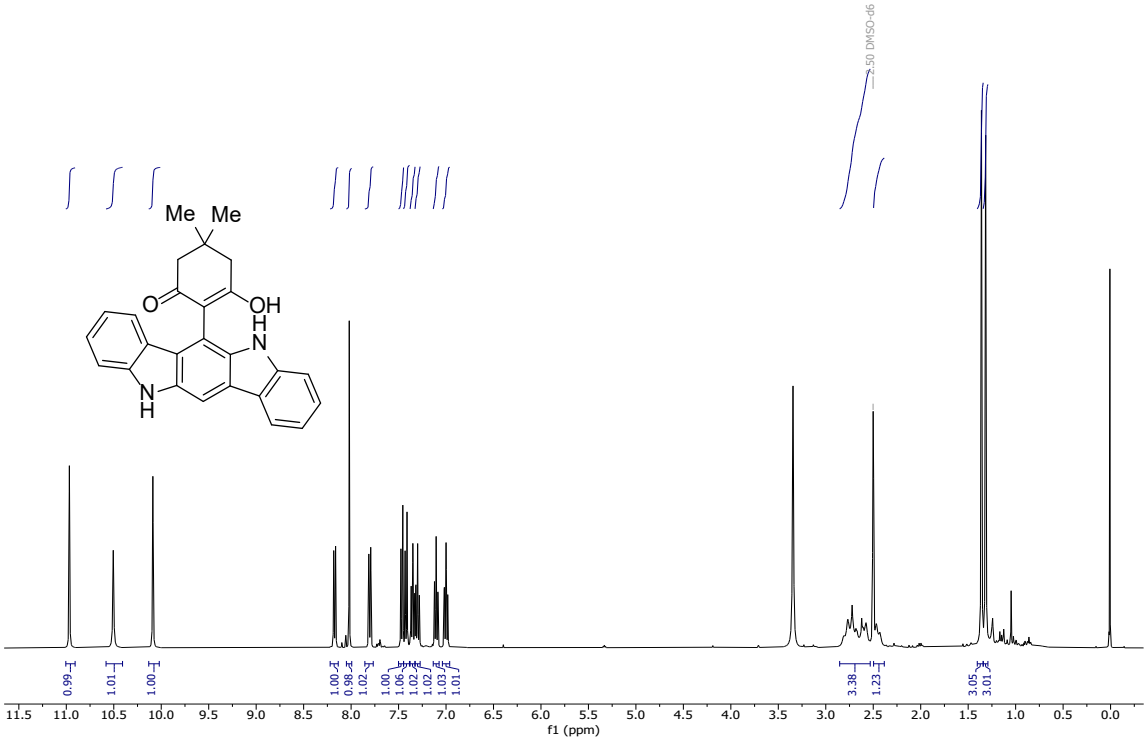

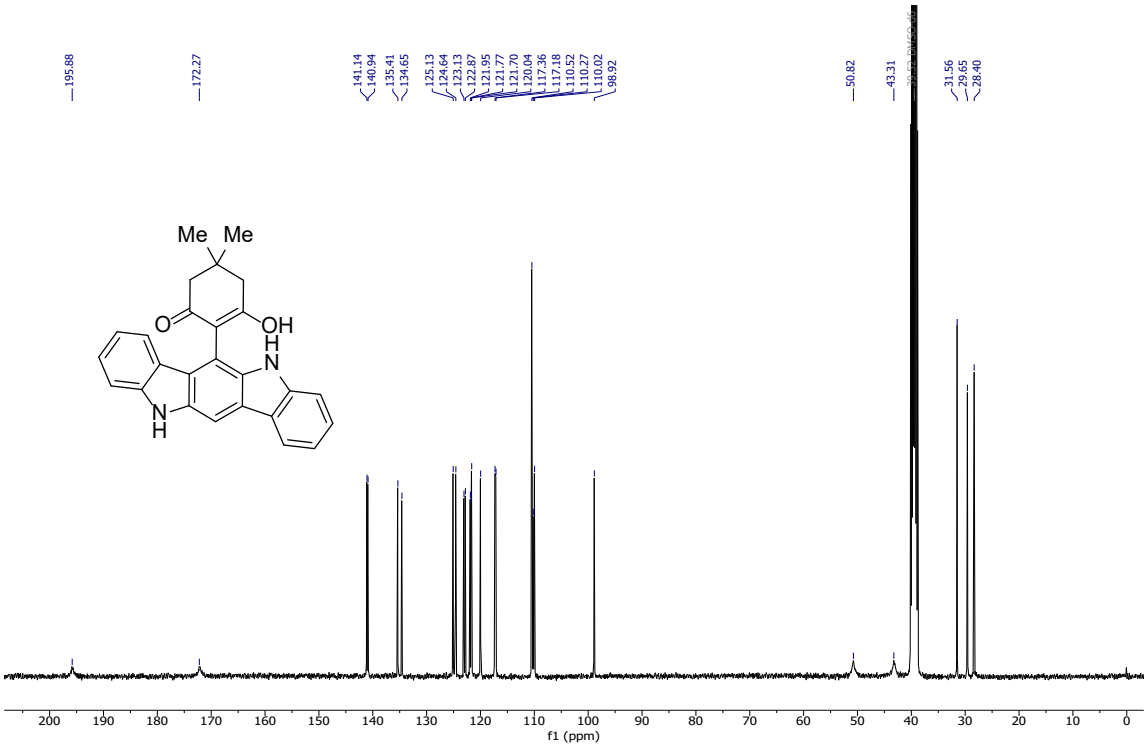

4-(5,11-Dihydroindolo[3,2-*b*]carbazole-6-yl)-5-hydroxyfuran-3(2*H*)-one (4b)

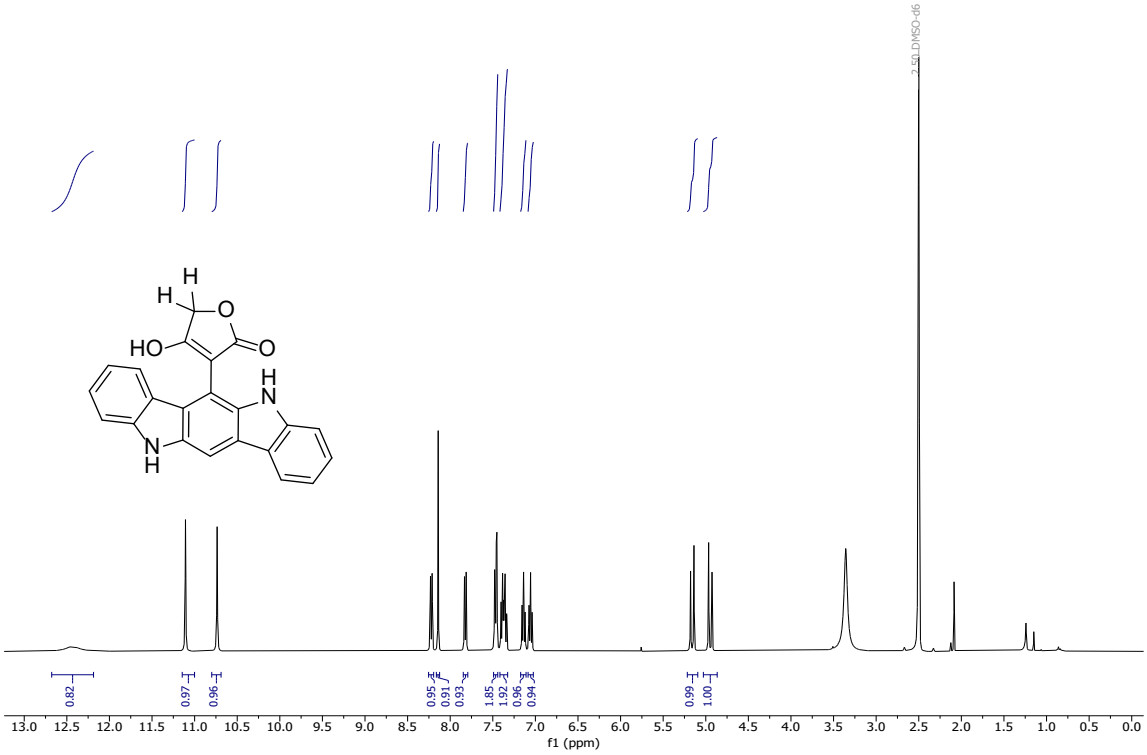

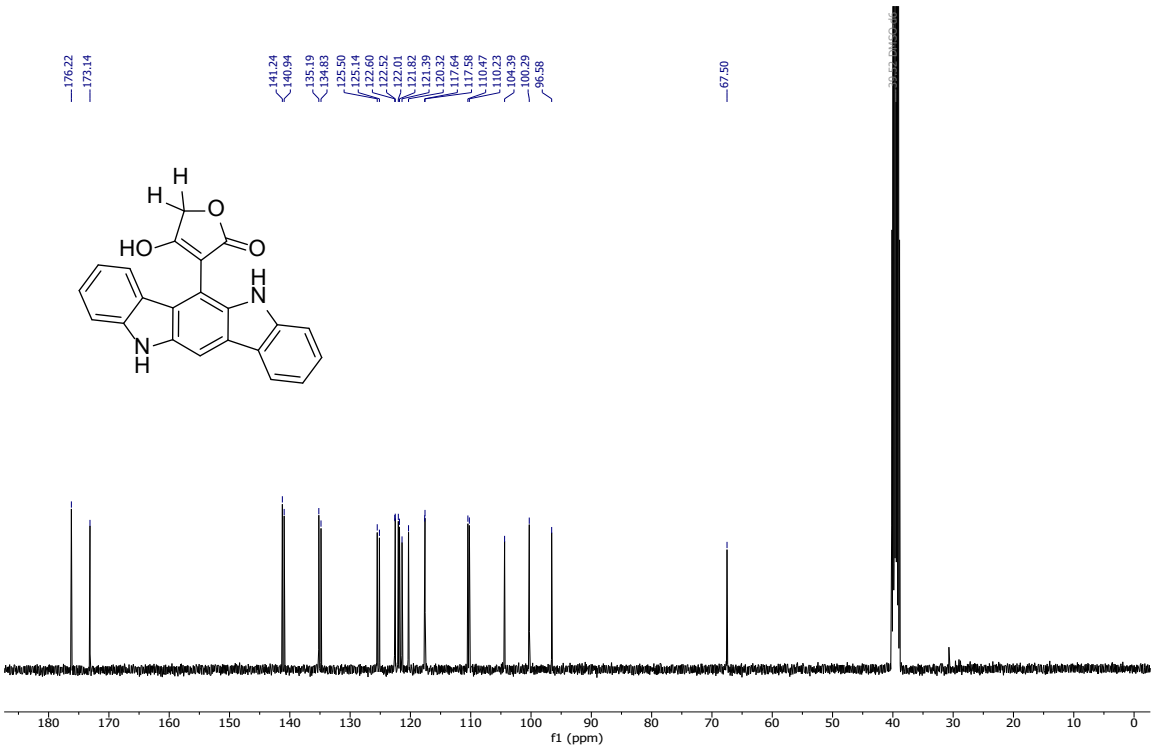

6-(5-Methoxy-1*H*-indol-3-yl)-5,11-dihydroindolo[3,2-*b*]carbazole (5a)

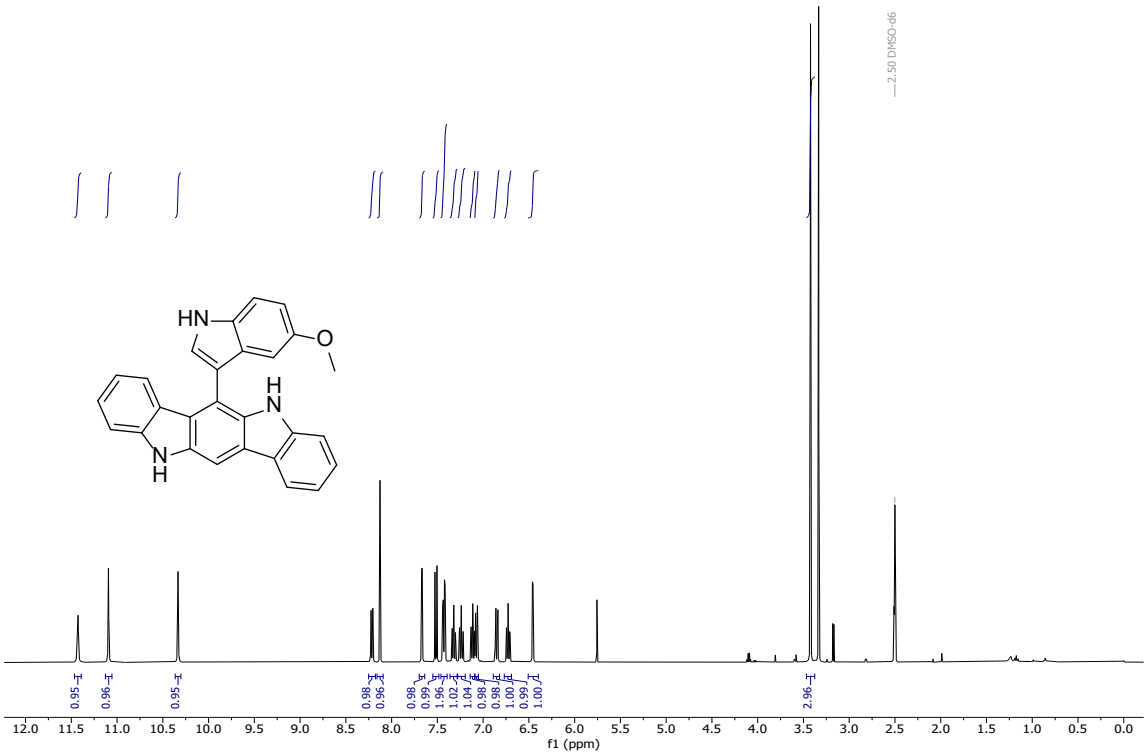

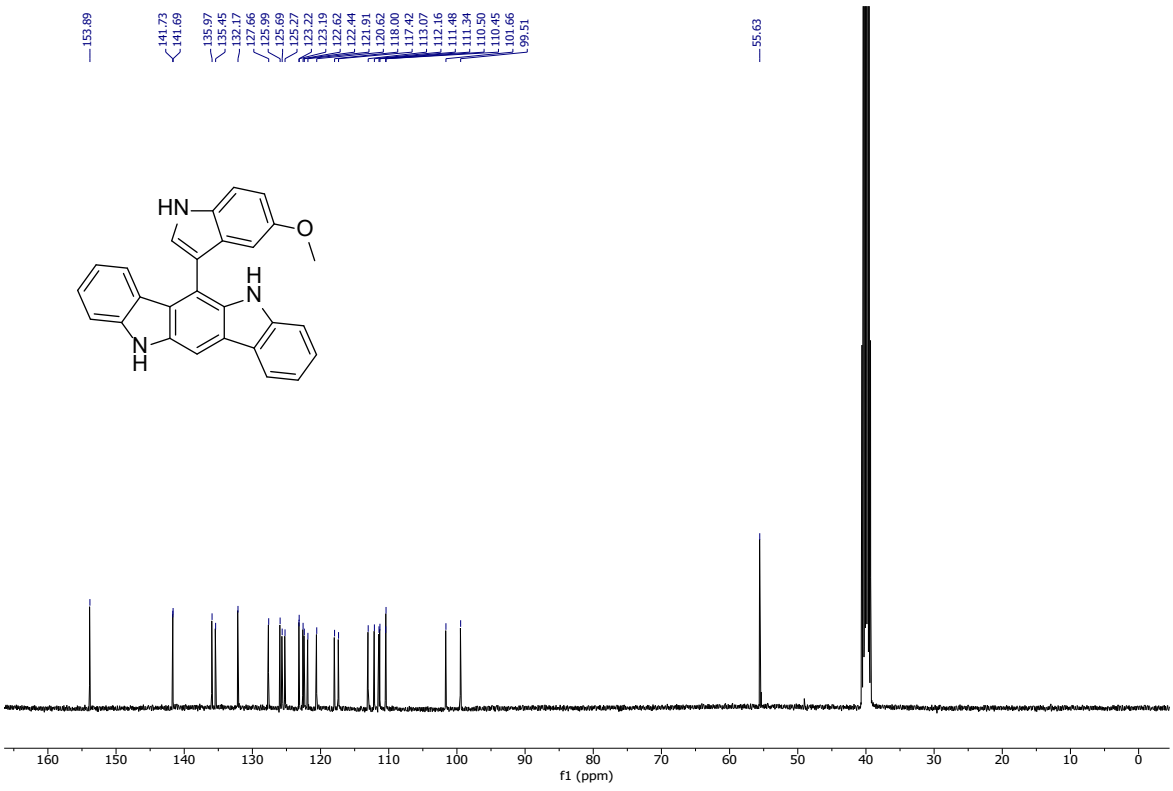

6-(5-Bromo-1*H*-indol-3-yl)-5,11-dihydroindolo[3,2-*b*]carbazole (5b)

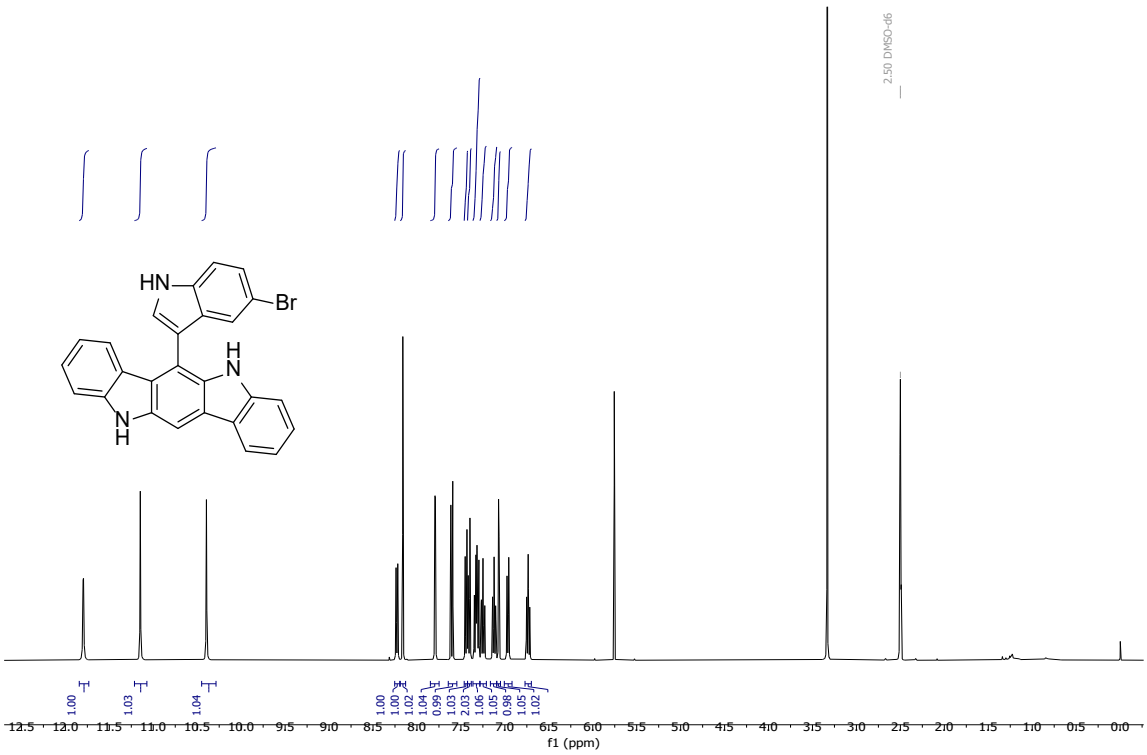

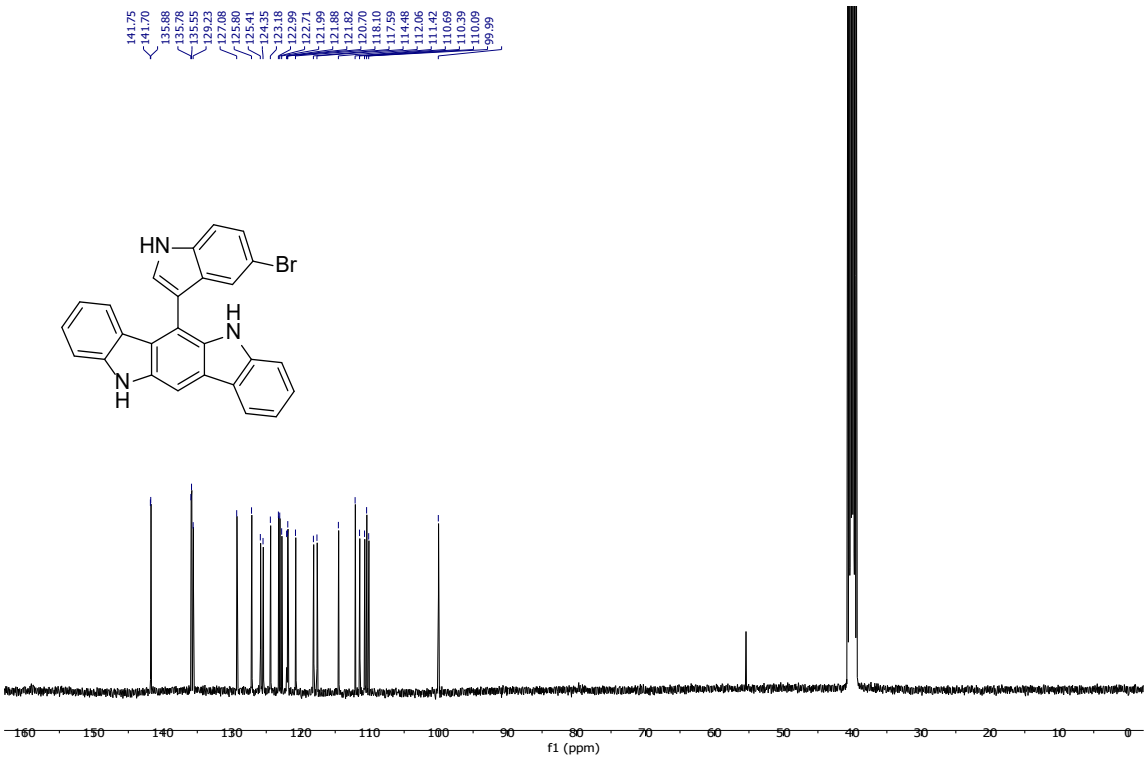

6-(1-Methyl-1*H*-indol-3-yl)-5,11-dihydroindolo[3,2-*b*]carbazole (5d)

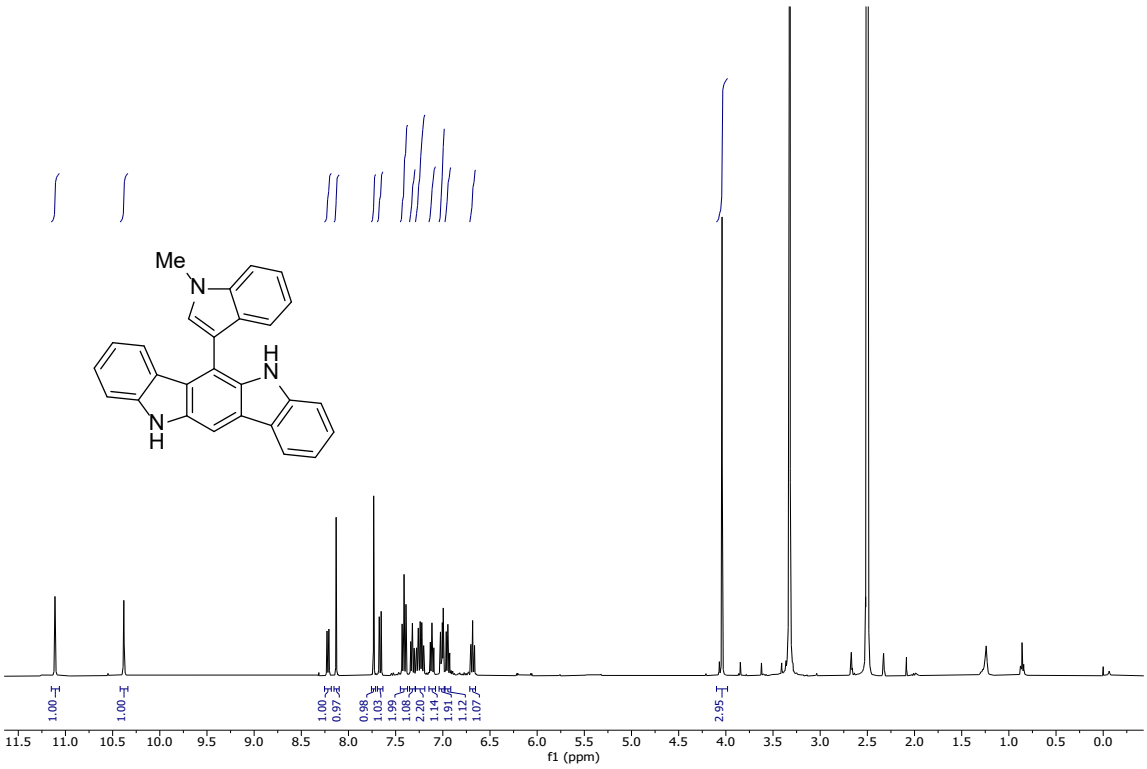

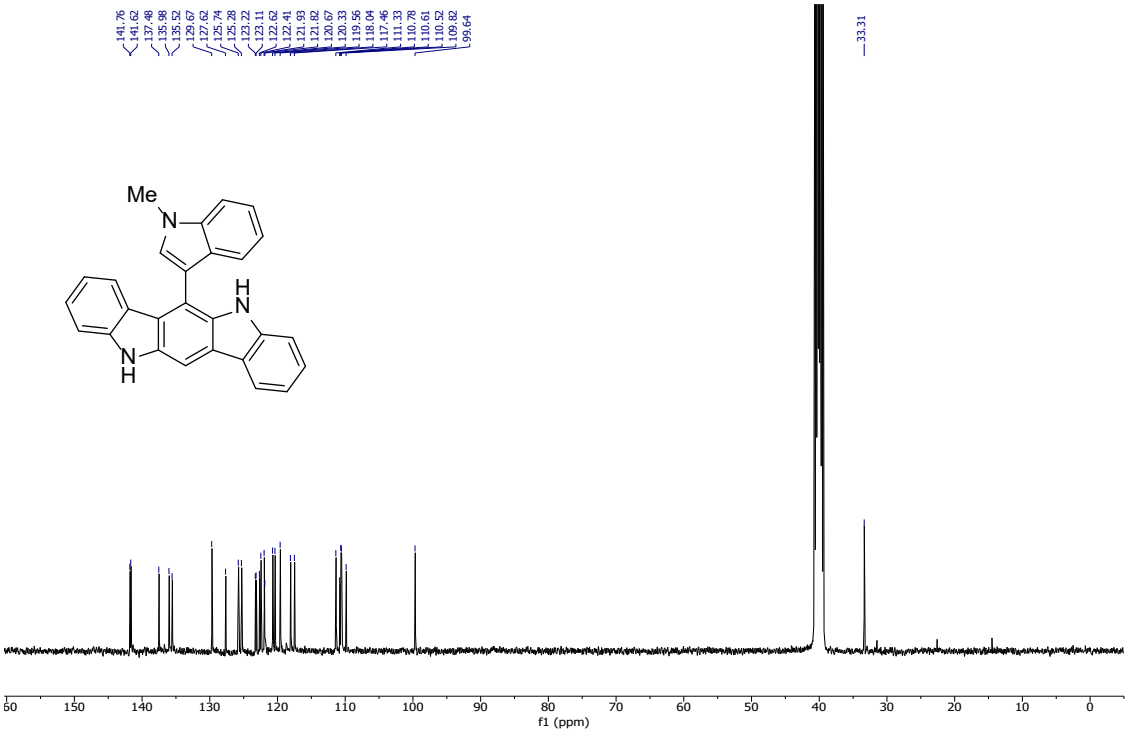

6-(2-Methyl-1*H*-indol-3-yl)-5,11-dihydroindolo[3,2-*b*]carbazole (5e)

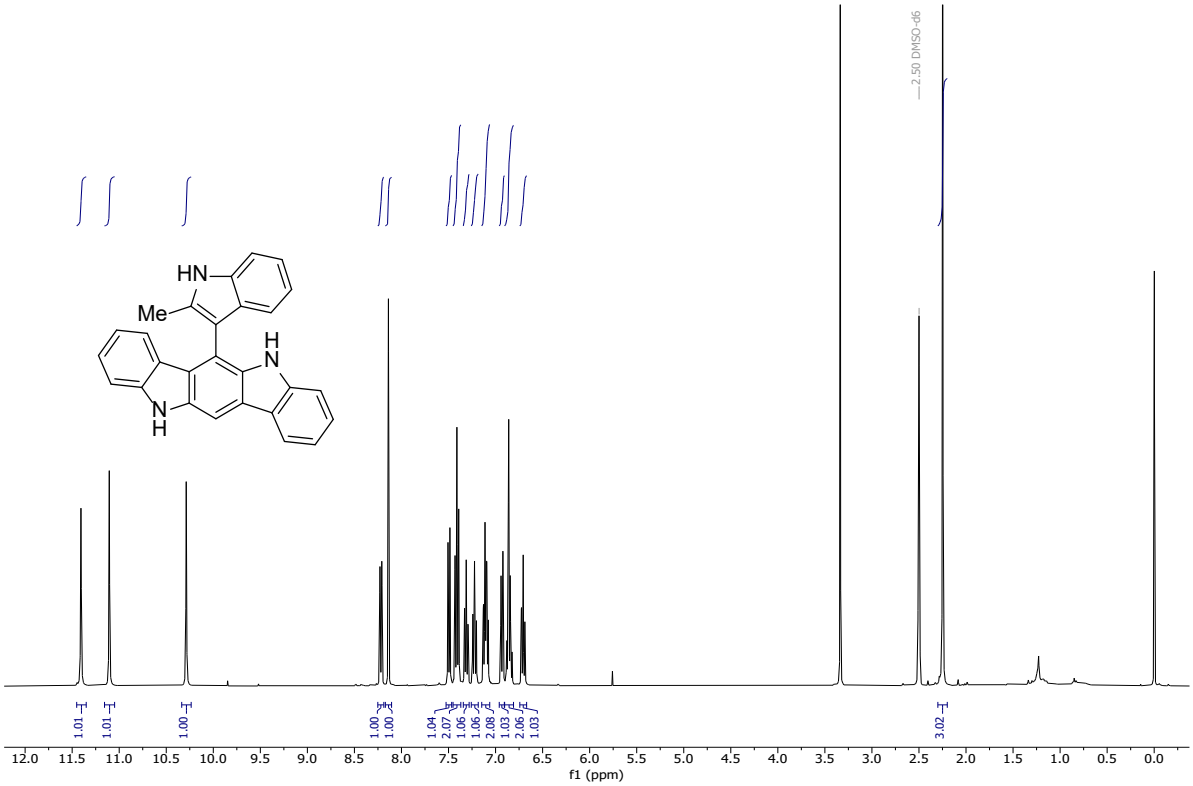

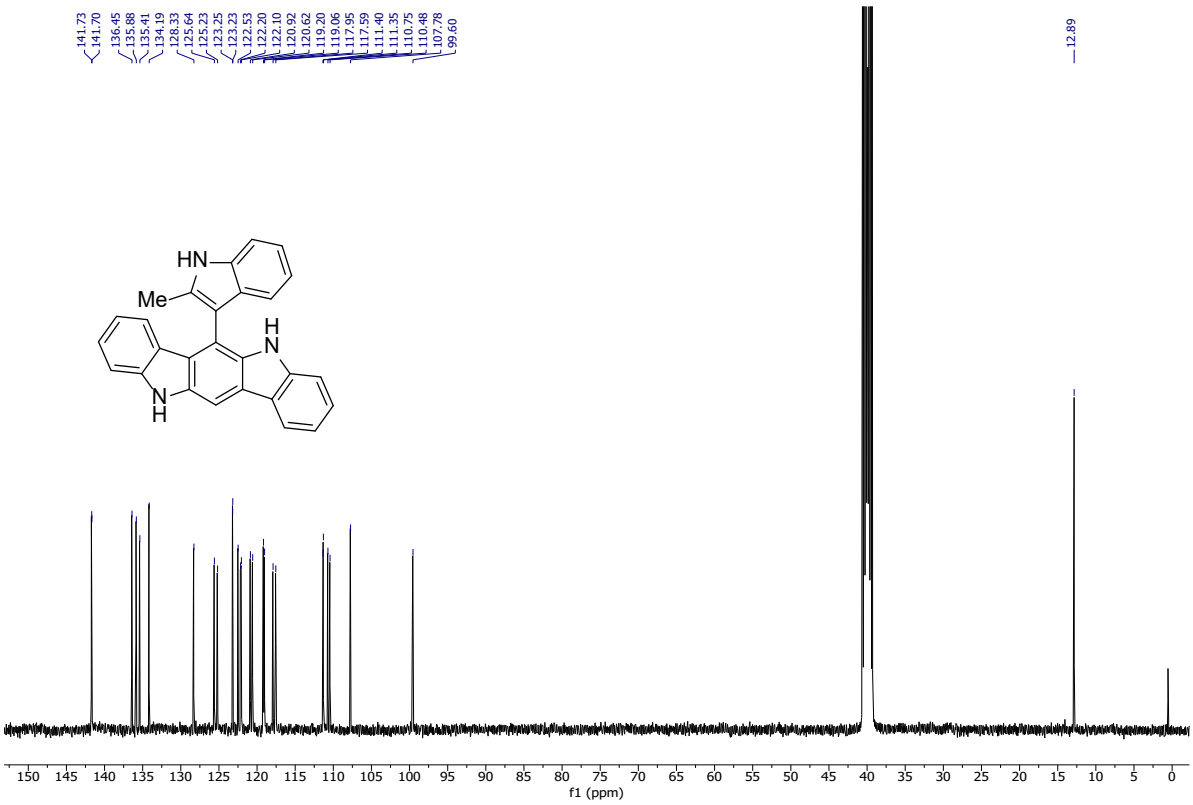

6-(4-Methyl-1*H*-indol-3-yl)-5,11-dihydroindolo[3,2-*b*]carbazole (5h)

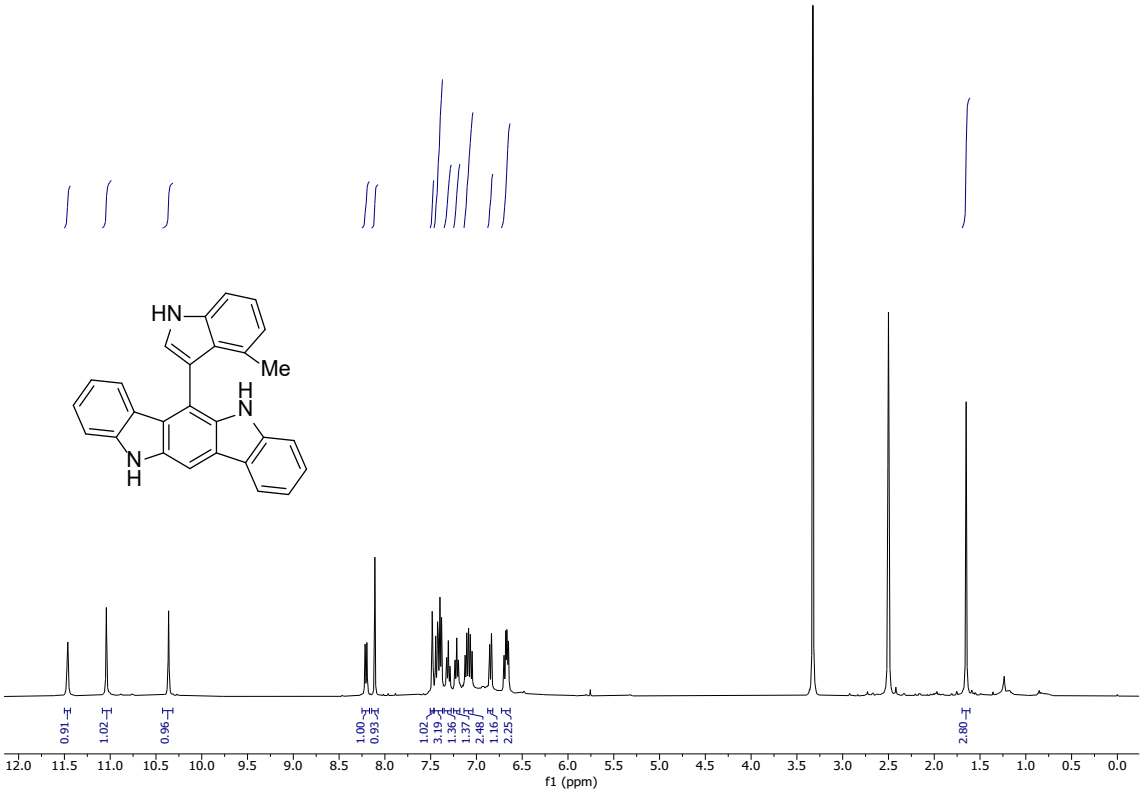

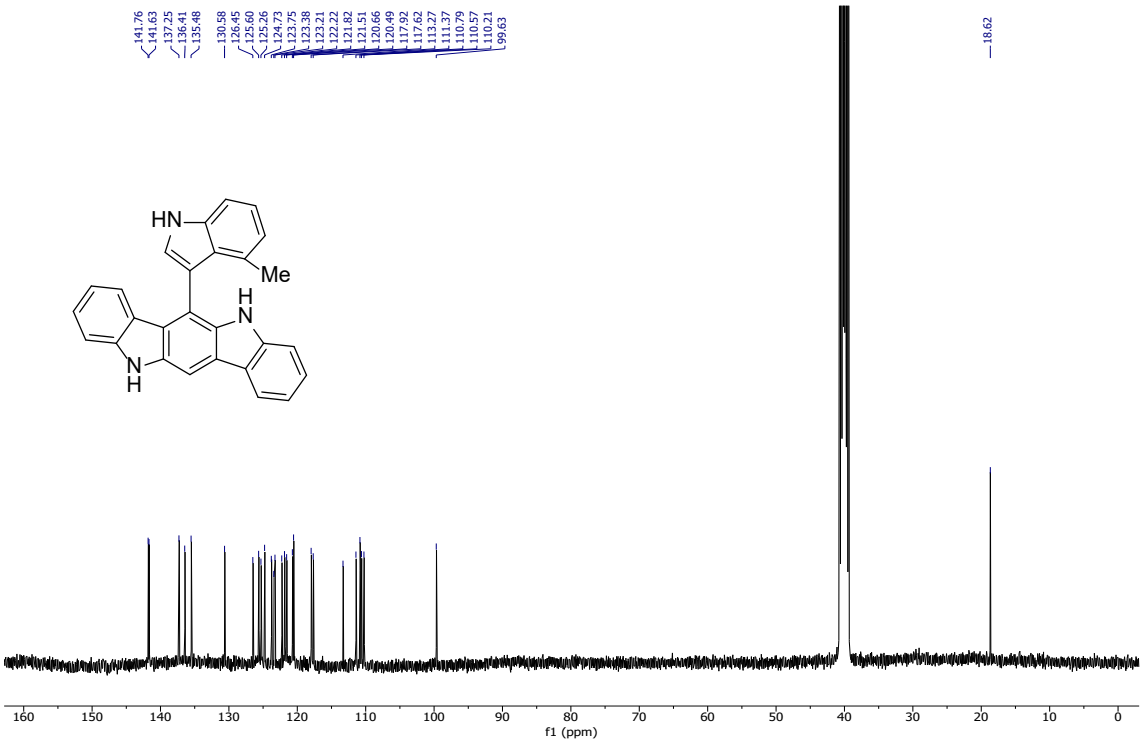

6-(7-Methyl-1*H*-indol-3-yl)-5,11-dihydroindolo[3,2-*b*]carbazole (5i)

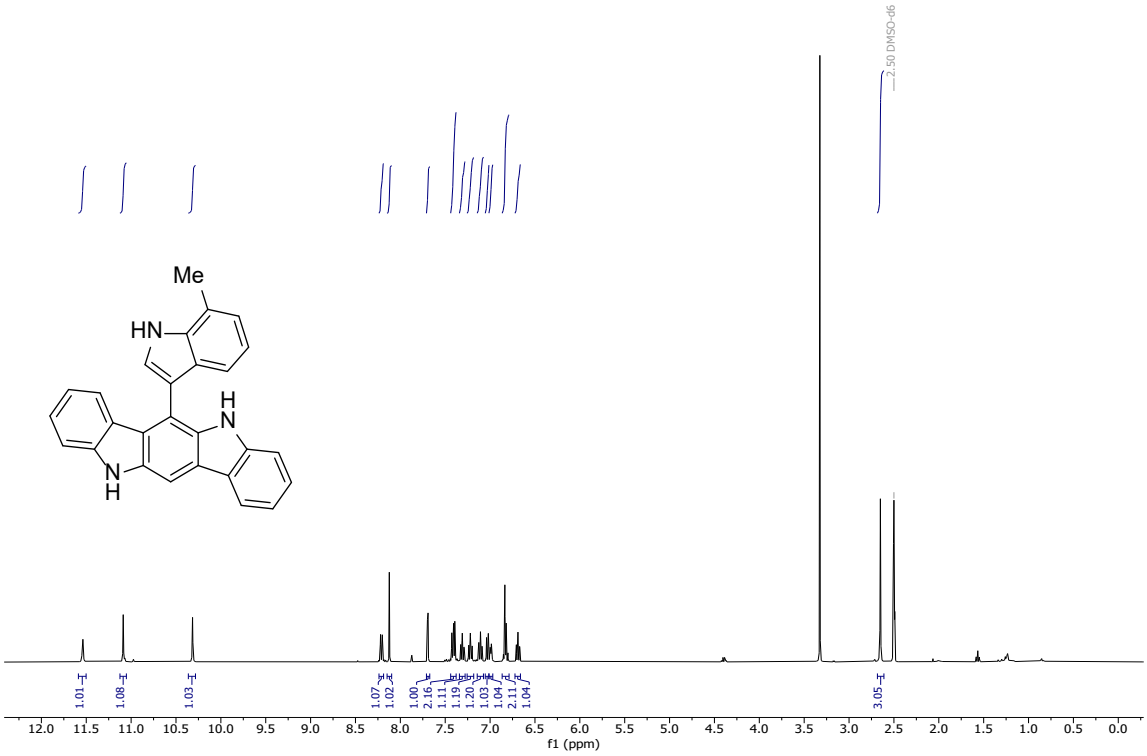

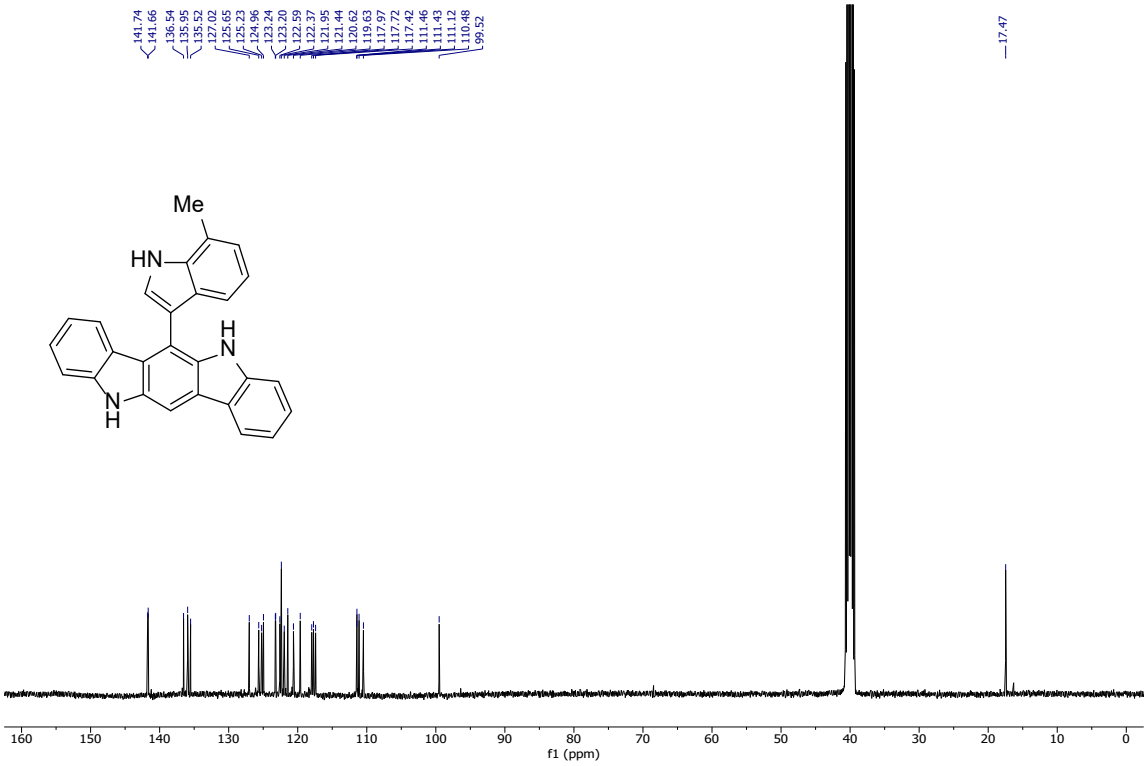

5,11-Dmethyl-6-(2-methyl-1*H*-indol-3-yl)-5,11-dihydroindolo[3,2-*b*]carbazole (5j)

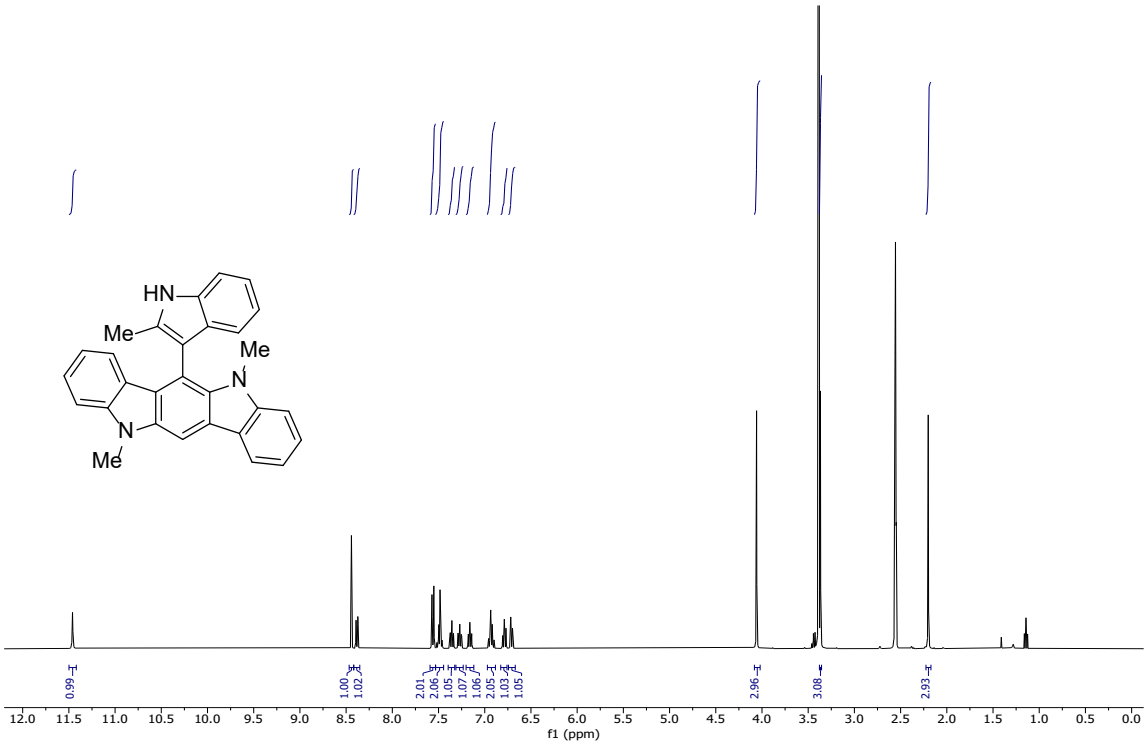

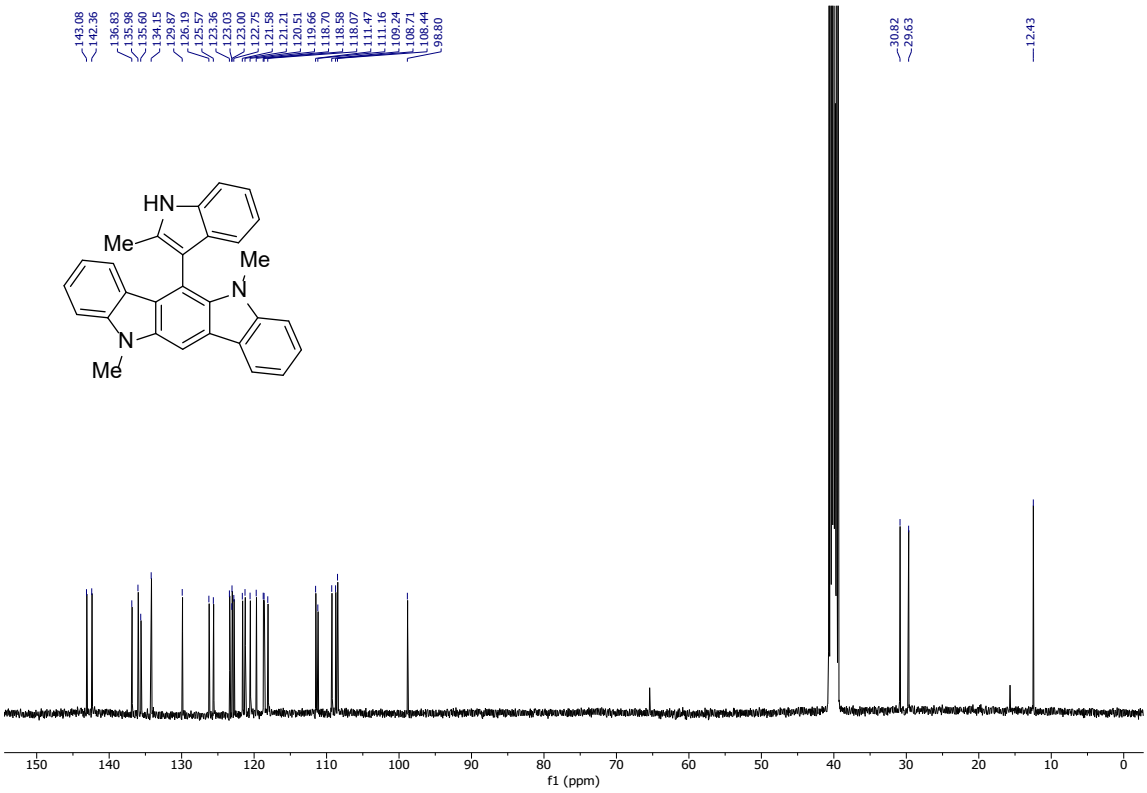

2,8-Difluoro-6-(2-methyl-1*H*-indol-3-yl)-5,11-dihydroindolo[3,2-*b*]carbazole (5k)

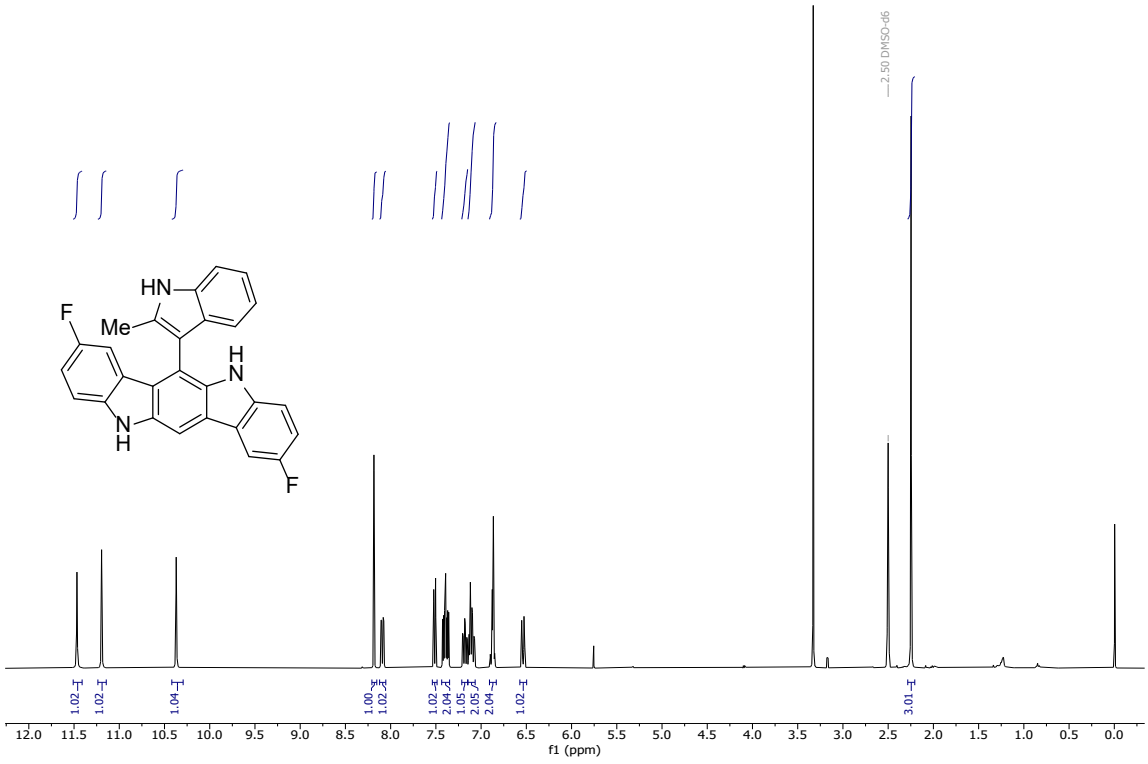

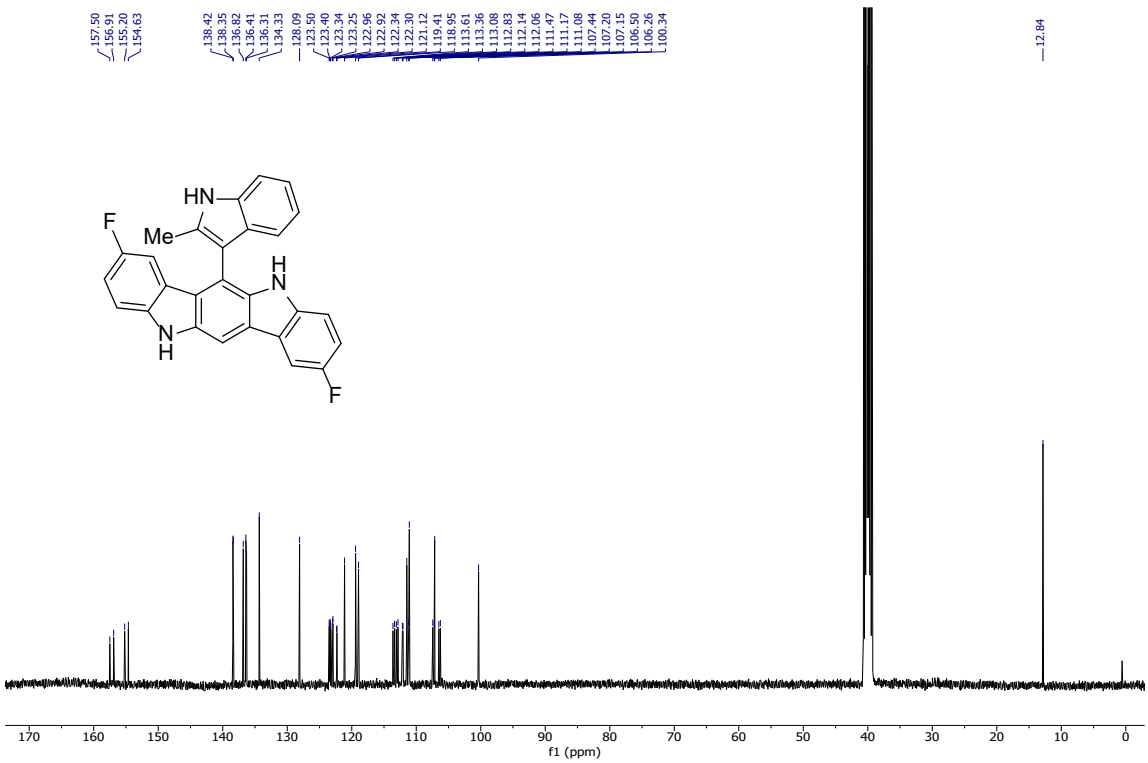

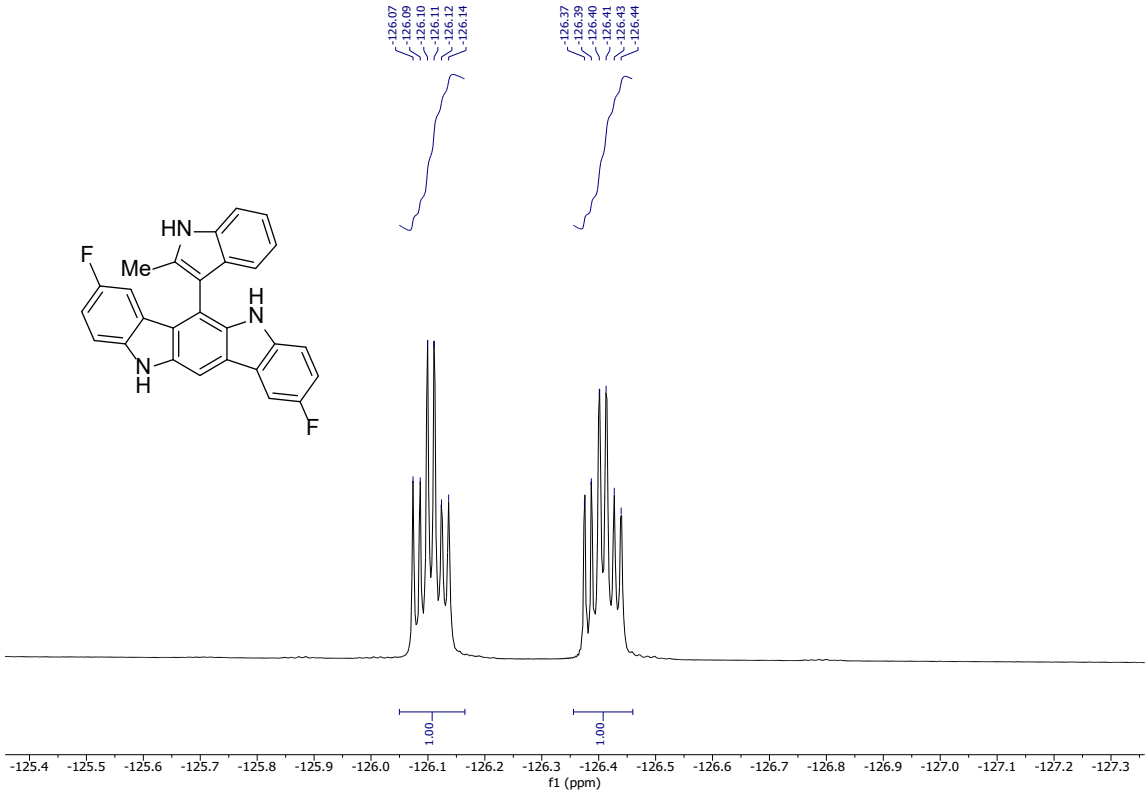
-126.07
-126.09
-126.10
-126.11
-126.12
-126.14
-126.37
-126.39
-126.40
-126.41
-126.43
-126.44
HN
F
Me
H
N
N
H
F
1.00
1.00
-125.4
-125.5
-125.6
-125.7
-125.8
-125.9
-126.0
-126.1
-126.2
-126.3
-126.4
-126.5
-126.6
-126.7
-126.8
-126.9
-127.0
-127.1
-127.2
-127.3
f1 (ppm)

2,8-Dimethoxy-6-(2-methyl-1*H*-indol-3-yl)-5,11-dihydroindolo[3,2-*b*]carbazole (5l)

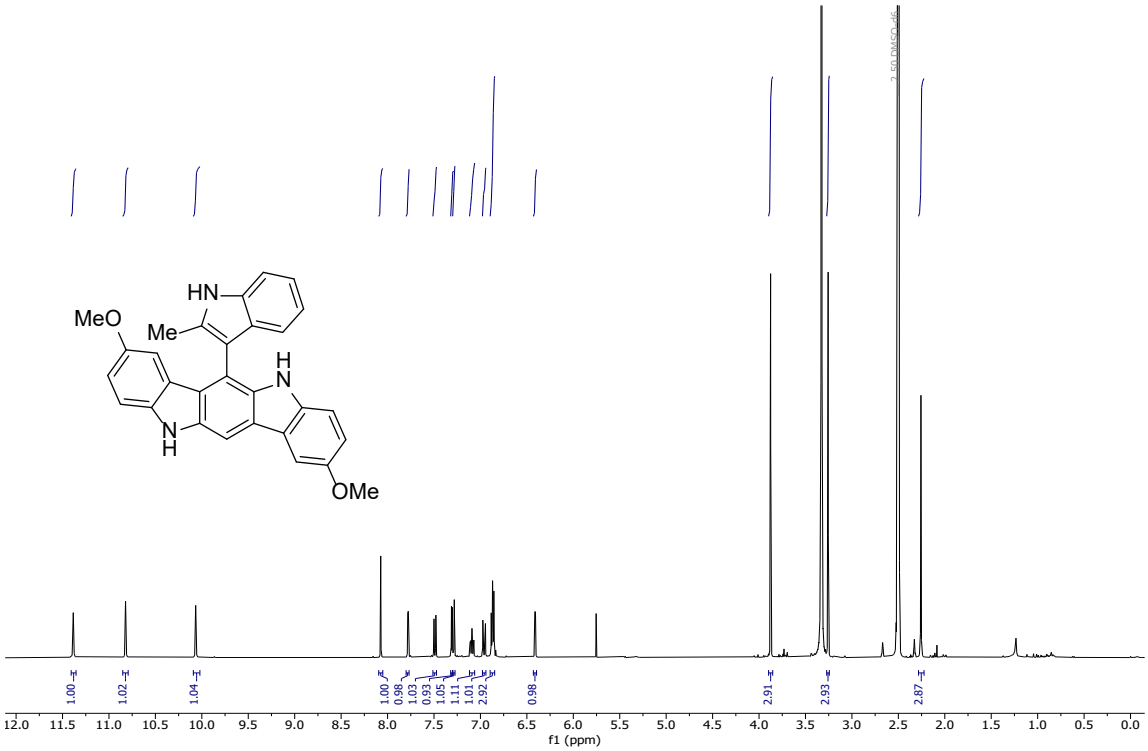

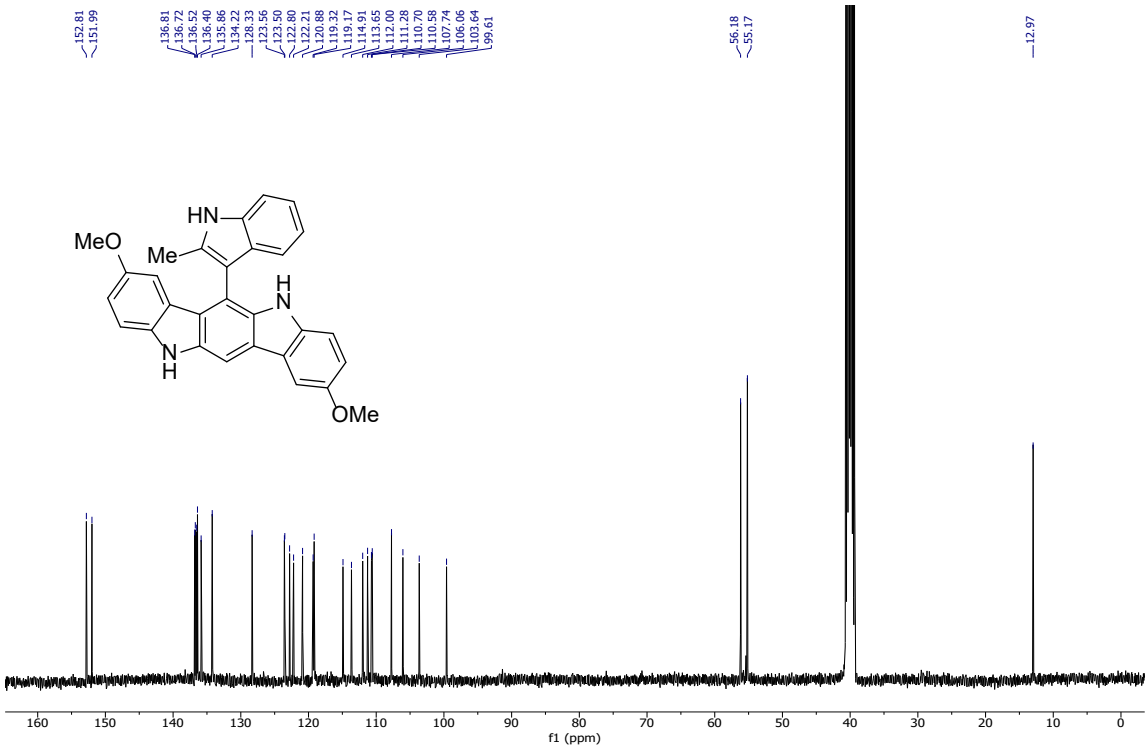

3-(5,11-Dihydroindolo[3,2-*b*]carbazole-6-yl)-1*H*-indole-6-carboxylic acid (5m)

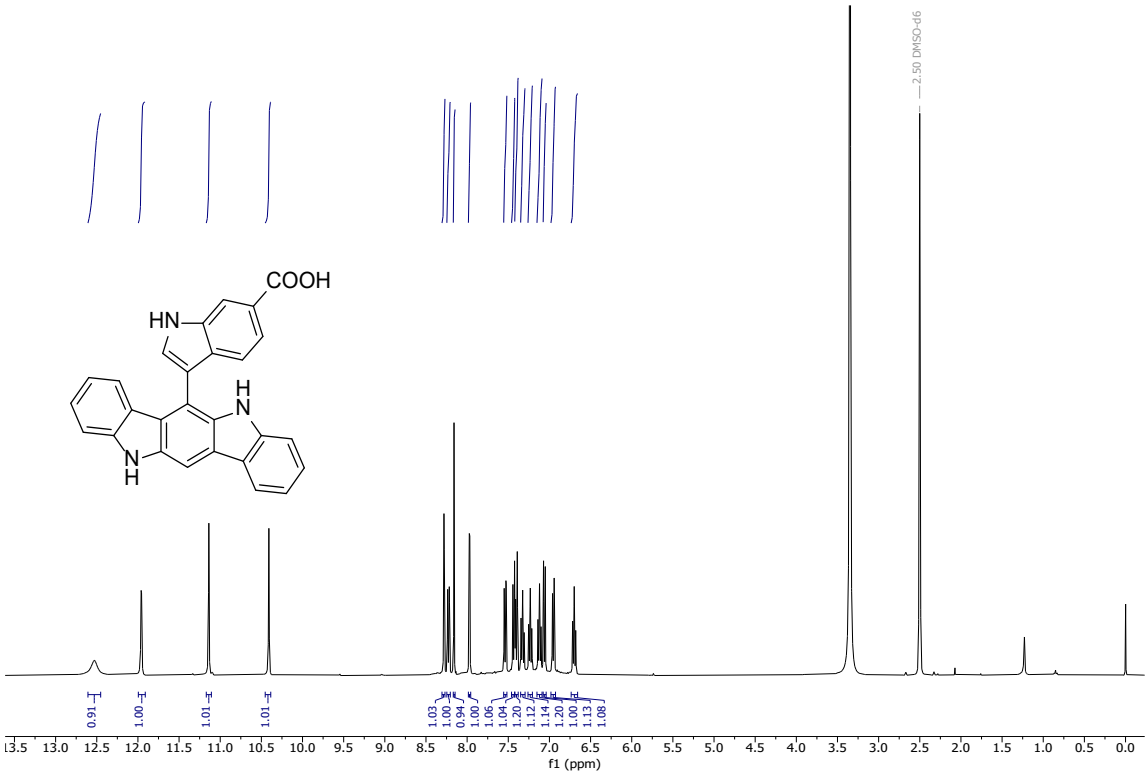

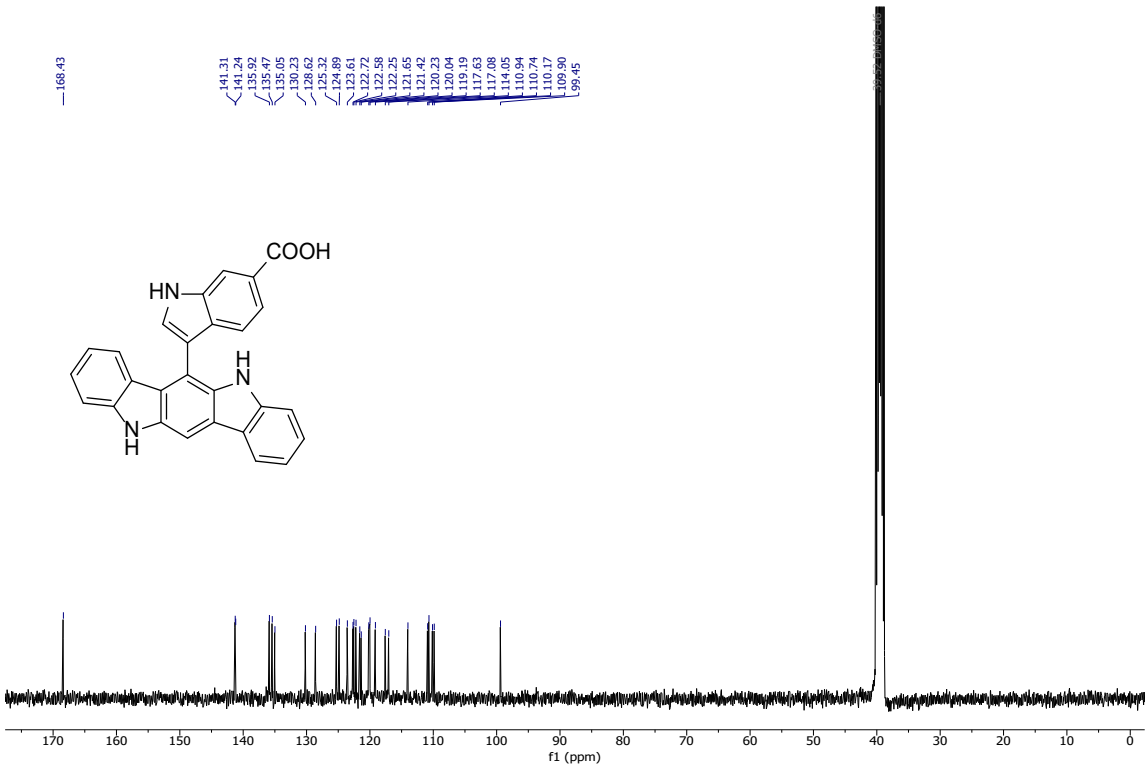

5-((1*H*-Indol-2-yl)methylene)-1,3-dimethylpyrimidine-2,4,6(1*H*,3*H*,5*H*)-trione (6a)
***N*-(4-(3-(5,11-Dihydroindolo[3,2-*b*]carbazol-6-yl)-1*H*-indol-5-yl)phenyl)methanesulfonamide (8a)**

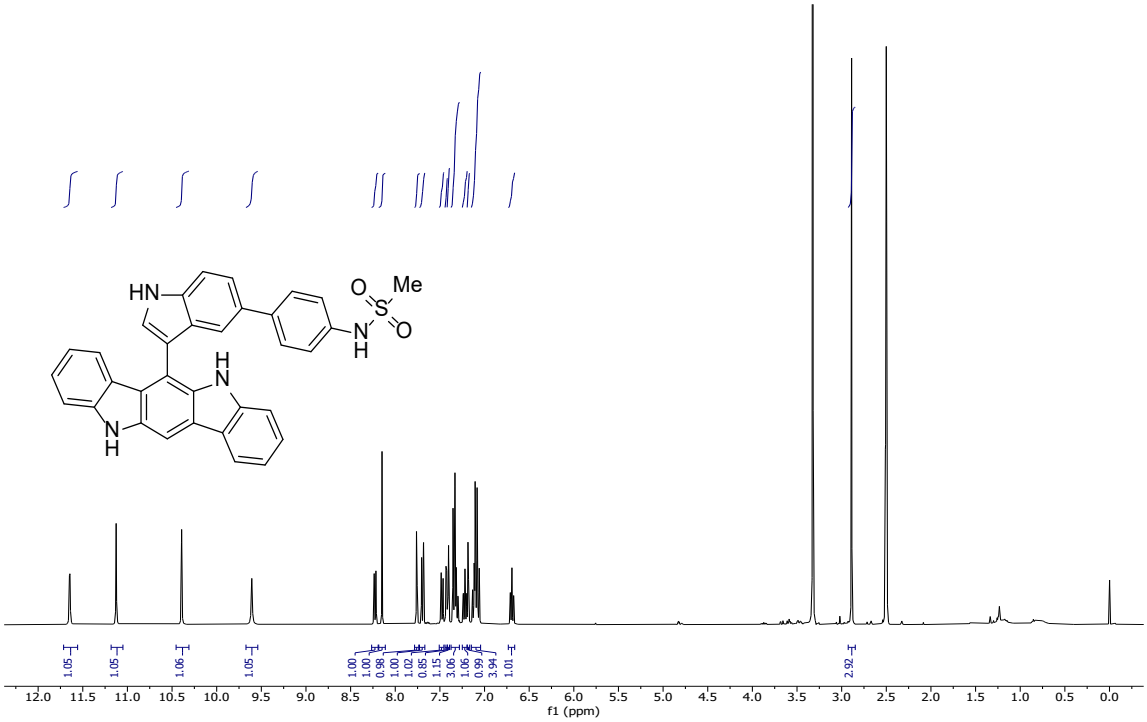

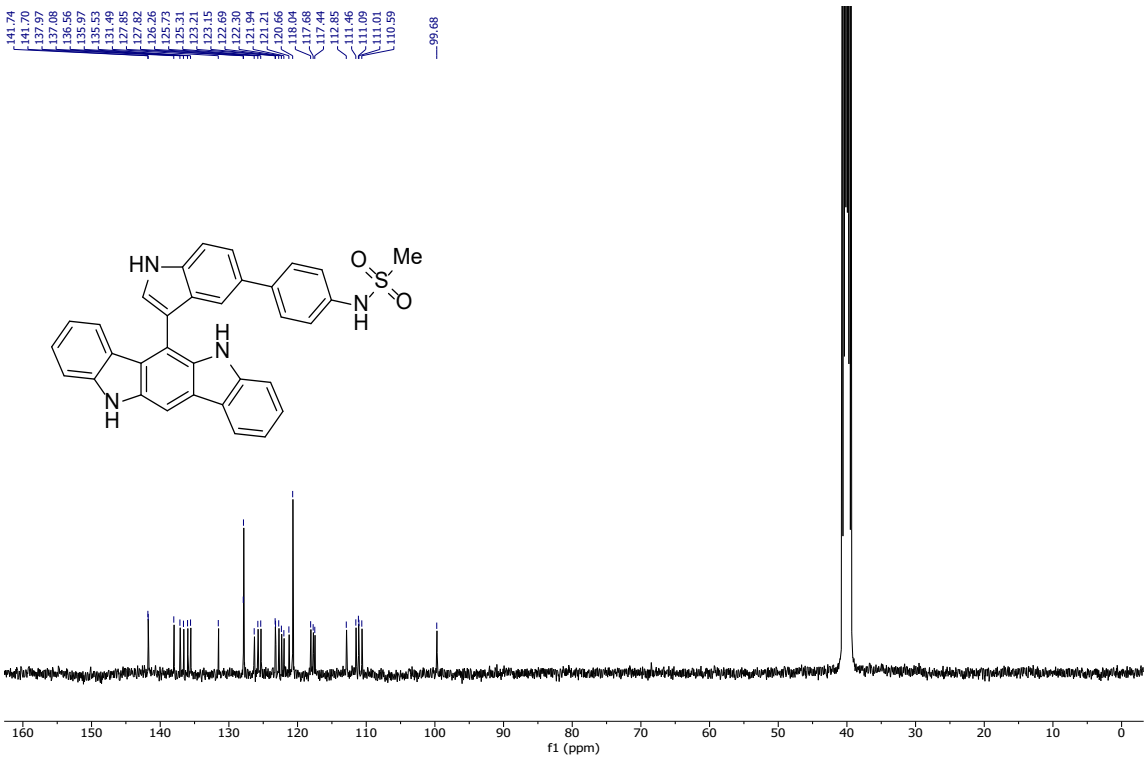

6-(5-(*p*-Tolylethynyl)-1*H*-indol-3-yl)-5,11-dihydroindolo[3,2-*b*]carbazole (8b)

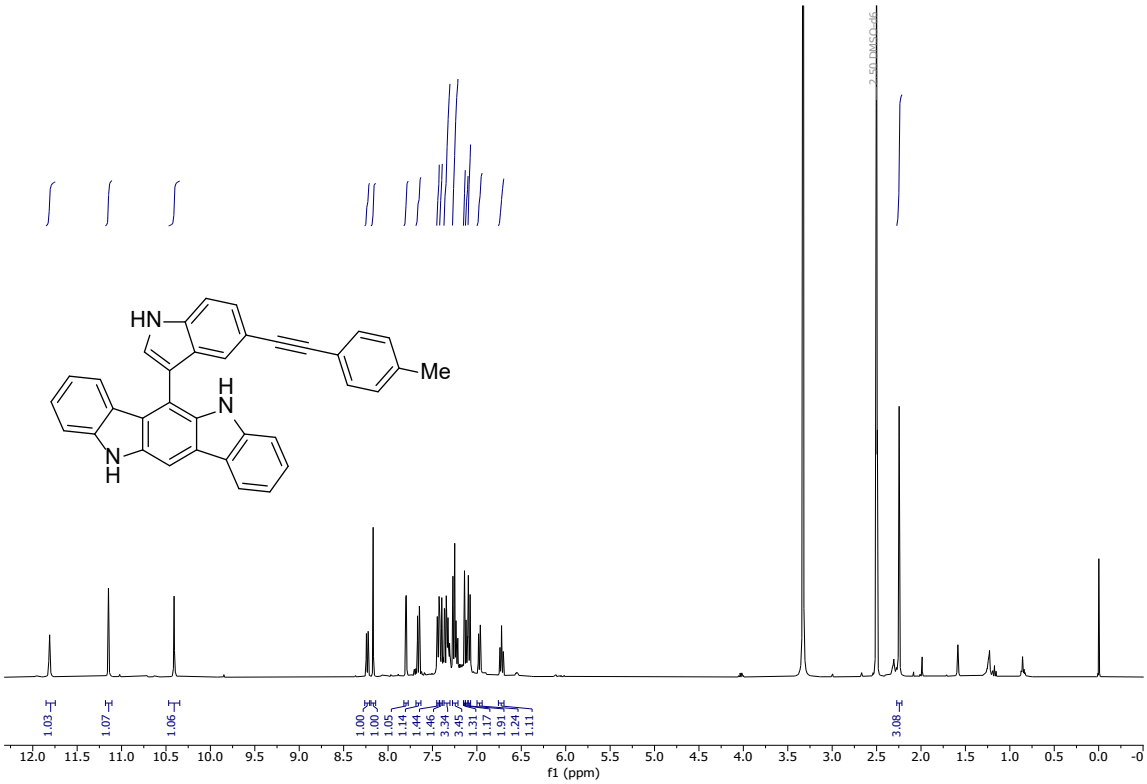

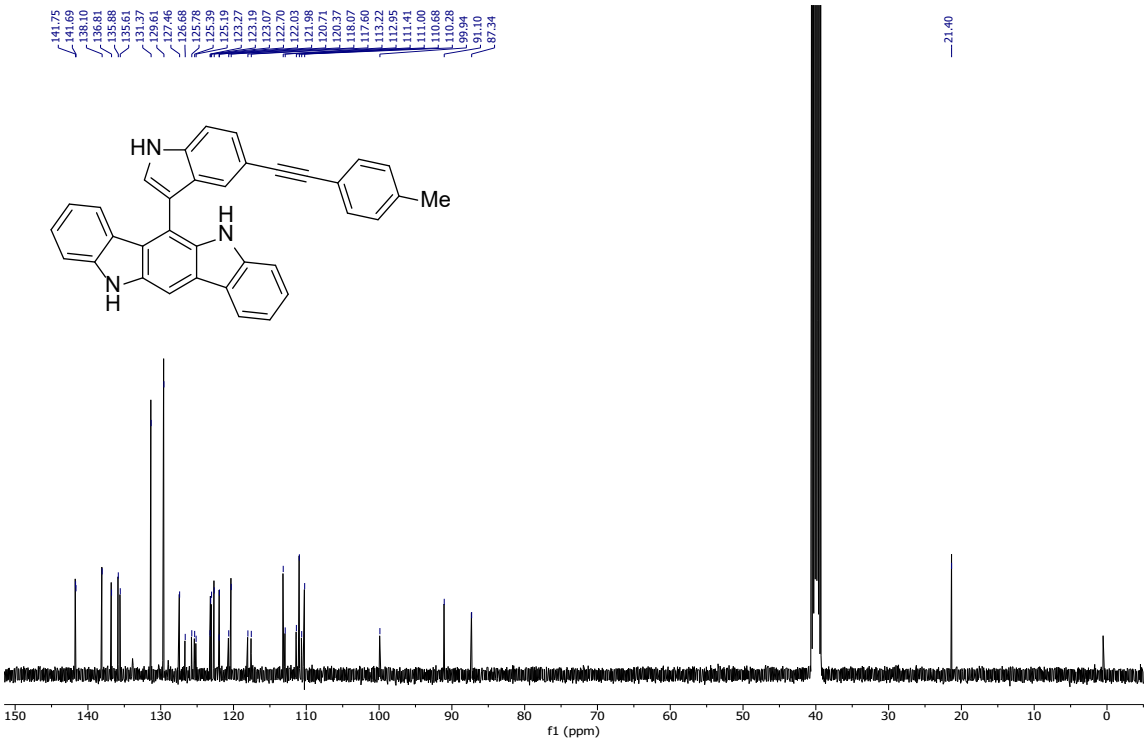

_N_-(2-(5,11-Dihydroindolo[3,2-_b_]carbazole-6-carbonyl)phenyl)acetamide (9)

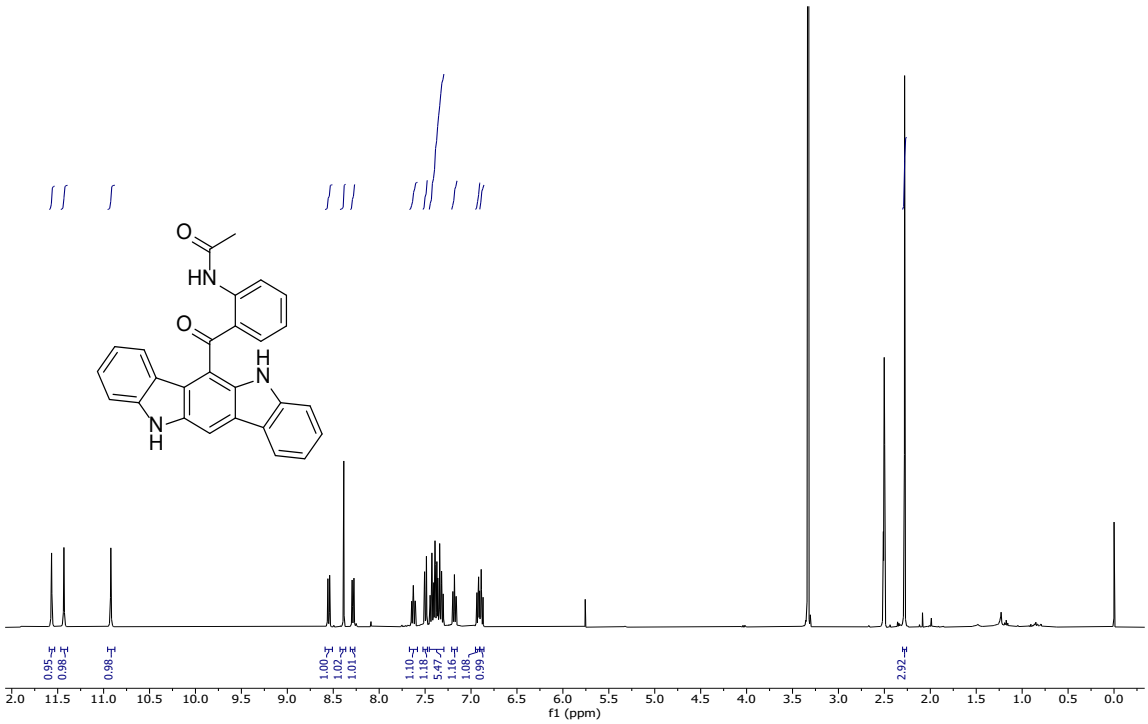

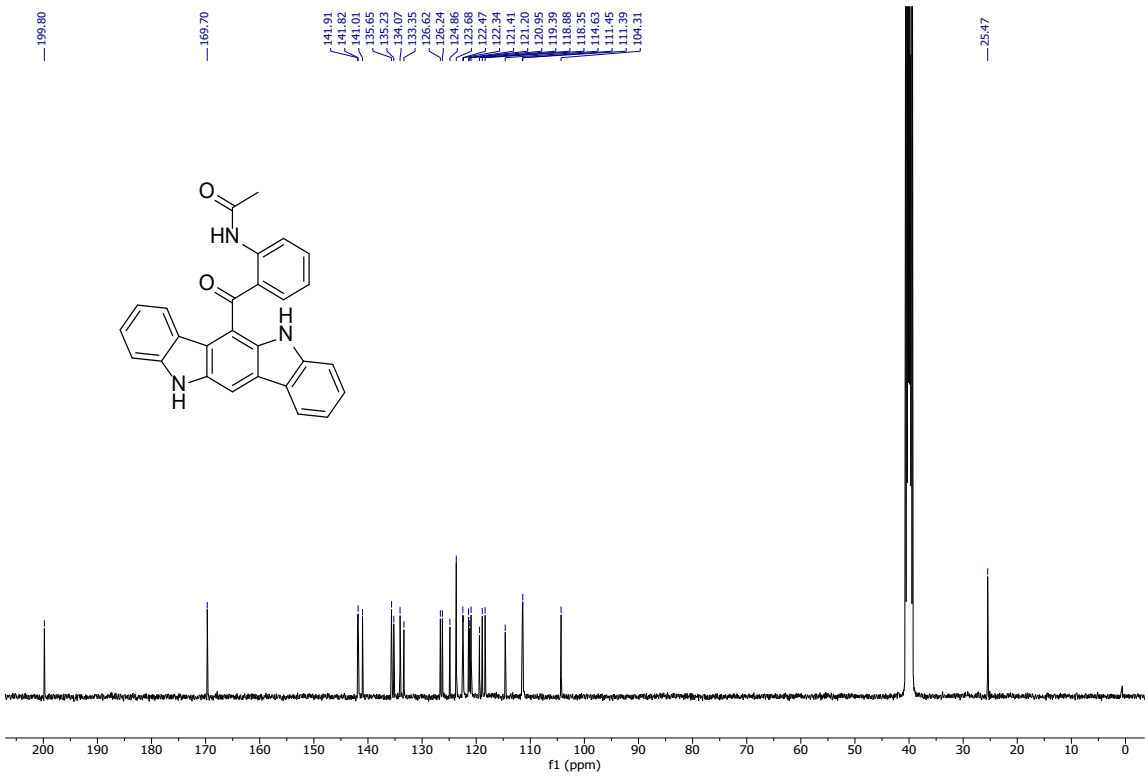

1-Acetyl-5'*H*-spiro[indoline-2,6'-indolo[3,2-*b*]carbazole]-3,12'(11'*H*)-dione (10)

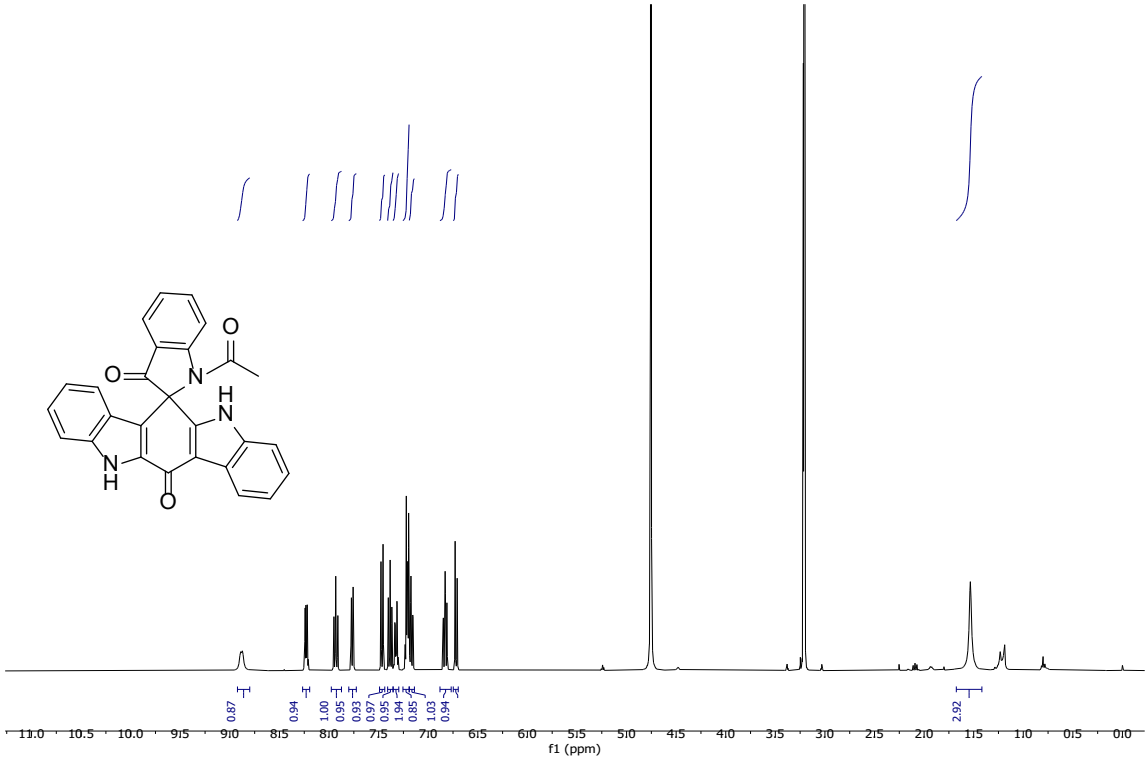

+

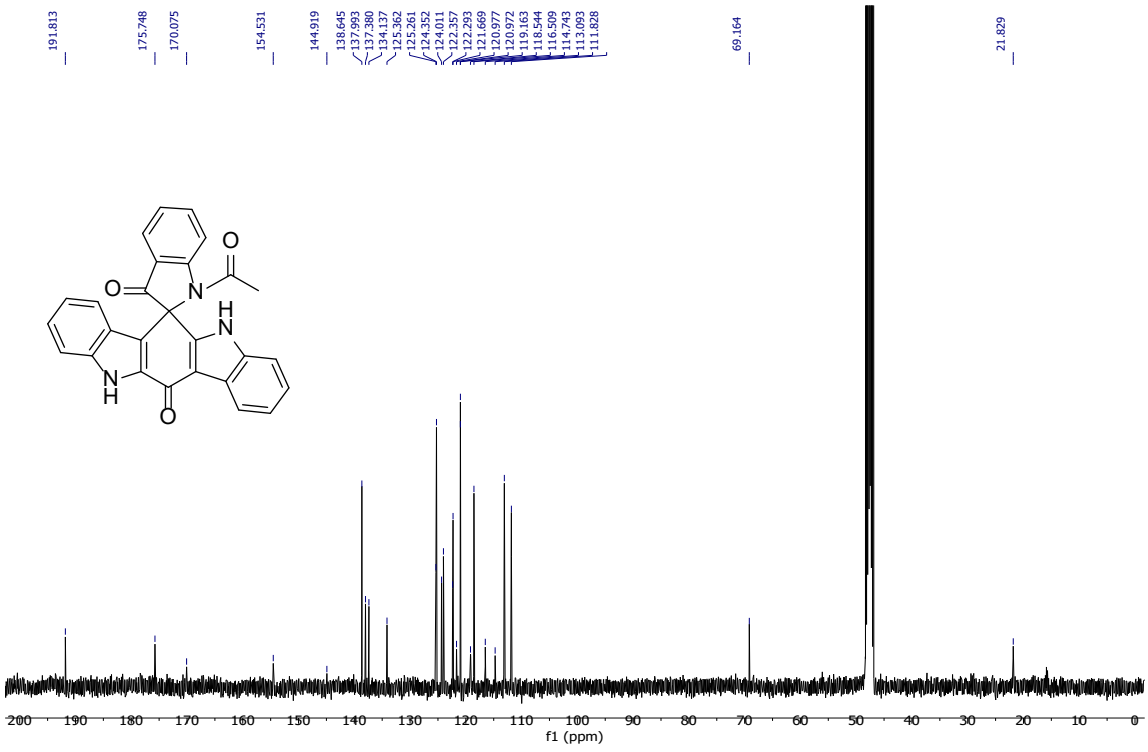

3-(5,11-Dihydroindolo[3,2-*b*]carbazole-6-yl)-*N*-pentyl-1*H*-indole-6-carboxamide (11a)

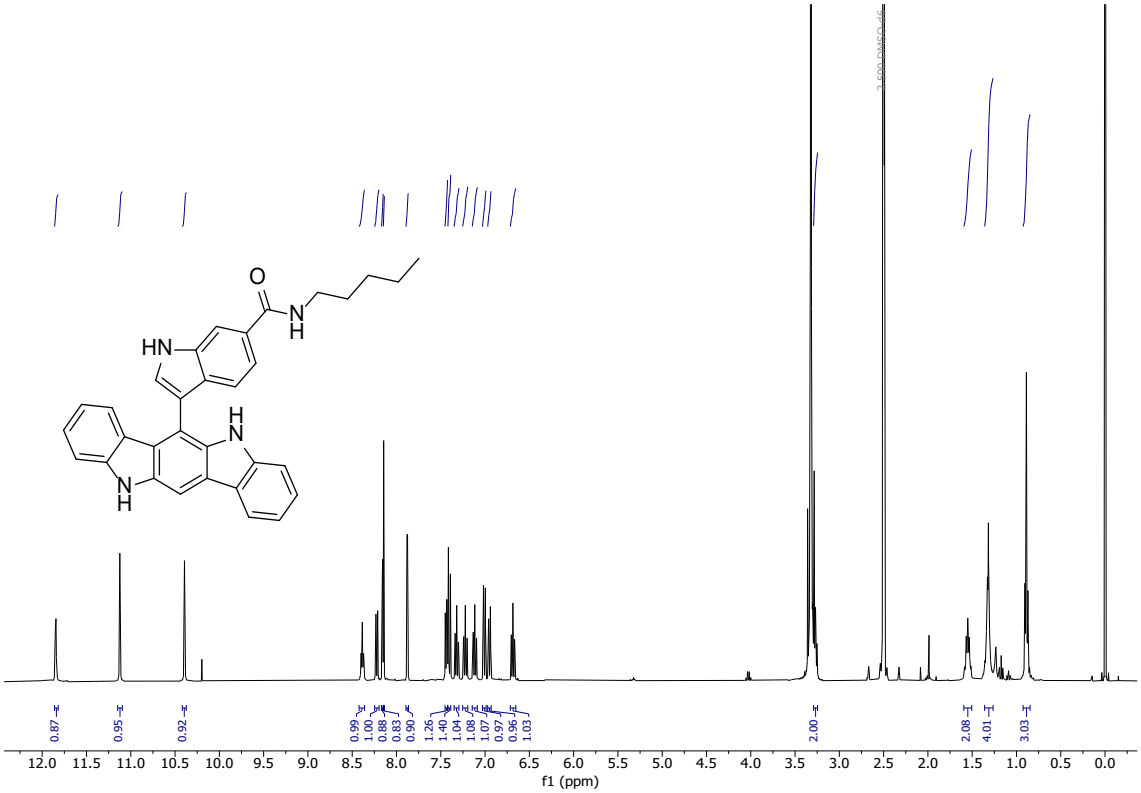

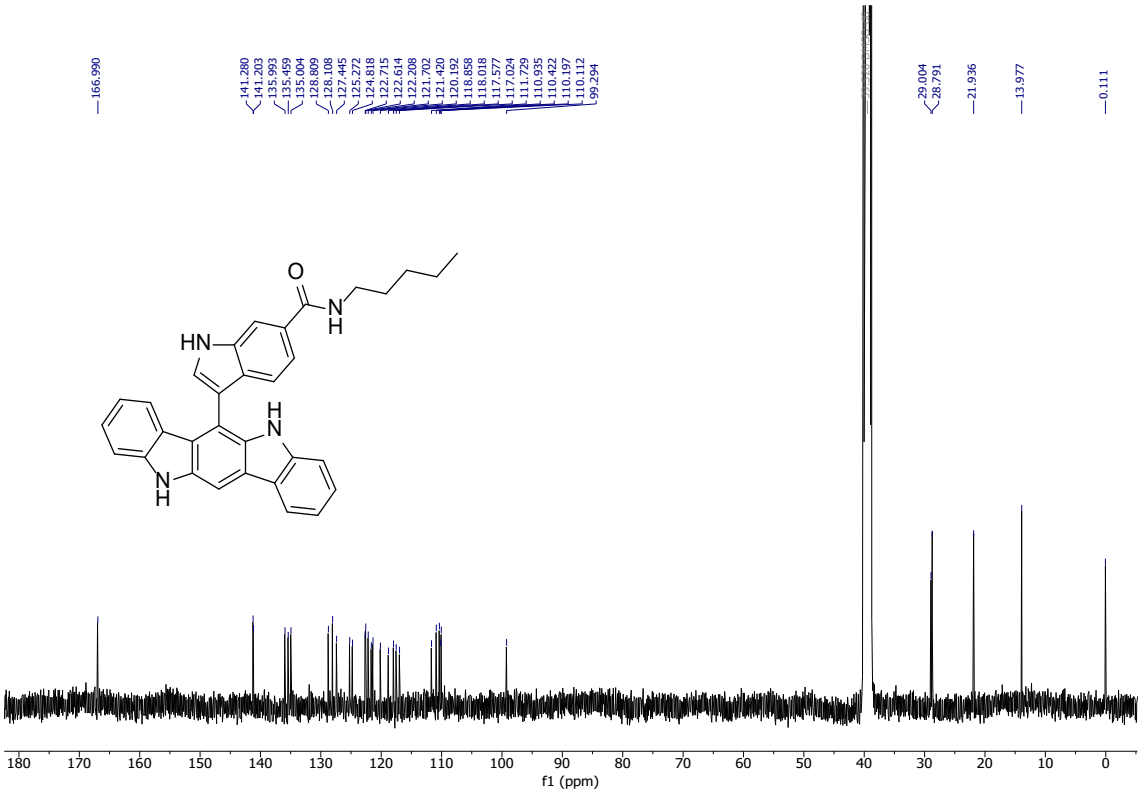

Indolocarbazole-PEG3-thalidomide (11b)

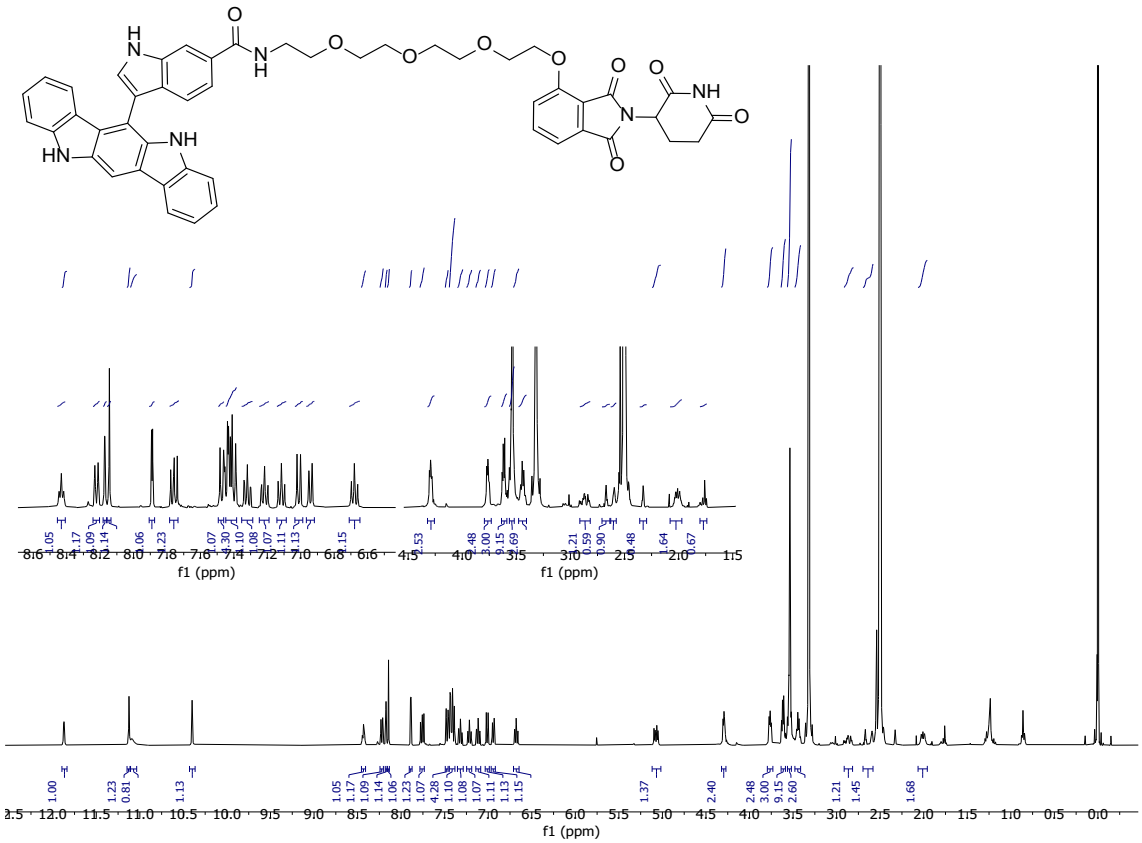

Diaminodecane-HomoPROTAC (11c)

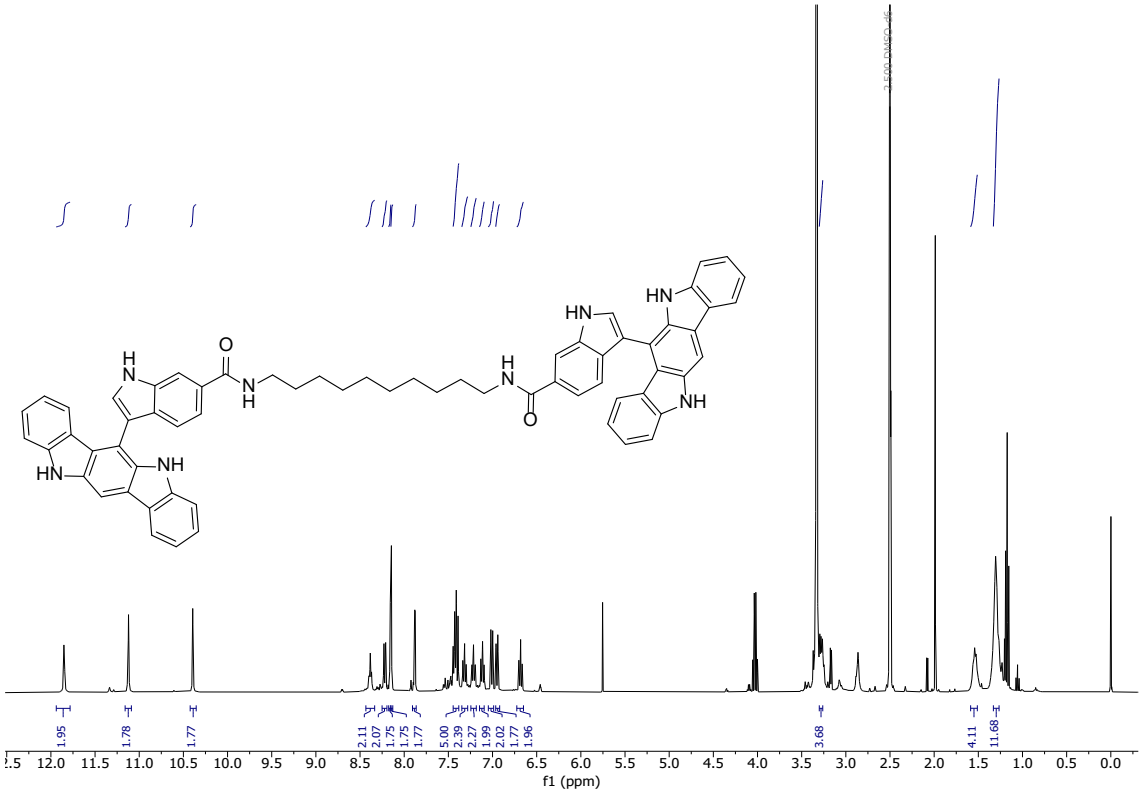

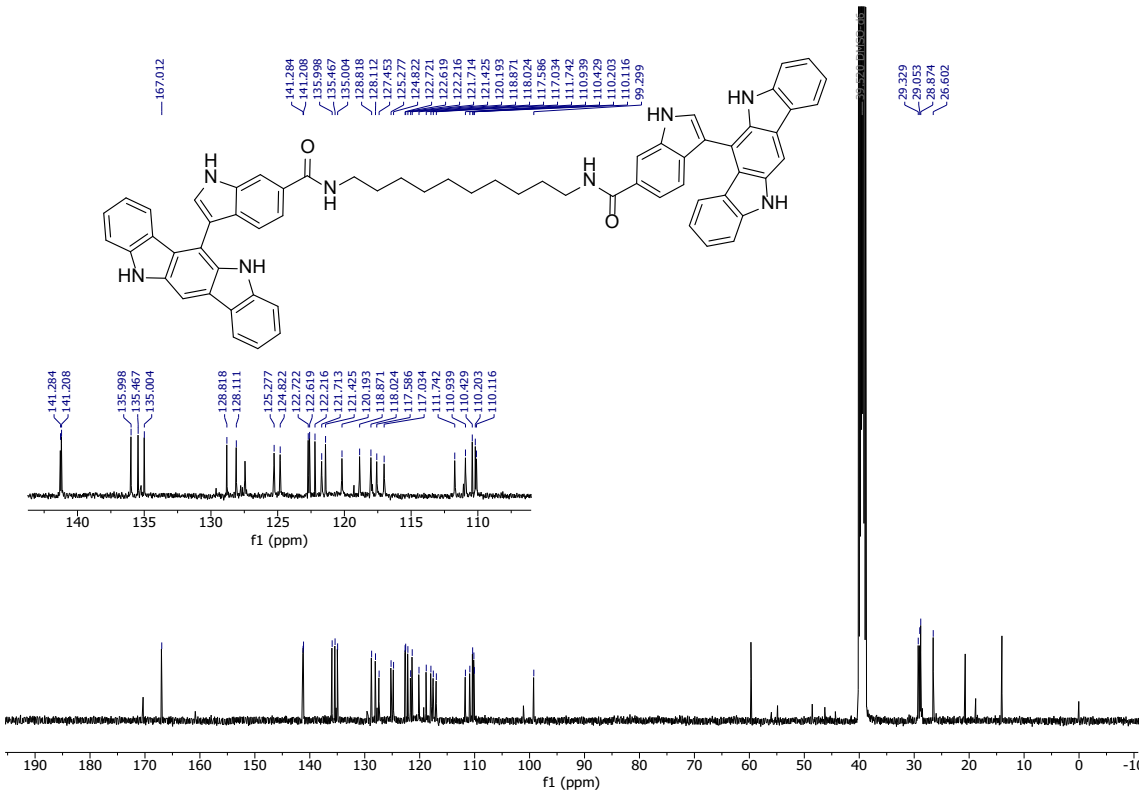

PEG3-HomoPROTAC (11c)

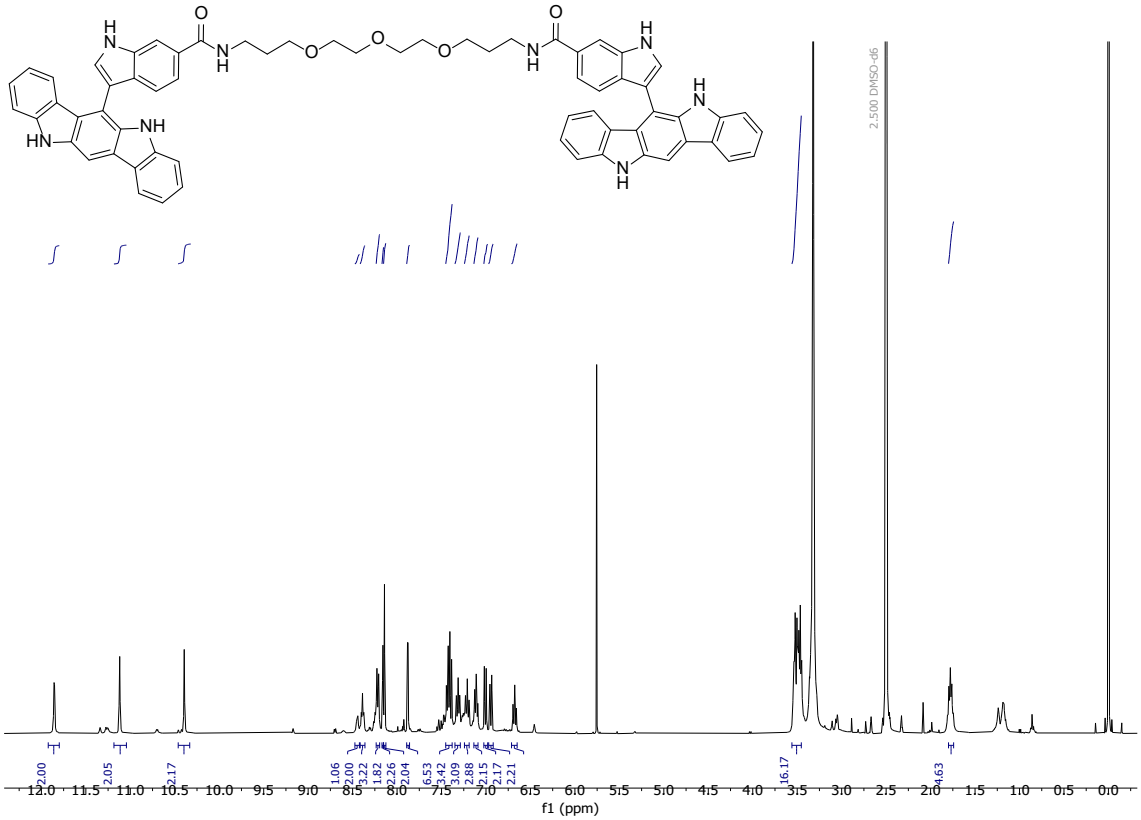

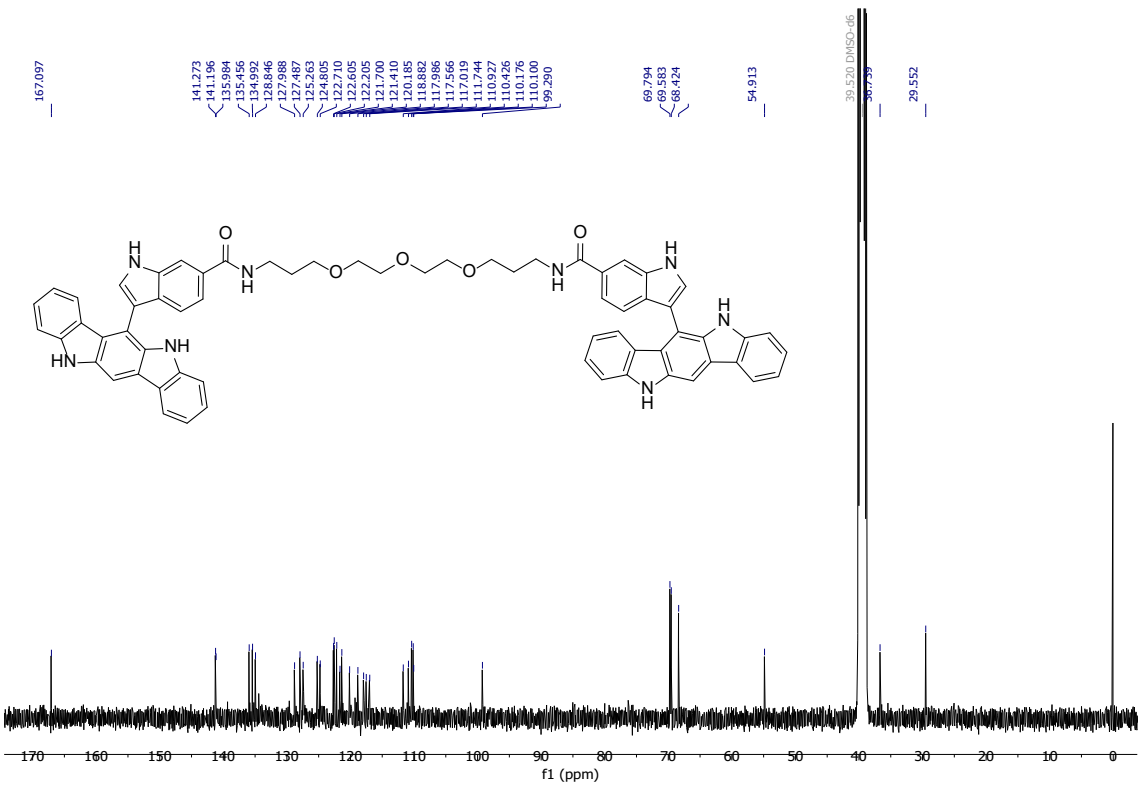

6-Ethoxy-5,11-dihydroindolo[3,2-*b*]carbazole (12)

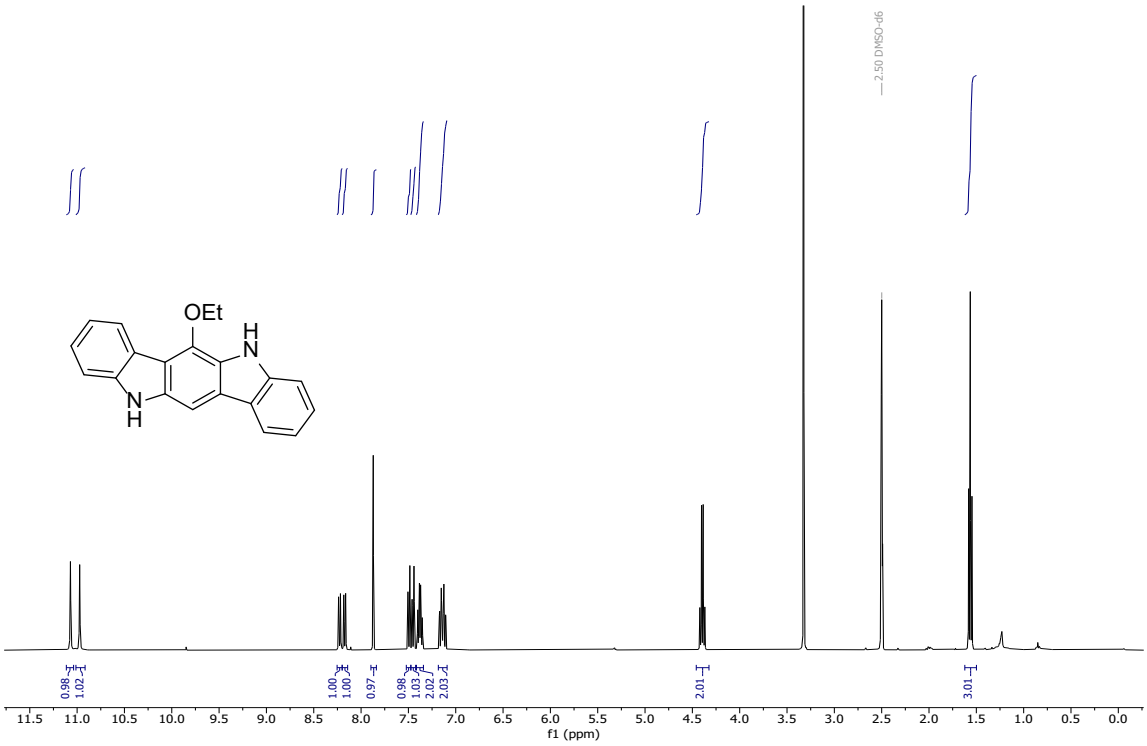

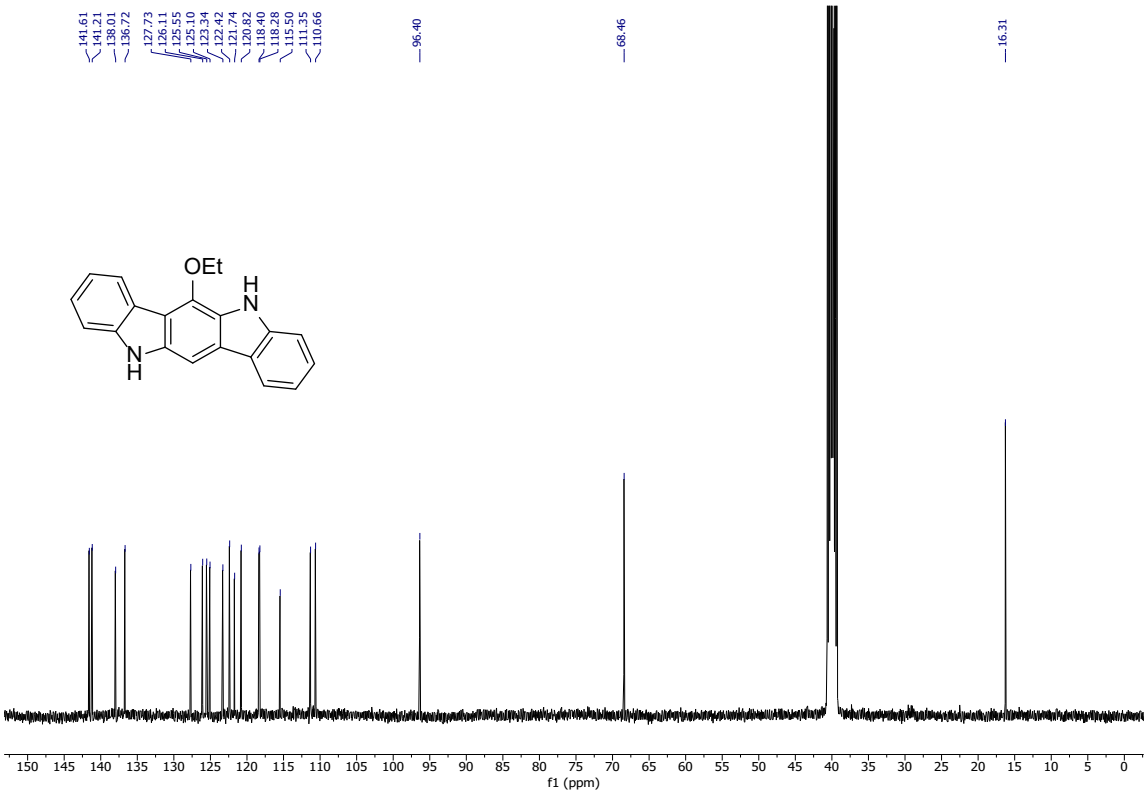

3. References

[1] V. Rothhammer, F.J. Quintana, *Nat. Rev. Immunol*. **2019**,*19*, 184–197.

[2] a) I. A. Murray, A. D. Patterson, G. H. Perdew, *Nat. Rev. Cancer* **2014**, *14*, 801-814. b) M. F. Torti, F. Giovannoni, F. J. Quintana, C. C. García, *Front. Immunol.* **2021**, *12*, 624293. c) Also see: J. Flegel, S. Shaaban, Z. J. Jia, B. Schulte, Y. Lian, A. Krzyzanowski, M. Metz, T. Schneidewind, F. Wesseler, A. Flegel, A. Reich, A. Brause, G. Xue, M. Zhang, L. Dötsch, I. D. Stender, J.-E. Hoffmann, R. Scheel, P. Janning, F. Rastinejad, D. Schade, C. Strohmann, A. P. Antonchick, S. Sievers, P. Moura-Alves, S. Ziegler, H. Waldmann, *J. Med. Chem*. **2022**, *65*, 16268−16289. d) C. A. Opitz, P. Holfelder, M. T. Prentzell, S. Trump, *Biochem. Pharmacol.* **2023**, *216*, 115798.

[3] M. G. Lebwohl, L. S. Gold, B. Strober, K. A. Papp, A. W. Armstrong, J. Bagel, L. Kircik, B. Ehst, H. Chih-Ho Hong, J. Soung, J. Fromowitz, S. Guenthner, S. C. Piscitelli, D. S. Rubenstein, P. M. Brown, A. M. Tallman, R. Bissonnette, *N. Engl. J. Med*. **2021**, *385*, 2219–2229.

[4] a) C. F. A. Vogel, L. S. Van Winkle, C. Esser, T. Haarmann-Stemmann, *Redox Biol*. **2020**, *34*, 101530. b) K. W. Bock*, Biochem. Pharmacol*. **2020**, *178*, 114093.

[5] a) K.Wiebke Schulte, E. Green, A. Wilz, M. Platten, O. Daumke. *Structure* **2017***, 25*, 1025–1033; b) S. Giani Tagliabue, S. C. Faber, S. Motta, M. S. Denison, L, Bonati. *Sci. Rep*.**2019**, *9*,10693; c) W. H. Bisson, D. C. Koch, E. F. O'Donnell, S. M. Khalil, N. I. Kerkvliet, R. L. Tanguay, R. Abagyan, S. K. Kolluri. *J. Med. Chem*. **2009**, *52*, 5635–5641; d) E. Goya-Jorge, R, M. Giner, M. Sylla-Iyarreta Veitía, R, Gozalbes, S, J. Barigye. *Chemosphere* **2020**, *256*, 127068.

[6] L. P. Nguyen, C, A. Bradfield. *Chem. Res. Toxicol*. **2008**, *21*, 102–116.

[7] C. Zhang, K. L. Creech, W. J. Zuercher, T. M. Willson. *Sci. Rep*. **2019**, *9*, 9982.

[8] G. Karageorgis, D. J. Foley, L. Laraia, S. Brakmann, H. Waldmann. *Angew. Chem. Int. Ed*. **2021**, *60,* 15705–15723.

[9] T. Janosik, A. Rannug, U. Rannug, N. Wahlström, J. Slätt, J. Bergman. *Chem. Rev*. **2018**, *118*, 9058–9128.

[10] For the only intriguing, reported example, see: S. Mula, N. Leclerc, P. Levéque, P. Retailleau, G. Ulrich, *J. Org. Chem.* **2018**, *83*, 14406−14418.

[11] a) J. Zhu, Q. Wang, M.-X. Wang, Eds. *Multicomponent Reactions in Organic Synthesis*; Wiley-VCH. Weinheim, Germany, 2015; b) Z. Wang, A. Dömling, *Multicomponent Reactions in Medicinal Chemistry*. In *Multicomponent Reactions towards Heterocycles;* E. van der Eycken, U. K. Sharma, Eds.Wiley-VCH:Weinhiem, Germany, 2022; pp. 91–137; e) P. Slobbe, E. Ruijter, R. V. A. Orru, *Medchemcomm* **2012**, *3*, 1189–1218.

[12] O. Ghashghaei, M. Pedrola, F. Seghetti, V. V. Martin, R. Zavarce, M. Babiak, J. Novacek, F. Hartung, K. Rolfes, T. Haarmann-Stemmann, R. Lavilla, *Angew. Chem. Int. Ed*. **2021**, *60*, 2603–2608.

[13] a) S. Gérard, A. Renzetti, B. Lefevre, A. Fontana, P. de Maria, J. Sapi. *Tetrahedron* **2010**, *66*, 3065–3069 and refs. cited therein; b) M. Shiri. *Chem. Rev*. **2012**, *112*, 3508–3549.

[14] V. Trudel, C.-H. Tien, A. Trofimova, A. K. Yudin. *Nat. Rev. Chem*. **2021**, *5*, 604-623.

[15] L. F. Tietze, G. Brasche, K. M. Gericke, *Domino Reactions in Organic Synthesis*; Wiley-VCH: Weinheim, 2006.

[16] M. Bandia, V. R. R. Ch. *J. Heterocycl. Chem*. **2017**, *54*, 3093–3098.

[17] D. Tejedor, F. García-Tellado, *Chem. Soc. Rev*. **2007**, *36*, 484–491.

[18] Likely following relative nucleophilicities in competition experiments. See: a) H. Mayr, A. R. Ofial. *Acc. Chem. Res*. **2016**, *49*, 952–956; b) H. Mayr, B. Kempf, A. R. Ofial. *Acc. Chem. Res*. **2003**, *36*, 66–77.

[19] Compound **5b**: CCDC 2360557.

[20] For a very recent report using 5-aminopyrazoles, see: G. Jan, D. Rajput, A. Gupta, D. Tsering, M. Karuppasamy, K. K. Kapoor, V. Sridharan. *Org. Chem. Front.* **2023**,*10*, 5978−5985.

[21] N. Llopis, P. Gisbert, A. Baeza, *Adv. Synth. Catal.* **2021**, *363*, 3245−3249.

[22] Compound **10**: CCDC 2360558.

[23] a) M. Shiri, M, A, Zolfigol, H. G. Kruger, Z. Tanbakouchian. *Chem. Rev*. **2010**, *110*, 2250–2293; b) V, Nair, K. G. Abhilash, N. Vidya. *Org. Lett*. **2005**, *7*, 5857–5859; c) M. Barbero, S. Cadamuro, S. Dughera, C. Magistris, P. Venturello. *Org. Biomol. Chem*. **2011**, *9*, 8393–8399.

[24] a) T-Z. Li; S-J. Liu; W. Tan, F. Shi. *Chem. Eur. J*. **2020**, *26*, 15779–15792; b) D. Bisag; D. Pecorari; A. Mazzanti; L. Bernardi, M. Fochi; G. Bencivenni; G. Bertuzzi; V. Corti. *Chem. Eur. J*. **2019**, *25*, 15694-15701; c) F. Jiang; K-W. Chen; P. Wu; Y-C. Zhang; Y. Jiao; F. Shi. *Angew. Chem. Int. Ed*. **2019**, *58*, 15104–15110; d) A. Kim; Y. Kwon. *Synlett* **2022**, *33*, 201–206.

[25] a) A. M. Armon, A. Bedi, V. Borin, I. Schapiro, O. Gidron. *Eur. J. Org. Chem.* **2021**, 5424–5429. b) A. Karton. *Chem. Phys. Lett*. **2014**, *614*, 156–161.

[26] a) R. Kumar, H. Aggarwal, A. Srivastava. *Chem. Eur. J*. 2020, *26*, 10653–10675. b) M. Rickhaus, M. Mayor, M. Jurıcek. *Chem. Soc. Rev*. **2017**, *46*, 1643–1660. c) M. Ball, Y. Zhong, Y. Wu, C. Schenck, F Ng, M. Steigerwald, S. Xiao, C. Nuckolls. *Acc. Chem. Res*. **2015**, *48*, 267−276.

[27] J. Gruszczyk, L. Grandvuillemin, J. Lai-Kee-Him, M. Paloni, C. G. Savva, P. Germain, M. Grimaldi, A. Boulahtouf, H.-S. Kwong, J. Bous, A. Ancelin, C. Bechara, A. Barducci, P. Balaguer, W. Bourguet, *Nat. Commun*. **2022**, *13*, 7010.

[28] S. G. Tagliabue, S. C. Faber, S. Motta, M. S. Denison, L. Bonati. *Sci. Rep*. **2019**, *9*, 10693.

[29] M. Cieslak, M. Słowianek, *Pharmaceutics* **2023**, *15*, 812.

[30] N. Ohoka, G. Tsuji, T. Shoda, T. Fujisato, M. Kurihara, Y. Demizu, M. Naito, *ACS Chem. Biol.* **2019**, *14*, 2822–2832.

[31] R. S. Pollenz, *Chem. Biol. Interact.* **2002**, *141*, 41–61.

[32] R. Bissonnette, E. S.-C. Proulx, C. Jack, C. Maari, *J. Eur. Acad. Dermatol. Venereol*. **2023**, *37*, 1168–1174.

[33] Y. Renert-Yuval, J. P. Thyssen, R. Bissonnette, T. Bieber, K. Kabashima, D. Hijnen, E. Guttman-Yassky, *J. Allergy. Clin. Immunol.* **2021**, *147*, 1174–1190.

[34] G. Brahmachari, S. Das. *RSC Adv*. **2014**, *4*, 7380–7388.

[35] A. Renzetti, E. Boffa, M. Colazzo, S. Gerard J. Sapi, T-H. Chan, H. Nakazawa, C. Villanie, A. Fontana. *RSC Adv*. **2014**, *4*, 47992–47999.

[36] SPARTAN, Wavefunction, Inc., 18401, Von Karman Avenue, Suite 435, Irvine CA 92612 USA.

General Conclusions

The research presented in this thesis supported the reaction space charting approach as a novel and efficient strategy to face some of the challenges associated with the early stages of drug discovery. In particular, it proved to be a useful tool for exploring the chemical space, leading to the discovery of new reactions and the generation of diverse chemical libraries with potential biomedical applications.

The findings highlight the relevance of MCRs in modern synthetic chemistry. In this regard, new multicomponent processes involving heterocycles (either as reactants or adducts) were discovered through the reaction space charting approach, which proved effective in identifying novel synthetic pathways and extending the reach of existing MCRs.

Moreover, the pivotal role that MCRs can play in the discovery of novel compounds with potential pharmaceutical applications was demonstrated. In this context, the modular nature of MCRs facilitated the efficient generation of diverse chemical libraries, providing a broad range of compounds for biological screening and potential drug development.

Privileged scaffolds, specifically 4-imidazolones and ICZ cores, were successfully generated through novel MCR processes. Their biological relevance and intrinsic reactivity were investigated, highlighting their potential as starting points for drug development, such as fluorescent probes, luciferase inhibitors, and transcription factor modulators.

The synthesised compounds were applied to the context of biomedical research, with their physicochemical properties and potential biological activity thoroughly investigated through relevant collaborations, including a predoctoral research stay at a chemical biology laboratory. These applications demonstrated the practical relevance of the developed chemistry to drug discovery and development processes.

Publications

Derived from the Thesis

Chapter I

Development of Heterocyclic Multicomponent Reactions Through Guided Exploration: Direct, Reasonable, and Unpredictable Processes

O. Ghashghaei, P. Nadal Rodríguez, R. Lavilla. *Synlett* **2022**, *33*, 822–835.

Heterocycle-Based Multicomponent Reactions in Drug Discovery: from Hit Finding to Rational Design.

P. Nadal Rodríguez, O. Ghashghaei, A. Bagán, C. Escolano, R. Lavilla. *Biomedicines* **2022**, *10*, 1488.

Reaction Space Charting as a Tool in Organic Chemistry Research and Development.

E. Lozano-Baró,[+] P. Nadal Rodríguez,[+] J. Juárez-Jiménez, O. Ghashghaei, R. Lavilla. *Adv. Synth. Catal.* **2024**, *366*, 551–573.

[+]These authors contributed equally to this work.

Chapter II

Charting the Chemical Reaction Space around a Multicomponent Combination: Controlled Access to a Diverse Set of Biologically Relevant Scaffolds

P. Nadal Rodríguez, O. Ghashghaei, A.M. Shoepf, S. Benson, M. Vendrell, R. Lavilla. *Angew. Chem. Int. Ed.* **2023**, *135*, e202303889.

Other Publications

The Prohibitin-Binding Compound Fluorizoline Activates the Integrated Stress Response through the eIF2α Kinase HRI

I. Sánchez-Vera, S. Núñez-Vázquez, J. Saura-Esteller, A. M. Cosialls, J. Heib, P. Nadal Rodríguez, O. Ghashghaei, R. Lavilla, G. Pons, J. Gil, D. Iglesias-Serret, *Int. J. Mol. Sci.* **2023**, *24*, 8064.

Annex I

Review Articles Derived from Chapter I

Synlett O. Ghashghaei et al. Account

Development of Heterocyclic Multicomponent Reactions through Guided Exploration: Direct, Reasonable and Unpredictable Processes

Ouldouz Ghashghaei
Pau Nadal Rodríguez
Rodolfo Lavilla*

Laboratory of Medicinal Chemistry, Faculty of Pharmacy and Food Sciences, and Institute of Biomedicine (IBUB), University of Barcelona, Av. de Joan XXIII, 27-31, 08028 Barcelona, SPAIN
rlavilla@ub.edu

This Account is dedicated to Prof. Mercedes Alvarez (University of Barcelona) on the occasion of her retirement, for her mentorship and support

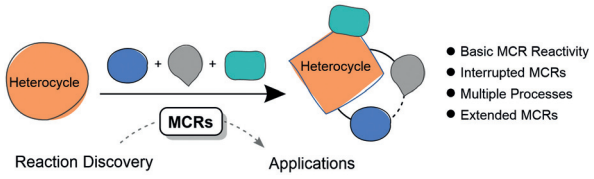

Received: 23.12.2021
Accepted after revision: 25.01.2022
Published online: 25.01.2022
DOI: 10.1055/a-1750-3185; Art ID: st-2021-a0473-a
Crowd-Reviewed

Abstract This Account summarizes the research of the group on the multicomponent reactions arena with fundamental heterocycles as substrates, using mechanistic considerations to hypothesize new processes and to rationalize results. Biomedical applications of the ensuing adducts were also envisaged, which brought about interesting discoveries.

Key words azines, azoles, heterocycles, multicomponent reactions, reaction discovery, reaction mechanism

1 Introduction and Context

It becomes evident that solutions to the most urgent challenges we are facing (health, food, environment, energy, etc.) would involve clever and imaginative use of chemistry. Creating new medicines and materials is thus closely related to our capacity of synthesizing complex and functional molecules. Therefore, organic synthesis is of uttermost importance and features like versatility and sustainability, as well as atom-, step-, redox-, and time-economies, define the practicality of the synthetic access to a given new compound.[1] In the 1980s, the preparation of complex natural products was a common playground, which fostered remarkable discoveries regarding innovative connectivities, often embodied in long stepwise sequences. Working in a Faculty of Pharmacy, we were exposed to the needs of modern medicinal chemistry, where the rapid preparation of bioactive compounds series with growing complexity is a priority. In this context, we were struck by the considerations on the vastness of the chemical space by Sharpless in his seminal paper on click chemistry,[1b] and later by the monumental and pioneering work of Ugi on multicomponent reactions (MCRs)[2] and its relation with combinatorial chemistry. Also, relevant here was its connection with domino reactions, where a single event triggers the sequential generation of several bonds, often in an intramolecular mode.[3]

MCRs are the transformations in which three or more reactants generate an adduct containing relevant portions of the starting materials, in a single operation through a unified reaction mechanism. They are pivotal in modern organic synthesis, showing high levels of reaction economies and bond-forming efficiency, while furnishing a wide array of connectivity patterns. Unfortunately, MCRs are not as abundant as the standard bimolecular transformations, the

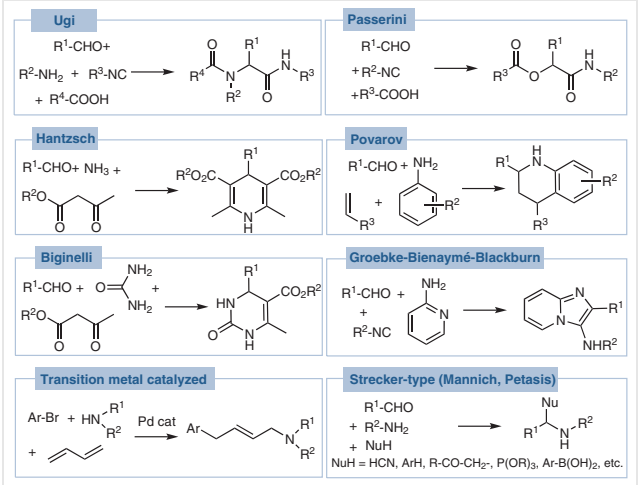

Scheme 1 Representative multicomponent reactions (MCRs)

© 2022. Thieme. All rights reserved.
Georg Thieme Verlag KG, Rüdigerstraße 14, 70469 Stuttgart, Germany

Downloaded by: Universidad de Barcelona. Copyrighted material.

main general processes being venerable named reactions of Passerini, Ugi, Strecker, Mannich, Biginelli, Hantzsch, and Povarov, together with modern contributions such as Petasis, Koevenagel-based cycloadditions, transition-metal-catalyzed and domino-anionic processes, radical-based transformations, etc. (Scheme 1).

Convergently, heterocycles predominate in medical chemistry and account for the most common structural motifs present in drugs. It should be noted that typically thousands of diverse heterocyclic compounds of increasing complexity must be prepared when launching a new drug. Therefore, the implicit synthetic issues involved, constitute one of the main goals in drug discovery.[4] The interplay of heterocycles with MCRs has typically been restricted to the presence of heterocyclic substituents in reactants taking part in well-known MCRs or to the synthesis of heterocyclic adducts through these processes.[2d,5]

With these thoughts in mind, we designed a research line combining all these concepts and, quite naïvely, outlined our approach as the use of basic heterocycles (common azines, azoles, and other N-, O-, S-heterocyclic nuclei) as reactants in MCRs (Scheme 2).[6] The project intended to gain basic knowledge in an underdeveloped area and to discover new, likely general transformations in order to eventually facilitate the preparation of bioactive compounds, i.e., drugs and bioprobes. Additionally, our feeling that the particularities of heterocyclic chemistry may tune or even drastically change the course of the multicomponent processes was an undeniable thrill. Our intention was to drive the reaction discovery through what we thought to be rational mechanistic hypotheses, based on fundamental heterocyclic reactivity. At least, this was the original plan.

Incidentally, before launching our MCR project, we had described a series of remarkable processes, in the context of our past work on the chemistry of pyridine derivatives. In

Biographical Sketches

Ouldouz Ghashghaei received her BSc and MSc in chemistry from Sharif University of Technology, (Iran) and a second MSc (2013), followed by her PhD (2017) in organic chemistry from Universitat de Barcelona (Spain), both under supervision of Prof. R. Lavilla. Currently, she is a postdoctoral researcher at the Faculty of Pharmacy, where she studies facilitated synthetic approaches to access heterocyclic systems of biomedical interest.

Pau Nadal received his degree in pharmacy from Universitat de Barcelona (Spain) in 2019. Then he joined the MedChem department in Glaxo Smith Kline in Stevenage (UK) through a year-long industrial placement. Since October 2020 he is pursuing his PhD under supervision of Profs. R. Lavilla and C. Escolano at Universitat de Barcelona.

Rodolfo Lavilla received his BA (1982), Master's (1983) and PhD (1987) degrees from the Faculty of Pharmacy, Universitat de Barcelona (Spain) under the supervision of Prof. Mercedes Alvarez. After a postdoctoral stage at the University of California San Diego (USA) with Prof. Ernest Wenkert, he joined the faculty at Universitat de Barcelona in 1990 where he is currently full professor of organic and medicinal chemistry at the Faculty of Pharmacy. He has co-authored over 130 research articles, reviews, book chapters and patents. His research interests include heterocyclic reactivity, multicomponent reactions, and applications to biomed projects.

Downloaded by: Universidad de Barcelona. Copyrighted material.

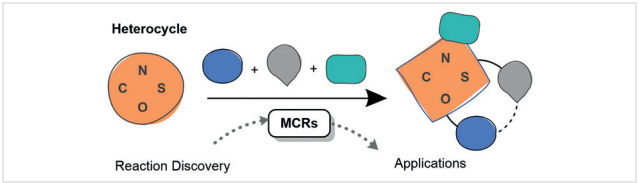

Scheme 2 Basic heterocycles as reactants in MCRs

these premonitory processes, several counterintuitive transformations took place in polar and radical reactions, overcoming the biomimetic tendency of dihydropyridines to suffer oxidation towards the pyridinium salt.[7] Instead, complex domino reactions took place, and we immediately felt a strong attraction to these MCR processes, where one substrate is incorporated twice into the final adduct but with different connectivity (ABB′ reactions, Scheme 3).[8] These findings further convinced us that the hidden aspects of the heterocyclic reactivity involved could justify our new MCR project.

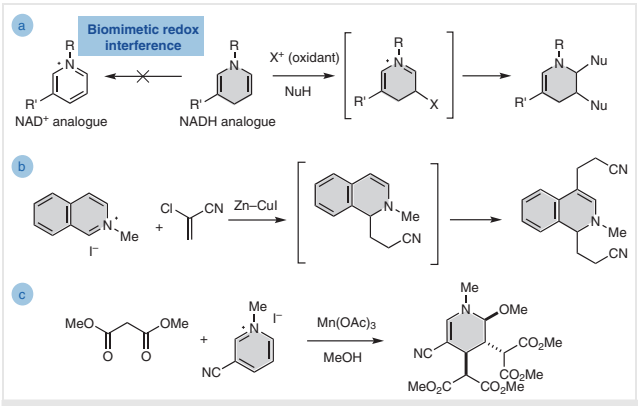

Scheme 3 ABB′ processes developed in the group prior to our MCR project

2 The Beginnings: Unexplored Heterocyclic Substrates

We started our work by analyzing the well-known Povarov MCR (Scheme 1)[9] using dihydropyridines (DHPs) as the activated olefins. The idea was to bypass the biomimetic redox reaction between imines and DHPs, because coenzyme NADH is a 1,4-DHP that reduces imines and carbonyls whilst becoming oxidized to NAD^+.[10,11] To this end, we found a way to avoid this interference using appropriate Lewis acid catalysis, as we observed that Sc^{3+} salts catalyzed the desired interaction while Mg^{2+} favored the unproductive redox process. In this way, *N*-alkyl-1,4-DHPs containing an electron-withdrawing group (EWG) at the β-position for stability, reacted with 4-methylaniline and ethyl glyoxylate to yield the desired naphthyridine adducts **1**, as usual with low stereoselective control, affording mixtures of *cis* and *trans* isomers (Scheme 4).[12] The mechanism of this formal aza-Diels–Alder cycloaddition likely involves a Mannich-type step between the enamine moiety and the *in situ* formed Schiff base **A**, followed by a Pictet–Spengler cyclization. Although there is strong evidence that many Povarov MCRs follow a concerted mechanism,[13] we believe that with highly polarized systems, the process evolves through the commented ionic pathway. The scope of the reaction includes a wide range of aromatic aldehydes and the highly activated carbonyl isatin, as well as the use of *N*-acyl-1,4-dihydropyridines. In contrast, the MCR was rather sensitive to the nature of the aniline component and, although the expected adducts were obtained in most cases, highly electron-deficient anilines such as 4-aminopyridine failed to perform the final Pictet–Spengler step of the reaction, whereas exceedingly electron-rich derivatives bypassed the DHP, trapping the imine instead. Highly substituted naphthyridines were obtained via a 4-component, one-pot tandem reaction in which the usual MCR was performed using an *in situ* generated γ-substituted DHP from its respective pyridinium salt. Adducts **2** containing cyano, phosphonate, and aminouracil residues at the C-4 position were prepared though this protocol (Scheme 4).

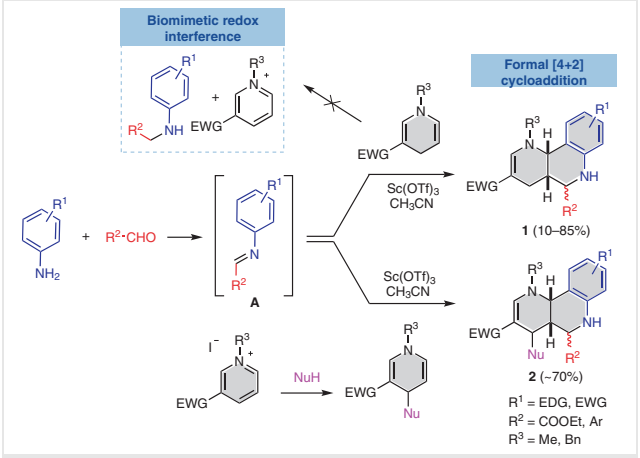

Scheme 4 The Povarov MCR with 1,4-DHPs, the biomimetic redox interference, and tandem processes

Next, we tested cyclic enamides following the described protocol. Both *exo*- and *endo*-cyclic unsaturated lactams yielded the expected products **3** and **4**, respectively, the former providing interesting spiro adducts (Scheme 5).[14] The incorporation of a methyl substitution at the α-position of the unsaturated lactams led to the interruption of the classical Povarov MCR (likely due to steric congestion) and provided different scaffolds depending on the carbonyl component. Whereas ethyl glyoxylate promoted a proton loss of the iminium intermediate with regeneration of the lactam after the Mannich step to yield enamides **5**, the more nucleophilic glyoxylic acid trapped the iminium ion to furnish adducts **6** (Scheme 5b).

© 2022. Thieme. All rights reserved.

Downloaded by: Universidad de Barcelona. Copyrighted material.

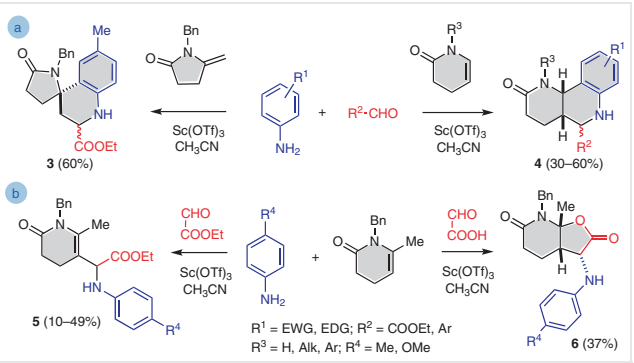

Scheme 5 The Povarov MCR with *endo*- and *exo*-cyclic enamides

Following this line, the reactivity of diverse heterocyclic substrates (imidazo-, oxazo-, and thiazolones) was explored under standard Povarov conditions. Pleasingly, a variety of fused adducts **7** were suitably obtained (Scheme 6).[15] It was observed that the heterocycle addition upon the imine took place in a regioselective manner, with the N atom pushing its β-position more efficiently than competing O, S atoms. To test the observed regioselectivity traits, we prepared the substrate **8** with the aromatic aldehyde moiety linked to the N atom of the thiazolone and reacted with an aniline under standard conditions. Although not strictly an MCR, the reaction yielded the desired all *cis*-pentacyclic adduct **9** with a remarkable regioselectivity reversal (Scheme 6b).

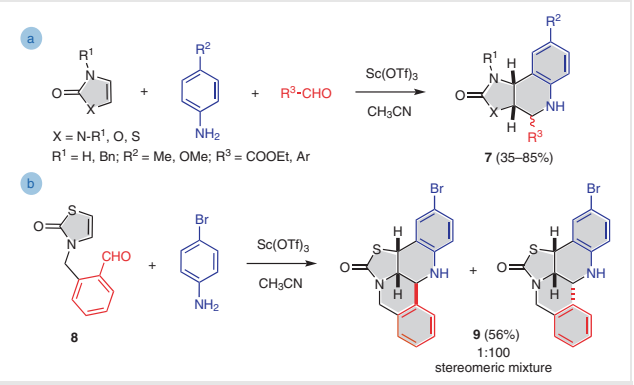

Scheme 6 Imidazolone-type heterocycles in Povarov MCRs

As said, the Povarov MCR usually leads to diastereomeric mixtures, and protocols with improved stereoselectivity require complex catalysts and present practical restrictions.[13b,16] Rather, we followed simple and general protocols in racemic series and obtained the relative stereochemistries. In some cases, to increase chemical diversity, we oxidized the crude products to generate the corresponding quinolines, which maintained all the crucial connectivity and functionalization introduced during the MCR, albeit with the loss of all stereochemical information (Scheme 7).[17] Both DDQ and MnO_2 served such purpose, the latter avoiding the known oxidation–elimination alternative pathway.[18] Some of the resulting quinolones **10–12** were found to exhibit an interesting multitrypanosomatid activity.[19] These adducts were also positively tested as inhibitors of human acetylcholinesterase (hAChE) and constituted a new family of anti-Alzheimer agents.[20]

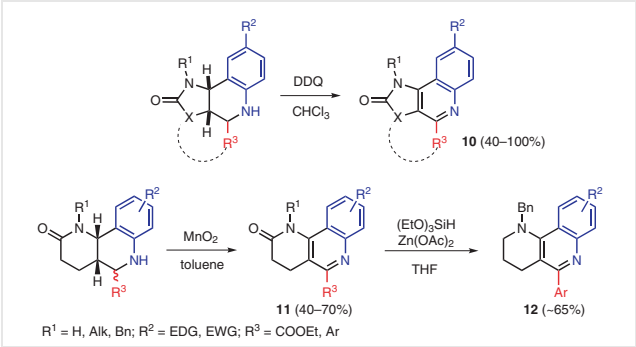

Scheme 7 Oxidation products of various heterocyclic Povarov adducts

Next, we turned to isocyanide-based MCRs (IMCRs),[2a,21] namely Ugi- and Passerini-type processes, to challenge DHPs and dihydropyranes under acidic conditions, in an attempt to generate the putative cationic intermediate which should react with the isocyanide (Scheme 8). As devised, the reactions were productive and using stoichiometric amounts of *p*-toluenesulfonic acid (*p*TSA), the protonation of the olefin moiety allowed for the nucleophilic attack of the isocyanide. The generated nitrilium intermediate provided the desired carboxamides **13** and **14** after final water quenching, accomplishing a one pot α-carbamoylation of DHPs and dihydrofuran/-pyran reactants (Scheme 8).[22] Substitutions at C-2 position of the enol ether afforded the corresponding adduct as a *trans*/*cis* (60:40) diastereomeric mixture. We also generated the reactive intermediate by means of other electrophilic species such as halogens and selenium derivatives. Despite initial concerns regarding the potential interference of isocyanides with halogen and selenium electrophiles, we were delighted to see that the MCRs successfully furnished the desired β-halo- or β-seleno-α-carbamoyl adducts **15–17**.[23] Remarkably, the transformation was stereoselective using DHPs as substrates, and only the *trans* isomers were detected (Scheme 8a). However, the reaction with enol ethers was unproductive using halogens (unstable adducts) and resulted in low yields with selenium reagents (Scheme 8b). Nevertheless, unavoidable biomimetic oxidations to the pyridinium salt caused by the oxidative nature of the halogens were observed, giving minor byproducts in some cases. Lastly, the halo and seleno derivatives offered the possibility to attempt post-transformations. Indeed, basic and oxidative eliminations were promoted from the initial products to yield the corresponding olefins.

Downloaded by: Universidad de Barcelona. Copyrighted material.

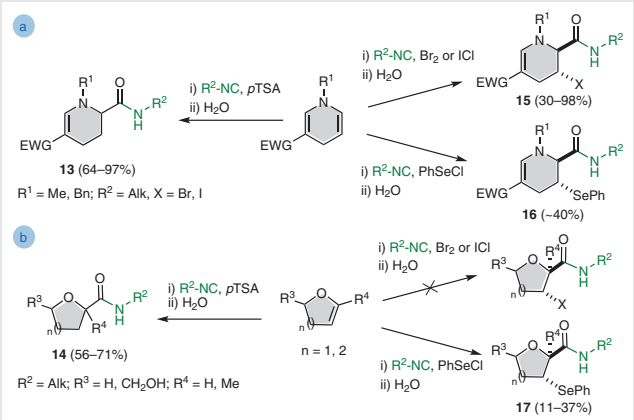

Scheme 8 Interaction of DHPs and dihydropyranes with isocyanides

Looking for other potential substrates for Ugi-type processes, we reacted various azines (mimicking cyclic imines) with acylating reagents, nicely producing the putative iminium ion intermediate, stabilized by the chloride anion, which was successfully attacked by the isocyanide. Once more, water acted as the final quencher of the transformation to yield the final Reissert-type adducts **18**, as a simple α-carbamoylation procedure for these important heterocyclic cores (Scheme 9).[24] Several chloroformates, among them the common N-protecting groups, gave respectable yields. Benzoyl and tosyl chlorides were also productive, although with lower yields. As for the azine scope, quinolines, isoquinolines, and their tricyclic analogues successfully afforded the desired products. However, as in classic Reissert processes,[25] pyridines failed to participate in this MCR. Moreover, the development of the reaction using a chloroformate resin, followed by a consequent oxidative cleavage allowed for the convenient obtention of the aromatic analogues **19** through a solid-phase protocol.[24]

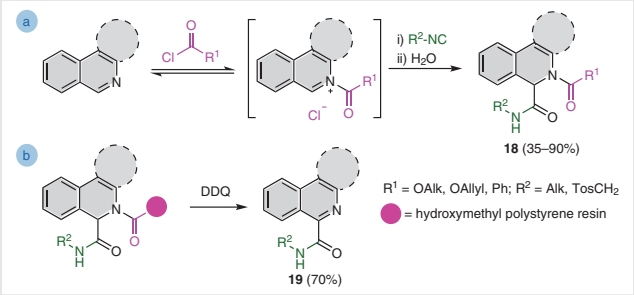

Scheme 9 MCR between acylated azines and isocyanides and their possible aromatization/oxidation

In this context, we embarked in an attractive application: to use MCRs for the fast development of tunable fluorescent probes.[26] We decided to synthesize a BODIPY-isocyanide and promote isocyanide-MCRs with it. The BODIPY core has been widely exploited as a fluorescent label due to its physicochemical and biological properties.[27] The targeted BODIPY-isocyanide **20** was successfully prepared through the standard aniline-to-formamide/dehydration protocol, and was then incorporated in several MCRs, namely Ugi, Passerini, and Groebke–Blackburn–Bienaymé (GBB) reactions (Scheme 10).[28] The BODIPY residue was not detrimental to the reactivity of the isocyanide, and all the new BODIPY adducts showed suitable fluorescence. Noticeably, the adduct **21c** (named PhagoGreen) showed an impressive performance as a pH-sensitive fluorescent probe and finely stained functional phagolysosomes in real time imaging, allowing the *in vivo* monitoring of these organelles. Incidentally, the imaging experiments were performed by the team of Prof. M. Vendrell (U. Edinburgh), a longstanding collaborator in most of the chemical biology projects.

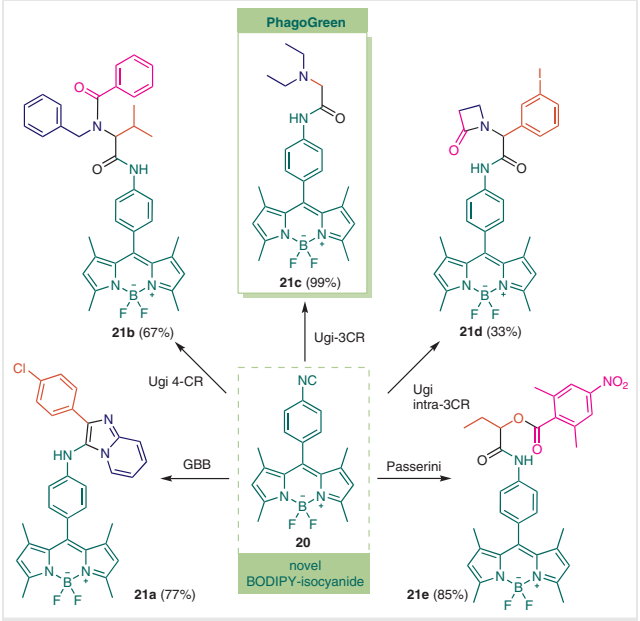

Scheme 10 Fluorescent adducts formed *via* MCRs with a BODIPY-isocyanide

3 Interrupted Processes

Thus far, we had investigated the basic guidelines for the MCRs with fundamental heterocycles, which mostly followed the usual trends for analogous processes in nonheterocyclic transformations. Next, we undertook a new exploratory chemistry involving drastic changes in the reactant scope, as a way to stress the mechanistic landscape. This would presumably force variations in the course of the reaction, i.e., interrupting the original process and rerouting the transformation towards new connectivity patterns.[29] First, we analyzed Povarov MCRs where the nature of the aniline component would determine the final Pictet–Spengler step. In this way, using an *N*-tryptophyl-DHP, an olefin component with ethyl glyoxylate and a deactivated

© 2022. Thieme. All rights reserved.

Downloaded by: Universidad de Barcelona. Copyrighted material.

(electron-deficient) aniline, the system evolved through the usual Mannich step, but was terminated with the electrophilic cyclization upon the much more reactive indole ring to yield the *trans*-indoloquinolizidine **22** in a stereoselective manner (Scheme 11a).[12a] Next, we tested the complete suppression of the cyclization using aliphatic amines, looking for alternative terminations. In this way, when *N*-alkyl-DHPs were treated with glyoxylate and primary amines, productive cascades ensued, affording formyl-tetrahydropyridines **23** and aminals **24** (Scheme11b).[30] The rationale here is that after the initial enamine addition upon the in situ generated imine, the resulting iminium ion intermediate **A** could evolve in two ways. It may suffer the hydrolysis by the generated water leading to the acyclic species **B** which, through an addition–elimination step, would yield tetrahydropyridine **23**. Alternatively, it can undergo an external attack by another equivalent of the primary amine leading to a diamine intermediate which would be quenched by the aldehyde reactant to form the bicyclic aminal **24**. Controlling the reaction conditions can direct the outcome, and in the presence of molecular sieves at low temperatures, the aminal predominates, whereas without removing the water and operating at higher temperatures, tetrahydro-pyridines become the major products. The obtained yields are around 40% (not bad for a pseudo five-component reaction) and the stereoselectivity favors the more stable *trans* adducts **23** and **24**.

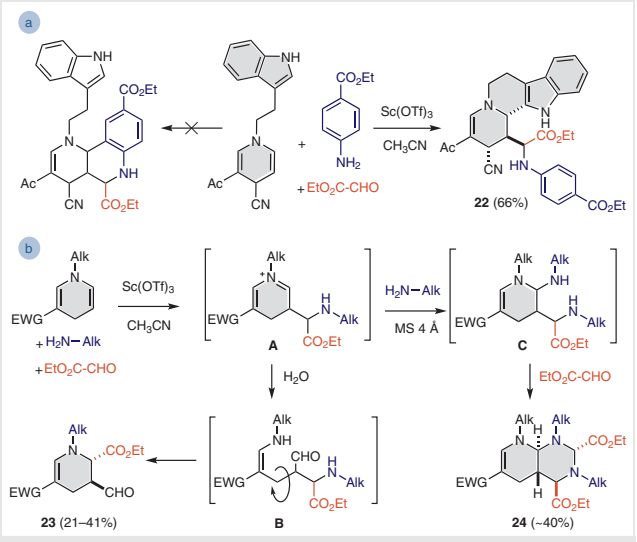

Scheme 11 Interrupted Povarov-type MCRs with dihydropyridines

Next, we challenged the system by adding a new component to a Povarov-type MCR: an external nucleophile (terminator) to switch off the aromatic cyclization and reach novel scaffold types. In this way, we tested the combination of a variety of amines, alcohols, aldehydes, and cyclic enol ethers under the usual Lewis acid catalysis. The first experiments involved deactivated anilines (nitro-substituted) and stoichiometric amounts of simple alcohols. The chemistry was productive and stereoselectively yielded the desired adducts **25** in respectful yields for a 4-component interaction, typically ranging from 40–80 % (Scheme 12a).[31] Even more, the system allowed variations including the use of activated anilines, aliphatic amines, internal trappings (leading to bridged or fused bicyclic adducts), the use of a variety of terminators (primary and secondary alcohols, water, and thiols) as well as a range of enol ethers including glycals (Scheme 12b). In the latter cases, the stereochemical induction conveniently gave access to a family of carbohydrate derivatives such as **25i**. It is worth mentioning that microwave activation and high-pressure conditions were key to the proper manipulation of sensitive substrates and allowed convenient preparation protocols. Finally, for reasons not fully understood (a euphemism meaning that we have no idea), some combinations yielded the 3-component Povarov adducts. As a rule of thumb, we accept that the kinetics capriciously favor one pathway over the rest. In this context, we described a series of post-transformations (oxidations, eliminations) that expanded the diversity of the synthetic outcome to generate quinoline adducts **26** and **27** (Scheme 12).

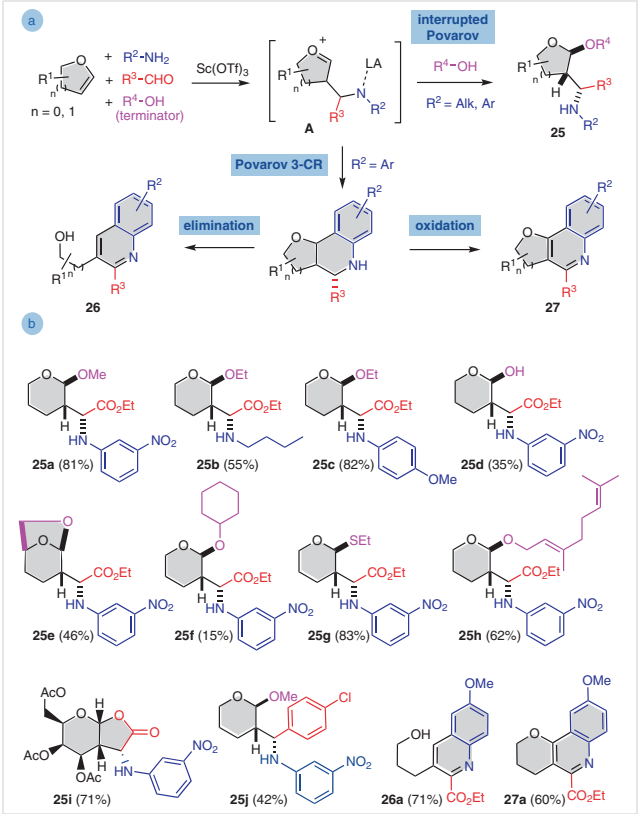

Scheme 12 a) Interrupted Povarov-type MCRs upon cyclic enol ethers. b) Accessible scaffolds through the developed 4-component MCR and representative post-transformations.

Downloaded by: Universidad de Barcelona. Copyrighted material.

At this point, we decided to test cyclic enol esters as substrates in Povarov MCRs. This seemingly trivial change may furnish lactone-type adducts instead of the common pyran-furan scaffolds. However, when experimentally testing the MCR under the standard conditions, we did not find the expected compound, and rearranged lactams **28** were produced instead (Scheme 13a).[32] The initially formed *cis* compounds were isomerized to the more stable *trans* derivatives by acid catalysis. Interestingly, the putative Mannich intermediate did not evolve through the usual electrophilic cyclization upon the aromatic ring, undergoing a competitive lactamization, likely releasing a neutral acetyl group in the elimination step. The generation of N-arylated γ- and δ-lactams is the major outcome of the novel MCR process. Some particularities, however, have to be considered. For instance, the presence of the methyl group in the olefin moiety seems to be critical for the reaction, as with vinyl acetate, a normal Povarov-type connectivity is observed, and the initial adduct **B** spontaneously yields quinoline scaffold **29** (Scheme 13b). Although a variety of substituted anilines undergo the described MCR, aliphatic amines do not promote the transformation. Moreover, aromatic aldehydes are much less reactive and only furnish Mannich-type adducts **30** upon the reaction with isopropenyl acetate, through which deacetylated products **31** were also obtained in some cases (Scheme 13c).

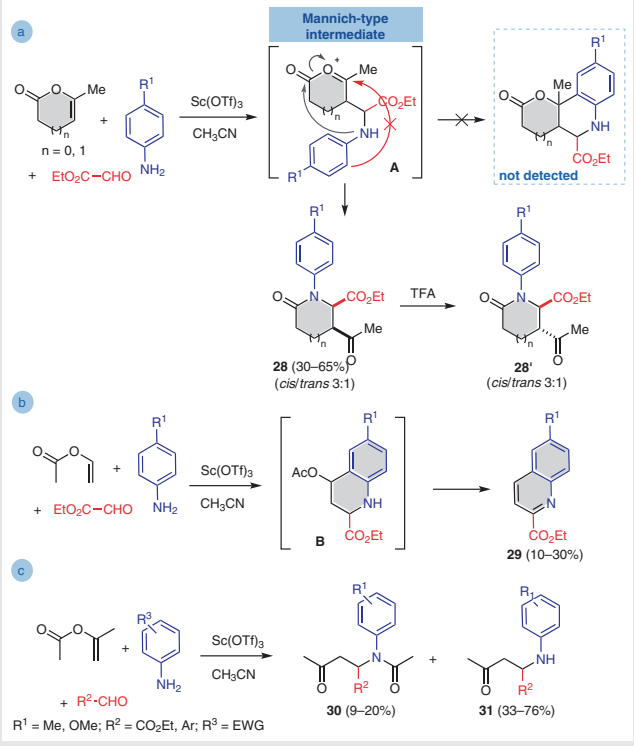

Scheme 13 Interrupted Povarov-type MCR with enol esters

Looking for other twists in the reactivity of the Povarov systems, we tested the behavior of cyclic imines. As, in principle, these substrates would naturally evolve to anti-Bredt adducts, we were intrigued by the outcome of this transformation. So, we decided to explore the interaction of a difluorinated pyrroline **32**, we had prepared for another project (serendipity sometimes helps the clueless chemists!),[33] with activated olefins under the typical conditions in our lab, that is, in acetonitrile solution with a mild acid catalysis. Remarkably, neither forbidden strained products nor dimers were generated. Instead, an impressive Ritter-terminated cycloadduct **33** was formed in a respectful yield (Scheme 14a).[34] It is interesting to note that had we started the experiments in other solvent systems, likely we would not have discovered this chemistry! Further studies confirmed that the process is quite general and a variety of cyclic imines (and even electron-deficient acyclic ones), olefins and nitriles generate the desired products **34**, with interesting exceptions. For instance, *tert*-butylcyanide does not promote the reaction, likely due to steric congestion. However, it is a good solvent for the process, a mild donor to stabilize cationic intermediates. This allows the use of the nitrile input in stoichiometric amounts, before this finding, we used excesses of this component.

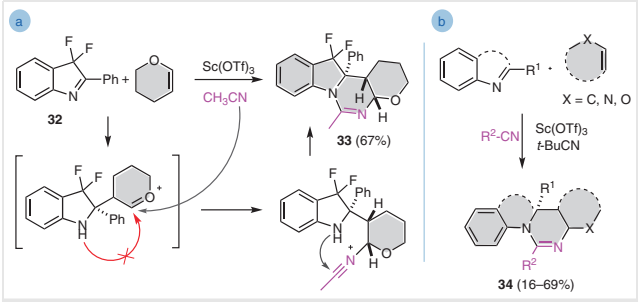

Scheme 14 Ritter terminated Povarov MCR

In continuation, we studied the interaction of cyclohexadiene as the reactive alkene in the system. We observed the formation of the imino-Diels–Alder adduct together with minor amounts of the Mannich–Ritter compound, showing complementary stereochemical patterns (Scheme 15).[35] Intrigued by the mechanism of this divergent process, we looked for advice from our computational expert, Prof. F. J. Luque (U. Barcelona), who determined that the topology of the interaction dictated its synthetic outcome. An *endo* approach led to a polarized transition state which evolved to the cationic intermediate **A**. This intermediate was then trapped by the nitrile to yield the MCR adduct **35**. However, the alternative more favorable *exo* pathway led to a less polarized transition state **B**, yielding adduct **36** through the [4+2] cycloaddition. Additional experiments with different nucleophiles confirmed this remarkable observation.

Downloaded by: Universidad de Barcelona. Copyrighted material.

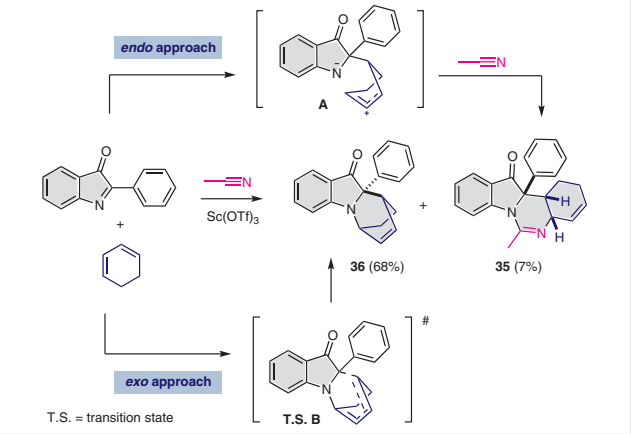

Scheme 15 Topology-dictated evolution of an MCR process

We have also observed interrupted processes studying isocyanide-based MCRs involving azines. After our description of the Ugi–Reissert transformations (see Scheme 9) and being aware of Ugi's initial observations on the addition of isocyanides to azinium salts,[36] we described the particular interaction of carboxamide-substituted pyridinium salts with isocyanides. In these processes, the carbamoylation takes place thanks to the intramolecular amide trapping, leading to its conversion into a cyanide group **37**, avoiding the *normal* evolution pathway (Scheme 16).[37] These studies clearly highlight the impact of a given substituent in the reaction course and the need for a detailed analysis of the scope, especially important in complex mechanistic processes such as MCRs.

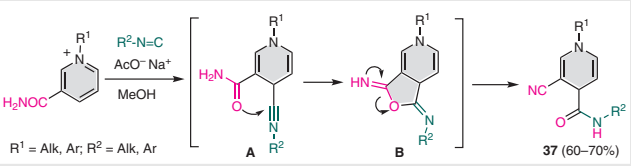

Scheme 16 Isocyanide additions upon carboxamide-azinium salts

In yet another example of a wrong hypothesis leading to interesting results, looking for an unprecedented 1,2-dicarbamoylation of double bonds, we tested the I_2-promoted isocyanide addition to dihydropyridines (Scheme 17).[38] We had in mind that a related process with Br_2 gave the β-bromo-α-carbamoyl adduct.[23] However, a striking reaction took place leading to benzimidazolium salts **38**, through an astonishing domino process. These salts were powders, and we could not crystallize them. Their structural assignment was a challenging task, which was done by extensive NMR analysis (mainly 2D methods), together with several mechanistic and labelling experiments. The use of deuterated dihydropyridines, and ^{13}C isocyanides was critical for the atomic mapping (Scheme 17b). Moreover, it was quite illustrative to find that pyridinium salts, as the likely oxidation products under the reaction conditions, were not the reactive intermediates. After considering dozens of crazy mechanistic hypotheses, we came across a rather reasonable one, which could explain the observed facts. The first interaction leads to the iodotetrahydropyridine nitrilium ion **A** (Scheme 17a). Then the attack of a second isocyanide unit followed by HI elimination gives rise to the nitrilium ion **B**, which is intramolecularly trapped by the enamine unit to form the bicyclic system **C**. An iodide-mediated fragmentation furnishes the iodoiminium intermediate **D**, which leads to the benzimidazolium salt **38** through ring closure and aromatization. The subtle differences between the halogens may account for the distinct behavior. The iodide role as a mild stabilizing agent for nitrilium ions, rendering them stable enough but still reactive to further evolve, can justify the interruption of the process at the initial Reissert stage towards the ensuing domino process. It is also a beautiful example (for us, at least) on how similar reactive combinations give totally different outcomes. In this context, the benzimidazolium salts thus produced were determined to be interesting small, nonpeptidic human prolyl oligopeptidase inhibitors, blood-brain-barrier permeable.[39]

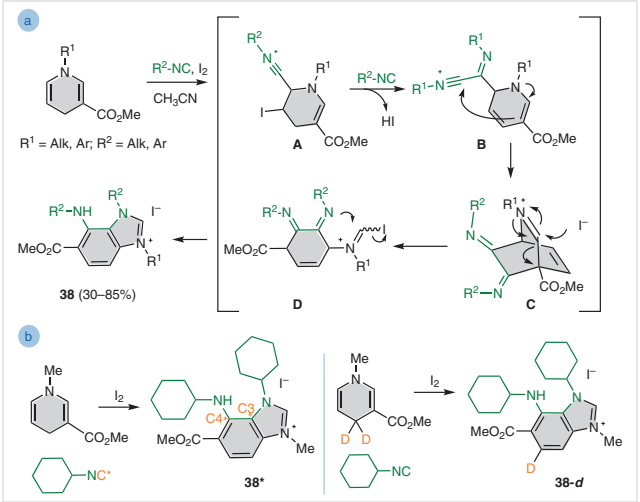

Scheme 17 Interrupted iodine-mediated dihydropyridine-isocyanide reactions

As is well known in heterocyclic chemistry, pyridines are reluctant to react in Reissert processes, as well as in our chloroformate-promoted Ugi–Reissert MCRs.[24] Looking for a stronger activation agent, we tested triflic anhydride to find that the isocyanides were massively degraded. Lowering the electrophilicity to trifluoroacetic anhydride (TFAA), the expected adduct was not detected. Strikingly again, we isolated the MCR adduct **39** with a completely reversed connectivity and an impressive acid fluoride moiety embedded in a dipolar scaffold.[40] This process works much better with isoquinolines (Scheme 18) and can be extended to a variety of difluoro-substituted anhydrides, delivering respectable yields of MCR adducts. It turns out that the initial N-acylaz-

Downloaded by: Universidad de Barcelona. Copyrighted material.

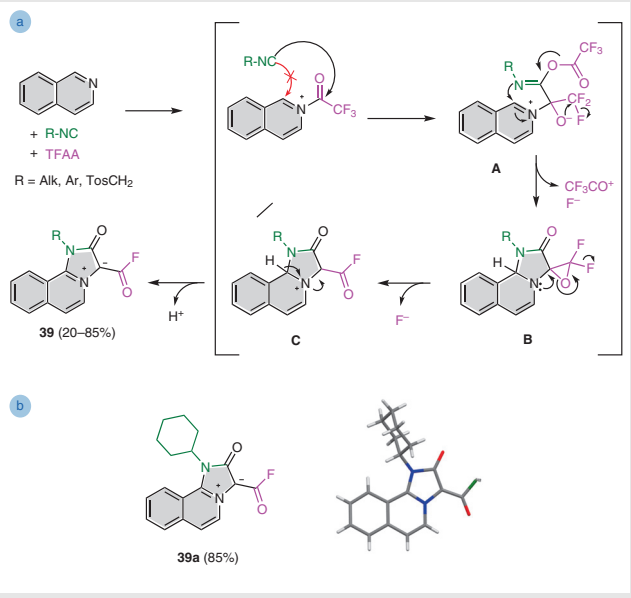

Scheme 18 a) TFAA-modified Ugi–Reissert MCR. b) X-ray crystal structure of the dipolar acid fluoride **39a**.

inium salt features two reactive sites: the α-position, leading to the standard Reissert processes (small amounts of these adducts were detected in some combinations), and the carbonyl center, which is much more activated by the adjacent fluorine atoms. These dramatically switch the course of the process, promoting the isocyanide interaction at this point. The event then triggers a domino process where the azinium ion **A** suffers the imine attack followed by the formation of a Darzens-type epoxide **B**, leading to the generation of the acid fluoride **C**. Finally, the release of an acidic proton furnishes the β-dicarbonyl anion and neutralizes the electric charge, delivering the stable dipole **39** (Scheme 18).

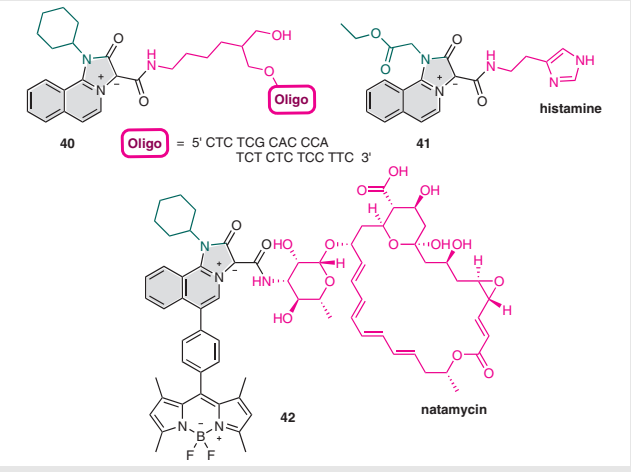

Scheme 19 TFAA MCR adducts with applications in biosciences

Surprisingly, the compounds are stable enough to be crystallized and, although reactive towards nucleophiles, they resist a standard water extraction, which was critical to the structural elucidation. As the NMR studies were, in our hands, inadequate to furnish a connectivity hypothesis, we relied on the X-ray crystallography to unravel the totally unexpected structure (Scheme 18b). After describing this impressive, interrupted process, we exploited the water compatibility of the acid fluoride, the intrinsic fluorescence of the nucleus and its productive interaction with N-nucleophiles, and we tuned the MCR to produce a variety of adducts suitable for labelling DNA oligonucleotides,[41] the specific monitoring of histamine levels in cells,[42] and the visualization of antifungal reagents (Scheme 19).[43]

4 Multiple Multicomponent Reactions: Problem of Selectivity

Multiple multicomponent reactions (MMCRs) have had a relevant impact on the facilitated access to complex assemblies.[44] In these transformations, the intelligent incorporation of polyfunctional substrates (amines, aldehydes, isocyanides, acids, etc.) in controlled concentrations drifts the sequence of MCRs away from random polymerization and directs the preorganized intermediates towards the favored macrocycles, molecular cages, dendrimers, peptidomimetics, etc. However, browsing the literature, we noticed a limited reaction scope, with Ugi and Passerini-type MCRs being predominant. Moreover, as heterocyclic substrates were rarely used in the context, we became interested in the idea of assembling fused heteroaromatic systems through heterocyclic MMCRs.

Being aware that the absolute majority of the research in the field depended on the *symmetric* polyfunctional substrates, we wondered how an MMCR cocktail would behave in the presence of a nonsymmetrical reactant. We were also curious to understand how the reaction course determines the formation of a mono-MCR adduct versus bis-/multiple MCR adducts. We believed that a selective, protecting-group-free access to mono-MCR adducts with polyfunctional substrates would notably expand the scope of MMCRs as the untouched functional groups could undergo further transformations. In other words, we were attracted to further explore the concept of (regio)selectivity in MMCRs.[45]

So, we took the diamino-diazines as model substrates and studied their reactivity under common GBB reaction conditions. Remarkably, the nonsymmetric 2,4-diaminopyrimidine exclusively yielded the single mono-GBB adducts **43** (and not **44** or **44′**) under mild Lewis acid catalysis, whereas under more drastic pTSA-catalyzed conditions, the bis-GBB adduct **45** was formed (Scheme 20). The structural assignment was done through X-ray crystal structure analyses, as the similarities among the connectivities of the fea-

Downloaded by: Universidad de Barcelona. Copyrighted material.

sible compounds did not allow proper NMR-based elucidation. In this way the selective synthesis of the nonsymmetric bis-GBB adducts **46** was achieved in a sequential fashion (Scheme 20a).[46] Switching to 3,6-diaminopyridazine, a similar trend was observed to furnish adducts **47**. Moreover, in the presence of suitable carboxylic acids, the corresponding GBB–Ugi adducts **48** were also isolated (Scheme 20b). Detailed computational studies determined the kinetic nature of the observed regioselectivity. The discovered selective MMCR platform turned out to be a powerful synthetic tool, as it paved the access to a variety of new scaffolds with full control over the decoration at 4-5 diversity points. These scaffolds also showed remarkable biomedical properties as antiviral agents against human adenovirus, as well as selective quadruplex DNA binders. Some derivatives exhibited pH- and environment-sensitive fluorescence. Moreover, GBB adducts of 2-pyridine carboxaldehyde yielded the unexpected 5-membered pseudo-BODIPY compound **49**, which exhibited promising photophysical properties for potential bioimaging applications (Scheme 20c). In this respect, it can be highlighted the performance of boron complex **49** as a promising fluorescent probe for live cell imaging. This compound shows good cell permeability and preferential accumulation in mitochondria, selectively staining these organelles (Figure 1).[46]

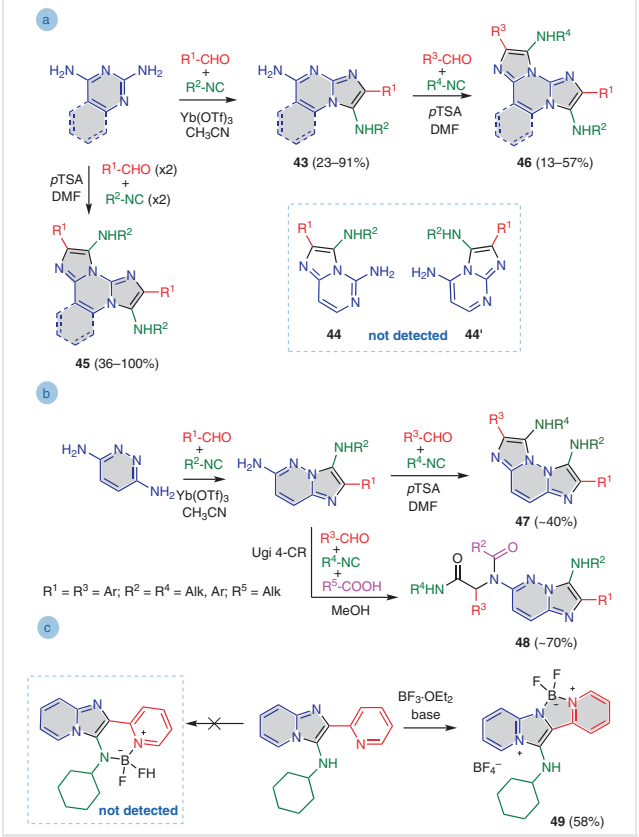

Scheme 20 Selective double GBB and GBB-Ugi reactions with α-diamino-diazines and related GBB-BODIPY adducts

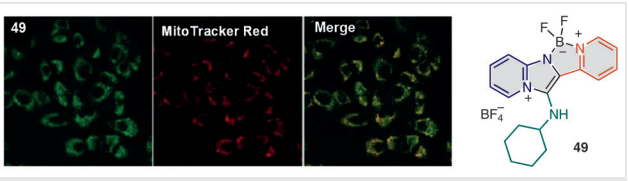

Figure 1 Living cell microscopy selective mitochondria staining with fluoroprobe **49**. Adapted from Ghashghaei *et al*. Multiple Multicomponent Reactions: Unexplored Substrates, Selective Processes, and Versatile Chemotypes in Biomedicine. *Chem. Eur. J.* **2018**, *24*, 14513–14521. Copyright Wiley-VCH GmbH. Reproduced with permission.

Finally, multiple GBBs over melamine, smoothly yielded novel, highly fused polyheterocyclic compounds **50**. The initial scaffold was further elaborated to more complex nano-sized tripodal systems **51** and **52** using suitable cross-coupling reactions upon the halo-aryl residues of the aldehyde component (Scheme 21).[46]

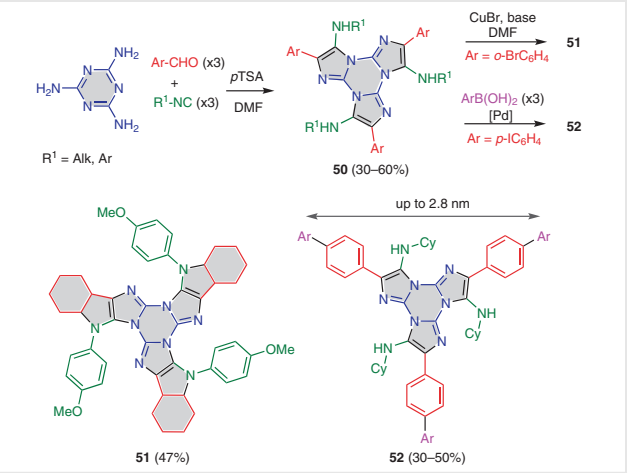

Scheme 21 Tripodal adducts of triple-GBBs with melamine and their late-stage diversification with inter-/intramolecular coupling reactions

Having a secure access to a mono-MCR adduct in a diaminopyrimidine system prompted us to tackle a biomedical application using our chemistry. Incidentally, there is an urgent global demand for novel medicines to fight microbial resistance and we saw the possibility of developing new antibiotic agents using the selective MMCRs. In this way we modified the marketed essential drug trimethoprim (TMP) through a selective GBB upon its 2,4-diaminopyrimidine moiety using the previously described protocol. The reaction of TMP with a range of aldehydes and isocyanides under acid catalysis yielded the mono- and bisadducts **53** and **54** (Scheme 22). This method allowed for the rapid and convenient synthesis of new antimicrobial compounds in a process comparable to a late-stage functionalization. The activity of the prepared adducts was tested against different bacterial strains. While the bisadducts were inactive, some of the monoadducts and combinations thereof

Downloaded by: Universidad de Barcelona. Copyrighted material.

showed promising results. They not only exhibited activities similar to TMP but, more importantly, with improved antibiotic kinetics, a key feature in clinics.[47] Moreover, further studies on the two lead compounds **53a** and **53b** in combination with sulfamethoxazole in the presence of colistin demonstrated a clear synergic effect and led to notable improvement of the antimicrobial potency, presumably due to the increased penetration of the antibiotic agents through the bacterial membrane (Scheme 22).[48]

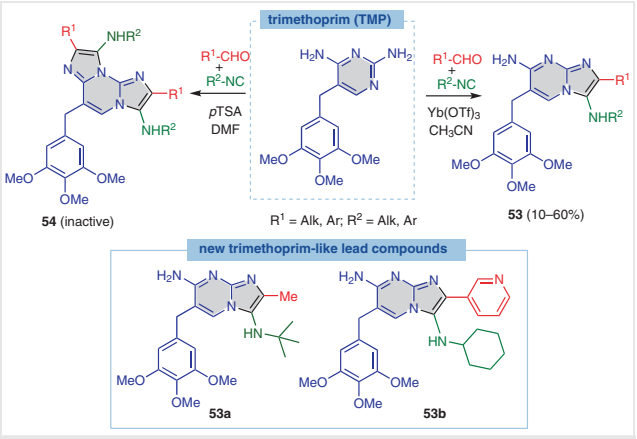

Scheme 22 The drugs-from-drugs approach: selective MCR-based modifications of the marketed antibiotic trimethoprim

This drugs-from-drugs approach, entirely based in selective MCRs upon polyfunctional systems, showcases the reach of the developed methodology. This approach may not be of universal application. For instance, if key recognition points at the initial drug are modified it will likely lose its activity. However, when relevant, it rapidly delivers a wide panel of derivatives leading to improved hits.

5 Extended Multicomponent Reactions

Linking MCRs to other reactions is widely popular in the field. Post-MCR transformations have significantly increased the structural diversity of the initial MCR adducts.[49] The union of MCRs, in which a series of MCRs is performed in a one-pot fashion, has also been previously reported by the community.[50] In these transformations, the product of a first MCR becomes a reactant of the next MCR.

The idea of extending a classical MCR first arose as the group performed a reported Reissert-type reaction of an azine and two units of isocyanides through an alternative TMSCl-catalyzed protocol. Surprisingly, in contrast to the previously described harsh acidic conditions, the silicon activation allowed the preparation of fused imizadolium salts under very mild conditions, with improved yields and significantly wider scope. The detailed computational and experimental study of the reaction mechanism confirmed that the key step was an unprecedented insertion of the second isocyanide equivalent into the N–Si bond of the initial Reissert-type intermediate **B**. These species then suffered a cascade of events (TMSOH elimination–cyclization–isomerization) to yield the final products **55** (Scheme 23a). Interestingly, the participation of some diazines gave access to novel mono- and bisadducts **56–58** in a single step, furnishing more complex heterocyclic cores (Scheme 23b). The synthesized benzimidazolium salts were confirmed to be potent antiparasitic compounds against *Trypanosoma brucei* and *cruzi*.[51]

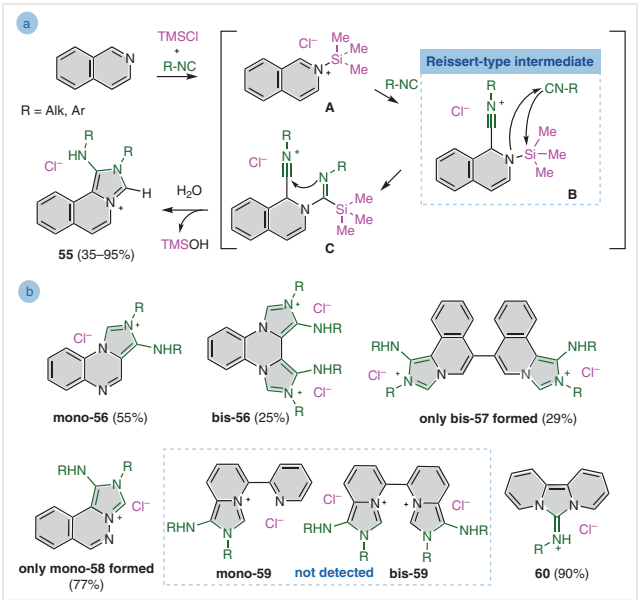

Scheme 23 TMSCl-mediated formation of benzimidazolium salts through extended Reissert reactions

Arguably, the best synthetic procedures regarding bond-forming efficiency are the domino reactions.[3] These fascinatingly elegant processes afford complex compounds thanks to the crafted arrangement of their substrates. These preorganized systems undergo a series of spontaneous, consecutive transformations after the first molecular event is triggered. Domino reactions are closely related to MCRs, as the latter can be considered intermolecular domino processes.

Despite the remarkable advantages of domino reactions, their general application in organic synthesis is limited. Domino substrates are rationally designed, complex entities and their preparation requires long multistep synthesis in most cases. We hypothesized that extended MCRs could bypass this bottleneck, in the sense that the domino substrates could get generated *in situ* through MCRs. This would require a chemical trigger that could activate the domino process once the initial MCR adduct is formed. In the meantime, while performing a classic MCR with indole carboxaldehydes in the group, we got inspired to use their dual nature as the trigger. Indole carboxaldehydes react as

Downloaded by: Universidad de Barcelona. Copyrighted material.

electrophiles during an MCR, whereas the resulting indole-MCR adduct has a nucleophilic nature. We speculated this polarity inversion would allow us to link MCRs with domino reactions (Scheme 24).

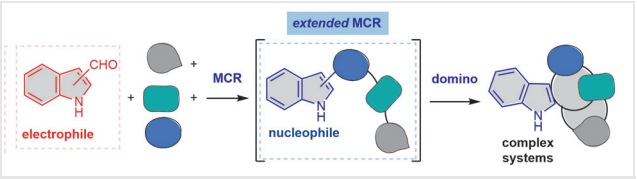

Scheme 24 The polarity inversion in extended MCRs with indole carboxaldehydes

We eventually found evidence on the feasibility of our hypothesis as we performed an open vessel GBB reaction with aminopyridine, indole 3-carboxaldehyde, and ethyl isocyanoacetate. The reaction led to the formation of the adduct **61**, whose origin may be traced back to a GBB adduct that had suffered a domino sequence of oxidation–Pictet–Spengler cyclization–oxidation steps.[52] Tuning reaction conditions and adding auxiliary oxidants resulted in the obtention of adduct **61** as the main product. Surprisingly, the use of iodine as the external oxidant rendered a rare Pictet–Spengler (PS) reaction upon the indole C4 position, affording a novel scaffold **62** (Scheme 25a). Optimal conditions, often exclusive for a particular input combination, were synthetically useful (30–60%). The scope spans a wide range of α-aminoazines and oxidizable isocyanide inputs. Moreover, indole 3-carbaldehyde was successfully swapped with similar components like, furfural, thiophene 2-carboxaldehde, electron-rich benzaldehydes, and indole 4-carbaldehyde (Scheme 25b).[52]

Finally, the incorporation of indole 2-carboxaldehyde directed the reaction towards a completely unexpected direction, yielding substituted indolocarbazoles **66** through a new nonoxidative ABC^3 version of the extended GBB. Much to our surprise, the very same reaction with cyclohexyl isocyanide at high temperatures (120 °C, μW), yielded a different polycyclic adduct **67** of spiranic nature and an ABC^3 composition (Scheme 26). The proposed unified mechanism accounts for the consecutive addition of two aldehyde units followed by altering cascades of acid-catalyzed dehydrations and cyclizations, both arising from the initial GBB adducts **A** (Scheme 26). Some of the synthesized compounds are potent activators of aryl hydrocarbon receptor (AhR), a promising target in current biomedical research.[52]

It is worth stating that, in our opinion, extended MCRs are not restricted to the examples presented. Thus, we firmly believe that exploring other MCR–domino combinations and their synthetic potentials is a promising research line.

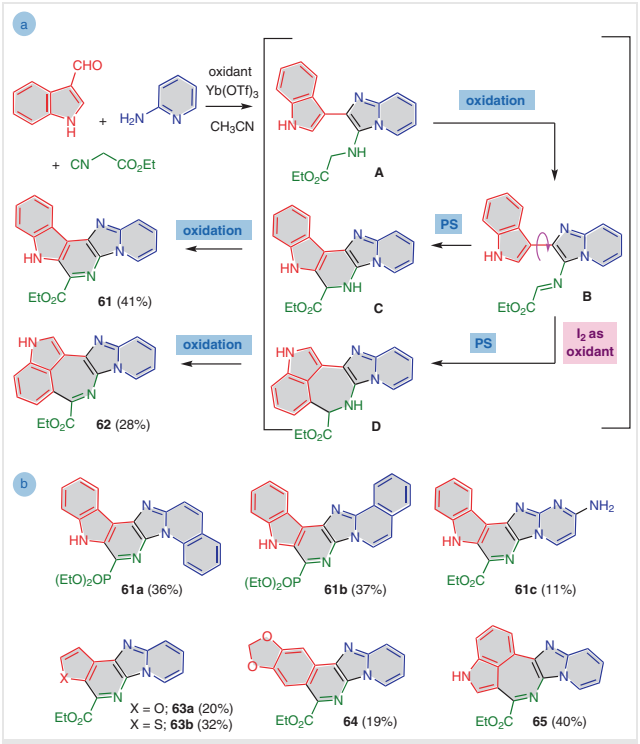

Scheme 25 Extended oxidative GBB adducts with 3-indole carboxaldehyde and related components

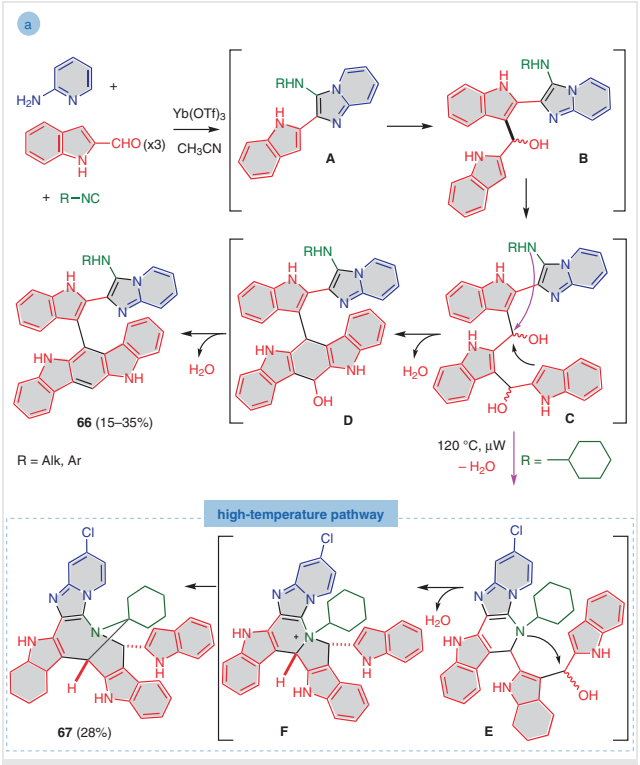

Scheme 26 Extended GBB pathways of indole 2-carboxaldehyde at different temperatures

© 2022. Thieme. All rights reserved.

Downloaded by: Universidad de Barcelona. Copyrighted material.

7 Conclusions and Wishes

During almost 20 years of continued work in the area, we are struck with a 'crazy' result almost every month. Our capacity in the analysis of these complex systems has slowly, but significantly evolved. Yet, we still cannot fully predict the outcome of a given heterocyclic MCR. However, we start to understand the reasons and extend their synthetic applications. These inputs trigger new explorations around chemically related space and thus the effects are propagated. Right now, with the actual level of knowledge, more basic reactivity explorations are needed, hopefully to establish general rules. The rich chemistry involved in the interactions of so many species (the 3 or more reactants, the solvent, the catalysts, and the ensuing intermediates), can often evolve in unpredictable, counterintuitive ways, bringing intricate connectivities, impossible to prepare otherwise. In many cases, as seen in the account, tiny differences in kinetics (caused by a solvent, an additive, or a small variation in a functional group) may fully rewire the mechanism and dramatically change the outcome of the process.

So, what would be our future direction? The search for new MCRs, whether heterocyclic or not, is a thrilling endeavor, already incredibly productive, delivering new concepts in reactivity and useful applications. The underlying reaction discovery may be approached in several ways. Although systematic searches and serendipity have furnished interesting results, we advocate for a hypothesis-driven research based in mechanistic considerations, often sparked by a careful analysis of minor byproducts detected in any process. We believe this synergic combination of rational science plus intentionally sought serendipity may furnish the right balance of chance and necessity for a fast progress in the field. In this respect, it is interesting to see how computers with artificial intelligence algorithms can speed up reaction discovery, and we believe an important task would be to teach these concepts to clever machines.[53]

To finish and considering the unquestionable need we have for novel scaffolds and meaningful compounds especially in medicine, we would like to send a couple messages to the academic community: one would be to specifically include MCRs at the undergraduate/graduate levels, and the second to contemplate this approach in the daily synthetic work. We consider these measures as investments from which our community may deeply benefit.

Conflict of Interest

The authors declare no conflict of interest.

Funding Information

Support from the Ministerio de Ciencia e Innovación-Spain (PID2019-107991RB-I00) is gratefully acknowledged. P.N.R. thanks Ministerio de Ciencia e Innovación for a predoctoral grant.

Acknowledgment

We warmly thank all past members of our research group for their talented dedication to the conception and development of the MCR project. Also, we acknowledge the collaborations we hold to back our research.

References

(1) For reflections on the ideal synthesis, see: (a) Trost, B. M. *Science* **1991**, *254*, 1471. (b) Kolb, H. C.; Finn, M. G.; Sharpless, K. B. *Angew. Chem. Int. Ed.* **2001**, *40*, 2004. (c) Burke, M. D.; Schreiber, S. L. *Angew. Chem. Int. Ed.* **2003**, *43*, 46. (d) Wender, P. A.; Verma, V. A.; Paxton, T. J.; Pillow, T. H. *Acc. Chem. Res.* **2008**, *41*, 40. (e) Newhouse, T.; Baran, P. S.; Hoffmann, R. W. *Chem. Soc. Rev.* **2009**, *38*, 3010. (f) Gaich, T.; Baran, P. S. *J. Org. Chem.* **2010**, *75*, 4657. (g) Hayashi, Y. *J. Org. Chem.* **2021**, *86*, 1.

(2) (a) Dömling, A.; Ugi, I. *Angew. Chem. Int. Ed.* **2000**, *39*, 3168. For overviews in the field, see: (b) *Multicomponent Reactions*; Zhu, J.; Bienaymé, H., Ed.; Wiley-VCH: Weinheim, **2005**. (c) *Multicomponent Reactions in Organic Synthesis*; Zhu, J.; Wang, Q.; Wang, M.-X., Ed.; Wiley-VCH: Weinheim, **2015**. (d) *Multicomponent Reactions towards Heterocycles*; Van der Eycken, E.; Sharma, U. K., Ed.; Wiley-VCH: Weinheim, **2021**.

(3) Tietze, L. F.; Brasche, G.; Gericke, K. M. *Domino Reactions in Organic Synthesis*; Wiley-VCH: Weinheim, **2006**.

(4) (a) Horton, D. A.; Bourne, G. T.; Smythe, M. L. *Chem. Rev.* **2003**, *103*, 893. For an overview of the field, see: (b) Wess, G.; Urmann, M.; Sickenberger, B. *Angew. Chem. Int. Ed.* **2001**, *40*, 3341. (c) Blakemore, D. C.; Castro, L.; Churcher, I.; Rees, D. C.; Thomas, A. W.; Wilson, D. M.; Wood, A. *Nat. Chem.* **2018**, *10*, 383.

(5) For representative examples, see: (a) Sunderhaus, J. D.; Martin, S. F. *Chem. Eur. J.* **2009**, *15*, 1300. (b) Jiang, B.; Rajale, T.; Wever, W.; Tu, S.-J.; Li, G. *Chem. Asian J.* **2010**, *5*, 2318. (c) Rotstein, B. H.; Zaretsky, S.; Rai, V.; Yudin, A. K. *Chem. Rev.* **2014**, *114*, 8323.

(6) For representative contributions of our group, see: (a) Isambert, N.; Lavilla, R. *Chem. Eur. J.* **2008**, *14*, 8444. (b) Vicente-García, E.; Kielland, N.; Lavilla, R. In *Multicomponent Reactions in Organic Synthesis*; Zhu, J.; Wang, Q.; Wang, M.-X., Ed.; Wiley-VCH: Weinheim, **2015**, 159. (c) Ghashghaei, O.; Pedrola, M.; Escolano, C.; Lavilla, R. In *Multicomponent Reactions towards Heterocycles*; Van der Eycken, E.; Sharma, U. K., Ed.; Wiley-VCH: Weinheim, **2021**, 1. See also: (d) Ibarra, I. A.; Islas-Jácome, A.; González-Zamora, E. *Org. Biomol. Chem.* **2018**, *16*, 1402.

(7) (a) Lavilla, R.; Kumar, R.; Coll, O.; Masdeu, C.; Spada, A.; Bosch, J.; Espinosa, E.; Molins, E. *Chem. Eur. J.* **2000**, *6*, 1763. (b) Lavilla, R.; Spada, A.; Bosch, J. *Org. Lett.* **2000**, *2*, 1533. (c) Lavilla, R.; Bernabeu, M. C.; Brillas, E.; Carranco, I.; Díaz, J. L.; Llorente, N.; Rayo, M.; Spada, A. *Chem. Commun.* **2002**, 850. (d) Lavilla, R.; Spada, A.; Carranco, I.; Bosch, J. *J. Org. Chem.* **2001**, *66*, 1487.

(8) Tejedor, D.; García-Tellado, F. *Chem. Soc. Rev.* **2007**, *36*, 484.

(9) (a) Kouznetsov, V. V. *Tetrahedron* **2009**, *65*, 2721. (b) Ghashghaei, O.; Masdeu, C.; Alonso, C.; Palacios, F.; Lavilla, R.

Downloaded by: Universidad de Barcelona. Copyrighted material.

Drug Discovery Today: Technol. **2018**, *29*, 71; and references cited therein.
(10) Lavilla, R. *Curr. Org. Chem.* **2004**, *8*, 715.
(11) Lavilla, R.; Coll, O.; Kumar, R.; Bosch, J. *J. Org. Chem.* **1998**, *63*, 2728.
(12) (a) Lavilla, R.; Bernabeu, M. C.; Carranco, I.; Díaz, J. L. *Org. Lett.* **2003**, *5*, 717. (b) Carranco, I.; Díaz, J. L.; Jiménez, O.; Vendrell, M.; Albericio, F.; Royo, M.; Lavilla, R. *J. Comb. Chem.* **2005**, *7*, 33.
(13) (a) Smith, C. D.; Gavrilyuk, J. I.; Lough, A. J.; Batey, R. A. *J. Org. Chem.* **2010**, *75*, 702. (b) Xu, H. J.; Zuend, S. G.; Woll, M.; Tao, Y. N.; Jacobsen, E. *Science* **2010**, *327*, 986. (c) Domingo, L. R.; Aurell, M. J.; Sáez, J. A.; Mekelleche, S. M. *RSC Adv.* **2014**, *4*, 25268.
(14) Vicente-García, E.; Catti, F.; Ramón, R.; Lavilla, R. *Org. Lett.* **2010**, *12*, 860.
(15) Vicente-García, E.; Ramón, R.; Lavilla, R. *Synthesis* **2011**, 2237.
(16) (a) Liu, H.; Dagousset, G.; Masson, G.; Retailleau, P.; Zhu, J. *J. Am. Chem. Soc.* **2009**, *131*, 4598. For an overview, see: (b) Fochi, M.; Caruana, L.; Bernardi, L. *Synthesis* **2014**, *46*, 135.
(17) Vicente-García, E.; Ramón, R.; Preciado, S.; Lavilla, R. *Beilstein J. Org. Chem.* **2011**, *7*, 980.
(18) Oku, A.; Kinugasa, M.; Kamada, T. *Chem. Lett.* **1993**, *22*, 165.
(19) di Pietro, O.; Vicente-García, E.; Taylor, M. C.; Berenguer, D.; Viayna, E.; Lanzoni, A.; Sola, I.; Sayago, H.; Riera, C.; Fisa, R.; Clos, M. V.; Pérez, B.; Kelly, J. M.; Lavilla, R.; Muñoz-Torrero, D. *Eur. J. Med. Chem.* **2015**, *105*, 120.
(20) (a) Camps, P.; Formosa, X.; Galdeano, C.; Muñoz-Torrero, D.; Ramírez, L.; Gómez, E.; Isambert, N.; Lavilla, R.; Badia, A.; Clos, M. V.; Bartolini, M.; Mancini, F.; Andrisano, V.; Arce, M. P.; Rodríguez-Franco, M. I.; Huertas, O.; Dafni, T.; Luque, F. J. *J. Med. Chem.* **2009**, *52*, 5365. (b) di Pietro, O.; Viayna, E.; Vicente-García, E.; Bartolini, M.; Ramón, R.; Juárez-Jiménez, J.; Clos, M. V.; Pérez, B.; Andrisano, V.; Luque, F. J.; Lavilla, R.; Muñoz-Torrero, D. *Eur. J. Med. Chem.* **2014**, *73*, 141. (c) di Pietro, O.; Pérez-Areales, F. J.; Juárez-Jiménez, J.; Espargaró, A.; Clos, M. V.; Pérez, B.; Lavilla, R.; Sabaté, R.; Luque, F. J.; Muñoz-Torrero, D. *Eur. J. Med. Chem.* **2014**, *84*, 107.
(21) Dömling, A. *Chem. Rev.* **2006**, *106*, 17.
(22) Masdeu, C.; Díaz, J. L.; Miguel, M.; Jiménez, O.; Lavilla, R. *Tetrahedron Lett.* **2004**, *45*, 7907.
(23) Masdeu, C.; Gómez, E.; Williams, N. A.; Lavilla, R. *QSAR Comb. Sci.* **2006**, *25*, 465.
(24) Díaz, J. L.; Miguel, M.; Lavilla, R. *J. Org. Chem.* **2004**, *69*, 3550.
(25) Kielland, N.; Lavilla, R. In *Synthesis of Heterocycles via Multicomponent Reactions II*; Orru, R. V. A.; Ruitjer, E., Ed.; Springer: Heidelberg, **2010**, 127.
(26) de Moliner, F.; Kielland, N.; Lavilla, R.; Vendrell, M. *Angew. Chem. Int. Ed.* **2017**, *56*, 3758.
(27) Loudet, A.; Burgess, K. *Chem. Rev.* **2007**, *107*, 4891.
(28) Vázquez-Romero, A.; Kielland, N.; Arévalo, M. J.; Preciado, S.; Mellanby, R. J.; Feng, Y.; Lavilla, R.; Vendrell, M. *J. Am. Chem. Soc.* **2013**, *135*, 16018.
(29) For an excellent review on interrupted reactions, see: Trudel, V.; Tien, C. H.; Trofimova, A.; Yudin, A. K. *Nat. Rev. Chem.* **2021**, *5*, 604.
(30) Carranco, I.; Díaz, J. L.; Jiménez, O.; Lavilla, R. *Tetrahedron Lett.* **2003**, *44*, 8449.
(31) Jiménez, O.; de la Rosa, G.; Lavilla, R. *Angew. Chem. Int. Ed.* **2005**, *44*, 6521.
(32) Isambert, N.; Cruz, M.; Arévalo, M. J.; Gómez, E.; Lavilla, R. *Org. Lett.* **2007**, *9*, 4199.
(33) Pérez-Perarnau, A.; Preciado, S.; Palmeri, C. M.; Moncunill-Massaguer, C.; Iglesias-Serret, D.; González-Gironés, D.; Miguel, M.; Karasawa, S.; Sakamoto, S.; Cosialls, A. M.; Rubio-Patiño, C.; Saura-Esteller, J.; Ramón, R.; Caja, L.; Fabregat, I.; Pons, G.; Handa, H.; Albericio, F.; Gil, J.; Lavilla, R. *Angew. Chem. Int. Ed.* **2014**, *53*, 10150.
(34) Preciado, S.; Vicente-García, E.; Llabrés, S.; Luque, F. J.; Lavilla, R. *Angew. Chem. Int. Ed.* **2012**, *51*, 6874.
(35) Llabrés, S.; Vicente-García, E.; Preciado, S.; Guiu, C.; Pouplana, R.; Lavilla, R.; Luque, F. J. *Chem. Eur. J.* **2013**, *19*, 13355.
(36) Ugi, I.; Böttner, E. *Liebigs Ann. Chem.* **1963**, *670*, 74.
(37) Williams, N. A. O.; Masdeu, C.; Díaz, J. L.; Lavilla, R. *Org. Lett.* **2006**, *8*, 5789.
(38) Masdeu, C.; Gómez, E.; Williams, N. A. O.; Lavilla, R. *Angew. Chem. Int. Ed.* **2007**, *46*, 3043.
(39) Tarragó, T.; Masdeu, C.; Gómez, E.; Isambert, N.; Lavilla, R.; Giralt, E. *ChemMedChem* **2008**, *3*, 1558.
(40) Arévalo, M. J.; Kielland, N.; Masdeu, C.; Miguel, M.; Isambert, N.; Lavilla, R. *Eur. J. Org. Chem.* **2009**, 617.
(41) Pérez-Rentero, S.; Kielland, N.; Terrazas, M.; Lavilla, R.; Eritja, R. *Bioconjugate Chem.* **2010**, *21*, 1622.
(42) Kielland, N.; Vendrell, M.; Lavilla, R.; Chang, Y.-T. *Chem. Commun.* **2012**, *48*, 7401.
(43) Sintes, M.; De Moliner, F.; Caballero-Lima, D.; Denning, D. W.; Read, N. D.; Kielland, N.; Vendrell, M.; Lavilla, R. *Bioconjugate Chem.* **2016**, *27*, 1430.
(44) Wessjohann, L. A.; Neves Filho, R. A. W.; Rivera, D. G. In *Isocyanide Chemistry: Applications in Synthesis and Materials Science*; Nenajdenko, V. G., Ed.; Wiley-VCH: Weinheim, **2012**, 233.
(45) For a detailed analysis, see: Ghashghaei, O.; Seghetti, F.; Lavilla, R. *Beilstein J. Org. Chem.* **2019**, *15*, 521.
(46) Ghashghaei, O.; Caputo, S.; Sintes, M.; Revés, M.; Kielland, N.; Estarellas, C.; Luque, F. J.; Aviñó, A.; Eritja, R.; Serna-Gallego, A.; Marrugal-Lorenzo, J. A.; Pachón, J.; Sánchez-Céspedes, J.; Treadwell, R.; de Moliner, F.; Vendrell, M.; Lavilla, R. *Chem. Eur. J.* **2018**, *24*, 14513.
(47) Pedrola, M.; Jorba, M.; Jardas, E.; Jardi, F.; Ghashghaei, O.; Viñas, M.; Lavilla, R. *Front. Chem.* **2019**, *7*, 475.
(48) Jorba, M.; Pedrola, M.; Ghashghaei, O.; Herráez, R.; Campos-Vicens, L.; Luque, F. J.; Lavilla, R.; Viñas, M. *Antibiotics* **2021**, *10*, 709.
(49) For a representative review, see: Sharma, U. K.; Sharma, N.; Vachhani, D. D.; Van der Eycken, E. *Chem. Soc. Rev.* **2015**, *44*, 1836.
(50) Zarganes-Tzitzikas, T.; Chandgude, A. L.; Dömling, A. *Chem. Rec.* **2015**, *15*, 981.
(51) Kishore, K. G.; Ghashghaei, O.; Estarellas, C.; Mestre, M. M.; Monturiol, C.; Kielland, N.; Kelly, J. M.; Francisco, A. F.; Jayawardhana, S.; Muñoz-Torrero, D.; Pérez, B.; Luque, F. J.; Gámez-Montaño, R.; Lavilla, R. *Angew. Chem. Int. Ed.* **2016**, *55*, 8994.
(52) Ghashghaei, O.; Pedrola, M.; Seghetti, F.; Martin, V. V.; Zavarce, R.; Babiak, M.; Novacek, J.; Hartung, F.; Rolfes, K.; Haarmann-Stemmann, T.; Lavilla, R. *Angew. Chem. Int. Ed.* **2021**, *60*, 2603.
(53) Granda, J. M.; Donina, L.; Dragone, V.; Long, D.-L.; Cronin, L. *Nature* **2018**, *559*, 377.

Downloaded by: Universidad de Barcelona. Copyrighted material.

biomedicines

MDPI

Review

Heterocycle-Based Multicomponent Reactions in Drug Discovery: From Hit Finding to Rational Design

Pau Nadal Rodríguez, Ouldouz Ghashghaei, Andrea Bagán, Carmen Escolano * and Rodolfo Lavilla *

Laboratory of Medicinal Chemistry, Faculty of Pharmacy and Food Sciences, University of Barcelona and Institute of Biomedicine (IBUB), Avda Joan XXIII 27–30, 08028 Barcelona, Spain; pnadal@ub.edu (P.N.R.); ghashghaei@ub.edu (O.G.); abaganpolonio@ub.edu (A.B.)

* Correspondence: cescolano@ub.edu (C.E.); rlavilla@ub.edu (R.L.)

Abstract: In the context of the structural complexity necessary for a molecule to selectively display a therapeutical action and the requirements for suitable pharmacokinetics, a robust synthetic approach is essential. Typically, thousands of relatively similar compounds should be prepared along the drug discovery process. In this respect, heterocycle-based multicomponent reactions offer advantages over traditional stepwise sequences in terms of synthetic economy, as well as the fast access to chemsets to study the structure activity relationships, the fine tuning of properties, and the preparation of larger amounts for preclinical phases. In this account, we briefly summarize the scientific methodology backing the research line followed by the group. We comment on the main results, clustered according to the targets and, finally, in the conclusion section, we offer a general appraisal of the situation and some perspectives regarding future directions in academic and private research.

Keywords: bioprobes; drug discovery; heterocycles; multicomponent reactions; reaction discovery

check for updates

Citation: Nadal Rodríguez, P.; Ghashghaei, O.; Bagán, A.; Escolano, C.; Lavilla, R. Heterocycle-Based Multicomponent Reactions in Drug Discovery: From Hit Finding to Rational Design. *Biomedicines* **2022**, *10*, 1488. https://doi.org/10.3390/biomedicines10071488

Academic Editors: Silvia Ortega-Gutierrez and María L. López-Rodríguez

Received: 31 May 2022
Accepted: 20 June 2022
Published: 23 June 2022

Publisher's Note: MDPI stays neutral with regard to jurisdictional claims in published maps and institutional affiliations.

Copyright: © 2022 by the authors. Licensee MDPI, Basel, Switzerland. This article is an open access article distributed under the terms and conditions of the Creative Commons Attribution (CC BY) license (https://creativecommons.org/licenses/by/4.0/).

1. Introduction

Modern drug discovery is a complex endeavor where pharmacology, biology and medicinal chemistry play important roles. Yet it unavoidably relies on a pivotal organic synthesis basis to ensure the access to the desired molecules. It has been estimated that thousands of new compounds are needed to launch a drug. This synthetic activity pervades all phases in drug development from the hit finding to production, and lately has experienced impressive advances [1–3]. Although all stages have specific requirements and are amenable to improvement, we believe that the synthetic methodology regarding aspects such as bond forming efficiency, structural diversity, and reaction economies are crucial points in this issue, the time factor being especially relevant [4–7].

The concern about the relevant chemical space in a given MedChem project, although capital, is often overlooked [8,9], considering that the dimension of drug-like space is around 10^{60} virtual molecules and, likely, we should go beyond this limit to find new medicines [10]. This situation can be confronted with the fact that at present, we have access to more than a 100 billion compounds, and the trillion level is in sight [11]. Furthermore, the broadcasted compounds are accessible through a limited set of well-established reactions, around 20 processes dominating the stepwise preparations in medicinal chemistry [12]. This only represents a minute fraction of the in principle feasible chemical connectivities, with most accessible scaffolds being overexploited. Thus, finding relevant drugs should arguably rely on the incorporation of new scaffolds, rather than overcrowding the existing ones [13].

To tackle the aforementioned problems, we became interested in multicomponent reactions (MCRs), processes where three or more reactants interact to form an adduct with most atoms of the starting materials, in one step, through a domino-type transformation involving a unified mechanism [14,15]. The development of MCRs continues at a considerable pace in reaction discovery, organic synthesis, etc., and their application in medicinal

chemistry is gaining momentum. The implementation of this methodology is having a deep impact on hit finding, greatly helping the production of combinatorial libraries (key for SAR studies), hit-to-lead (H2L) stage, lead optimization and large-scale preparation of complex medicines [16–18].

Our group has been involved in the development of new MCRs based on the use of fundamental heterocycles as substrates. The following reasons may justify this approach: (a) the limited knowledge available on these processes; (b) the presence of heterocyclic motifs in the majority of drugs and (c) the convenience of the MCR approach to tackle defined MedChem projects, both from a conceptual and practical point of view (Figure 1) [19–22]. In this review, we summarize the biomedical impact of our research, classified according to the biological targets upon which the MCR adducts interact, their mode of action and their purpose. The following sections comprise enzymes, transcription factors, chemotherapeutics, fluorescent probes, and neuroactive compounds. Finally, some considerations will be disclosed as conclusions and future outlook.

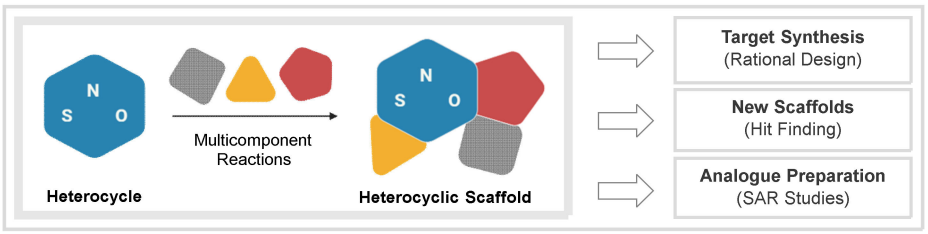

Figure 1. Heterocycle-based MCRs for MedChem applications.

2. Enzymes

2.1. Acetyl-Cholinesterase (AChE)

In this section, we account for the research targeting the dual inhibition of the acetylcholinesterase (AChE). Although blocking the enzyme improves the symptoms of Alzheimer disease (AD), Inestrosa et al. demonstrated that the enzyme itself promotes amyloid peptide aggregation, in vitro and in vivo, through binding at a peripheral site [23]. At this point, P. Camps and D. Muñoz-Torrero (UB), who had prepared novel classes of extremely potent AChE inhibitors [24], contacted us to address a challenging task: the dual inhibition of AChE at the active and peripheral sites [25]. Since the putative binding site of the amyloid peptide at the enzyme surface is quite flat, the plan was to drive the inhibitor into the peripheral site, while efficiently blocking the catalytic site with a known blocker, a tacrine derived unit, both linked by a flexible chain to fill the gorge that communicates both sites (Figure 2a). Preliminary docking studies backed the design of the final compounds. As the peripheral site binder, a planar pyrano-quinoline nucleus was chosen and the retrosynthesis relied on a Povarov MCR [26], a process which is progressively used in medicinal chemistry [27]. In this way, the condensation of an aniline, an aromatic aldehyde, and an activated olefin afforded the corresponding MCR adducts **1** as a mixture of stereoisomers, which were subjected to DDQ oxidation to afford the fused aromatic systems (Figure 2b). The resulting fragment was coupled with an amino-chlorotacrine to yield the designed compound **2a** in a remarkable three-step preparation (Figure 2c). Compound **2a** exhibited impressive performance, displaying potent central inhibition at nanomolar level, together with spontaneous and AChE-mediated inhibition of the amyloid aggregation. Interestingly, it showed a suitable PAMPA profile, as well as an unexpected BACE inhibition (Figure 2c) [28]. Refined computational calculations, done by F. J. Luque (UB), showed a favored pose of the dual inhibitor blocking the active site with its tacrine moiety, filling the gorge with the flexible chain, and nicely disposing the MCR-derived unit at the peripheral site, sandwiched between a tyrosine and a tryptophan (Figure 2d).

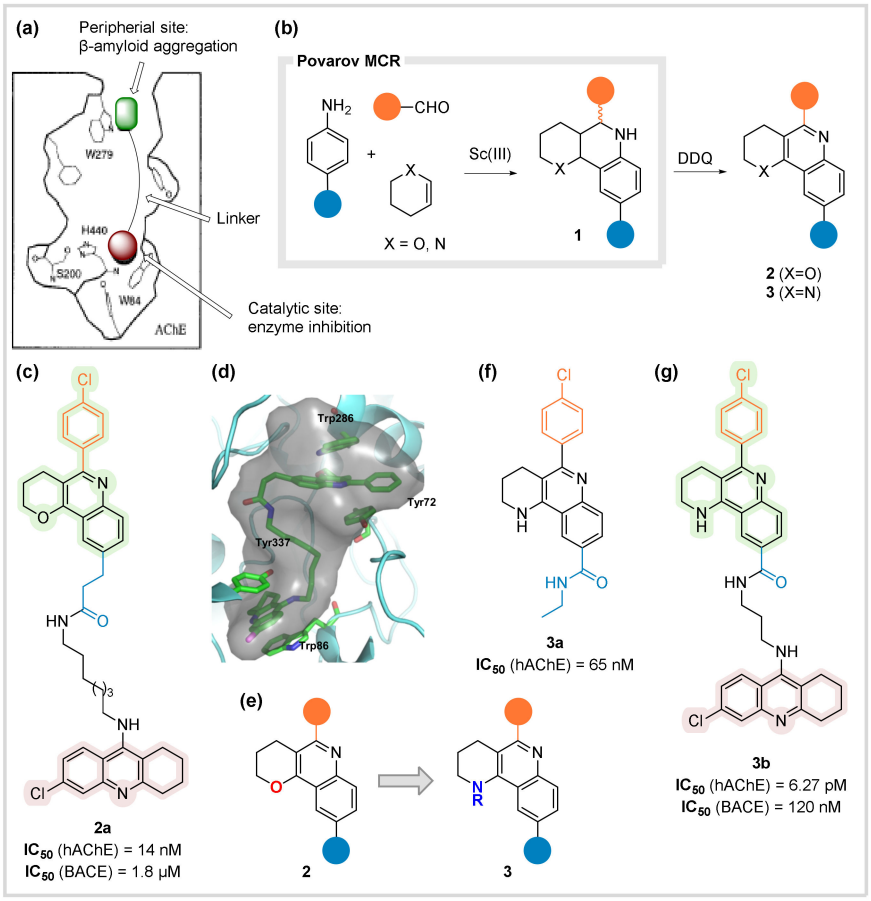

Figure 2. AChE inhibitors. (**a**) Outline of the AChE dual inhibition. (**b**) The Povarov MCR and subsequent oxidation leading to the new peripheral site inhibitors. (**c**) Structure and pharmacological data for the dual AChE inhibitor **2a**. (**d**) Docking simulation showing the interactions at the catalytic and peripheral sites. From ref. [28] (P. Camps et al., *J. Med. Chem.* **2009**, *52*, 5365), reproduced with permission. Copyright 2009 ACS. (**e**) Isosteric modification in the peripheral site inhibitor core. (**f**) Structure and pharmacological data of small molecule peripheral site inhibitor **3a**. (**g**) Structure and pharmacological data for the dual AChE inhibitor **3b**.

Careful analysis of the observed interactions suggested a structural change to maximize the binding at the peripheral site which has an anionic nature: to isosterically replace the oxygen atom at the pyran ring with a nitrogen. This would ensure the amine protonation at physiological pH, reinforcing the affinity with the aromatic amino acid residues involved by adding a cation-π interaction (Figure 2e). In this way, a related Povarov MCR with tetrahydropyridines conveniently afforded the desired adducts, only requiring tactical modifications such as the introduction of substitution at the nitrogen in the precursors or the use of a Boc group to generate the final NH derivatives after deprotection. In this way, we prepared a chemset of exclusively allosteric binders with potency levels reaching low nanomolar range, a remarkable result for small molecules tackling the peripheral site (**3a**, Figure 2f) [29]. The mode of action is an allosteric inhibition, in agreement with enzymatic data and supported by molecular modeling studies. Furthermore, following this research line, a dual inhibitor was envisaged, linking this peripheral unit to the chlorotacrine moiety. Docking studies suggested an attractive interaction of the amide group with an amino acid residue at the gorge, resulting in a deeper penetration of the quinoline substructure (in comparison with dihydropyrane-fused derivatives), recommending a shorter linkage for optimal binding. In this way, derivative **3b** was designed and prepared through a straightforward MCR-based synthesis (Figure 2g). It displayed outstanding potency against AChE with a single digit picomolar activity. Moreover, it showed a good BACE-blocking profile

at nanomolar level while remarkably inhibiting the amyloid peptide and tau aggregations [30]. Incidentally, this new class of allosteric binders, having clear analogies with antiparasitic aminoquinolines, were also tested against trypanosomatid causing agents (*Trypanosoma cruzi, T. brucei and Leishmania infantum*), displaying low micromolar levels of IC_{50} and IC_{90}, albeit with lesser efficacy in front of epi- and pro-mastigotes and with low safety indexes [31]. In our opinion, the presented results clearly demonstrate how the intelligent implication of the MCR strategy combined with the suitable computational platform can lead to highly efficient production of meaningful chemical libraries and eventual lead compounds.

2.2. Dihydrofolate Reductase (DHFR)

Another research line in our laboratories aims at the construction of new drugs from existing ones through a sort of late-stage derivatization via MCRs. This *Drugs from Drugs* approach relies on two premises: (a) the existence of drugs that can act as substrates in MCR processes and (b) the suitability of the resulting MCR adducts to keep meaningful structural information and to maintain activity against the initial target (Figure 3a). In this way, we may diversify the original entity and tackle a variety of aspects including drug selectivity, resistance, etc. In this context, MCRs would greatly accelerate the drug discovery process and simultaneously enable serious structural modifications. We focused on the Groebke-Blackburn-Bienaymé MCR (GBBR), the interaction of an aminopyridine, and aldehyde and an isocyanide to yield substituted imidazopyrididine adducts [32,33] knowing that several drugs display a diaminopyrimidine motif. Such is the case of trimethoprim (TMP), a WHO essential medicine for the treatment of lower urinary tract infections and bacterial dysentery. TMP blocks the folic acid route by inhibiting dihydrofolate reductase (DHFR) and is usually used combination with sulfamethoxazole (SMX). The synergistic effect efficiently interrupts DNA synthesis in bacteria (in contrast, humans get the folic acid from diet). Currently, TMP treatments face increasing problems with drug resistant infections, which have become a serious challenge in chemotherapy. Interestingly, TMP was eligible for the MCR-based modification, as the resulting adducts retained a relevant part of the structural binding motif (Figure 3b). Therefore, we tackled the derivatization of TMP to expand the chemical diversity around its core and optimize the activity of the formed derivatives. Accordingly, we promoted selective GBBRs involving TMP, an array of aldehydes and isocyanides to build a representative chemset of 15 TMP mono- and bis-derivatives **4** and **5** (Figure 3b. For further discussion of the exclusive formation of adducts 4 and 5 under mild and harsh conditions respectively, see Section 4.2.

This collection was tested against *Escherichia coli*, *Pseudomonas aeruginosa* and several strains of methicillin-resistant *Staphylococcus aureus*, to find that double adducts **5** were inactive, whereas derivatives **4** displayed different levels of potency, useful to establish a preliminary SAR. Although *Pseudomonas* were resistant to all new adducts, some of them displayed relevant activity in the low micromolar range. The best hit was derivative **4a**, which, albeit with MIC figures very similar to the parent TMP (Figure 3c), provided a remarkably faster mode of action, a key feature in clinical treatments (Figure 3d) [34]. This was shown in combination experiments with SMX both against *E. coli* and *S. aureus*, prompting new research on its mechanism of action. Additional determinations revealed that the selected compound **4a** was active in biofilm prevention in tests with *P. aeruginosa*, even though similar to TMP, it could not fully eradicate those from *S. aureus*. Furthermore, its toxicity against cell lines (HepG2 and L-929) was extremely low at the usual antibiotic concentrations. *P. aeruginosa* is naturally resistant to TMP and its derivatives, likely due to its efflux systems. Accordingly, treatment with adduct **4a**, SMX and an efflux pump inhibitor (PAβN), enhanced its potency in a quite remarkable manner (15-fold). Similarly, colistin (a peptide used to permeabilize membranes) also exhibits a synergistic effect in resistant bacteria, rendering these microorganisms sensible to TMP-like adducts. Furthermore, in the presence of these inhibitors, the enzyme activity can be fully restored by adding increasing concentration of the NADPH cofactor. To explain this fact and gain knowledge on the

mode of action, we explored the binding of MCR adduct **4a** to a model of DHFR from *E. coli*. After refined docking calculations, and comparisons with the PDB from the interaction of the parent TMP with the same enzyme, it was concluded that our compounds present a different binding mode in the pocket. Derivative **4a** is accommodated in a completely rearranged form, sterically colliding with the NADPH cofactor (Figure 3e) [35]. These findings reinforce the need for new scaffolds and validate the hypothesis of using existing drugs to find new relevant derivatives through MCRs.

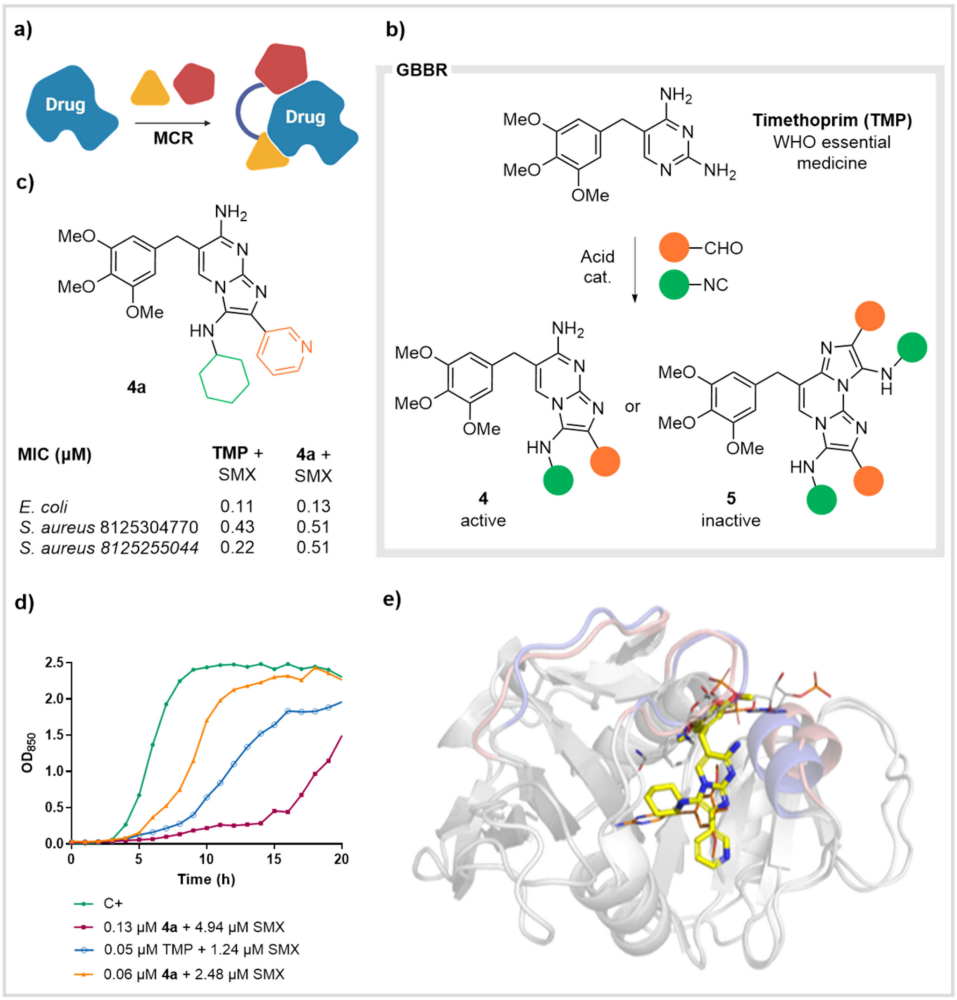

Figure 3. DHFR inhibitors. (**a**) Concept of the *Drugs form Drugs* approach. (**b**) Structure of trimethoprim and GBBR leading to mono- and bis- adducts **4** and **5**, respectively. (**c**) Structure and activity data of lead compound **4a**. (**d**) Growth curve of *E. coli* with TMP and **4a** in combination with SMX. (**e**) Docked position of adduct **4a** (yellow) in DHFR (homology model from *E. coli*). The location of TMP (orange) and NADPH (gray) is also shown.

3. Transcription Factors

Aryl Hydrocarbon Receptor (AhR)

The Aryl hydrocarbon Receptor (AhR) pathway is associated with a vast variety of physiological processes. Interestingly, both activation and inhibition of this pathway result in distinct biological responses. Therefore, its controlled regulation is considered as a potentially promising therapeutic approach for a range of diseases including cancers and immune system disorders. At present, AhR-based drug discovery campaigns face serious challenges. First, as the active site of the receptor is not fully described, the development of novel small-molecule AhR ligands mainly relies on compound screening rather than rational design. On the other hand, the majority of currently known AhR ligands raise

cytotoxicity concerns due to their alarming poly(hetero)aromatic structures. Finally, the generation of relevant screening libraries around limited (complex) scaffolds requires multi-step synthetic routes, slowing down the progress in the area.

In this context, our group reported an MCR-based pathway to assemble complex fused polyheterocyclic systems through oxidative and non-oxidative extensions of GBBR with indole carboxaldehydes, yielding adducts **6–8** (Figure 4a) [36]. Remarkably, the incorporation of indole 2-carboxaldehydes yielded GBBR adducts **6** featuring indolocarbazole nuclei (Figure 4a). Interestingly, these compounds shared the same structural motif of FICZ, a biosynthetic derivative of tryptophan and a potent activating ligand of AhR, commonly used as a positive control (Figure 4b). Inspired by this resemblance, a selection of synthesized compounds was tested. The results confirmed the substituted indolocarbazoles **6a–c** to be AhR pathway activators (Figure 4c,d). Remarkably, compound **8a**, featuring a complex 7-membered connectivity in a polycyclic framework, demonstrated similar behavior, despite lacking the indolocarbazole residue [36]. Considering the easy access to structurally diverse AhR ligand libraries through one-pot operations, further studies are being conducted to develop novel AhR pathway modulators with potential biomedical applications.

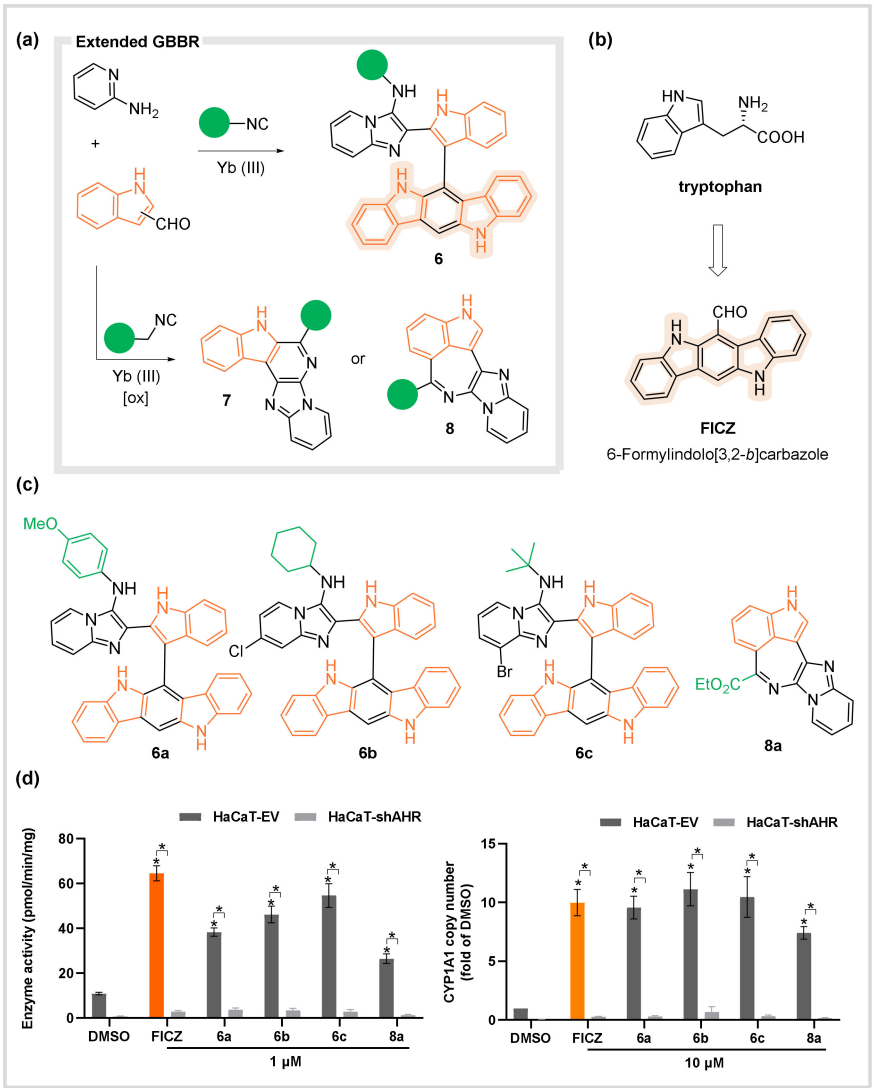

Figure 4. AhR Activators. (**a**) The extended GBBRs with indole carboxaldehydes. (**b**) FICZ ligand structure. (**c**) Novel MCR-based indolocarbazole ligands. (**d**) The AhR-activating properties of the synthesized compounds in keratinocytes (related to cytochrome P450 activity and expression). * $p \leq 0.05$.

4. Chemotherapeutic Agents

Compound screening continues to be a highly influential approach in modern drug discovery. This strategy is particularly useful in case of limited knowledge about the disease development mechanisms, the complexity of the physiological pathways, or insufficient information on the function/structures of the biological targets involved. On such occasions, as computational approaches may not be fully implied, the drug discovery campaigns heavily rely on the screening of relevant libraries. In this context, MCRs are powerful tools for the rapid development of small-molecule collections around promising scaffolds or diversity-oriented motifs [37]. Here, we summarize the applications of the heterocycle-based MCRs discovered in the group to develop novel *tunable* chemotherapeutic agents via compound screening.

4.1. Antiparacitic Agents against Trypanosoma

Chagas disease and Sleeping sickness, arising from *Trypanosoma cruzi* and *Trypanosoma brucei*, respectively, figure among the concerning global health problems. These pathologies dramatically affect the lives of large populations and impose considerable economical charge on several countries. Additionally, because of our dynamic lifestyle, they are not geographically restricted to endemic regions anymore. Moreover, as the currently available therapies are not efficient enough, the treatments are long-term, and the patients normally suffer a range of side-effects, experiencing chronic stages and developing resistance. These aspects intensify their socio-economical effects and imply an urgent need for treatments arising from new/modified scaffolds with improved efficiency and safety.

In this context, Robello et al. reported the anti-trypanosomal activity of simple imidazolium salts against Chagas disease [38]. Based on their findings, symmetrically N-Substituted imidazolium salts like compound **MLB** showed improved potency and safety against *Trypanosoma cruzi*, compared to the commonly prescribed benznidazole (Figure 5a). In the meantime, our group described the convenient assembly of tetra-substituted imidazolium salts **10** through the acid-catalyzed reaction of propargylamines **9** and isocyanides. The reaction was successfully coupled with the classic A^3-MCR (Aldehyde-Amine-Alkyne condensation) to prepare the intermediate substrates **9** through the condensations of aldehydes, amines, and alkynes (Figure 5b). The simple (one-pot) preparation and the wide scope of the reaction furnished a small library of imidazolium salts **10** with four diversity points, allowing the incorporation of both aromatic and aliphatic residues [39]. A selection of synthesized compounds was tested against both African and American Trypanosoma. Among them, salts **10a** and **10b** displayed particularly encouraging antiparasitical activity against *Trypanosoma cruzi* at sub-μM level and moderate safety indexes. Surprisingly, these compounds were confirmed to be highly active against *Trypanosoma brucei* (at nanomolar-level) with exceptional safety indexes (Figure 5c) [40].

Interestingly, Robello's report also suggested the (less potent) antiparasitic activity of a benzimidazolium derivative called **MLJ** (Figure 5d) [38]. Meanwhile, the group was also developing a novel TMSCl-mediated mechanism for the reaction of isocyanides and azines to give amino benzimidazolium salts **11** through a Reissert type MCR (Figure 5e) [41]. This unprecedented mild activation significantly amplified the scope of the reaction, giving access to a diverse collection of aminobenzimidazolium salts. These compounds featured a wide range of aliphatic/aromatic substituents (coming from the isocyanides) as well as variety of azines/diazines. The novelty and features of the synthesized library encouraged us to determine their antiparasitic activity. To our delight, several derivatives including **11a–c** exhibited micromolar-level activity against *Trypanosoma cruzi* with safety indexes comparable to the previous series (Figure 5f). Furthermore, they also confirmed to have remarkable nano-molar potencies and excellent safety indexes against *Trypanosoma brucei.* Having promising pharmacochemical properties, compound **11c** (featuring an added nitrogen atom on the heterocyclic scaffold) was selected for an in vivo study on mice and it was unexpectedly inactive probably due to a poor bioavailability [41]. However, these results confirm the promising potential of scaffolds **10** and **11** as new classes of antiparasitic

agents against both African and American Trypanosoma. Moreover, considering the described multicomponent access, their performance and pharmaco-physical properties could be further improved by structural modifications upon the existing diversity points.

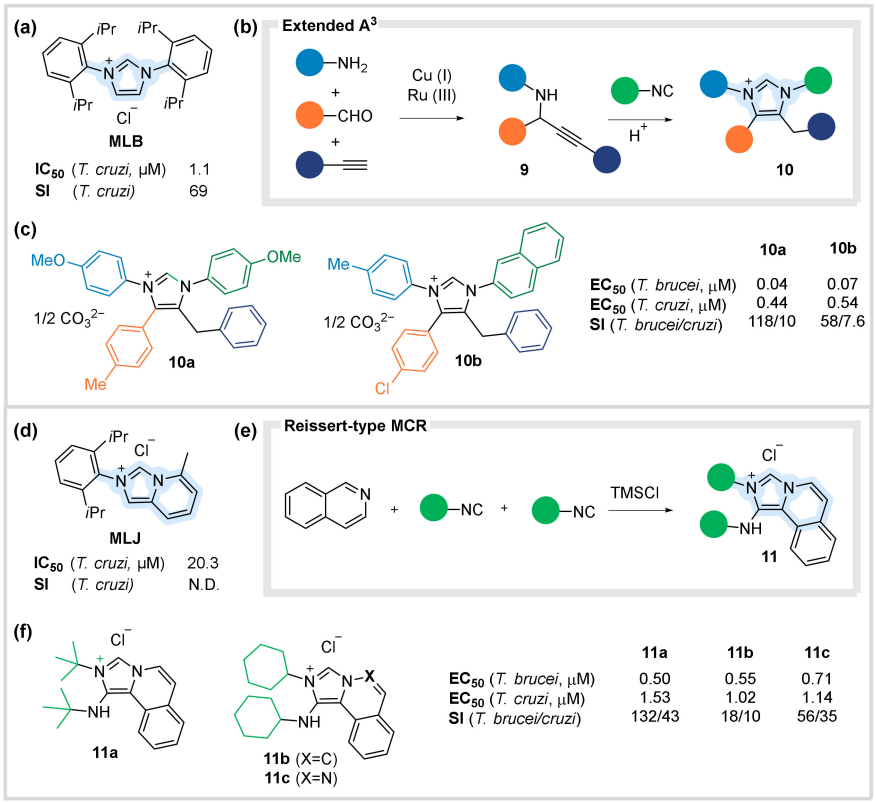

Figure 5. MCR-based antiparasitic agents. (**a**) Imidazolium salt MLB with antiparasitic activity against Chagas disease. (**b**) MCR pathway to tetrasubstituted imidazolium salts. (**c**) Biological activities of promising derivatives. (**d**) Benzimidazolium salt MLJ with mild antiparasitic activity against Chagas disease. (**e**) TMSCl-promoted MCR synthesis of benzimidazolium salts. (**f**) Biological activities of selected derivatives.

4.2. Antiviral Agents against Human Adenovirous

Viral diseases (including influenza and related infections) affect large human/animal populations, especially during outbreaks. Moreover, these infections seriously threaten individuals with weakened immune systems. Unfortunately, despite being fatal for high-risk groups, several specific antiviral treatments are not yet available. On the other hand, due to their mechanisms of action, frequent mutations, and developed resistance, there is a constant demand for new scaffolds/derivatives with improved performance.

In this context, a project in the group led to the discovery of multiple GBBRs upon a variety of unexplored aminoazine substrates. The structural diversity, selectivity, scope, and a variety of post-transformations established a unique synthetic platform for screening libraries (Figure 6a) [32]. Inspired by the relevance of the benzimidazole core in medicinal chemistry, especially in anti-infectious compounds, a selection of our GBBR adducts were tested against human adenovirus (Figure 6b). Remarkably, bis-GBBR compounds **13a–c** exhibited micromolar activity, whereas their mono-GBBR precursors **12a–b** were inactive. Surprisingly, compound **13a′**, a close derivative of **13a** with only a slight modification on one isocyanide residue was inactive. Compounds **13a–b** also exhibited remarkable selectivity indexes. We believe that exploiting the structural diversity and synthetic facility of these reactions to further expand the observed SAR may lead to the discovery of specific antiviral agents for human adenovirus and related infections.

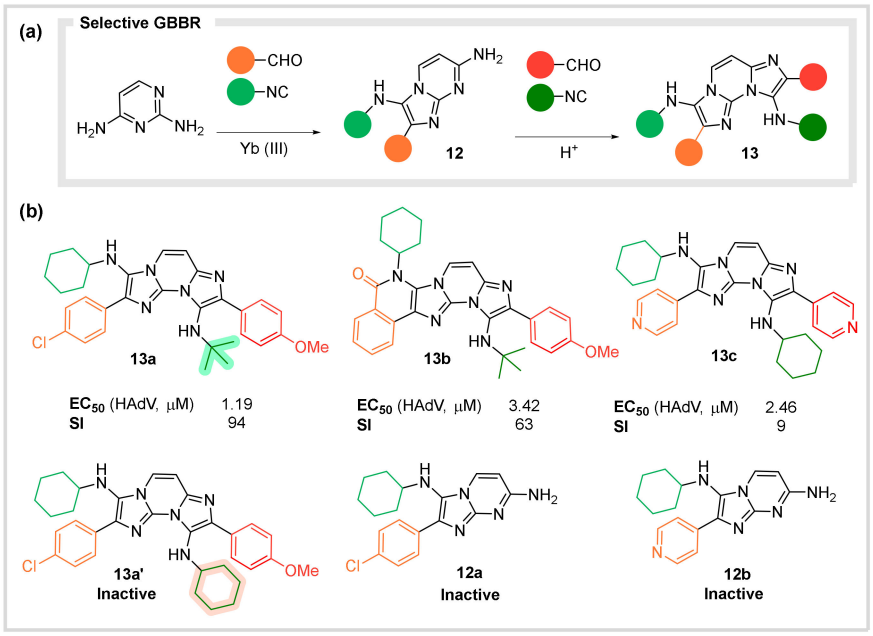

Figure 6. GBBR approach to antivirals. (**a**) Selective GBBRs upon diaminoazines. (**b**) Antiviral activity of the representative GBBR compounds against human Adenovirus.

5. Fluorescent Bioprobes

The ability of chemical entities to fluoresce upon light excitation has been long exploited in biomedicine and bioimaging [42–44]. The development of new fluorescent probes encompasses a compromise between suitable photophysical properties (high fluorescence, quantum yields, etc.) and adequate properties for biological use (good affinity and permeability, low toxicity, etc.). A representative example is the BODIPY scaffold (Figure 7a), one of the most versatile fluorescent probes exploited so far, which plays an extremely important role in bioimaging [45,46]. Taking into account the relevance of isocyanide based MCRs as well as the group's previous work in the field, we envisioned the participation of a BODIPY derivative in such transformations to rapidly build new fluoroprobes. In this way, we synthesized the unprecedented isonitrile-functionalised BODIPY (14), following a standard preparation protocol form the corresponding anilino-BODIPY derivative. Compound 14 maintained the excellent photophysical properties of the parent BODIPY core (Figure 7b) [47]. Then, isocyanide **14** was used as the substrate in several well-known MCRs, namely Ugi, Passerini and GBBR (Figure 7b) to generate a series of BOPIDY-derivatized analogues **15**, which showed remarkable cell permeability. Imaging experiments were planned and supervised by M. Vendrell (U. Edinburgh). While most derivatives indiscriminately stained the whole cytoplasm, derivative **15a** ($pK_a \approx 5.76$, Figure 7c) showed selective bright fluorescence in subcellular acidic compartments, as confirmed by co-incubation with acidotropic dye LysoTracker Red (Figure 7d). In light of these remarkable properties, we evaluated the imaging of phagosomal acidification by treating RAW 264.7 macrophages with probe **15a** before and after incubation with zymosan, a glucan that induces phagosomal acidification. It was determined that the fluorescence intensity was proportional to the activation with zymosan (unlike LysoTracker Red), proving that emission of **15a** is ratiometric and depends on macrophages acidification as it decreased upon inhibition of a key ATPase for phagosomal acidification with bafilomycin A (Figure 7e).

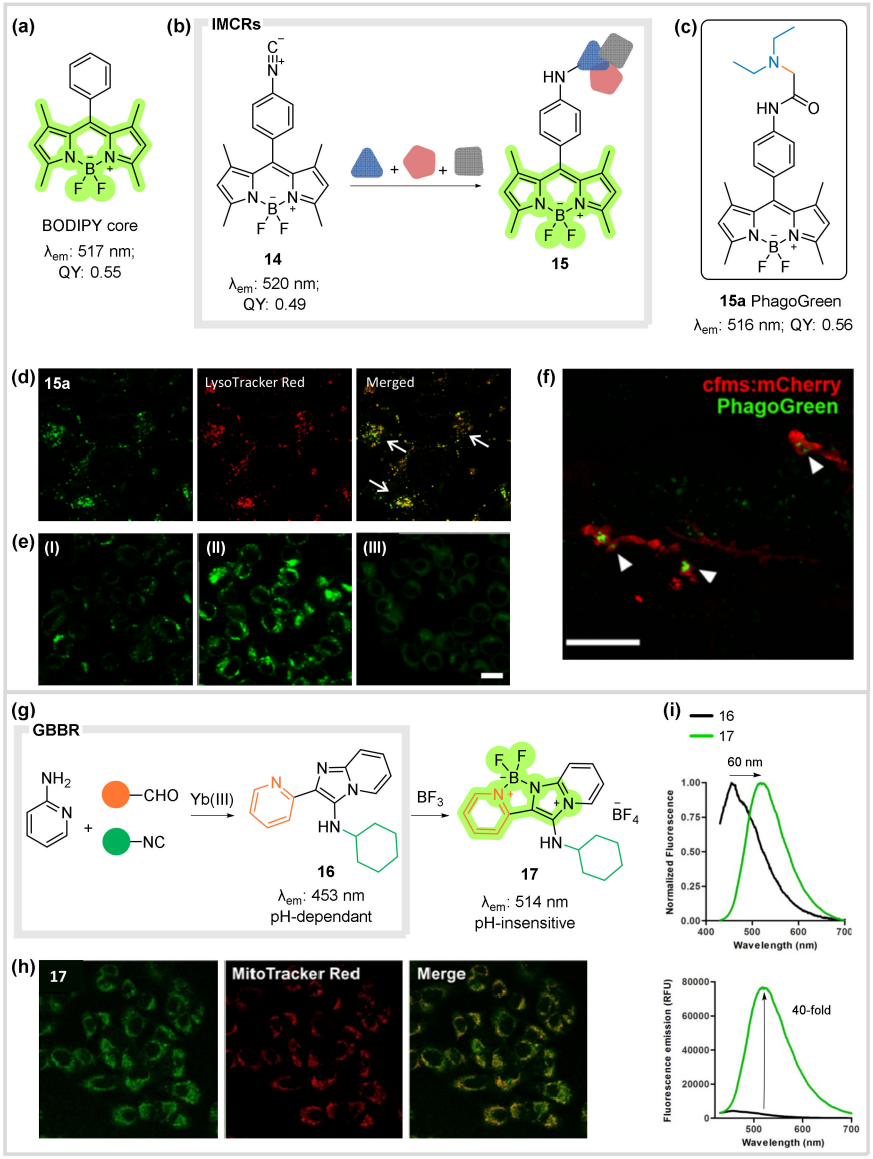

Figure 7. (**a**) Structure and photophysical properties of the BODIPY core. (**b**) Isocyanide derivatized BODIPY scaffold and generation of compounds **15** through various IMCRs. (**c**) Structure and photophysical properties of selected probe **15a**, Phagogreen. (**d**) Co-incubation of **15a** and LysoTracker Red in A549 cells. (**e**) RAW 264.7 macrophages were treated with **15a**. Fluorescence of **15a** in (**I**) non-activated macrophages, (**II**) zymosan-activated macrophages, and (**III**) zymosan-activated macrophages treated with bafilomycin A. (**f**) Still from time-lapse imaging of transgenic zebrafish with m-Cherry-labelled macrophages treated with PhagoGreen. Scale bars: 20 µm. Sections (**d**–**f**) from ref. [47] (O. Vázquez-Romero et al, *J. Am. Chem. Soc*. **2013**, *135*, 16018) reproduced with permission. Copyright 2013 ACS. (**g**) GBBR access to BODIPY-adduct **17**. (**h**) Human A549 epithelial cells upon incubation with compound **17** and MitoTracker Red. Scale bar: 10 µm. (**i**) Fluorescent properties of probe **17** vs. GBBR adduct 16. Sections (**h**,**i**) From ref. [32] (O. Ghashghaei et al., *Chem. Eur. J*. **2018**, *24*, 14513), reproduced with permission Copyright Wiley-VCH GmbH.

We confirmed that compound **15a**, named PhagoGreen, was neither toxic nor altered macrophage biology. Thus, we tackled the in vivo imaging of activated macrophages by incubating zebrafish embryos expressing m-Cherry labelled phagocytic macrophages with PhagoGreen **15a**, and no staining of early phagosomes was observed, whereas bright fluorescence was detected in actively phagocytic macrophages (Figure 7f).

Moreover, we believed that our previous work in MCRs using heterocyclic substrates [22] provided an optimal framework for the development of de novo fluorophores. In this regard, as the group was developing a GBBR-based chemset [32], we envisaged that the input of pyridine-2-carboxaldehyde would lead to generation of compounds resembling the BODIPY scaffold upon BF_3 post-condensation. Thus, GBBR adduct 16 was synthesised and its BODIPY-like analogue 17 suitably obtained, rendering a non-conventional 5-membered ring BODIPY derivative (Figure 7g). Although the GBBR adduct is somewhat fluorescent, the boron bridging greatly improves the photophysical properties. Probe 17 displays an impressive 60 nm red-shift and a 40-fold fluorescence increase (compared with 16) while being pH independent, making it a valuable fluorophore for bioimaging applications under a range of conditions (Figure 7h). Its potential in live-cell imaging was confirmed by incubation of compound 17 with human lung A549 epithelial cells, showing remarkable cell permeability and exhibiting preferential accumulation in mitochondria (Figure 7i).

In the context of de novo synthesis of fluorescent scaffolds, we also described a new MCR from azines, isocyanides and trifluoroacetic acid anhydride that yielded mesoionic acid fluorides (Figure 8a) [48]. Their remarkable stability to hydrolysis together with their photochemical properties made this scaffold promising to detect amino containing analytes through amide formation. When we reacted adduct 18 with a series of signaling molecules, mainly hormones and neurotransmitters, in PBS solution, we found that it exhibited an excellent selectivity towards histamine. Moreover, a significant bathochromic shift was observed, and clear differences between the probe (named Histamine Blue) and the histamine adduct 19 could be observed (Figure 8b). Then, we evaluated its ability to image histamine in live RBL-2H3 basophils and RAW 264.7 macrophages. Histamine Blue (18) selectively stained the histamine-storing granules of basophils, without inducing cytotoxicity or affecting their morphology. As for the macrophages, probe 18 did not stain the cells, which under normal conditions contain low levels of histamine. However, macrophages were brightly stained after either histamine uptake or treatment with thapsigargin, which induces de novo synthesis of histamine (Figure 8c) [48].

Based on these results, we also tackled the preparation of new labelling agents by modifying our acid fluoride probe with well-established fluorophores, following facilitated procedures for sophisticated constructs [49]. We realized that linking the BODPIY scaffold to our mesoionic acid fluorides would potentially provide labels for amine-containing biomolecules endowed with remarkable properties. Indeed, when the BODIPY isoquinoline 20 took part in the MCR, it suitably yielded the corresponding dipolar acid fluoride 21 (Figure 8d) [50]. As expected, the probe maintained the spectral properties of the BODIPY dye as well as the resistance to hydrolysis and exclusive reactivity towards amines of the initial acid fluorides and validated it for use as a label. In this regard, we tackled the visual detection of natamycin through this approach. This macrolide selectively binds to ergosterol, a key component of fungal cell membranes, thus inhibiting their growth. It also contains a free amino group eligible for coupling with our probe. Thus, the fluorescent natamycin amide 22 could serve as a probe for the detection of fungal infection sites (Figure 8e). Moreover, this compound displayed remarkable environment sensitivity towards hydrophobic media, showing a 70-fold fluorescence increase in 1,4-dioxane (mimicking the lipid bilayer) over PBS (mimicking the intracellular media) (Figure 8f). Its use as a fluorescent probe for the imaging of fungal cells was assessed by incubation with several fungal pathogens (*Fusarium solani*, *F. oxysporum*, and *Aspergillus flavus*) and bacteria (*Pseudomonas aeruginosa*). While the ergosterol-containing fungi species displayed bright fluorescence upon uptake of the probe (detected by confocal microscopy); bacteria, lacking ergosterol, were not stained, confirming the potential application of BODIPY-natamycin derivative 22 as a fluorescent probe for imaging fungal infections (Figure 8g).

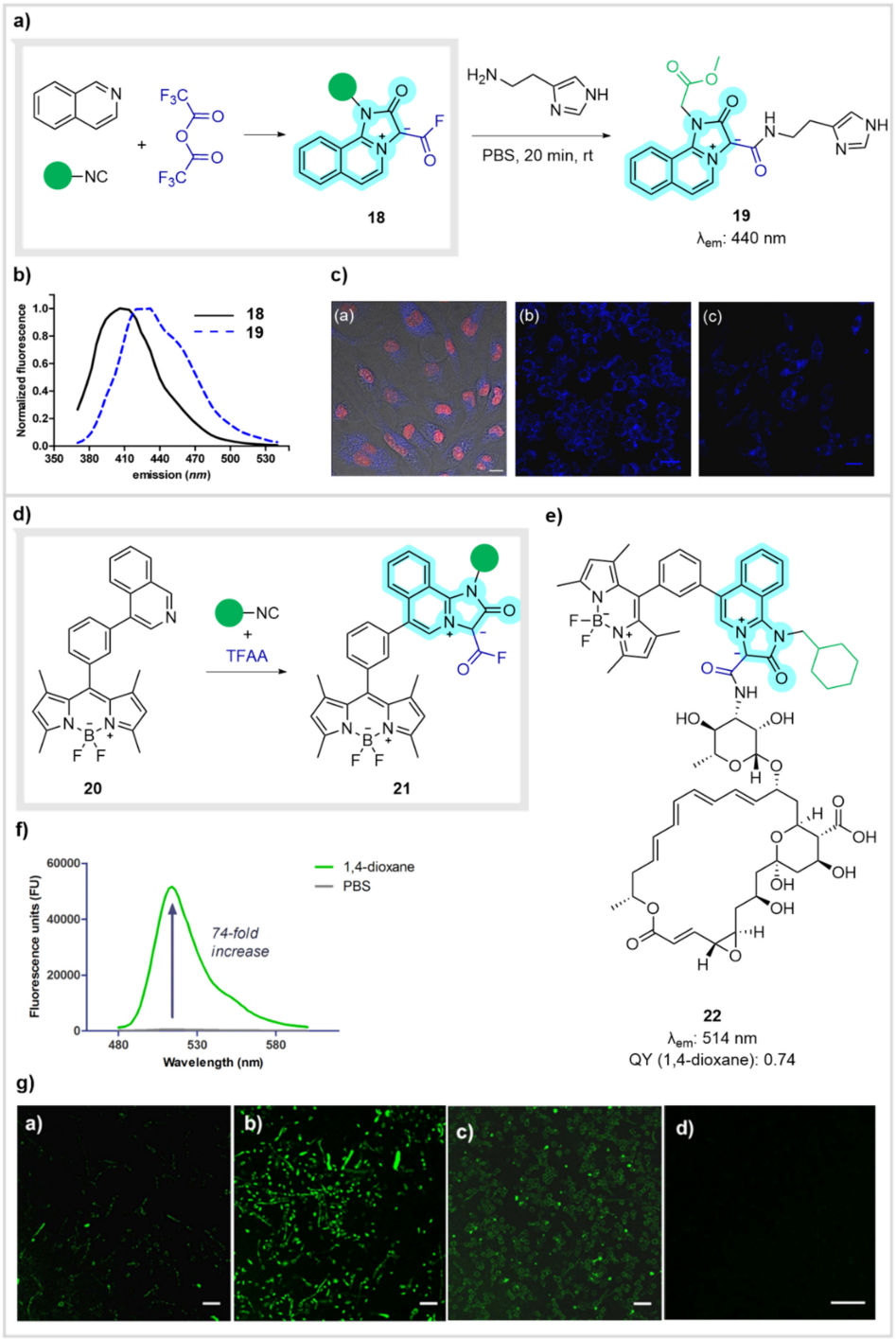

Figure 8. (**a**) MCR access to probe **18** for imaging of histamine in live cells. (**b**) Normalized fluorescence of probe **18** (black) and histamine adduct **19** (blue). (**c**) Microscopy images of: (**a**) RBL-2H3 basophils upon incubation of probe **18** with DRAQ5 as nuclear counterstaining; (**b**) RAW 264.7 macrophages after incubation with Histamine blue and upon histamine uptake and (**c**) after treatment with thapsigargin. Sections (b,c) from ref [48] (N. Kielland et al., *Chem. Commun*. **2012**, *48*, 7401) reproduced with permission form the Royal Society of Chemistry. (**d**) MCR to the BODIPY dipolar acid fluoride **21**. (**e**) Structure of probe **22**, from conjugation of **21** with natamycin. (**f**) Fluorescent properties of probe **22** in 1,4-dioxane and in PBS. (**g**) Fluorescence images of fungal and bacterial cells upon incubation with **20**: (**a**) *F. solani*, (**b**) *F. oxysporum*, (**c**) *A. flavus* and (**d**) *P. Aeruginosa*. Scale bar: 20 μm. Sections (**f**,**g**) from ref [50] (M. Sintes et al. *Bioconjug. Chem*. **2016**, *27*, 1340) reproduced with permission. Copyright 2016 ACS.

6. Receptors

This section describes the development of neuroactive agents via MCRs and related processes. These receptor modulators address symptomatic treatment for neurodegenerative diseases, aiming to improve cognitive and behavioral signs. This goal is very challenging, as no new cognitive enhanced drug has reached the market in more than two decades. In this context, we were attracted by imidazoline I_2 receptors (I2-IR), located in central and peripheral nervous system, as well as many organs and tissues [51]. I_2-IR are imidazoline nonadrenergic binding sites recognized by the tritiated radioligands idazoxan and *p*-aminoclonidine [52,53]. Although, I_2-IR are heterogeneous and lack detailed structural definition, their implication in physiological and pathological processes has been described by using well-characterized I_2-IR ligands. These ligands have proven that I_2-IR level dysregulations are a hallmark in analgesia, inflammation, and human brain disorders such as AD, Parkinson's and Huntington diseases, depression, and glial tumors [54–56].

Known I_2-IR ligands share common structural features, namely a 2-substituted imidazoline (Figure 9a) [57–59]. As substitution in the 4 and 5-positions of the imidazoline ring had remained unexplored, we tackled these structural changes to generate new families of I_2-IR ligands with enhanced pharmacological properties. To achieve a fast and convenient access to these imidazoline scaffolds, we applied the Orru MCR, which involves the use of carbonyls, amines and isocyanides bearing an acidic α-position (Figure 9b) [60,61]. We specifically studied the role of diethyl isocyanomethylphosphonate (PhosMic) in these processes and reported the silver-catalyzed MCR synthesis of a diverse library of 2-(imidazoline-4-yl)phosphonates **23** [62]. The pharmacological profile and selectivity of the selected compounds were evaluated through competition binding studies against the tritiated selective radioligands for I_2-IR (2-BFI) and α_2-adrenoreceptors (AR) such as 2-methoxyidazoxan. The studies were performed in membranes from postmortem human frontal cortex, a brain area with significant density of both receptors. Compounds **23a** and **23b** emerged as the most promising ligands. Imidazoline **23a** showcased a much better I_2/α_2- AR selectivity than the standard idazoxan, while analogue **23b** displayed remarkable nanomolar-range affinity for I_2-IR (Figure 9c) [63].

With the impressive results of our new I_2-IR ligands, we explored their anti-AD properties. Accordingly, in vivo studies in mice showed that acute treatments with MCR adducts **23a** and **23b** in the mice hippocampus significantly increased the ratio of oligomeric FAS-associated protein with death domain (FADD) phosphorylated at ser191 (p-FADD) to total dimeric FADD, an index of cell survival and neuroplasticity. Both compounds also induced mild hypothermia, a well-stablished neuroprotective effect in cerebral ischemia, regulated mechanisms of apoptotic pathways and inhibited p35 cleavage into neurotoxic p25 [63]. Moreover, in vivo studies in the model of neurodegeneration senescence accelerated mouse prone 8 mice (SAMP8) with compounds **23b** and **23c** (endowed with high affinity and selectivity for I_2-IR) produced beneficial effects in behavior and cognition. Changes in molecular pathways implicated in oxidative stress, inflammation, synaptic plasticity, and apoptotic cell death supported the improvement in the whole condition of the treated animals. This study was the first experimental evidence to demonstrated that I_2-IR are putative targets for cognitive impairment [64]. Therefore, I_2-IR could be considered as a putative new therapeutic target for AD, and its modulation constitutes an encouraging option for treating this unmet medical need. Additionally, in vivo studies in SAMP8 animals treated with adduct **23b** ameliorated both behavioral and psychological symptoms of dementia and cognitive decline by attenuating depressive-like and fear-anxiety-like behavior and improving cognitive performance. Amelioration of molecular pathways underlying depression and anxiety phenotypes were observed, suggesting I_2-IR as an alternative target for slowing down AD progression (Figure 9d) [65].

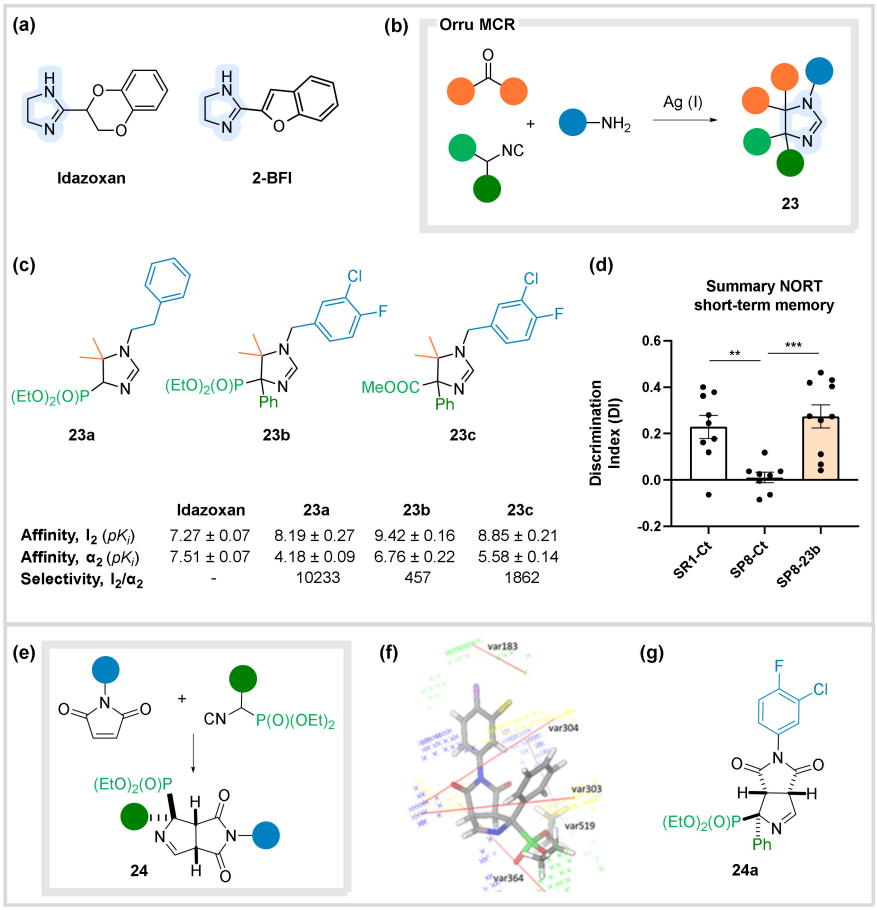

Figure 9. I_2 Imidazoline receptors. (**a**) Structure of known I_2IR ligands. (**b**) MCR access to substituted 2-imidazolines **23**. (**c**) Structure and binding affinities of the selected compounds. (**d**) In vivo data of compound **23b**. (**e**) Condensation between maleimides and PhosMIC derivatives leading to new I_2-IR ligands **24**. (**f**) 3D-QSAR series **24**. (**g**) Structure of the selected analogue **24a**. Values represented in (**d**) are mean ± Standard error of the mean (SEM); n = 36 (SR1-Ct n = 11; SP8-Ct n = 11; SP8-23b n = 14). ** $p < 0.01$; *** $p < 0.001$.

In parallel, we described a related process (not a MCR this time) that involved the interaction of a PhosMic component with a maleimide, to yield a formal [3 + 2] cycloadduct, displaying an alternative substitution pattern [66]. In this way, another chemset of 36 bicyclic adducts **24** was conveniently prepared (Figure 9e). These bicyclic adducts showed outstanding affinity and selectivity values upon I_2-IR and constituted the first example of I_2-IR ligands without a 2-imidazoline unit. Interestingly, 3D-QSAR studies with these series helped to rationalize the results and, circumventing the limited structural information of the receptor, guided the design of the future improved ligands (Figure 9f). In this way, the mapping of the receptor suggested the type and polarity of further substitutions in the scaffold. Preliminary ADME and a safety panel led us to select a representative compound **24a** (Figure 9g) for in vivo studies [67], which demonstrated hypothermic properties and neuroprotection in a murine model of neurodegeneration [68]. Additionally, the treatment of SAMP8 murine model with **24a** revealed a beneficial effect by improving cognition and ameliorating anxiety-like behavior. Modulation of I_2-IR with compound **24** reduces neuroinflammation, oxidative stress and calcineurin protein levels in SAMP8 [69].

The suitable access to undescribed 2-(imidazoline-4-yl)phosphonate and related scaffolds, enabled by judicious use of MCRs, has increased the chemical diversity of the I_2-IR modulating ligands and importantly unveiled their implication in neurodegenerative diseases. Further progress in the area will be supported by the robust chemistry developed ensuring the convenient preparation of the required ligands.

7. Conclusions and Outlook

The incorporation of MCRs to the synthetic arsenal in biomedical projects greatly empowers the targeted preparation of defined structures and combinatorial libraries, as well as enabling the exploration of the dark chemical space. It constitutes an attractive strategy, already delivering useful scaffolds and hits impossible to prepare otherwise. The development of new transformations belonging to this family of reactions is an ongoing task in several research groups and it will surely help in the colonization of these uncharted regions. The presented results dealing with directed synthesis based on rational design, combinatorial approaches and diversity-oriented (exploratory) preparations spanning a variety of targets including enzymes (AChE, DHFR), transcription factors (AhR), receptors (I2-IR), chemotherapeutical hits (viruses, bacteria) and fluorescent probes (for histamine, lysosomes, etc.), validate the hypothesis. In summary, we have developed rationally designed enzyme inhibitors, prepared through previously described MCRs, with unprecedented potency and selectivity. Moreover, in a sort of late-stage functionalization, we have deeply modified a useful antibiotic and improved its properties. The use of well-established MCRs also paved the way to access new classes of receptor ligands which were much improved through medicinal chemistry principles. We have synthesized a useful and diversifiable fluorophore precursor (BODIPY isocyanide) and generated useful bioprobes via standard MCRS. Finally, through reaction discovery, we have disclosed new chemotherapeutic compounds, labeling agents and transcription factor ligands. Future work along fundamental reactivity exploration and meaningful use of MCRs, mainly based in heterocycles, will likely increase the impact of the methodology and expand its reach in medicinal chemistry, encompassing all phases of the drug discovery and drug development.

Author Contributions: P.N.R., O.G., A.B., C.E. and R.L. contributed to the conception, writing, and editing of the review. All authors have read and agreed to the published version of the manuscript.

Funding: This research was funded by the Ministerio de Ciencia e Innovación (Spain), grant number PID2019-107991RB-I00.

Institutional Review Board Statement: Not applicable.

Informed Consent Statement: Not applicable.

Data Availability Statement: Data sharing not applicable.

Acknowledgments: We warmly thank all past members of our research group for their dedication to the conception and development of the MCR project. Additionally, we acknowledge the collaborations we hold to back our research. Useful suggestions and support form F. J. Luque (UB), X. Barril (UB) and L. Campos-Vicens (UB) are acknowledged. P. N. R. and A. B. thank Ministerio de Ciencia e Innovación for predoctoral grants. Figures 1 and 3a were created with BioRender.com (accessed on 30 May 2022).

Conflicts of Interest: The authors declare no conflict of interest. The funders had no role in the design of the study; in the collection, analyses, or interpretation of data; in the writing of the manuscript, or in the decision to publish the results.

Abbreviations

AChE	Acetylcholinesterase
AD	Alzheimer disease
DDQ	2,3-Dichloro-5,6-dicyano-1,4-benzoquinone
BACE	Beta secretase
GBBR	Groebke-Blackburn-Bienaymé MCR
TMP	Trimethoprim
WHO	World Health Organization
MIC	Minimum inhibition concentration
PDB	Protein data bank
DHFR	Dihydrofolate reductase

SMX	Sulfamethoxazole
PaβN	Phenylalanine-arginine β-naphthylamide
NADPH	Reduced nicotinamide adenine dinucleotide phosphate
AhR	Hydrocarbon Receptor
FICZ	6-Formylindolo [3,2-b]carbazole
SAR	Structure-Activity Relationship
Trp	Tryptophan
TMSCl	Trimethylsilyl chloride
PBS	Phosphate buffer saline
AR	α_2-Adrenoreceptors
PhosMic	Diethyl isocyanomethylphosphonate

References

1. Gioiello, A.; Piccinno, A.; Lozza, A.M.; Cerra, B. The Medicinal Chemistry in the Era of Machines and Automation: Recent Advances in Continuous Flow Technology. *J. Med. Chem.* **2020**, *63*, 6624–6647. [CrossRef]
2. Blakemore, D.C.; Castro, L.; Churcher, I.; Rees, D.C.; Thomas, A.W.; Wilson, D.M.; Wood, A. Organic Synthesis Provides Opportunities to Transform Drug Discovery. *Nat. Chem.* **2018**, *10*, 383–394. [CrossRef]
3. Cernak, T.; Dykstra, K.D.; Tyagarajan, S.; Vachal, P.; Krska, S.W. The Medicinal Chemist's Toolbox for Late Stage Functionalization of Drug-like Molecules. *Chem. Soc. Rev.* **2016**, *45*, 546–576. [CrossRef] [PubMed]
4. Kolb, H.C.; Finn, M.G.; Sharpless, K.B. Click Chemistry: Diverse Chemical Function from a Few Good Reactions. *Angew. Chem. Int. Ed.* **2001**, *40*, 2004–2021. [CrossRef]
5. Burke, M.D.; Schreiber, S.L.; Burke, M.D. A Planning Strategy for Diversity-Oriented Synthesis. *Angew. Chem. Int. Ed.* **2004**, *43*, 46–58. [CrossRef] [PubMed]
6. Newhouse, T.; Baran, P.S.; Hoffmann, R.W. The Economies of Synthesis. *Chem. Soc. Rev.* **2009**, *38*, 3010–3021. [CrossRef]
7. Hayashi, Y. Time Economy in Total Synthesis. *J. Org. Chem.* **2021**, *86*, 1–23. [CrossRef]
8. Lipinski, C.; Hopkins, A. Navigating Chemical Space for Biology and Medicine. *Nature* **2004**, *432*, 855–861. [CrossRef]
9. Dobson, C.M. Chemical Space and Biology. *Nature* **2004**, *432*, 824–828. [CrossRef]
10. Doak, B.C.; Over, B.; Giordanetto, F.; Kihlberg, J. Oral Druggable Space beyond the Rule of 5: Insights from Drugs and Clinical Candidates. *Chem. Biol.* **2014**, *21*, 1115–1142. [CrossRef]
11. Grygorenko, O.O.; Radchenko, D.S.; Dziuba, I.; Chuprina, A.; Gubina, K.E.; Moroz, Y.S. Generating Multibillion Chemical Space of Readily Accessible Screening Compounds. *iScience* **2020**, *23*, 101681. [CrossRef] [PubMed]
12. Brown, D.G.; Boström, J. Analysis of Past and Present Synthetic Methodologies on Medicinal Chemistry: Where Have All the New Reactions Gone? *J. Med. Chem.* **2016**, *59*, 4443–4458. [CrossRef] [PubMed]
13. Zhao, H.; Akritopoulou-Zanze, I. When Analoging Is Not Enough: Scaffold Discovery in Medicinal Chemistry. *Expert Opin. Drug Discov.* **2010**, *5*, 123–134. [CrossRef] [PubMed]
14. Zhu, J.; Bienaymé, H. *Multicomponent Reactions*; Zhu, J., Bienaymé, H., Eds.; Wiley-VCH: Weinheim, Germany, 2005.
15. Zhu, J.; Wang, Q.; Wang, M.-X. *Multicomponent Reactions in Organic Synthesis*; Zhu, J., Wang, Q., Wang, M.-X., Eds.; Wiley-VCH: Weinheim, Germany, 2015.
16. Hulme, C. Applications of Multicomponent Reactions in Drug Discovery—Lead Generation to Process Development. In *Multicomponent Reactions*; Zhu, J., Bienayme, H., Eds.; Wiley-VCH: Weinheim, Germany, 2005; pp. 311–341.
17. Wang, Z.; Domling, A. Multicomponent Reactions in Medicinal Chemistry. In *Multicomponent Reactions towards Heterocycles*; van der Eycken, E., Sharma, U.K., Eds.; Wiley-VCH: Weinhiem, Germany, 2022; pp. 91–137.
18. Slobbe, P.; Ruijter, E.; Orru, R.V.A. Recent Applications of Multicomponent Reactions in Medicinal Chemistry. *Medchemcomm* **2012**, *3*, 1189–1218. [CrossRef]
19. Isambert, N.; Lavilla, R. Heterocycles as Key Substrates in Multicomponent Reactions: The Fast Lane towards Molecular Complexity. *Chem. Eur. J.* **2008**, *14*, 8444–8454. [CrossRef] [PubMed]
20. Vicente-García, E.; Kielland, N.; Lavilla, R. Functionalization of Heterocycles by MCRs. In *Multicomponent Reactions in Organic Synthesis*; Zhu, J., Wang, Q., Wang, M., Eds.; Wiley-VCH: Weinheim, Germany, 2015; pp. 159–182.
21. Ghashghaei, O.; Pedrola, M.; Escolano, C.; Lavilla, R. Heterocycles as Inputs in MCRs: An Update. In *Multicomponent Reactions towards Heterocycles*; van der Eycken, E., Sharma, U.K., Eds.; Wiley-VCH: Weinheim, Germany, 2022; pp. 1–43.
22. Ghashghaei, O.; Nadal Rodríguez, P.; Lavilla, R. Development of Heterocyclic Multicomponent Reactions through Guided Exploration: Direct, Reasonable and Unpredictable Processes. *Synlett* **2022**, *33*, 822–835. [CrossRef]
23. Inestrosa, N.C.; Alvarez, A.; Pérez, C.A.; Moreno, R.D.; Vicente, M.; Linker, C.; Casanueva, O.I.; Soto, C.; Garrido, J. Acetylcholinesterase Accelerates Assembly of Amyloid-Peptides into Alzheimer's Fibrils: Possible Role of the Peripheral Site of the Enzyme. *Neuron* **1996**, *16*, 881–891. [CrossRef]
24. Munoz-Torrero, D.; Camps, P. Dimeric and Hybrid Anti-Alzheimer Drug Candidates. *Curr. Med. Chem.* **2006**, *13*, 399–422. [CrossRef]
25. Cavalli, A.; Bolognesi, M.L.; Capsoni, S.; Andrisano, V.; Bartolini, M.; Margotti, E.; Cattaneo, A.; Recanatini, M.; Melchiorre, C. A Small Molecule Targeting the Multifactorial Nature of Alzheimer's Disease. *Angew. Chem. Int. Ed.* **2007**, *46*, 3689–3692. [CrossRef]

26. Kouznetsov, V. Recent Synthetic Developments in a Powerful Imino Diels-Alder Reaction (Povarov Reaction): Application to the Synthesis of N-Polyheterocycles and Related Alkaloids. *Tetrahedron* **2009**, *65*, 2721–2750. [CrossRef]
27. Ghashghaei, O.; Masdeu, C.; Alonso, C.; Palacios, F.; Lavilla, R. Recent Advances of the Povarov Reaction in Medicinal Chemistry. *Drug Discov. Today Technol.* **2018**, *29*, 71–79. [CrossRef] [PubMed]
28. Camps, P.; Formosa, X.; Galdeano, C.; Muñoz-Torrero, D.; Ramírez, L.; Gómez, E.; Isambert, N.; Lavilla, R.; Badia, A.; Clos, M.V.; et al. Pyrano[3,2-c]Quinoline-6-Chlorotacrine Hybrids as a Novel Family of Acetylcholinesterase-and β-Amyloid-Directed Anti-Alzheimer Compounds. *J. Med. Chem.* **2009**, *52*, 5365–5379. [CrossRef]
29. Di Pietro, O.; Viayna, E.; Vicente-García, E.; Bartolini, M.; Ramón, R.; Juárez-Jiménez, J.; Clos, M.V.; Pérez, B.; Andrisano, V.; Luque, F.J.; et al. 1,2,3,4-Tetrahydrobenzo[h][1,6]Naphthyridines as a New Family of Potent Peripheral-to-Midgorge-Site Inhibitors of Acetylcholinesterase: Synthesis, Pharmacological Evaluation and Mechanistic Studies. *Eur. J. Med. Chem.* **2014**, *73*, 141–152. [CrossRef] [PubMed]
30. Di Pietro, O.; Pérez-Areales, F.J.; Juárez-Jiménez, J.; Espargaró, A.; Clos, M.V.; Pérez, B.; Lavilla, R.; Sabaté, R.; Luque, F.J.; Muñoz-Torrero, D. Tetrahydrobenzo[h][1,6]Naphthyridine-6-Chlorotacrine Hybrids as a New Family of Anti-Alzheimer Agents Targeting β-Amyloid, Tau, and Cholinesterase Pathologies. *Eur. J. Med. Chem.* **2014**, *84*, 107–117. [CrossRef]
31. Di Pietro, O.; Vicente-Garcia, E.; Taylor, M.; Berenguer, D.; Viayna, E.; Lanzoni, A.; Sola, I.; Sayago, H.; Riera, C.; Fisa, R.; et al. Multicomponent Reaction-Based Synthesis and Biological Evaluation of Tricyclic Heterofused Quinolines with Multi-Trypanosomatid Activity. *Eur. J. Med. Chem.* **2015**, *105*, 120–137. [CrossRef] [PubMed]
32. Ghashghaei, O.; Caputo, S.; Sintes, M.; Revés, M.; Kielland, N.; Estarellas, C.; Luque, F.J.; Aviñó, A.; Eritja, R.; Serna-Gallego, A.; et al. Multiple Multicomponent Reactions: Unexplored Substrates, Selective Processes, and Versatile Chemotypes in Biomedicine. *Chem. Eur. J.* **2018**, *24*, 14513–14521. [CrossRef]
33. Boltjes, A.; Dömling, A. The Groebke-Blackburn-Bienaymé Reaction. *Eur. J. Org. Chem.* **2019**, *2019*, 7007–7049. [CrossRef]
34. Pedrola, M.; Jorba, M.; Jardas, E.; Jardi, F.; Ghashghaei, O.; Viñas, M.; Lavilla, R. Multicomponent Reactions Upon the Known Drug Trimethoprim as a Source of Novel Antimicrobial Agents. *Front. Chem.* **2019**, *7*. [CrossRef]
35. Jorba, M.; Pedrola, M.; Ghashghaei, O.; Herráez, R.; Campos-Vicens, L.; Luque, F.J.; Lavilla, R.; Viñas, M. New Trimethoprim-Like Molecules: Bacteriological Evaluation and Insights into Their Action. *Antibiotics* **2021**, *10*, 709. [CrossRef]
36. Ghashghaei, O.; Pedrola, M.; Seghetti, F.; Martin, V.V.; Zavarce, R.; Babiak, M.; Novacek, J.; Hartung, F.; Rolfes, K.M.; Haarmann-Stemmann, T.; et al. Extended Multicomponent Reactions with Indole Aldehydes: Access to Unprecedented Polyheterocyclic Scaffolds, Ligands of the Aryl Hydrocarbon Receptor. *Angew. Chem. Int. Ed.* **2021**, *60*, 2603–2608. [CrossRef]
37. Muñoz-Torrero, D.; Lavilla, R.; Pérez-Areales, F.J.; Ghashghaei, O. Multicomponent Reactions: A Mighty Journey Partner for Infectious Tropical Disease Drug Discovery. In *Medicinal Chemistry Approaches to Malaria and Other Tropical Diseases*; Chibale, K., Ed.; Academic Press: Cambridge, MA, USA, 2019; pp. 181–217. ISBN 9780128205518.
38. Faral-Tello, P.; Liang, M.; Mahler, G.; Wipf, P.; Robello, C. Imidazolium Compounds Are Active against All Stages of Trypanosoma Cruzi. *Int. J. Antimicrob. Agents* **2014**, *43*, 262–268. [CrossRef] [PubMed]
39. Ghashghaei, O.; Revés, M.; Kielland, N.; Lavilla, R. Modular Access to Tetrasubstituted Imidazolium Salts through Acid-Catalyzed Addition of Isocyanides to Propargylamines. *Eur. J. Org. Chem.* **2015**, *15*, 4383–4388. [CrossRef]
40. Ghashghaei, O.; Kielland, N.; Revés, M.; Taylor, M.C.; Kelly, J.M.; Di Pietro, O.; Muñoz-Torrero, D.; Pérez, B.; Lavilla, R. Tetrasubstituted Imidazolium Salts as Potent Antiparasitic Agents against African and American Trypanosomiases. *Molecules* **2018**, *23*, 177. [CrossRef] [PubMed]
41. Kishore, K.G.; Ghashghaei, O.; Estarellas, C.; Mestre, M.M.; Monturiol, C.; Kielland, N.; Kelly, J.M.; Francisco, A.F.; Jayawardhana, S.; Muñoz-Torrero, D.; et al. Insertion of Isocyanides into N–Si Bonds: Multicomponent Reactions with Azines Leading to Potent Antiparasitic Compounds. *Angew. Chem. Int. Ed.* **2016**, *55*, 8994–8998. [CrossRef] [PubMed]
42. Zhang, J.; Campbell, R.E.; Ting, A.Y.; Tsien, R.Y. Creating New Fluorescent Probes for Cell Biology. *Nat. Rev. Mol. Cell Biol.* **2002**, *3*, 906–918. [CrossRef]
43. Kikuchi, K. Design, Synthesis and Biological Application of Chemical Probes for Bio-Imaging. *Chem. Soc. Rev.* **2010**, *39*, 2048–2053. [CrossRef]
44. Fu, Y.; Finney, N.S. Small-Molecule Fluorescent Probes and Their Design. *RSC Adv.* **2018**, *8*, 29051–29061. [CrossRef]
45. Kaur, P.; Singh, K. Recent Advances in the Application of BODIPY in Bioimaging and Chemosensing. *J. Mater. Chem. C.* **2019**, *7*, 11361–11405. [CrossRef]
46. Loudet, A.; Burgess, K. BODIPY Dyes and Their Derivatives: Syntheses and Spectroscopic Properties. *Chem. Rev.* **2007**, *107*, 4891–4932. [CrossRef]
47. Vázquez-Romero, A.; Kielland, N.; Arévalo, M.J.; Preciado, S.; Mellanby, R.J.; Feng, Y.; Lavilla, R.; Vendrell, M. Multicomponent Reactions for de Novo Synthesis of Bodipy Probes: In Vivo Imaging of Phagocytic Macrophages. *J. Am. Chem. Soc.* **2013**, *135*, 16018–16021. [CrossRef]
48. Kielland, N.; Vendrell, M.; Lavilla, R.; Chang, Y.T. Imaging Histamine in Live Basophils and Macrophages with a Fluorescent Mesoionic Acid Fluoride. *ChemComm* **2012**, *48*, 7401–7403. [CrossRef] [PubMed]
49. De Moliner, F.; Kielland, N.; Lavilla, R.; Vendrell, M. Modern Synthetic Avenues for the Preparation of Functional Fluorophores. *Angew. Chem. Int. Ed.* **2017**, *56*, 3758–3769. [CrossRef] [PubMed]
50. Sintes, M.; de Moliner, F.; Caballero-Lima, D.; Denning, D.W.; Read, N.D.; Kielland, N.; Vendrell, M.; Lavilla, R. Electrophilic, Activation-Free Fluorogenic Reagent for Labeling Bioactive Amines. *Bioconjug. Chem.* **2016**, *27*, 1430–1434. [CrossRef] [PubMed]

51. Ruggiero, D.A.; Regunathan, S.; Wang, H.; Milner, T.A.; Reis, D.J. Immunocytochemical Localization of an Imidazoline Receptor Protein in the Central Nervous System. *Brain Res.* **1998**, *780*, 270–293. [CrossRef]
52. Li, J.X. Imidazoline I2 Receptors: An Update. *Pharmacol. Ther.* **2017**, *178*, 48–56. [CrossRef]
53. Bousquet, P.; Hudson, A.; García-Sevilla, J.A.; Li, J.X. Imidazoline Receptor System: The Past, the Present, and the Future. *Pharmacol. Rev.* **2020**, *72*, 50–79. [CrossRef]
54. Rovati, L.C.; Brambilla, N.; Blicharski, T.; Connell, J.; Vitalini, C.; Bonazzi, A.; Giacovelli, G.; Girolami, F.; D'Amato, M. Efficacy and Safety of the First-in-Class Imidazoline-2 Receptor Ligand CR4056 in Pain from Knee Osteoarthritis and Disease Phenotypes: A Randomized, Double-Blind, Placebo-Controlled Phase 2 Trial. *Osteoarthr. Cartil.* **2020**, *28*, 22–30. [CrossRef]
55. Smith, K.L.; Jessop, D.S.; Finn, D.P. Modulation of Stress by Imidazoline Binding Sites: Implications for Psychiatric Disorders. *Stress* **2009**, *12*, 97–114. [CrossRef]
56. Callado, L.F.; Martín-Gómez, J.I.; Ruiz, J.; Garibi, J.M.; Meana, J.J. Imidazoline I2 Receptor Density Increases with the Malignancy of Human Gliomas. *J. Neurol. Neurosurg. Psychiatry* **2004**, *75*, 785–787. [CrossRef]
57. Dardonville, C.; Rozas, I. Imidazoline Binding Sites and Their Ligands: An Overview of the Different Chemical Structures. *Med. Res. Rev.* **2004**, *24*, 639–661. [CrossRef]
58. Rodriguez-Arévalo, S.; Bagán, A.; Griñán-Ferré, C.; Vasilopoulou, F.; Pallàs, M.; Brocos-Mosquera, I.; Callado, L.F.; Loza, M.I.; Martínez, A.L.; Brea, J.; et al. Benzofuranyl-2-Imidazoles as Imidazoline I2 Receptor Ligands for Alzheimer's Disease. *Eur. J. Med. Chem.* **2021**, *222*, 113540. [CrossRef] [PubMed]
59. Vasilopoulou, F.; Rodríguez-Arévalo, S.; Bagán, A.; Escolano, C.; Griñán-Ferré, C.; Pallàs, M. Disease-Modifying Treatment with I2 Imidazoline Receptor Ligand LSL60101 in an Alzheimer's Disease Mouse Model: A Comparative Study with Donepezil. *Br. J. Pharmacol.* **2021**, *178*, 3017–3033. [CrossRef] [PubMed]
60. Elders, N.; Schmitz, R.F.; de Kanter, F.J.J.; Ruijter, E.; Groen, M.B.; Orru, R.V.A. A Resource-Efficient and Highly Flexible Procedure for a Three-Component Synthesis of 2-Imidazolines. *J. Org. Chem.* **2007**, *72*, 6135–6142. [CrossRef] [PubMed]
61. Elders, N.; Ruijter, E.; de Kanter, F.J.J.; Groen, M.B.; Orru, R.V.A. Selective Formation of 2-Imidazolines and 2-Substituted Oxazoles by Using a Three-Component Reaction. *Chem. Eur. J.* **2008**, *14*, 4961–4973. [CrossRef]
62. Abás, S.; Estarellas, C.; Luque, F.J.; Escolano, C. Easy Access to (2-Imidazolin-4-Yl)Phosphonates by a Microwave Assisted Multicomponent Reaction. *Tetrahedron* **2015**, *71*, 2872–2881. [CrossRef]
63. Abás, S.; Erdozain, A.M.; Keller, B.; Rodríguez-Arévalo, S.; Callado, L.F.; García-Sevilla, J.A.; Escolano, C. Neuroprotective Effects of a Structurally New Family of High Affinity Imidazoline I2 Receptor Ligands. *ACS Chem. Neurosci.* **2017**, *8*, 737–742. [CrossRef]
64. Griñán-Ferré, C.; Vasilopoulou, F.; Abás, S.; Rodríguez-Arévalo, S.; Bagán, A.; Sureda, F.X.; Pérez, B.; Callado, L.F.; García-Sevilla, J.A.; García-Fuster, M.J.; et al. Behavioral and Cognitive Improvement Induced by Novel Imidazoline I2 Receptor Ligands in Female SAMP8 Mice. *Neurotherapeutics* **2019**, *16*, 416–431. [CrossRef]
65. Vasilopoulou, F.; Bagan, A.; Rodriguez-Arevalo, S.; Escolano, C.; Griñán-Ferré, C.; Pallàs, M. Amelioration of BPSD-Like Phenotype and Cognitive Decline in SAMP8 Mice Model Accompanied by Molecular Changes after Treatment with I2-Imidazoline Receptor Ligand MCR5. *Pharmaceutics* **2020**, *12*, 475. [CrossRef]
66. Arróniz, C.; Molina, J.; Abás, S.; Molins, E.; Campanera, J.M.; Luque, F.J.; Escolano, C. First Diastereoselective [3 + 2] Cycloaddition Reaction of Diethyl Isocyanomethylphosphonate and Maleimides. *Org. Biomol. Chem.* **2013**, *11*, 1640–1649. [CrossRef]
67. Abás, S.; Rodríguez-Arévalo, S.; Bagán, A.; Griñán-Ferré, C.; Vasilopoulou, F.; Brocos-Mosquera, I.; Muguruza, C.; Pérez, B.; Molins, E.; Luque, F.J.; et al. Bicyclic α-Iminophosphonates as High Affinity Imidazoline I2 Receptor Ligands for Alzheimer's Disease. *J. Med. Chem.* **2020**, *63*, 3610–3633. [CrossRef]
68. Escolano, C.; Pallás, M.; Griñán-Ferreé, C.; Abás, S.; Callado, L.F.; García-Sevilla, J.A. Synthetic I2 Imidazoline Receptor Ligands for Prevention or Treatment of Human Brain Disorders. Patent No. WO2019121853, 27 June 2019.
69. Vasilopoulou, F.; Griñán-Ferré, C.; Rodríguez-Arévalo, S.; Bagán, A.; Abás, S.; Escolano, C.; Pallàs, M. I2 Imidazoline Receptor Modulation Protects Aged SAMP8 Mice against Cognitive Decline by Suppressing the Calcineurin Pathway. *GeroScience* **2020**, *43*, 965–983. [CrossRef] [PubMed]

Check for updates

REVIEWS doi.org/10.1002/adsc.202301205 Advanced Synthesis & Catalysis

Very Important Publication

Reaction Space Charting as a Tool in Organic Chemistry Research and Development

Eloy Lozano Baró,[+a] Pau Nadal Rodríguez,[+a] Jordi Juárez-Jiménez,[b] Ouldouz Ghashghaei,[a,*] and Rodolfo Lavilla[a,*]

[a] Laboratory of Medicinal Chemistry, Faculty of Pharmacy and Food Sciences. University of Barcelona and Institute of Biomedicine UB (IBUB). Av. Joan XXIII, 27–31, 08028 Barcelona, Spain
E-mail: ghashghaei@ub.edu; rlavilla@ub.edu

[b] Department of Pharmacy and Pharmaceutical Technology and Physical Chemistry, Faculty of Pharmacy and Food Sciences, and Institute of Theoretical and Computational Chemistry (IQTCUB), University of Barcelona, Av. Joan XXIII, 27-31, 08028 Barcelona, Spain

[+] These authors contributed equally to this work.

Manuscript received: October 20, 2023; Revised manuscript received: January 16, 2024;
Version of record online: January 31, 2024

Dedicated with admiration and affection to Prof. Miquel A. Pericàs.

© 2024 The Authors. Advanced Synthesis & Catalysis published by Wiley-VCH GmbH. This is an open access article under the terms of the Creative Commons Attribution Non-Commercial NoDerivs License, which permits use and distribution in any medium, provided the original work is properly cited, the use is non-commercial and no modifications or adaptations are made.

Abstract: The chemical and reaction spaces are incredibly vast and special procedures are required to study them. Their complex and multiparametric nature encompass myriads of compounds and interactions and endless modifications involving the distinct impact of relevant variables (temperature, solvent, stoichiometry, etc.). This often calls for the design, collection, and analysis/interpretation of large datasets. Reaction charting, the systematic scanning, description, analysis, and guided modifications of a given process, stands as the most promising approach. It offers fast and accurate solutions as well as expanding the knowledge about the systems. This deeper understanding enables reliable predictions, improvement of the productivity (yields, scope), eventually leading to sustainable, economic, and safe applications. The present review introduces the topic, analyzing selected examples and recent advancements in different organic chemistry-related fields. The covered methodologies range from classical experimentation modifying one factor at a time, to Design of Experiments and more modern computational approaches involving Machine Learning and Artificial Intelligence. In this way, the impact of charting in process development, biological and medicinal chemistry, catalysis, reaction discovery and computational methods is accounted. Finally, the conclusion/outlook section gives a general appraisal and a prospect on the future implementation of the methodology.

Keywords: Computational chemistry; Medicinal chemistry; Molecular diversity; Reaction discovery; Synthesis design

1. Introduction

A chart can be defined as a map for the use of navigators. And is in this sense that the reaction space can be explored and described to fully understand the processes involved, with the aim of exploiting all possibilities, extending its reach, or developing new applications. Thus, charting is the act of actively exploring the reaction space of a system, with the intent of gaining enough knowledge to rationalize how

© 2024 The Authors. Advanced Synthesis & Catalysis published by Wiley-VCH GmbH

Eloy Lozano Baró received his degree in Pharmacy from Universitat de Barcelona (UB) in 2022. Then he joined the Laboratory of Organic Chemistry at UB as a research trainee, where he is pursuing his PhD under the supervision of Prof. R. Lavilla and Dr. O. Ghashghaei.

Pau Nadal Rodríguez received his degree in Pharmacy from Universitat de Barcelona (UB) in 2019. Then he joined the MedChem department of Glaxo Smith Kline in Stevenage (UK) through an Industrial Placement. He is now pursuing his PhD under the supervision of Prof. R. Lavilla and Dr. O. Ghashghaei at UB.

Jordi Juárez-Jiménez obtained his BA (2008), Master (2010) and PhD (2014) degrees from Universitat de Barcelona (Faculty of Pharmacy). After postdoctoral stages at the University of Florida and the University of Edinburgh, in 2020 he returned to the Faculty of Pharmacy of the University of Barcelona as a Lecturer in Physical Chemistry. He has co-authored 20 scientific publications and his research interests are centered around the molecular modelling of biomolecular and chemical processes.

Ouldouz Ghashghaei received her BSc. in Chemistry from Sharif University of Technology (Iran), followed by her MSc. (2013) and PhD (2017) in Organic Chemistry from Universitat de Barcelona, both under supervision of Prof. R. Lavilla. Currently, she is an adjunct professor of Organic Chemistry at UB. She has co-authored 20 scientific publications and is focused on novel synthetic approaches to access biologically relevant heterocyclic systems.

Rodolfo Lavilla received his BA (1982), Master (1983) and PhD (1987) degrees from Universitat de Barcelona (Faculty of Pharmacy). After a postdoctoral stage at the UC-San Diego with Prof. E. Wenkert, he joined the faculty of Pharmacy at UB, where he is now Full Professor of Organic & Medicinal Chemistry. He has co-authored over 130 research articles, reviews, and patents. His research interests include heterocyclic reactivity, multicomponent reactions, and applications to biomed projects.

changes in the system may affect the outcome, rather than having to perform individual experiments to elucidate every possible result. This is especially appealing in the context of the current societal challenges we are facing, which are tackled through chemistry: the need to cleanly generate a variety of substances, the fast synthesis of complex bioactive compounds (especially for drug discovery), the expansion of the catalytic and preparative arsenals, the biosafety and environmental issues, etc.[1,2]

To present a clear task, we first discuss some features of the chemical and reactivity spaces (see Table 1 for some useful definitions).

The chemical space, the annotated collection of feasible molecules, is strikingly broad. To have manageable sets, some restrictions (molecular weight, stability, feasibility, properties, etc.) are often applied to efficiently guide the study of specific problems.[3–7] Next, the interactions of these molecules, especially those dealing with their preparation and activity, should be looked at. We can define the reaction space of a given chemical transformation as the network of all feasible interactions connecting the involved species and ensued intermediates.[8,9] The accurate description of the reaction space will improve our global knowledge of the system, providing a deep understanding of the interactions, explaining the scope, catalysis by different species, the role of the solvent, temperature, stoichiometry, etc. This would allow to expand the reach of the transformation, enabling reliable predictions and eventually, tuning the conditions for suitable applications (sustainability, produc-

© 2024 The Authors. Advanced Synthesis & Catalysis published by Wiley-VCH GmbH

16154169, 2024, 4, Downloaded from https://onlinelibrary.wiley.com/doi/10.1002/adsc.202301205 by Readcube (Labtiva Inc.), Wiley Online Library on [02/07/2024]. See the Terms and Conditions (https://onlinelibrary.wiley.com/terms-and-conditions) on Wiley Online Library for rules of use; OA articles are governed by the applicable Creative Commons License

Table 1. Glossary terms.

Term	Definition
Chemical Space	Virtual collection of all feasible molecules resulting from standard bond connections. Usually restricted to limitations (Molecular Weight in most cases, properties, etc.).
Reaction Space	Virtual collection of all meaningful interactions among a collection of chemical species belonging to a determined system.
Design of Experiments (DOE)	A statistical approach to reaction optimization that allows the variation of multiple factors simultaneously to screen the reaction space around a particular process. DOE enables the evaluation of a large number of parameters in a relatively small number of experiments.
Artificial Intelligence (AI)	A branch of computer science to develop machines that simulate human intelligence. AI can process large amounts of data, unsuitable for humans, and recognize patterns, make decisions, plan future experimentation, etc.
Machine Learning (ML)	A discipline of AI which enables the autonomous learning of computers, without specific programming.
Training Data Set	Set of examples used to fit the parameters for a given model to be used in a supervised learning method.

tivity, safety, etc.). Due to the vastness of the chemical and reaction spaces involved, special methods are needed, often one step forward from traditional methods based on intuition, fragmentary experimentation, rational speculation, or serendipity (Figure 1). The methodologies used for the study and description of the reaction space range from the straightforward modification of one factor at a time (often guided by chemical intuition), the Design of Experiments (DOE) tackling several variables simultaneously, to the more modern computational approaches where Artificial Intelligence (AI) and Machine Learning (ML) protocols efficiently cope with large data amounts. Although the two latter are being actively developed nowadays, relevant results are mentioned, but the review is not centered on these approaches.

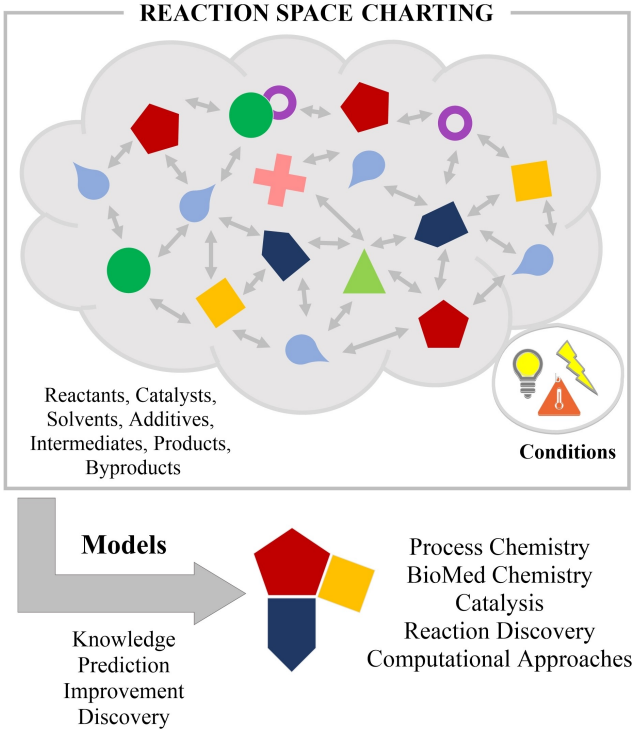

Figure 1. The concept of reaction space charting.

Charting the reaction space is in line with systems chemistry, where the precise analysis of a given model may furnish significant data to gain meaningful insights and likely address new expansions in different directions.[10,11] In this respect, the irruption of AI and ML protocols anticipate the tempting view of the reaction prediction. However, the quality and reliability of AI models will entirely depend on our ability to generate appropriately sized and annotated data, which entails massive experimentation and curation efforts. In this regard, the need to build more equilibrated datasets, including negative results that are not easily extracted from the existing literature, should be stressed.[12–14] Filling current gaps in dataset availability and development of new models are two linked developments, that are essential to make AI descriptions better suited to the real system needs.[15] Charting the reaction space is especially useful in multifactorial processes, where prediction out of basic principles is not straightforward or even more, cannot be unraveled from sophisticated computational modelling or massive standard experimentation. For an appraisal of the field focusing on the reaction optimization methods, see the excellent revision by Taylor, Lapkin, and coworkers.[16]

Charting the chemical reactivity space is having a deep impact in modern organic synthesis. In this appraisal, rather than bringing an exhaustive description, we summarize representative cases where this burgeoning approach is applied. First, we comment the impact of the concept in different fields/contexts (process chemistry, medicinal and biological chemistry, catalysis, reaction discovery and development, computational approaches), although in some cases they are closely intertwined; to end with a conclusion section.

© 2024 The Authors. Advanced Synthesis & Catalysis published by Wiley-VCH GmbH

16154169, 2024, 4, Downloaded from https://onlinelibrary.wiley.com/doi/10.1002/adsc.202301205 by Readcube (Labtiva Inc.), Wiley Online Library on [02/07/2024]. See the Terms and Conditions (https://onlinelibrary.wiley.com/terms-and-conditions) on Wiley Online Library for rules of use; OA articles are governed by the applicable Creative Commons License

2. Process Chemistry

The process chemistry for the production of chemicals and especially drugs, pioneered the implementation of the charting approaches. In this challenging context, where safety is carefully adjusted at all levels (contents of the Active Pharmaceutical Ingredient, impurities, crystallographic forms, etc.), the procedures are tightly regulated. For preparative purposes, many items (robustness, sustainability, economies, safety, complexity, etc.) are carefully analyzed and parametrized. Then, scores for determined parameters are calculated with specific programs to stablish the global suitability of the process.[17] In this context, changes in the concentrations, reaction times, additives, reactor shapes, temperatures etc. can introduce relevant modifications. This often leads to rejection of the produced batch, the failure to authorize the modified process or problems to transfer it to a different site. Formerly, the mapping was performed by describing the reaction space, modifying one factor at a time to determine the suitable values of all parameters for a given transformation in a specific experimental set. The data acquisition was done at a relatively slow pace. DOE greatly improved the situation, allowing to establish suitable conditions through a reduced number of experiments, where several factors are modified in each determination. This methodology is relevantly present in modern process chemistry, as well as in other endeavors.[18] FDA expects DOE approaches to be included in new drug submissions. Moreover, to guarantee compliance with the Green Chemistry Principles, optimized protocols using safe reagents/solvents and in smaller quantities are required. In this context, Murray, Sheppard, and team disclosed the selection of the appropriate solvent for a given transformation, a capital issue in drug development.[19]

Although the improvement through the use of DOE alone is clear, there are still serious concerns in the modification of organic transformations at large scales, while permanently keeping the required standards.[20] To address this issue, instead of progressively adding more data to cover all productive environments, a new way was devised: the concept of a design space (DS).[21] DS includes a careful description of the transformation, especially contemplating the nature of the process, its mechanistic profile, kinetics, side reactions, etc. This ideally leads to the identification of critical quality attributes, acceptance criteria (starting materials, solvents, impurities, etc.), defining process controls and specifications. Thus, after determining the proven acceptable ranges for all meaningful parameters, a multidimensional combination and interaction network of all these items, with proven impact in the quality, is built. Working within this DS is formally allowed and is therefore advisable. On the contrary, staying out of the authorized region is considered a change and requires a regulatory post-approval adjustment.

As a relevant example, scientists at Bristol Myers-Squibb developed a DS approach to manufacture asunaprevir (to treat chronic hepatitis C infection).[22] In this case, once the impurities and the critical factors were determined, the dynamic model of DS was built through a critical assessment of the elementary step kinetics, cross checked, and validated with several relevant experiments. The system of study involves the interaction of the polyfunctional alcohol derivative **1** with α-haloisoquinoline **2** in an aromatic nucleophilic substitution, using a strong base to generate the alkoxide reactive intermediate (Figure 2A). Apart from the desired adduct **3**, some impurities were detected arising from several side reactions (compounds **4**–**9**, Figure 2A). In this way, mainly focusing on the temperature and the number of base equivalents, the key impurities were kept at low levels, and the overall yield was improved within a range of values for each parameter. Moreover, the dynamic model was experimentally challenged, displaying good correlation with the predicted values (Figure 2B–D).

Flow chemistry has positively impacted this field, greatly improving many features of process chemistry, in comparison with classical batch procedures. This approach results in faster, safer, more eco-friendly protocols, with higher quality products and access to intrinsically complex transformations.[23] Despite the obvious advantages, these innovative processes face specific problems dealing with the reaction space. For instance, extensive experimentation in microfluidics may be monitored with desorption electrospray ionization mass spectrometry to accelerate determined processes and to predict their outcome.[24] In this way, the best conditions (solvent, stoichiometry, temperature) for the benzylation of a wide range of amines were determined in a fast manner.

At the forefront of this section are the self-optimizing continuous flow platforms for the improvement of chemical processes.[25] These systems significantly reduce the need for repetitive and extensive experimentation by using algorithms. A key point relies on the use of a multitasking Bayesian optimization with prior information based in the chemical knowledge of the reaction. A striking application involves C–C couplings by metal-catalyzed C–H activation processes, key in the fragment-based drug design. Thus, using optimal, known regions of the chemical reaction space, the protocol fixes the ligand, solvent, reaction time and temperature to get much improved yields in a surprisingly low number of experiments (Figure 3A).

Even further, the combination of self-learning systems with experimental automation is poised to dramatically affect how chemists will conduct experiments in the near future. The underlying idea is that

© 2024 The Authors. Advanced Synthesis & Catalysis published by Wiley-VCH GmbH

16154169, 2024, 4, Downloaded from https://onlinelibrary.wiley.com/doi/10.1002/adsc.202301205 by Readcube (Labtiva Inc.), Wiley Online Library on [02/07/2024]. See the Terms and Conditions (https://onlinelibrary.wiley.com/terms-and-conditions) on Wiley Online Library for rules of use; OA articles are governed by the applicable Creative Commons License

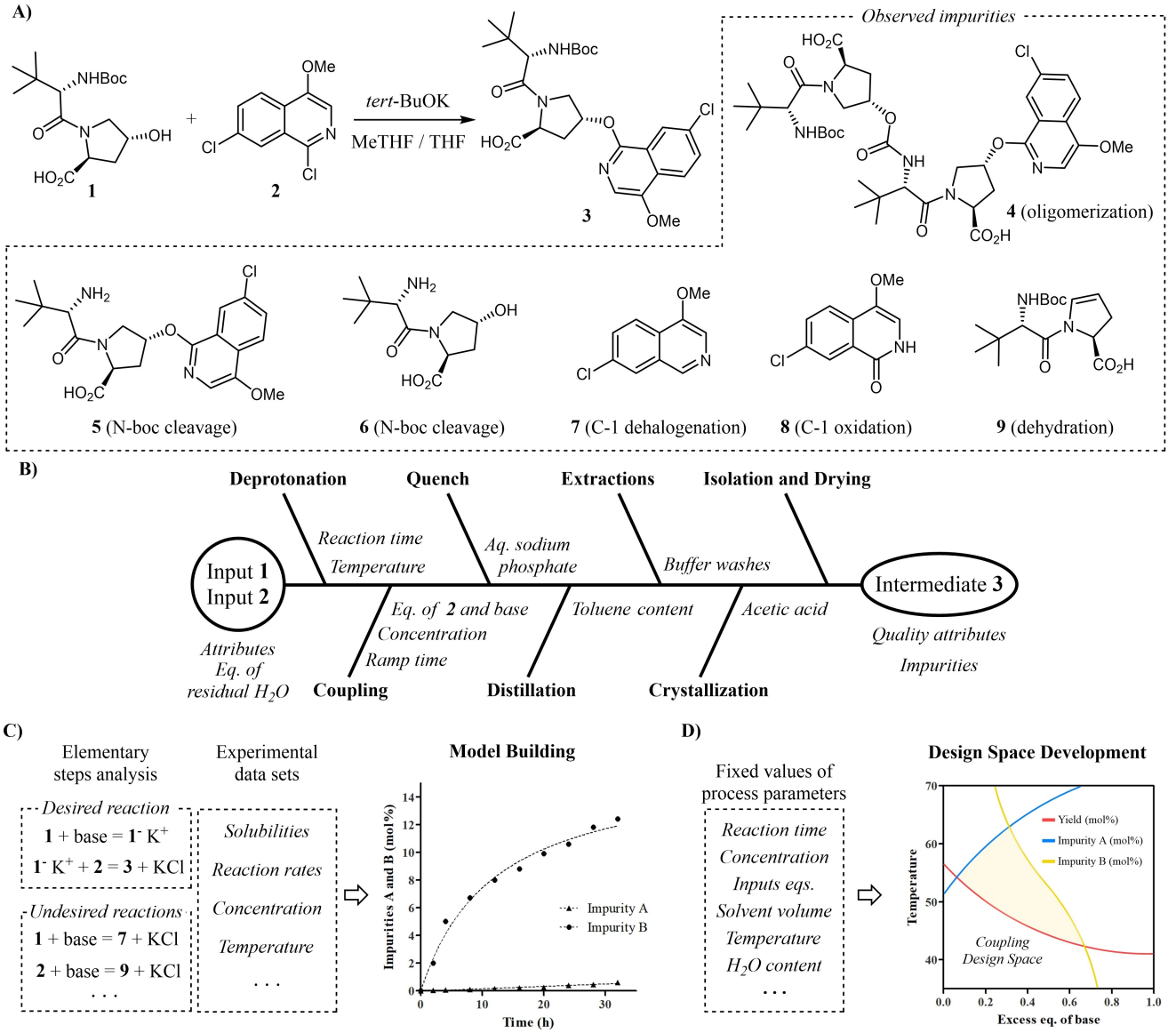

Figure 2. Charting in process chemistry I. A) Asunaprevir key transformation. B) Ishikawa diagram. C) Model building steps. D) Design space development.

organic synthesis will be ultimately performed by introducing a series of steps to be performed on a computer or even a series of final compounds to be obtained. ML algorithms will find the optimal experimental conditions and automated hardware will conduct the reaction and purification steps (Figure 3B). The potential applications and developmental challenges of this so-called self-driving laboratories have been recently reviewed by Aspuru-Guzik.[26] For example, the combination of a natural language processor with a modular automated system able to perform basic organic synthesis operations, allowed the automated synthesis of a dozen organic compounds. This was achieved using natural language descriptions of the synthetic procedures, akin to the descriptions usually found on the methodological sections of the scientific literature in a remarkable contribution by Cronin and team.[27] More recently, Sigman, Aspuru-Guzik, and Hein demonstrated that stablishing a feedback loop between the analysis of the synthetic outcome and the and the driving ML algorithm allowed to approach the optimization of the reaction conditions for a Suzuki-Miyaura coupling as a multivariate process optimization problem. Namely, only 192 experiments were carried out over 96 h to determine the reaction temperature, the phosphine to palladium ratio, the palladium loading and the phosphine ligand that yielded ca. 70% of the desired product. In contrast, the systematic exploration of combinatorial possibilities (3 continuous parameters

© 2024 The Authors. Advanced Synthesis & Catalysis published by Wiley-VCH GmbH

16154169, 2024, 4, Downloaded from https://onlinelibrary.wiley.com/doi/10.1002/adsc.202301205 by Readcube (Labtiva Inc.), Wiley Online Library on [02/07/2024]. See the Terms and Conditions (https://onlinelibrary.wiley.com/terms-and-conditions) on Wiley Online Library for rules of use; OA articles are governed by the applicable Creative Commons License

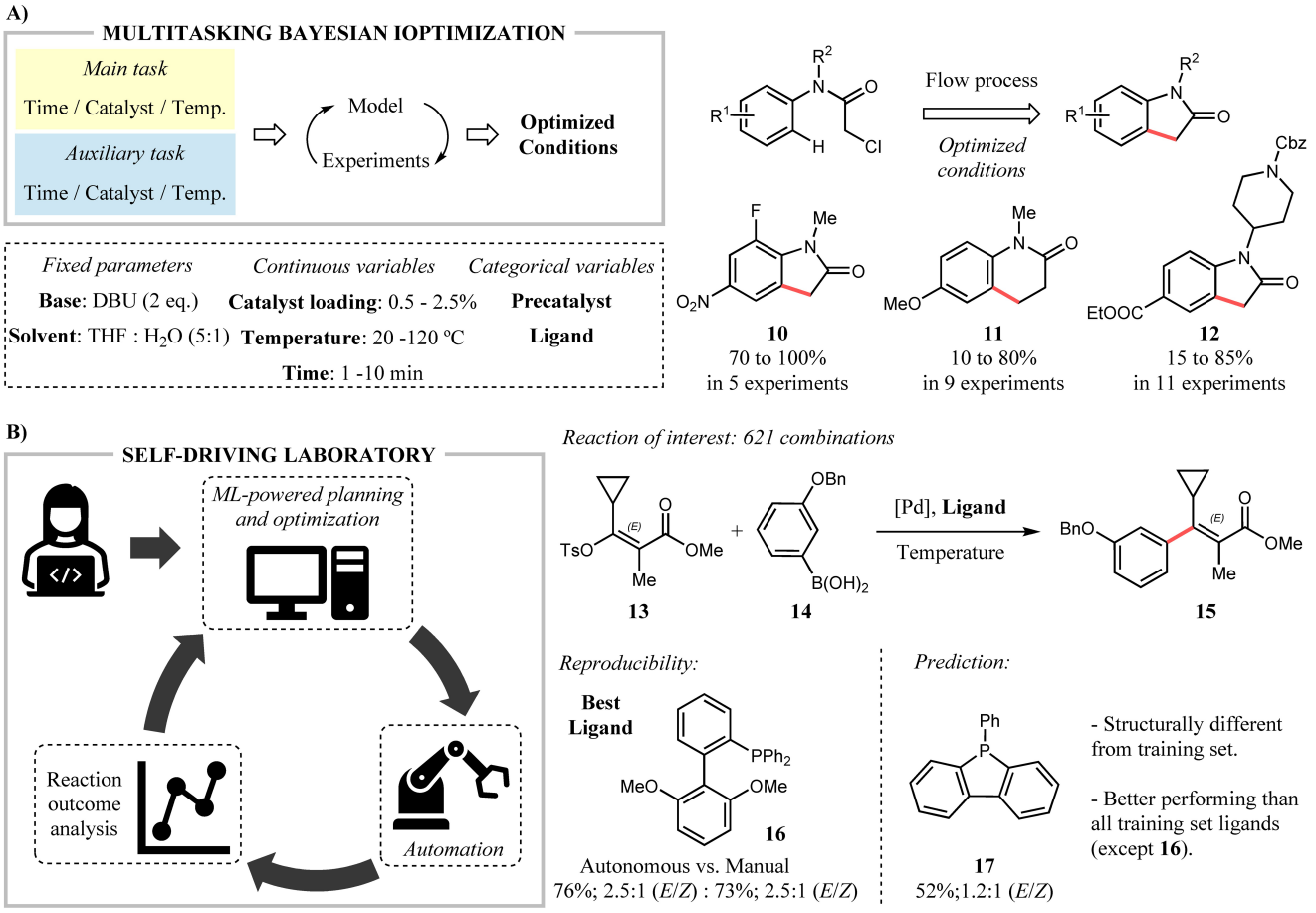

Figure 3. Charting in process chemistry II. A) Flow C–H activation processes. B) A self-driving laboratory process.

plus 23 possible phosphine ligands) would have required 621 experiments (Figure 3B).[28]

A very recent development by Gomes has been the introduction of a multi-large language model- based agent capable of autonomously execute different stages of automated chemical synthesis (from planning based on scientific literature to writing commands for a cloud laboratory to solve optimization problems based on observed results). Although the experimental capabilities of the authors limited the compound space that could be explored, the combination of these semi-autonomous agents with more advanced automated synthesis hardware could lead to transformative changes in process chemistry in the upcoming years.[29]

3. Biological and Medicinal Chemistry

The bioactivity of drugs and probes, from their design to preparation and testing, is very hard to predict. This is due to the diversity and complexity of the living systems and the variety of processes involved, many of them apparently unrelated, *i. e.* absorption, metabolism, compartmentalization, affinity, selectivity excretion, etc. Thus, charting procedures are almost mandatory to inclusively address all the involved features (Figure 4).[30] In this way, a programmed mapping of the

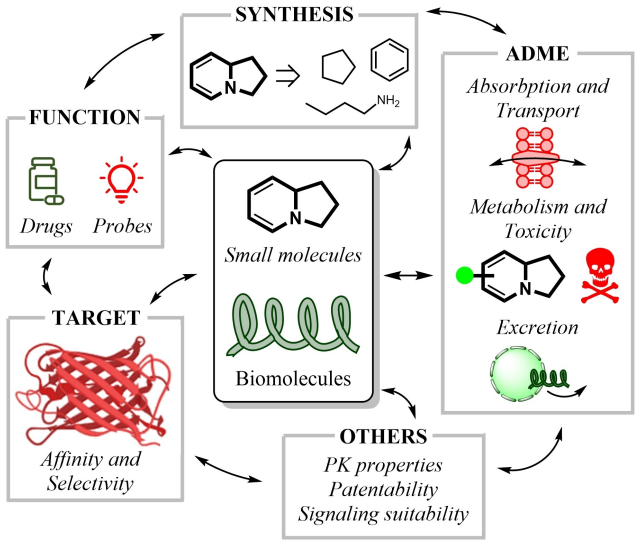

Figure 4. Complexity of the systems involved in biological and medicinal chemistry.

© 2024 The Authors. Advanced Synthesis & Catalysis published by Wiley-VCH GmbH

16154169, 2024, 4, Downloaded from https://onlinelibrary.wiley.com/doi/10.1002/adsc.202301205 by Readcube (Labtiva Inc.), Wiley Online Library on [02/07/2024]. See the Terms and Conditions (https://onlinelibrary.wiley.com/terms-and-conditions) on Wiley Online Library for rules of use; OA articles are governed by the applicable Creative Commons License

interaction of the drug/probe with the biomolecule (in vitro or *in vivo* conditions) would provide useful information on the system. Incidentally, the implementation of charting procedures such as systematic structural modifications, iterative experimentation, etc. may be developed to get the description of the system. This approach is analogous to the usual mapping of any standard chemical transformation. Moreover, it can also be considered in a complementary manner: using a molecular entity to map the structural and functional features of a larger biomolecule or the living system itself. To illustrate this section, we may mention a few relevant examples.

Dealing with basic cell elements, the formation of functional membranes and organelle-like vesicles constitutes a key issue in the generation of artificial cells with several implications, from the origin of life to physiological issues, etc.[31] These entities are prepared according to the nature of their lipidic components. For instance, Paleos has reported the generation of a family of functional vesicles from a wide choice of components. Their synthetic accessibility is an important prerequisite, as several structures should be combined in different stoichiometries. (mixtures of compounds **18**–**19** or **20**–**21**, Figure 5A).[32] In a related environment, Devaraj showed that functional droplets can internalize a variety of compounds (proteins, oligonucleotides, probes, etc.), enabling enzyme mediated reactions and even performing tasks such as cell-free protein synthesis or signaling events.[33,34] Key to the performance of these structures, are the nature of the hydrophobic species and their relative stoichiometry (compounds **22**–**23**, Figure 5B).

The development of functional probes is also affected by a series of complex events (permeabilization, compartmentalization, aggregation, potent and selective response, etc.), which determine their performance, *i.e.* a good read out. Ideally, a proper balance among all these features gives rise to a useful probe. In this respect, combinatorial approaches to generate a family of derivatives around a particular scaffold should be regarded to progress towards the development of a suitable compound in a programmed manner.[35] For instance, Vendrell developed the Near

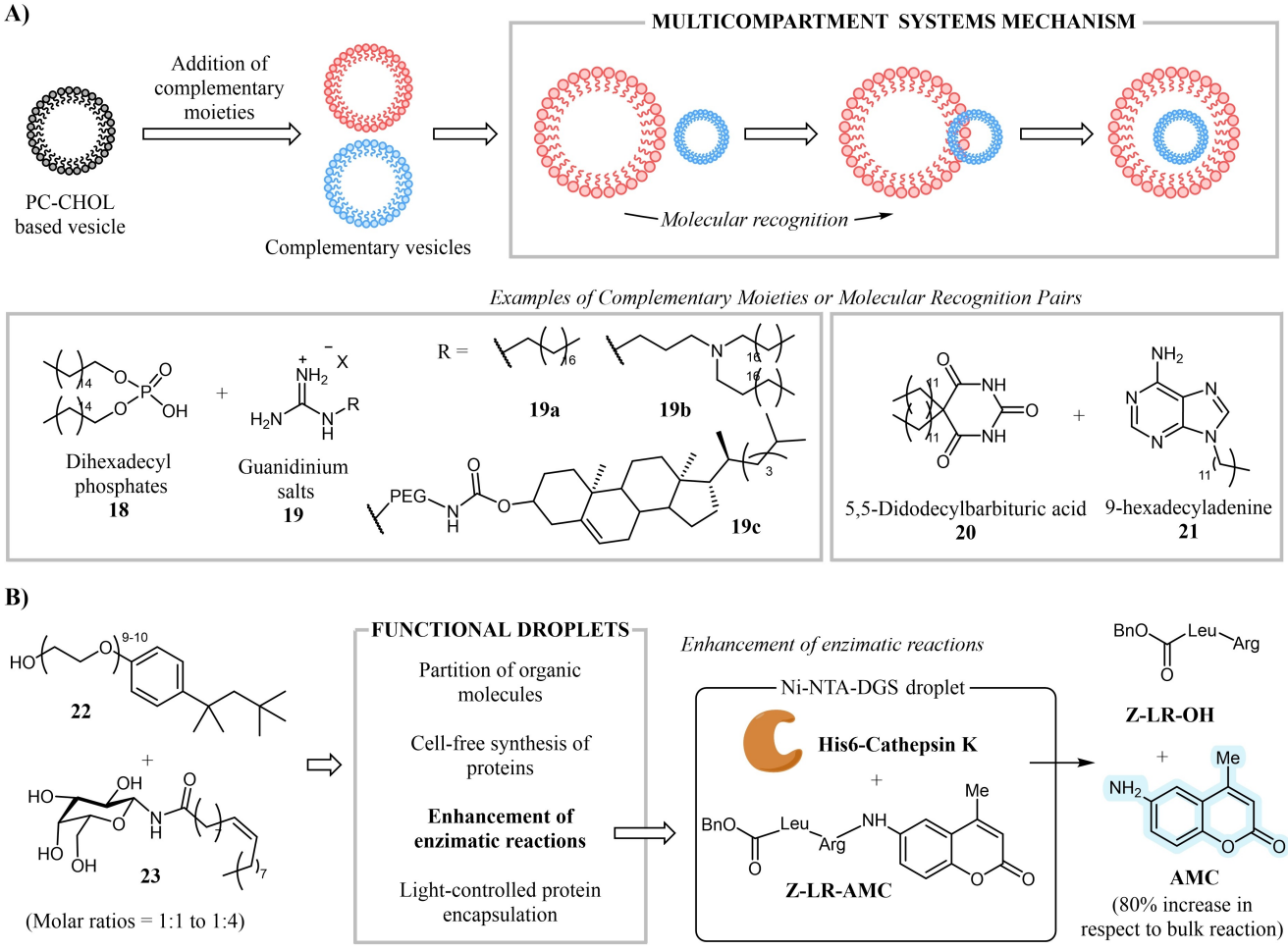

Figure 5. Charting in biological chemistry I. A) Paleos' vesicles. B) Devaraj's functional droplets.

© 2024 The Authors. Advanced Synthesis & Catalysis published by Wiley-VCH GmbH

16154169, 2024, 4, Downloaded from https://onlinelibrary.wiley.com/doi/10.1002/adsc.202301205 by Readcube (Labtiva Inc.), Wiley Online Library on [02/07/2024]. See the Terms and Conditions (https://onlinelibrary.wiley.com/terms-and-conditions) on Wiley Online Library for rules of use; OA articles are governed by the applicable Creative Commons License

Infrared BODIPY probe **25** based in a multicomponent approach, where the diversification points were mapped to optimize the fluorescent emission, selectivity in front of the target cells and the solubility of the final adduct (Figure 6A).[36]

In a related topic, Bush and team developed efficient reactive probes **26** based on aryl sulfur (VI) fluorides, to covalently tag lysine, tyrosine, histidine, and serine residues in proteins. By profiling the overall reactivity, the selectivity among the distinct nucleophilic amino acids, the aqueous stability and the solubility, a panel of derivatives featuring a *p*-carbonyl group enriched a large number of proteins, expanding the liganded proteome (Figure 6B).[37] The use of this procedure allowed the discovery of ligands for determined target proteins, once a fragment was attached to the reactive sulfur fluoride moiety.[38]

Finally, in a bright approach to chart protein epitopes surrounding the binding site, MacMillan has developed the selective generation of trifluoromethylcarbenes via a suitable ligand linked to an Ir photocatalyst **27** (Figure 6C). The rationale being that after the ligand selectively nests in the binding site, the diazirine precursor **28** is transformed by the photocatalyst and the generated carbene rapidly inserts mainly in the vicinity. In this way, the site can be described after the analysis of the modified amino acids. Importantly, this has allowed the description of proteins lacking crystal 3D structures.[39]

Medicinal chemistry is perhaps a field in which charting was applied well before the concept was

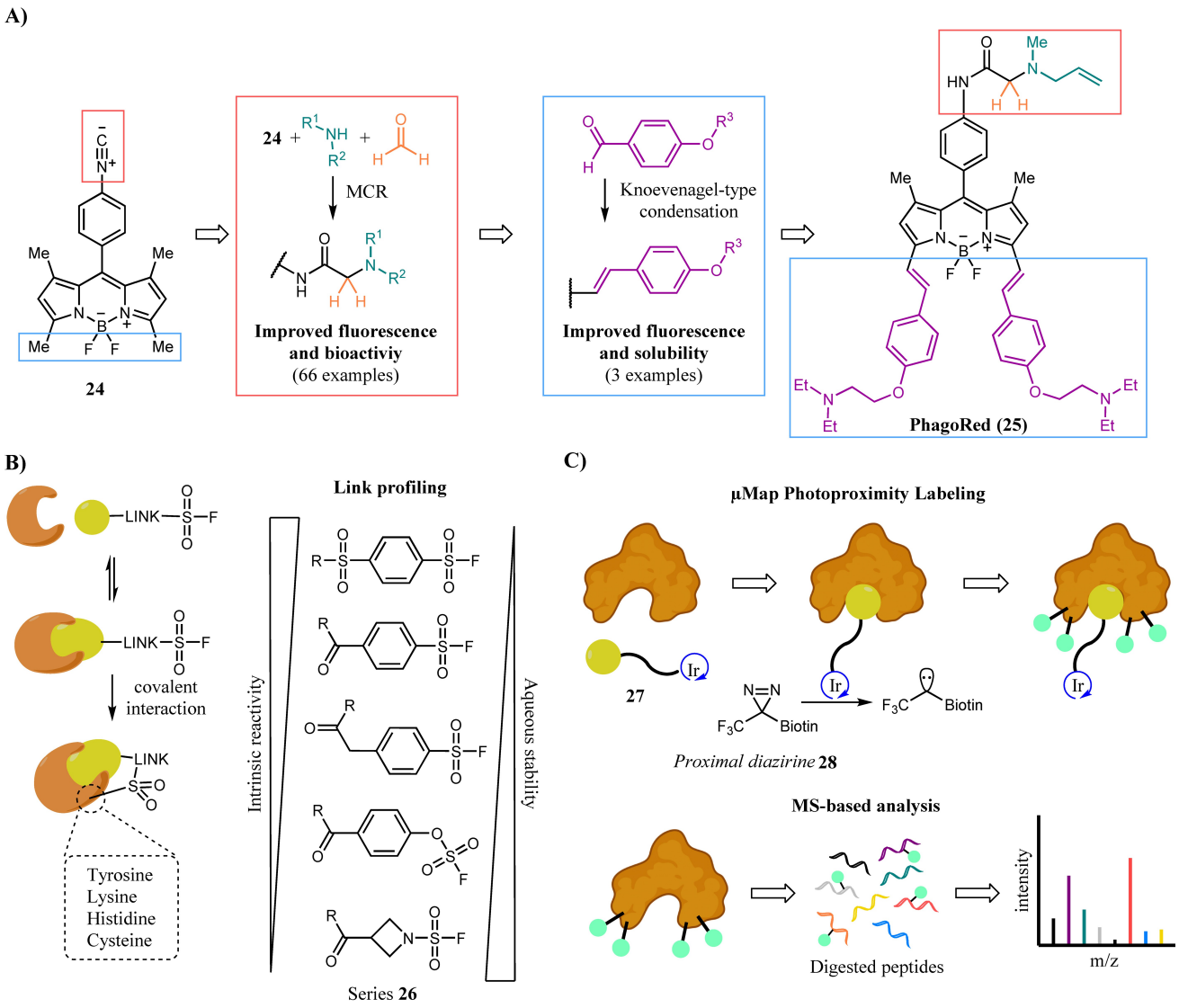

Figure 6. Charting in biological chemistry II. A) Vendrell's NIR BODIPY probe. B) Bush's covalent probes. C) MacMillan's mapping of protein epitopes.

© 2024 The Authors. Advanced Synthesis & Catalysis published by Wiley-VCH GmbH

16154169, 2024, 4, Downloaded from https://onlinelibrary.wiley.com/doi/10.1002/adsc.202301205 by Readcube (Labtiva Inc.), Wiley Online Library on [02/07/2024]. See the Terms and Conditions (https://onlinelibrary.wiley.com/terms-and-conditions) on Wiley Online Library for rules of use; OA articles are governed by the applicable Creative Commons License

coined. Especially in the drug discovery process, where finding the "needle in the stack" (the drug in the chemical space) not only includes the astonishing size of the latter,[4,40] but also the seemingly capricious biological profiles of the selected compounds. Moreover, synthetic approaches, efficacy, safety, legal and economic aspects, etc. also play important roles. In this context, there is a strong interplay with organic synthesis to fulfill the preparation of thousands of compounds needed to develop a drug.[41,42]

A series of novel methodologies have emerged featuring charting elements. The late-stage functionalization (LSF) involves the systematic modification of C–H bonds (often by metal-catalyzed processes) of a determined compound to reach a family of structurally related derivatives decorated with a variety of substituents.[43] Ackermann and Johansson have reviewed the field and disclosed the extensive derivatization of simple drugs (Figure 7A) using different reactions (C–H activation processes involving the formation of C–C, C–S, C–P, C–X bonds).[44–45] The approach uses the innate reactivity of the structure itself (meaning the higher tendency to suffer the desired transformation by certain atoms in the molecule) or a guided mode (when a coordinating group is present or attached close to the reacting site, stabilizing in this way the organometallic intermediate). These transformations can be triggered by a variety of modern activation modes including photoredox, electrochemical, and enzymatic approaches. For instance, the marketed drugs diazepam[45] and loratadine[46] have been diversified in this way (Figures 7B–C). Overall, LSF allows the efficient generation of several derivatives out of a single substrate, notably diminishing the synthetic effort towards a new drug, which otherwise would need a set of multistep sequences.

A complementary approach deals with a programmed variation of the scaffold itself. Thus, molecular editing aims at the modification of the initial skeleta in different ways (insertion, deletion, or atom exchange).[47,48] Although, this approach is still being developed, remarkable examples illustrate its power and timely usefulness to prepare new tridimensional scaffolds for drug discovery. For instance, Sarpong and

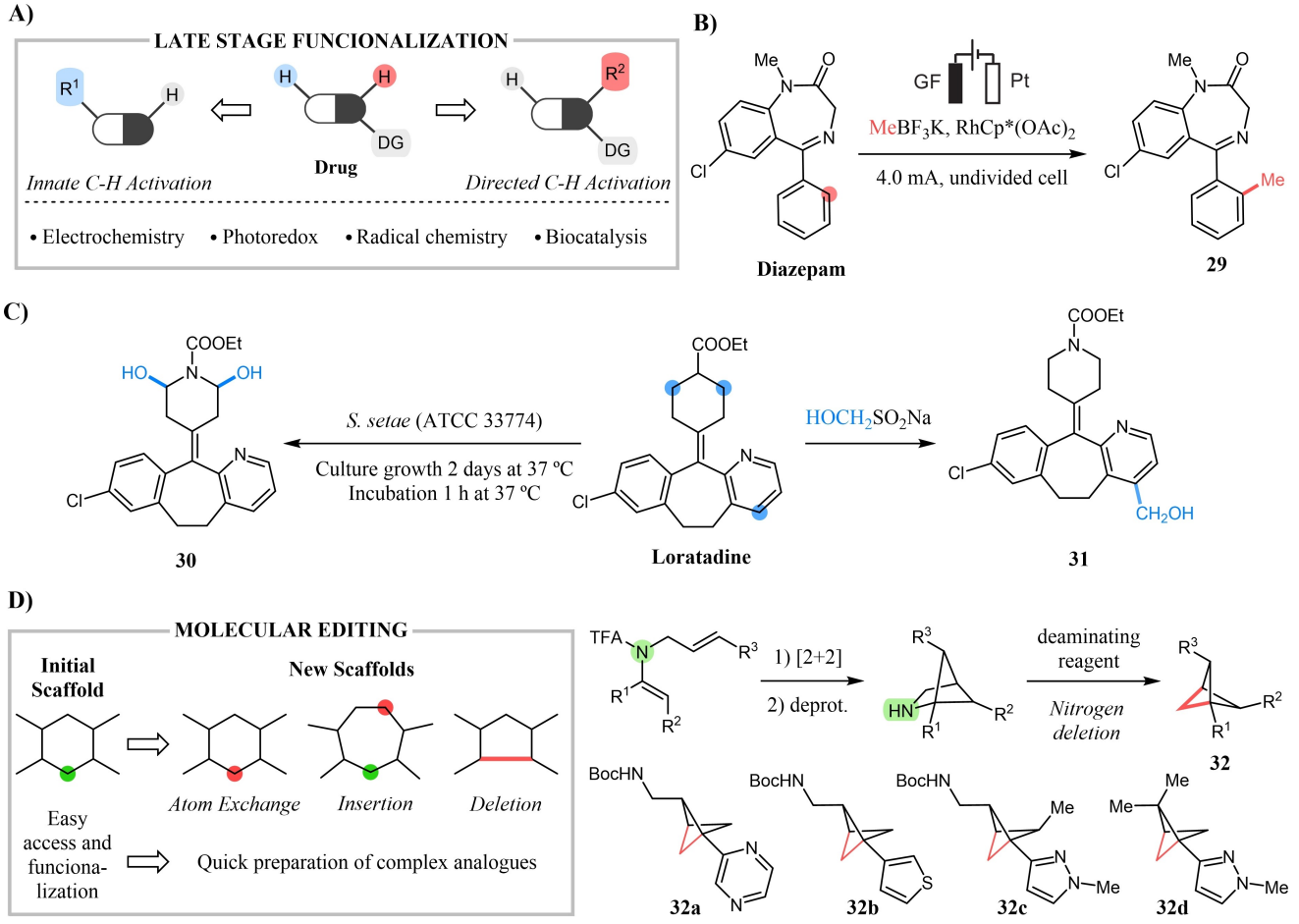

Figure 7. Charting in medicinal chemistry I. A) Late-stage functionalization of known drugs. B) Ackermann's LSF of diazepam. C) Lall's LSF of loratadine. D) Molecular editing: concept and Sarpong's approach to bicyclo[1.1.1]pentanes.

© 2024 The Authors. Advanced Synthesis & Catalysis published by Wiley-VCH GmbH

16154169, 2024, 4, Downloaded from https://onlinelibrary.wiley.com/doi/10.1002/adsc.202301205 by Readcube (Labtiva Inc.), Wiley Online Library on [02/07/2024]. See the Terms and Conditions (https://onlinelibrary.wiley.com/terms-and-conditions) on Wiley Online Library for rules of use; OA articles are governed by the applicable Creative Commons License

Lebold have edited a suitably accessible azabicyclic structure to yield functionalized and substituted bicyclo[1.1.1]pentanes **32** in a fast manner (Figure 7D).[49] In this respect, we may also mention the work of Levin to generalize the aromatic nitrogen scanning in the molecular edition of aromatic rings to directly generate a programmed set of pyridine derivatives.[50]

Structure-Activity Relationship (SAR) plays a central role in medicinal chemistry. This classic concept involves the use of systematic charting procedures. In addition to computational refinements (see below), a new approach by Carragher and Unciti-Broceta has been recently disclosed.[51] Starting from a promiscuous kinase inhibitor **33**, they developed a highly potent and SCR-kinase selective pyrazolopyrimidine **34** by analogue search targeting a broad spectrum of cancer-kinases. The phenotypic screening against a mammary adenocarcinoma cell line generated SAR data, biased the ensuing design (Figure 8A).

In order to integrate an intuitive vision of the process, Bajorath has introduced the SAR matrix method to bridge the properties visualization and compound design, giving a more user-friendly appraisal of the large data obtained (Figure 8B).[52] The SAR matrixes are systematically built by selecting compound series with well-defined structural relationships and setting them in matrices that parallel the well-known R-group tables. Key to the method is the matched molecular pair concept, defined as a couple of compounds that differ by a structural change at a single site.

In this section, the related Biology Oriented Synthesis (BIOS) and pseudo-Natural Product (NP) approaches, two relevant contributions by Waldmann, should be mentioned.[5–3–56] They are based in the coevolution of proteins and NPs, the latter being a privileged source of ligands, well recognized in medicinal chemistry. However, considerations on their tough total synthesis, low availability, and reduced number of structural variants, seriously hinder their use. The innovative structural charting that the methodology proposes, involves a guided modification of the NP connectivities. In this manner, protocols based on the distortion/recombination of simpler scaffolds amenable to decoration, allow the obtention and analysis of complex, yet readily prepared and manageable compounds. The generated products show impressive bioactivity profiles and constitute a first-class source for discovery in biology and medicine (Figure 9). To cite a few relevant findings unraveled through this methodology, we may highlight pseudo-NPs as selective inhibitors of glucose transporter[57] novel chemo-

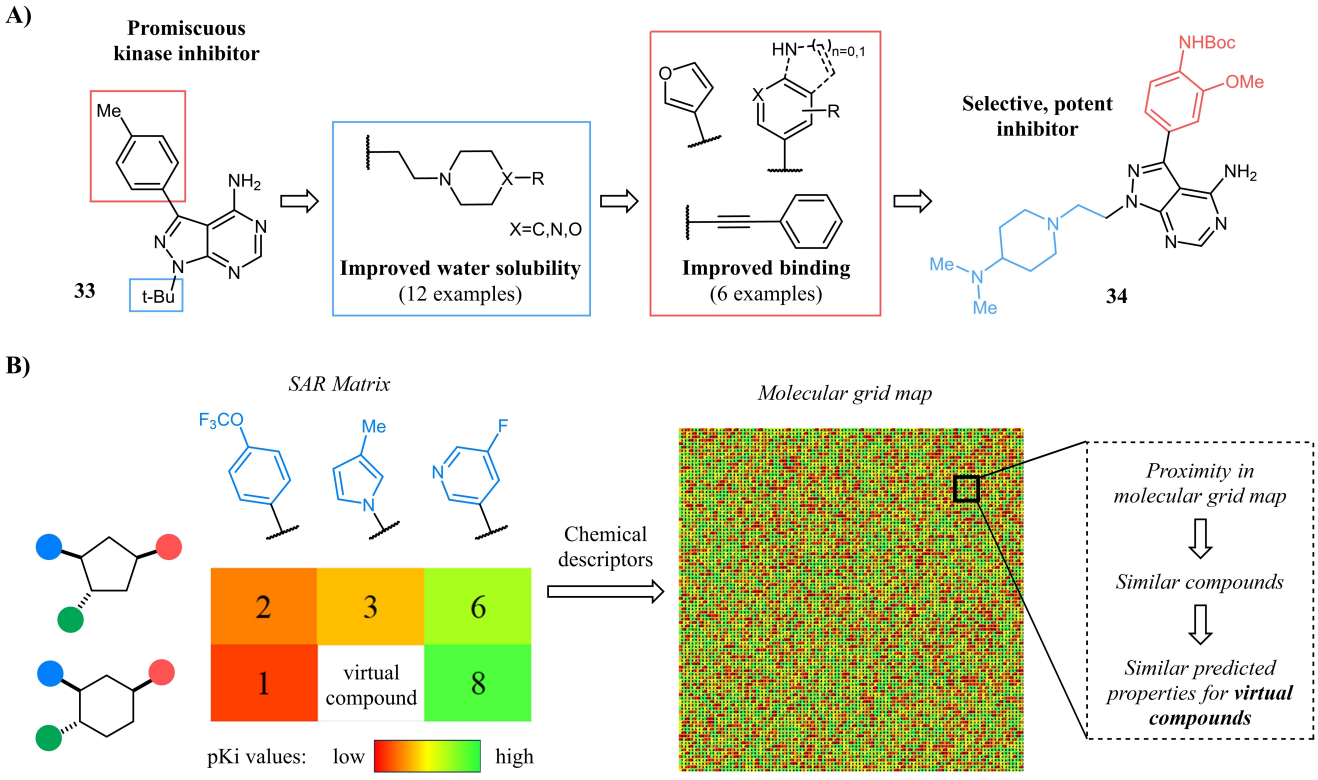

Figure 8. Charting in medicinal chemistry II. A) SAR Phenotypic screen by Carragher-Unciti Broceta. B) Matrix SAR and grid by Bajorath.

© 2024 The Authors. Advanced Synthesis & Catalysis published by Wiley-VCH GmbH

16154169, 2024, 4, Downloaded from https://onlinelibrary.wiley.com/doi/10.1002/adsc.202301205 by Readcube (Labtiva Inc.), Wiley Online Library on [02/07/2024]. See the Terms and Conditions (https://onlinelibrary.wiley.com/terms-and-conditions) on Wiley Online Library for rules of use; OA articles are governed by the applicable Creative Commons License

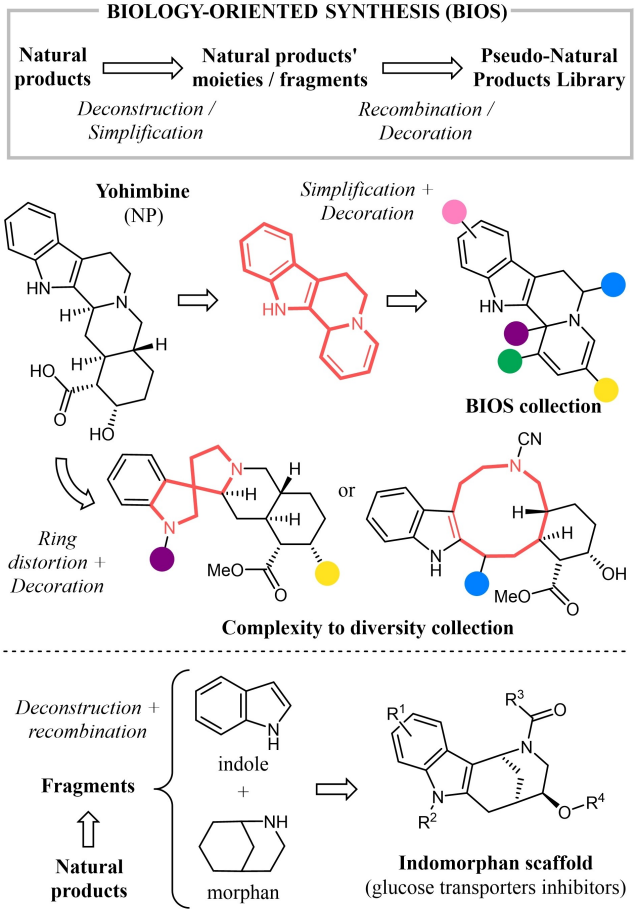

Figure 9. Waldmann's BIOS/pseudo-NPs approach.

types for Hedgehog signaling[58] and RNA binders-degraders.[59]

4. Catalysis

The complexity of the catalytic processes (recognition, binding, lowering the energy barrier, catalyst release, etc.) demand a charting approach to get optimized efficiencies, and recent results show its power compared with classical approaches. Research in the field ranges from expanding organometallic, photochemical or asymmetric catalysis, to facilitating a previously hard or inaccessible transformation. These works mainly consist of catalyst discovery and the exploration of the conditions (additives, solvent, catalytic load, temperature, etc.) necessary to optimize the overall performance and applicability of a given reaction. Here we highlight some remarkable findings in the field that fall into the charting philosophy, or that provide tools and methodologies to map a catalytical chemical space.

An adaptive dynamic homogeneous catalysis platform is presented by König to provide good-yielding general conditions for photocatalyzed cross-coupling reactions.[60] The concept relies on the capability of the catalytic system to self-adapt to the reaction environment. The optimal requirements of the catalytic complex (electronics, coordination, geometry, etc.) are solely driven by the nature of the (proto)nucleophile, while the electrophile, the photocatalyst, and the nickel salt remain unchanged. In this way, the nucleophile scope is mapped depending on the additive needed (if any) to promote the transformation, resulting in nine different C(sp^2)-X bond forming reactions leading to compounds 35. Aside from its simplicity, the system stands out for its predictability, displaying consistent reproducibility across all nucleophilic groups, thus providing a general picture of the reactivity space of this cross-coupling transformation, exemplified with compounds 36–37 (Figure 10A).

One of the main concerns in the field is the applicability of a catalytic system to a wide range of reactants, usually referred to as substrate generality. However, the development of new catalytic processes typically relies on its performance upon a particular substrate, and transferability to a broader scope is often unsatisfactory. To overcome this challenge, Kagan introduced the multi-substrate approach,[61] essentially postulating the charting of the reaction space of catalytic reactions. Over the last two decades, the concept has been applied in asymmetric catalysis.[62–64] For instance, List uses the multi-substrate approach to develop a general organocatalyst for the asymmetric Diels-Alder cycloaddition of cyclopentadiene with various enals 38.[65] In this way, different dienophile substrates are mixed with cyclopentadiene and the corresponding catalyst in the same reaction vessel. The results are analyzed by chiral gas chromatography, giving indicators of reaction performance (yield and stereoselectivity) for all substrates at once. While screening on a single substrate would likely result in missing the "best-for-all" catalyst, the multi-substrate approach provides a suitable entry for generality (Figure 10B). Yet, a huge drawback is associated to screening and determining enantiomeric excesses (e.e.) from a large number of substrate-catalyst combinations. To overcome this hurdle, Jacobsen developed a methodology based on supercritical fluid chromatography-mass spectrometry (SFC-MS), to rapidly provide e.e. values.[66] The approach is tested on an enantioselective Pictet-Spengler reaction. The selected chiral catalysts are screened against representative combinations of *N*-benzyl tryptamines 40 and aldehydes 41. In this way, a SPINOL-phosphoric acid is found to provide remarkable levels of generality. The optimized model is then tested against new reactant combinations to validate the methodology (Figure 10B).

Data science is materializing as one of the main players in the field of catalysis,[67] specifically focusing on prediction tools for the development of general catalytic processes.[68]. An unsupervised ML algorithm

© 2024 The Authors. Advanced Synthesis & Catalysis published by Wiley-VCH GmbH

16154169, 2024, 4, Downloaded from https://onlinelibrary.wiley.com/doi/10.1002/adsc.202301205 by Readcube (Labtiva Inc.), Wiley Online Library on [02/07/2024]. See the Terms and Conditions (https://onlinelibrary.wiley.com/terms-and-conditions) on Wiley Online Library for rules of use; OA articles are governed by the applicable Creative Commons License

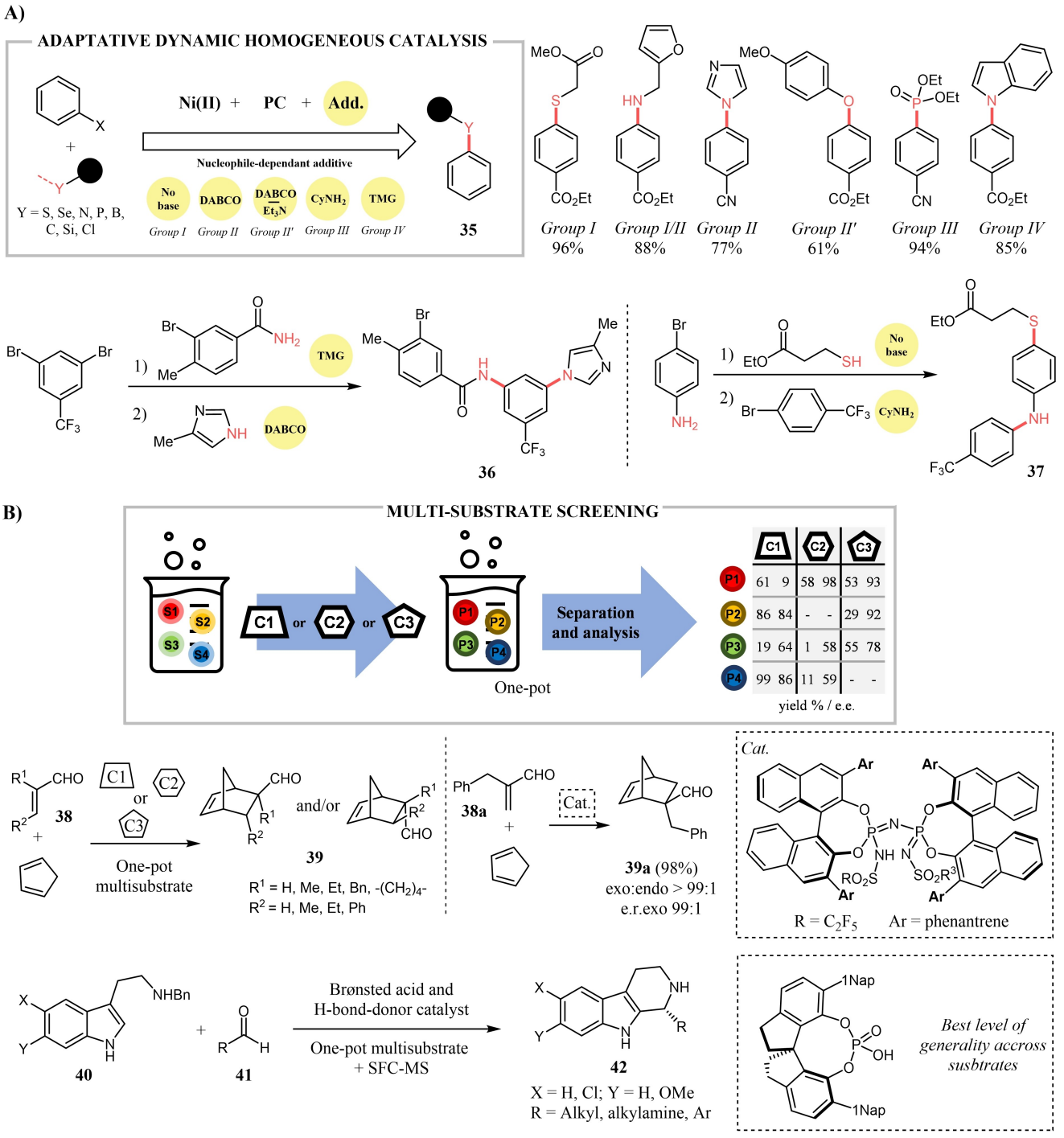

Figure 10. Catalysis I. A) König's adaptive dynamic homogeneous catalysis. B) List's application of the multi-substrate approach and Jacobsen's methodology for the rapid determination of e.e. to assess reaction generality.

developed by Reid serves to describe the generality of described catalysts for asymmetric Mannich-type reactions towards adducts 43.[69] In this case, the authors not only aim at substrate generality (broad scope), but also reaction generality (development of connectivity variants). In this respect, mechanistic insights show that hydrogen bonding interactions offer clear advantages over covalent catalysis. Moreover, the authors apply the findings to experimentally target new reactions to validate the developed workflow (Figure 11A). Sigman showcases the practicality of data science for the *de novo* design of a chiral phosphoric acid (CPA) catalyst.[70] A data-driven selection of fragments is incorporated into the single-point chiral

© 2024 The Authors. Advanced Synthesis & Catalysis published by Wiley-VCH GmbH

16154169, 2024, 4, Downloaded from https://onlinelibrary.wiley.com/doi/10.1002/adsc.202301205 by Readcube (Labtiva Inc.), Wiley Online Library on [02/07/2024]. See the Terms and Conditions (https://onlinelibrary.wiley.com/terms-and-conditions) on Wiley Online Library for rules of use; OA articles are governed by the applicable Creative Commons License

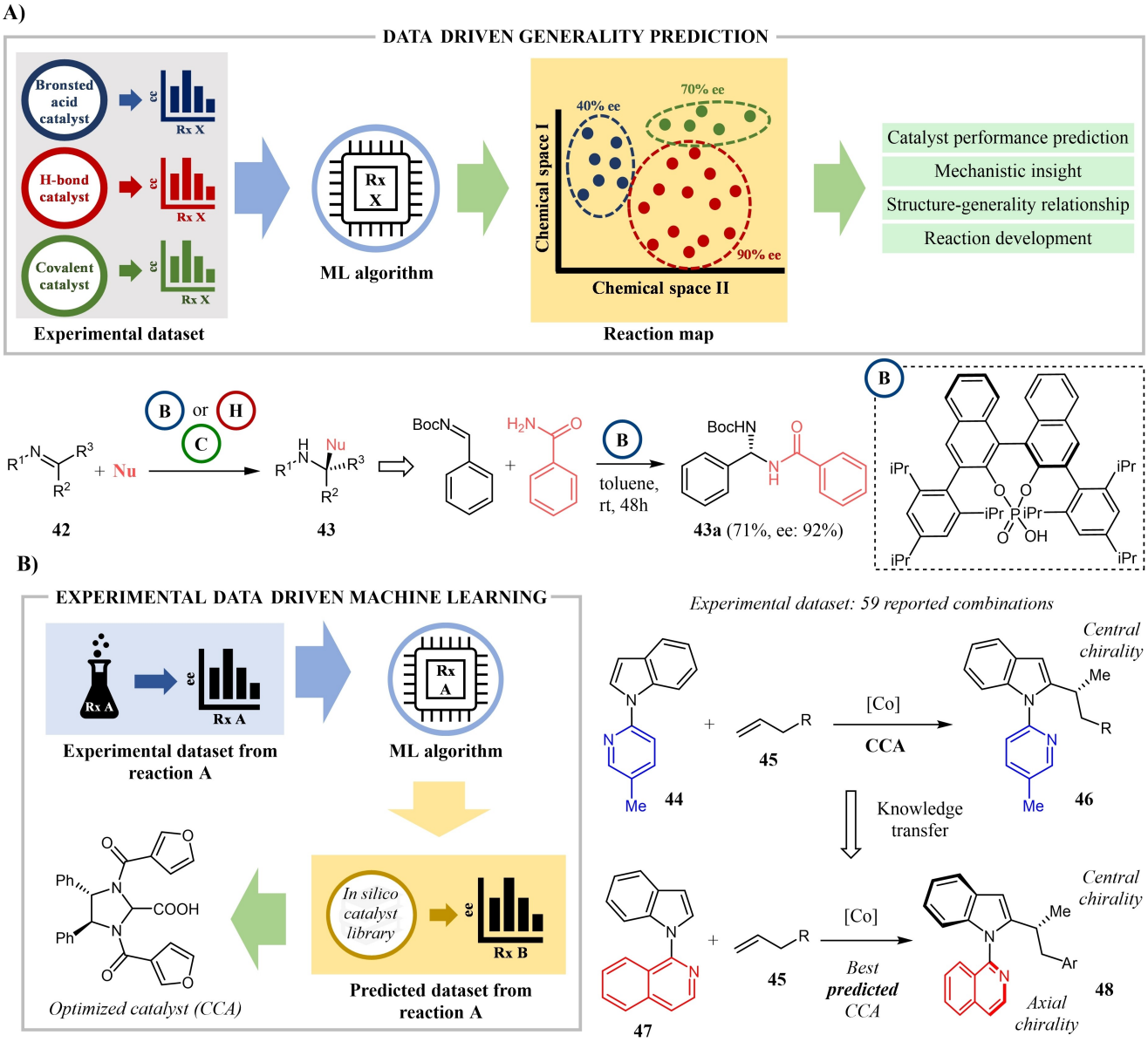

Figure 11. Catalysis II. A) Reid's workflow for generality in asymmetric catalysis. B) Data-driven knowledge transfer strategy by Ackermann.

CPAs, resulting in an experimental training set of 20 catalysts, which are tested in an asymmetric hydrogenation of 8-aminoquinolines. A thorough study reveals key features for selectivity, allowing to predict whether a catalyst would generate enantioselectivity or not depending on the residues. Since synthesizing a family of chiral catalysts and screening for e.e. are laborious tasks, the available data of asymmetric systems to train ML algorithms is scarce. Using the construction of indoles with C-central and C–N axial chirality as a model, Ackermann proposes a data-driven knowledge transfer strategy.[71] An ML algorithm is trained on experimental data from a related reaction without axial chirality adducts 46, which is then used as an accurate e.e. virtual prediction tool for an *in-silico* library of catalysts applied to the target reaction. The methodology was verified with experimental data from the best performing catalysts leading to pure atropoisomeric compounds 48 (Figure 11B).

5. Reaction Discovery and Development

With the recent advances in computational techniques, structure-based molecular function prediction is becoming more and more accessible. However, despite immense advances in fundamental organic synthesis, we still have restricted access to large regions of the chemical space. This is particularly serious when it

© 2024 The Authors. Advanced Synthesis & Catalysis published by Wiley-VCH GmbH

16154169, 2024, 4, Downloaded from https://onlinelibrary.wiley.com/doi/10.1002/adsc.202301205 by Readcube (Labtiva Inc.), Wiley Online Library on [02/07/2024]. See the Terms and Conditions (https://onlinelibrary.wiley.com/terms-and-conditions) on Wiley Online Library for rules of use; OA articles are governed by the applicable Creative Commons License

comes to chemical scaffolds, resulting in a limited number of cores in functional materials.[72] In this context, reaction discovery/development campaigns are expected to provide robust, general, and green reactions, giving convenient access to unexplored scaffolds or novel decorative features. Several approaches have been used to discover new reactions/reactivity modes ranging from serendipity to rational and empirical approaches. In this section, we briefly discuss representative examples where the idea of charting chemical reaction space is clearly involved. Although these discoveries cover a wide range of reactivity patterns and technological aspects, they share a common concept: several reactant sets are screened under a variety of conditions (additives, reaction conditions, etc.) in search for a *hit*, a combination that demonstrates new chemical reactivity. This *hit* is then evaluated for its usefulness and elaborated into a more general transformation upon the detailed description of its scope, mechanism, etc.

Screening-based reaction discovery appeared upon the success of combinatorial chemistry. While the dominant paradigm was to synthesize chemical libraries or optimize known reactions, Glorius and others started to apply combinatorial setups to spot new reactions. This allowed screening large numbers of random or pre-selected combinations under a matrix of reaction parameters looking for novel transformations. Over the years, enabling technologies like automated workflows and modern analytical techniques further accelerated the pace of discovery. As a result, an impressive number of new reactions have been reported using this approach.[73] In this context, Glorius investigated the key quenching step of a particular photocatalytic reaction to chart the catalytic reaction space, leading to the discovery of new substrates and reactivity.[74] Coined *mechanism-based screening*, the authors study the ability of a set of 100 substrates to quench an excited Ir photocatalyst. Luminescence spectroscopy is used to identify benzotriazoles and phenols as novel classes of substrates in situ. The appropriate photocatalyst is matched to a particular quencher for optimal results. This approach not only serves to expand the chemical space of photochemical reactions, but also provides mechanistic insights and facilitates the development of new visible-light-promoted reactions. The knowledge gained from the charting allows the authors to rationally design proof-of-concept reactions of benzotriazoles 49 and phenols 51 to generate compounds 50 and 52 respectively (Figure 12A).

In an alternative perspective, MacMillan employed the idea of charting as a tool to boost serendipity. His team used an automated high throughput platform coupled with GC-MS chromatography to screen the interactions of random substrates with common functional groups in the presence of a variety of metal catalysts. Starting from a detected *hit* coupling reaction between N,N-dimethylaniline and 1,4-dicyanobenzene (1,4-DCB) with $Ir(ppy)_2(dtbbpy)$ PF_6 as catalyst and evaluating its potential interest for medicinal chemistry, they developed a new and general photoredox amine C–H arylation protocol under mild and convenient conditions to access substituted aromatics 54 (Figure 12B).[75] In a similar approach reported by Hartwig, the screening led to the discovery and development of new and general metal-catalyzed hydroamination reactions.[76] In an interesting example, Liu charted the chemical reaction space around the azide coupling reactions using a DNA-encoded substrate platform. By deep screening of reaction conditions, they detected a Ru(II) catalyzed azide-nitrile coupling reaction. Switching to non-DNA-encoded substrates and tuning the reaction, they developed a mild visible-light catalyzed azide reduction to a variety of primary amines 57, with remarkable chemoselectivity in front of a variety of potentially problematic functional groups like disulfides, aldehydes, alkynes, etc. It also showed excellent biocompatibility even in the presence of an enzyme without effecting their performance (Figure 12C).[77]

New reactions often arise from alternative coupling modes of known combinations. In an illustrative example, Cernak mapped all the reactivity possibilities of a highly studied combination (amines 58 and carboxylic acids 59, Figure 13A) to clearly show that its reactivity map can go far beyond the conventional amide formation. They made a computationally examined chart of plausible couplings and experimentally confirmed the feasibility of some combinations as proof of concept, for instance yielding compounds 60–63 (Figure 13A). They also demonstrated the impact of the approach by applying these alternative couplings to complex, biologically relevant amines.[78] This can be elaborated to other coupling partners, arguably suggesting a vast playground for reaction discovery. The approach can be useful in the context of multicomponent reactions (MCRs), where the reaction space and the network of reactivities are far more complex. Our lab has recently applied charting as a convenient tool to expand the synthetic reach of MCRs, allowing for the selective generation of several scaffolds out of a given set of reactants. As a model, the chemical reaction space around a known MCR combination was carefully charted. The studied set of aldehydes/ketones 64, amines 65 and isocyanoacetates 66 has been known to yield 2-imidazolines 67. The charting however showed that changes in the reaction chemical space can direct the same set to selectively afford 4-imidazolones 68. Consequent mapping around the amine component unraveled novel reactivity modes, giving rise to the formation of 2-aminoimidazolones 69 and coelenterazine-type derivatives 70 (Figure 13B).[79]

© 2024 The Authors. Advanced Synthesis & Catalysis published by Wiley-VCH GmbH

16154169, 2024, 4, Downloaded from https://onlinelibrary.wiley.com/doi/10.1002/adsc.202301205 by Readcube (Labtiva Inc.), Wiley Online Library on [02/07/2024]. See the Terms and Conditions (https://onlinelibrary.wiley.com/terms-and-conditions) on Wiley Online Library for rules of use; OA articles are governed by the applicable Creative Commons License

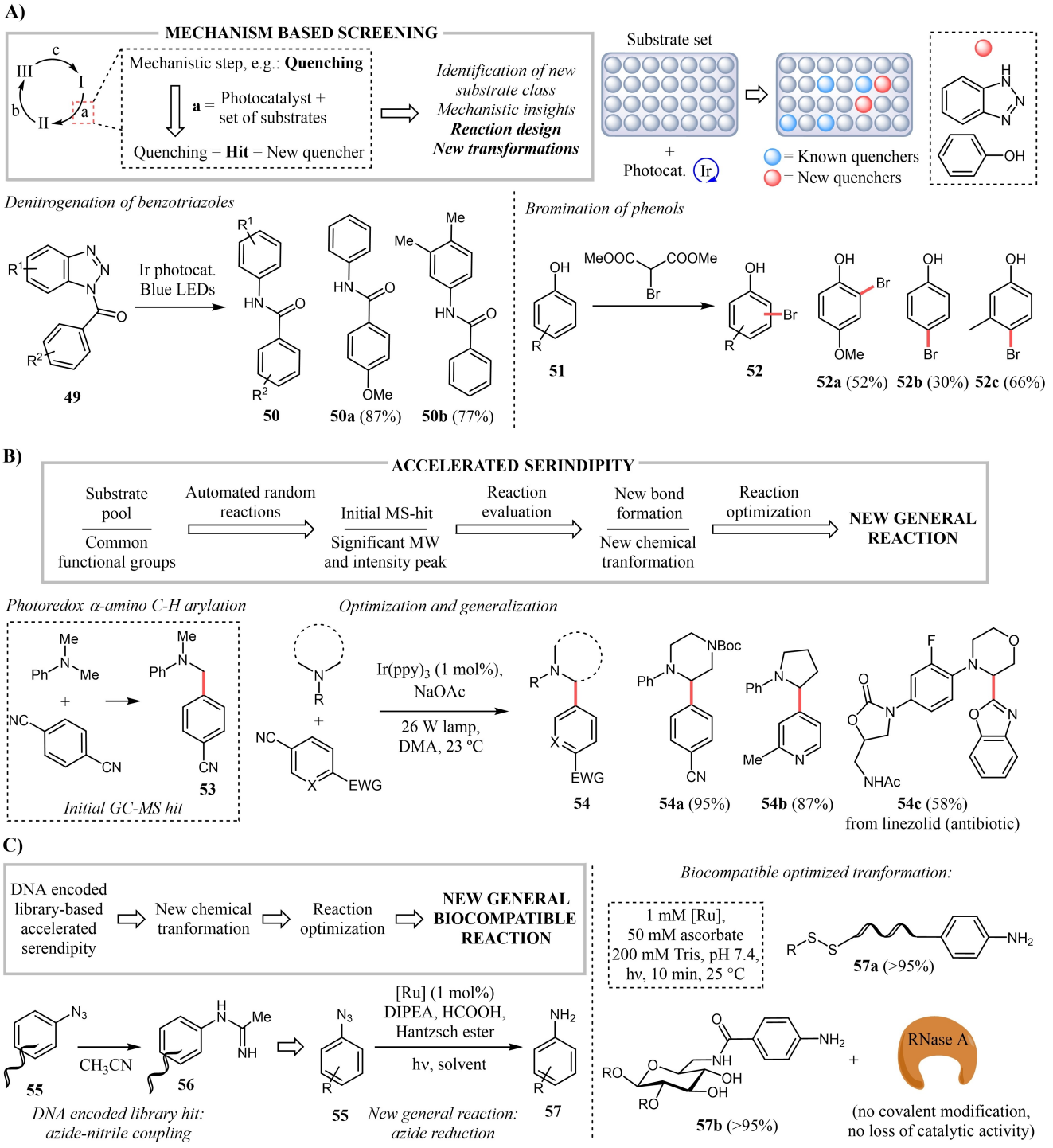

Figure 12. *Screening-based* reaction discovery and development. A) Glorius' mechanism-based screening. B) MacMillan's accelerated serendipity concept. C) Liu's DNA encoded library method.

Interrupted reactions are another approach to develop new transformations. These reactions are rooted in the mechanistic alteration of known processes, in the sense that the chain of events take a different path at some point, delivering unexpected connectivites. Yudin has shown that this approach has a general character,[80] and a wide range of organic reactions can be interrupted, giving rise to remarkable expansion in the structural and mechanistical diversity of the parent transformation. For instance, interrupted versions of the classical Povarov MCR described by Fañanás, Rodríguez and our team, are clear examples

© 2024 The Authors. Advanced Synthesis & Catalysis published by Wiley-VCH GmbH

16154169, 2024, 4, Downloaded from https://onlinelibrary.wiley.com/doi/10.1002/adsc.202301205 by Readcube (Labtiva Inc.), Wiley Online Library on [02/07/2024]. See the Terms and Conditions (https://onlinelibrary.wiley.com/terms-and-conditions) on Wiley Online Library for rules of use; OA articles are governed by the applicable Creative Commons License

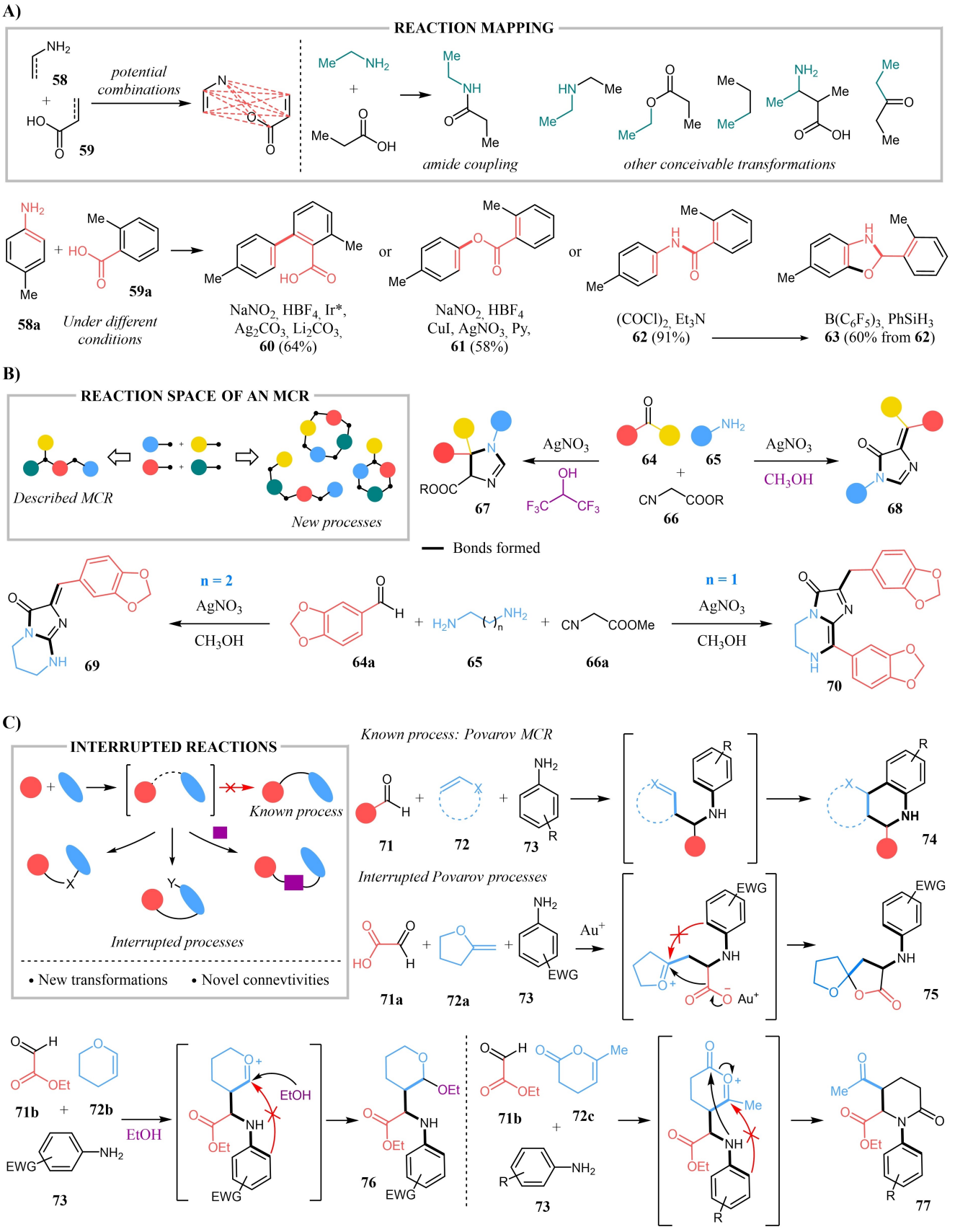

Figure 13. Alternative connectivities in reaction discovery and development. A) Cernak's reaction mapping. B) MCR space charting. C) Interrupted processes.

© 2024 The Authors. Advanced Synthesis & Catalysis published by Wiley-VCH GmbH

16154169, 2024, 4, Downloaded from https://onlinelibrary.wiley.com/doi/10.1002/adsc.202301205 by Readcube (Labtiva Inc.), Wiley Online Library on [02/07/2024]. See the Terms and Conditions (https://onlinelibrary.wiley.com/terms-and-conditions) on Wiley Online Library for rules of use; OA articles are governed by the applicable Creative Commons License

of charting the reactivity space, leading to new transformations which in many cases are hard to predict or rationally design (Figure 13C).[81–84]

As previously mentioned, any newly discovered transformation needs further refinement to become a useful tool in organic synthesis. This would normally require precise description of the scope and reaction mechanism. Mapping also contributes to the robustness and generality of the discovered process. In a relevant example, MacMillan reports the rapid improvement and generalization of a challenging decarboxylative arylation, using an additive screening approach to identify phthalimide as the most promising one, followed by efficient suppression of side reactions and improved results with non-activated carboxylic acids and electron-rich aryl bromides. In other words, charting the additives of a given reaction not only unravels the most efficient ones, but also provides deep insights into the reaction mechanism, eventually contributing to the generality of the reaction.[85] Moreover, Glorius describes a procedure to rapidly assess the robustness of a given reaction. Taking a common Buchwald-Hartwig reaction as a model, they map the compatibility of the reaction regarding the functional groups and residues. by simply adding equimolar quantities of readily available compounds bearing analogous structural features to the reaction media. By monitoring the yield and additive recovery, a compatibility chart was built. Finally, they examine the usefulness of the obtained data as a prediction tool, by performing the coupling reaction on complex substrates bearing these features, displaying remarkable proximity between predicted and experimental results (Figure 14).[86]

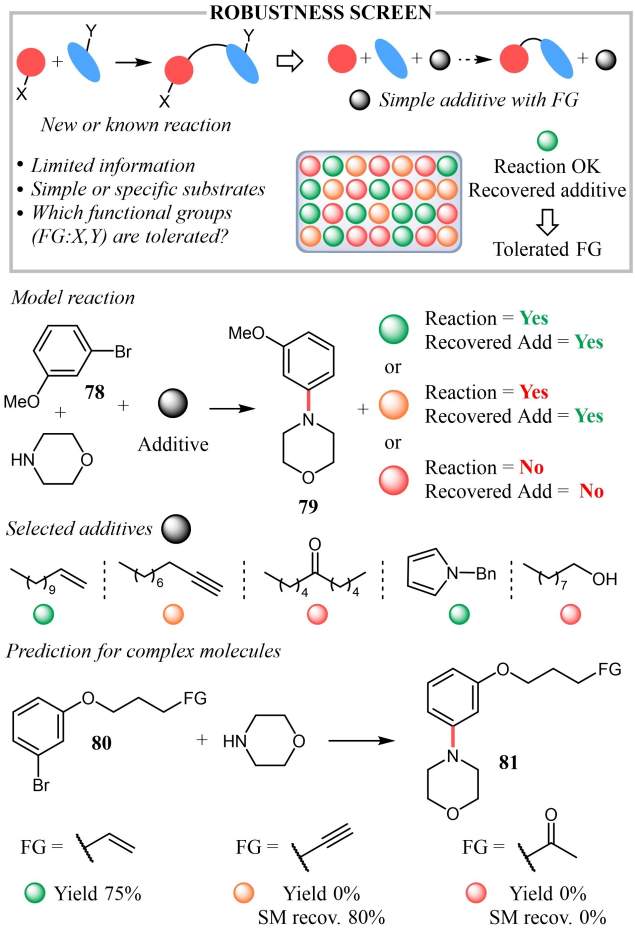

Figure 14. Glorius' reactivity scope appraisal.

Finally, the examples above illustrate that charting is highly associated with analytical methods, data processing, design of experiment, and computational approaches, especially when larger campaigns are on the agenda. To better address this point, Cernak lab has developed Phactor™, a high throughput screening platform to handle experiment planning and output analysis of reaction discovery campaigns, broadcasted as a free web service for the scientific community.[87] Cronin has showed how an automated robotic set-up can handle a reaction discovery process from design to analysis.[88]

6. Computational Approaches

As seen above, charting the reaction space requires the development of suitable computational frameworks that are synergistic with experimental approaches. Indeed, the accurate prediction of chemical reactivity from mixtures of reactants and reagents remains one of the most relevant challenges in the field of computational chemistry and Norrby recently provided a detailed review of the different approaches currently being developed to understand and predict organic reactivity.[89] They can be roughly divided in three groups: atomistic simulations, rule-based expert systems and data-driven approaches. Among those, expert systems have decreased in popularity over the last decade and are oftentimes seen as poorly scalable and difficult to impossible to generalize.[90] Next, atomistic models rely on the description of structural and conformational determinants of the reacting species involved.[89] As they use highly accurate quantum calculations, these approaches are often computationally expensive and require too much human input to virtually screen large sets of reactions, although they can assist in providing mechanistical insights into unexpected reactivity (Figure 15A).[91–94] Over the last decade, there has been interesting developments using neural-network wavefunctions to speed up ab-initio quantum chemistry calculations, however the field remains in early stages.[95,96] In parallel, leveraging ML models to perform atomistic simulations of an accuracy similar to quantum mechanics calculations at a fraction of the cost has become a very active area of research. The most popular approaches rely on training

© 2024 The Authors. Advanced Synthesis & Catalysis published by Wiley-VCH GmbH

16154169, 2024, 4, Downloaded from https://onlinelibrary.wiley.com/doi/10.1002/adsc.202301205 by Readcube (Labtiva Inc.), Wiley Online Library on [02/07/2024]. See the Terms and Conditions (https://onlinelibrary.wiley.com/terms-and-conditions) on Wiley Online Library for rules of use; OA articles are governed by the applicable Creative Commons License

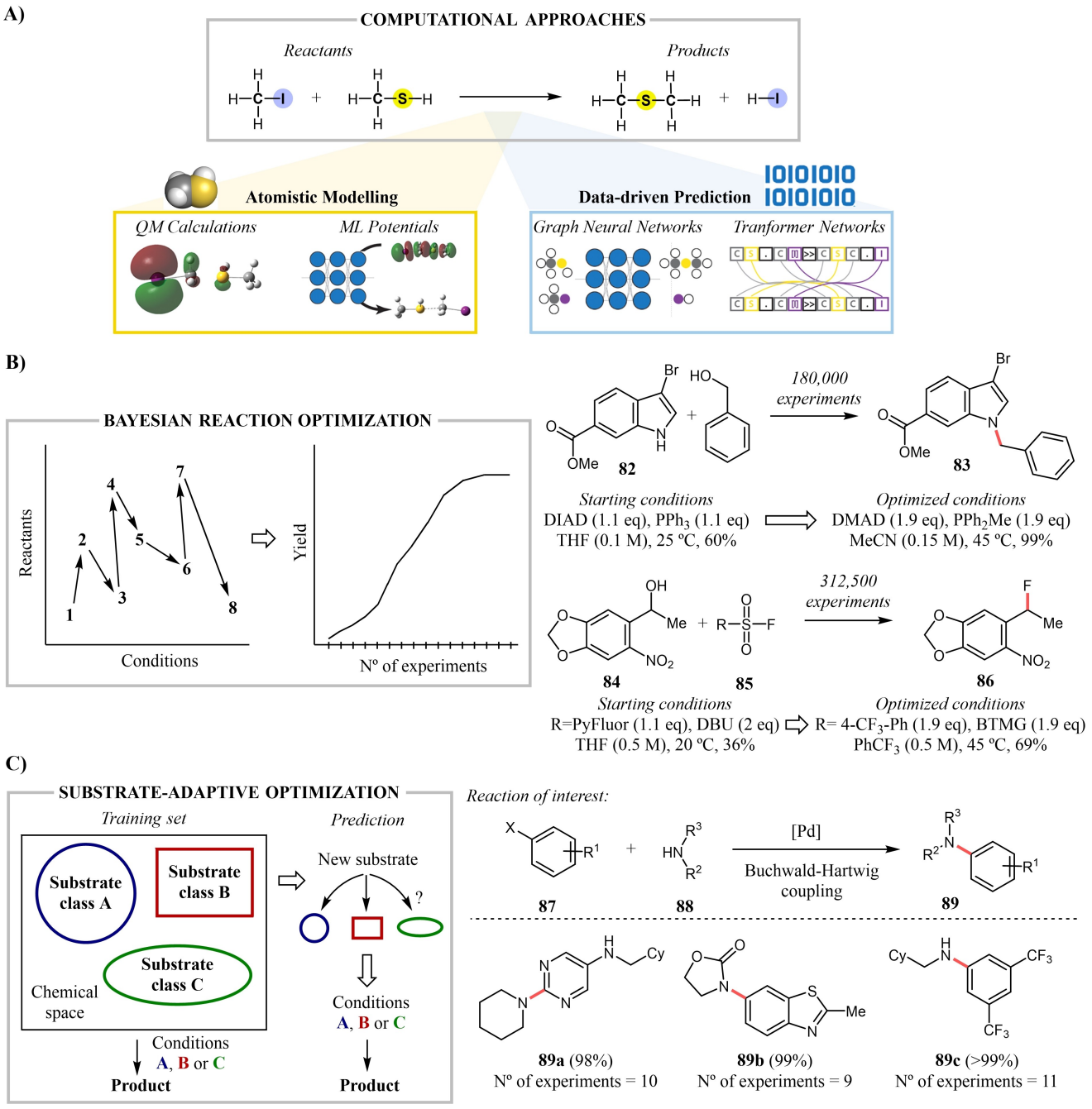

Figure 15. Computational approaches. A) Atomistic modelling and data-driven approaches to reaction prediction for chemical space charting. B) Doyle's Bayesian reaction optimization. C) Denmark's substrate-adaptative model.

an ML model (usually a neural network) to predict the potential energy surface associated to a chemical configuration, using results of quantum chemical calculations of model systems as input training data, leading to so called machine learning potentials (MLPs).[97] Building on this idea put forward by Behler and Parrinello, Isayev and Roitberg developed ANI-1,[98] deemed the first transferable neural network for organic molecules, whose accuracy was subsequently improved in later iterations to be comparable to coupled cluster approaches.[99] The latest ANI-1 version (ANI-1xnr) was recently used to study a small set of chemical processes in condensed-phase.[100] Furthermore, different MLPs have been successfully applied to predict reaction dynamics of Diels-Alder reactions,[101] to describe the reaction network of methane combustion,[9] to screen the thermal half-lives of thousands of azobenzene derivatives,[102] and to

© 2024 The Authors. Advanced Synthesis & Catalysis published by Wiley-VCH GmbH

16154169, 2024, 4, Downloaded from https://onlinelibrary.wiley.com/doi/10.1002/adsc.202301205 by Readcube (Labtiva Inc.), Wiley Online Library on [02/07/2024]. See the Terms and Conditions (https://onlinelibrary.wiley.com/terms-and-conditions) on Wiley Online Library for rules of use; OA articles are governed by the applicable Creative Commons License

predict gas-phase activation energies,[103,104] and transition states (Figure 15A).[105]

The applicability domain of MLP is restricted by the diversity of the initial training set (for example the initial ANI iteration was trained for a set of few elements, namely C, H, N and O). The interesting concept of element-embracing atom-centered symmetry functions was recently introduced,[106] with the objective of developing lifelong MLPs that do not need to be retrained for every system at hand. However, massive computational efforts would still be required before developing generally applicable models for reaction charting when less common solvents and transition metal-based catalyst are involved.[9]

Data-driven methods require less intensive human input than atomistic methods and, once trained, the inference stage is usually orders of magnitude faster than any physics-based simulation, offering an extremely appealing path for computer-aided reaction charting (Figure 15A). Early attempts at using ML to predict chemical reactivity date from a decade ago and different applications of ML methods to the different aspects of chemical reactivity have been comprehensively reviewed recently.[107] Here we highlight recent developments on the field that likely will find wider application in reaction charting. When the reaction space to be explored is well defined, for example with the aim to find the optimal conditions for a particular reaction, it is possible to build *ad-hoc* models that are more efficient than systematic exploration at identifying the optimal regions of the reaction space. An example is the use of Bayesian optimization to navigate the chemical spaces of the Mitsunobu and the deoxyfluorination reactions by Doyle (Figure 15B).[108] An alternative to optimization approaches is the use of Cernak and Zimmerman's transfer learning.[109] In this regard, Bigler, Fantasia, and Denmark optimized Pd-catalyzed couplings through a substrate-adaptative model by identifying those regions of the chemical space that are the closest to the involved reactants (Figure 15C).[110] When the scope of the prediction is wider, an approach that has gained momentum is to use graph neural networks (GNNs) to predict reaction outcomes based on the reactants, reagents, and solvents (Figure 15A).[111] This approach yields straightforward models, because the familiar bidimensional representation of organic molecules is easily translated into graphs, where atoms become nodes and bonds become edges. Furthermore, these models have been reported to be very accurate, some of them being able to predict even minor products.[112] On the other hand, the need to map the reacting atoms makes these models very dependent on the presence of a large amount (*ca.* tens of thousands) of correctly labeled examples on the dataset.[113] Different automated mapping models have been developed[113–115] to surpass the overreliance on curated data. Alternatively, the combination of the so-called generalized reaction templates (GRTs), which encode reaction rules learnt from a few thousand simple type reactions, and GNNs[116] or the implementation of unsupervised pretraining approaches could also alleviate the need to curate large, annotated datasets (Figure 15A).[117]

In later years, the development of attention-based mechanism and the related transformer networks (TNs) have emerged as an alternative to GNNs to predict chemical reactivity.[113] The main advantage of these models is that they do not require the atom-to-atom mapping of the reactions in the training set and, instead, are able to identify patterns from the dataset in an unsupervised manner.[113] However, because these are text-based models (based on reaction SMILES) their outputs are typically more difficult to interpret. In that sense, the theory-infused neural network (TinNet),[118] which combines d-band chemisorption DFT calculations with deep neural networks; the quantum mechanics augmented graph neural network (ml-QM-GNN)[119] that combines attention-based architectures and GNNs; or the T5Chem[120] that leverages multitask learning, are examples of models aiming to provide results that are more easily interpreted.

The main limitation of both GNNs and TNs is that, ultimately, their results are highly dependent on the quality of their training data set. The need for data also increases with the complexity of the model, but to date, most curated chemical reaction data sets are proprietary and not readily available to researchers,[12] with the prominent exception of the USPTO dataset, compiled from reactions appearing in patents filled in the United States of America,[121] and the datasets that stem from it. To contribute to the advancement of data-driven approaches, the Open Reaction Database (ODR)[12] initiative was recently proposed as a community-driven effort to provide high quality chemical data. Their authors conceived it as a "live document" that should be highly adaptable to different needs of its community of users. This approach could potentially attenuate the well documented problem of biases towards high-yield reactions that is prevalent in datasets. However, it remains to be seen if this kind of open approaches will be enough to fulfill the needs for the most data-hungry models, especially regarding reactions for which generating large amounts of labeled data is too time-consuming or expensive. Another commonly cited short-coming of trained models is their ability to predict reactions not represented in the training dataset. In that sense, recent efforts have attempted to address this limitation by developing models able to reliably perform so-called zero-shot predictions of reactivity not seen in the dataset.[122,123] In summary, computational models are an essential component of reaction charting efforts and their importance is likely to keep increasing in the coming years, especially if the already present syner-

© 2024 The Authors. Advanced Synthesis & Catalysis published by Wiley-VCH GmbH

16154169, 2024, 4, Downloaded from https://onlinelibrary.wiley.com/doi/10.1002/adsc.202301205 by Readcube (Labtiva Inc.), Wiley Online Library on [02/07/2024]. See the Terms and Conditions (https://onlinelibrary.wiley.com/terms-and-conditions) on Wiley Online Library for rules of use; OA articles are governed by the applicable Creative Commons License

gies with automation efforts developed in parallel are fully leveraged.[27]

7. Conclusions and Outlook

In this appraisal we have presented several charting approaches dealing with distinct endeavors, unified by the common nexus of organic chemistry. The philosophy of scanning experimental, computational, or structural parameters either systematically or in a hypothesis-driven manner greatly helps to gain global knowledge of the system. Moreover, it yields valuable results in a fast way, especially while dealing with complex systems where prediction-based approaches may not be straightforward, as the final outcome depends on the combination of many parameters. It has to be said that several classical works appearing in the review were not quoted by the authors as charting or mapping. However, in our opinion, they broadly involve the concept, as they define the reaction space around a system, often through a classical screening approach. Remarkable examples have been commented belonging to process chemistry, biological and medicinal chemistry, catalysis, reaction discovery, and computational methods, which are becoming landmarks in the field. Considering the already established success of the approach in disentangling complex questions in different contexts, we firmly believe that charting approaches will have a key role in organic chemistry research, especially when dealing with multiparametric problems.

Acknowledgements

Funding from Ministerio de Ciencia e Innovación (Spain), the Agencia Estatal de Investigación and the European Regional Development Fund (EDFR) (PID2022-139180OB-I00 and PID2020-115683GA-I00) is gratefully acknowledged. P.N.R. thanks Ministerio de Ciencia e Innovación (Spain) for a predoctoral grant. J J.-J is member of the Computational Biology and Drug Design Consolidated Research Group supported by the Generalitat de Catalunya (2021SGR00671) and acknowledges support from grant CEX2021-001202-M financed by MCIN/AEI/10.13039/501100011033. We warmly thank Dr Antonio Ramirez (Bristol Myers-Squibb Company, New Brunswick (USA) for useful comments. The authors acknowledge BioRender.com for assistance with figure creation.

References

[1] G. S. Omenn, *Science* **2006**, *314*, 1696–1704.
[2] I. Ojima, *Front. Chem.* **2017**, *5*, 52, DOI: 10.3389/fchem.2017.00052.
[3] J.-L. Reymond, *Acc. Chem. Res.* **2015**, *48*, 722–730.
[4] C. M. Dobson, *Nature* **2004**, *432*, 824–828.
[5] P. S. Gromski, A. B. Henson, J. M. Granda, L. Cronin, *Nat. Chem. Rev.* **2019**, *3*, 119–128.
[6] C. Lipinski, A. Hopkins, *Nature* **2004**, *432*, 855–861.
[7] O. O. Grygorenko, D. S. Radchenko, I. Dziuba, A. Chuprina, K. E. Gubina, Y. S. Moroz, *iScience* **2020**, *23*, 101681.
[8] P. M. Murray, S. N. G. Tyler, J. D. Moseley, *Org. Process Res. Dev.* **2013**, *17*, 40–46.
[9] S. Stocker, G. Csányi, K. Reuter, J. T. Margraf, *Nat. Commun.* **2020**, *11*, 5505, DOI: 10.1038/s41467-020-19267-x.
[10] G. Ashkenasy, T. M. Hermans, S. Otto, A. F. Taylor, *Chem. Soc. Rev.* **2017**, *46*, 2543–2554.
[11] E. O. Johnson, D. T. Hung, *ACS Chem. Biol.* **2019**, *14*, 2497–2511.
[12] S. M. Kearnes, M. R. Maser, M. Wleklinski, A. Kast, A. G. Doyle, S. D. Dreher, J. M. Hawkins, K. F. Jensen, C. W. Coley, *J. Am. Chem. Soc.* **2021**, *143*, 18820–18826.
[13] M. C. Kozlowski, *Org. Lett.* **2022**, *24*, 7247–7249.
[14] M. P. Maloney, C. W. Coley, S. Genheden, N. Carson, P. Helquist, P.-O. Norrby, O. Wiest, *J. Org. Chem.* **2023**, *88*, 5239–5241.
[15] H. Shalit Peleg, A. Milo, *Angew. Chem. Int. Ed.* **2023**, *62*, e202219070. *Angew. Chem.* **2023**, *135*, e202219070.
[16] C. J. Taylor, A. Pomberger, K. C. Felton, R. Grainger, M. Barecka, T. W. Chamberlain, R. A. Bourne, C. N. Johnson, A. A. Lapkin, *Chem. Rev.* **2023**, *123*, 3089–3126.
[17] D. Kaiser, J. Yang, G. Wuitschik, *Org. Process Res. Dev.* **2018**, *22*, 1222–1235.
[18] S. A. Weissman, N. G. Anderson, *Org. Process Res. Dev.* **2015**, *19*, 1605–1633.
[19] P. M. Murray, F. Bellany, L. Benhamou, D.-K. Bučar, A. B. Tabor, T. D. Sheppard, *Org. Biomol. Chem.* **2016**, *14*, 2373–2384.
[20] Guidance for Industry. Q11 Development and Manufacture of Drug Substances. US Department of Health and Human Services. Food and Drug Administration. Center for Drug Evaluation and Research (CDER). Center for Biologics Evaluation and Research (CBER). November 2012 ICH.
[21] J. L. Burt, A. D. Braem, A. Ramirez, B. Mudryk, L. Rossano, S. Tummala, *J. Pharm. Innov.* **2011**, *6*, 181–192.
[22] A. Ramirez, D. M. Hallow, M. D. B. Fenster, S. Lou, N. R. Domagalski, S. Tummala, S. Srivastava, L. A. Hobson, *Org. Process Res. Dev.* **2016**, *20*, 1781–1791.
[23] M. Baumann, T. S. Moody, M. Smyth, S. Wharry, *Org. Process Res. Dev.* **2020**, *24*, 1802–1813.
[24] B. P. Loren, H. S. Ewan, L. Avramova, C. R. Ferreira, T. J. P. Sobreira, K. Yammine, H. Liao, R. G. Cooks, D. H. Thompson, *Sci. Rep.* **2019**, *9*, 14745.
[25] C. J. Taylor, K. C. Felton, D. Wigh, M. I. Jeraal, R. Grainger, G. Chessari, C. N. Johnson, A. A. Lapkin, *ACS Cent. Sci.* **2023**, *9*, 957–968.
[26] F. Häse, L. M. Roch, A. Aspuru-Guzik, *Trends Chem.* **2019**, *3*, 282–291.

© 2024 The Authors. Advanced Synthesis & Catalysis published by Wiley-VCH GmbH

16154169, 2024, 4, Downloaded from https://onlinelibrary.wiley.com/doi/10.1002/adsc.202301205 by Readcube (Labtiva Inc.), Wiley Online Library on [02/07/2024]. See the Terms and Conditions (https://onlinelibrary.wiley.com/terms-and-conditions) on Wiley Online Library for rules of use; OA articles are governed by the applicable Creative Commons License

[27] S. H. M. Mehr, M. Craven, A. I. Leonov, G. Keenan, L. Cronin, *Science* **2020**, *370*, 101–108.
[28] M. Christensen, L. P. E. Yunker, F. Adedeji, F. Häse, L. M. Roch, T. Gensch, G. dos Passos Gomes, T. Zepel, M. S. Sigman, A. Aspuru-Guzik, J. E. Hein, *Commun. Chem.* **2021**, *4*, 112, DOI: 10.1038/s42004-021-00550-x.
[29] M. D. A. Boiko, R. MacKnight, B. Kline, G. Gomes, *Nature* **2023**, *624*, 570–578.
[30] M. Mammen, S.-K. Choi, G. M. Whitesides, *Angew. Chem. Int. Ed.* **1998**, *37*, 2754–2794. *Angew. Chem.* **1998**, *110*, 2908–2953.
[31] J. A. Vance, N. K. Devaraj, *J. Am. Chem. Soc.* **2021**, *143*, 8223–8231.
[32] C. M. Paleos, A. Pantos, *Acc. Chem. Res.* **2014**, *47*, 1475–1482.
[33] K. A. Podolsky, N. K. Devaraj, *Nat. Chem. Rev.* **2021**, *5*, 676–694.
[34] A. Bhattacharya, H. Niederholtmeyer, K. A. Podolsky, R. Bhattacharya, J.-J. Song, R. J. Brea, C.-H. Tsai, S. K. Sinha, N. K. Devaraj, *PNAS* **2020**, *117*, 18206–18215.
[35] M. Vendrell, D. Zhai, J. C. Er, Y.-T. Chang, *Chem. Rev.* **2012**, *112*, 4391–4420.
[36] A. Fernandez, N. Kielland, A. Makda, N. O. Carragher, M. C. González-García, L. Espinar-Barranco, J. A. González-Vera, A. Orte, R. Lavilla, M. Vendrell, *RSC Chem. Biol.* **2022**, *3*, 1251–1259.
[37] K. E. Gilbert, A. Vuorinen, A. Aatkar, P. Pogány, J. Pettinger, E. K. Grant, J. M. Kirkpatrick, K. Rittinger, D. House, G. A. Burley, J. T. Bush, *ACS Chem. Biol.* **2023**, *18*, 285–295.
[38] A. Aatkar, A. Vuorinen, O. E. Longfield, K. Gilbert, R. Peltier-Heap, C. D. Wagner, F. Zappacosta, K. Rittinger, C. Chung, D. House, N. C. O. Tomkinson, J. T. Bush, *ACS Chem. Biol.* **2023**, *18*, 1926–1937.
[39] S. W. Huth, J. V. Oakley, C. P. Seath, J. B. Geri, A. D. Trowbridge, D. L. Parker, F. P. Rodriguez-Rivera, A. G. Schwaid, C. Ramil, K. A. Ryu, C. H. White, O. O. Fadeyi, R. C. Oslund, D. W. C. MacMillan, *J. Am. Chem. Soc.* **2023**, *145*, 16289–16296.
[40] A. Cherkasov, *Nat. Chem. Biol.* **2023**, *19*, 667–668.
[41] D. C. Blakemore, L. Castro, I. Churcher, D. C. Rees, A. W. Thomas, D. M. Wilson, A. Wood, *Nat. Chem.* **2018**, *10*, 383–394.
[42] O. O. Grygorenko, D. M. Volochnyuk, S. V. Ryabukhin, D. B. Judd, *Chem. Eur. J.* **2020**, *26*, 1196–1237.
[43] T. Cernak, K. D. Dykstra, S. Tyagarajan, P. Vachal, S. W. Krska, *Chem. Soc. Rev.* **2016**, *45*, 546–576.
[44] L. Guillemard, N. Kaplaneris, L. Ackermann, M. J. Johansson, *Nat. Chem. Rev.* **2021**, *5*, 522–545.
[45] Y. Wang, S. Dana, H. Long, Y. Xu, Y. Li, N. Kaplaneris, L. Ackermann, *Chem. Rev.* **2023**, *123*, 11269–11335.
[46] M. S. Lall, A. Bassyouni, J. Bradow, M. Brown, M. Bundesmann, J. Chen, G. Ciszewski, A. E. Hagen, D. Hyek, S. Jenkinson, B. Liu, R. S. Obach, S. Pan, U. Reilly, N. Sach, D. J. Smaltz, D. K. Spracklin, J. Starr, M. Wagenaar, G. S. Walker, *J. Med. Chem.* **2020**, *63*, 7268–7292.
[47] A. M. Szpilman, E. M. Carreira, *Angew. Chem. Int. Ed.* **2010**, *49*, 9592–9628. *Angew. Chem.* **2010**, *122*, 9786–9823.
[48] C. Hui, Z. Wang, S. Wang, C. Xu, *Org. Chem. Front.* **2022**, *9*, 1451–1457.
[49] B. A. Wright, A. Matviitsuk, M. J. Black, P. García-Reynaga, L. E. Hanna, A. T. Herrmann, M. K. Ameriks, R. Sarpong, T. P. Lebold, *J. Am. Chem. Soc.* **2023**, *145*, 10960–10966.
[50] T. J. Pearson, R. Shimazumi, J. L. Driscoll, B. D. Dherange, D.-I. Park, M. D. Levin, *Science* **2023**, *381*, 1474–1479.
[51] C. Fraser, J. C. Dawson, R. Dowling, D. R. Houston, J. T. Weiss, A. F. Munro, M. Muir, L. Harrington, S. P. Webster, M. C. Frame, V. G. Brunton, E. E. Patton, N. O. Carragher, A. Unciti-Broceta, *J. Med. Chem.* **2016**, *59*, 4697–4710.
[52] A. Yoshimori, T. Tanoue, J. Bajorath, *ACS Omega* **2019**, *4*, 7061–7069.
[53] H. van Hattum, H. Waldmann, *J. Am. Chem. Soc.* **2014**, *136*, 11853–11859.
[54] G. Karageorgis, D. J. Foley, L. Laraia, S. Brakmann, H. Waldmann, *Angew. Chem. Int. Ed.* **2021**, *60*, 15705–15723. *Angew. Chem.* **2021**, *133*, 15837–15855.
[55] R. J. Young, S. L. Flitsch, M. Grigalunas, P. D. Leeson, R. J. Quinn, N. J. Turner, H. Waldmann, *JACS Au* **2022**, *2*, 2400–2416.
[56] M. Grigalunas, S. Brakmann, H. Waldmann, *J. Am. Chem. Soc.* **2022**, *144*, 3314–3329.
[57] J. Ceballos, M. Schwalfenberg, G. Karageorgis, E. S. Reckzeh, S. Sievers, C. Ostermann, A. Pahl, M. Sellstedt, J. Nowacki, M. A. Carnero Corrales, J. Wilke, L. Laraia, K. Tschapalda, M. Metz, D. A. Sehr, S. Brand, K. Winklhofer, P. Janning, S. Ziegler, H. Waldmann, *Angew. Chem. Int. Ed.* **2019**, *58*, 17016–17025; *Angew. Chem.* **2019**, *131*, 17172–17181.
[58] J. Liu, J. Flegel, F. Otte, A. Pahl, S. Sievers, C. Strohmann, H. Waldmann, *Angew. Chem. Int. Ed.* **2021**, *60*, 21384–21395. *Angew. Chem.* **2021**, *133*, 21554–21565.
[59] Y. Tong, Y. Lee, X. Liu, J. L. Childs-Disney, B. M. Suresh, R. I. Benhamou, C. Yang, W. Li, M. G. Costales, H. S. Haniff, S. Sievers, D. Abegg, T. Wegner, T. O. Paulisch, E. Lekah, M. Grefe, G. Crynen, M. Van Meter, T. Wang, Q. M. R. Gibaut, J. L. Cleveland, A. Adibekian, F. Glorius, H. Waldmann, M. D. Disney, *Nature* **2023**, *618*, 169–179.
[60] I. Ghosh, N. Shlapakov, T. A. Karl, J. Düker, M. Nikitin, J. V. Burykina, V. P. Ananikov, B. König, *Nature* **2023**, *619*, 87–93.
[61] X. Gao, H. B. Kagan, *Chirality* **1998**, *10*, 120–124.
[62] T. Satyanarayana, H. B. Kagan, *Adv. Synth. Catal.* **2005**, *347*, 737–748.
[63] A. Duursma, A. J. Minnaard, B. L. Feringa, *Tetrahedron* **2002**, *58*, 5773–5778.
[64] J. Rein, S. D. Rozema, O. C. Langner, S. B. Zacate, M. A. Hardy, J. C. Siu, B. Q. Mercado, M. S. Sigman, S. J. Miller, S. Lin, *Science* **2023**, *380*, 706–712.

© 2024 The Authors. Advanced Synthesis & Catalysis published by Wiley-VCH GmbH

16154169, 2024, 4, Downloaded from https://onlinelibrary.wiley.com/doi/10.1002/adsc.202301205 by Readcube (Labtiva Inc.), Wiley Online Library on [02/07/2024]. See the Terms and Conditions (https://onlinelibrary.wiley.com/terms-and-conditions) on Wiley Online Library for rules of use; OA articles are governed by the applicable Creative Commons License

[65] H. Kim, G. Gerosa, J. Aronow, P. Kasaplar, J. Ouyang, J. B. Lingnau, P. Guerry, C. Farès, B. List, *Nat. Commun.* **2019**, *10*, 770, DOI: 10.1038/s41467-019-08374-z.
[66] C. C. Wagen, S. E. McMinn, E. E. Kwan, E. N. Jacobsen, *Nature* **2022**, *610*, 680–686.
[67] J. M. Lassaletta, *Nat. Commun.* **2020**, *11*, 3787.
[68] N. H. Angello, V. Rathore, W. Beker, A. Wołos, E. R. Jira, R. Roszak, T. C. Wu, C. M. Schroeder, A. Aspuru-Guzik, B. A. Grzybowski, M. D. Burke, *Science* **2022**, *378*, 399–405.
[69] I. O. Betinol, J. Lai, S. Thakur, J. P. Reid, *J. Am. Chem. Soc.* **2023**, *145*, 12870–12883.
[70] J. P. Liles, C. Rouget-Virbel, J. L. H. Wahlman, R. Rahimoff, J. M. Crawford, A. Medlin, V. S. O'Connor, J. Li, V. A. Roytman, F. D. Toste, M. S. Sigman, *Chem* **2023**, *9*, 1518–1537.
[71] Z.-J. Zhang, S.-W. Li, J. C. A. Oliveira, Y. Li, X. Chen, S.-Q. Zhang, L.-C. Xu, T. Rogge, X. Hong, L. Ackermann, *Nat. Commun.* **2023**, *14*, 3149, DOI: 10.1038/s41467-023-38872-0.
[72] H. Zhao, I. Akritopoulou-Zanze, *Expert Opin. Drug Discovery* **2010**, *5*, 123–134.
[73] K. D. Collins, T. Gensch, F. Glorius, *Nat. Chem.* **2014**, *6*, 859–871.
[74] M. N. Hopkinson, A. Gómez-Suárez, M. Teders, B. Sahoo, F. Glorius, *Angew. Chem. Int. Ed.* **2016**, *55*, 4361–4366. *Angew. Chem.* **2016**, *128*, 4434–4439.
[75] A. McNally, C. K. Prier, D. W. C. MacMillan, *Science* **2011**, *334*, 1114–1117.
[76] D. W. Robbins, J. F. Hartwig, *Science* **2011**, *333*, 1423–1427.
[77] Y. Chen, A. S. Kamlet, J. B. Steinman, D. R. Liu, *Nat. Chem.* **2011**, *3*, 146–153.
[78] B. Mahjour, Y. Shen, W. Liu, T. Cernak, *Nature* **2020**, *580*, 71–75.
[79] P. Nadal Rodríguez, O. Ghashghaei, A. M. Schoepf, S. Benson, M. Vendrell, R. Lavilla, *Angew. Chem. Int. Ed.* **2023**, *62*, e202303889. *Angew. Chem.* **2023**, *135*, e202303889.
[80] V. Trudel, C. H. Tien, A. Trofimova, A. K. Yudin, *Nat. Chem. Rev.* **2021**, *5*, 604–623.
[81] S. Preciado, E. Vicente-García, S. Llabrés, F. J. Luque, R. Lavilla, *Angew. Chem. Int. Ed.* **2012**, *51*, 6874–6877. *Angew. Chem.* **2012**, *124*, 6980–6983.
[82] N. Isambert, M. Cruz, M. J. Arévalo, E. Gómez, R. Lavilla, *Org. Lett.* **2007**, *9*, 4199–4202.
[83] O. Jiménez, G. de la Rosa, R. Lavilla, *Angew. Chem. Int. Ed.* **2005**, *44*, 6521–6525. *Angew. Chem.* **2005**, *117*, 6679–6683.
[84] L. Cala, A. Mendoza, F. J. Fañanás, F. Rodríguez, *Chem. Commun.* **2013**, *49*, 2715–2717.
[85] C. N. Prieto Kullmer, J. A. Kautzky, S. W. Krska, T. Nowak, S. D. Dreher, D. W. C. MacMillan, *Science* **2022**, *376*, 532–539.
[86] K. D. Collins, F. Glorius, *Nat. Chem.* **2013**, *5*, 597–601.
[87] B. Mahjour, R. Zhang, Y. Shen, A. McGrath, R. Zhao, O. G. Mohamed, Y. Lin, Z. Zhang, J. L. Douthwaite, A. Tripathi, T. Cernak, *Nat. Commun.* **2023**, *14*, 3924, DOI: 10.1038/s41467-023-38872-0.
[88] J. M. Granda, L. Donina, V. Dragone, D. L. Long, L. Cronin, *Nature* **2018**, *559*, 377–381.
[89] K. Jorner, A. Tomberg, C. Bauer, C. Sköld, P.-O. Norrby, *Nat. Chem. Rev.* **2021**, *5*, 240–255.
[90] K. Molga, S. Szymkuć, B. A. Grzybowski, *Acc. Chem. Res.* **2021**, *54*, 1094–1106.
[91] W.-B. Liu, D. P. Schuman, Y.-F. Yang, A. A. Toutov, Y. Liang, H. F. T. Klare, N. Nesnas, M. Oestreich, D. G. Blackmond, S. C. Virgil, S. Banerjee, R. N. Zare, R. H. Grubbs, K. N. Houk, B. M. Stoltz, *J. Am. Chem. Soc.* **2017**, *139*, 6867–6879.
[92] M. Lanzi, T. Rogge, T. S. Truong, K. N. Houk, J. Wencel-Delord, *J. Am. Chem. Soc.* **2023**, *145*, 345–358.
[93] C. Xu, H. Zhang, S. Lan, J. Liu, S. Yang, Q. Zhang, X. Fang, *Angew. Chem. Int. Ed.* **2023**, *62*, e202219064. *Angew. Chem.* **2023**, *135*, e202219064.
[94] S. Llabrés, E. Vicente-García, S. Preciado, C. Guiu, R. Pouplana, R. Lavilla, F. J. Luque, *Chem. Eur. J.* **2013**, *19*, 13355–13361.
[95] J. Hermann, J. Spencer, K. Choo, A. Mezzacapo, W. M. C. Foulkes, D. Pfau, G. Carleo, F. Noé, *Nat. Chem. Rev.* **2023**, *7*, 692–109.
[96] P. Schwaller, D. Probst, A. C. Vaucher, V. H. Nair, D. Kreutter, T. Laino, J. L. Reymond, *Nat. Mach. Intell.* **2021**, *3*, 144–152.
[97] J. Behler, M. Parrinello, *Phys. Rev. Lett.* **2007**, *98*, 146401, DOI: 10.1103/PhysRevLett.98.146401.
[98] J. S. Smith, O. Isayev, A. E. Roitberg, *Chem. Sci.* **2017**, *8*, 3192–3203.
[99] J. S. Smith, B. T. Nebgen, R. Zubatyuk, N. Lubbers, C. Devereux, K. Barros, S. Tretiak, O. Isayev, A. E. Roitberg, *Nat. Commun.* **2019**, *10*, 2903, DOI: 10.1038/s41467-019-10827-4.
[100] S. Zhang, M. Z. Makós, R. B. Jadrich, E. Kraka, K. Barros, B. T. Nebgen, S. Tretiak, O. Isayev, N. Lubbers, R. A. Messerly, J. S. Smith, **2022**, ChemRxiv preprint DOI: 10.26434/chemrxiv-2022-15ct6-v3.
[101] T. A. Young, T. Johnston-Wood, H. Zhang, F. Duarte, *Phys. Chem. Chem. Phys.* **2022**, *24*, 20820–20827.
[102] S. Axelrod, E. Shakhnovich, R. Gómez-Bombarelli, *ACS Cent. Sci.* **2023**, *9*, 166–176.
[103] C. A. Grambow, L. Pattanaik, W. H. Green, *J. Phys. Chem. Lett.* **2020**, *11*, 2992–2997.
[104] E. Marques, S. de Gendt, G. Pourtois, M. J. van Setten, *J. Chem. Inf. Model.* **2023**, *63*, 1454–1461.
[105] S. Choi, *Nat. Commun.* **2023**, *14*, 1168, DOI: 10.1038/s41467-023-36823-3.
[106] M. Eckhoff, M. Reiher, *J. Chem. Theory Comput.* **2023**, *19*, 3509–3525.
[107] M. Meuwly, *Chem. Rev.* **2021**, *121*, 10218–10239.
[108] B. J. Shields, J. Stevens, J. Li, M. Parasram, F. Damani, J. I. Martinez Alvarado, J. M. Janey, R. P. Adams, A. G. Doyle, *Nature* **2021**, *590*, 89–96.
[109] E. Shim, J. A. Kammeraad, Z. Xu, A. Tewari, T. Cernak, P. M. Zimmerman, *Chem. Sci.* **2022**, *13*, 6655–6668.

© 2024 The Authors. Advanced Synthesis & Catalysis published by Wiley-VCH GmbH

16154169, 2024, 4, Downloaded from https://onlinelibrary.wiley.com/doi/10.1002/adsc.202301205 by Readcube (Labtiva Inc.), Wiley Online Library on [02/07/2024]. See the Terms and Conditions (https://onlinelibrary.wiley.com/terms-and-conditions) on Wiley Online Library for rules of use; OA articles are governed by the applicable Creative Commons License

[110] N. I. Rinehart, R. K. Saunthwal, J. Wellauer, A. F. Zahrt, L. Schlemper, A. S. Shved, R. Bigler, S. Fantasia, S. E. Denmark, *Science* **2023**, *381*, 965–972.
[111] C. W. Coley, W. Jin, L. Rogers, T. F. Jamison, T. S. Jaakkola, W. H. Green, R. Barzilay, K. F. Jensen, *Chem. Sci.* **2019**, *10*, 370–377.
[112] C. W. Coley, R. Barzilay, T. S. Jaakkola, W. H. Green, K. F. Jensen, *ACS Cent. Sci.* **2017**, *3*, 434–443.
[113] P. Schwaller, B. Hoover, J.-L. Reymond, H. Strobelt, T. Laino, *Sci. Adv.* **2021**, *7*, eabe4166.
[114] W. Jaworski, S. Szymkuć, B. Mikulak-Klucznik, K. Piecuch, T. Klucznik, M. Kaźmierowski, J. Rydzewski, A. Gambin, B. A. Grzybowski, *Nat. Commun.* **2019**, *10*, 1434, DOI: 10.1038/s41467-019-09440-2.
[115] A. Lin, N. Dyubankova, T. I. Madzhidov, R. I. Nugmanov, J. Verhoeven, T. R. Gimadiev, V. A. Afonina, Z. Ibragimova, A. Rakhimbekova, P. Sidorov, A. Gedich, R. Suleymanov, R. Mukhametgaleev, J. Wegner, H. Ceulemans, A. Varnek, *Mol. Inf.* **2022**, *41*, 2100138, DOI: 10.1002/minf.202100138.
[116] S. Chen, Y. Jung, *Nat. Mach. Intell.* **2022**, *4*, 772–780.
[117] M. Wen, S. M. Blau, X. Xie, S. Dwaraknath, K. A. Persson, *Chem. Sci.* **2022**, *13*, 1446–1458.
[118] S.-H. Wang, H. S. Pillai, S. Wang, L. E. K. Achenie, H. Xin, *Nat. Commun.* **2021**, *12*, 52808, DOI: 10.10.1038/s41467-021-25639-8.
[119] T. Stuyver, C. W. Coley, *J. Chem. Phys.* **2022**, *156*, 084104, DOI: 10.1063/5.0079574.
[120] J. Lu, Y. Zhang, *J. Chem. Inf. Model.* **2022**, *62*, 1376–1387.
[121] [dataset] D. Lowe, **2017**, Chemical reactions from US patents (1976-Sep2016), figshare. Dataset, DOI: 10.6084/m9.figshare.5104873.v1.
[122] P. Seidl, P. Renz, N. Dyubankova, P. Neves, J. Verhoeven, J. K. Wegner, M. Segler, S. Hochreiter, G. Klambauer, *J. Chem. Inf. Model.* **2022**, *62*, 2111–2120.
[123] A. Su, X. Wang, L. Wang, C. Zhang, Y. Wu, X. Wu, Q. Zhao, H. Duan, *Phys. Chem. Chem. Phys.* **2022**, *24*, 10280–10291.

© 2024 The Authors. Advanced Synthesis & Catalysis published by Wiley-VCH GmbH

16154169, 2024, 4, Downloaded from https://onlinelibrary.wiley.com/doi/10.1002/adsc.202301205 by Readcube (Labtiva Inc.), Wiley Online Library on [02/07/2024]. See the Terms and Conditions (https://onlinelibrary.wiley.com/terms-and-conditions) on Wiley Online Library for rules of use; OA articles are governed by the applicable Creative Commons License

Annex II

Other Publications Derived from the Thesis

International Journal of
Molecular Sciences

MDPI

Article

The Prohibitin-Binding Compound Fluorizoline Activates the Integrated Stress Response through the eIF2α Kinase HRI

Ismael Sánchez-Vera [1], Sonia Núñez-Vázquez [1], José Saura-Esteller [1], Ana M. Cosialls [1], Judith Heib [1], Pau Nadal Rodríguez [2], Ouldouz Ghashghaei [2], Rodolfo Lavilla [2], Gabriel Pons [1], Joan Gil [1,*,†] and Daniel Iglesias-Serret [3,4,*,†]

1 Departament de Ciències Fisiològiques, Facultat de Medicina i Ciències de la Salut, Universitat de Barcelona, Oncobell-IDIBELL (Institut d'Investigació Biomèdica de Bellvitge), 08907 L'Hospitalet de Llobregat, Spain; isanchezvera@ub.edu (I.S.-V.)
2 Laboratory of Medical Chemistry, Faculty of Pharmacy and Food Sciences, Institute of Biomedicine (IBUB), University of Barcelona, 08028 Barcelona, Spain
3 Departament d'Infermeria Fonamental i Medicoquirúrgica, Facultat de Medicina i Ciències de la Salut, Universitat de Barcelona, 08907 L'Hospitalet de Llobregat, Spain
4 Facultat de Medicina, Universitat de Vic-Universitat Central de Catalunya (UVic-UCC), 08500 Vic, Spain
* Correspondence: jgil@ub.edu (J.G.); d.iglesias.serret@ub.edu (D.I.-S.); Tel.: +34-934-029-095 (J.G.); +34-934-024-225 (D.I.-S.)
† These authors contributed equally to this work.

Abstract: Fluorizoline is a synthetic molecule that induces apoptosis, by selectively targeting prohibitins (PHBs), through induction of the BH3-only protein NOXA. This induction is transcriptionally regulated by the integrated stress response (ISR)-related transcription factors ATF3 and ATF4. Here, we evaluate the role of the four eIF2α kinases, to decipher which is responsible for the mechanism of ISR activation triggered by fluorizoline in HeLa and HAP1 cells. First, we demonstrated the involvement of the eIF2α kinases using ISR inhibitor (ISRIB) and by simultaneous downregulation of all four eIF2α kinases, as both approaches were able to increase cell resistance to fluorizoline-induced apoptosis. Furthermore, we confirmed that fluorizoline treatment results in endoplasmic reticulum (ER) stress, as evidenced by PERK activation. Despite PERK activation, this kinase was not directly involved in the ISR activation by fluorizoline. In this regard, we found that the eIF2α kinases are capable of compensating for each other's loss of function. Importantly, we demonstrated that the mitochondrial-stress-related eIF2α kinase HRI mediates ISR activation after fluorizoline treatment.

Keywords: fluorizoline; prohibitin; apoptosis; ER-stress; mitochondrial-stress; ISR; HRI

check for updates

Citation: Sánchez-Vera, I.; Núñez-Vázquez, S.; Saura-Esteller, J.; Cosialls, A.M.; Heib, J.; Nadal Rodríguez, P.; Ghashghaei, O.; Lavilla, R.; Pons, G.; Gil, J.; et al. The Prohibitin-Binding Compound Fluorizoline Activates the Integrated Stress Response through the eIF2α Kinase HRI. *Int. J. Mol. Sci.* **2023**, *24*, 8064. https://doi.org/10.3390/ijms24098064

Academic Editor: Gabriella Simbula

Received: 24 March 2023
Revised: 24 April 2023
Accepted: 27 April 2023
Published: 29 April 2023

Copyright: © 2023 by the authors. Licensee MDPI, Basel, Switzerland. This article is an open access article distributed under the terms and conditions of the Creative Commons Attribution (CC BY) license (https://creativecommons.org/licenses/by/4.0/).

1. Introduction

Fluorizoline is a synthetic molecule that induces apoptosis through selective binding to prohibitin 1 and 2 (PHB1 and PHB2) [1,2]. These proteins are mainly located in the inner mitochondrial membrane (IMM), conforming hetero-oligomeric ring-like complexes. In the IMM, the PHB complex can regulate several processes related to survival, apoptosis, and cell proliferation, among others [3,4].

A growing body of evidence links prohibitins to tumor development. Thus, it has been demonstrated that PHBs mediate cell survival and tumor progression [5–7]. Moreover, PHB1 and PHB2 are highly expressed in a wide variety of primary tumors [3], which further supports this pro-tumorigenic role of PHBs. Interestingly, fluorizoline treatment induces apoptosis in a wide range of cancer cell lines [1,2,8–12] and primary samples derived from leukemia and lymphoma patients [13–16]. Therefore, fluorizoline binding to PHBs clearly inhibits its pro-survival function, emerging as a potential target for cancer treatment.

We have previously described that fluorizoline mainly accumulates in the mitochondria, likely due to its binding to mitochondrial PHBs [1,2]. This binding causes mitochondrial fragmentation, cristae disruption, and reactive oxygen species (ROS) [2,8]. These

findings suggest a stressed mitochondrial network, which is compatible with defects in the PHB–mitochondrial complex [17]. Interestingly, one of the best-characterized responses to mitochondrial stress is the mitochondrial unfolded protein response (UPR^{mt}), which in turn converges on integrated stress response (ISR) activation [18].

The ISR is a central and evolutionarily conserved adaptive network that is activated in response to various extracellular or intracellular stresses [19]. This pathway has as its central event the phosphorylation of the eukaryotic initiation factor 2 alpha (eIF2α) on Ser51, which leads to general suppression of cap-dependent translation. Thereby, only a subset of mRNAs can be translated in a cap-independent manner, such as the activating transcription factor 4 (ATF4), which can promote pro-survival or pro-apoptotic processes, depending on the stress duration and severity [20–22]. Four eIF2α kinases are responsible for the phosphorylation of this factor in response to various stress stimuli: protein kinase double-stranded RNA-dependent (PKR) was initially found to directly react to viral infection, PKR-like ER kinase (PERK) is activated upon ER-stress, haeme-regulated inhibitor (HRI) responds to haeme deprivation, and amino acid deprivation induces the activation of general control non-derepressible-2 (GCN2) kinase. Although each kinase was initially identified as responding to these stimuli, they can also respond to other types of stresses. Moreover, they can eventually cooperate and compensate for the loss of each other [19].

We have recently reported that fluorizoline activates the ISR signaling pathway in different cell lines. On the one hand, we described in HeLa and HAP1 cells that NOXA and apoptosis induction by fluorizoline or PHB downregulation are mediated by the ISR-related transcription factors ATF4 and ATF3 [9]. On the other hand, in HEK293T and U2OS cells, the activation of this pathway showed a protective role upon fluorizoline treatment [8]. Thus, depending on the cellular context, the activation of this pathway by fluorizoline has shown pro-apoptotic or pro-survival roles.

Although PHBs are mainly located in the mitochondria, we have also reported ER-stress induction after fluorizoline treatment in different cell lines, denoted by the splicing of XBP1 through the ER-stress sensor inositol-requiring enzyme 1α (IRE1α) [8]. Disturbances to different ER-related homeostatic processes can impair protein folding efficiency, leading to an accumulation of unfolded or misfolded proteins (so-called ER-stress). This pathway is regulated by PERK, IRE1α, and ATF6 in the ER membrane. Therefore, as ER-stress leads to the activation of PERK, it subsequently triggers the activation of ISR [23].

Therefore, considering that fluorizoline may be triggering both ER and mitochondrial stress, we investigated the role of the four eIF2α kinases, to determine which stress pathway was responsible for the ISR activation in HeLa and HAP1 cells. Here, we describe the role of the ISR in apoptosis execution upon fluorizoline treatment. Moreover, we identify compensatory mechanisms among the four eIF2α kinases, but strikingly the mitochondrial-stress-related kinase HRI emerges as the main driver of the ISR activation in response to fluorizoline treatment.

2. Results

2.1. ISR Inhibition Increases Cell Resistance to Apoptosis Induction by Fluorizoline

We have previously described the relevance of the transcription factor ATF4 for the induction of NOXA and apoptosis after fluorizoline treatment in HeLa and HAP1 cells [9]. Therefore, we first aimed to determine whether ATF4 was increased by the phosphorylation of eIF2α and thus by the activation of any of the eIF2α kinases. In order to investigate the eIF2α kinases' involvement, we decided to inhibit the pathway at the eIF2α level using the ISR inhibitor (ISRIB), which is capable of avoiding the effect of eIF2α phosphorylation through the activation of the eIF2B complex [19,24]. Importantly, ISRIB pretreatment significantly reduced the induction of apoptosis by fluorizoline in HeLa and HAP1 cells (Figure 1A,B). ISRIB caused a significant inhibition of ATF4 and CHOP induction (Figure 1C–F). This result confirmed that the increase in ATF4 is the consequence of the ISR activation after fluorizoline treatment. Furthermore, these data point towards the involvement of the eIF2α kinases in fluorizoline-induced apoptosis.

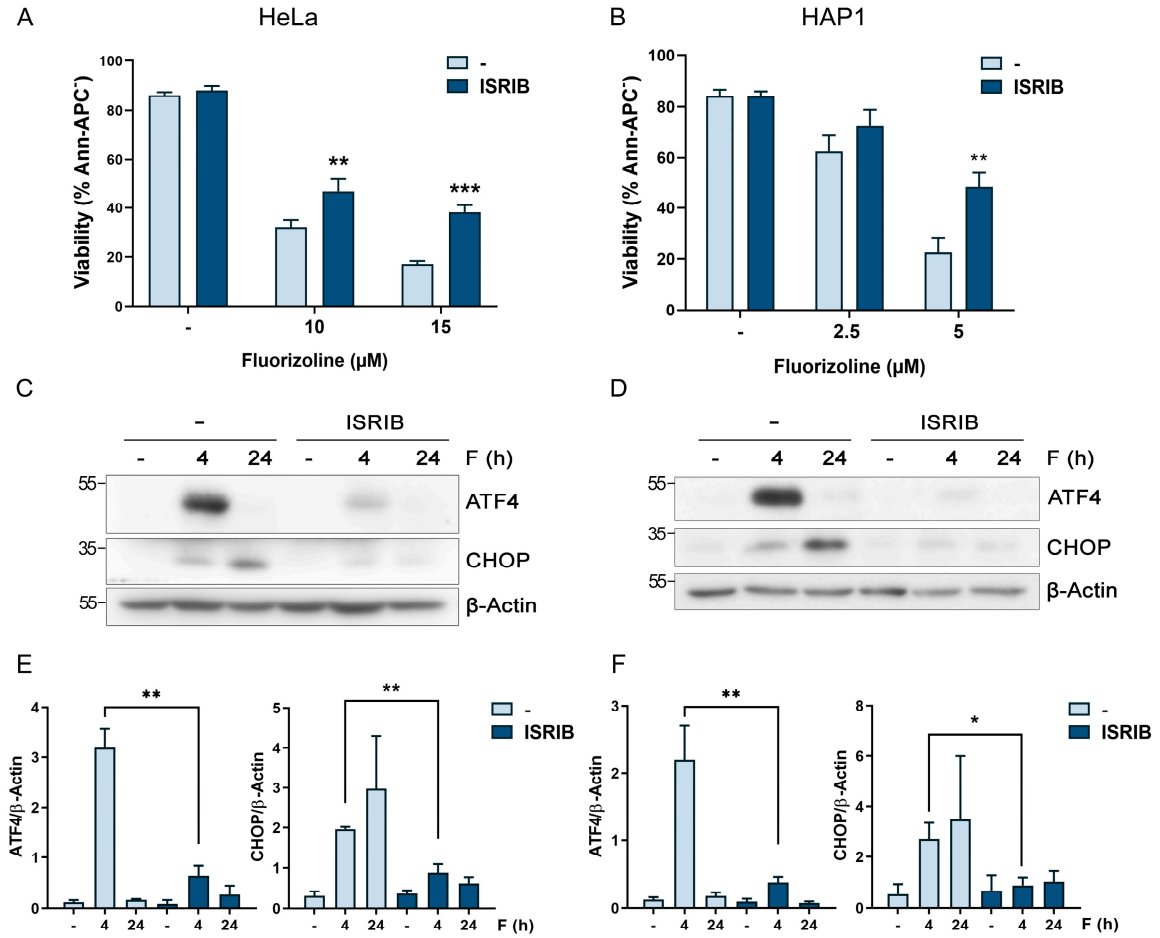

Figure 1. ISR inhibition by ISRIB increases cell resistance to fluorizoline-induced apoptosis. (**A**,**C**,**E**) HeLa and HAP1 (**B**,**D**,**F**) cells were pretreated with 15 μM ISRIB for 1 h. Then, HeLa and HAP1 cells were either untreated (-) or treated with the indicated doses of fluorizoline (F). (**A**,**B**) Cell viability was measured using flow cytometry after 24 h of fluorizoline treatment, and it is expressed as the mean ± SEM ($n \geq 3$) of the percentage of non-apoptotic cells (Ann-APC$^-$). Protein extracts from (**C**) HeLa and (**D**) HAP1 cells either untreated (-) or treated for the indicated times with 10 and 5 μM fluorizoline, respectively, were analyzed with Western blot. β-Actin was used as a loading control. These are representative images of at least three independent experiments. (**E**,**F**) Bars represent the quantification of ATF4 and CHOP relative to β-Actin band intensity. Data show the mean ± SE+M ($n \geq 3$) of the relative band intensity. * $p < 0.05$, ** $p < 0.01$, *** $p < 0.001$.

2.2. PERK Activation by Fluorizoline-Induced Stress Is Not Responsible for the Activation of the ISR

The central event of the ISR is the phosphorylation of eIF2α by any of the four eIF2α kinases. As it has been described that each kinase preferentially reacts to different environmental stresses [25,26], we investigated which kinase is activated in response to fluorizoline treatment. We previously described the presence of ER-stress after fluorizoline treatment in HEK293T and U2OS cell lines [8], and thus the eIF2α kinase PERK emerged as the first candidate to be analyzed.

To this end, we first analyzed the activation of PERK upon fluorizoline treatment. HeLa and HAP1 cells treated with fluorizoline showed an increase in PERK phosphorylation in Thr982, together with the previously reported ATF4 induction at 4 h (Figure 2A,B). These data demonstrated that fluorizoline treatment results in PERK activation. Therefore, we assessed the involvement of PERK activation after fluorizoline treatment using the PERK inhibitor AMG44 [27]. HeLa and HAP1 cells were pretreated with AMG44 and then, cells were treated with fluorizoline or thapsigargin. As expected, ATF4 induction by the ER stress inducer thapsigargin, which activates the ISR through the eIF2α

kinase PERK, was efficiently inhibited upon AMG44 pretreatment (Figure 2C,D). Otherwise, fluorizoline-induced ATF4 protein levels were not affected by the presence of AMG44 in both cell lines, indicating that ISR was still being activated independently of PERK activation (Figure 2C,D). Accordingly, chemical inhibition of PERK did not inhibit fluorizoline-induced apoptosis (Figure 2E,F).

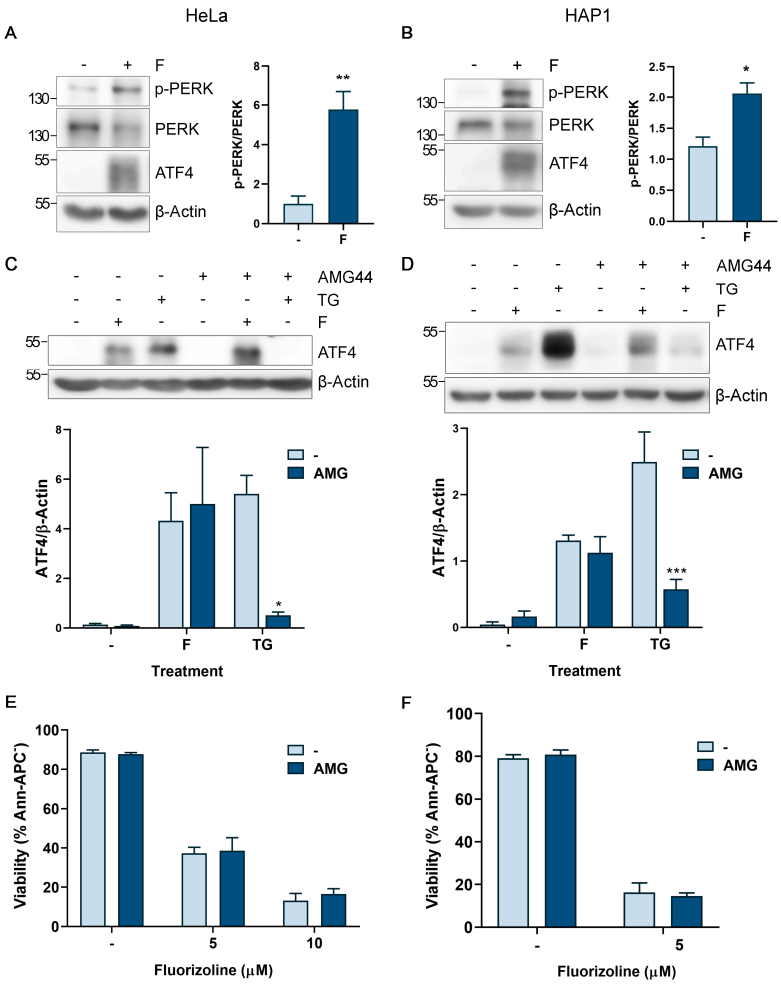

Figure 2. PERK activation is not required for fluorizoline-induced ISR activation and apoptosis. (**A**,**C**,**E**) HeLa and (**B**,**D**,**F**) HAP1 cells were either untreated (-) or pretreated (where indicated) with 2.5 μM AMG44 for 1 h. Then, cells were either untreated (-) or treated with (**A**,**C**) 10 μM fluorizoline (F) or 10 μM thapsigargin (TG) and with (**B**,**D**) 5 μM fluorizoline or 5 μM of thapsigargin. Other doses of fluorizoline are indicated in the figure. (**A**–**D**) Protein extracts from HeLa and HAP1 cells either untreated (-) or treated with fluorizoline for 4 h were analyzed with Western blot. β-Actin was used as a loading control. These are representative images of at least three independent experiments. Bars represent the quantification of (**A**,**B**) p-PERK relative to PERK band intensity and (**C**,**D**) ATF4 relative to β-Actin band intensity. Phosphorylated PERK: p-PERK. Data show the mean ± SEM (n = 3) of the relative band intensity. (**E**,**F**) Cell viability was measured using flow cytometry after 24 h of fluorizoline treatment, and it is expressed as the mean ± SEM (n = 3) of the percentage of non-apoptotic cells (Ann-APC$^-$). * $p < 0.05$, ** $p < 0.01$, *** $p < 0.001$.

We further investigated the PERK involvement in HeLa and HAP1 cells using an acute downregulation approach and also using stable cell lines downregulated for PERK expression. First, PERK was efficiently downregulated using specific siRNA (Figure 3A–F). Afterwards, apoptosis and ISR activation were assessed upon fluorizoline treatment. Additionally, thapsigargin and the mitochondrial stress inductor CCCP were used as controls for PERK and HRI activation, respectively. Importantly, neither ATF4 induction

(Figure 3A,B,D,E) nor fluorizoline-induced apoptosis (Figure 3C,F) were affected by the downregulation of PERK in HeLa and HAP1 cells.

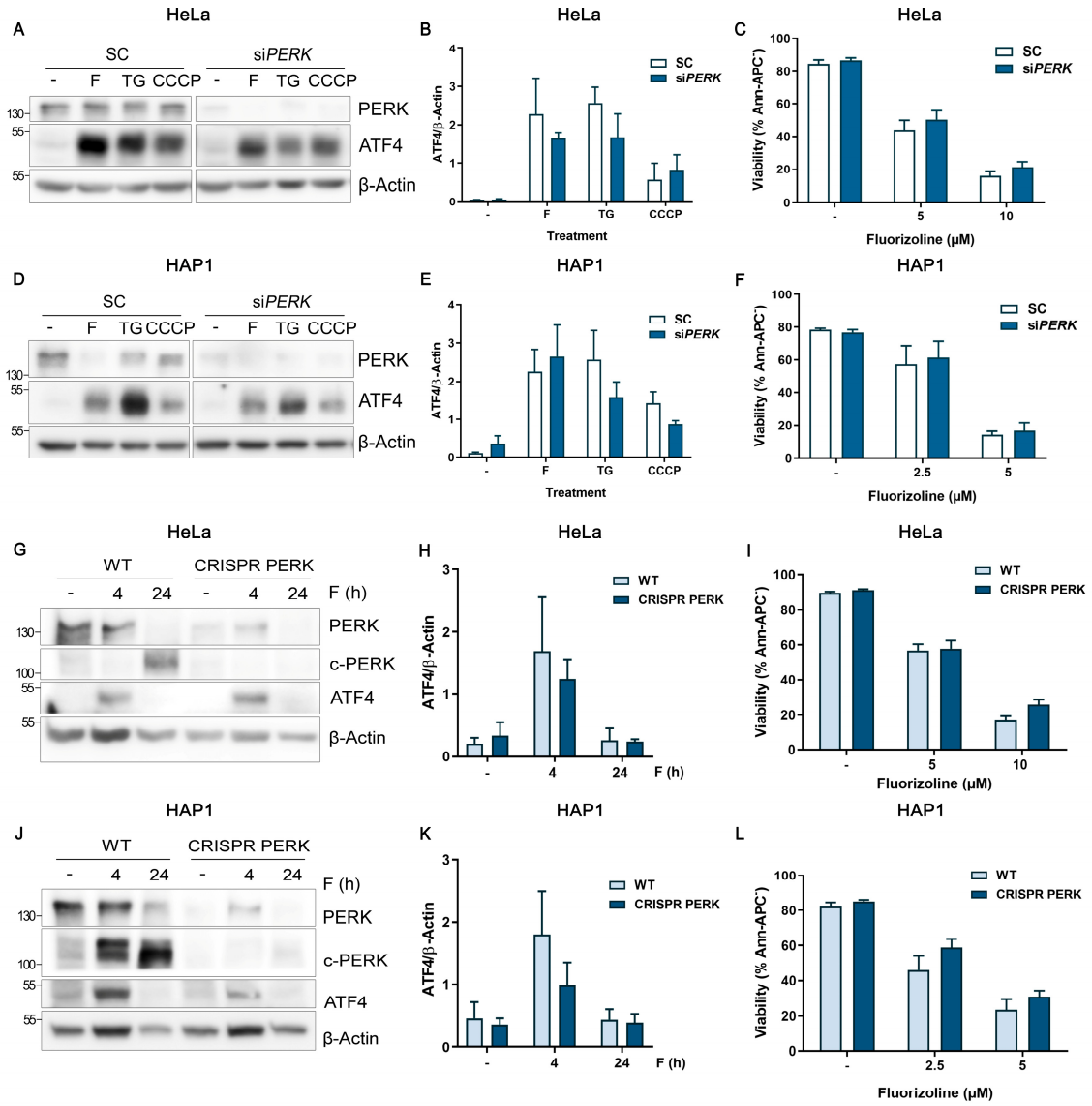

Figure 3. Fluorizoline induces the activation of ISR and apoptosis independently of PERK. (**A**–**C**) HeLa and (**D**–**F**) HAP1 cells were transfected with scramble (SC) or PERK siRNA (siPERK) for 48 h. Then, cells were either untreated (-) or treated with (**A**) 10 μM fluorizoline (F), 10 μM thapsigargin (TG), or 10 μM CCCP; or with (**D**) 5 μM fluorizoline, 5 μM thapsigargin, or 5 μM CCCP for 4 h. (**G**–**I**) HeLa and (**J**–**L**) HAP1 parental cells (WT) and cells lacking PERK (CRISPR PERK) were either untreated (-) or treated with (**G**–**I**) 10 μM or (**J**–**L**) 5 μM fluorizoline, respectively, for the indicated times. Other doses of fluorizoline are indicated in the figure. (**A**,**G**) Protein extracts from HeLa cells either untreated (-) or treated with 10 μM F, TG, and CCCP, and (**D**,**J**) protein extracts from HAP1 cells either untreated (-) or treated with 5 μM of F, TG, and CCCP were analyzed with Western blot for 4 h of treatment or for the indicated times. β-Actin was used as a loading control. Cleaved PERK: c-PERK. These are representative images of at least three independent experiments. (**B**,**E**,**H**,**K**) Bars represent the quantification of ATF4 relative to β-Actin band intensity. Data show the mean ± SEM ($n = 3$) of the relative band intensity. (**C**,**F**,**I**,**L**) Cell viability was measured by flow cytometry after 24 h of treatment, and it is expressed as the mean ± SEM ($n \geq 3$) of the percentage of non-apoptotic cells (Ann-APC).

Next, we generated pools of HeLa and HAP1 cells downregulated for PERK expression using CRISPR/Cas9 technology (CRISPR PERK) (see Section 4.3). Western blot analysis showed a clear PERK downregulation, although residual PERK protein levels remained, due to the heterogeneity of the cells (Figure 3G,J). WT and CRISPR PERK cells were analyzed for 4 and 24 h after fluorizoline treatment. Treatment with fluorizoline resulted in a significant reduction in overall PERK protein levels. Meanwhile, an increase in a lower band (c-PERK), compatible with that decrease in total PERK, was observed. The downregulation of both bands in CRISPR PERK cells demonstrated that these bands represent specific forms of PERK (Figure 3G,J). This finding was totally reverted upon effector caspases inhibition, indicating that PERK cleavage is produced after effector caspases activation.

According to PERK chemical inhibition, stable downregulation of PERK could not prevent fluorizoline-induced apoptosis in HeLa and HAP1 cells (Figure 3I,L). Indeed, PERK downregulation did not inhibit ATF4 induction by fluorizoline (Figure 3G,H,J,K).

Our results indicate that fluorizoline can still induce the activation of the ISR and apoptosis in the absence of PERK. Altogether, these data indicate that PERK and ER stress are not directly involved in the mechanism of apoptosis induction by fluorizoline.

2.3. Analysis of the eIF2α Kinases in Fluorizoline-Induced Apoptosis

Since chemical inhibition and molecular downregulation of PERK did not prevent fluorizoline-induced ISR activation, we next analyzed the other three eIF2α kinases, to identify which kinase mediates the activation of the ISR after fluorizoline treatment.

HRI, PKR, and GCN2 were efficiently downregulated in HeLa and HAP1 cells (Figure 4A,B). Afterwards, apoptosis and ISR activation were assessed after fluorizoline treatment. Thapsigargin and CCCP were used as ER and mitochondrial stress control treatments. Regarding ISR activation, HRI-downregulated cells showed reduced ATF4 induction upon mitochondrial stress control treatment CCCP, which validated the HRI downregulation (Figure 4A,B). Despite HRI, PKR, and GCN2 downregulation, the ATF4 induction after fluorizoline treatment remained unaffected in both cell lines (Figure 4A,B). Moreover, individual downregulation of the eIF2α kinases did not prevent HeLa and HAP1 cells from undergoing apoptosis upon fluorizoline treatment (Figure 4C,D).

As shown, downregulation of each of the four eIF2α kinases did not show any significant effect on fluorizoline-induced ISR activation, suggesting compensatory mechanisms between the eIF2α kinases upon fluorizoline-induced stress. Indeed, it has been reported that these kinases eventually can cooperate and compensate for the loss of the other eIF2α kinases [25,26]. To test this, we decided to downregulate all four eIF2α kinases simultaneously.

HeLa and HAP1 cells were efficiently downregulated for each eIF2α kinase (EIF2AK) simultaneously, using specific siRNAs (Figure 5A–D). Moreover, we could validate this approach using the stress inducers thapsigargin and CCCP, as EIF2AK downregulation inhibited ATF4 induction with control treatments (Figure 5A,B,E,F). Interestingly, simultaneous downregulation of the EIF2AKs was able to significantly inhibit the ATF4 induction with 4 h of fluorizoline treatment (Figure 5A,B,E,F), indicating that interfering with the compensatory mechanism among the four eIF2α kinases abrogates the activation of the ISR.

Next, we investigated the relevance of the eIF2α kinases in the apoptotic execution triggered by fluorizoline. Interestingly, the HeLa and HAP1 cells simultaneously downregulated for the four eIF2α kinases showed significant resistance to fluorizoline-induced apoptosis at 12 h, although these differences decreased at 24 h (Figure 6A,B). Of note, fluorizoline-induced apoptosis did not increase significantly from 12 to 24 h in the control group, whereas in the EIF2AKs downregulated cells, apoptotic cell death significantly increased at the latest time-point of 24 h (Figure 6A,B). This result indicates that the ISR inhibition through EIF2AKs downregulation delayed the apoptosis execution in HeLa and HAP1 cells.

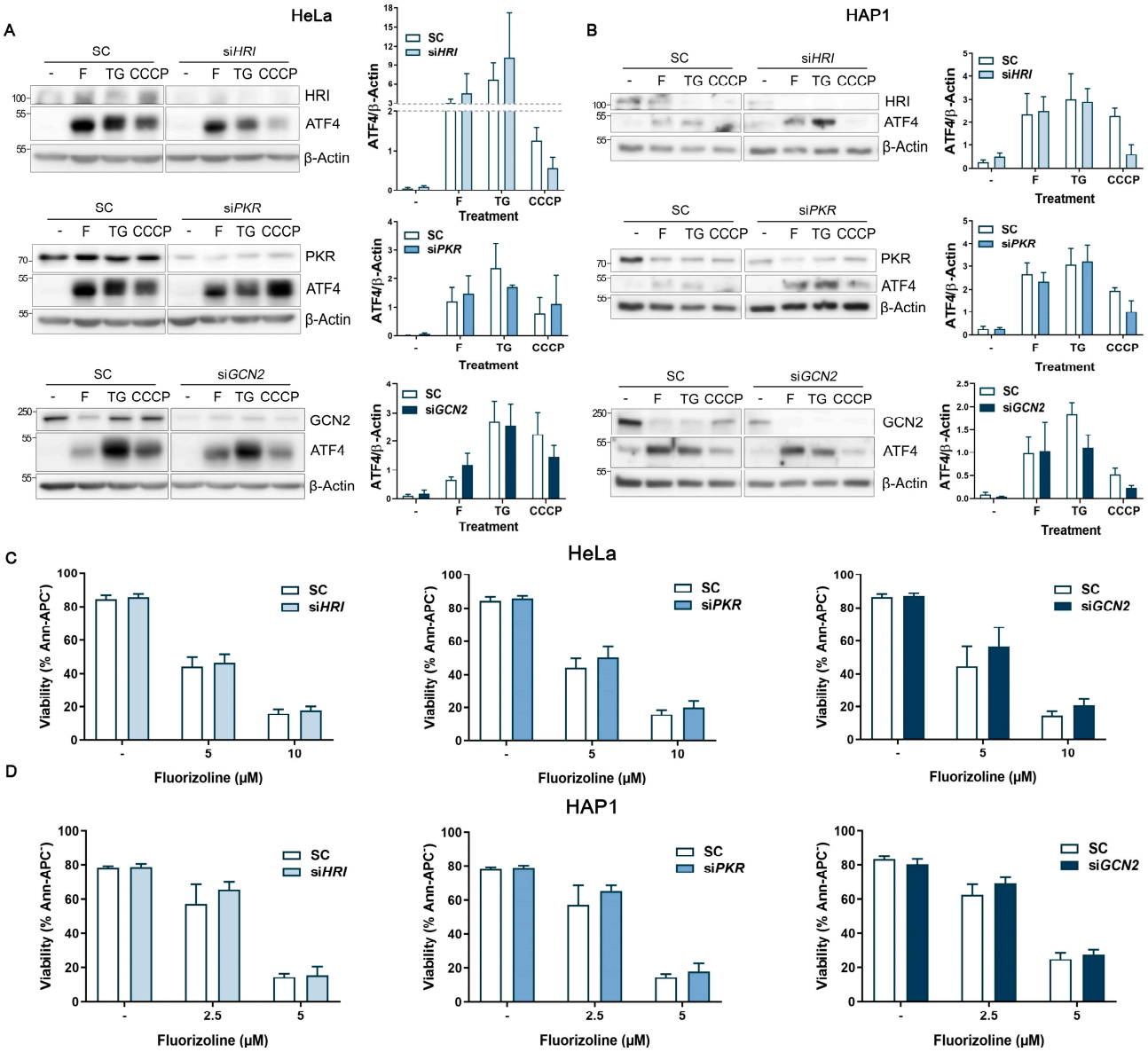

Figure 4. Individual downregulation of HRI, PKR, or GCN2 does not affect the ISR activation and apoptosis induction triggered by fluorizoline treatment. (**A**,**C**) HeLa and (**B**,**D**) HAP1 cells were transfected with scramble (SC) or individually with HRI siRNA (siHRI), PKR siRNA (siPKR), or GCN2 siRNA (siGCN2) for 48 h. Then, cells were either untreated (-) or treated with (**A**) 10 μM fluorizoline (F), 10 μM thapsigargin (TG), or 10 μM CCCP; or with (**B**) 5 μM of fluorizoline, 5 μM thapsigargin or 5 μM CCCP for 4 h. (**A**,**B**) Protein extracts from HeLa and HAP1 cells either untreated (-) or treated (F, TG, CCCP) for 4 h were analyzed with western blot. β-Actin was used as a loading control. These are representative images of at least three independent experiments. Bars represent the quantification of ATF4 relative to β-Actin band intensity. Data show the mean ± SEM ($n = 3$) of the relative band intensity. (**C**,**D**) Cell viability was measured by flow cytometry after 24 h with the indicated doses of fluorizoline, and this is expressed as the mean ± SEM ($n \geq 3$) of the percentage of non-apoptotic cells (Ann-APC$^-$).

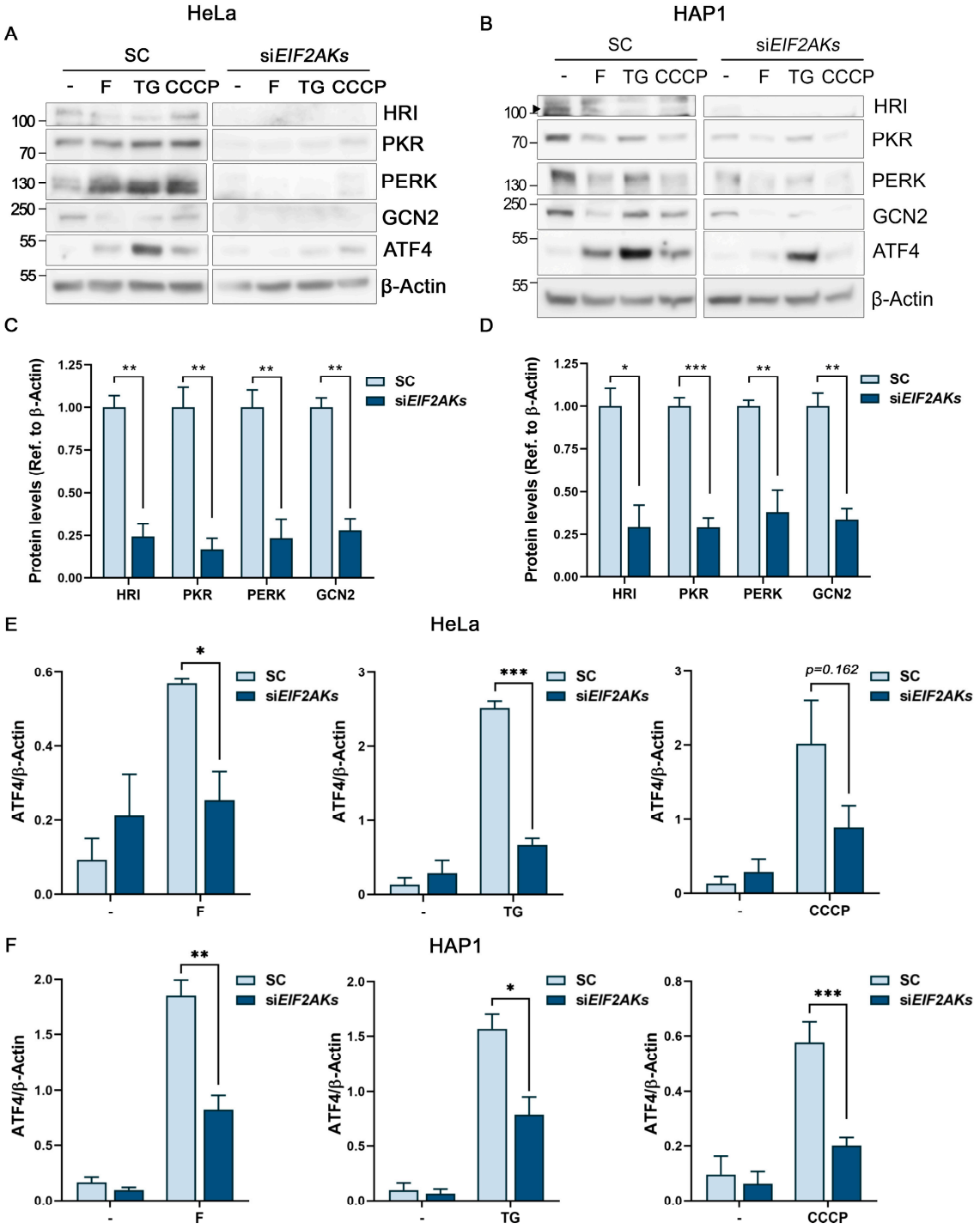

Figure 5. Simultaneous eIF2α kinase downregulation significantly inhibits the ISR activation by fluorizoline. (**A**,**C**,**E**) HeLa and (**B**,**D**,**F**) HAP1 cells were transfected with scramble (SC) or simultaneously with HRI, PKR, PERK, and GCN2 siRNAs (siEIF2AKs) for 48 h. Then, cells were either untreated (-) or treated with (**A**) 10 μM fluorizoline (F), 10 μM thapsigargin (TG), or 10 μM of CCCP; or with (**B**) 5 μM fluorizoline, 5 μM thapsigargin, or 5 μM CCCP for 4 h. (**A**,**B**) Protein extracts from cells were analyzed with Western blot. β-Actin was used as a loading control. These are representative images of at least three independent experiments. Bars represent the quantification of (**C**,**D**) basal levels of HRI, PKR, PERK, and GCN2, and (**E**,**F**) ATF4 inductions relative to β-Actin band intensity. Data show the mean ± SEM ($n \geq 3$) of the relative band intensity. * $p < 0.05$, ** $p < 0.01$, *** $p < 0.001$.

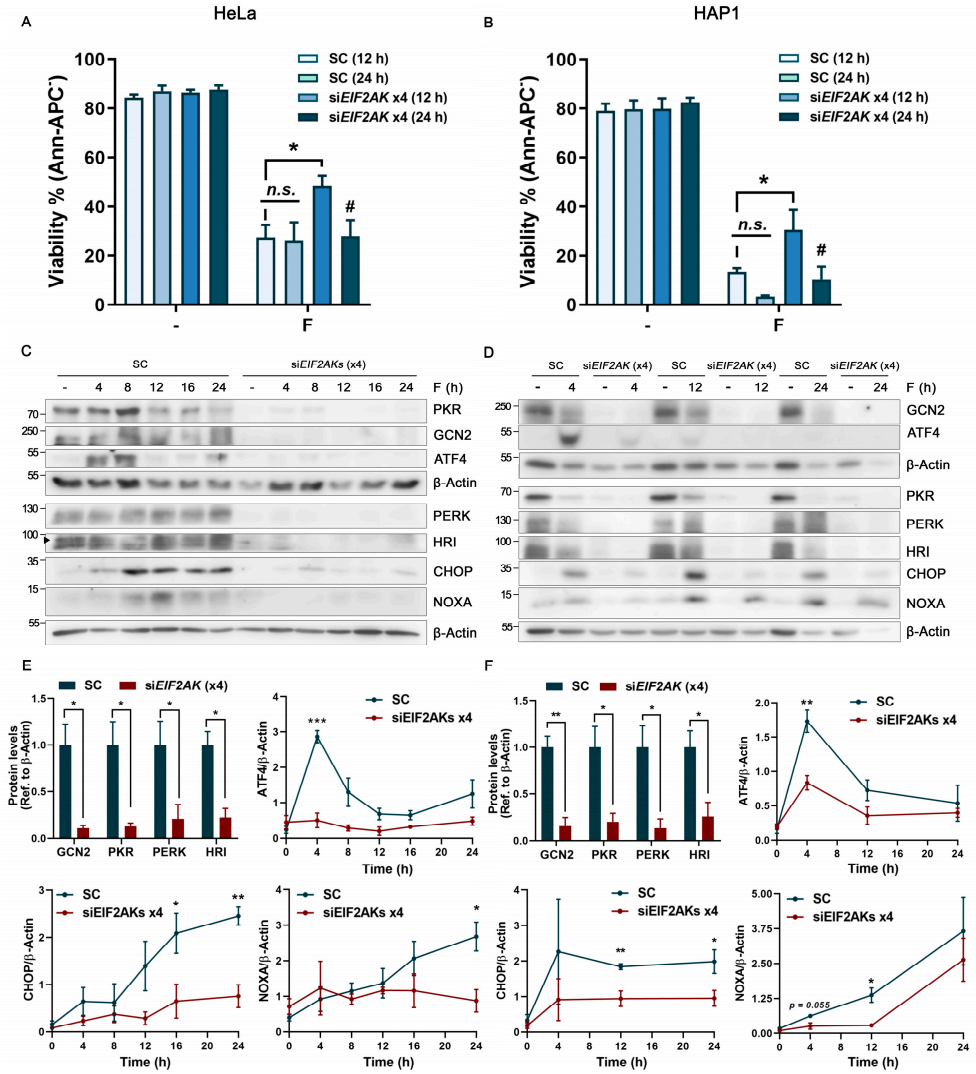

Figure 6. Simultaneous eIF2α kinase downregulation significantly delayed NOXA induction and increased cell resistance to apoptosis after fluorizoline treatment. (**A**,**C**,**E**) HeLa and (**B**,**D**,**F**) HAP1 cells were transfected with scramble (SC) or simultaneously with HRI, PKR, PERK, and GCN2 siRNAs (siEIF2AKs ×4) for 48 h. Then, HeLa and HAP1 cells were either untreated (-) or treated with 10 and 5 μM of fluorizoline (F), respectively, for the indicated times. (**A**,**B**) Cell viability was measured using flow cytometry after 12 and 24 h of treatment, and this is expressed as the mean ± SEM ($n \geq 3$) of the percentage of non-apoptotic cells (Ann-APC$^-$). (**C**,**D**) Protein extracts from HeLa and HAP1 cells were analyzed with Western blot for the indicated times. β-Actin was used as a loading control. These are representative images of at least three independent experiments. (**E**,**F**) Graphs represent the quantification of basal levels of HRI, PKR, PERK, and GCN2, and ATF4, CHOP, and NOXA inductions relative to β-Actin band intensity for all timings analyzed. Data show the mean ± SEM ($n \geq 3$) of the relative band intensity. * $p < 0.05$, ** $p < 0.01$, *** $p < 0.001$, not statistically significant: *n.s.*, SC versus siEIF2AKs ×4 transfected cells; # $p < 0.05$ 12 h versus 24 h of fluorizoline treatment.

As stated above, we recently reported that the induction of the pro-apoptotic protein NOXA after fluorizoline treatment was mainly mediated by ATF4 in HeLa and HAP1 cells [9]. Therefore, we analyzed ATF4 and its downstream factors CHOP and NOXA after fluorizoline treatment (Figure 6C,D). In concordance with the viability profile, EIF2AKs-downregulated cells showed a significant inhibition of the ATF4 induction peak at 4 h after fluorizoline treatment. Similarly, a significant inhibition of CHOP induction over time was observed. NOXA protein levels remained significantly inhibited until the 12 h time point in both cell lines analyzed. In particular, in HeLa cells, NOXA inductions were completely

inhibited throughout the entire time course, whereas in HAP1 cells, NOXA induction was restored at 24 h of fluorizoline treatment (Figure 6C–F).

All these data indicate that the inhibition of the ISR at the EIF2AK level significantly reduces ATF4 induction, being less efficient in inducing CHOP, NOXA, and apoptosis.

This result further demonstrated that ATF4 induction by fluorizoline can be carried out by any of the eIF2α kinases through the activation of the ISR. Furthermore, it supports the hypothesis that more than one of the eIF2α kinases, which have overlapping functions, could play a role in the mechanism of action of fluorizoline, perhaps due to cooperation among them or through compensatory mechanisms.

2.4. Fluorizoline Treatment Activates the eIF2α Kinase HRI to Induce the ISR

To overcome potential compensatory mechanisms among the eIF2α kinases, we designed an approach to analyze the role of each kinase in the fluorizoline-induced ISR, without the overlapping effects of the other kinases. As it was essential to achieve high downregulation efficiencies, HeLa cells were selected for this approach. To this end, we simultaneously downregulated three of the four eIF2α kinases, allowing one of them to be physiologically expressed. Then, cells were treated with fluorizoline or with thapsigargin for 4 h. High downregulation efficiency was obtained in each interference combination (Figure 7A,B). This experiment was validated using thapsigargin as a PERK-dependent control treatment, which showed that cells exclusively expressing PERK could induce ATF4 to the same extent as the control cells (Figure 7C,D). Interestingly, we found that after fluorizoline treatment where HRI was the unique non-downregulated eIF2α kinase, ATF4 protein levels were induced to the same extent as the control cells (Figure 7C,D). These results demonstrated that HRI is the main kinase that senses fluorizoline-induced stress to trigger the activation of the ISR.

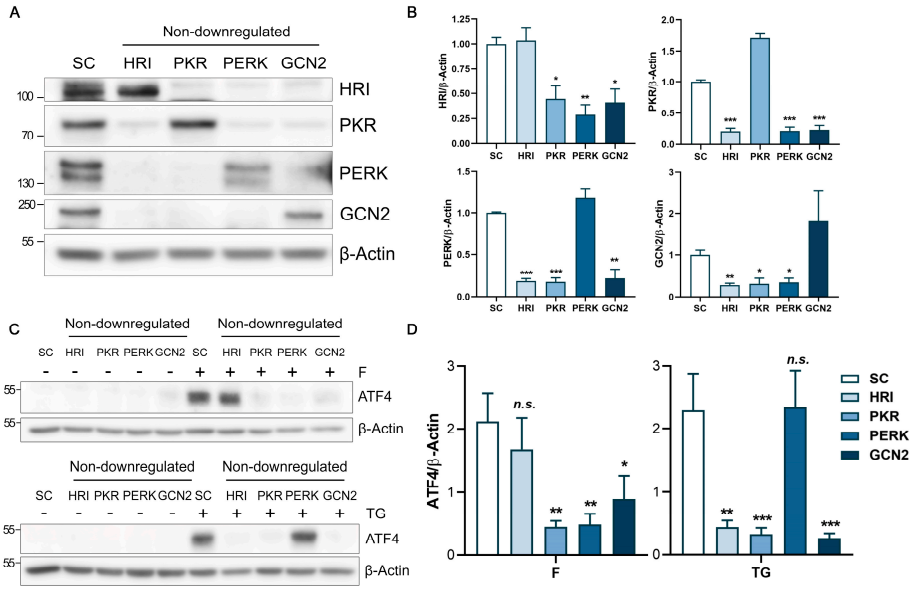

Figure 7. Fluorizoline primarily induces the activation of the ISR through HRI. (**A**–**D**) HeLa cells were transfected with scramble (SC) or simultaneously with a triple combination of the EIF2AKs siRNAs for 48 h, allowing the endogenous expression of one of them. Each combination is defined by the kinase that was not downregulated: HRI, PKR, PERK, or GCN2. Then, cells were untreated (-) or treated with (**C**) 10 μM fluorizoline (F) and 10 μM thapsigargin (TG) for 4 h. Protein levels were analyzed with western blot. β-Actin was used as a loading control. These are representative images of three independent experiments. Bars represent the quantification of (**B**) HRI, PKR, PERK, or GCN2 and (**D**) treatment-induced ATF4 relative to β-Actin band intensity. Data show the mean ± SEM ($n = 3$) of the relative band intensity. Statistically significant reductions: * $p < 0.05$, ** $p < 0.01$, *** $p < 0.001$, not statistically significant: *n.s.*

3. Discussion

In this article, we investigated the involvement of the eIF2α kinases in the activation of the ISR, and their role in the mechanism of apoptosis induction by fluorizoline. Our findings demonstrate that fluorizoline-induced apoptosis is attenuated or delayed when the ISR activation is compromised at the eIF2α kinase level. Importantly, we demonstrated that fluorizoline mainly triggers the activation of the ISR through the eIF2α kinase HRI.

Previous results have already pointed out that fluorizoline-induced ER stress could be the cause of the activation of the ISR. We could identify the activation of IRE1α through the splicing of XBP1 in HEK293T and U2OS cells [8]. Moreover, other studies also related the activation of the ISR after fluorizoline treatment to ER stress [10]. In this work, we confirmed the presence of ER stress, by identifying PERK activation in response to fluorizoline treatment in HeLa and HAP1 cells. Although all these data indicated that the activation of the ISR may be due to ER stress, PERK chemical inhibition and molecular downregulation had no effect in the activation of the ISR and apoptosis execution. Therefore, ER stress is not the initial source of the stress induced by fluorizoline and responsible for triggering the ISR activation and the apoptotic outcome. However, we cannot discard PERK involvement at a later stage. The mechanism by which fluorizoline binding to PHBs induces ER stress remains to be elucidated. PHBs are not located in the ER, but there is growing and consistent evidence describing mitochondria and ER associations, mitochondrial-associated membranes (MAMs), as key regulators of calcium homeostasis, proteostasis, mitochondrial bioenergetics, apoptosis, and autophagy [28]. Furthermore, the presence of PHB at MAMs fractions has been observed [29]. In this regard, we reported Ca^{2+} mobilization after treating U2OS cells with fluorizoline [8], which was also observed in A549 cells by other researchers [10]. Interestingly, PHBs have been reported to interact with the voltage-dependent anion channel (VDAC) in the outer mitochondrial membrane (OMM). VDAC is involved in Ca^{2+} signaling from the ER to the mitochondria at MAMs, through its interaction with the mitochondrial calcium uniporter (MCU) in IMM and with IP_3 receptor at the ER membrane [28]. Thus, fluorizoline may impair ER-Ca^{2+} homeostasis. Furthermore, a direct localization of PERK in MAMs has been found. Indeed, PERK-depleted cells showed a decrease in ER-mitochondria contact sites and an increased apoptosis resistance against agents that induce ER stress through ROS production [30]. These data, together with previous results describing ROS production after fluorizoline treatment [2,8] might explain the activation of PERK (Figure 8).

In this study, we found that individual downregulation of the eIF2α kinases failed to identify the involvement of any of the four kinases in ATF4 induction by fluorizoline, suggesting compensatory mechanisms between them. This result is consistent with previous data describing ATF4 as a key regulator of the mitochondrial stress response, whereby individual eIF2α kinases downregulation did not abolish ATF4 induction [31]. In addition, the general activation of all four eIF2α kinases upon stress has been reported [21]. For instance, compensatory functions between PERK and GCN2 kinases have also been described in mouse models and HeLa cells [26,32,33].

We demonstrated that the ISR activation by the eIF2α kinases participates in the apoptotic induction upon fluorizoline treatment in HeLa and HAP1 cells, as the inhibition of the pathway by ISRIB could decrease fluorizoline-induced apoptosis. Interestingly, we demonstrated that the activation of the ISR was driven by one of the eIF2α kinases, as the simultaneous downregulation of all four kinases significantly inhibited the ATF4 induction by fluorizoline. Furthermore, this interference significantly increased the cell resistance to fluorizoline-induced apoptosis in HeLa and HAP1 cells at 12 h, which was reduced at the longer time point of 24 h. Accordingly, NOXA inductions were inhibited, especially up to the 12 h time point. However, NOXA induction was restored at the latest time point in HAP1 cells, which may indicate the activation of an ISR-independent mechanism of NOXA induction. These data suggest that fluorizoline induces an acute overactivation of the ISR, to induce apoptosis. Moreover, our findings indicate that when the ISR activation is compromised, either by ISRIB or by EIF2AK downregulation, the apoptotic outcome is

delayed. Finally, as the fluorizoline-induced stress is sustained over time, the attenuated ISR activation could be sufficient to eventually induce the apoptotic outcome.

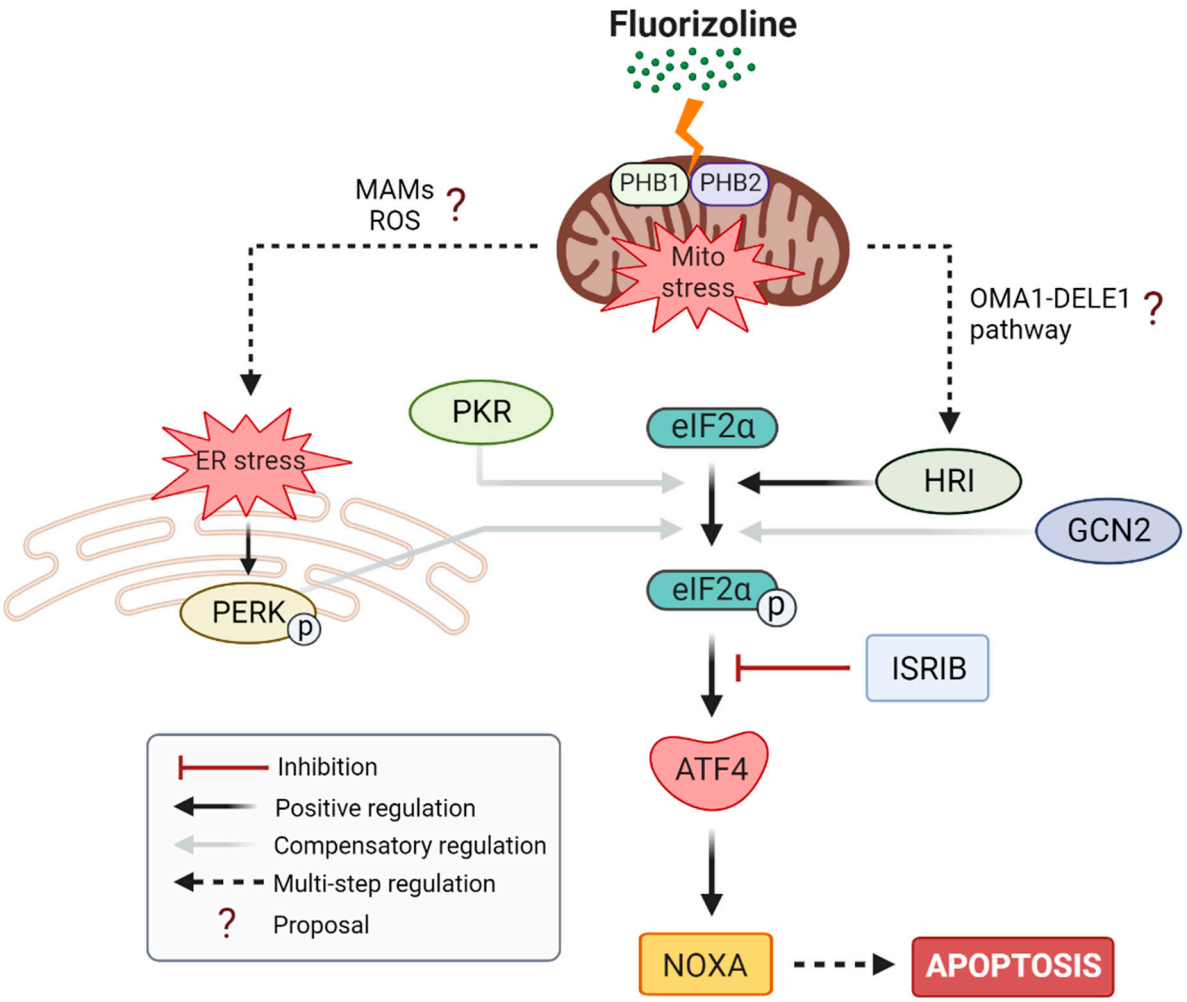

Figure 8. Schematic representation of the proposed fluorizoline mechanism of action. Fluorizoline molecules bind to PHB1 and PHB2 in the inner membrane of mitochondria, disrupting their normal functions and leading to mitochondrial stress. Upon this stress, the ISR pathway is mainly activated through the eIF2α kinase HRI, perhaps through the OMA1-DELE1-HRI pathway. Compensatory mechanisms within all four eIF2α kinases were found. Alternatively, fluorizoline treatment resulted in ER stress and PERK activation, perhaps due to the close relation of mitochondria and ER in MAMs or as a consequence of fluorizoline-induced ROS. Finally, the activation of this pathway converged in ATF4-induced NOXA protein upregulation and apoptosis execution.

To overcome these compensatory mechanisms of each eIF2α kinase, we performed an approach that allowed us to analyze the eIF2α kinase involvement, while avoiding their overlapping activities upon fluorizoline treatment. Strikingly, by using this approach, we could identify HRI as the kinase responsible for the activation of the ISR upon fluorizoline treatment, likely due to the mitochondrial stress induced by fluorizoline (Figure 8). The eIF2α kinase analysis here described upon fluorizoline treatment is consistent with other previous data indicating different compensatory mechanisms for sensing mitochondrial stress within the cell [34]. These data may rule out the notion of a unique pathway relating mitochondrial stress to the activation of the ISR. Instead, it seems that distinct molecular mechanisms are able to sense this stress, depending on the cellular context.

Recently, a molecular pathway linking mitochondrial stress to the activation of HRI has been described. This pathway is coordinated by the IMM protease OMA1, which

proteolyzes the intermembrane space (IMS) small protein DELE1 to activate HRI [35,36]. Therefore, this pathway is compatible with the HRI involvement in the ISR activation triggered by fluorizoline described here. Moreover, several studies have also related mitochondrial dysfunction, such as electron transport system (ETS) inhibition or mitochondrial ROS to GCN2 activation [34,37]. Therefore, it is plausible that the initial stress induced by the fluorizoline binding to PHBs at the mitochondria triggers a molecular pathway leading to the activation of cytosolic eIF2α kinases, and thus GCN2 could compensate for the loss of HRI. Interestingly, it has been pointed out that ATF4 can still be induced in HRI or DELE1 downregulated cells with a time delay [35], further suggesting the notion of these compensatory activities among the eIF2α kinases.

Mitochondrial PHB complexes are closely related to mitochondrial quality control processes such as OXPHOS assembly, ROS formation, mitochondrial DNA organization, and mitophagy [4,38]. Furthermore, we and others have found an activation of the ISR upon PHB depletion in human cancer cells and in *C. elegans* [8,9,39]. According to these PHB functions, targeting PHBs with fluorizoline treatment led to mitochondrial fragmentation, cristae disorganization, and mitochondrial ROS production; a clear mitochondrially stressed phenotype compatible with the PHB-downregulated cells [1,40]. Moreover, mitochondrial PHBs complexes serve as scaffolds for the reciprocal stabilization of some proteins, including SLP2 and, interestingly, OMA1 [41]. As a result of this interaction between PHBs and OMA1, it has been reported that downregulation of PHBs can lead to the stabilization of the OMA1 active form [42,43]. Accordingly, a recent study related the activation of the ISR to mitochondrial stress through the activation of OMA1 triggered by the disruption of the interaction between PHBs and SLP2 [44]. All these data further reinforce that fluorizoline could be inducing HRI activation through the OMA1-DELE1-HRI pathway.

Here, we describe that the inhibition of the ISR in HeLa and HAP1 cells increased cell resistance to fluorizoline-induced apoptosis. Furthermore, we previously described that, in HEK293T and U2OS cells, inhibition of the ISR caused an increased sensitization to fluorizoline-induced apoptosis [8]. These data support the notion that the different basal stress states that are present in human cancer cells from different origins may lead to distinct responses to treatments that induce ISR activation. Therefore, either reducing or increasing ISR activation can impair cancer cell survival upon a stressful stimulus. For instance, in cancer treatment, some approaches have focused on overloading the stress that a cell can handle [45–47]. Conversely, upregulation of the ISR has been related to the development of drug resistance in cancer [22,48]. Hence, opposite approaches have been developed to inhibit some components of the ISR, to overcome such resistance, such as eIF2α kinases inhibitors [49–52], and eIF2B activators, such as ISRIB and 2BAct [53,54]. Therefore, further efforts should be made to better understand the regulation of the ISR in cancer, in order to adequately modulate the ISR, as a promising targeting pathway for cancer treatment [55].

In conclusion, in this article, we characterized the fluorizoline-induced stress response and apoptosis in HeLa and HAP1 cells. Interestingly, the apoptosis induced by fluorizoline was found to be the result of a potent activation of the ISR mediated by HRI, likely due to mitochondrial stress. These results improve our understanding of the cell response to treatment with the PHB-binding compound fluorizoline, which in turn could be valuable in developing future therapeutic applications targeting PHBs in cancer treatment.

4. Materials and Methods

4.1. Cell Lines

A HeLa cell line, derived from cervical cancer cells, was supplied by the European Collection of Authenticated Cell Cultures (ECACC). HAP1 cells, a near-haploid human cell line that was derived from the male chronic myelogenous leukemia (CML) cell line KBM-7 were by supplied Horizon Discovery. HeLa cells were cultured in Dulbecco's Modified Eagle Medium (DMEM) and HAP1 cells were cultured in Iscove's Modified Dulbecco's Medium (IMDM). DMEM and IMDM were supplemented with 10% fetal bovine serum

(FBS) and heat-inactivated FBS (FBSi), respectively, and 100 ng/mL gentamycin. DMEM was also supplemented with 2 mM L-glutamine (all from Biological Industries, Israel). Cells were cultured at 37 °C in a humidified atmosphere containing 5% carbon dioxide.

4.2. Reagents

The synthesis of fluorizoline was performed as previously described (Pérez-Perarnau et al., 2014b). DMSO, ISRIB, thapsigargin, and CCCP were supplied by Sigma-Aldrich (Merck, Saint Louis, MI, USA).

4.3. CRISPR/Cas9

To generate a pool of HeLa and HAP1 cells lacking a specific protein, we used the system previously described in [56]. Different short guide RNAs (sgRNA) were designed to target PERK (5′-AAACAGACCGTGAAAGCATGGAAAC-3′). The sgRNA sequences were cloned into the pSpCas9(BB)-2A-puro vector (supplied by Adgene, Watertown, MA, USA), which encodes an RNA Polymerase III promotor for the transcription of the guide, the Cas9 endonuclease and a gene providing resistance to puromycin. HeLa cells were transfected overnight with Lipofectamine® LTX Reagent (Thermo Fisher Scientific, Waltham MA, USA) and HAP1 cells with Turbofectin from Origene (Rockville, MD, USA). An empty vector without sgRNA was used as a negative control. Puromycin was added for 24 h at 2 and 1 µg/mL for HeLa and HAP1 cells, respectively, to select PERK-depleted cells. The selected cells were tested for gene deletion using a mismatch cleavage assay and checked for protein knock-down with an immunoblot. Only those cell cultures showing clear PERK downregulation were used for experiments.

4.4. Cell Viability

Cell viability was assessed by measuring phosphatidylserine exposure with annexin V APC staining and analyzed with flow cytometry using FACSCantoTM and FACSDivaTM software 6.1.3 (Becton Dickinson, NJ, USA). Cells were incubated with annexin binding buffer and annexin V-APC for 15 min in the dark before analysis. Cell viability was expressed as the percentage of the annexin V-APC-negative population, which corresponds to the non-apoptotic cells.

4.5. Small Interfering RNA Transfection

HeLa cells were transfected with siRNA of *EIF2AK1* (HRI, S25800), *EIF2AK2* (PKR, S11185), *EIF2AK3* (PERK, S18102), *EIF2AK4* (GCN2, S532694), and their negative control (4404021) using Lipofectamine® RNAiMax Reagent (all purchased from Thermo Fisher Scientific, Waltham, MA, USA). DMEM and IMDM were replaced with OptiMEM (Gibco, ThermoFisher), and complexes were added into cells dropwise and incubated for 4–6 h and then replaced again with their respective fresh media. The efficiency of the downregulation was assessed through Western blot.

4.6. Western Blot

Whole-cell protein extracts were obtained by lysing cells with Laemmli sample buffer. Protein concentration was measured with a Micro BCA Protein Assay Reagent kit (Pierce, Rockford, IL, USA). Protein extracts (20–40 µg) were subjected to reducing conditions, loaded onto a polyacrylamide gel, and then transferred to Immobilon-P membranes from Millipore (Billerica, MA, USA). One hour after blocking with 5% (*w*/*v*) non-fatty milk in Tris-buffered saline solution with Tween® 20, membranes were incubated with the following specific primary antibodies: β-Actin (AC-15, Sigma-Aldrich), ATF4 (D4B8, Cell Signaling), CHOP (2895, Cell Signaling), NOXA (114C307, Abcam), HRI (MBS2538144, MyBioSource), PKR (3072S, Cell Signaling), PERK (C33E10, Cell Signaling), p-PERK (Thr982) (PA5-102853, Invitrogen), and GCN2 (3302S, Cell Signaling). Antibody binding was detected using a secondary antibody conjugated to horseradish peroxidase, and an enhanced

chemiluminescence detection system (Amersham, Little Chalfont, UK). Raw quantification of band intensities was performed using Multi Gauge software V3.0 (Fujifilm Corporation).

4.7. Statistical Analysis

The results are shown as the mean ± standard error of the mean (SEM) of values obtained in three or more independent experiments. Statistical analysis was performed using Student's *t*-test (two-tailed) for simple comparisons or ANOVA–Tukey for multiple comparisons, using GraphPad Prism 6.0c Software Inc. Differences were considered significant at p values below 0.05 (* $p < 0.05$; ** $p < 0.01$; *** $p < 0.001$).

Author Contributions: Conceptualization, I.S.-V., J.G. and D.I.-S.; Funding acquisition, J.G.; Investigation, I.S.-V., S.N.-V., J.S.-E., A.M.C., J.H. and G.P.; Methodology, I.S.-V.; Project administration, J.G.; Resources, P.N.R., O.G. and R.L.; Supervision, J.G. and D.I.-S.; Writing—original draft, I.S.-V., G.P., J.G. and D.I.-S.; Writing—review and editing, S.N.-V., J.S.-E., A.M.C., J.H., G.P., J.G. and D.I.-S. All authors have read and agreed to the published version of the manuscript.

Funding: This work was supported by a grant from the Ministerio de Ciencia e Innovación and ERDF (PID2020-120537RB-I00 to J.G. and PID2019-107991RB-I00 to R.L.). I.S.-V. is recipient of a research fellowship from Ministerio de Ciencia e Innovación.

Institutional Review Board Statement: Not applicable.

Informed Consent Statement: Not applicable.

Data Availability Statement: Not applicable.

Acknowledgments: We want to thank the Scientific and Technological Centers of the Bellvitge Campus at the University of Barcelona. Schematic representation was created using BioRender.com.

Conflicts of Interest: The authors declare no conflict of interest.

References

1. Pérez-Perarnau, A.; Preciado, S.; Palmeri, C.M.; Moncunill-Massaguer, C.; Iglesias-Serret, D.; González-Gironès, D.M.; Miguel, M.; Karasawa, S.; Sakamoto, S.; Cosialls, A.M.; et al. A Trifluorinated Thiazoline Scaffold Leading to Pro-Apoptotic Agents Targeting Prohibitins. *Angew. Chem. Int. Ed.* **2014**, *53*, 10150–10154. [CrossRef]
2. Moncunill-Massaguer, C.; Saura-Esteller, J.; Pérez-Perarnau, A.; Palmeri, C.M.; Núñez-Vázquez, S.; Cosialls, A.M.; González-Gironès, D.M.; Pomares, H.; Korwitz, A.; Preciado, S.; et al. A Novel Prohibitin-Binding Compound Induces the Mitochondrial Apoptotic Pathway through NOXA and BIM Upregulation. *Oncotarget* **2015**, *6*, 41750–41765. [CrossRef]
3. Yang, J.; Li, B.; He, Q.Y. Significance of Prohibitin Domain Family in Tumorigenesis and Its Implication in Cancer Diagnosis and Treatment. *Cell Death Dis.* **2018**, *9*, 580. [CrossRef] [PubMed]
4. Tatsuta, T.; Langer, T. Prohibitins. *Curr. Biol.* **2017**, *27*, R629–R631. [CrossRef]
5. Thuaud, F.; Ribeiro, N.; Nebigil, C.G.; Désaubry, L. Prohibitin Ligands in Cell Death and Survival: Mode of Action and Therapeutic Potential. *Chem. Biol.* **2013**, *20*, 316–331. [CrossRef] [PubMed]
6. Han, J.; Yu, C.; Souza, R.F.; Theiss, A.L. Prohibitin 1 Modulates Mitochondrial Function of Stat3. *Cell. Signal.* **2014**, *26*, 2086–2095. [CrossRef]
7. Ma, L.L.; Shen, L.; Tong, G.H.; Tang, N.; Luo, Y.; Guo, L.L.; Hu, C.T.; Huang, Y.X.; Huang, G.; Jing, F.Y.; et al. Prohibitin, Relocated to the Front Ends, Can Control the Migration Directionality of Colorectal Cancer Cells. *Oncotarget* **2017**, *8*, 76340. [CrossRef]
8. Saura-Esteller, J.; Sánchez-Vera, I.; Núñez-Vázquez, S.; Cosialls, A.M.; Gama-Pérez, P.; Bhosale, G.; Mendive-Tapia, L.; Lavilla, R.; Pons, G.; Garcia-Roves, P.M.; et al. Activation of the Integrated Stress Response and ER Stress Protect from Fluorizoline-Induced Apoptosis in HEK293T and U2OS Cell Lines. *Int. J. Mol. Sci.* **2021**, *22*, 6117. [CrossRef]
9. Núñez-Vázquez, S.; Sánchez-Vera, I.; Saura-Esteller, J.; Cosialls, A.M.; Noisier, A.F.M.; Albericio, F.; Lavilla, R.; Pons, G.; Iglesias-Serret, D.; Gil, J. NOXA Upregulation by the Prohibitin-Binding Compound Fluorizoline Is Transcriptionally Regulated by Integrated Stress Response-Induced ATF3 and ATF4. *FEBS J.* **2021**, *288*, 1271–1285. [CrossRef]
10. Jin, X.; Xie, J.; Zabolocki, M.; Wang, X.; Jiang, T.; Wang, D.; Désaubry, L.; Bardy, C.; Proud, C.G. The Prohibitin-Binding Compound Fluorizoline Affects Multiple Components of the Translational Machinery and Inhibits Protein Synthesis. *J. Biol. Chem.* **2020**, *295*, 9855–9867. [CrossRef] [PubMed]
11. Takagi, H.; Moyama, C.; Taniguchi, K.; Ando, K.; Matsuda, R.; Ando, S.; Ii, H.; Kageyama, S.; Kawauchi, A.; Chouha, N.; et al. Fluorizoline Blocks the Interaction between Prohibitin-2 and γ-Glutamylcyclotransferase and Induces P21Waf1/Cip1 Expression in MCF7 Breast Cancer Cells. *Mol. Pharm.* **2022**, *101*, 78–86. [CrossRef]
12. Yurugi, H.; Marini, F.; Weber, C.; David, K.; Zhao, Q.; Binder, H.; Désaubry, L.; Rajalingam, K. Targeting Prohibitins with Chemical Ligands Inhibits KRAS-Mediated Lung Tumours. *Oncogene* **2017**, *36*, 4778–4789. [CrossRef] [PubMed]

13. Cosialls, A.M.; Pomares, H.; Iglesias-Serret, D.; Saura-Esteller, J.; Núñez-Vázquez, S.; González-Gironès, D.M.; de La Banda, E.; Preciado, S.; Albericio, F.; Lavilla, R.; et al. The Prohibitin-Binding Compound Fluorizoline Induces Apoptosis in Chronic Lymphocytic Leukemia Cells through the Upregulation of NOXA and Synergizes with Ibrutinib, 5-Aminoimidazole-4-Carboxamide Riboside or Venetoclax. *Haematologica* **2017**, *102*, 1587–1593. [CrossRef] [PubMed]
14. Cosialls, A.M.; Sánchez-Vera, I.; Pomares, H.; Perramon-Andújar, J.; Sanchez-Esteban, S.; Palmeri, C.M.; Iglesias-Serret, D.; Saura-Esteller, J.; Núñez-Vázquez, S.; Lavilla, R.; et al. The BCL-2 Family Members NOXA and BIM Mediate Fluorizoline-Induced Apoptosis in Multiple Myeloma Cells. *Biochem. Pharm.* **2020**, *180*, 114198. [CrossRef]
15. Pomares, H.; Palmeri, C.M.; Iglesias-Serret, D.; Moncunill-Massaguer, C.; Saura-Esteller, J.; Núñez-Vázquez, S.; Gamundi, E.; Arnan, M.; Preciado, S.; Albericio, F.; et al. Targeting Prohibitins Induces Apoptosis in Acute Myeloid Leukemia Cells. *Oncotarget* **2016**, *7*, 64987–65000. [CrossRef]
16. Wierz, M.; Pierson, S.; Chouha, N.; Désaubry, L.; François, J.H.; Berchem, G.; Paggetti, J.; Moussay, E. The Prohibitin-Binding Compound Fluorizoline Induces Apoptosis in Chronic Lymphocytic Leukemia Cells Ex Vivo but Fails to Prevent Leukemia Development in a Murine Model. *Haematologica* **2018**, *103*, e154–e157. [CrossRef] [PubMed]
17. Merkwirth, C.; Dargazanli, S.; Tatsuta, T.; Geimer, S.; Löwer, B.; Wunderlich, F.T.; Von Kleist-Retzow, J.C.; Waisman, A.; Westermann, B.; Langer, T. Prohibitins Control Cell Proliferation and Apoptosis by Regulating OPA1-Dependent Cristae Morphogenesis in Mitochondria. *Genes Dev.* **2008**, *22*, 476–488. [CrossRef]
18. Anderson, N.S.; Haynes, C.M. Folding the Mitochondrial UPR into the Integrated Stress Response. *Trends Cell Biol.* **2020**, *30*, 428–439. [CrossRef]
19. Costa-Mattioli, M.; Walter, P. The Integrated Stress Response: From Mechanism to Disease. *Science* **2020**, *368*, eaat5314. [CrossRef]
20. Ron, D. Translational Control in the Endoplasmic Reticulum Stress Response. *J. Clin. Investig.* **2002**, *110*, 1383–1388. [CrossRef]
21. Pakos-Zebrucka, K.; Koryga, I.; Mnich, K.; Ljujic, M.; Samali, A.; Gorman, A.M. The Integrated Stress Response. *EMBO Rep.* **2016**, *17*, 1374–1395. [CrossRef]
22. Kalkavan, H.; Chen, M.J.; Crawford, J.C.; Quarato, G.; Fitzgerald, P.; Tait, S.W.G.; Goding, C.R.; Green, D.R. Sublethal Cytochrome c Release Generates Drug-Tolerant Persister Cells. *Cell* **2022**, *185*, 3356–3374.e22. [CrossRef]
23. Iurlaro, R.; Muñoz-Pinedo, C. Cell Death Induced by Endoplasmic Reticulum Stress. *FEBS J.* **2016**, *283*, 2640–2652. [CrossRef]
24. Zyryanova, A.F.; Weis, F.; Faille, A.; Abo Alard, A.; Crespillo-Casado, A.; Sekine, Y.; Harding, H.P.; Allen, F.; Parts, L.; Fromont, C.; et al. Binding of ISRIB Reveals a Regulatory Site in the Nucleotide Exchange Factor EIF2B. *Science* **2018**, *359*, 1533–1536. [CrossRef] [PubMed]
25. Hamanaka, R.B.; Bennett, B.S.; Cullinan, S.B.; Diehl, J.A. PERK and GCN2 Contribute to EIF2α Phosphorylation and Cell Cycle Arrest after Activation of the Unfolded Protein Response Pathway. *Mol. Biol. Cell* **2005**, *16*, 5493–5501. [CrossRef]
26. Lehman, S.L.; Ryeom, S.; Koumenis, C. Signaling through Alternative Integrated Stress Response Pathways Compensates for GCN2 Loss in a Mouse Model of Soft Tissue Sarcoma. *Sci. Rep.* **2015**, *5*, srep11781. [CrossRef] [PubMed]
27. Smith, A.L.; Andrews, K.L.; Beckmann, H.; Bellon, S.F.; Beltran, P.J.; Booker, S.; Chen, H.; Chung, Y.A.; D'Angelo, N.D.; Dao, J.; et al. Discovery of 1*H*-Pyrazol-3(2*H*)-Ones as Potent and Selective Inhibitors of Protein Kinase R-like Endoplasmic Reticulum Kinase (PERK). *J. Med. Chem.* **2015**, *58*, 1426–1441. [CrossRef]
28. Prudent, J.; McBride, H.M. The Mitochondria-Endoplasmic Reticulum Contact Sites: A Signalling Platform for Cell Death. *Curr. Opin. Cell Biol.* **2017**, *47*, 52–63. [CrossRef]
29. Su, Y.; Huang, X.; Huang, Z.; Huang, T.; Xu, Y.; Yi, C. STAT3 Localizes in Mitochondria-Associated ER Membranes Instead of in Mitochondria. *Front. Cell Dev. Biol.* **2020**, *8*, 274. [CrossRef]
30. Verfaillie, T.; Rubio, N.; Garg, A.D.; Bultynck, G.; Rizzuto, R.; Decuypere, J.P.; Piette, J.; Linehan, C.; Gupta, S.; Samali, A.; et al. PERK Is Required at the ER-Mitochondrial Contact Sites to Convey Apoptosis after ROS-Based ER Stress. *Cell Death Differ.* **2012**, *19*, 1880–1891. [CrossRef] [PubMed]
31. Quirós, P.M.; Prado, M.A.; Zamboni, N.; D'Amico, D.; Williams, R.W.; Finley, D.; Gygi, S.P.; Auwerx, J. Multi-Omics Analysis Identifies ATF4 as a Key Regulator of the Mitochondrial Stress Response in Mammals. *J. Cell Biol.* **2017**, *216*, 2027–2045. [CrossRef] [PubMed]
32. Devi, L.; Ohno, M. Deletion of the EIF2α Kinase GCN2 Fails to Rescue the Memory Decline Associated with Alzheimer's Disease. *PLoS ONE* **2013**, *8*, e77335. [CrossRef] [PubMed]
33. Roobol, A.; Roobol, J.; Bastide, A.; Knight, J.R.P.; Willis, A.E.; Smales, C.M. P58IPK Is an Inhibitor of the EIF2α Kinase GCN2 and Its Localization and Expression Underpin Protein Synthesis and ER Processing Capacity. *Biochem. J.* **2015**, *465*, 213–225. [CrossRef]
34. Mick, E.; Titov, D.V.; Skinner, O.S.; Sharma, R.; Jourdain, A.A.; Mootha, V.K. Distinct Mitochondrial Defects Trigger the Integrated Stress Response Depending on the Metabolic State of the Cell. *eLife* **2020**, *9*, e49178. [CrossRef] [PubMed]
35. Fessler, E.; Eckl, E.M.; Schmitt, S.; Mancilla, I.A.; Meyer-Bender, M.F.; Hanf, M.; Philippou-Massier, J.; Krebs, S.; Zischka, H.; Jae, L.T. A Pathway Coordinated by DELE1 Relays Mitochondrial Stress to the Cytosol. *Nature* **2020**, *579*, 433. [CrossRef] [PubMed]
36. Guo, X.; Aviles, G.; Liu, Y.; Tian, R.; Unger, B.A.; Lin, Y.H.T.; Wiita, A.P.; Xu, K.; Correia, M.A.; Kampmann, M. Mitochondrial Stress Is Relayed to the Cytosol by an OMA1–DELE1–HRI Pathway. *Nature* **2020**, *579*, 427–432. [CrossRef]
37. Baker, B.M.; Nargund, A.M.; Sun, T.; Haynes, C.M. Protective Coupling of Mitochondrial Function and Protein Synthesis via the EIF2α Kinase GCN-2. *PLoS Genet.* **2012**, *8*, e1002760. [CrossRef] [PubMed]

38. Artal-Sanz, M.; Tavernarakis, N. Prohibitin Couples Diapause Signalling to Mitochondrial Metabolism during Ageing in *C. elegans*. *Nature* **2009**, *461*, 793–797. [CrossRef]
39. Hernando-Rodríguez, B.; Artal-Sanz, M. Mitochondrial Quality Control Mechanisms and the PHB (Prohibitin) Complex. *Cells* **2018**, *7*, 238. [CrossRef]
40. Merkwirth, C.; Langer, T. Prohibitin Function within Mitochondria: Essential Roles for Cell Proliferation and Cristae Morphogenesis. *Biochim. Biophys. Acta BBA—Mol. Cell Res.* **2009**, *1793*, 27–32. [CrossRef]
41. Signorile, A.; Sgaramella, G.; Bellomo, F.; Rasmo, D. De Prohibitins: A Critical Role in Mitochondrial Functions and Implication in Diseases. *Cells* **2019**, *8*, 71. [CrossRef] [PubMed]
42. Sato, S.I.; Murata, A.; Orihara, T.; Shirakawa, T.; Suenaga, K.; Kigoshi, H.; Uesugi, M. Marine Natural Product Aurilide Activates the OPA1-Mediated Apoptosis by Binding to Prohibitin. *Chem. Biol.* **2011**, *18*, 131–139. [CrossRef] [PubMed]
43. Zhang, K.; Li, H.; Song, Z. Membrane Depolarization Activates the Mitochondrial Protease OMA1 by Stimulating Self-Cleavage. *EMBO Rep.* **2014**, *15*, 576. [CrossRef] [PubMed]
44. Cheng, M.; Yu, H.; Kong, Q.; Wang, B.; Shen, L.; Dong, D.; Sun, L. The Mitochondrial PHB2/OMA1/DELE1 Pathway Cooperates with Endoplasmic Reticulum Stress to Facilitate the Response to Chemotherapeutics in Ovarian Cancer. *Int. J. Mol. Sci.* **2022**, *23*, 1320. [CrossRef] [PubMed]
45. Hartleben, G.; Schorpp, K.; Kwon, Y.; Betz, B.; Tsokanos, F.; Dantes, Z.; Schäfer, A.; Rothenaigner, I.; Kuhn, J.M.M.; Morigny, P.; et al. Combination Therapies Induce Cancer Cell Death through the Integrated Stress Response and Disturbed Pyrimidine Metabolism. *EMBO Mol. Med.* **2021**, *13*, e12461. [CrossRef] [PubMed]
46. Narita, T.; Ri, M.; Masaki, A.; Mori, F.; Ito, A.; Kusumoto, S.; Ishida, T.; Komatsu, H.; Iida, S. Lower Expression of Activating Transcription Factors 3 and 4 Correlates with Shorter Progression-Free Survival in Multiple Myeloma Patients Receiving Bortezomib plus Dexamethasone Therapy. *Blood Cancer J.* **2015**, *5*, e373. [CrossRef]
47. Zhang, Y.; Zhou, L.; Safran, H.; Borsuk, R.; Lulla, R.; Tapinos, N.; Seyhan, A.A.; El-Deiry, W.S. EZH2i EPZ-6438 and HDACi Vorinostat Synergize with ONC201/TIC10 to Activate Integrated Stress Response, DR5, Reduce H3K27 Methylation, ClpX and Promote Apoptosis of Multiple Tumor Types Including DIPG. *Neoplasia* **2021**, *23*, 792–810. [CrossRef]
48. Dey, S.; Sayers, C.M.; Verginadis, I.I.; Lehman, S.L.; Cheng, Y.; Cerniglia, G.J.; Tuttle, S.W.; Feldman, M.D.; Paul, P.J.; Fuchs, S.Y.; et al. ATF4-Dependent Induction of Heme Oxygenase 1 Prevents Anoikis and Promotes Metastasis. *J. Clin. Investig.* **2015**, *125*, 2592. [CrossRef]
49. Jammi, N.V.; Whitby, L.R.; Beal, P.A. Small Molecule Inhibitors of the RNA-Dependent Protein Kinase. *Biochem. Biophys. Res. Commun.* **2003**, *308*, 50–57. [CrossRef]
50. Kato, Y.; Kunimasa, K.; Sugimoto, Y.; Tomida, A. BCR-ABL Tyrosine Kinase Inhibition Induces Metabolic Vulnerability by Preventing the Integrated Stress Response in K562 cells. *Biochem. Biophys. Res. Commun.* **2018**, *504*, 721–726. [CrossRef]
51. Mohamed, E.; Sierra, R.A.; Trillo-Tinoco, J.; Cao, Y.; Innamarato, P.; Payne, K.K.; de Mingo Pulido, A.; Mandula, J.; Zhang, S.; Thevenot, P.; et al. The Unfolded Protein Response Mediator PERK Governs Myeloid Cell-Driven Immunosuppression in Tumors through Inhibition of STING Signaling. *Immunity* **2020**, *52*, 668–682.e7. [CrossRef] [PubMed]
52. Rosen, M.D.; Woods, C.R.; Goldberg, S.D.; Hack, M.D.; Bounds, A.D.; Yang, Y.; Wagaman, P.C.; Phuong, V.K.; Ameriks, A.P.; Barrett, T.D.; et al. Discovery of the First Known Small-Molecule Inhibitors of Heme-Regulated Eukaryotic Initiation Factor 2α (HRI) Kinase. *Bioorg. Med. Chem. Lett.* **2009**, *19*, 6548–6551. [CrossRef] [PubMed]
53. Sidrauski, C.; McGeachy, A.M.; Ingolia, N.T.; Walter, P. The Small Molecule ISRIB Reverses the Effects of EIF2α Phosphorylation on Translation and Stress Granule Assembly. *eLife* **2015**, *4*, e05033. [CrossRef] [PubMed]
54. Wong, Y.L.; Lebon, L.; Basso, A.M.; Kohlhaas, K.L.; Nikkel, A.L.; Robb, H.M.; Donnelly-Roberts, D.L.; Prakash, J.; Swensen, A.M.; Rubinstein, N.D.; et al. EIF2B Activator Prevents Neurological Defects Caused by a Chronic Integrated Stress Response. *eLife* **2019**, *8*, e42940. [CrossRef] [PubMed]
55. Tian, X.; Zhang, S.; Zhou, L.; Seyhan, A.A.; Hernandez Borrero, L.; Zhang, Y.; El-Deiry, W.S. Targeting the Integrated Stress Response in Cancer Therapy. *Front. Pharm.* **2021**, *12*, 2621. [CrossRef] [PubMed]
56. Ran, F.A.; Hsu, P.D.; Wright, J.; Agarwala, V.; Scott, D.A.; Zhang, F. Genome Engineering Using the CRISPR-Cas9 System. *Nat. Protoc.* **2013**, *8*, 2281–2308. [CrossRef]

Disclaimer/Publisher's Note: The statements, opinions and data contained in all publications are solely those of the individual author(s) and contributor(s) and not of MDPI and/or the editor(s). MDPI and/or the editor(s) disclaim responsibility for any injury to people or property resulting from any ideas, methods, instructions or products referred to in the content.

Detailed Index